ISSN 2301-1092 • ISSN (en línea) 2301-1106

MEMORIA

INVESTIGACIONES EN INGENIERÍA

Nº 30

FACULTAD DE INGENIERÍA

UM
UNIVERSIDAD DE MONTEVIDEO

MEMORIA

Investigaciones en Ingeniería

ISSN 2301-1092 • ISSN (en línea) 2301-1106

Núm. 30 (2026)

Sumario

Págs.

Editorial – Ingeniería aplicada, sostenible y emergente.

La Revista Memoria Investigaciones en Ingeniería presenta su Número 30 reafirmando su compromiso con la difusión de conocimiento científico y tecnológico que responda a los desafíos contemporáneos de la ingeniería. Esta edición reúne contribuciones originales y de revisión que reflejan el carácter multidisciplinario de nuestra publicación, integrando enfoques experimentales, numéricos, de diseño, manufactura avanzada, optimización, sostenibilidad y validación en campo, con aplicaciones concretas en el ámbito industrial, energético, ambiental, estructural y de telecomunicaciones.

Los artículos de este número evidencian una agenda investigativa dinámica y alineada con problemáticas actuales. En el campo de materiales e ingeniería mecánica, se incluye una caracterización mecánica comparativa de compuestos de PVC reciclado y madera–plástico, aportando evidencia relevante para el uso de materiales más sostenibles y de alto desempeño. La edición también incorpora avances en manufactura aditiva, destacando la fabricación por escritura directa con tinta de óxido cúprico, demostrando el potencial de estas técnicas para el desarrollo de componentes funcionales con propiedades específicas.

Desde la perspectiva de los procesos de unión y manufactura, se presenta un estudio termomecánico mediante elementos finitos sobre los efectos de parámetros de soldadura SMAW en uniones disímiles, así como un trabajo que aborda la ubicación óptima del cordón de soldadura para mejorar la integridad estructural en la fabricación de tubos perfilados. Estas contribuciones fortalecen el vínculo entre modelado, optimización de proceso y confiabilidad estructural.

La línea de ingeniería civil y gestión del riesgo se ve representada con una evaluación del desempeño sísmico de un edificio multifamiliar en Surco, Lima, considerando diferentes niveles de amenaza y aplicando el estándar ATC-40, lo cual constituye una referencia importante para el diseño, diagnóstico y reforzamiento estructural en contextos urbanos expuestos a sismicidad.

En el ámbito de ingeniería industrial y mejora de procesos, se propone un análisis orientado a determinar la correlación entre balanceo de línea y productividad, aportando herramientas metodológicas para la toma de decisiones basada en evidencia en entornos de manufactura. De forma complementaria, este número incluye aportes en optimización paramétrica de materiales y procesos, como el estudio del acero EN-31 mediante mecanizado por descarga eléctrica (EDM), evidenciando la importancia de seleccionar adecuadamente variables operativas para maximizar desempeño y eficiencia.

El enfoque ambiental y energético se desarrolla mediante una revisión sobre captura y separación de carbono, tema central en las estrategias de mitigación del cambio climático. Asimismo, se presentan investigaciones en sensado y nanomateriales, con una evaluación comparativa de nanoestructuras de CeO_2 modificadas con sílice para detección de amoníaco a temperatura ambiente, contribuyendo al desarrollo de tecnologías de monitoreo más precisas y accesibles.

La edición también amplía su alcance con trabajos orientados a robótica y monitoreo ambiental, incluyendo el diseño a nivel de sistema y validación en exteriores de un robot móvil solar para monitorización autónoma, resaltando el valor de la integración entre diseño, energía renovable y pruebas reales. En el área de comportamiento dinámico de materiales, se analiza el efecto del recargue superficial (hardfacing) sobre características de amortiguamiento de acero ASTM A516 Grado 70, aportando conocimiento para aplicaciones sometidas a vibración y fatiga.

En la intersección entre modelado físico y técnicas de datos, se presenta un enfoque híbrido termodinámico–aprendizaje automático para la predicción del punto de inflamación de mezclas orgánicas binarias, reforzando la tendencia actual hacia soluciones basadas en modelos interpretables y herramientas predictivas robustas. Además, el número incluye contribuciones en telecomunicaciones, con el modelado de cobertura 4G mediante Matlab y su validación con mediciones reales, trabajo que destaca por su aplicabilidad en planificación y diagnóstico de redes. En el área de electrónica y sistemas embebidos, se propone una arquitectura de bajo costo para el control temporal repetible en estaciones de prueba, orientada a confiabilidad y replicabilidad experimental. Finalmente, se incorpora una simulación de convección libre

https://doi.org/10.36561/ING.30.1
ISSN 2301-1092 • ISSN (en línea) 2301-1106

laminar totalmente desarrollada entre placas paralelas verticales, contribuyendo al entendimiento de fenómenos fundamentales de transferencia de calor y flujo.

Este número es también el resultado del esfuerzo conjunto de autores, evaluadores y equipo editorial. A todos ellos extendemos nuestro reconocimiento por su rigor, dedicación y compromiso con la calidad científica. La revista mantiene su objetivo de ofrecer un espacio confiable para la comunicación académica, promoviendo buenas prácticas de investigación y una evaluación por pares que fortalece la solidez de los resultados publicados.

Invitamos a la comunidad académica, profesional e industrial a explorar esta edición, utilizar sus hallazgos como base para nuevas investigaciones y continuar aportando con trabajos que impulsen la innovación, la sostenibilidad y el desarrollo tecnológico en nuestros países y en el entorno global.

Dr. Ing. Rafael Sotelo
Editor en Jefe
Facultad de Ingeniería
Universidad de Montevideo

https://doi.org/10.36561/ING.30.1
ISSN 2301-1092 • ISSN (en línea) 2301-1106

Comparative Mechanical Characterization of Recycled PVC and Wood–Plastic Composites

Caracterización mecánica comparativa de compuestos de PVC reciclado y madera-plástico

Caracterização Mecânica Comparativa de PVC Reciclado e Compósitos de Madeira-Plástico

Eylia Abbas Jafri [1], Shaheryar A. Khan [2] (*), Ifrah Asif [3], Sohail Hasnain [4], M. Areeb Rizwan Siddiqui [5],

Recibido: 28/07/2025 Aceptado: 24/11/2025

Summary. - Recycled polymers offer opportunities for circular material use, yet their mechanical performance is often limited by feedstock variability. This study provides a controlled comparison of neat, recycled PVC and WPC (PVC + 20 wt.% wood flour) processed under identical extrusion and compression-molding conditions. Tensile, flexural and hardness tests were conducted according to ASTM standards, and results are reported as mean ± standard deviation (n = 5). The WPC exhibited modest but measurable increases in tensile strength (~12%), flexural strength (~8%), and Shore D hardness (~8.5%), while tensile and flexural moduli remained statistically comparable between the two materials. Flexural modulus exceeded tensile modulus for both materials, consistent with surface-dominated stress distributions in bending. The findings demonstrate that incorporating 20 wt.% wood flour into recycled PVC can enhance selected mechanical properties without compromising stiffness, offering a performance profile consistent with material-substitution pathways in circular-economy strategies. The study also highlights the influence of recycled feedstock variability and identifies the need for future microstructural characterization to confirm the hypothesized deformation and failure mechanisms.

Keywords: wood–plastic composite, recycled PVC, tensile tests, flexural tests, hardness, ASTM standards, mechanical properties, sustainability.

(*) Corresponding author.

[1] Senior Lecturer, Department of Mechanical Engineering, PNEC-NUST (Pakistan), eylia@pnec.nust.edu.pk,
ORCID iD: https://orcid.org/0009-0009-0859-4134

[2] Associate Professor and Head of Mechanical Engineering, DHA Suffa University (Pakistan), shaheryar.atta@dsu.edu.pk,
ORCID iD: https://orcid.org/0000-0003-1600-7322

[3] Lecturer, Department of Mechanical Engineering, NEDUET (Pakistan), ifrahasif@neduet.edu.pk,
ORCID iD: https://orcid.org/0000-0001-7551-2199

[4] Lecturer, Department of Mechanical Engineering, NEDUET (Pakistan), sohail@neduet.edu.pk,
ORCID iD: https://orcid.org/0009-0005-2970-2908

[5] Student, Department of Mechanical Engineering, NEDUET (Pakistan), engr.areebriz@gmail.com,
ORCID iD: https://orcid.org/0009-0008-2635-6116

Memoria Investigaciones en Ingeniería, núm. 30 (2026). pp. 3-13
https://doi.org/10.36561/ING.30.2
ISSN 2301-1092 • ISSN (en línea) 2301-1106 – Universidad de Montevideo, Uruguay

Resumen. - *Los polímeros reciclados ofrecen oportunidades para el uso circular de materiales, pero su rendimiento mecánico suele estar limitado por la variabilidad de la materia prima. Este estudio proporciona una comparación controlada de PVC reciclado puro y WPC (PVC + 20 % en peso de harina de madera) procesados bajo condiciones idénticas de extrusión y moldeo por compresión. Se realizaron ensayos de tracción, flexión y dureza según las normas ASTM, y los resultados se presentan como media ± desviación estándar (n = 5). El WPC mostró incrementos modestos pero medibles en la resistencia a la tracción (~12 %), la resistencia a la flexión (~8 %) y la dureza Shore D (~8,5 %), mientras que los módulos de tracción y flexión se mantuvieron estadísticamente comparables entre ambos materiales. El módulo de flexión superó al módulo de tracción en ambos materiales, lo que concuerda con las distribuciones de tensión dominadas por la superficie en la flexión. Los hallazgos demuestran que la incorporación de un 20 % en peso de harina de madera al PVC reciclado puede mejorar ciertas propiedades mecánicas sin comprometer la rigidez, ofreciendo un perfil de rendimiento consistente con las vías de sustitución de materiales en las estrategias de economía circular. El estudio también destaca la influencia de la variabilidad de la materia prima reciclada e identifica la necesidad de una caracterización microestructural futura para confirmar los mecanismos de deformación y falla hipotetizados.*

Palabras clave: *compuesto de madera y plástico, PVC reciclado, ensayos de tracción, ensayos de flexión, dureza, normas ASTM, propiedades mecánicas, sostenibilidad*

Resumo *. -* *Polímeros reciclados oferecem oportunidades para o uso circular de materiais, porém seu desempenho mecânico é frequentemente limitado pela variabilidade da matéria-prima. Este estudo apresenta uma comparação controlada entre PVC reciclado puro e WPC (PVC + 20% em peso de farinha de madeira) processados sob condições idênticas de extrusão e moldagem por compressão. Ensaios de tração, flexão e dureza foram conduzidos de acordo com as normas ASTM, e os resultados são apresentados como média ± desvio padrão (n = 5). O WPC exibiu aumentos modestos, porém mensuráveis, na resistência à tração (~12%), resistência à flexão (~8%) e dureza Shore D (~8,5%), enquanto os módulos de tração e flexão permaneceram estatisticamente comparáveis entre os dois materiais. O módulo de flexão excedeu o módulo de tração para ambos os materiais, o que é consistente com a distribuição de tensões predominantemente superficiais na flexão. Os resultados demonstram que a incorporação de 20% em peso de farinha de madeira ao PVC reciclado pode aprimorar propriedades mecânicas selecionadas sem comprometer a rigidez, oferecendo um perfil de desempenho consistente com as vias de substituição de materiais em estratégias de economia circular. O estudo também destaca a influência da variabilidade da matéria-prima reciclada e identifica a necessidade de caracterização microestrutural futura para confirmar os mecanismos de deformação e falha hipotetizados.*

Palavras-chave: *compósito madeira-plástico, PVC reciclado, ensaios de tração, ensaios de flexão, dureza, normas ASTM, propriedades mecânicas, sustentabilidade*

1. Introduction. - Global plastic production exceeds 300 million tons annually, driven by versatility, durability, and low production cost [1], [2], [3]. However, the environmental burden of plastic waste, particularly its persistence, non-renewable origin, and low biodegradability, has become a critical global concern [4]. Plastic debris contaminates terrestrial and aquatic ecosystems, adversely affecting biodiversity and human health [5]. As pressure mounts to reduce environmental footprints, researchers and industries are increasingly turning to recycling and composite technologies to extend the utility of plastic waste [6].

Among commonly recycled thermoplastics, polyvinyl chloride (PVC) stands out due to its extensive use in construction, packaging, and consumer goods. PVC exhibits desirable characteristics such as flame retardancy, corrosion resistance, and dimensional stability. However, its recycling is complicated by the presence of additives like plasticizers, stabilizers, and residual contaminants that can hinder reprocessing and reduce mechanical integrity [7], [8]. Still, the abundance of post-consumer PVC waste, particularly from pipes, cables, and siding, offers a valuable feedstock for secondary applications if properly reformulated [9].

One strategy to potentially enhance the properties or sustainability profile of recycled PVC involves hybridizing it with bio-based fillers, such as wood flour, to create wood–plastic composites (WPCs). WPCs are typically fabricated by melt-compounding wood flour with thermoplastics, followed by extrusion or molding [10]. This approach leverages the natural stiffness and renewability of lignocellulosic biomass while potentially reducing dependence on virgin polymers. Moreover, WPCs support circular economy principles by valorizing both plastic and biomass waste streams [11], [12].

WPCs are increasingly used in decking, fencing, automotive interiors, and furniture [13]. However, their mechanical performance is influenced by many factors, including wood particle size and morphology, polymer–filler ratio, processing conditions (like mixing methods and temperature profiles), and interfacial adhesion [10], [14], [15]. Generally, adding wood flour increases composite stiffness and hardness but can impact ductility and strength depending on the specific formulation and interface quality. This performance balance is often attributed to the inherent incompatibility between hydrophobic polymer matrices (like PVC) and hydrophilic cellulosic fillers, potentially leading to stress concentrations and microvoids at the interface [16], [17], [18]. The quality of the recycled matrix itself can also influence final composite properties [8], [19].

Furthermore, studies have demonstrated that chemical treatment of wood flour or the use of coupling agents can substantially affect composite performance [20]. For instance, coupling agents and compatibilizers can improve adhesion between filler and matrix, potentially resulting in higher strength and moisture resistance [21], [22], [23]. Similarly, the thermal stability of WPCs depends on the nature and content of the lignocellulosic material used [24]. Such parameters must be carefully optimized to tailor composites for specific end-use applications.

Despite numerous studies on WPCs (often based on polyolefins) and recycled PVC separately [10], [19], [25], few have offered a systematic mechanical comparison between recycled PVC and its corresponding WPC variant under identical processing and testing protocols. This study aims to address this gap by presenting a controlled, comparative investigation of key mechanical properties – specifically tensile, flexural, and Shore D hardness of recycled PVC and its 20% wood-filled composite under consistent, ambient conditions.

2. Material and Methods. -

2.1. Materials. - Recycled PVC pellets (derived from post-consumer pipes and sheets) and kiln-dried hardwood sawdust (wood flour, particle size <250 μm) were procured. The wood flour was further dried at 80°C for 30 minutes just before use to remove any leftover moisture content. No additional additives or compatibilizers were introduced during reprocessing and therefore, the material reflects a heterogeneous mixture of commercial uPVC formulations typical of construction waste with the composition unknown.

2.2. Composite Fabrications. - Formulations containing 0% (PVC) and 20% wood flour by weight were dry-blended (WPC). Compounding was performed using a co-rotating twin-screw extruder (L/D = 40:1) with a screw speed of 100 rpm and barrel zone temperatures set between 150–170°C, consistent with typical processing windows for PVC-based WPCs [10]. Torque and melt pressure were monitored continuously to ensure process stability [29]. The extrudate was pelletized (diameter ≈ 3 mm) and subsequently compression molded at 160°C under 5 MPa pressure for 10 minutes into sheets approximately 3 mm thick and released hot. The molded sheets were allowed to cool at room temperature for 2 hours. Post-cure annealing was conducted at 80°C for 2 hours to minimize residual stresses [30]. Test specimens were precisely laser cut according to ASTM D638 Type I (tensile), ASTM D790 (flexural), and ASTM D2240 (hardness) dimensions [26], [27], [28].

2.3. Mechanical Testing. - All mechanical tests were conducted in a controlled ambient laboratory environment maintained at 23 ± 2°C and 50 ± 5% Relative Humidity (RH), logged using an environmental chamber compliant with ISO 291 [31]. For each material condition (PVC and WPC), five tensile specimens (n = 5), five flexural specimens (n = 5), and five hardness specimens (n = 5) were tested in accordance with the respective ASTM standards. All specimens were produced from the same compression-molded sheet batch to ensure consistency. Prior to testing, specimens were inspected for machining defects, edge cracks, or dimensional deviations greater than ±1%. One PVC tensile specimen and one WPC flexural specimen were rejected due to visible edge chipping from laser cutting and were replaced to maintain the required sample size.

Tensile tests: Performed according to ASTM D638 (Type I specimens) using a universal testing machine at a crosshead speed of 5 mm/min [26]. Strain was measured accurately using an extensometer [7]. Young's modulus, tensile strength, and elongation at break were determined.

Flexural tests: Conducted according to ASTM D790 using a three-point bending setup [27]. The support span-to-depth ratio was maintained at 16:1, and the crosshead speed was 2 mm/min [18]. Flexural modulus and flexural strength were calculated.

Hardness tests: Measured according to ASTM D2240 using a Shore D durometer mounted on an operating stand to ensure perpendicularity and consistent load application [28]. Measurements were taken after a dwell time of 15 seconds. Five indentations were made on each specimen at different locations [3]. None of the samples were rejected.

Data acquisition systems sampled load and displacement/strain data at 1 kHz, filtered using a 10 Hz low pass filter, to generate high-resolution stress–strain curves. Load cells and extensometers were calibrated per ASTM E4 and standard procedures prior to testing series.

3. Results. -

3.1. Tensile Behavior. - The uniaxial tensile stress vs strain curve for a typical PVC and WPC sample is illustrated in Figure 1. The stress vs strain curve of PVC is illustrated with a solid blue line whereas that of WPC is illustrated with a dashed red line. The tensile stress–strain curves in Figure 1 show a typical elastic region followed by a short yield-like transition without a well-defined plateau for both materials, indicating semi-ductile behavior. Neither PVC nor WPC exhibited classical strain hardening; instead, both curves rose monotonically until reaching their respective maximum stresses, followed by an abrupt load drop, characteristic of polymer composites with limited plastic deformation. The PVC curve shows a smoother transition to failure, while the WPC curve displays a slightly steeper post-yield slope, consistent with modest reinforcement from wood flour.

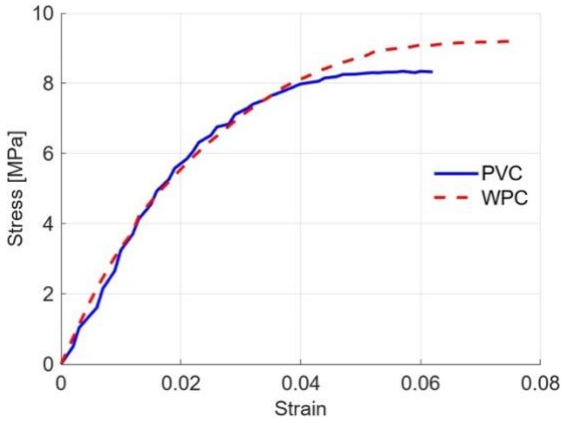

Figure I. The uniaxial tensile stress vs strain curves for neat, recycled PVC and WPC (PVC + 20 wt.% wood flour) samples.

The tensile properties are reported as mean ± standard deviation for n = 5 specimens per material. PVC exhibited an elastic modulus of 395 ± 32 MPa. Its ultimate tensile strength was measured at 8.2 ± 0.85 MPa, with an elongation at break of 6.2 ± 0.13%.

The incorporation of 20% wood flour into PVC to create the WPC resulted in notable changes. The elastic modulus remained comparable at approximately 398 ± 27 MPa. However, the tensile strength increased to 9.2 ± 1.1 MPa, representing an approximate 12% increase compared to neat PVC. The WPC sample showed a slightly increased elongation at break of 7.5 ± 0.18%.

The observed increase in tensile strength for the WPC, despite similar stiffness, is likely attributed to the reinforcing effect of the cellulose fibers within the wood flour. These fibers may contribute to load-bearing capacity, particularly after the PVC matrix yields, enhancing the composite's overall strength before fracture. The effect on ductility requires careful consideration of failure modes.

3.2. Flexural Behavior. - The three-point bending stress vs strain curves for a typical PVC and WPC sample is illustrated in Figure 2. The stress vs strain curve of PVC is illustrated with a solid blue line whereas that of WPC is illustrated with a dashed red line. The flexural stress–strain curves in Figure 2 show a linear elastic region up to approximately 2–2.5% strain for both materials, after which the curves begin to deviate due to matrix microcracking and the onset of tensile-side yielding typical of thermoplastic composites under bending. Neither material exhibited a distinct yield plateau; instead, the curves increased steadily to a peak flexural stress before showing a sharp drop associated with catastrophic failure. The WPC curve demonstrates slightly higher peak stress and marginally improved strain tolerance.

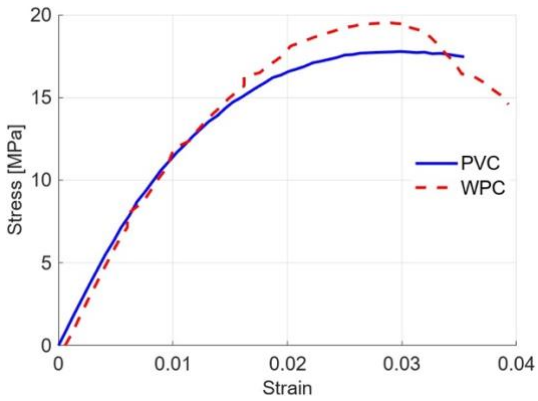

Figure II. The three-point bending stress vs strain curves for neat recycled PVC and WPC (PVC + 20 wt.% wood flour) samples

Flexural properties (n = 5 per material) are presented as mean ± standard deviation. Both PVC and WPC showed similar initial stiffness in bending, with calculated flexural moduli in the range of 1650 ± 365 MPa and 1680 ± 294 MPa, respectively. As expected, these values are substantially higher than the elastic moduli observed in tension due to the stress gradient inherent in bending.

The flexural strength of PVC was determined to be 18.1 ± 1.75 MPa. The WPC sample demonstrated a higher flexural strength, measured at 19.5 ± 1.95 MPa, approximately 8% greater than the PVC.

The strain at which failure or substantial load drop occurred in bending was approximately 0.035 ± 0.009 for PVC and slightly higher, around 0.038 ± 0.011, for WPC. This suggests the WPC could withstand slightly more bending deformation before failure compared to PVC under these test conditions.

The tensile and flexural test results indicate that while the incorporation of 20% wood flour does not alter the stiffness (Young's/Flexural Modulus) compared to PVC, it enhances both the tensile and flexural strength. This improvement is attributed to the reinforcing contribution of the wood fibers within the composite structure. The WPC also showed comparable or slightly increased strain tolerance before failure in bending.

3.3. Hardness Measurements. - The Shore D hardness values are presented in Table 1.

	Shore D Hardness									
Sample No.	**PVC**					**WPC**				
1	29	30	30	29	28	33	32	31	32	32
2	31	29	30	30	29	31	32	34	32	32
3	30	29	30	29	30	31	32	33	32	32
4	30	29	30	29	30	32	30	32	32	32
5	30	29	30	30	29	32	32	33	32	32

Table I. The Shore-D harness for neat, recycled PVC and WPC (PVC + 20 wt.% wood flour) samples.

Shore D hardness measurements showed a consistent increase with the addition of wood flour. This represents an 8.5% increase, paralleling trends sometimes observed with increased stiffness or filler content. The hardness enhancement likely results from the presence of the harder wood particles and potentially restricted polymer chain mobility near the filler surface, consistent with literature findings [3], [10].

Property	**Unit**	**PVC (mean ± SD)**	**WPC (mean ± SD)**	**n**
Young’s modulus	MPa	395 ± 32	398 ± 27	5
Tensile strength	MPa	8.2 ± 0.85	9.2 ± 1.10	5
Elongation at break	%	6.2 ± 0.13	7.5 ± 0.18	5
Flexural modulus	MPa	1650 ± 365	1680 ± 294	5
Flexural strength	MPa	18.1 ± 1.75	19.5 ± 1.95	5
Flexural strain at failure	Unitless	0.035 ± 0.009	0.038 ± 0.011	5
Shore D hardness	–	29.60 ± 0.50	32 ± 0.74	25

Table II. Summary of results.

4. Discussion. - The observed mechanical property changes upon adding 20% wood flour to recycled PVC reflect typical composite behavior. While simple models like the rule-of-mixtures might approximate modulus trends [9], the strength properties are more complexly governed by factors such as flaw distributions (e.g., micro-voids) and, critically,

the quality of interfacial adhesion between the relatively hydrophobic PVC matrix and the hydrophilic wood filler [10], [18], [21]. Poor adhesion can lead to ineffective stress transfer from the matrix to the reinforcing filler, potentially limiting the strength enhancement [20].

The flexural modulus for both materials was substantially higher than the tensile modulus, which is expected for semi-rigid polymers and wood–plastic composites. In three-point bending, the specimen experiences a strong through-thickness stress gradient: the outermost fibres carry the highest stresses while the inner core remains relatively unstressed. As a consequence, the measured stiffness is governed primarily by the behavior of the surface layers, which respond more rigidly than the bulk polymer under uniform tensile loading. Additionally, bending constrains lateral contraction more strongly than tension, reducing Poisson expansion and further increasing the apparent modulus. From a microstructural standpoint, the wood flour present in the WPC improves surface stiffness under bending because fibers located near outer surfaces engage more effectively in load transfer. In contrast, tensile testing probes the entire cross-section uniformly, including regions containing micro-voids, imperfect filler dispersion or weak polymer–filler adhesion, which collectively reduce the effective tensile modulus.

Micro-voids, potentially formed during extrusion due to moisture release from wood flour or air entrapment, can act as stress concentrators, possibly initiating cracks under tensile and bending loads [18], [29]. The increase in tensile (~12%) and flexural (~8%) strength observed here suggests some reinforcing effect from the wood fibers, but also potentially indicates non-optimal interfacial bonding, which is common in untreated WPCs [20]. The particle size and aspect ratio of the wood flour also play a significant role in determining the reinforcing efficiency [14], [15]. Although these tests were conducted in a controlled dry state, the inherent hydrophilicity of wood fillers could introduce variability or affect long-term performance under ambient humidity due to moisture sorption at the interface, potentially degrading both the filler and the interface itself [32], [33], [34].

The slightly higher strain at failure observed in bending for the WPC, compared to PVC, is not contradictory to the tensile ductility trends. This difference arises because tensile and flexural failures are governed by different mechanisms. In bending, failure initiates in the highly stressed outer surface while the neutral axis remains relatively unstressed, allowing limited redistribution of strain before catastrophic fracture. Local microcrack blunting or fiber-bridging effects in the WPC can delay surface crack propagation, permitting a slightly greater strain before failure. Under uniaxial tension, however, the entire gauge length is uniformly stressed, making the material more sensitive to internal defects such as voids, fiber pull-out sites and poor interfacial bonding. These internal imperfections promote earlier tensile fracture, even if the same material shows slightly improved surface deformation behavior in bending. Thus, the flexural strain-to-failure trend is consistent with the expected difference in dominant failure mechanisms between the two loading modes.

When interpreting the magnitude of the observed strength improvements, approximately 12% in tensile strength and 8% in flexural strength, it is important to consider their relevance within the context of typical design safety factors and target application domains. For many structural or semi-structural applications involving PVC and WPCs such as decking boards, facade components, low-load automotive interior panels, safety factors typically range from 2 to 4. Within this framework, strength increments of the order reported here may be viewed as modest in absolute terms and, in some cases, comparable to batch-to-batch variation commonly observed in recycled polymer composites. Nonetheless, these improvements remain meaningful for several reasons. First, the increases in strength occurred without compromising stiffness or hardness and without the use of coupling agents, indicating that even unmodified wood flour can contribute positively to load-bearing capacity. Second, for high-volume applications where material cost and environmental impact are key considerations, incremental gains in strength can translate to reductions in material usage, improved durability, or expanded suitability for low to medium-load components. Finally, from a sustainability perspective, demonstrating that recycled PVC can achieve enhanced performance with renewable fillers underscores the potential for performance-neutral or performance-positive material substitutions that support circular-economy principles.

It is important to emphasize that the discussion regarding micro-void formation, interfacial debonding, and potential moisture-related effects is grounded in mechanisms widely documented in the literature for PVC and WPC-based composites, rather than in direct microstructural observations from the present study. Because no microscopy or fractographic characterization was performed on the tested specimens, these interpretations should be regarded as literature-supported hypotheses rather than experimentally confirmed mechanisms. Future investigations incorporating detailed morphological characterization would be valuable for validating the proposed deformation and failure mechanisms and for establishing more definitive structure–property correlations.

This study provides comparative mechanical benchmarks that are relevant for industrial quality control and materials selection, particularly in applications such as automotive components, façade panels, and construction elements where recycled or resource-efficient materials are increasingly considered [13], [19]. Rather than making explicit environmental claims, the present work should be viewed as contributing to material substitution strategies that are broadly consistent with circular economy principles and supportive of Sustainable Development Goals (SDGs) 9 and 12, which emphasize responsible production and sustainable infrastructure development [9], [35]. Achieving enhanced performance in recycled PVC or WPC-based systems typically requires attention to interfacial engineering, such as the use of coupling agents including maleated polyolefins or silanes, as well as process optimization to reduce defects and improve fusion quality. Future research may also explore hybrid composite formulations to simultaneously improve mechanical performance and maintain or enhance the environmental benefits associated with the use of recycled and bio-based constituents [18], [20], [21], [36].

5. Conclusion. - This study presented a controlled comparative mechanical evaluation of neat recycled polyvinyl chloride (PVC) and a wood–plastic composite (WPC) containing 20 wt.% wood flour, processed via extrusion and compression molding. The results demonstrated that incorporating wood flour achieved performance enhancements consistent with a reinforcing effect:

- Stiffness: The WPC exhibited comparable stiffness (Young's modulus and Flexural modulus) to PVC.
- Strength: The WPC showed modestly enhanced tensile strength (~12% increase) and flexural strength (~8% increase).
- Hardness: A systematic and consistent increase in surface hardness was observed, with Shore D hardness improving by approximately 8.5%.
- Ductility: While tensile elongation at break was slightly higher for WPC, the composite also demonstrated a slightly higher strain at failure in bending compared to PVC.

These strength and hardness improvements are meaningful, as they confirm that PVC can accept a bio-filler without compromising mechanical integrity, highlighting a performance-positive material substitution relevant to circular economy principles.

The selection between PVC and WPC depends on specific application requirements such as, WPCs offer benefits in stiffness consistency, strength, and hardness, while utilizing wood waste for enhanced sustainability. Given the inherent heterogeneity of recycled feedstocks and the lack of coupling agents in this formulation, achieving optimal long-term performance requires further investigation into interfacial engineering and process optimization to minimize defects and moisture effects. Future research, ideally incorporating microstructural characterization (e.g., fractography), is recommended to validate the hypothesized failure mechanisms (micro-voids and interfacial debonding) and to establish definitive structure–property correlations for these sustainable composites

Data availability. - The dataset supporting the results of this study can be requested from the corresponding author.

References

[1] Bläsing M, Amelung W. Plastics in soil: Analytical methods and possible sources. Sci Total Environ. 2018;612:422–35.
[2] Borrelle SB, Ringma J, Schmidt C, et al. Predicted growth in plastic waste exceeds efforts to mitigate plastic pollution. Science. 2020;369(6510):1515–8.
[3] Ferdous W, Manalo A, Lokuge W. Recycling of landfill wastes (tyres, plastics and glass) in construction. Resour Conserv Recycl. 2021;173:105745.
[4] Muthukumar A, Veerappapillai S. Biodegradation of plastics – A brief review. J Polym Environ. 2022;36:1–11.
[5] Rodrigues MO, Abrantes N, Gonçalves F, et al. Impacts of plastic products used in daily life on the environment and human health: What is known? Environ Toxicol Pharmacol. 2019;72:103239.
[6] La Mantia FP, Morreale M. Green composites: A brief review. Compos Part A Appl Sci Manuf. 2011;42(6):579–88.
[7] Miranda Yañez LA, Ramírez C, Ortega MA. Improving the bond strength of a new PVC-based adhesive. Int J Adhes Adhes. 2023;127:103500.
[8] Sadat-Shojai M, Bakhshandeh GR. Recycling of PVC wastes. Polym Degrad Stabil. 2011;96(4):404–15.
[9] La Mantia FP, Mistretta MC. Recycling of PVC: Challenges and opportunities. Polymers (Basel). 2022;14(4):799.
[10] Klyosov AA. Wood-Plastic Composites. Hoboken (NJ): John Wiley & Sons; 2007.
[11] Evode N, Bahers JB, Amor B, et al. Plastic waste and its management strategies for environmental sustainability. Case Stud Chem Environ Eng. 2021;4:100142.
[12] Rodrigues AC, Lopes AC, Costa MR, et al. Hybrid composites of recycled thermoplastics reinforced with lignocellulosic fibers. J Polym Environ. 2019;27:1583–94.
[13] Ashori A. Wood–plastic composites as promising green-composites for automotive industries! Bioresour Technol. 2008;99(11):4661–7.
[14] Schirp A, Wolcott MP. Influence of particle size and mixing processes on the mechanical properties and dimensional stability of wood–plastic composites. Wood Fiber Sci. 2005;37(4):653–66.
[15] Teuber L, Schirp A, Hentges D. Influence of wood species and particle dimensions on the mechanical properties of wood-plastic composites (WPC) manufactured by extrusion. Pro Ligno. 2016;12(4):115–22.
[16] Clemons C. Wood–plastic composites in the United States: The interfacing of two industries. Forest Prod J. 2002;52(6):10–8.
[17] Kirchhoff C, Meier B, Reif D. Effect of fibre surface treatment on mechanical properties and moisture absorption of WPCs. Compos Sci Technol. 2012;72(9):1055–60.
[18] Tan YW, Liew CM. Mechanical behaviour of wood–plastic composites: Effect of interface and voids. Compos Interfaces. 2024;31(2):134–48.
[19] Najafi SK. Use of recycled plastics in wood plastic composites – A review. Waste Manag. 2013;33(9):1898–1905.
[20] Pickering KL, Efendy MG A, Le TM. A review of recent developments in natural fibre composites and their mechanical properties. Compos Part A Appl Sci Manuf. 2016;83:98–112.
[21] George J, Sreekala MS, Thomas S. A review on interface modification and characterization of natural fiber reinforced plastic composites. Polym Eng Sci. 2001;41(9):1471–85.
[22] Stark NM, Rowlands RE. Effects of wood fiber characteristics on mechanical properties of wood/polypropylene composites. Wood Fiber Sci. 2003;35(2):167–74.
[23] Gao Q, Xie Y, Wang Q. Effect of chemical modification of wood flour on the mechanical properties of wood–plastic composites. Constr Build Mater. 2014;62:238–42.
[24] Mengeloglu F, Karakus K. Thermal degradation behavior of agricultural residues-based fibre–polymer composites. Bioresour Technol. 2008;99(7):2327–35.
[25] Selke SE, Wichman I. Wood fiber/polyolefin composites. Compos Part A Appl Sci Manuf. 2004;35(3):321–6.
[26] ASTM International. ASTM D638, Standard Test Method for Tensile Properties of Plastics. West Conshohocken (PA): ASTM International.
[27] ASTM International. ASTM D790, Standard Test Methods for Flexural Properties of Unreinforced and Reinforced Plastics and Electrical Insulating Materials. West Conshohocken (PA): ASTM International.

[28] ASTM International. ASTM D2240, Standard Test Method for Rubber Property—Durometer Hardness. West Conshohocken (PA): ASTM International.
[29] Domadia M, Shah M, Rahman MN. Characterization of WPC with high wood content. J Kejuruteraan. 2024;36(3):210–22.
[30] Rosli R, Zakaria M. Water resistance of WPCs with hybrid fillers. J Kejuruteraan. 2025;37(1):47–58.
[31] Hasan MM, Talib AH. Water uptake and mechanical loss in outdoor-grade WPCs. J Kejuruteraan. 2025;37(2):77–86.
[32] Fabiyi JS, McDonald AG, Wolcott MP, et al. Wood plastic composites weathering: Natural and accelerated weathering using FTIR spectroscopy. Polym Degrad Stabil. 2008;93(8):1405–14.
[33] Ali K, Musa NA, Zainol R. Moisture degradation in natural fiber and PVC-based composites. Mater Res Express. 2024;11(3):035301.
[34] Ali R, Omar MI, Zakaria Z. Moisture effects on WPC interface adhesion: A micromechanical analysis. J Reinf Plast Compos. 2024;43(1):1–14.
[35] United Nations. Transforming our world: The 2030 Agenda for Sustainable Development. 2015. Available from: https://sustainabledevelopment.un.org/post2015/transformingourworld/publication
[36] Majid HA, Rahim MA. Hybrid fillers for moisture resistance in WPC. J Polym Compos. 2024;45(2):123–31.

Author contribution:

1. Conception and design of the study

2. Data acquisition

3. Data analysis

4. Discussion of the results

5. Writing of the manuscript

6. Approval of the last version of the manuscript

IA has contributed to: 1, 2, 3, 4, 5 and 6.

EAJ has contributed to: 1, 2, 3, 4, 5 and 6.

SH has contributed to: 1, 2, 3, 4, 5 and 6.

MAR has contributed to: 1, 2, 3, 4, 5 and 6.

SAK has contributed to: 1, 2, 3, 4, 5 and 6.

Acceptance Note: This article was approved by the journal editors Dr. Rafael Sotelo and Mag. Ing. Fernando A. Hernández Gobertti.

Additive Manufacturing of Cupric Oxide via Direct Ink Writing

Fabricación aditiva de óxido cúprico mediante escritura directa con tinta

Fabricação aditiva de óxido cúprico por escrita direta de tinta

Muhammad Ali [1], Shaheryar A. Khan [2] (*), Aqueel Shah [3], Antash Najib [4], Abbas Hussain [5]

Recibido: 18/08/2025 Aceptado: 24/11/2025

Summary. - The DIW approach offers numerous benefits, including expedited prototyping, cost-effectiveness, reduced waste in manufacturing, and enhanced design flexibility. It's currently a popular production method for building materials and has great potential for porous and electronic materials. In this study, porous cupric oxide (CuO) ceramics were fabricated using a direct ink writing (DIW) approach based on a copper particle–laden aqueous precursor. The ink formulation was optimized to achieve stable extrusion and crack-free green bodies, yielding a final composition of 68.0 wt% Cu, 31.3 wt% water, and 0.6 wt% CMC. Following oxidation and sintering in air, the printed structures exhibited a bulk density of 3.60 ± 0.20 g cm^{-3} and a corresponding theoretical porosity of 43.7 ± 0.9%. X-ray diffraction confirmed nearly phase-pure monoclinic CuO with no detectable Cu or Cu_2O residues. The printed components exhibited an interconnected, porous microstructure and a four-point-probe resistivity of 10.5 ± 0.3 Ω·m at 25 °C, reflecting the influence of high porosity on charge transport. The DIW route demonstrated here provides a controllable pathway for producing porous CuO architectures with tunable microstructure and moderate electrical conductivity. These characteristics suggest potential applicability in gas filtration, catalytic supports, and electrochemical sensing; however, device-level validation is still required to fully assess functional performance.

Keywords: Advanced Ceramics, Direct Ink Writing, Additive Manufacturing, Copper Oxide, Cupric Oxide, Binder, Ceramics, Green Body, Brown Body, Sintered Ceramic, Resistivity Analysis of Ceramic, Aqueous Binder Slurry, Particle Laden Slurry

(*) Corresponding author.

[1] Postgraduate Student, National University of Sciences and Technology (Pakistan), ime.322.ali@gmail.com,
ORCID iD: https://orcid.org/0009-0006-8014-5737

[2] Associate Professor and Head of the Department of Mechanical Engineering., DHA Suffa University (Pakistan), shaheryar.atta@dsu.edu.pk,
ORCID iD: https://orcid.org/0000-0003-1600-7322

[3] Professor, National University of Sciences and Technology (Pakistan), a.shah@smme.nust.edu.pk,
ORCID iD: https://orcid.org/0000-0003-2814-3073

[4] Assistant Professor, National University of Sciences and Technology (Pakistan), antash.najib@pnec.nust.edu.pk,
ORCID iD: https://orcid.org/0000-0002-4845-9350

[5] Assistant Professor, National University of Sciences and Technology (Pakistan), abbas.hussain@pnec.nust.edu.pk,
ORCID iD: https://orcid.org/0009-0008-1680-6507

Memoria Investigaciones en Ingeniería, núm. 30 (2026). pp. 14-29
https://doi.org/10.36561/ING.30.3
ISSN 2301-1092 • ISSN (en línea) 2301-1106 – Universidad de Montevideo, Uruguay

Resumen. - *El método DIW ofrece numerosas ventajas, como la creación rápida de prototipos, la rentabilidad, la reducción de residuos en la fabricación y una mayor flexibilidad de diseño. Actualmente es un método de producción popular para materiales de construcción y tiene un gran potencial para materiales porosos y electrónicos. En este estudio, se fabricaron cerámicas porosas de óxido cúprico (CuO) utilizando un método de escritura directa con tinta (DIW) basado en un precursor acuoso cargado con partículas de cobre. La formulación de la tinta se optimizó para lograr una extrusión estable y cuerpos verdes sin grietas, obteniendo una composición final de 68,0 % en peso de Cu, 31,3 % en peso de agua y 0,6 % en peso de CMC. Tras la oxidación y sinterización al aire, las estructuras impresas mostraron una densidad aparente de 3,60 ± 0,20 g cm⁻³ y una porosidad teórica correspondiente de 43,7 ± 0,9 %. La difracción de rayos X confirmó CuO monoclínico casi puro en fase, sin residuos detectables de Cu o Cu_2O. Los componentes impresos exhibieron una microestructura porosa interconectada y una resistividad de cuatro puntas de 10,5 ± 0,3 Ω·m a 25 °C, lo que refleja la influencia de la alta porosidad en el transporte de carga. La ruta de impresión directa con tinta (DIW) demostrada aquí proporciona una vía controlable para producir arquitecturas porosas de CuO con microestructura ajustable y conductividad eléctrica moderada. Estas características sugieren una posible aplicabilidad en filtración de gases, soportes catalíticos y detección electroquímica; sin embargo, aún se requiere una validación a nivel de dispositivo para evaluar completamente su rendimiento funcional.*

Palabras clave: *Cerámica avanzada, Impresión directa con tinta, Fabricación aditiva, Óxido de cobre, Óxido cúprico, Aglutinante, Cerámica, Cuerpo verde, Cuerpo marrón, Cerámica sinterizada, Análisis de resistividad de cerámica, Suspensión acuosa de aglutinante, Suspensión con partículas*

Resumo. ***-*** *A abordagem de escrita direta de tinta (DIW) oferece inúmeros benefícios, incluindo prototipagem acelerada, custo-benefício, redução de desperdício na fabricação e maior flexibilidade de design. Atualmente, é um método de produção popular para materiais de construção e tem grande potencial para materiais porosos e eletrônicos. Neste estudo, cerâmicas porosas de óxido cúprico (CuO) foram fabricadas utilizando uma abordagem de escrita direta de tinta (DIW) baseada em um precursor aquoso carregado com partículas de cobre. A formulação da tinta foi otimizada para obter extrusão estável e corpos verdes sem trincas, resultando em uma composição final de 68,0% em peso de Cu, 31,3% em peso de água e 0,6% em peso de CMC. Após oxidação e sinterização ao ar, as estruturas impressas apresentaram uma densidade aparente de 3,60 ± 0,20 g cm⁻³ e uma porosidade teórica correspondente de 43,7 ± 0,9%. A difração de raios X confirmou a presença de CuO monoclínico quase puro, sem resíduos detectáveis de Cu ou Cu_2O. Os componentes impressos exibiram uma microestrutura porosa interconectada e uma resistividade de quatro pontos de 10,5 ± 0,3 Ω·m a 25 °C, refletindo a influência da alta porosidade no transporte de carga. A rota DIW demonstrada aqui fornece um caminho controlável para produzir arquiteturas porosas de CuO com microestrutura ajustável e condutividade elétrica moderada. Essas características sugerem potencial aplicabilidade em filtração de gases, suportes catalíticos e sensores eletroquímicos; no entanto, a validação em nível de dispositivo ainda é necessária para avaliar completamente o desempenho funcional.*

Palavras-chave: *Cerâmicas Avançadas, Impressão Direta de Tinta, Manufatura Aditiva, Óxido de Cobre, Óxido Cúprico, Aglutinante, Cerâmicas, Corpo Verde, Corpo Marrom, Cerâmica Sinterizada, Análise de Resistividade de Cerâmica, Suspensão Aquosa de Aglutinante, Suspensão com Partículas*

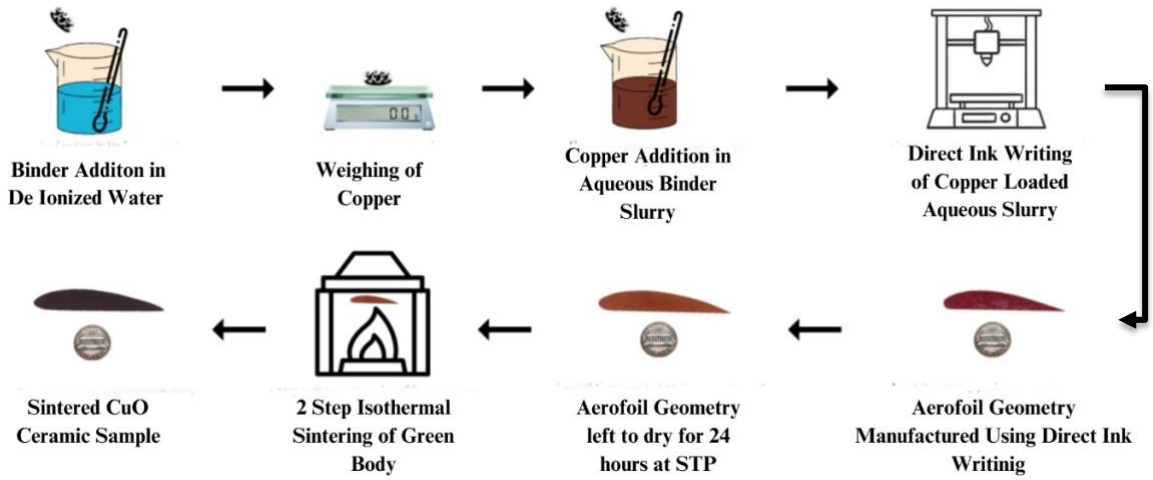

Graphical abstract.

1. Introduction. - The demand for materials with enhanced performance has created an everlasting need for the emergence of advanced materials. In today's world, advanced ceramics have primarily supplanted traditional materials. This technological change is motivated and boosted by the Asian markets in Japan and China [1].

Ceramics are well-known materials among other inorganic materials for their peculiar characteristics due to their chemical and physical properties [2]. High hardness, high strength, low thermal conductivity, and biocompatibility are some of the unique characteristics of advanced ceramics [3–6]. These materials have an enhanced resistance to wear governed by their microstructures that enable their application in various areas such as aerospace, biomedical, solar cells, fuel cells, heat exchangers, turbines, and piezo-electric devices [7].

Cupric oxide (CuO) is a black-colored ceramic material known as cupric oxide or copper (ii) oxide [8]. It is a transition metal oxide with a high surface-to-volume ratio, porosity, and monoclinic crystal structure [9,10]. It holds unique importance due to its comparable efficiency as a catalytic agent, superconducting property, anti-microbial agent, and energy-storing characteristics [9,11,12]. It is used in various domains today, including electronics, biomedical devices, energy harvesting systems, chemical catalysts for different chemical reactions, solid self-lubricants, and anti-microbial textiles [13–15]. It is used as a p-type semiconductor and magnetic storage media, finding its application in capacitors, electrodes, and different gas-sensing probes [16–19]. It is used to sense gases in the atmosphere and different biomedical sensing devices, including but not limited to CO_2, NO_2, H_2, H_2S, CO, benzyne, alcohol, ethanol, and methanol [10,20–24]. Studies show that CuO has the potential to replace the graphite anodes in lithium-ion batteries, as it is less expensive, safer, and more environmentally favorable than graphite [25]. CuO-based biomedical instruments detect blood protein patterns and blood glucose levels [16]. CuO also serves the environment by removing pollutants from the aqueous environment, including fluorides, arsenic, benzene, and toluene [26–28]. Its adsorption property removes lead, acrylic acid, and ciprofloxacin from different media, making CuO a good choice as a water-treating agent [26].

Conventional techniques for producing monolithic ceramic parts have many disadvantages, such as reliance on molds, lengthy production cycles, low material utilization rate, high material waste, high production cost, limited production volume, poor repeatability, and lack of microstructure control. [29]. These techniques include dry pressing, casting, micromachining, and injection molding [30,31]. Dry pressing and casting have similar limitations, such as the requirement for molds and the inability to produce complex shapes readily [32]. Fractures, porosity, and warpage are a few of the defects that can occur during the dry pressing and casting of ceramics. Nevertheless, these processes are protracted processes that frequently result in a product with an unstable microstructure [30].

Micromachining in ceramics is limited to low-volume production due to the high cost of the required machining tools, the geometric constraints that impede the production of intricate patterns, and the material's fragility [30].

Additive manufacturing (AM) has disrupted the manufacturing space and is being utilized to circumvent the limitations of conventional manufacturing techniques [33–35]. The technique builds monolithic parts layer-by-layer using 3D CAD data, resulting in the fabrication of complex geometries and reducing machining costs [36–38]. The technique provides freedom of design, increased finish quality, and reduced design-to-production lead time [39].

AM techniques have been developed for different materials [40,41], however, the Direct Ink Writing (DIW) technique is the most flexible, which can additively manufacture polymers, metals, ceramics, composites, and biological materials [42–44]. The DIW technique employs viscous pastes termed “inks” to produce monolithic parts [45]. The inks can be loaded with particles of ceramics to produce ceramic green bodies that can be later sintered in a furnace to produce a monolithic ceramic part [46]. Furthermore, pre-ceramic metal powder may also be utilized, which will oxidize in the furnace to produce ceramic parts[47].

The composition of the ink can be customized based on the specific application and desired properties of the printed part [43]. The combination of solid particles, solvents, binders, surfactants, plasticizers, rheology modifiers, and crosslinkers allows for a wide range of ink formulations that can be optimized for different printing methods, materials, and part geometries [45,48–51].

Despite extensive research on DIW of ceramic materials, the additive manufacturing of cupric oxide remains largely unexplored, particularly when derived from metallic copper precursors. Existing DIW studies on ceramics primarily utilize oxide powders, sol–gel routes, or UV-curable suspensions, whereas the transformation of a water-based metallic copper ink into a monolithic CuO ceramic through controlled oxidation and sintering has not been previously reported. In this study, we establish a reproducible process window for printing crack-free CuO structures using an aqueous CMC-based binder formulation with optimized copper loading. The work further demonstrates that the resulting 3D-printed CuO exhibits a combination of high porosity and measurable electrical conductivity, enabling its potential use in sensing and filtration applications. This contribution distinguishes the present study from prior DIW efforts and provides a scalable, low-cost pathway for fabricating functional CuO architectures.

This paper presents the additive manufacturing of copper oxide via the Direct Ink Writing (DIW) technique. A pre-ceramic green body was produced using an aqueous ink loaded with copper particles. The green body was sintered to form a monolithic ceramic part and characterized for its density, structure, and electrical conductivity. The results demonstrate that DIW is a viable technique for the manufacturing of monolithic parts from CuO. Unlike most existing DIW ceramics that utilize oxide powders, sol-gel routes, or UV-curable suspensions, this work establishes the first reported transformation of a water-based metallic copper ink into a monolithic CuO ceramic through a controlled oxidation and sintering process.

2. Materials and methods. - Copper powder, DI water (De-Ionized Water), and CMC (Carboxymethyl Cellulose) binder were the three components used for this research. Copper powder with a particle size of 10µm was purchased and imported from Vanuatu. The DI water was used in this experiment to ensure that no impurity was added to the materials during the manufacturing process, affecting the chemical composition of the slurry. CMC binder, holding CAS number 9000-11-7, was purchased from Purge Chemical Industries, Karachi, Pakistan.

2.1 Preparation of copper-loaded pre-ceramic ink. - The pre-ceramic ink was formulated as a copper particle–laden aqueous binder system. The aqueous binder was first prepared by dissolving 0.20 g of CMC in 10.0 g of deionized water, followed by manual stirring for 3 minutes to ensure complete homogenization. Subsequently, 21.7 g of copper powder was incorporated into the binder solution. The copper powder was added intermittently and stirred continuously to promote uniform wetting and dispersion. Manual stirring throughout this process ensured homogeneous distribution of the metallic particles within the aqueous matrix. The final ink composition on a mass–mass basis consisted of 68.0 wt% copper, 31.3 wt% water, and 0.6 wt% CMC.

Multiple solid loadings were evaluated to identify the optimal formulation for DIW. Copper contents lower than 68 wt% resulted in insufficient structural integrity during drying, leading to cracking of the green bodies. Conversely, higher copper loadings produced excessively dense pastes that consistently clogged the nozzle during extrusion. The polymeric binder concentration also governed drying behaviour: CMC levels above 0.6 wt% increased shrinkage and deformation during solvent removal, whereas lower binder contents led to cracking due to inadequate particle–particle bridging. Based on these observations, the composition of 68.0 wt% Cu and 0.6 wt% CMC in a 31.3 wt% aqueous phase was identified as the optimal mass fraction combination for achieving stable extrusion, shape retention, and crack-free green bodies.

Although the ink was formulated and optimized on a mass–mass basis, its rheological behavior was also considered during process development, as DIW printability is strongly governed by viscosity, shear-thinning characteristics, and yield stress. While full rheological profiling (e.g., viscometry or oscillatory shear measurements) was not performed in this study, the formulation exhibited all qualitative indicators of DIW-compatible flow behavior. Specifically, the ink demonstrated continuous filament formation under extrusion, maintained structural integrity after deposition, and showed no signs of uncontrolled spreading, all of which are consistent with shear-thinning pastes reported in DIW literature. The absence of nozzle clogging or die swell further suggests that the yield stress lies within a suitable range for stable extrusion. The optimized solid and binder mass fractions (68.0 wt% Cu and 0.6 wt% CMC) were therefore selected not only for their influence on drying and green-body integrity, but also for their empirically validated rheological performance during printing.

2.2 Direct Ing Writing. - Parts were manufactured using a modified Creality Ender-3 platform that was adapted for direct ink writing (DIW) through mechanical and control-system modifications. The stock thermoplastic extruder assembly was removed and replaced with a custom-designed DIW print head. The print head consisted of a 50 mL pneumatic dispensing cartridge fitted with a tapered nozzle of 0.4 mm exit diameter, which deposited the copper-loaded pre-ceramic slurry onto a glass build platform. Extrusion was actuated by a regulated pneumatic pressure system (0–1 MPa), supplied by a laboratory compressor and controlled by an electronic solenoid valve interfaced with the printer's control board. Fine adjustment of the extrusion pressure was achieved using an inline pressure regulator to ensure stable and continuous filament formation.

The Ender-3 is originally designed for stepper-driven thermoplastic extrusion and, therefore, its firmware was modified so that the E-axis extrusion commands in the G-code toggled the solenoid valve rather than driving a stepper motor. Geometric parameters, including layer height, nozzle speed, infill pattern, and wall thickness, were defined in the slicing software (Ultimaker Cura), while the extrusion rate was governed exclusively by pneumatic pressure. These modifications enabled reliable deposition of the high-viscosity CuO precursor paste while preserving the positional accuracy inherent to the FFF motion system.

All samples were manufactured under controlled laboratory conditions of 25 ± 1 °C and 50% relative humidity. Fig. 1 illustrates the modified DIW setup along with the part geometry selected for DIW-based CuO ceramic fabrication, and the corresponding DIW process parameters are summarized in Table 1. The printed aerofoil specimen (NACA 2412) had an overall chord length of 100 mm, a maximum thickness of 15.54 mm, and a span of 3 mm (z-axis). The outer shell thickness was set to 0.8 mm, with a rectilinear infill density of 100%. These dimensions were chosen to minimize drying-induced warpage and to promote uniform shrinkage during sintering.

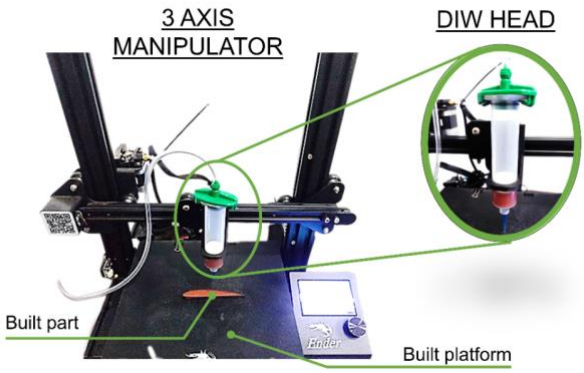

Figure I. The Direct Ink Writing (DIW) setup.

Parameter	Value
Nozzle Diameter	0.4 mm
Layer Height	0.2 mm
Extrusion Width	0.4 mm
Linear Speed	20 $mm.s^{-1}$
Raster Angle	45 degrees
Infill Pattern	Rectilinear
Infill Density	100%
Wall thickness	0.8 mm
Air Pressure	0.2 MPa

Table I. Parameters of the Direct Ink Writing Process.

2.3 Drying, demolding, and sintering. - The printed green bodies were dried at room temperature for 24 h and subsequently sintered in a programmable air furnace concurrently. The temperature schedule consisted of an initial heating step from room temperature to 400 °C at a rate of 5 °C/min, followed by a dwell of 45 min to ensure complete binder burnout. The temperature was then increased from 400 to 900 °C at 5 °C/min, where the samples were held for 180 min to promote oxidation and densification. After sintering, the furnace was allowed to cool naturally to room temperature at an uncontrolled rate. All specimens were sintered in ambient air without additional oxygen flow. The multi-step sintering regime is illustrated in Figure II.

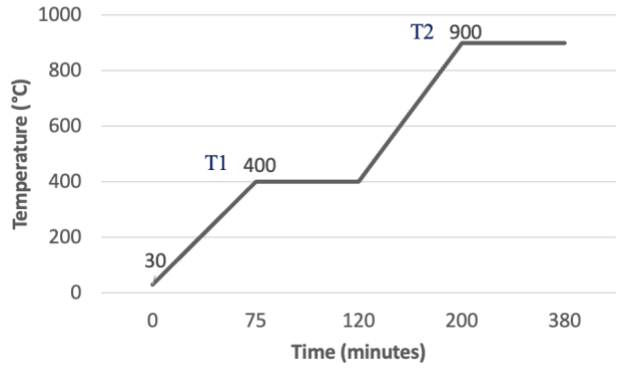

Figure II. The Direct Ink Writing (DIW) setup.

3. Results and discussion. -

3.1 Sintered ceramic body. - The transformation of the DIW sample to the final sintered ceramic body is illustrated in Figure III. The technique can produce monolithic parts using pre-ceramic slurry without cracking and warping. An

isotropic shrinkage of 4.1 ± 0.2 % (n=5) was observed from the CAD model to the sintered body. It can be concluded that the DIW technique is a viable option for the manufacturing of monolithic ceramic parts. Simple and complex part geometries can be designed in a CAD environment and implemented readily for function-specific applications.

Figure III. Transformation from the DIW part to the sintered monolithic ceramic body (Aerofoil Geometry).

3.2 XRD Analysis. - The X-ray diffractogram of the sintered CuO sample is illustrated in Figure IV. The XRD analysis demonstrates that the Cu particles have uniformly oxidized into CuO as the experimental pattern shows an excellent match with the monoclinic CuO reference pattern (Crystallography Open Database) [52]. A quantitative analysis by Rietveld refinement using FullProf software was performed to identify the phase ratio. The results of the refinement indicated that the sample is 99.8 % phase-pure CuO. No significant secondary phases, such as residual Cu or Cu_2O, were detected above the instrument's detection limit.

The degree of crystallinity was determined by integrating the area under the crystalline peaks and the background amorphous hump. Using the peak analyser tool in OriginLab software, the crystallinity degree of the sample was calculated to be 65.78%.

The crystallite size of the XRD patterns was estimated using Scherrer's equation:

$$D = \frac{k\,\lambda}{\beta \cos\theta} \qquad (1)$$

where D is the crystallite size, k is the so-called shape factor (0.9), λ is the wavelength (0.15418 nm, CuKα), β is the Full Width at Half Maximum (FWHM), and θ is the diffraction angle [53]. To ensure an accurate representation, the crystallite size was calculated using the FWHM of the three most intense peaks: $(11\bar{1})$, (111), and (200) located at approximately 35.5°, 38.7°, and 39.8° 2Theta, respectively). The FWHM values were corrected for instrumental broadening using a standard LaB6 reference sample. Exploiting the average of the data derived from these three peaks, an average crystallite size of 71.75 nm was determined, with an estimated standard deviation (error) of 2.1 nm is reported for the measurement. The sample was identified as having a Monoclinic Crystal System with refined lattice parameters.

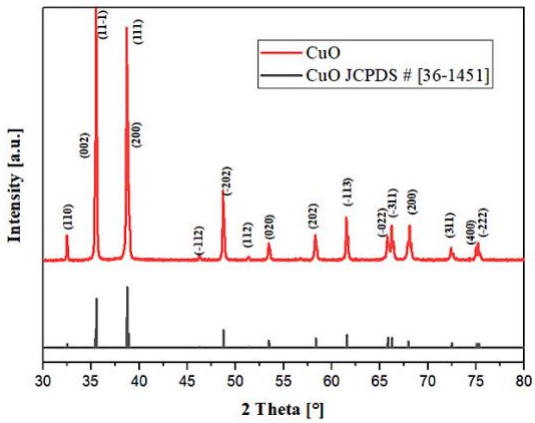

Figure IV. X-ray diffractogram of sintered CuO sample.

The refined lattice parameters of the sintered phase were found to be a = 4.68370 Å, b = 3.42260 Å, c = 5.12880 Å, and β = 99.54°. These values are in excellent agreement with the reported unit-cell dimensions for monoclinic CuO (tenorite), which are typically quoted as a ≈ 4.68 Å, b ≈ 3.42 Å, c ≈ 5.13 Å, and β ≈ 99.5° in standard crystallographic databases and the literature. The close match between the extracted parameters and the reference values indicates that the as-sintered material is phase-pure CuO with negligible lattice distortion. Any minor differences are within expected experimental uncertainty and may arise from instrument calibration, residual micro-strain introduced during the oxidation/sintering cycle, or slight non-stoichiometry. Peak broadening observed in the diffractogram (Scherrer crystallite size ≈ 72 nm) is consistent with the finite crystallite size and could also contribute to small uncertainties in the refined cell metrics.

3.3 Morphology. - The morphology of copper powder and the sintered CuO ceramic was studied under a Scanning Electron Microscope. SEM micrographs of copper powder in Fig. 5 (a and b) depict the powder having an average particle size of 10µm. The SEM micrographs demonstrate the agglomeration of the copper powder. The copper powder was not subjected to ball milling to prevent it from early oxidation.

Figure V (c and d) shows the SEM images of the CuO sintered sample manufactured using additive manufacturing. The micrographs show that powder particles have sintered into a porous structure. This porosity allows for the application of additively manufactured CuO parts in applications such as gas sensing and pollutant filtration [54].

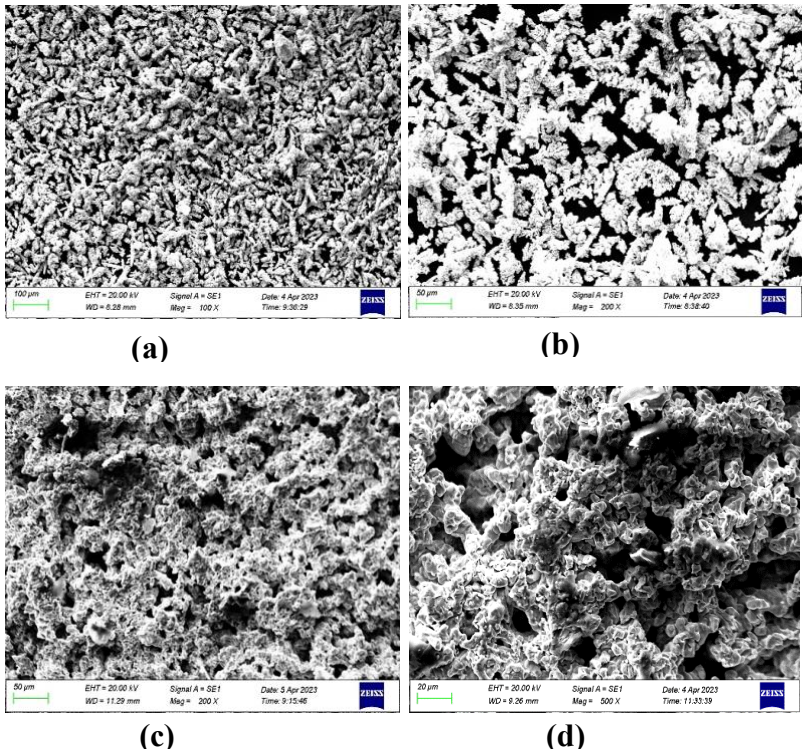

Figure V. (a) SEM image of copper powder at x100 magnification. (b) SEM image of copper powder at x200 magnification. (c) SEM image of sintered CuO ceramic at x200 magnification. (d) SEM image of sintered CuO ceramic at x500 magnification.

3.4 Porosity and Density. - The surface porosity of the sintered sample was estimated through pixel intensity analysis using the ImageJ software. Pixel intensity analysis is illustrated in Figure VI, where the porous regions are mapped with red color. The software estimates a mean surface porosity of 40.4%.

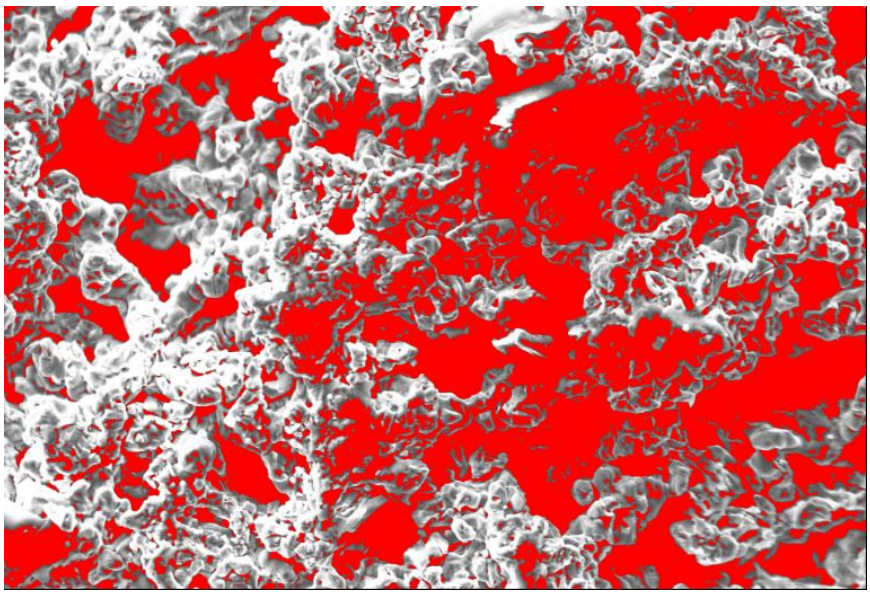

Figure VI. Porosity Analysis of SEM Image of CuO Ceramic Sample using ImageJ Software

The bulk density of the sintered CuO samples was determined using the liquid infiltration method following ASTM C830–00 [55]. Each sample was first weighed in the dry state using an analytical balance to obtain the dry mass (m_{dry}), then immersed in distilled water until complete saturation of open pores was achieved. The samples were gently blotted to remove excess surface liquid and reweighed to obtain the wet mass (m_{wet}).

The bulk volume (V_{bulk}) of each sample was calculated using the relation:

$$V_{bulk} = \frac{m_{dry}}{\rho_{theoratical}} + \frac{m_{wet} - m_{dry}}{\rho_{liquid}} \quad (1)$$

The bulk density of each sample was calculated as:

$$\rho_{bulk} = \frac{m_{dry}}{V_{bulk}} \quad (2)$$

The porosity of each sample was determined by:

$$\%P = 1 - \frac{\rho_{bulk}}{\rho_{theoratical}} \quad (3)$$

The measured dry and wet masses, calculated bulk densities, and porosities for the five samples are summarized in Table 2. The average bulk density was found to be 3.6 ± 0.2 g/cm³, corresponding to a calculated porosity of 43.7 ± 0.9%. The density of the sample can be further increased by secondary infiltration post-sintering for specific applications.

Sample	Dry Mass (g)	Wet Mass (g)	Bulk Density (g/cm³)	Porosity (%)
1	9.45	10.63	3.44	44.6
2	9.75	10.93	3.57	44.3
3	9.95	11.14	3.61	43.7
4	10.20	11.40	3.65	42.9
5	10.45	11.68	3.69	42.3

Table II. Results of bulk density measurements.

The close agreement between the bulk (43.7%) and surface (40.4%) porosity values confirms that the CuO ceramic exhibits a homogeneously distributed porous microstructure. The slight variance, where the bulk value is marginally higher, is primarily attributed to the inclusion of closed porosity in the 3D density calculation, which is inherently

excluded from the 2D surface projection, further supporting the conclusion that the additive manufacturing approach successfully produced a high-porosity ceramic structure suitable for the intended applications.

3.5 Resistivity Analysis. - The resistivity was determined using the four-probe resistivity technique [56]. The voltage was measured at the two inner probes, while the current was injected using the two outer probes. The schematic of the four-probe resistivity technique is illustrated in Figure VII.

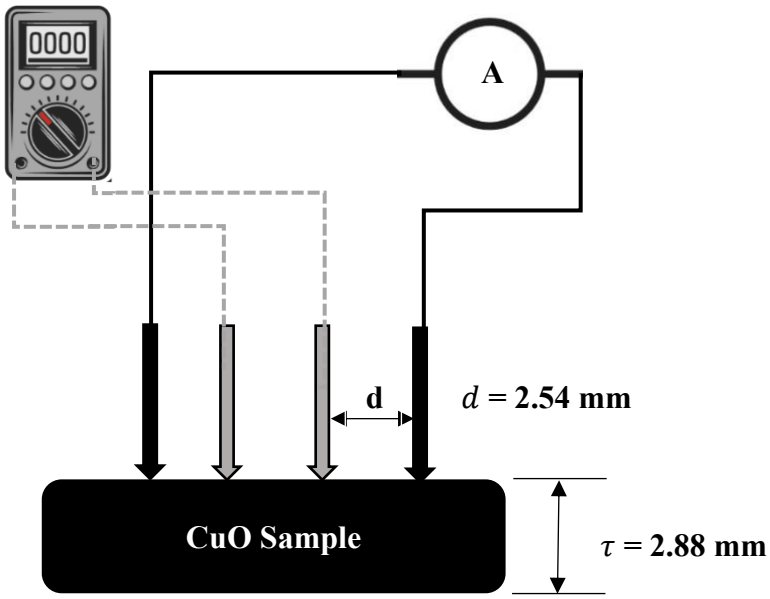

Figure VII. The schematic of the four-probe resistivity technique.

The printed and sintered CuO aerofoil samples had an average thickness of 2.88 mm, while the probe spacing (d) of the four-point probe head was fixed at 2.54 mm. The measurements were performed directly on the as-sintered surface without additional polishing or metallization, as the intrinsic conductivity of the CuO matrix was sufficient for stable contact formation. All measurements were conducted at a controlled room temperature of 25 ± 1°C and 50% relative humidity. To ensure the validity of the measurement, the current *I* was swept across a range of 1 mA to 10 mA, and the resulting *I-V* curve was confirmed to be linear ($R^2 > 0.999$), indicating Ohmic contact behavior within the measurement range and validating the use of the following resistivity formula for bulk material:

The computations were conducted using the resistivity formula for the bulk material [54].

$$\rho = \frac{V}{I}\, x\, \frac{\pi\, \tau}{\ln\left(\frac{\sinh\,(\tau/d)}{\sinh\,(\tau/2d)}\right)} \qquad (4)$$

where V is the recorded voltage, I is the injected current, τ is the thickness of the sample, and d is the probe spacing. The resistivity of the CuO sample was computed to be 10.5 ± 0.3 $\Omega\, m$ (n=5) which corresponds to a conductivity of (9.5 ± 0.3) $x10^{-2}$ S/m.

The electrical conductivity indicates the potential for the additively manufactured CuO parts to function as active components, such as electrodes or catalytic membranes. This is enabled by the synergy between this foundational conductivity and the high surface area derived from the 43.7 % theoretical porosity. Therefore, while the bulk electrical measurement establishes the viability for charge conduction, the true potential for specific applications, including electrochemical sensing, supercapacitors, and heterogeneous catalysis, must be confirmed through subsequent device-level proof-of-concept (PoC) studies that evaluate charge transfer kinetics and functional performance.

3.6 Efficacy of the DIW technique. - The results demonstrate that the DIW technique is a viable alternative to produce monolithic ceramic parts from CuO, circumventing the limitations of conventional ceramic manufacturing techniques. Complex geometries could be designed in a CAD environment and manufactured readily. The SEM, porosity, and XRD analyses show that the resulting part shall be porous and may be employed in various applications such as filtering of microbial and chemical pollutants. The electrical conductivity will enable the utilization of the sintered part in biological sensing and gas sensing applications. The developed technique can be explored for the manufacturing of other functional metal oxides, such as Al2O3 and TiO2.

The physical and electrical properties achieved via this novel Direct Ink Writing (DIW) route demonstrate a successful balance between a desirable architecture and inherent material characteristics when compared to traditional CuO ceramics and functional films.

The measured bulk density of 3.60 ± 0.20 g/cm³ is significantly lower than the theoretical density of fully dense CuO (often cited near 6.31 g/cm³ [52]), which is a direct consequence of the resulting high porosity of 40.4%. This structured, high-porosity is a key feature of the DIW process, ensuring the high surface area required for functional applications such as gas sensors and catalytic applications, where morphology and enhanced surface reaction sites are critical for performance [22].

Furthermore, the measured bulk resistivity of 10.5 ± 0.3 Ω m is characteristic of the material's semiconducting behavior. CuO is widely studied as a p-type semiconductor [23], and this resistivity confirms that the 3D-printed, porous ceramic possesses the required electrical properties to function as an active layer in conductometric devices, distinguishing it from fully insulating ceramic structures [23].

Despite the functional advantages of high porosity, this architecture presents inherent trade-offs, which must be acknowledged. This high porosity inherently limits mechanical strength and structural rigidity. The interconnected pore network facilitates charge transport pathways and enhances active surface exposure, but it also reduces the load-bearing solid fraction, making the parts more susceptible to brittle failure under mechanical stress.

Similarly, the measured bulk resistivity of 10.5 ± 0.3 Ω m is characteristic of the material's p-type semiconducting behaviour [23], but is significantly higher than that of dense sintered CuO. This elevated resistivity reflects both the porous morphology and the reduced percolation pathways for charge transport. The presence of air-filled voids, oxide necks between particles, and incomplete densification restricts electron mobility, further illustrating an intrinsic trade-off between porosity-driven functional advantages and the deterioration of both electrical and mechanical properties. Future studies should therefore focus on tuning the sintering schedule, solid loading, or post-processing treatments (e.g., partial densification, infiltration) to balance porosity with improved conductivity and structural robustness depending on the intended application.

4. Conclusion. - This study demonstrated the successful fabrication of porous CuO ceramics using a direct ink writing (DIW) route starting from a copper particle–laden aqueous binder system. The optimized ink formulation (68.0 wt% Cu, 31.3 wt% water, and 0.6 wt% CMC) enabled stable extrusion and the formation of crack-free green bodies. Following oxidation and sintering, the printed structures exhibited a bulk density of 3.60 ± 0.20 g/cm³, corresponding to a theoretical porosity of 43.7 ± 0.9 %. SEM analysis confirmed a porous interconnected microstructure and the formation of monoclinic CuO as the dominant crystalline phase.

Electrical characterization using a four-point probe configuration yielded a bulk resistivity of 10.5 ± 0.3 Ω m and a corresponding conductivity of $(9.5 \pm 0.3) \times 10^{-2}$ S/m at 25 ± 1 °C. These values reflect the influence of the high porosity and incomplete densification on charge-transport behavior. The combined microstructural and electrical results indicate that the additively manufactured CuO components possess the foundational properties required for functional applications where surface area, diffusion, and moderate conductivity are desirable.

While the present work establishes the feasibility of DIW-based CuO fabrication, the potential applicability of these structures in gas sensing, filtration, catalysis, or electrochemical systems remains conditional and will require dedicated device-level testing to evaluate performance, stability, and charge-transfer characteristics. Future studies may focus on controlling densification, tailoring porosity, or incorporating post-processing treatments to further optimize the balance between electrical, structural, and functional requirements.

Declaration Conflict of Interest. - The authors of this research announce that they have no known contending monetary interests or individual connections that may have impacted the work detailed in this paper.

Data and Code Availability. - Data and code shall be made available upon request to the corresponding author.

References

[1] W.R. Matizamhuka, Advanced ceramics — The new frontier in modern-day technology: Part I, J South Afr Inst Min Metall 118 (2018) 757–764. https://doi.org/10.17159/2411-9717/2018/V118N7A9.

[2] T. Ayode Otitoju, P. Ugochukwu Okoye, G. Chen, Y. Li, M. Onyeka Okoye, S. Li, Advanced ceramic components: Materials, fabrication, and applications, Journal of Industrial and Engineering Chemistry 85 (2020) 34–65. https://doi.org/10.1016/J.JIEC.2020.02.002.

[3] C.Barry. Carter, M.Grant. Norton, Ceramic materials: science and engineering, (2013). https://books.google.com/books/about/Ceramic_Materials.html?id=WRg_AAAAQBAJ (accessed March 26, 2023).

[4] R. Danzer, On the relationship between ceramic strength and the requirements for mechanical design, J Eur Ceram Soc 34 (2014) 3435–3460. https://doi.org/10.1016/J.JEURCERAMSOC.2014.04.026.

[5] F. Klocke, Modern approaches for the production of ceramic components, J Eur Ceram Soc 17 (1997) 457–465. https://doi.org/10.1016/S0955-2219(96)00163-X.

[6] H. Budharaju, S. Suresh, M.P. Sekar, B. De Vega, S. Sethuraman, D. Sundaramurthi, D.M. Kalaskar, Ceramic materials for 3D printing of biomimetic bone scaffolds – Current state-of-the-art & future perspectives, Mater Des 231 (2023) 112064. https://doi.org/10.1016/J.MATDES.2023.112064.

[7] M. Laborie, A. Naveau, A. Menard, CAD-CAM resin-ceramic material wear: A systematic review, J Prosthet Dent (2022). https://doi.org/10.1016/J.PROSDENT.2022.01.027.

[8] Susilawati, T.I. Nasution, M. Hasanah, Y.A. Sihombing, Fabrication of Ceramic Composites Based on CuO-ZnO, (2018). https://dupakdosen.usu.ac.id/handle/123456789/69927 (accessed April 1, 2023).

[9] D. Renuga, J. Jeyasundari, S. Athithan, Y. Brightson, A. Jacob, Synthesis and characterization of copper oxide nanoparticles using Brassica oleracea var. italic extract for its antifungal application, Mater. Res. Express 7 (2020) 45007. https://doi.org/10.1088/2053-1591/ab7b94.

[10] S. Steinhauer, E. Brunet, T. Maier, G.C. Mutinati, A. Köck, O. Freudenberg, C. Gspan, W. Grogger, A. Neuhold, R. Resel, Gas sensing properties of novel CuO nanowire devices, Sens Actuators B Chem 187 (2013) 50–57. https://doi.org/10.1016/J.SNB.2012.09.034.

[11] D.G. Desai, G.R. Navale, D.J. Late, M.S. Dharne, P.S. Walke, Size does matter: antibacterial activities and cytotoxic evaluation of polymorphic CuO nanostructures, J Mater Sci 58 (2023) 2782–2800. https://doi.org/10.1007/S10853-023-08157-4/METRICS.

[12] A.P. Cabello, M.A. Ulla, J.M. Zamaro, In situ growth of nanostructured copper and zinc mixed oxides on brass supports as efficient microreactors for the catalytic CO oxidation, Journal of Materials Science 2022 57:27 57 (2022) 12797–12809. https://doi.org/10.1007/S10853-022-07391-6.

[13] B.K. Singh, State-of-Art on Self-Lubricating Ceramics and Application of Cu/CuO as Solid Lubricant Material, Https://Doi.Org/10.1080/0371750X.2022.2149625 (2023). https://doi.org/10.1080/0371750X.2022.2149625.

[14] L.E. Román, C. Villalva, C. Uribe, F. Paraguay-Delgado, J. Sousa, J. Vigo, C.M. Vera, M.M. Gómez, J.L. Solís, Textiles Functionalized with Copper Oxides: A Sustainable Option for Prevention of COVID-19, Polymers 2022, Vol. 14, Page 3066 14 (2022) 3066. https://doi.org/10.3390/POLYM14153066.

[15] A.M. Anand, A. Raj, R. Adithya Nath, J.A. Salam, R. Jayakrishnan, Self-powered UV photodetector based on self-assembled CuO and spin-coated ZnO heterostructure, J Mater Sci 58 (2023) 11000–11015. https://doi.org/10.1007/S10853-023-08726-7/METRICS.

[16] R. Ahmad, M. Vaseem, N. Tripathy, Y.B. Hahn, Wide linear-range detecting nonenzymatic glucose biosensor based on CuO nanoparticles inkjet-printed on electrodes, Anal Chem 85 (2013) 10448–10454. https://doi.org/10.1021/AC402925R.

[17] K. Abdelkarem, R. Saad, A.M. Ahmed, M.I. Fathy, M. Shaban, H. Hamdy, Efficient room temperature carbon dioxide gas sensor based on barium doped CuO thin films, J Mater Sci 58 (2023) 11568–11584. https://doi.org/10.1007/S10853-023-08687-X/TABLES/3.

[18] D.Y. Tiba, L.L. Name, R. Landers, T.C. Canevari, Copper oxide nanostructures with nanoneedles shape obtained by direct reaction with nitrogen-doped carbon quantum dots: development of an electrochemical sensor to glyphosate, J Mater Sci 58 (2023) 12569–12583. https://doi.org/10.1007/S10853-023-08827-3/METRICS.

[19] U.A.A. Yasin, M.M. Ahmed, J. Zhang, Z. Jia, T. Guo, R. Zhao, J. Shi, J. Du, Engineering the band structure of CuO via decoration with AgBr to enhance its photocatalytic degradation performance, J Mater Sci 58 (2023) 7333–7346. https://doi.org/10.1007/S10853-023-08487-3/METRICS.

[20] N. Bin Tanvir, C. Wilbertz, S. Steinhauer, A. Köck, G. Urban, O. Yurchenko, Work Function Based CO2 Gas Sensing Using Metal Oxide Nanoparticles at Room Temperature, Mater Today Proc 2 (2015) 4190–4195. https://doi.org/10.1016/J.MATPR.2015.09.002.
[21] O. Baranov, K. Bazaka, T. Belmonte, C. Riccardi, H.E. Roman, M. Mohandas, S. Xu, U. Cvelbar, I. Levchenko, Recent innovations in the technology and applications of low-dimensional CuO nanostructures for sensing, energy and catalysis, Nanoscale Horiz (2023). https://doi.org/10.1039/D2NH00546H.
[22] O. Lupan, V. Postica, N. Ababii, M. Hoppe, V. Cretu, I. Tiginyanu, V. Sontea, T. Pauporté, B. Viana, R. Adelung, Influence of CuO nanostructures morphology on hydrogen gas sensing performances, Microelectron Eng 164 (2016) 63–70. https://doi.org/10.1016/J.MEE.2016.07.008.
[23] F. Shao, F. Hernández-Ramírez, J.D. Prades, C. Fàbrega, T. Andreu, J.R. Morante, Copper (II) oxide nanowires for p-type conductometric NH 3 sensing, Appl Surf Sci 311 (2014) 177–181. https://doi.org/10.1016/J.APSUSC.2014.05.038.
[24] S. Wang, S. Gao, J. Tian, Q. Wang, T. Wang, X. Hao, F. Cui, A stable and easily prepared copper oxide catalyst for degradation of organic pollutants by peroxymonosulfate activation, J Hazard Mater 387 (2020) 121995. https://doi.org/10.1016/J.JHAZMAT.2019.121995.
[25] T.H. Tran, V.T. Nguyen, Review Article Copper Oxide Nanomaterials Prepared by Solution Methods, Some Properties, and Potential Applications: A Brief Review, (2014). https://doi.org/10.1155/2014/856592.
[26] J.O. Ighalo, P.A. Sagboye, G. Umenweke, O.J. Ajala, F.O. Omoarukhe, C.A. Adeyanju, S. Ogunniyi, A.G. Adeniyi, CuO nanoparticles (CuO NPs) for water treatment: A review of recent advances, Environ Nanotechnol Monit Manag 15 (2021). https://doi.org/10.1016/J.ENMM.2021.100443.
[27] S. Saif, S.F. Adil, M. Khan, M.R. Hatshan, M. Khan, F. Bashir, Adsorption Studies of Arsenic(V) by CuO Nanoparticles Synthesized by Phyllanthus emblica Leaf-Extract-Fueled Solution Combustion Synthesis, Sustainability 2021, Vol. 13, Page 2017 13 (2021) 2017. https://doi.org/10.3390/SU13042017.
[28] L. Mohammadi, E. Bazrafshan, M. Noroozifar, A. Ansari-Moghaddam, F. Barahuie, D. Balarak, Adsorptive Removal of Benzene and Toluene from Aqueous Environments by Cupric Oxide Nanoparticles: Kinetics and Isotherm Studies, J Chem 2017 (2017). https://doi.org/10.1155/2017/2069519.
[29] Z. Liu, C. Ma, Z. Chang, P. Yan, F. Li, Advances in crack formation mechanism and inhibition strategy for ceramic additive manufacturing, J Eur Ceram Soc 43 (2023) 5078–5098. https://doi.org/10.1016/J.JEURCERAMSOC.2023.05.008.
[30] S.S. Hossain, K. Lu, Recent progress of alumina ceramics by direct ink writing: Ink design, printing and post-processing, Ceram Int 49 (2023) 10199–10212. https://doi.org/10.1016/J.CERAMINT.2023.01.143.
[31] J. xin Wen, T. bin Zhu, Z. peng Xie, W. bin Cao, W. Liu, A strategy to obtain a high-density and high-strength zirconia ceramic via ceramic injection molding by the modification of oleic acid, International Journal of Minerals, Metallurgy and Materials 24 (2017) 718–725. https://doi.org/10.1007/S12613-017-1455-9/METRICS.
[32] S.M. Olhero, P.M.C. Torres, J. Mesquita-Guimarães, J. Baltazar, J. Pinho-da-Cruz, S. Gouveia, Conventional versus additive manufacturing in the structural performance of dense alumina-zirconia ceramics: 20 years of research, challenges and future perspectives, J Manuf Process 77 (2022) 838–879. https://doi.org/10.1016/J.JMAPRO.2022.02.041.
[33] A. Vevers, A. Kromanis, E. Gerins, J. Ozolins, Additive Manufacturing and Casting Technology Comparison: Mechanical Properties, Productivity and Cost Benchmark, Latvian Journal of Physics and Technical Sciences 55 (2018) 56–63. https://doi.org/10.2478/LPTS-2018-0013.
[34] Y. Lin, D. Wang, C. Yang, W. Zhang, Z. Wang, An Al-Al interpenetrating-phase composite by 3D printing and hot extrusion, International Journal of Minerals, Metallurgy and Materials 30 (2023) 678–688. https://doi.org/10.1007/S12613-022-2543-Z/METRICS.
[35] Y. tao Gao, T. hua Wu, Y. Zhou, Application and prospective of 3D printing in rock mechanics: A review, International Journal of Minerals, Metallurgy and Materials 28 (2021) 1–17. https://doi.org/10.1007/S12613-020-2119-8/METRICS.
[36] A. Zocca, P. Colombo, C.M. Gomes, J. Günster, Additive Manufacturing of Ceramics: Issues, Potentialities, and Opportunities, Journal of the American Ceramic Society 98 (2015) 1983–2001. https://doi.org/10.1111/JACE.13700.
[37] R. Galante, C.G. Figueiredo-Pina, A.P. Serro, Additive manufacturing of ceramics for dental applications: A review, Dental Materials 35 (2019) 825–846. https://doi.org/10.1016/J.DENTAL.2019.02.026.

[38] B. Diepold, N. Vorlaufer, S. Neumeier, T. Gartner, M. Göken, Optimization of the heat treatment of additively manufactured Ni-base superalloy IN718, International Journal of Minerals, Metallurgy and Materials 27 (2020) 640–648. https://doi.org/10.1007/S12613-020-1991-6/METRICS.
[39] S. Ford, M. Despeisse, Additive manufacturing and sustainability: an exploratory study of the advantages and challenges, J Clean Prod 137 (2016) 1573–1587. https://doi.org/10.1016/J.JCLEPRO.2016.04.150.
[40] M. Srivastava, S. Rathee, V. Patel, A. Kumar, P.G. Koppad, A review of various materials for additive manufacturing: Recent trends and processing issues, (2022). https://doi.org/10.1016/j.jmrt.2022.10.015.
[41] H. Liu, J. Wu, S. Wang, J. Duan, H. Shao, Effect of Sr2+ on 3D gel-printed Sr3−xMgx(PO4)2 composite scaffolds for bone tissue engineering, International Journal of Minerals, Metallurgy and Materials 30 (2023) 2236–2244. https://doi.org/10.1007/S12613-023-2638-1/METRICS.
[42] M.A.S.R. Saadi, A. Maguire, N.T. Pottackal, M.S.H. Thakur, M.M. Ikram, A.J. Hart, P.M. Ajayan, M.M. Rahman, Direct Ink Writing: A 3D Printing Technology for Diverse Materials, Advanced Materials 34 (2022). https://doi.org/10.1002/ADMA.202108855.
[43] S.B. Balani, S.H. Ghaffar, M. Chougan, E. Pei, E. Şahin, Processes and materials used for direct writing technologies: A review, Results in Engineering 11 (2021) 100257. https://doi.org/10.1016/J.RINENG.2021.100257.
[44] S.A. Khan, I. Lazoglu, Development of additively manufacturable and electrically conductive graphite–polymer composites, Progress in Additive Manufacturing 5 (2020) 153–162. https://doi.org/10.1007/s40964-019-00102-9.
[45] L. del-Mazo-Barbara, M.P. Ginebra, Rheological characterisation of ceramic inks for 3D direct ink writing: A review, J Eur Ceram Soc 41 (2021) 18–33. https://doi.org/10.1016/J.JEURCERAMSOC.2021.08.031.
[46] F. Abdeljawad, D.S. Bolintineanu, A. Cook, H. Brown-Shaklee, C. DiAntonio, D. Kammler, A. Roach, Sintering processes in direct ink write additive manufacturing: A mesoscopic modeling approach, Acta Mater 169 (2019) 60–75. https://doi.org/10.1016/J.ACTAMAT.2019.01.011.
[47] S.A. Legett, X. Torres, A.M. Schmalzer, A. Pacheco, J.R. Stockdale, S. Talley, T. Robison, A. Labouriau, Balancing Functionality and Printability: High-Loading Polymer Resins for Direct Ink Writing, Polymers 2022, Vol. 14, Page 4661 14 (2022) 4661. https://doi.org/10.3390/POLYM14214661.
[48] D. Graf, J. Jung, T. Hanemann, Formulation of a Ceramic Ink for 3D Inkjet Printing, Micromachines (Basel) 12 (2021). https://doi.org/10.3390/MI12091136.
[49] Y. De Hazan, J. Heinecke, A. Weber, T. Graule, High solids loading ceramic colloidal dispersions in UV curable media via comb-polyelectrolyte surfactants, J Colloid Interface Sci 337 (2009) 66–74. https://doi.org/10.1016/J.JCIS.2009.05.012.
[50] Z. Xing, W. Liu, Y. Chen, W. Li, Effect of plasticizer on the fabrication and properties of alumina ceramic by stereolithography-based additive manufacturing, Ceram Int 44 (2018) 19939–19944. https://doi.org/10.1016/J.CERAMINT.2018.07.259.
[51] T. Chen, A. Sun, C. Chu, H. Wu, J. Wang, J. Wang, Z. Li, J. Guo, G. Xu, Rheological behavior of titania ink and mechanical properties of titania ceramic structures by 3D direct ink writing using high solid loading titania ceramic ink, J Alloys Compd 783 (2019) 321–328. https://doi.org/10.1016/J.JALLCOM.2018.12.334.
[52] S. Gražulis, A. Daškevič, A. Merkys, D. Chateigner, L. Lutterotti, M. Quirós, N.R. Serebryanaya, P. Moeck, R.T. Downs, A. Le Bail, Crystallography Open Database (COD): An open-access collection of crystal structures and platform for world-wide collaboration, Nucleic Acids Res 40 (2012). https://doi.org/10.1093/NAR/GKR900.
[53] J.I. Langford, X-ray diffraction procedures for polycrystalline and amorphous materials by H. P. Klug and L. E. Alexander, J Appl Crystallogr 8 (1975) 573–574. https://doi.org/10.1107/S0021889875011399.
[54] D. Jung, S. Hwang, H.J. Kim, J.H. Han, H.N. Lee, Characterization of Porous CuO Films for H2S Gas Sensors, Materials 15 (2022) 7270. https://doi.org/10.3390/MA15207270/S1.
[55] A. Shahzad, S.A. Khan, A. Paksoy, Ö. Balcı-Çağıran, I. Lazoglu, Negative additive manufacturing of Al2O3-Al cermet material by fused deposition and Direct Ink Writing, Mater Today Commun 33 (2022). https://doi.org/10.1016/J.MTCOMM.2022.104739.
[56] D. Schroder, Semiconductor material and device characterization, IEEE Press; Wiley, Piscataway NJ; Hoboken N.J., 2006.

Author contribution:

1. Conception and design of the study

2. Data acquisition

3. Data analysis

4. Discussion of the results

5. Writing of the manuscript

6. Approval of the last version of the manuscript

MA has contributed to: 1, 2, 3, 4, 5 and 6.

SAK has contributed to: 1, 2, 3, 4, 5 and 6.

AS has contributed to: 1, 2, 3, 4, 5 and 6.

AN has contributed to: 1, 2, 3, 4, 5 and 6.

AH has contributed to: 1, 2, 3, 4, 5 and 6.

Acceptance Note: This article was approved by the journal editors Dr. Rafael Sotelo and Mag. Ing. Fernando A. Hernández Gobertti.

Thermo-Mechanical FEM Study of SMAW Parameter Effects in S355J2+N / ASTM A572 Gr.50 Dissimilar Steel Joints

Estudio termomecánico mediante el método de elementos finitos de los efectos de los parámetros de la soldadura SMAW en uniones de aceros disímiles S355J2+N / ASTM A572 Gr.50.

Estudo termomecânico por elementos finitos dos efeitos dos parâmetros de soldagem SMAW em juntas de aços dissimilares S355J2+N / ASTM A572 Gr.50

Syed Farrukh Haider [1], Shaheryar A. Khan [2 (*)], Aqueel Shah [3], Muhammad Nasir Bashir [4], Asif Mansoor [5], Abbas Hussain [6], M. Mahmood Ali [7], Salman Nisar [8]

Recibido: 09/09/2025 Aceptado: 24/11/2025

Summary. - Shielded Metal Arc Welding (SMAW) is widely employed in structural steel fabrication; however, the thermo-mechanical response of dissimilar structural steel joints remains insufficiently explored through numerical modeling. In this study, a three-dimensional transient thermo-mechanical finite element model is developed to investigate SMAW of dissimilar S355J2+N and ASTM A572 Grade 50 steel plates. Goldak's double-ellipsoidal heat source is implemented to represent arc heat input, and a Box–Behnken design is employed to systematically examine the influence of welding current, voltage, and travel speed. The analysis focuses on peak temperature, out-of-plane distortion, and elastic stress indicators derived from a linear thermo-elastic formulation. The results indicate that welding current predominantly governs peak temperature, while travel speed has the strongest influence on thermal gradients and distortion behavior; voltage exhibits a secondary but non-negligible effect on heat distribution. Simulated thermal and deformation trends are benchmarked against published experimental and numerical studies on comparable structural steels and show consistent qualitative behavior. Owing to the absence of plasticity, temperature-dependent material properties, and direct experimental validation, stress results are interpreted solely as qualitative indicators rather than physically realistic residual stresses. The study provides a structured thermo-elastic FEM and design-of-experiments–based sensitivity framework for a dissimilar structural steel combination not previously reported in SMAW numerical studies, offering practical insight into parameter screening for thermal and distortion control in structural steel fabrication.

(*) Corresponding author.

[1] Postgraduate Student, National University of Sciences and Technology (Pakistan), syedhaider270@yahoo.com,
ORCID iD: https://orcid.org/0009-0007-2560-2664

[2] Associate Professor and Head of the Department of Mechanical Engineering., DHA Suffa University (Pakistan), shaheryar.atta@dsu.edu.pk,
ORCID iD: https://orcid.org/0000-0003-1600-7322

[3] Professor, National University of Sciences and Technology (Pakistan), a.shah@smme.nust.edu.pk,
ORCID iD: https://orcid.org/0000-0002-4845-9350

[4] Assistant Professor, National University of Sciences and Technology (Pakistan), mnasir@ceme.nust.edu.pk,
ORCID iD: https://orcid.org/0000-0001-9620-5980

[5] Assistant Professor, National University of Sciences and Technology (Pakistan), asif.mansure@pnec.nust.edu.pk,
ORCID iD: https://orcid.org/0000-0002-2127-0961

[6] Assistant Professor, National University of Sciences and Technology (Pakistan), abbas.hussain@pnec.nust.edu.pk,
ORCID iD: https://orcid.org/0009-0008-1680-6507

[7] Lecturer, Atlantic Technological University (Ireland), Muhammad.Ali@atu.ie,
ORCID iD: https://orcid.org/0000-0001-8236-2459

[8] Assistant Professor, Taibah University (Kingdom of Saudi Arabia), snahmed@taibahu.edu.sa,
ORCID iD: https://orcid.org/0000-0003-4307-6278

Memoria Investigaciones en Ingeniería, núm. 30 (2026). pp. 30-55
https://doi.org/10.36561/ING.30.4
ISSN 2301-1092 • ISSN (en línea) 2301-1106 – Universidad de Montevideo, Uruguay

Keywords: Finite Element Method (FEM); Goldak's double ellipsoidal model; SMAW; Solid Mechanics; Thermal distribution.

Resumen. - *La soldadura por arco metálico protegido (SMAW) se emplea ampliamente en la fabricación de acero estructural; sin embargo, la respuesta termomecánica de las uniones de aceros estructurales disímiles aún no se ha explorado suficientemente mediante modelado numérico. En este estudio, se desarrolla un modelo tridimensional transitorio termomecánico de elementos finitos para investigar la SMAW de placas de acero disímiles S355J2+N y ASTM A572 Grado 50. Se implementa la fuente de calor elipsoidal doble de Goldak para representar el aporte de calor del arco, y se emplea un diseño Box-Behnken para examinar sistemáticamente la influencia de la corriente de soldadura, el voltaje y la velocidad de avance. El análisis se centra en la temperatura máxima, la distorsión fuera del plano y los indicadores de tensión elástica derivados de una formulación termoelástica lineal. Los resultados indican que la corriente de soldadura rige predominantemente la temperatura máxima, mientras que la velocidad de avance tiene la mayor influencia en los gradientes térmicos y el comportamiento de distorsión; el voltaje exhibe un efecto secundario, pero no despreciable, en la distribución del calor. Las tendencias térmicas y de deformación simuladas se comparan con estudios experimentales y numéricos publicados sobre aceros estructurales comparables y muestran un comportamiento cualitativo consistente. Debido a la ausencia de plasticidad, propiedades del material dependientes de la temperatura y validación experimental directa, los resultados de tensión se interpretan únicamente como indicadores cualitativos, en lugar de tensiones residuales físicamente realistas. Este estudio proporciona un marco de sensibilidad termoelástico estructurado basado en el método de elementos finitos (MEF) y el diseño de experimentos para una combinación de aceros estructurales diferentes, no reportada previamente en estudios numéricos de soldadura por arco con electrodo revestido (SMAW). Esto ofrece información práctica para la selección de parámetros para el control térmico y de distorsión en la fabricación de acero estructural.*

Palabras clave: *Método de elementos finitos (MEF); Modelo elipsoidal doble de Goldak; SMAW; Mecánica de sólidos; Distribución térmica.*

Resumo. ***-*** *A soldagem a arco com eletrodo revestido (SMAW) é amplamente empregada na fabricação de aço estrutural; no entanto, a resposta termomecânica de juntas de aço estrutural dissimilares permanece insuficientemente explorada por meio de modelagem numérica. Neste estudo, um modelo tridimensional transiente de elementos finitos termomecânicos é desenvolvido para investigar a soldagem a arco com eletrodo revestido de chapas de aço dissimilares S355J2+N e ASTM A572 Grau 50. A fonte de calor de duplo elipsoide de Goldak é implementada para representar a entrada de calor do arco, e um planejamento Box-Behnken é empregado para examinar sistematicamente a influência da corrente de soldagem, da tensão e da velocidade de deslocamento. A análise concentra-se na temperatura máxima, na distorção fora do plano e nos indicadores de tensão elástica derivados de uma formulação termoelástica linear. Os resultados indicam que a corrente de soldagem governa predominantemente a temperatura máxima, enquanto a velocidade de deslocamento tem a influência mais forte nos gradientes térmicos e no comportamento de distorção; a tensão apresenta um efeito secundário, mas não desprezível, na distribuição de calor. As tendências térmicas e de deformação simuladas são comparadas com estudos experimentais e numéricos publicados sobre aços estruturais comparáveis e mostram um comportamento qualitativo consistente. Devido à ausência de plasticidade, propriedades do material dependentes da temperatura e validação experimental direta, os resultados de tensão são interpretados apenas como indicadores qualitativos, em vez de tensões residuais fisicamente realistas. O estudo fornece uma estrutura de sensibilidade termoelástica baseada no método dos elementos finitos (MEF) e no planejamento de experimentos para uma combinação de aços estruturais distintos, não relatada anteriormente em estudos numéricos de soldagem com eletrodo revestido (SMAW), oferecendo informações práticas sobre a seleção de parâmetros para o controle térmico e de distorção na fabricação de aço estrutural.*

Palavras-chave: *Método dos Elementos Finitos (MEF); Modelo elipsoidal duplo de Goldak; SMAW; Mecânica dos Sólidos; Distribuição térmica.*

1. Introduction. - Welding is one of the most widely used fabrication processes for permanently joining metallic components in structural, pressure vessel, shipbuilding, and repair applications. In fusion welding processes, the joint is formed by localized melting of the base (parent) material with or without the addition of a consumable filler metal, followed by solidification to create a welded joint or weldment [1], [2]. The selection of welding consumables is typically guided by compatibility with the parent materials in order to achieve acceptable metallurgical integrity and mechanical performance of the joint.

Among conventional arc welding techniques, Shielded Metal Arc Welding (SMAW), also referred to as stick welding, remains one of the most versatile and widely adopted processes due to its simplicity, portability, and applicability in both indoor and outdoor environments. SMAW is extensively employed in construction, shipbuilding, maintenance, and repair industries. In this process, an electric arc is established between a flux-coated consumable electrode and the workpiece, generating the heat required for melting the base metal and filler material. The decomposition of the flux coating produces shielding gases and slag, which protect the molten weld pool from atmospheric contamination such as oxygen and hydrogen, thereby reducing defects such as porosity and cracking [2–4]. A schematic representation of the SMAW process and its associated heat source modeling framework is shown in Fig. 1. The figure illustrates the interaction between the welding arc, consumable electrode, base metals, and the implementation of the moving heat source within the finite element domain.

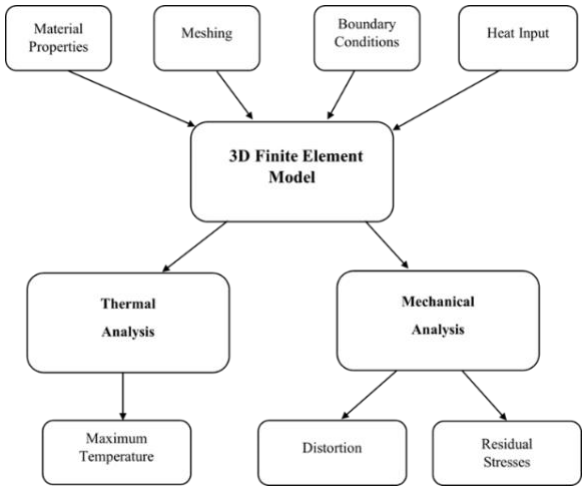

Figure I. Schematic representation of the Shielded Metal Arc Welding (SMAW) process and numerical modeling framework adopted in the present study. [4].

Despite its widespread industrial use, SMAW involves highly localized and transient thermal cycles that induce steep temperature gradients within the weldment. These thermal gradients, in turn, govern the evolution of microstructure, distortion, and residual stresses, which critically influence the dimensional accuracy and service performance of welded components. As a result, understanding the influence of welding parameters, such as current, voltage, and travel speed, on thermal and mechanical responses remains a central concern in welding science and engineering.

In recent decades, finite element modeling (FEM) has emerged as a powerful tool for analyzing welding processes, offering detailed insight into transient temperature fields, deformation behavior, and stress development that are difficult to measure experimentally. Numerous studies have investigated the effects of welding parameters on similar and dissimilar materials using both experimental and numerical approaches.

Table I summarizes representative experimental and numerical studies investigating the influence of welding parameters on thermal, mechanical, and metallurgical responses for various arc welding processes and materials [4–40].

	Author(s)	Welding Process	Material	Findings
1	M. E. Aalami-Aleagha et al [4]	SMAW	Steel pipe API 5L grade	Moderate Current produced optimum hardness.
2	Hunchul Jeong et al. [5]	GTAW	Aluminum A16061	reverse polarity produced more heat input than straight polarity.
3	Chao Wang et al. [6]	GMAW	SM400A	Residual stresses more with welding increased local heating and cutting.
4	Dong Ho Bae et al. [7]	GTAW	SUS304L	Longitudnal Residual Stress = 300 MPa; wider stress zones obtained with double ellipsoid model than ramp heat input model.
5	Chang-Sung Seok et al. [8]	MIG	High tensile steel H-plate	Maximum tensile residual stress found at center of thickness.
6	Chang-Sung Seok et al. [9]	GMAW	Steel Pipe	C-seam weldment on pipe produced larger longitudinal bending deformation than the L-seam pipe.
7	Dong-Yoon Kim et al. [10]	GMAW	Hot press forming steel sheets	Low Wire feed speed produced and current produced high tensile strength.
8	Yong Hua Shi et al. [11]	K-TIG	Q345	Segmentation LSTM Model has 95.2% accuracy to recognize the weld penetration state.
9	Zeng Liu et al. [12]	GMAW	High nitrogen and martensitic low alloy steel	ER 307Mo filler metal produced lower porosity and optimum joint strength as compared to ER 2209 and ER 120 S-G.
10	M. Mazar Atabaki et al. [13]	HLAW	High strength quenched and tempered steel	Stand-off distance had more impact on weld quality and penetration as compared to welding speed and power.
11	Qiang Lang et al. [14]	TIG	Transformation induced plasticity (TRIP) Steel	Addition of Laser to low current TIG increased weld depth and changed the fracture form from brittle to ductile.
12	Guoqing Wu et al. [15]	Tungsten-Argon Welding	LA141 alloy plates	With argon protection device and homogenous welding wires, the tensile strength increased to 124 MPa i.e 95% of base metal and microhardness improved.
13	A. G. Kamble et al. [16]	GMAW	AISI 321 SS plates	Bead penetration is increased with an increase in speed, gas flow rate, and wire feed rate.
14	Rohit Jha et al. [17]	TIG	MS	Maximum tensile strength at the highest current of 110 A and a welding speed of 157.80 mm/min.
15	Afnan Dadi et al. [18]	SMAW	MS SA-516 Gr. 70	Highest tensile strength obtained at a current of 120 A.
16	R. A. Mohammed et al. [19]	SMAW	Medium Carbon Steel	Highest hardness and tensile strength but lower impact strength obtained at HAZ than weldment and parent metal.
17	Brijesh Sharma et al. [20]	SMAW and GMAW	MS 2062	Maximum penetration and optimum bead obtained with SMAW, at current = 100 A, voltage = 24 V and arc length = 3mm, as compared to GMAW.
18	Asibeluo et al. [21]	SMAW	A-36 steel	Highest hardness of 114 HB was obtained at lowest current of 70 A.
19	J.O. Olawale et al [22]	SMAW	Low carbon steel	Increase in current increased the tensile strength and hardness but reduced impact strength.
20	Abhishek Shukla et al. [23]	SMAW	AISI 1020	RSM and experimental results are closer and maximum current of 120 A provided the highest tensile strength of 259 MPa.

21	Randy Chiong et al. [24]	SMAW	AISI 1018	Maximum hardness and tensile strength, 452 MPa and 195 HV, respectively, obtained at highest current.
22	Deepak Pathak et al. [25]	SMAW	Low carbon steel	Highest tensile strength observed at DCEN polarity and highest current.
23	S.H. Zoalfakar et al. [26]	SMAW	ST 37/2, ST 44/2, and ST 52/3 steel plates	Increasing Carbon equivalent (C.E) % and groove angle, increased the tensile strength and hardness.
24	Edi Widodo et al. [27]	SMAW	SS AISI 304	Highest tensile strength of 632 MPa obtained at highest current of 90 A.
25	Dhananjay Kumar et al. [28]	TIG and SMAW	SS 304L	Distortion of TIG was lesser as compared to SMAW.
26	A.K. Rude et al. [29]	SMAW	MS	Micro hardness decreases with increase in welding current but increases with number of layers.
27	Rajiv Selvam et al. [30]	SMAW	Carbon steel pipes	E- 6010 and E-7018 filler metals produced greater hardness, ductility, and toughness as compared to E-7010 and E-7018.
28	L. S. Sisira K Weerasekralage et al. [31]	SMAW	MS	Highest weldment quality obtained with current of 123 A, voltage of 27 V, and 60 º included angle.
29	Digambar Benne et al. [32]	SMAW	MS	With increase in current, voltage, and speed, the hard-faced part's hardness and impact strength was increased.
30	Talabi et al. [33]	SMAW	Low carbon steel	Increase in current and voltage increased the tensile strength and yield strength but reduced the hardness.
31	U.S. Patil et al. [34]	SMAW	SS 304 and MS 1018	With the current = 85 A, welding speed = 8 mm/s, electrode angle of 30 º, and root gap of 0.75 mm. the highest tensile strength of 403 N/mm^2 is obtained.
32	Mahmud Khan et al.[35]	SMAW and TIG	SS AISI 304 and MS AISI 1020	TIG produced the highest tensile strength, % elongation and yield strength as compared to SMAW.
33	Mauricio Andres Rojas Nova et al. [36]	SMAW	A 36 Steel	Increase in travel speed decreases the maximum temperature. Optimum welding speed is obtained when temperature of source produces temperature just above the melting point of base metal.
34	M Matuszewski [37]	TIG and MIG	Aluminum alloy 6060 sheet	TIG with argon shielded with addition of metallic wire; MIG determined the fusion zone of sheets.
35	Sajeeb A.M. [38]	TIG	Aluminum alloy 6061-T6	Weld penetration was increased by increase in current and deacrease in stand-off distance. Current is found to be the most significant parameter.
36	A. Boudiaf et al. [39]	GTAW	AISI 316L	The highest temperature was observed at the ceneter of the source; 2D model is closer to experminetal results.
37	Cronje M [40]	SMAW	MS	Maximum distortion observed at the edge of geometry due to less heat dissipation and decreasing heat sink effect.

Table I. Examples of welding parameters' effect on Steel Specimen from Literature.

Across these studies, welding current is consistently reported as the dominant parameter governing heat input, with higher currents leading to increased peak temperatures, deeper penetration, and enhanced hardness or tensile strength in carbon and structural steels [4, 14, 18–24, 33]. Welding voltage primarily influences arc stability and bead geometry, indirectly affecting thermal distribution and residual stress development [3, 17, 20]. In contrast, welding travel speed is repeatedly shown to act as a controlling parameter for heat input density, where increased speed reduces peak temperature, limits fusion zone width, and mitigates distortion and residual stress accumulation [25, 33, 37, 40]. Several studies further highlight that excessive heat input, while improving penetration, can adversely increase distortion and tensile residual stresses, emphasizing the need for balanced parameter selection [6, 9, 28]. Despite these advances, the majority of reported investigations focus on similar material joints or experimental optimization, with comparatively fewer studies addressing three-dimensional transient thermo-mechanical modeling of dissimilar structural steel welds using systematic DOE-based sensitivity analysis.

However, a careful examination of the existing literature reveals two important gaps. First, while extensive work exists on SMAW of carbon steels, stainless steels, and aluminum alloys, numerical investigations focusing specifically on dissimilar structural steel combinations remain limited. Second, although response surface methodologies (RSM) and design of experiments (DOE) techniques have been successfully applied to welding processes, their integration with three-dimensional transient thermo-mechanical FEM for SMAW remains relatively underexplored, particularly for dissimilar steel joints.

Notably, to the best of our knowledge, no prior numerical study has reported on SMAW welding between S355J2+N and ASTM A572 Grade 50 structural steel plates, despite the widespread industrial use of both materials in load-bearing applications. These steels are commonly employed in construction and infrastructure projects, where dimensional stability and thermal distortion control are critical. Understanding the sensitivity of their thermo-mechanical response to welding parameters is therefore of practical importance.

In this study, a three-dimensional transient thermo-mechanical finite element model of the SMAW process for dissimilar S355J2+N / ASTM A572 Gr.50 steel plates is developed using COMSOL Multiphysics. Goldak's double-ellipsoidal heat source formulation is employed to represent the arc heat input. A Box–Behnken design (BBD) is adopted to systematically investigate the effects of welding current, voltage, and travel speed on key response variables, namely maximum temperature, distortion, and elastic stress indicators. Regression and analysis of variance (ANOVA) techniques are used to quantify the relative influence of process parameters and to identify dominant trends in the thermo-mechanical response.

The novelty of the present work does not lie in proposing a new welding model, but rather in providing a systematic thermo-elastic and DOE-based sensitivity assessment for a dissimilar structural steel joint that has not been previously reported in SMAW numerical studies. The results offer quantitative insight into the relative importance of welding parameters on thermal and distortion behavior, thereby providing a parameter-screening framework that can assist in distortion control and process planning for structural steel fabrication.

2. Research Methodology. –

2.1 Materials Selection and Geometry. - There are two different materials in this research for welding simulation which include S355J2+N and ASTM A572 Gr.50 structural steel plates. The filler material has been assumed to be one of the base metals i.e., S355J2+N. Table II shows the material properties and chemical composition of metals. The material properties were adopted from published literature and standard material databases commonly used in numerical welding simulations [36], [37], [40]. The thermal conductivity and specific heat capacity were adopted from the standard steel material library available in COMSOL Multiphysics and commonly used literature sources. At the same time, density values were taken from experimentally reported ranges for the selected steels. In the present study, all thermal and mechanical properties were assumed to be temperature-independent. This simplification was adopted to focus on the comparative influence of welding parameters on thermal distribution and deformation, while

maintaining reasonable computational efficiency. Although temperature-dependent properties are known to influence residual stress development, their inclusion was beyond the scope of the current thermo-elastic framework.

Material	Material Properties			Chemical Composition				
	Young's Modulus (GPa)	Density ($\frac{Kg}{m^3}$)	Poison ratio	C	Mn	P	S	Si
S355J2+N	200	7700 to 8030	0.3	0.22	1.60	0.035	0.035	0.55
ASTM A572 Gr. 50	190 - 210	7800	0.27-0.30	0.23	1.35	0.030	1.03	0.40

Table II. Material Properties and Chemical Composition of Metals.

The joint geometry of the dissimilar metals is shown in Figure 2. As per ISO-9692, the joint preparation of structural steel plates was carried out on AutoCAD 2021 and 3D design was made on SolidWorks 2016.

The 2D model was designed keeping in view the recommended root gap, root face, material thickness, and bevel angle. (Figures II(a) and II(b)) shows that the geometry consists of a root gap of 3 mm, a root face of 3 mm, and an included angle of 60 °. The dimensions are given in millimeters.

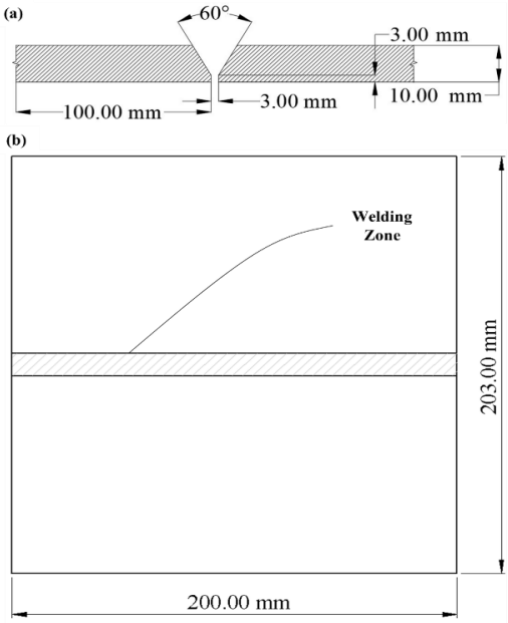

Figure II. Three-dimensional finite element model of the dissimilar S355J2+N / ASTM A572 Gr.50 butt joint used for thermo-mechanical simulation. [43]

2.2 Heat Source Modelling. - The current simulation work involves the use of Goldak's double ellipsoidal heat source model for simulating the SMAW process to provide a real-life experimental experience. This model is based on the Gaussian distribution of power density and offers versatility to both deep and shallow penetration welds. The heat source model has a steeper thermal gradient at the front and slightly steeper at the rear side of the ellipsoid [44], [45].

In cartesian coordinates, the power density distribution for the front and rear is given as follows [46]:

The distribution for the front quadrant:

$$q_f(x,y,z,t) = \frac{6\sqrt{3}f_f Q}{abc_f \pi\sqrt{\pi}} exp\left\{-3\left(\frac{x^2}{a^2} + \frac{y^2}{b^2} + \frac{(z+vt)^2}{{c_f}^2}\right)\right\} \quad [1]$$

Likewise, for the rear quadrant:

$$q_r(x,y,z,t) = \frac{6\sqrt{3}f_r Q}{abc_r\pi\sqrt{\pi}} exp\left\{-3\left(\frac{x^2}{a^2} + \frac{y^2}{b^2} + \frac{(z+vt)^2}{{c_r}^2}\right)\right\} \quad [2]$$

where, x, y, and z are the local spatial coordinates.

$$Q = \eta V I \quad [3]$$

where V is the Voltage (V), I is the current (A), and η is the thermal efficiency (%).

The product of the voltage (V), current (I), and thermal efficiency (η), is typically 80% for SMAW, which means that power provided by the welding source is 80% converted to the thermal energy required for welding. ν is the welding speed and t is the present time.

The f_f and f_r are the heat fraction parameters for the front and rear quadrants respectively, and their sum is equal to two. The recommended values stated by Goldak et al. (1984) are f_f = 0.6 and f_r = 1.4.

The thermal analysis of the 3D model involves the most important factor known to be the conservation of energy.

The governing equation related to transient heat transfer analysis in welding is denoted by (Equation [3]) [47].

$$\rho c \frac{\partial T}{\partial t}(x,y,z,t) = \nabla.\vec{q}(x,y,z,t) + Q(x,y,z,t) \quad [4]$$

where, ρ is the density of materials ($\frac{Kg}{m^3}$), c is the specific heat capacity, T is the current temperature, $\vec{q}$ is the flux vector, Q is the internal rate of heat generation, x, y, and z are the coordinates in the reference system, and t is time.

It is assumed that there will be radiation losses from the outer surface of the plates by both, convection, and radiation. The heat losses will be prominent around and in the weldment via radiation whereas the area away from the weld zone will experience heat loss through convection [48], [49]. Hence, a combined heat transfer coefficient is used and computed from (Equation [5]) [50].

$$\tilde{h} = \frac{\varepsilon_{em}\sigma_{bol}\left((T+273)^4 - (T_{amb}+273)^4\right)}{(T-T_{amb})} + h_{con} \quad [5]$$

where, $\tilde{h}$ is the combined heat transfer coefficient, ε_{em} is the emissivity σ_{bol} the Stefan Boltzmann constant, T_{amb} is the ambient temperature, and h_{con} is the convective heat transfer coefficient.

The parameters in the 3D double ellipsoidal model are given in the following Table III and the welding parameters in Table IV. Goldak's double ellipsoidal 3D heat source model is validated with the experimental results obtained by Christensen et al [50].

Parameters	**Value**	
Length of the front ellipsoid	c_f	12.9 mm
Length of the rear ellipsoid	c_r	10.3mm
Depth of penetration	b	3 mm
Width of heat source	a	8 mm
Front heat fraction	f_f	0.6
Rear heat fraction	f_r	1.4

Table III. Double ellipsoidal heat source parameters [51].

Welding Parameters	Values			
Arc Voltage	V	22 V	24 V	26 V
Current	I	120 A	140 A	160 A
Welding Speed	vel	3 mm/s	5 mm/s	7 mm/s
Heat Source Efficiency	η	80%		

Table IV. Welding Parameters for SMAW [39].

2.3 Design of Experiments (DOE). - The excessive current and voltage during the welding process may induce stresses and distortion in the welding geometry along with other defects. Also, the lower current and voltage settings may result in incomplete joint penetration and more spatter. Moreover, slow welding speed leads to concentrated heat input at a particular weld location which causes distortion. On the other hand, the fast-welding speed leads to incomplete weld penetration but less distortion. These effects cause weak welding strength and poor weld quality.

To cater to this issue, the process parameters require optimization either via several experiments or through a parametric numerical simulation. So, the simulation tool for analysis and optimization of SMAW process parameters is to be used. Therefore, a 3D simulation of weld geometry with modules coupled (Heat transfer with Solid Mechanics) in COMSOL Multiphysics 5.5 simulation software is built for the present study.

The Box-Behnken Design (BBD) is a form of response surface methodology (RSM) that requires at least three levels to run a single experiment. In this study, the three-level-three-factor BBD technique was applied to obtain the best combination of welding variables for the sound quality of the weld [52], [53], [54], [55], [56]. Table V represents the chosen welding variables along with their levels.

Order No.	LEVELS USING BBD			ACTUAL VALUES		
	V	I	vel	V	I	vel
	-1	-1	0	22	120	0.005
	-1	1	0	22	160	0.005
	1	-1	0	26	120	0.005
	1	1	0	26	160	0.005
	-1	0	-1	22	140	0.003
	-1	0	1	22	140	0.007
	1	0	-1	26	140	0.003
	1	0	1	26	140	0.007
	0	-1	-1	24	120	0.003
	0	-1	1	24	120	0.007
	0	1	-1	24	160	0.003
	0	1	1	24	160	0.007
	0	0	0	24	140	0.005
	0	0	0	24	140	0.005
	0	0	0	24	140	0.005

Table V. Assigning Levels to the Process Parameters.

There are three levels i.e., -1, 0, and 1 for each parameter which corresponds to the lowest level, central level, and the highest level of parameter values. Table V shows 15 different combinations of input process parameters with the levels assigned and the actual values of the input parameters.

2.4 Simulation Procedure. - The 3D graphical model of the welded joint was developed in SOLIDWORKS 2016 and imported into COMSOL Multiphysics 5.5 for the thermo-mechanical simulation of the SMAW process. The geometry consists of two steel plates (S355J2+N and ASTM A572 Gr.50) and a central weld region configured as a Single-V groove butt joint, following ISO-9692 recommendations for joint preparation [43].

The Heat Transfer in Solids and Solid Mechanics physics interfaces were applied in a coupled manner to capture both the transient thermal response and the resulting elastic deformation. Goldak's double-ellipsoidal heat source formulation was implemented according to the procedure described in [44–46], and the associated welding parameters are summarized in Table VI. The initial temperature was set at 25 °C, and heat losses from external surfaces were treated using convection and radiation boundary conditions based on the methodology described in [48–50]. The total heat input was calculated using the arc efficiency for SMAW reported in [51].

Parameter	Value	Description
x0	-0.10 m	Heat source center x-coordinate
y0	0 m	Heat source center y-coordinate
z0	-0.002 m	Heat source center z-coordinate
vel	0.003 m/s	Welding speed
V	22 V	Welding voltage
I	120 A	Welding current
u	0.8	Weld efficiency
af	0.0129 m	Length of front ellipsoidal
ar	0.0103 m	Length of rear ellipsoidal
b	0.003 m	Depth of penetration
c	0.005 m	Width of heat source
Ff	0.6	Heat fraction (front)
Fr	1.4	Heat fraction (rear)
cf	0.0129 m	Front length of the weld pool
cr	0.0103 m	Rear length of the weld pool
Q	3200	Heat input

a	0.008 m	Weld width/2
q01	1.1574×10^{10}	Power density Distribution for the front part
q02	3.3823×10^{10}	Power density distribution for the rear part
p	1.0133×10^{8} Pa	Pressure

Table VI. Defining the parameters for the 3D geometry.

The resulting transient temperature field was then used as a thermal load in the structural analysis. All materials were modelled as linear elastic, consistent with the simplified thermo-elastic welding models commonly reported in earlier studies [57], [58]. Temperature-dependent mechanical properties, plasticity, creep, and phase transformation effects were not included, and therefore the mechanical results represent elastic strain-based indicators of deformation rather than true physical residual stress magnitudes. Accordingly, the von Mises stress values are interpreted only for comparative analysis between welding conditions, not as actual residual stresses.

A free boundary condition was applied to allow unconstrained deformation of the plates. No external clamps or fixtures were used. The absence of mechanical constraints allows free distortion and therefore represents an upper-bound estimate of deformation, while constrained welding conditions would be expected to reduce out-of-plane displacement but increase residual stresses.

The simulation was run as a time-dependent study from 0 to 67 s, corresponding to the weld-travel time at 0.003 m/s, while higher speeds (0.005 and 0.007 m/s) reduced the welding duration to approximately 40 s.

The mesh was generated using physics-controlled tetrahedral elements, with refinement along the weld line to capture steep thermal gradients. This meshing strategy follows recommendations in prior finite element welding simulations [36], [37], [40]. Figure 3 shows the final meshed geometry.

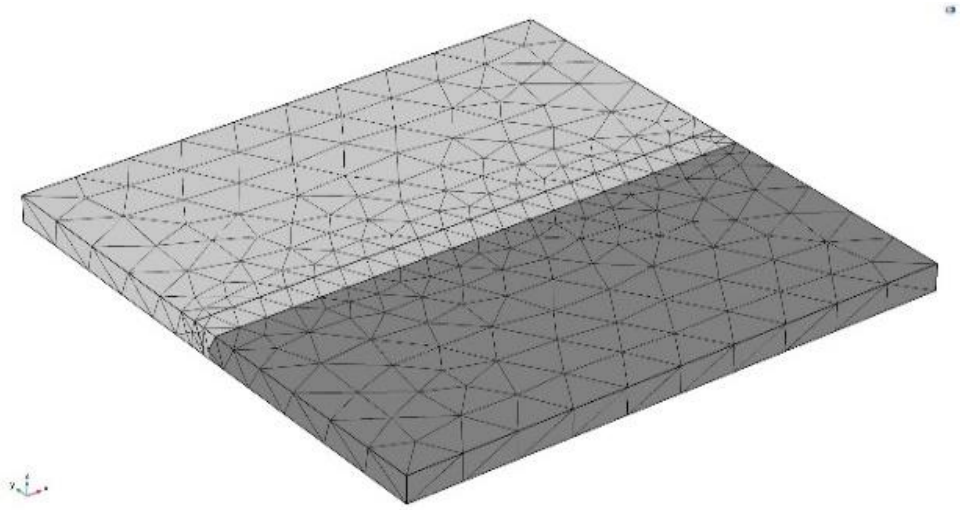

Figure III. Meshing strategy employed for the SMAW numerical model

In this study, the simulation time range was set from 0 to 67 s with a time step of 0.05 s. At a welding speed of 0.003 m/s, the 200 mm weld length requires approximately 67 s for completion in a single pass. At higher speeds of 0.005 m/s and 0.007 m/s, the same weld length is completed in approximately 40 s.

2.5 Temperature Profiles. - Figure 4 illustrates the evolution of the temperature field as the Goldak double-ellipsoidal heat source moves along the weld line in the x-direction. Welding begins from the left-hand side of the joint, and the transient temperature contours at four representative times (t = 15 s, 25 s, 30 s, and 35 s) are shown in Figures 4(a–d). The highest temperatures occur in the weld pool and the immediate heat-affected zone, while temperatures decrease rapidly away from the heat source due to conduction and surface heat losses.

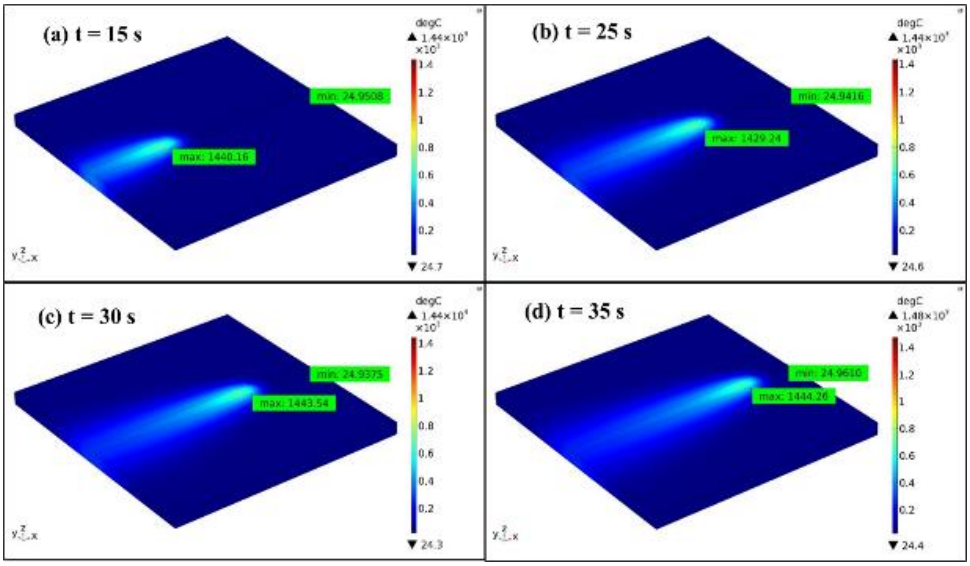

Figure IV. Goldak double-ellipsoidal heat source representation used to model arc heat input in the SMAW process (a) t = 15s, (b) t = 25s, (c) t = 30s, (d) t =35s.

Figures 5(a) and 5(b) present the temperature distribution along the depth (z-axis) and the transverse direction (y-axis), respectively. As expected, the temperature decreases with depth below the weld centerline and laterally across the plate thickness. Once the local temperature exceeds approximately 1425 °C, melting initiates, and the weld metal begins to form the fusion bond at the joint interface.

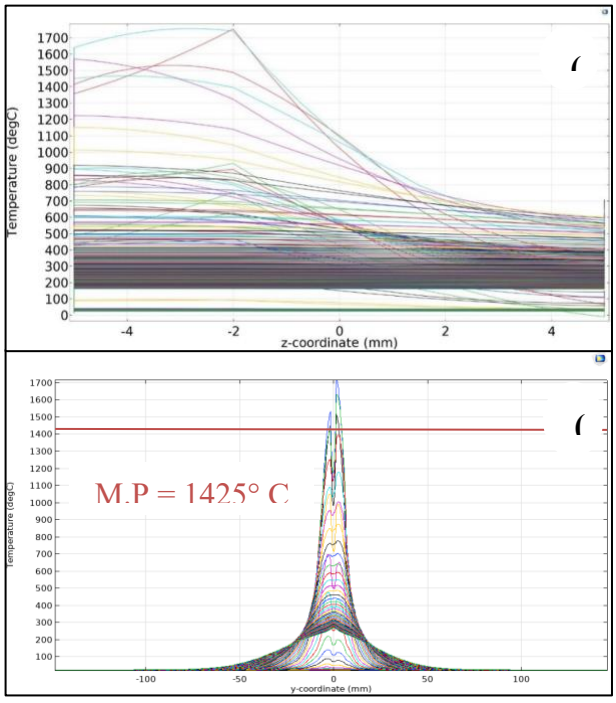

Figure V. Transient temperature distribution. (a)Temperature vs Z-coordinate, and (b) Temperature vs Y-coordinates.

2.6 Structural Stresses and Deformation. - Figures 6(a) and 6(b) present the elastic von Mises stress indicator obtained from the thermo-elastic structural model. As noted earlier, the mechanical analysis was performed using linear-elastic material behaviour; therefore, the reported von Mises values represent qualitative elastic stress indicators rather than physical residual stress magnitudes. These indicators highlight regions where the thermal cycle generates high elastic strain and provide insight into the relative stress distribution during and immediately after welding.

Elevated elastic stress indicators appear near the weld centerline, where the material experiences the largest thermal gradients and volumetric expansion. Away from the weld pool, the indicator decreases rapidly as the temperature field becomes more uniform. Along the transverse (y-axis) direction, the maximum indicator occurs near the weld centerline, while along the longitudinal (x-axis) direction the distribution varies with the non-uniform heat input and the progression of the heat source. These trends are shown in Figures 7(a) and 7(b).

The deformation field resulting from thermal expansion and subsequent cooling is shown in Figures 8(a–c). The predicted distortion reflects the accumulated elastic strains, with maximum displacement occurring near the edges and corners of the welded plates. The Z-component displacement illustrates upward bending near the weld region, which is consistent with typical distortion behavior in butt-welded joints subjected to steep temperature gradients.

These qualitative results demonstrate how variations in heat input influence the overall deformation pattern. While quantitative residual stress predictions require elastic–plastic, temperature-dependent modelling, the present thermo-elastic simulation provides useful comparative insight into the effect of welding parameters on the distribution and magnitude of elastic strain and distortion.

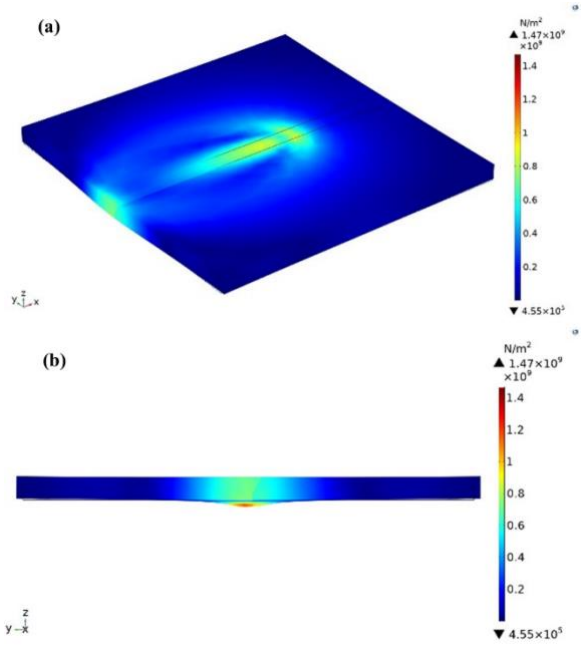

Figure VI. Elastic von Mises stress indicator distribution obtained from the linear thermo-elastic structural model at V = 24 V, I = 150 A, and welding speed = 0.004 m/s at t = 14 s: (a) y–z plane section through the weld centerline; (b) isometric view. The plotted values represent qualitative elastic stress indicators and do not correspond to true residual stresses.

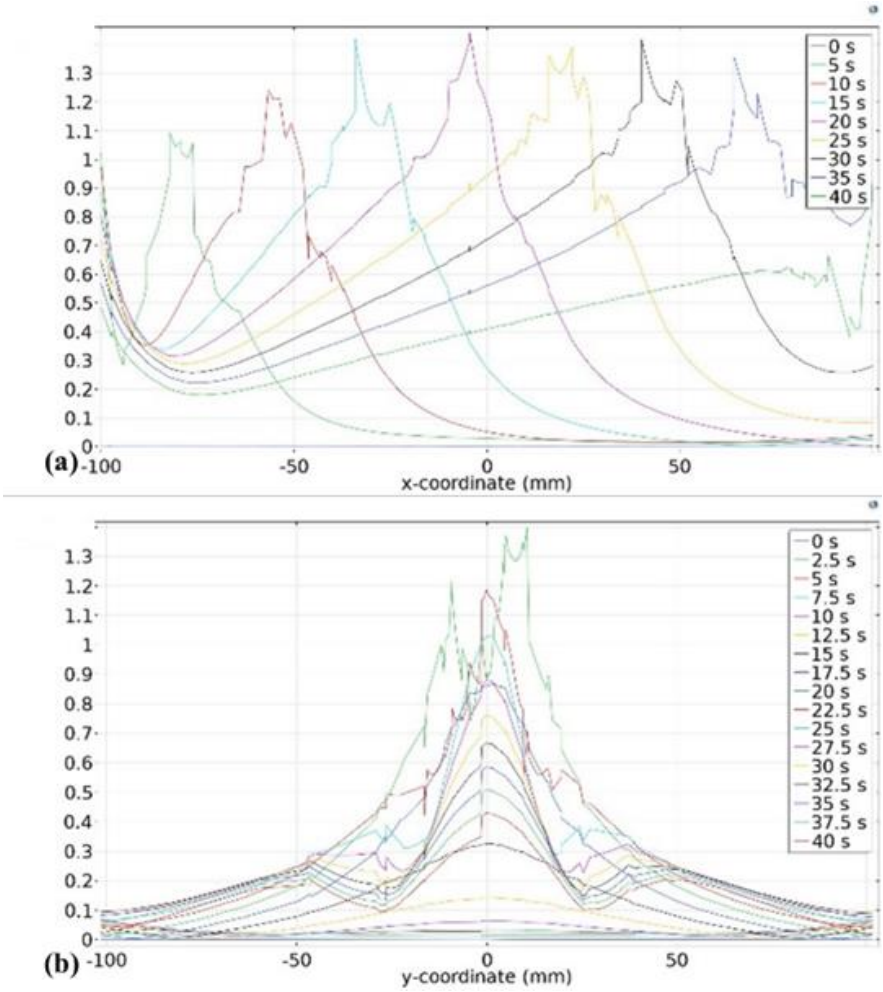

Figure VII. Distribution of the elastic von Mises indicator along (a) the longitudinal (x) direction and (b) the transverse (y) direction relative to the weld centerline.

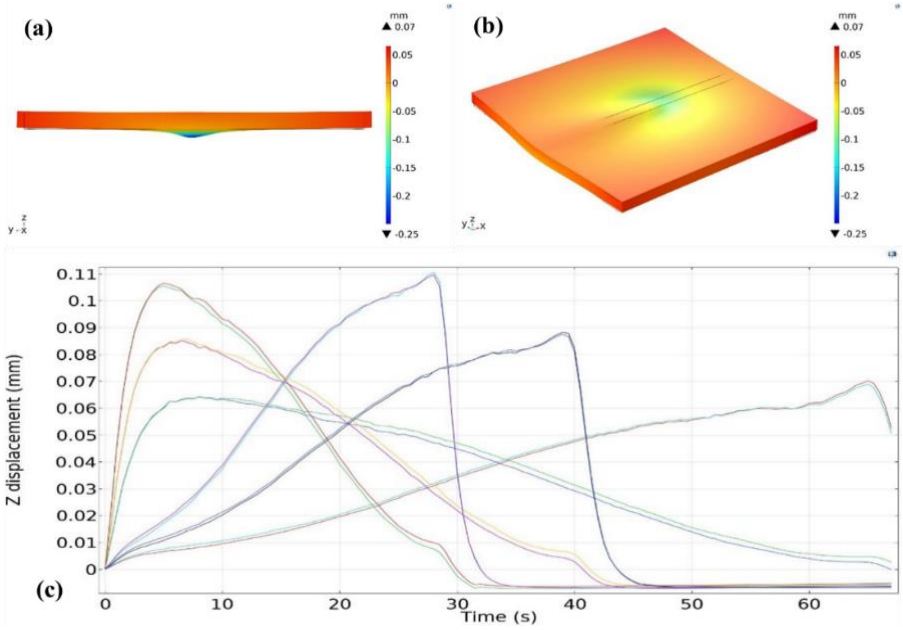

Figure VIII. Predicted displacement field from transient thermal loading: (a) global displacement magnitude, (b) isometric view of deformation, (c) Z-component displacement illustrating out-of-plane distortion after cooling.

3. Results and Discussion. -

3.1 Design of Experiments and Statistical Modelling. - A Box–Behnken Design (BBD) with three factors and three levels was employed to evaluate the influence of welding voltage, current, and welding speed on the thermo–mechanical responses of the welded joint. Multiple regression analysis was conducted following the procedures described in [59], using the response data summarized in Table VII.

Because the structural model was linear-elastic, the von Mises output (Res_Str) represents an elastic stress indicator rather than a physical residual stress. Therefore, quantitative regression and ANOVA were performed only for the physically meaningful responses, namely the Z-displacement (Td) and the maximum temperature (T_max). The elastic stress indicator (Res_Str) is retained in Table VII for qualitative comparison only and was not used to develop empirical equations.

A general parametric relationship of the form presented below was fitted to the log-transformed data for Td and T_max:.

$$Y_i = b_{0i} + b_{1i}X_1 + b_{2i}X_2 + b_{3i}X_3 \quad [6]$$

where Y_i corresponds to log(Td) or log(T_max), $X_1 = log(V)$, $X_2 = log(I)$, and $X_3 = log(vel)$.

A log-linear model of the form shown in Equation [6] was fitted to log-transformed responses, where the predictors correspond to log(V), log(I), and log(vel). The regression coefficients were estimated using Microsoft Excel based on the approach in [59].

Order No.	Levels Defined			Actual Values			Response Parameters		
	V	I	vel	V	I	vel	Res_Str (GPa)	Td (mm)	T_max (°C)
1	-1	-1	0	22	120	0.005	3.581E+09	0.0679	1090.2
2	-1	1	0	22	160	0.005	4.638E+09	0.0939	1585
3	1	-1	0	26	120	0.005	3.122E+09	0.0805	1334.9
4	1	1	0	26	160	0.005	1.468E+09	0.0486	2506.5
5	-1	0	-1	22	140	0.003	1.722E+09	0.062	2538.8
6	-1	0	1	22	140	0.007	1.13E+09	0.0573	1924.7
7	1	0	-1	26	140	0.003	1.679E+09	0.0555	3044.9
8	1	0	1	26	140	0.007	5.578E+09	0.0942	1500.8
9	0	-1	-1	24	120	0.003	2.32E+09	0.07	1994.7
10	0	-1	1	24	120	0.007	3.094E+09	0.0738	1103.7
11	0	1	-1	24	160	0.003	2.702E+09	0.0544	3494.1
12	0	1	1	24	160	0.007	3.315E+09	0.0992	1618.6
13	0	0	0	24	140	0.005	5.912E+09	0.0885	1488.2
14	0	0	0	24	140	0.005	5.912E+09	0.0884	1483.1
15	0	0	0	24	140	0.005	5.912E+09	0.0894	1489.3

Table VII. BBD Design and Output response values of Residual Stress (Res_Str), Displacement (Td), and Maximum Temperature (T_max)

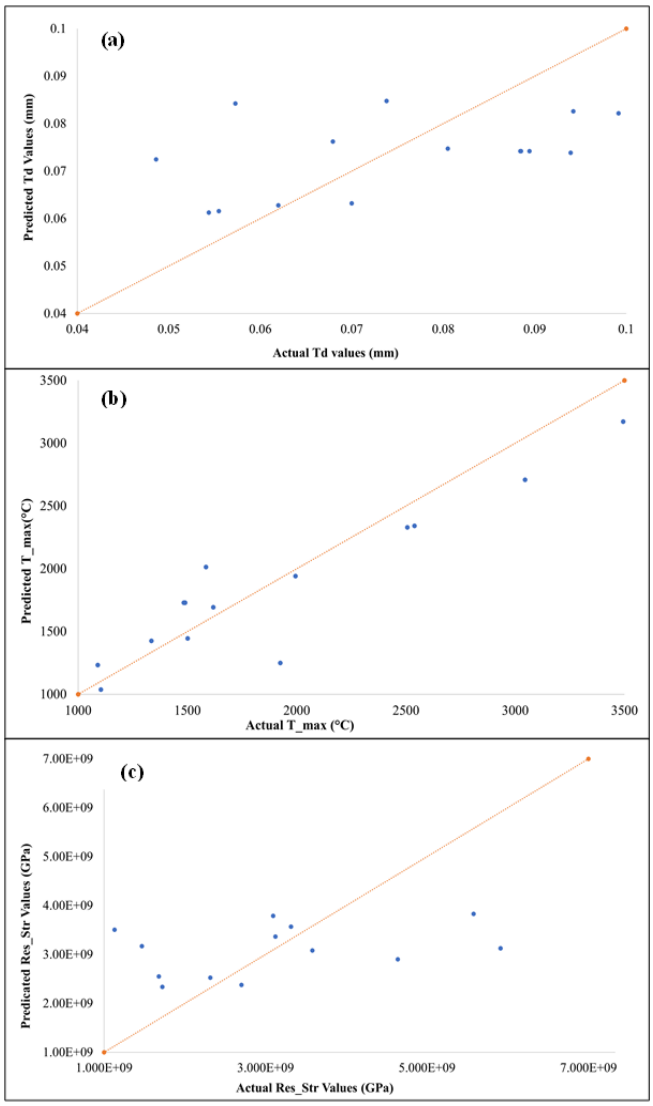

Figure IX. Scatter plots comparing actual and predicted responses for (a) distortion (Td) and (b) maximum temperature (T_max) based on log-linear regression models. The elastic stress indicator (Res_Str) is shown for completeness but was not used for regression analysis.

The regression results are summarized in Table VIII. The scatter plots of actual versus predicted values for Td and T_max are shown in Figures 9(a–b), demonstrating reasonable agreement between the predicted and observed responses, consistent with the use of log-transformed linear models [61–64].

	log Res_Str		log Td		log T_max	
Source	F-value	p-value	F-value	p-value	F-value	p-value
Model	0.3441	0.0535	1.1130	0.9738	13.0007	0.0477
log V	-	0.8352	-	0.9072	-	0.2897
log I	-	0.8879	-	0.8514	-	0.0031
log vel	-	0.3467	-	0.0971	-	0.0005
R-sq	0.0858		0.2328		0.7800	
R-sq (adj)	-0.1635		0.0236		0.7200	

Table VIII. ANOVA results for log Res_Str, log Td, and log T_max

The low R^2 value for Td indicates that a first-order log-linear model is insufficient to fully capture deformation behaviour, which is influenced by geometric stiffness and boundary effects beyond primary process parameters. The ANOVA results indicate that welding current exhibits the strongest statistical influence on T_max, as evidenced by the lowest p-value, followed by welding speed and voltage. For Td, the p-values are comparatively higher, indicating weaker explanatory power. This aligns with the sensitivity considerations described widely in welding DOE literature [65–69], in which T_max is generally more sensitive to heat-input variations than displacement.

Because Res_Str is an elastic indicator and not a physical residual stress, no empirical equation or sensitivity expression is provided for that quantity.

A formal optimization or multi-objective decision-making procedure was not performed; therefore, the results are interpreted as parametric trends rather than optimized welding conditions.

3.2 Thermal Response. - Figures 10(a) and 10(b) illustrate the maximum temperature variation along the weld line (x-axis) and through the depth (z-axis). The temperature rises rapidly once the arc initiates, reaches a peak sufficient for melting and fusion, and fluctuates slightly along the x-direction due to the evolving heat-sink effect of the surrounding base metal. Along the z-axis, the temperature decreases with depth as heat is conducted away from the active fusion zone. These thermal cycles govern melting, fusion, and the subsequent development of distortion.

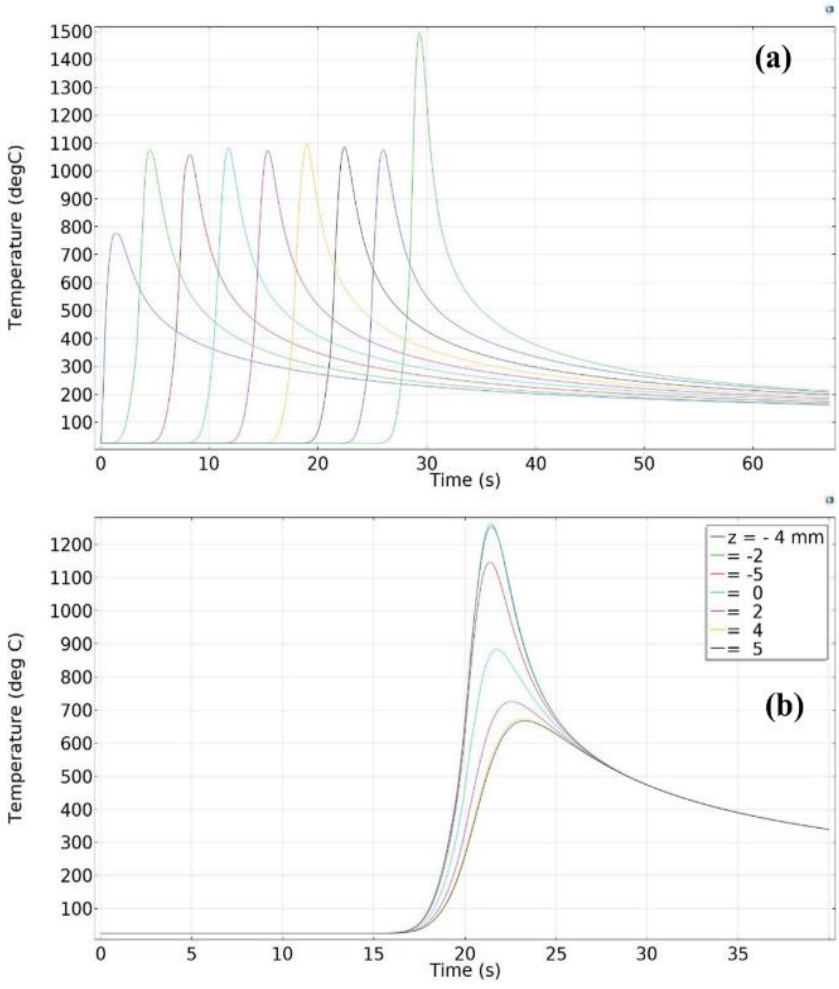

Figure X. Variation of maximum temperature (T_max) along (a) the weld line (x-axis) and (b) through the plate thickness (z-axis) during welding.

The thermal expansion and contraction associated with the heating and cooling cycle induce elastic strain fields, which are represented by the elastic von Mises indicator (Res_Str). As discussed earlier, this quantity does not represent true residual stress but provides a qualitative map of regions experiencing higher thermo-elastic loading during welding. Distortion (Td) reflects the cumulative effect of these elastic strains and the steep temperature gradients in the joint. Minimizing weld volume, optimizing heat input, and controlling inter-pass timing are common methods for reducing distortion in welded joints, as reported in previous studies [70], [71]. These general concepts are consistent with the qualitative trends observed in the present thermo-elastic model.

3.3 Heat Source benchmarking. - The Goldak double-ellipsoidal volumetric heat source implemented in this study was benchmarked by examining the thermal field behaviour, fusion-zone dimensions, and the temperature-time response at points adjacent to the weld line. The objective was to ensure that the implemented heat input parameters reproduced the characteristic features of SMAW thermal behaviour reported in the literature.

Figure IV shows the transient thermal distribution as the heat source travels along the weld line. The predicted peak temperatures exceed the melting range of the steel (~1425–1500 °C), followed by rapid cooling once the heat source moves forward. This behaviour is consistent with established SMAW thermal cycles, where peak temperatures remain concentrated in the fusion zone and decrease sharply within a few millimeters of the weld centreline [44–46], [48–50].

The predicted fusion-zone width and depth estimated from the isotherms near the melting temperature agree in magnitude with typical SMAW fusion zones reported for similar heat inputs and plate thicknesses in earlier numerical and experimental studies [36], [40], [57]. The predicted fusion zone depth of ~3 mm falls within the 2.5–3.5 mm range reported by Goldak et al.[50] for comparable SMAW heat inputs.Although the present model does not include phase transformations, the overall size and shape of the molten region fall within expected ranges for comparable voltage, current, and travel speed combinations.

The temperature–time history extracted along the weld line (Figure 11(a)) demonstrates the expected progression from rapid heating to steep cooling. The temperature fluctuations along the x-direction, including the lower temperature observed immediately at arc initiation and the slight peak towards the end of the weld, are characteristic of Goldak-type heat input profiles and reflect the evolving heat-sink conditions of the surrounding base metal. The temperature variation through the depth (Figure 11(b)) shows decreasing temperature with increasing depth, as documented in earlier SMAW simulations [47], [48].

Overall, the shape of the fusion zone, the magnitude and gradient of peak temperatures, and the transient behaviour of the temperature field confirm that the implemented Goldak heat source is physically consistent and aligns well with previously published numerical welding models.

3.4 Discussion. - The thermo–mechanical simulations performed in this study provide a clear understanding of how SMAW process parameters influence the thermal field, elastic strain distribution, and deformation in a Single-V butt joint configuration. The predicted temperature distribution is consistent with the behaviour expected from a Goldak double-ellipsoidal heat source, where the highest temperatures occur near the weld pool and rapidly decrease away from the fusion zone due to conduction and surface heat losses. The thermal gradients observed in Figures 4 and 5 follow the characteristic pattern reported in earlier numerical welding studies [44–46], [48–50], confirming correct representation of heat input and boundary conditions.

The thermal results further show that welding current and welding speed significantly influence peak temperature levels (T_max). Higher current increases heat input per unit length, resulting in a wider and deeper fusion zone, whereas higher speed reduces the time available for heat accumulation, thereby decreasing T_max. These parametric trends are consistent with SMAW physics and with previous findings in the literature [36], [40], [57]. The temperature evolution along the weld line and through the depth (Figure 11) confirms that the weld pool experiences a rapid heating phase, followed by accelerated cooling once the heat source moves forward. This behaviour governs the molten pool development and the subsequent formation of the fusion zone.

The elastic von Mises indicator (Res_Str) provides qualitative insight into regions experiencing high thermo-elastic loading during and immediately after welding. As expected, the highest elastic indicator values appear near the weld centreline, where steep thermal gradients induce differential expansion. Although these values do not represent true residual stresses due to the absence of plasticity in the structural model, the spatial trends in Figures 6 and 7 help identify zones with the greatest deformation potential. Similar qualitative stress–distribution patterns have been reported in simplified thermo-elastic welding simulations [57], [58].

The deformation results reveal that the dominant distortion mode is out-of-plane bending (Z-displacement), with peak deflection occurring near the plate edges and corners (Figures 8(a–c)). This is consistent with classical distortion mechanisms associated with butt welding, where asymmetric heating causes upward bending due to non-uniform expansion and contraction. The magnitude and distribution of Td are strongly influenced by heat input, aligning with the behaviour noted in prior experimental and numerical work [65–69].

The DOE and regression analysis provide further insight into parameter influence. The ANOVA results (Table VIII) show that welding current exerts the strongest statistical effect on T_max, followed by welding speed, while Td exhibits comparatively weak sensitivity to all three parameters. This behaviour reflects the dual dependence of distortion on both thermal gradients and the structural stiffness of the plates. The relatively low R^2 values for Td also indicate that deformation is influenced by geometric effects beyond the primary welding parameters, a trend also observed in earlier welding DOEs [62–64].

Although direct experimental validation for the S355J2+N / ASTM A572 Gr.50 joint was not available, the simulated trends, namely the increase of peak temperature with welding current and its reduction with increasing welding speed, are consistent with experimental and numerical observations reported for comparable arc-welded structural steels in the literature [21, 22, 29]. Furthermore, the predicted distortion magnitudes fall within the ranges reported for butt-welded steel plates subjected to similar heat inputs and boundary conditions [24–26].

Overall, the present simulation framework successfully captures the key qualitative relationships between welding parameters, thermal fields, and deformation. While the thermo-elastic model does not produce quantitative residual stress values, it provides reliable comparative trends that can guide parameter selection for reducing distortion. Incorporating temperature-dependent elastoplastic properties and phase transformation effects in future work will enable accurate prediction of residual stress magnitudes and allow for full validation against experimental data.

3.5 Significance of the Study. - This study provides an integrated thermo–mechanical and design-of-experiments assessment of the SMAW process for a Single-V butt joint of S355J2+N and ASTM A572 Gr.50 steels. By combining a transient Goldak-type heat source model with thermo-elastic structural analysis and a Box–Behnken design, the work establishes a coherent framework for understanding how voltage, current, and welding speed influence weld-pool thermal cycles and distortion. The results clarify the dominant role of welding current in controlling peak temperatures and demonstrate how increases in welding speed can effectively reduce thermal accumulation and limit out-of-plane deformation.

Although the structural model is elastic and therefore does not predict true residual stress magnitudes, the elastic von Mises indicator provides valuable qualitative insight into regions experiencing elevated thermo-elastic loading. This enables identification of distortion-prone zones and supports the interpretation of deformation mechanisms without requiring a full elastoplastic formulation.

The combined simulation–DOE approach offers a practical methodology for parameter screening in welded structures where distortion control is critical. The insights derived here can guide the selection of welding parameters for reducing deformation in industrial fabrication settings. Moreover, the modelling structure developed in this work provides a foundation for future enhancements involving temperature-dependent elastoplastic laws, phase-transformation effects, and experimental validation. These extensions will further strengthen the predictive capability of numerical welding simulations and contribute to optimized process planning in structural steel applications.

4. Conclusion and Future Work. - A three-dimensional transient thermo-mechanical finite element framework was developed to investigate the influence of SMAW process parameters on the thermal and deformation behavior of dissimilar S355J2+N and ASTM A572 Grade 50 steel plates. Based on the numerical simulations and parametric analysis, the following conclusions can be drawn:

1. Welding current is the dominant parameter governing peak temperature, producing a strong increase in maximum thermal response with increasing current, whereas travel speed significantly moderates thermal gradients by controlling heat input per unit length.

2. Travel speed exerts the strongest influence on out-of-plane distortion, indicating its critical role in deformation control during SMAW of structural steel joints. Voltage shows a secondary effect on both thermal distribution and deformation behavior.

3. Elastic stress fields obtained from the linear thermo-elastic analysis reveal spatial stress localization associated with thermal gradients; however, due to the absence of plasticity, stress relaxation, and temperature-dependent material properties, these results are interpreted solely as qualitative elastic stress indicators rather than physically realistic residual stresses.

4. Regression and ANOVA analyses support the qualitative identification of dominant parameters for peak temperature and distortion; nevertheless, low coefficients of determination for certain responses indicate the limitations of first-order models and restrict their use to trend interpretation rather than prediction or optimization.

5. Benchmark comparisons with published experimental and numerical studies on comparable structural steels demonstrate consistency in thermal and deformation trends, supporting the credibility of the numerical framework within its stated scope.

The primary contribution of this work lies in providing a transparent thermo-elastic FEM and design-of-experiments–based sensitivity assessment for a dissimilar structural steel combination not previously reported in SMAW numerical studies. The limitations associated with the material model and the absence of direct experimental validation are explicitly acknowledged. Future work will focus on incorporating temperature-dependent material behavior, plasticity, and experimental measurements to enable physically realistic residual stress prediction and quantitative model validation.

Future research will extend the present numerical framework by incorporating temperature-dependent thermo-physical and mechanical material properties, as well as elastic–plastic constitutive behavior, to enable physically realistic prediction of residual stresses and permanent deformation. The inclusion of phase transformation effects and stress relaxation mechanisms will further improve the fidelity of the mechanical response during heating and cooling cycles. Experimental measurements of temperature histories, fusion zone geometry, and distortion for the S355J2+N / ASTM A572 Gr.50 joint will be pursued to provide direct quantitative validation of the numerical model. In addition, refined response surface models incorporating higher-order and interaction terms, combined with formal multi-response optimization techniques, will be employed to support predictive parameter selection and process optimization. These extensions will allow the framework developed in the present study to evolve from qualitative parameter screening toward quantitatively validated welding process design.

Declaration Conflict of Interest. - The authors of this research announce that they have no known contending monetary interests or individual connections that may have impacted the work detailed in this paper.

Data and Code Availability. - Data and code shall be made available upon request to the corresponding author.

Nomenclature. –

SMAW	Shielded Metal Arc Welding
FEM	Finite Element Method
HAZ	Heat Affected Zone
C	Carbon
Si	Silicon
Mn	Manganese
vel	Welding Speed
V	Voltage
I	Current
ρ	Density of materials
c	Specific heat capacity
T	Present temperature
$\vec{q}$	Flux vector
Q	Internal rate of heat generation
x, y, z	Coordinates in the reference system
t	Time
$\tilde{h}$	Combined heat transfer coefficient
ε_{em}	Emissivity
σ_{bol}	Stefan Boltzmann Constant
T_{amb}	Ambient temperature
h_{con}	Convective heat transfer Coefficient.
η	Thermal Efficiency
c_f	Length of the front ellipsoid
GMAW	Gas Metal Arc Welding
BBD	Box-Behnken Design
RSM	Response Surface Methodology
c_r	Length of the rear ellipsoid
a	Width of heat source
b	Depth of Penetration
f_f	Front heat fraction
MS	Mild Steel
f_r	Rear heat fraction
HB	Hardness Brinell
PWHT	Post-Weld Heat Treatment
DCEN	Direct Current Electrode Negative
DCEP	Direct Current Electrode Positive
AISI	American Iron and Steel Institute
ASTM	American Society for Testing and Materials
UTS	Ultimate Tensile Strength
EL%	Percentage Elongation
TIG	Tungsten Inert Gas
GTAW	Gas Tungsten Arc Welding
LPG	Liquefied Petroleum Gas
G	Groove
F	Fillet
SS	Stainless Steel
S355	Structural Steel with a minimum yield strength of minimum 355 MP

References

[1] "What is Welding? - Definition, Processes and Types of Welds - TWI." Accessed: Oct. 28, 2022. [Online]. Available: https://www.twi-global.com/technical-knowledge/faqs/what-is-welding

[2] "Shielded Metal Arc Welding (SMAW) [SubsTech]." Accessed: Jan. 03, 2023. [Online]. Available: https://www.substech.com/dokuwiki/doku.php?id=shielded_metal_arc_welding_smaw

[3] N. M. Kohlhorst, K. M. Faraone, R. G. Miller, G. Muralidharan, G. B. Ulrich, and J. C. Zhao, "A Technique for the Quantitative Characterization of Weld Microstructure and Application to Mo Welds," Metallurgical and Materials Transactions B: Process Metallurgy and Materials Processing Science, vol. 54, no. 3, pp. 1434–1448, Jun. 2023, doi: 10.1007/S11663-023-02771-Y/METRICS.

[4] M. E. Aalami-Aleagha and A. M. Rashidi, "Correlated macrostructural parameters of weld and weld current in the SMAW of small pipes," Journal of Mechanical Science and Technology, vol. 26, no. 1, pp. 181–185, 2012, doi: 10.1007/s12206-011-0939-1.

[5] H. Jeong, K. Park, and J. Cho, "Numerical analysis of variable polarity arc weld pool," Journal of Mechanical Science and Technology, vol. 30, no. 9, pp. 4307–4313, 2016, doi: 10.1007/s12206-016-0845-7.

[6] C. Wang and J. W. Kim, "Numerical analysis of distortions by using an incorporated model for welding-heating-cutting processes of a welded lifting lug," Journal of Mechanical Science and Technology, vol. 32, no. 12, pp. 5855–5862, 2018, doi: 10.1007/s12206-018-1134-4.

[7] D. H. Bae, C. H. Kim, S. Y. Cho, J. K. Hong, and C. L. Tsai, "Numerical analysis of welding residual stress using heat source models for the multi-pass weldment," KSME International Journal, vol. 16, no. 9, pp. 1054–1064, 2002, doi: 10.1007/BF02984424.

[8] C. S. Seok, M. W. Suh, and J. H. Park, "Investigation of welding residual stress of high tensile steel by finite element method and experiment," KSME International Journal, vol. 13, no. 12, pp. 879–885, 1999, doi: 10.1007/BF03184755.

[9] C. Wu, C. Lee, and J. W. Kim, "Numerical simulation of bending deformation induced by multi-seam welding of a steel-pipe structure," Journal of Mechanical Science and Technology, vol. 34, no. 5, pp. 2121–2131, 2020, doi: 10.1007/s12206-020-0433-8.

[10] D. Y. Kim, T. H. Lee, C. Kim, M. Kang, and J. Park, "Gas metal arc welding with undermatched filler wire for hot-press-formed steel of 2.0 GPa strength: Influence of filler wire strength and bead geometry," Mater Today Commun, vol. 34, no. December 2022, 2023, doi: 10.1016/j.mtcomm.2022.105244.

[11] Y. H. Shi, Z. S. Wang, X. Y. Chen, Y. X. Cui, T. Xu, and J. Y. Wang, "Real-time K-TIG welding penetration prediction on embedded system using a segmentation-LSTM model," Adv Manuf, 2023, doi: 10.1007/s40436-023-00437-1.

[12] Z. Liu et al., "Investigation of the weldability of dissimilar joint between high nitrogen steel and low alloy steel by comparing filler metals," Mater Today Commun, vol. 35, no. 92, p. 105551, 2023, doi: 10.1016/j.mtcomm.2023.105551.

[13] M. Mazar Atabaki, N. Yazdian, and R. Kovacevic, "Hybrid laser/arc welding of thick high-strength steel in different configurations," Adv Manuf, vol. 6, no. 2, pp. 176–188, 2018, doi: 10.1007/s40436-017-0193-6.

[14] Q. Lang, X. Zhang, G. Song, and L. Liu, "Effects of different laser power and welding speed on the microstructure and mechanical properties of TRIP joints in laser-TIG arc hybrid lap filler wire welding," Mater Today Commun, vol. 29, no. July, p. 102925, 2021, doi: 10.1016/j.mtcomm.2021.102925.

[15] G. Wu, D. Zhao, and L. Sun, "Microstructure and mechanical properties of wire-filled tungsten argon arc welded joints for LA141 magnesium-lithium-aluminum alloy," Mater Today Commun, vol. 23, no. December 2019, p. 100881, 2020, doi: 10.1016/j.mtcomm.2019.100881.

[16] A. G. Kamble and R. V. Rao, "Experimental investigation on the effects of process parameters of GMAW and transient thermal analysis of AISI321 steel," Adv Manuf, vol. 1, no. 4, pp. 362–377, 2013, doi: 10.1007/s40436-013-0041-2.

[17] A. K. J. Rohit Jha, "Influence of Welding Current and Joint Design on the Tensile Properties of SMAW Welded Mild Steel Joints," International Journal of Engineering Research and Application, vol. 4, no. 6, pp. 106–111, 2014.

[18] A. Dadi, P. B. Goyal, and H. Patel, "A Review Paper on 'Optimization of Shielded Metal Arc Welding Parameters for Welding of (Ms) Sa-516 Gr . 70 Plate by Using Taguchi Approach"," Int J Sci Res Sci Technol, vol. 4, no. 5, pp. 1536–1543, 2018.

[19] R. A. Mohammed, M. Abdulwahab, and E. T. Dauda, "Properties evaluation of shielded metal arc welded medium carbon steel material.," Int J Innov Res Sci Eng Technol, vol. 2, no. 8, pp. 3351–3357, 2013.
[20] B. Sharma and S. Goyal, "Parametric Optimization of Shielded Metal Arc Welding of Milsd Steel (MS) 2062 using Taguchi Method," ADR Journals, vol. 3, no. 3. pp. 11–18, 2016.
[21] I. S. Asibeluo and E. Emifoniye, "Effect of Arc Welding Current on the Mechanical Properties of A36 Carbon Steel Weld Joints," SSRG International Journal of Mechanical Engineering, vol. 2, no. 9, pp. 79–87, 2015.
[22] J. O. O. * et Al, "Correlation between Process Variables in Shielded Metal-Arc Welding (SMAW) Process and Post Weld Heat Treatment (PWHT) on Some Mechanical Properties of Low Carbon Steel Welds," Journal of Minerals and Materials Characterization and Engineering, vol. 11, no. 09, pp. 896–903, 2012, doi: 10.4236/jmmce.2012.119085.
[23] M. E, J. Nehru, E. College, A. Shukla, and V. S. Joshi, "Experimental Study of Shielded metal Arc Welding Parameter on Weld Strength for AISI 1020 Using Response Surface Methodology," no. 9, pp. 1123–1126, 2017.
[24] R. Chiong, N. Khandoker, S. Islam, and E. Tchan, "Effect of SMAW parameters on microstructure and mechanical properties of AISI 1018 low carbon steel joints: An experimental approach," IOP Conf Ser Mater Sci Eng, vol. 495, no. 1, 2019, doi: 10.1088/1757-899X/495/1/012093.
[25] D. Pathak, R. P. Singh, S. Gaur, and V. Balu, "Experimental investigation of effects of welding current and electrode angle on tensile strength of shielded metal arc welded low carbon steel plates," Mater Today Proc, no. xxxx, pp. 1–3, 2020, doi: 10.1016/j.matpr.2020.01.146.
[26] S. H. Zoalfakar and A. A. Hassan, "Analysis and Optimization of Shielded Metal Arc Welding Parameters on Mechanical Properties of Carbon Steel Joints by Taguchi Method," no. 01, pp. 1431–1444, 2017.
[27] E. Widodo, I. Iswanto, M. A. Nugraha, and K. Karyanik, "Electric current effect on mechanical properties of SMAW-3G on the stainless steel AISI 304," MATEC Web of Conferences, vol. 197, pp. 1–4, 2018, doi: 10.1051/matecconf/201819712003.
[28] D. Kumar, M. Dharamvir, and *, "Study and Analysis of the Effect of Welding Process on Distortion With 304L Stainless Steel Weld Joints," vol. 6, no. 2, pp. 212–216, 2017.
[29] A.K.Rude and Pimpalgaonkar, "Optimization Of Process Parameter In Hardfacing By Shield Metal Arc Welding (SMAW)," International Research Journal of Engineering and Technology (IRJET), vol. 05, no. 01, pp. 232–236, 2018.
[30] R. Selvam and S. Jacob, "Experimental investigation and analysis of SMAW processed carbon steel pipes," International Journal of Mechanical and Production Engineering Research and Development, vol. 8, no. 5, pp. 29–40, 2018, doi: 10.24247/ijmperdoct20185.
[31] L. S. Sisira and K. Weeraskaralage, "Optimization of Shielded Metal Arc Welding (SMAW) process for mild steel Optimization of Shielded Metal Arc Welding (SMAW) process for mild steel," Journal ENGINEER, no. August, 2019, doi: 10.13140/RG.2.2.23458.58560.
[32] D. Benne and D. Choudhary, "Experimentation and Analysis of Strength and Microstructural Parameters of Mild Steel Specimen Hardfaced by Chromium Zedalloy-350 Using Shielded Metal Arc Welding (SMAW) Process .," vol. 2, no. 1, pp. 1–5, 2018.
[33] S. I. Talabi, O. B. Owolabi, J. A. Adebisi, and T. Yahaya, "Effect of welding variables on mechanical properties of low carbon steel welded joint," Advances in Production Engineering And Management, vol. 9, no. 4, pp. 181–186, 2014, doi: 10.14743/apem2014.4.186.
[34] U. S. Patil and M. S. Kadam, "Microstructural analysis of SMAW process for joining stainless steel 304 with mild steel 1018 and parametric optimization by using response surface methodology," Mater Today Proc, vol. 44, pp. 1811–1815, 2021, doi: 10.1016/j.matpr.2020.12.008.
[35] M. Khan, M. W. Dewan, and M. Z. Sarkar, "Effects of welding technique, filler metal and post-weld heat treatment on stainless steel and mild steel dissimilar welding joint," J Manuf Process, vol. 64, no. December 2020, pp. 1307–1321, 2021, doi: 10.1016/j.jmapro.2021.02.058.
[36] M. A. Rojas Nova, L. M. Calderon Vergel, A. D. Pertuz Comas, and O. Bohorquez Becerra, "Efecto de la velocidad de avance en procesos de soldadura por arco eléctrico usando el método de elementos finitos," Ciencia en Desarrollo, vol. 12, no. 2, pp. 67–72, 2021, doi: 10.19053/01217488.v12.n2.2021.13419.
[37] M. Matuszewski, "Modeling of 3D temperature field in butt welded joint of 6060 alloy sheets using the ANSYS program," IOP Conf Ser Mater Sci Eng, vol. 659, no. 1, 2019, doi: 10.1088/1757-899X/659/1/012034.

[38] A. M. Sajeeb, "Parametric studies on weld penetration on plate of aluminium alloy 6061-T6 using FEM simulation," Applied Mechanics and Materials, vol. 367, pp. 90–95, 2013, doi: 10.4028/www.scientific.net/AMM.367.90.
[39] A. Boudiaf and M. E. A. Djeghlal, "Modeling and Numerical Simulation of Thermal Cycles During GTAW Welding," SSRN Electronic Journal, no. November, pp. 4–10, 2019, doi: 10.2139/ssrn.3389786.
[40] M. Cronje, "Finite Element Modelling of Shielded Metal Arc Welding," no. December, pp. 1–110, 2005.
[41] "S355J2(+N) / 1.0570(dubl) - SteelNumber - Chemical composition, equivalent, properties." Accessed: Jan. 29, 2023. [Online]. Available: http://www.steelnumber.com/en/steel_composition_eu.php?name_id=850
[42] "Ovako S355J2 S355J2(M) Steel, +AR." Accessed: Jan. 29, 2023. [Online]. Available: https://www.matweb.com/search/datasheet.aspx?matguid=3c36b268408a4cc1ae7f789bd605d6c6&ckck=1
[43] "ISO - ISO 9692-1:2013 - Welding and allied processes — Types of joint preparation — Part 1: Manual metal arc welding, gas-shielded metal arc welding, gas welding, TIG welding and beam welding of steels." Accessed: Feb. 26, 2023. [Online]. Available: https://www.iso.org/standard/62520.html
[44] K. Sripriyan, M. Ramu, P. R. Thyla, and K. Anantharuban, "Weld bead characterization of flat wire electrode in gmaw process part II: a numerical study," Journal of Mechanical Science and Technology, vol. 35, no. 6, pp. 2615–2622, 2021, doi: 10.1007/s12206-021-0532-1.
[45] N. U. Dar, E. M. Qureshi, and M. M. I. Hammouda, "Analysis of weld-induced residual stresses and distortions in thin-walled cylinders," Journal of Mechanical Science and Technology, vol. 23, no. 4, pp. 1118–1131, 2009, doi: 10.1007/s12206-008-1012-6.
[46] G. Fu, J. Gu, M. I. Lourenco, M. Duan, and S. F. Estefen, "Parameter determination of double-ellipsoidal heat source model and its application in the multi-pass welding process," Ships and Offshore Structures, vol. 10, no. 2, pp. 204–217, 2015, doi: 10.1080/17445302.2014.937059.
[47] A. Kiran, Y. Li, J. Hodek, M. Brázda, M. Urbánek, and J. Džugan, "Heat Source Modeling and Residual Stress Analysis for Metal Directed Energy Deposition Additive Manufacturing," Materials, vol. 15, no. 7, 2022, doi: 10.3390/ma15072545.
[48] J. Zhou and H. L. Tsai, Welding heat transfer. Woodhead Publishing Limited, 2005. doi: 10.1533/9781845690939.1.32.
[49] T. F. Flint, J. a Francis, and J. R. Yates, "Analytical solutions of the transient thermal field induced in finite bodies with insulating and convective boundary conditions subjected to a welding heat source," 2013.
[50] J. Goldak, A. Chakravarti, and M. Bibby, "A new finite element model for welding heat sources," Metallurgical Transactions B, vol. 15, no. 2, pp. 299–305, 1984, doi: 10.1007/BF02667333.
[51] Material Welding, "What is efficiency in welding & welding efficiency for SMAW, GMAW,TIG, FCAW and SAW?," 2022, [Online]. Available: https://www.materialwelding.com/what-is-efficiency-in-welding-welding-efficiency-for-smaw-gmawtig-fcaw-and-saw/
[52] P. Vigneshwaran and M. P. Prabakaran, "Weld Strength Optimization by using Box-Behnken Design," no. April 2014, 2019, [Online]. Available: www.ijert.org
[53] M. Alhajabdalla, H. Mahmoud, M. S. Nasser, I. A. Hussein, R. Ahmed, and H. Karami, "Application of response surface methodology and box-behnken design for the optimization of the stability of fibrous dispersion used in drilling and completion operations," ACS Omega, 2021, doi: 10.1021/acsomega.0c04272.
[54] N. Ferreira et al., "Application of response surface methodology and box–behnken design for the optimization of mercury removal by Ulva sp.," J Hazard Mater, vol. 445, no. November 2022, 2023, doi: 10.1016/j.jhazmat.2022.130405.
[55] S. L. C. Ferreira et al., "Box-Behnken design: An alternative for the optimization of analytical methods," Anal Chim Acta, vol. 597, no. 2, pp. 179–186, 2007, doi: 10.1016/j.aca.2007.07.011.
[56] P. Sathiya, P. M. Ajith, and R. Soundararajan, "Genetic algorithm based optimization of the process parameters for gas metal arc welding of AISI 904 L stainless steel," Journal of Mechanical Science and Technology, vol. 27, no. 8, pp. 2457–2465, 2013, doi: 10.1007/s12206-013-0631-8.
[57] H. Cui et al., "Numerical Simulation of the Interaction Between Arc Plasma and Molten Slag in Electric Arc Furnace for High-Titania Slag Smelting," Metallurgical and Materials Transactions B: Process Metallurgy and Materials Processing Science, vol. 54, no. 4, pp. 1687–1704, Aug. 2023, doi: 10.1007/S11663-023-02775-8/METRICS.

[58] S. H. Zargar, M. Farahani, and M. K. B. Givi, "Numerical and experimental investigation on the effects of submerged arc welding sequence on the residual distortion of the fillet welded plates," Proc Inst Mech Eng B J Eng Manuf, vol. 230, no. 4, pp. 654–661, 2016, doi: 10.1177/0954405414560038.
[59] "S355J2 steel plate,S355J2 sheet,S355J2 coil - Carbon steel", [Online]. Available: https://www.steelss.com/Carbon-steel/s355j2.html
[60] M. M. Ali, F. Dave, R. Sherlock, A. Mcilhagger, and D. Tormey, "Simulated Effect of Carbon Black on High Speed Laser Transmission Welding of Polypropylene With Low Line Energy," Front Mater, vol. 8, no. September, pp. 1–14, 2021, doi: 10.3389/fmats.2021.737689.
[61] S. Kannan, S. S. Kumaran, and L. A. Kumaraswamidhas, "Optimization of friction welding by taguchi and ANOVA method on commercial aluminium tube to Al 2025 tube plate with backing block using an external tool," Journal of Mechanical Science and Technology, vol. 30, no. 5, pp. 2225–2235, 2016, doi: 10.1007/s12206-016-0432-y.
[62] F. Reyes-Calderón, R. Vences-Hernández, J. A. Salazar-Torres, H. J. Vergara-Hernández, I. Aguilera-Navarrete, and V. Pérez-González, "Parameter optimization: Force (F), time (T) and current intensity (I), in the RSW welding process of DP-290 steel plates using the taguchi method," Soldagem e Inspecao, vol. 23, no. 2, pp. 157–167, 2018, doi: 10.1590/0104-9224/SI2302.04.
[63] S. C. Bodkhe and D. R. Dolas, "Optimization of Activated Tungsten Inert Gas Welding of 304L Austenitic Stainless Steel," Procedia Manuf, vol. 20, pp. 277–282, 2018, doi: 10.1016/j.promfg.2018.02.041.
[64] B. Trembach, A. Grin, M. Turchanin, N. Makarenko, O. Markov, and I. Trembach, "Application of Taguchi method and ANOVA analysis for optimization of process parameters and exothermic addition (CuO-Al) introduction in the core filler during self-shielded flux-cored arc welding," International Journal of Advanced Manufacturing Technology, vol. 114, no. 3–4, pp. 1099–1118, 2021, doi: 10.1007/s00170-021-06869-y.
[65] S. Karaoğlu and A. Seçgin, "Sensitivity analysis of submerged arc welding process parameters," J Mater Process Technol, vol. 202, no. 1–3, pp. 500–507, Jun. 2008, doi: 10.1016/J.JMATPROTEC.2007.10.035.
[66] Z. Chen, C. Li, X. Han, X. Gao, and H. Gao, "Sensitivity analysis of the MIG welding process parameters based on response surface method," J Adhes Sci Technol, vol. 35, no. 6, pp. 590–609, 2021, doi: 10.1080/01694243.2020.1816778.
[67] J. Luukkonen, A. Pohjonen, S. Louhenkilpi, J. Miettinen, M. J. Sillanpää, and E. Laitinen, "Gradient Boosted Regression Trees for Modelling Onset of Austenite Decomposition During Cooling of Steels," Metallurgical and Materials Transactions B: Process Metallurgy and Materials Processing Science, vol. 54, no. 4, pp. 1705–1724, 2023, doi: 10.1007/s11663-023-02782-9.
[68] P. Merico, M. Faccoli, and G. Cornacchia, "Analysis of Ancient Slag Inclusion-Metal Systems as a Method to Disclose Processing Thermo-chemical Parameters: The Case Study of a Medieval Lombard Steel Bar from Northern Italy," Metallurgical and Materials Transactions B: Process Metallurgy and Materials Processing Science, vol. 54, no. 3, pp. 1408–1421, 2023, doi: 10.1007/s11663-023-02769-6.
[69] Y. Zhang, H. Liu, T. Coetsee, Z. Wang, and C. Wang, "Identifying Oxygen Transfer Pathways During High Heat Input Submerged Arc Welding: A Case Study into CaF2-SiO2-CaO-TiO2 Fluxes," Metallurgical and Materials Transactions B: Process Metallurgy and Materials Processing Science, vol. 54, no. 6, pp. 2875–2880, Dec. 2023, doi: 10.1007/S11663-023-02922-1/METRICS.
[70] B. Kiran, K. Mishra, Y. R. Singh, and D. Nagaraju, "Structural and thermal analysis of butt joint GTAW of similar and dissimilar materials with distinct groove angles through simulation and mathematical modelling," FME Transactions, vol. 48, no. 3, pp. 667–680, 2020, doi: 10.5937/FME2003667B.
[71] J. Wang, H. Yuan, N. Ma, and H. Murakawa, "Recent research on welding distortion prediction in thin plate fabrication by means of elastic FE computation," Marine Structures, vol. 47, pp. 42–59, 2016, doi: 10.1016/j.marstruc.2016.02.004.

Author contribution:

1. Conception and design of the study
2. Data acquisition
3. Data analysis
4. Discussion of the results
5. Writing of the manuscript
6. Approval of the last version of the manuscript

SFH has contributed to: 1, 2, 3, 4, 5 and 6.

SAK has contributed to: 1, 2, 3, 4, 5 and 6.

AS has contributed to: 1, 2, 3, 4, 5 and 6.

MNB has contributed to: 1, 2, 3, 4, 5 and 6.

AM has contributed to: 1, 2, 3, 4, 5 and 6.

AN has contributed to: 1, 2, 3, 4, 5 and 6.

MMA has contributed to: 1, 2, 3, 4, 5 and 6.

SN has contributed to: 1, 2, 3, 4, 5 and 6.

Acceptance Note: This article was approved by the journal editors Dr. Rafael Sotelo and Mag. Ing. Fernando A. Hernández Gobertti.

Ubicación Óptima de la Soldadura para Mayor Integridad en la Fabricación de Tubos Perfilados

Optimal Weld Seam Placement for Enhanced Integrity in Profiled Tubes Manufacturing

Posicionamento ideal da costura de solda para maior integridade na fabricação de tubos perfilados.

Sergey V. Parshin [1] (*), Anastasiya A. Parshina [2]

Recibido: 11/09/2025 Aceptado: 24/11/2025

Resumen. - La producción de tubos de gran diámetro con perfiles complejos, como estrellas de múltiples puntas, a menudo depende de tubos soldados debido a la escasez y alto costo de tubos sin costura. Sin embargo, la soldadura presenta una ductilidad entre un 5-10% menor que el metal base, aumentando el riesgo de falla durante la conformación plástica del perfil. Este estudio emplea modelado por elementos finitos (MEF) para simular el proceso de perfilado de un tubo con forma de estrella de seis puntas, con el objetivo de identificar la ubicación óptima de la soldadura que minimice la intensidad de deformación y maximice la integridad estructural. Los resultados identificaron zonas de deformación mínima en los puntos de inflexión de la curvatura del perfil, permitiendo una estrategia práctica de rotación del tubo antes del conformado para posicionar la costura en estas áreas. El estudio concluye que esta metodología ofrece una solución efectiva y potencialmente costo-eficiente para la fabricación industrial de tubos perfilados soldados, mitigando el riesgo de falla.

Palabras clave: ubicación de soldadura; tubos perfilados; modelado por elementos finitos; intensidad de deformación; integridad estructural

[1] Doctor en Ciencias Técnicas (Ingeniería), Profesor. Universidad Federal de los Urales, Facultad de Nuevos Materiales y Tecnologías, svparshin@urfu.ru, ORCID iD: https://orcid.org/0000-0002-7814-1247

[2] Candidato en Ciencias Técnicas (Ingeniería), Profesor Asociado. Universidad Federal de los Urales, Facultad de Nuevos Materiales y Tecnologías, a.a.parshina@urfu.ru, ORCID iD: https://orcid.org/0000-0001-8633-4690

Memoria Investigaciones en Ingeniería, núm. 30 (2026). pp. 56-63
https://doi.org/10.36561/ING.30.5
ISSN 2301-1092 • ISSN (en línea) 2301-1106 – Universidad de Montevideo, Uruguay

Summary. - *The production of large-diameter profiled pipes, such as multi-ray stars, often relies on welded blanks due to the scarcity and high cost of seamless alternatives. However, the weld seam has 5-10% lower ductility than the base metal, increasing the risk of failure during profiling. This study uses finite element modeling (FEM) to simulate the profiling process of a six-ray star-shaped pipe, aiming to identify the optimal weld seam placement that minimizes deformation intensity and maximizes structural integrity. Results identified zones of minimal deformation at the inflection points of the profile's curvature, enabling a practical strategy of pipe rotation before forming to position the seam in these areas. The study concludes that this methodology offers an effective and potentially cost-efficient solution for the industrial manufacturing of welded profiled pipes, mitigating the risk of failure.*

Palabras clave: *weld seam placement; profiled pipes; finite element modeling; deformation intensity; structural integrity.*

Resumo *.* ***-*** *A produção de tubos perfilados de grande diâmetro, como os em formato de estrela de múltiplos raios, frequentemente depende de blanks soldados devido à escassez e ao alto custo de alternativas sem costura. No entanto, a junta de solda apresenta ductilidade 5-10% menor que a do metal base, aumentando o risco de falha durante a perfilação. Este estudo utiliza modelagem por elementos finitos (MEF) para simular o processo de perfilação de um tubo em formato de estrela de seis raios, com o objetivo de identificar o posicionamento ideal da junta de solda que minimize a intensidade da deformação e maximize a integridade estrutural. Os resultados identificaram zonas de mínima deformação nos pontos de inflexão da curvatura do perfil, possibilitando uma estratégia prática de rotação do tubo antes da conformação para posicionar a junta nessas áreas. O estudo conclui que essa metodologia oferece uma solução eficaz e potencialmente economicamente eficiente para a fabricação industrial de tubos perfilados soldados, mitigando o risco de falha.*

Palavras-chave: *posicionamento da junta de solda; tubos perfilados; modelagem por elementos finitos; intensidade da deformação; integridade estrutural.*

1. Introducción. - La producción de tubos perfilados de gran diámetro, como las configuraciones multi-punta, enfrenta desafíos debido a la disponibilidad limitada y el alto costo de los blanks de tubos sin costura [1]. Los tubos soldados son una alternativa viable, pero sus costuras de soldadura, con una ductilidad entre un 5% y 10% menor que el metal base, son propensas a fallar bajo deformación plástica significativa durante el perfilado [2]–[4] o en operaciones posteriores como la expansión. Estudios previos destacan el impacto de las imperfecciones de la soldadura y los esfuerzos residuales en el riesgo de falla [3], [4], sin embargo, las estrategias para optimizar la ubicación de la costura de soldadura permanecen poco exploradas. El hidroconformado de tubos (THF) y el conformado por rodillos son métodos comunes de perfilado, pero ambos enfrentan desafíos relacionados con la deformación de la costura de soldadura [5], [6]. En el THF, la ductilidad reducida de la soldadura aumenta el riesgo de fractura por tracción en zonas de alta curvatura [6]. El modelado por elementos finitos (MEF) se ha utilizado para predecir distribuciones de tensión y deformación en perfiles complejos [7], [8], lo que ofrece información valiosa sobre el comportamiento de la costura. Por ejemplo, estudios sobre esfuerzos residuales en uniones soldadas [9] y sobre hidroconformado de tubos soldados a medida [10] enfatizan la importancia de la optimización de la ubicación de la soldadura. Este estudio tiene como objetivo identificar ubicaciones óptimas para la costura de soldadura utilizando MEF para minimizar el daño inducido por la deformación y mejorar la integridad estructural en la fabricación de tubos perfilados, centrándose en un perfil en forma de estrella de seis puntas.

2. Materiales y métodos. -

2.1 Diseño del estudio. - Este estudio empleó modelado tridimensional por elementos finitos (MEF) para simular el proceso de perfilado de tubos soldados con una sección transversal en forma de estrella de seis puntas. El modelo analizó la intensidad de deformación (deformación plástica equivalente, ε~i~) y los estados de tensión (σ~i~) para identificar zonas óptimas de ubicación de la costura de soldadura.

2.2 Modelado por Elementos Finitos. - El modelo MEF se desarrolló utilizando ANSYS Multiphysics para replicar el perfilado multietapa. Se utilizó un modelo tridimensional de elementos finitos para simular el proceso de perfilado, utilizando elementos tetraédricos SOLID187 capaces de capturar geometrías complejas y soportar malla adaptativa. Este tipo de elemento proporciona alta precisión para modelar los intrincados perfiles de los tubos y maneja eficientemente las interacciones de contacto. La malla se refinó considerando la geometría del tubo y las regiones de máxima deformación: a lo largo del espesor de la pared del tubo, se utilizaron hasta 3-4 elementos. Se aplicó una malla adaptativa en la zona de soldadura para capturar con precisión las concentraciones de tensión y deformación en esta área. En otros lugares, se empleó una malla más gruesa para equilibrar la eficiencia computacional y la precisión. Las condiciones de contorno incluyeron restricciones de simetría (simetría BC), que redujeron la carga computacional al explotar la simetría del perfil. La interacción entre los rodillos de perfilado y el tubo se modeló mediante condiciones de contacto, se utilizó una formulación de contacto penal. El coeficiente de fricción entre los rodillos y el tubo se estableció en 0.15, un valor típico para interacciones acero-acero. Un análisis de sensibilidad preliminar mostró que la localización de las zonas de deformación mínima es poco sensible a variaciones razonables (±0.05) en este parámetro. Teniendo en cuenta el posible deslizamiento y la presión ejercida por los rodillos. El modelo replicó una secuencia de perfilado multietapa típica, con 3 pasos de formación progresiva. En cada paso, se aplicó un desplazamiento prescrito a los rodillos para lograr la deformación incremental del perfil. El análisis se realizó en condiciones estáticas, con propiedades elasto-plásticas del material especificadas según las características del metal base. El comportamiento del material se definió mediante un modelo elasto-plástico isotrópo con endurecimiento cinemático y el criterio de fluencia de von Mises. La curva tensor-deformación para el metal base se obtuvo de ensayos de tracción (tabla I). La ductilidad reducida (5-10%) de la soldadura se implementó mediante una límite de deformación plástica equivalente (fracture strain) inferior en la zona afectada por el calor (zac), manteniéndose las mismas propiedades de resistencia y endurecimiento que el metal base para simplificar el modelo, enfoque justificable para el objetivo de ubicación óptima. La deformación plástica se modeló utilizando leyes constitutivas elasto-plásticas estándar. Los esfuerzos y deformaciones residuales se despreciaron en el modelo, lo cual es aceptable para optimizar la ubicación de la soldadura asumiendo que no influyen significativamente en el comportamiento de deformación del perfil. Esta suposición se justifica en el contexto de este estudio, ya que los esfuerzos residuales de soldadura superpuestos a los esfuerzos de conformado pueden afectar los niveles absolutos de tensión, pero es poco probable que cambien la ubicación relativa

de los mínimos de deformación a lo largo de la circunferencia del perfil, siendo esta ubicación el objetivo principal del análisis. Las conclusiones son más fiables para casos con calidad de soldadura alta y distribuciones típicas de esfuerzos residuales. El análisis implicó identificar los puntos de deformación y tensión máximas y mínimas, permitiendo determinar las zonas con deformación mínima, correspondientes a las ubicaciones óptimas de la costura de soldadura. Los parámetros clave incluyeron: Propiedades del Material: propiedades del metal base y de la soldadura, con la ductilidad de la soldadura establecida entre un 5-10% menor que la del metal base [2], [11]. Trayectoria de Deformación: los criterios basados en curvatura, derivados de la segunda derivada de la geometría del perfil, identificaron zonas de deformación mínima [8]. El criterio de optimalidad formalizado fue: 1) minimizar la intensidad de deformación plástica equivalente (ε_i) a lo largo de la línea de soldadura, y 2) preferir regiones donde el estado de tensiones locales durante el conformado evite valores máximos de tracción. Los puntos de inflexión, donde la segunda derivada de la curva del perfil es máxima, satisfacen este criterio. Condiciones de Contorno: se simuló una deformación multietapa, reflejando las restricciones industriales del conformado por rodillos [7]. El modelo calculó la intensidad de deformación y los estados de tensión en la sección transversal del tubo, centrándose en puntos característicos (crestas, valles, zonas de transición).

Propiedad	Valor
Módulo de Elasticidad (E)	210 GPa
Límite de Fluencia (σ_y)	350 MPa
Coeficiente de Poisson (ν)	0.3
Curva de Endurecimiento ($\sigma = K\varepsilon^n$)	K = 650 MPa, n = 0.18
Deformación plástica equivalente a la fractura (ε_f)	0.25

Tabla I. Propiedades del material del metal base (acero aleado).

2.3 Análisis de Datos. - Se analizaron las distribuciones de intensidad de deformación y estado de tensiones en puntos clave del perfil. El punto de inflexión se identificó maximizando la derivada de la función de curvatura. Para cuantificar la ventaja de la ubicación óptima, se compararon los valores de ε_i en diferentes puntos característicos (tabla II). Los resultados se validaron con predicciones teóricas y estudios previos [9].

Ubicación en el Perfil	Valor de ε_i
Cresta (Punto 4, superficie interna)	0.15
Valle (Punto 1)	0.08
Punto de Inflexión (Punto 2)	**0.02**

Tabla II. Comparación cuantitativa de la intensidad de deformación (ε_i).

3. Resultados. - El modelado por elementos finitos reveló variaciones significativas en la intensidad de deformación (ε_i) y el estado de tensiones (σ_i) a través de la sección transversal del tubo en forma de estrella de seis puntas (Figura I).

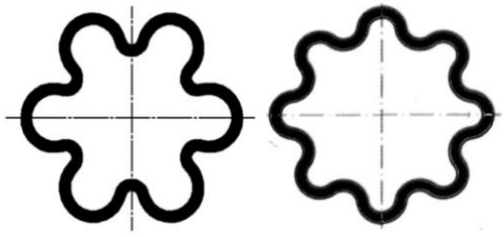

Figura I. Perfiles transversales de tubos multirradiados, con especial atención al perfil estrellado de seis radios.

La Figura I ilustra los perfiles seccionales de tubos multi-punta, destacando la configuración de seis puntas utilizada en este estudio.

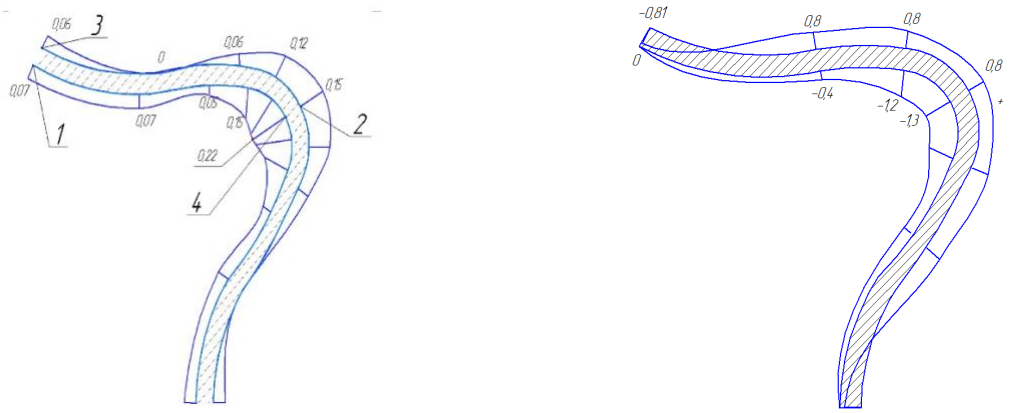

(a) (b)

Figura II.- Distribución de (a) la intensidad de deformación y (b) el estado de tensiones durante el conformado. Los puntos 1 y 3 representan los valles, los puntos 2 y 4 representan las crestas, con el punto de inflexión entre crestas y valles.

La Figura II(a) muestra que la máxima intensidad de deformación ocurrió en las superficies internas de las crestas (punto 4, $\varepsilon_i \approx 0.15$), mientras que se observó una deformación mínima en los puntos de inflexión (punto 2, $\varepsilon_i \approx 0$). La Figura II(b) indica una transición de tensiones de tracción a compresión en el punto de inflexión, minimizando las concentraciones de tensiones.

Para el perfil de seis puntas, se identificaron 12 zonas óptimas de ubicación de la costura de soldadura, correspondientes a los puntos de inflexión de la curvatura externa de cada punta, lo que permite una implementación práctica mediante la rotación del tubo.

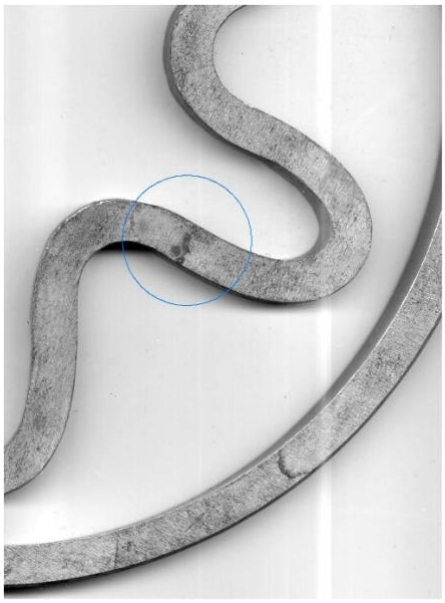

Figura III. Ubicación óptima de la soldadura en un tubo perfilado con forma de estrella de seis radios.

La foto (Figura III) presenta un espécimen físico de un tubo perfilado en forma de estrella de seis puntas fabricado de acuerdo con los parámetros optimizados derivados del análisis de elementos finitos. La costura de soldadura se posiciona a lo largo del punto de inflexión de la curvatura externa del perfil, donde el modelado computacional predijo una intensidad de deformación mínima ($\varepsilon_i \approx 0$). Esta ubicación crítica se determinó mediante un análisis sistemático de los patrones de distribución de deformación en la sección transversal del tubo durante la simulación de perfilado. La línea de soldadura visible demuestra una fusión adecuada y una penetración uniforme, confirmando la viabilidad

de la implementación industrial. La superficie del tubo exhibe transiciones suaves entre las puntas sin defectos visibles, validando el enfoque de modelado para la mitigación de deformaciones en tubos perfilados soldados.

4. Discusión. - Posicionar las costuras de soldadura en los puntos de inflexión de la curvatura del perfil reduce significativamente el daño inducido por la deformación, alineándose con hallazgos previos sobre optimización del pie de soldadura [11]. Este enfoque mitiga los esfuerzos residuales y las deformaciones pico, ofreciendo una alternativa práctica a los tratamientos posteriores a la soldadura. En comparación con las estrategias de hidroconformado [10], la rotación del tubo antes del perfilado es más simple y potencialmente más rentable, aunque se necesita un análisis de costo-beneficio más profundo. Estudios sobre tubos corrugados laterales (LCTs) muestran que la geometría del perfil influye en la distribución de deformaciones [12]. El método propuesto se alinea con las técnicas de conformado incremental inverso (ICF) [13], donde los ajustes de parámetros reducen errores de forma. Las 12 zonas óptimas proporcionan flexibilidad para aplicaciones industriales, similar a las estrategias para minimizar el movimiento de la línea de soldadura en hidroconformado [10]. Limitaciones y generalización: el estudio se centra en un perfil específico de seis puntas. Sin embargo, la metodología propuesta (identificar zonas de deformación mínima mediante mef y posicionar la soldadura en esos puntos) es generalizable a otros perfiles, como tubos cuadrados, rectangulares o estrellas con diferente número de puntas. La regla heurística de "soldar en los puntos de inflexión" se espera que sea válida para perfiles con curvatura alternada (crestas y vallos), aunque la ubicación exacta de dichos puntos debe reevaluarse para cada geometría particular mediante simulación. Las principales limitaciones del modelo incluyen la negligencia de esfuerzos residuales y la falta de un criterio explícito de daño por fractura; la evaluación de integridad se basa en proxies de deformación/tensión, no en una predicción directa de falla. Las limitaciones incluyen el enfoque en un perfil de seis puntas, que puede no generalizarse a otras geometrías. Trabajos futuros deberían validar el enfoque en diversas configuraciones y entornos reales.

5. Conclusiones. - Este estudio demuestra que colocar las costuras de soldadura en zonas de deformación mínima, identificadas mediante modelado por elementos finitos, mejora la integridad estructural de los tubos perfilados. Para perfiles en forma de estrella de seis puntas, la rotación del tubo para alinear las costuras con los puntos de inflexión ofrece una solución rentable para la fabricación industrial. La validación cualitativa mediante un espécimen físico fabricado (figura III), de acero aleado de 3 mm de espesor y 250 mm de diámetro, perfilado en 3 pasos, confirmó la ausencia de grietas o defectos visibles cuando la soldadura se ubicó en la posición óptima. Ensayos informales previos con soldaduras en posiciones no óptimas (e.g., en las crestas) mostraron mayor propensión al agrietamiento, apoyando cualitativamente los resultados numéricos. Investigaciones futuras deberían validar este enfoque en diversas geometrías de tubos e integrar optimización paramétrica para mejorar aún más la confiabilidad.

Referencias

[1] A. Abrass, T. Kessler, and P. Groche; "Optimizing roll forming processes with the aid of a new numerical algorithm," *Key Eng. Mater.*, 2012. 504–506: p. 857–862.
[2] A. A. Bogatov; *Welded Cold-Formed Pipes*, 1991, Metallurgiya: Moscow, Russia.
[3] V. V. Yakovlev, V. I. Krylov, and A. N. Ivanov; "Methods for improving the quality of cold-formed welded pipes," *Stal'*, 1988. (1): p. 60–62.
[4] V. M. Vlasov; "Production of thin-walled welded pipes with reduced internal burr," *Stal'*, 1983. (7): p. 50–51.
[5] A. Alaswad, K. Y. Benyounis, and A. G. Olabi; "Tube hydroforming process: A reference guide," *Mater. Des.*, 2012. 33: p. 328–339.
[6] Y.-M. Hwang and Y.-K. Lin; "Analysis and finite element simulation of the tube bulge hydroforming process," *J. Mater. Process. Technol.*, 2002. 125–126: p. 821–825.
[7] Y. Yan and Q. Li; "FEM modeling and mechanics analysis of flexible roll forming," *Appl. Mech. Mater.*, 2010. 44–47: p. 132–137.
[8] B. Abeyrathna, B. Rolfe, P. Hodgson, and M. Weiss; "Local deformation in roll forming," *Int. J. Adv. Manuf. Technol.*, 2017. 88: p. 2405–2415.
[9] D. E. Katsareas, A. Youtsos, and C. F. T. Mattas; "Finite element simulation of welding in pipes: A sensitivity analysis," in *Residual Stress and Its Effects on Fatigue and Fracture*, A. G. Youtsos, Ed., 2006, Springer: Dordrecht, Netherlands. p. 15–26.
[10] R. A. F. Valente, R. M. N. Jorge, A. D. Santos, and L. M. J. S. Dinis; "Simulation of dissimilar tailor-welded tubular hydroforming processes using EAS-based solid finite elements," *Int. J. Adv. Manuf. Technol.*, 2008. 37: p. 670–689.
[11] Y. Wang, Z. Li, and X. Zhang; "Applying weld toe process design in finite element analysis of super large structure," *J. Mech. Sci. Technol.*, 2017. 31(12): p. 5865–5873.
[12] X. Deng, X. Liu, and Y. Zhang; "On the crashworthiness analysis and design of a lateral corrugated tube," *Int. J. Mech. Sci.*, 2018. 140: p. 30–41.
[13] J.-C. Park, D.-Y. Yang, M. Cha, and D. Kim; "Investigation of a new incremental counter forming in flexible roll forming," *Int. J. Mach. Tools Manuf.*, 2014. 86: p. 68–80.

Author contribution:

1. Conception and design of the study

2. Data acquisition

3. Data analysis

4. Discussion of the results

5. Writing of the manuscript

6. Approval of the last version of the manuscript

SVP has contributed to: 1, 2, 3, 4, 5 and 6.

AAP has contributed to: 1, 2, 3, 4, 5 and 6.

Acceptance Note: This article was approved by the journal editors Dr. Rafael Sotelo and Mag. Ing. Fernando A. Hernández Gobertti.

Evaluación del Desempeño Sísmico de un Edificio Multifamiliar Ubicado en el Distrito de Surco, Lima; ante Diferentes Niveles de Amenaza, aplicando la Norma ATC – 40

Seismic Performance Assessment of a Multi-Family Building Located in the Surco District, Lima, Under Different Threat Levels, applying the ATC-40 Standard

Avaliação do Desempenho Sísmico de um Edifício Multifamiliar Localizado no Bairro Surco, Lima, sob Diferentes Níveis de Ameaça, aplicando a Norma ATC-40

Josimar Guillen [1] (*), Oliberth Huaman [2], Genner Villarreal [3]

Recibido: 06/10/2025 Aceptado: 12/01/2026

Resumen. - El estudio evaluó el desempeño sísmico de un edificio multifamiliar en Surco, Lima, bajo diferentes niveles de amenaza sísmica, utilizando la norma ATC-40. Se empleó un enfoque cuantitativo, descriptivo y explicativo, modelando la estructura en software especializado y aplicando análisis estático, dinámico espectral y pushover. Se encontró un período fundamental de vibración de 0.706 segundos en X y 0.400 segundos en Y. La fuerza cortante basal estática fue de 288.74 Tonf en X y 679.50 Tonf en Y, con derivas máximas de entrepiso de 0.000908 en X y 0.000798 en Y, todas dentro de los límites normativos. El análisis pushover mostró cargas laterales tentativas de hasta 185.68 Tonf en X y 294.57 Tonf en Y, y se detectaron ratios de refuerzo longitudinal superiores a los recomendados, llegando a 2.40 en columnas, señalando zonas vulnerables. En conclusión, el edificio mostró buen desempeño ante sismos moderados, pero presentó debilidades ante amenazas sísmicas más altas. La norma ATC-40 facilitó la identificación de estas áreas críticas, siendo una herramienta útil para el reforzamiento y mejora estructural en zonas sísmicas.

Palabras clave: Desempeño sismico, norma ATC-40, método pushover, edificio multifamiliar.

[1] Ingeniero Civil. Universidad de San Martin de Porres, oliberth_huaman@usmp.pe, ORCID iD: https://orcid.org/0009-0007-8669-3846

[2] Ingeniero Civil. Universidad de San Martin de Porres, josimar_guillem@usmp.pe, ORCID iD: https://orcid.org/0009-0003-9453-6673

[3] PhD. Universidad de San Martin de Porres, gvillarrealc@usmp.pe, ORCID iD: https://orcid.org/0000-0003-1768-646X

Summary. - *This study evaluated the seismic performance of a multi-family building in Surco, Lima, under different seismic hazard levels, using the ATC-40 standard. A quantitative, descriptive, and explanatory approach was used, modeling the structure in specialized software and applying static, dynamic spectral, and pushover analysis. A fundamental vibration period of 0.706 seconds in X and 0.400 seconds in Y was found. The static basal shear force was 288.74 Tonf in X and 679.50 Tonf in Y, with maximum story drifts of 0.000908 in X and 0.000798 in Y, all within the regulatory limits. The pushover analysis showed tentative lateral loads of up to 185.68 Tonf in X and 294.57 Tonf in Y, and longitudinal reinforcement ratios higher than recommended were detected, reaching 2.40 in columns, indicating vulnerable areas. In conclusion, the building showed good performance under moderate earthquakes, but presented weaknesses under higher seismic hazards. The ATC-40 standard facilitated the identification of these critical areas, being a useful tool for structural reinforcement and improvement in seismic zones.*

Palabras clave: *Seismic performance, ATC-40 standard, pushover method, multi-family building.*

***Resumo*. -** *Este estudo avaliou o desempenho sísmico de um edifício multifamiliar em Surco, Lima, sob diferentes níveis de risco sísmico, utilizando a norma ATC-40. Foi utilizada uma abordagem quantitativa, descritiva e explicativa, modelando a estrutura em software especializado e aplicando análises estáticas, espectrais dinâmicas e de pushover. Foi encontrado um período fundamental de vibração de 0,706 segundos em X e 0,400 segundos em Y. A força cortante basal estática foi de 288,74 Tonf em X e 679,50 Tonf em Y, com deslocamentos máximos entre pavimentos de 0,000908 em X e 0,000798 em Y, todos dentro dos limites regulamentares. A análise de pushover mostrou cargas laterais provisórias de até 185,68 Tonf em X e 294,57 Tonf em Y, e foram detectadas taxas de armadura longitudinal superiores às recomendadas, atingindo 2,40 nas colunas, indicando áreas vulneráveis. Em conclusão, o edifício apresentou bom desempenho sob terremotos moderados, mas apresentou fragilidades sob riscos sísmicos mais elevados. A norma ATC-40 facilitou a identificação dessas áreas críticas, sendo uma ferramenta útil para reforço estrutural e melhoria em zonas sísmicas.*

Palavras-chave: *Desempenho sísmico, norma ATC-40, método pushover, edifício multifamiliar.*

1. Introducción. - Los terremotos son eventos naturales que impactan profundamente en la seguridad estructural y la estabilidad social de las regiones afectadas, especialmente en áreas urbanas densamente pobladas donde el colapso de edificaciones puede ocasionar pérdidas humanas y materiales incalculables. Aunque las normativas de diseño sismorresistente han avanzado significativamente, su implementación práctica varía ampliamente, exponiendo a muchas construcciones a niveles inadecuados de protección. Este panorama global exige la adopción de herramientas de evaluación como la Norma ATC-40, la cual permite analizar el desempeño sísmico de edificaciones considerando diferentes niveles de amenaza, lo que resulta esencial en regiones de alta actividad sísmica como Lima, Perú.

En América Latina, la vulnerabilidad estructural frente a sismos es un problema persistente debido a la confluencia de factores como la informalidad en la construcción, la falta de recursos económicos y el crecimiento urbano desordenado. Países como Chile y México han avanzado en la aplicación de normativas sismorresistentes, mientras que, en otros, como Perú, las deficiencias en el diseño y la supervisión estructural generan un entorno de alta exposición al riesgo. Estas condiciones subrayan la necesidad de investigaciones que adapten estándares internacionales, como el ATC-40, al contexto regional para mejorar la seguridad y resiliencia de las edificaciones.

El distrito de Surco, en Lima, combina características de alto crecimiento inmobiliario con una alta densidad poblacional, lo que lo convierte en un caso de estudio relevante para evaluar la aplicabilidad de normativas internacionales. Este proyecto busca analizar el desempeño sísmico de un edificio multifamiliar bajo diferentes escenarios de amenaza sísmica, contribuyendo a la seguridad estructural y ofreciendo soluciones que puedan replicarse en otras zonas del país. Esta evaluación no solo es técnica, sino también estratégica, ya que identifica oportunidades para optimizar el diseño y la normativa local, reduciendo riesgos y aumentando la resiliencia frente a desastres.

Los Antecedentes de investigación son:

Castellanos y Jara (2021) en su investigación "Evaluación de desempeño sísmico del edificio de la Universidad Internacional SEK ubicado en el Campus Felipe Segovia Olmo" el objetivo principal del estudio fue analizar técnica y detalladamente el comportamiento lineal y no lineal de la estructura de hormigón armado del edificio Felipe Segovia Olmos, ubicado en el campus centro de la Universidad Internacional SEK en Quito. Se buscó evaluar el desempeño sísmico del edificio conforme a las normativas ecuatorianas y a códigos internacionales como el ASCE 41-13, NIST y ACI 318. La investigación comenzó con la recopilación de información en campo y la realización de ensayos no destructivos para verificar el uso actual de los espacios y las propiedades de los materiales estructurales. Se utilizó un modelo estático lineal para analizar la respuesta estructural ante sismos, y posteriormente se aplicaron análisis estáticos no lineales Pushover mediante elementos finitos para obtener la curva de capacidad del edificio y determinar el punto de desempeño según el método del espectro de capacidad ASCE41-13 NPS. Los resultados indicaron que la infraestructura no colapsa y mantiene niveles aceptables de seguridad para los ocupantes, concluyendo en la importancia de adecuar el diseño sísmico al cambio de uso del edificio para garantizar la protección tanto de las personas como de la estructura.

Montero (2022) establece como objetivo general de su investigación evaluar el desempeño sísmico de un edificio de pórticos de hormigón armado utilizando el método lineal ACI369.1-17. La metodología aplicada incluyó la modelación del edificio en el software SAP2000, considerando rigideces efectivas y distribuyendo las fuerzas sísmicas mediante un análisis estático lineal, obteniendo las demandas internas de fuerza y desplazamiento. Los resultados indicaron que el edificio cumple con las limitaciones del método estático lineal, sin embargo, no todos sus elementos cumplen con los objetivos de desempeño establecidos. Por ejemplo, las columnas interiores del primer nivel presentaron una razón demanda-capacidad de 0.879. En conclusión, la estructura cumple parcialmente con los criterios de aceptación de la normativa ACI369.1-17, destacando la importancia de mejorar algunos elementos estructurales para cumplir completamente con los objetivos de desempeño esperados.

Lagos (2024) indica en su investigación como objetivo general evaluar el desempeño sísmico de estructuras con marcos arriostrados excéntricamente (EBF) que utilizan enlaces reemplazables cortos, de acuerdo con la normativa chilena NCh433. La metodología emplea el análisis no lineal estático y dinámico siguiendo las pautas del FEMA P695,

utilizando modelos estructurales en la plataforma OpenSees para simular diferentes alturas de edificios (3, 9 y 15 pisos), zonas sísmicas y tipos de suelo. Los resultados indican que la sobre resistencia decrece con la altura, con valores promedios de 4.3, 2.74 y 2.12 para edificios de 3, 9 y 15 pisos respectivamente. Asimismo, el análisis dinámico reveló que el promedio del CMR fue 1.60, 1.40 y 1.53 para estas alturas, incumpliendo los criterios del FEMA P695. En conclusión, se sugiere que la normativa NCh433 es conservadora para edificios de menor altura, pero sobreestima la capacidad de aquellos con 15 pisos, destacando la necesidad de revisar los factores de modificación de respuesta estructural para EBF con enlaces reemplazables.

Bula (2022) estableció como objetivo general en su investigación el evaluar el desempeño sísmico de un edificio de 12 pisos ubicado en Bucaramanga, Santander, siguiendo las normas de diseño sismo-resistente aplicables. La metodología se basa en el uso del programa SAP2000 para el análisis estructural y en procedimientos de diseño detallados para los elementos estructurales, como columnas y vigas de concreto armado. Se realizaron tanto análisis modales espectrales como análisis no lineales (pushover y cronológicos) para obtener las fuerzas internas y desplazamientos del sistema. Los resultados cuantitativos muestran que las derivas máximas se mantuvieron dentro de los límites aceptables según la normativa, con un cortante basal que alcanzó valores de hasta 100,000 kN. En conclusión, el edificio presentó un comportamiento adecuado bajo las condiciones de carga sísmica analizadas, cumpliendo con los criterios de desempeño estructural esperados.

Gálvez y Zapata (2022) en su investigación evaluaron el desempeño sísmico de tres edificios de pórticos de concreto armado de distintas alturas, diseñados según la norma ecuatoriana NEC-15, utilizando análisis estático no lineal. La metodología incluyó la modelación de los edificios en el software ETABS y la aplicación de cargas laterales para simular las condiciones sísmicas, verificando el cumplimiento de los niveles de desempeño establecidos en FEMA 356. Los resultados cuantitativos muestran que los edificios de 2, 4 y 8 pisos cumplieron con los niveles de seguridad de vida y prevención del colapso, con factores de ductilidad de desplazamiento entre 3 y 5, y factores de sobre resistencia superiores a 1. En conclusión, se verificó que la altura influye en el desempeño sísmico, reduciendo la rigidez lateral y la sobre resistencia conforme aumenta la altura del edificio.

Chancafe y Gonzales (2021) en su investigación “Evaluación del desempeño sísmico de un edificio multifamiliar de concreto armado de 8 pisos mediante un Análisis Pushover, distrito de Santiago de Surco”, el objetivo del estudio fue evaluar el desempeño sísmico del edificio multifamiliar "La Merced" utilizando el Análisis Estático No Lineal (Pushover), con el fin de determinar su curva de capacidad frente a diversos niveles sísmicos. Se aplicaron métodos de identificación de puntos de desempeño de acuerdo con normas internacionales como FEMA 440 y ASCE 41-13, así como los niveles del comité Visión 2000. Empleando el software ETABS y en cumplimiento con la Norma de Diseño Sismorresistente E030, se obtuvieron derivas máximas de 0.0051 en la dirección X y 0.0013 en la dirección Y, cumpliendo con los límites establecidos. Los desplazamientos objetivos, evaluados mediante el espectro de capacidad y el método de coeficientes, indicaron que el desempeño sísmico del edificio es óptimo, garantizando la seguridad estructural y la funcionalidad bajo diversas condiciones sísmicas. Esto es esencial para mitigar pérdidas económicas y humanas en zonas vulnerables como la costa del Perú.

Carmelo y Kaqui (2022) en su investigación “Evaluación del desempeño sísmico de un edificio de concreto armado diseñado con la norma E030 del 2003 mediante un Análisis No Lineal Estático” el objetivo del estudio fue evaluar el desempeño sísmico de un edificio multifamiliar de 8 pisos en San Isidro, diseñado originalmente bajo la norma E030-2003, mediante el uso del análisis no lineal estático (pushover) para compararlo con los estándares actuales de la norma E030-2018. La investigación se basó en un enfoque aplicado con metodología cuantitativa y nivel descriptivo, utilizando Excel y ETABS para los cálculos y el modelado estructural. Se emplearon modelos de comportamiento estructural como Hognestad, Kent y Park, y Mander, integrados con modelos de plasticidad según la norma FEMA 356. Los resultados mostraron que la estructura cumplía con los requisitos de seguridad de vida en la dirección X y de ocupación inmediata en la dirección Y bajo el sismo de diseño. Sin embargo, se observó que la ductilidad demandada era menor a la requerida en ambos ejes. En conclusión, la investigación destacó la necesidad de actualizar el diseño estructural para cumplir con los estándares más recientes de seguridad sísmica y ductilidad especificados por la normativa vigente.

Tinipuclla (2020) en su investigación "Evaluación del diseño sismorresistente aplicando un análisis sísmico no lineal de un edificio multifamiliar, San Juan de Lurigancho", el estudio tuvo como objetivo evaluar el diseño sismorresistente de un edificio multifamiliar mediante el análisis sísmico no lineal, utilizando específicamente el método Pushover. La metodología se centró en analizar la capacidad de la estructura para resistir fuerzas horizontales incrementales, caracterizando su comportamiento no lineal durante eventos sísmicos. Se trató de un estudio de diseño no experimental y de nivel explicativo, en el que se realizó un análisis no lineal de vigas y columnas para identificar las rótulas plásticas y determinar las derivas laterales. Los resultados subrayaron la evaluación del nivel de desempeño sísmico conforme a normas como ATC-40, FEMA 440 y SEAOC, concluyendo que el método Pushover es efectivo para verificar el cumplimiento del diseño sismorresistente según la norma E030 y para entender el comportamiento estructural durante eventos sísmicos.

Ramos (2021) en su investigación "Evaluación del desempeño sísmico de edificaciones multifamiliares mediante métodos convencionales, edificio multifamiliar Benjamín Del Solar, Sachaca, Arequipa" tuvo como objetivo evaluar el desempeño sísmico del Edificio Multifamiliar Benjamín del Solar en Sachaca, Arequipa, utilizando métodos convencionales de análisis estático, dinámico modal y análisis no lineal estático. Se aplicó una metodología científica con un diseño experimental y un enfoque explicativo. Los resultados indicaron que la estructura resistió 444.93 Tonf. en la dirección X-X y 472.46 Tonf. en la dirección Y-Y durante un sismo severo, clasificándose como segura para la vida según la categorización del desempeño sísmico. La investigación concluyó que la normativa sismorresistente peruana proporciona una resistencia conservadora para edificaciones de concreto armado, limitando las derivas de entrepiso al 7 por mil. Además, el análisis no lineal reveló un balance adecuado entre rigidez y ductilidad en la estructura, lo cual se evidenció en las curvas de capacidad obtenidas.

Miranda & Torres (2023) en su investigación realizaron un análisis sísmico lineal y no lineal para evaluar el desempeño sísmico de una vivienda multifamiliar de cuatro niveles en Tacna, aplicando la norma ATC-40. La metodología empleada incluyó la recopilación de datos y modelado estructural utilizando el software ETABS. Se realizaron análisis tanto lineales como no lineales del comportamiento sísmico de la estructura, con énfasis en la determinación de derivas, fuerzas cortantes y desplazamientos. En cuanto a los resultados cuantitativos, el análisis no lineal determinó que la fuerza cortante en la base en la dirección X fue de 317.51 Tonf, con un desplazamiento de 0.207 m, mientras que en la dirección Y, la fuerza cortante fue de 221.77 Tonf, con un desplazamiento de 0.105 m. En conclusión, la evaluación del desempeño sísmico indicó que la edificación tiene un nivel de ocupación inmediata tanto en las direcciones X como Y, cumpliendo así con los requisitos de seguridad establecidos en la norma ATC-40.

Norma E.030. - La Norma Técnica Peruana E.030, "Diseño Sismorresistente", es la regulación nacional vigente que establece el método para diseñar edificios capaces de resistir terremotos. Este criterio adopta un concepto de seguridad estructural que asegura la vida de los habitantes y minimiza los daños. La E.030 contiene criterios para la selección de materiales, disposición estructural y métodos de análisis de manera que los edificios se diseñen para resistir las fuerzas sísmicas anticipadas, de modo que ningún edificio colapse y los daños no sean irreparables (Choque y Luque, 2019).

Algunos de los puntos más importantes a considerar al aplicar Norma E.030, según autores como Delgado (2015), son:

- Análisis sísmico: Es fundamental realizar un análisis dinámico y estático de las estructuras para asegurar su resistencia frente a sismos.
- Zonificación sísmica: El diseño debe ajustarse a la zona de sismo donde se halla el proyecto, ya que Perú está dividido en varias zonas según el riesgo sísmico.
- Materiales estructurales: Se deben seleccionar y diseñar adecuadamente materiales resistentes a fuerzas sísmicas, como el concreto armado y el acero.
- Simetría y configuración estructural: La norma enfatiza que las edificaciones deben tener una forma y disposición estructural que distribuyan las fuerzas sísmicas de manera equilibrada.

Norma ATC – 40. - La norma ATC-40 (Applied Technology Council 40), publicada en 1996, instaura procesos para evaluar y rediseñar de estructuras con base en su desempeño sísmico. Esta normativa utiliza un enfoque basado en el análisis no lineal, como el análisis "Pushover", y clasifica el desempeño de una edificación en diferentes niveles según su capacidad de resistir sismos de distintos grados de intensidad. La ATC-40 define tres niveles de peligro de sismo principales: sismo de servicio (SE), sismo máximo (ME) y sismo de diseño (DE), que corresponden a diferentes probabilidades de ocurrencia y magnitudes esperadas durante la vida útil que una estructura tiene. Estos niveles de peligro se combinan con objetivos de desempeño de la estructura, como ocupación inmediata, estabilidad estructural y seguridad de vida, con el fin de evaluar la capacidad de la edificación para que se soporte sismos sin comprometer la seguridad quienes lo ocupan o la funcionalidad de la construcción (Guevara, 2020).
Los pasos clave que deben seguirse para aplicar el código ATC-40 son descritos por Muñoz y Tapara (2020) y se muestra a continuación:

- Niveles de desempeño estructural: El ATC-40 categoriza las estructuras en varios niveles de desempeño, como ocupación inmediata, seguridad estructural y seguridad de vida. Todos se refieren a los diferentes niveles de daño estructural, desde muy poco daño que permite la ocupación hasta mucho daño que significa que el edificio no es muy habitable.
- Niveles de peligro sísmico: El ATC-40 establece tres criterios de peligro de sismo para el propósito del diseño estructural: terremoto de servicio (SE), terremoto de diseño (DE) y terremoto máximo (ME). Cada nivel corresponde a diferentes probabilidades de ocurrencia y niveles de severidad sísmica, que forman el trasfondo para determinar la respuesta de las estructuras a varias intensidades de un evento sísmico.
- Método de espectro de capacidad: Es uno de los métodos principales del ATC-40, donde se aplica el método del espectro de capacidad, cuya finalidad es determinar los puntos de desempeño de un edificio sometido a cargas sísmicas empleando la curva de capacidad de la estructura. Este enfoque tiene en cuenta la respuesta no lineal de la estructura y es uno de los que se aplican más para evaluaciones de desempeño.
- Evaluación de los elementos estructurales y no estructurales: Se reconoce en la norma el diferente comportamiento de estos elementos y cómo impactan el comportamiento del edificio bajo acción sísmica. Estos componentes se evalúan por separado, determinando los niveles de daño correspondientes.
- Objetivos de desempeño sísmico: El ATC-40 selecciona niveles de desempeño esperados para los edificios bajo distintos escenarios sísmicos. El propósito de seguridad básica implica que, bajo un sismo de diseño, el edificio tiene que alcanzar el nivel de "seguridad de vida", mientras que, bajo un sismo máximo, el nivel requerido es de "estabilidad de la estructura".

Comparación entre la norma E.030 y ATC -40. -

Aspecto	Norma E030	Norma ATC-40
Enfoque	Diseño basado en fuerzas	Diseño basado en el desempeño
Método de análisis	Análisis lineal estático y dinámico	Análisis no lineal (Pushover) y espectro de capacidad
Niveles de desempeño	No especifica niveles de desempeño claros	Define ocupación inmediata, seguridad de vida y estabilidad estructural
Evaluación estructural	Enfoque en seguridad de vida y resistencia estructural	Evalúa componentes estructurales y no estructurales
Objetivo principal	Garantizar que las edificaciones soporten sismos según la zona sísmica	Evaluar el desempeño de las estructuras bajo diferentes intensidades sísmicas

Tabla I. Comparación entre la norma E030 y ATC -40. ***Nota.*** Elaboración propia.

2. Análisis Sísmico. -

2.1. Niveles de desempeño sísmico según ATC-40. -

Niveles de Desempeño para Elementos Estructurales:

- Ocupación Inmediata (SP-1): Daños muy limitados; la resistencia y capacidad del sistema de cargas verticales y laterales permanecen usualmente intactas. La estructura es segura para su uso inmediato y no se muestran pérdidas humanas.
- Daño Controlado (SP-2): Estado de daño entre seguridad de vida y ocupación inmediata. Aunque la vida de las personas que ocupan el lugar no se encuentra en peligro, todavía se pueden ver afectados.
- Seguridad de Vida (SP-3): Daños significativos sin agotar totalmente los márgenes de seguridad contra un colapso posible. El riesgo de vida es muy bajo para los ocupantes, aunque pueden requerirse reparaciones antes de reocupar la estructura.
- Seguridad Limitada (SP-4): Daño entre la estabilidad estructural y los niveles de seguridad de vida. Ciertas partes de la estructura pueden necesitar ser reforzadas para asegurar la seguridad.
- Estabilidad Estructural (SP-5): Daño severo; la estructura tiene amplias posibilidades de colapsar parcial o totalmente. Hay una pérdida sustancial de resistencia y rigidez, con alto riesgo de colapso ante réplicas posibles.
- No Considerado (SP-6): No es un nivel de desempeño, sin embargo, se utiliza cuando no se evalúan los componentes estructurales.

Niveles de Desempeño para Elementos No Estructurales:

- Operacional (NP-A): Los elementos no estructurales, maquinarias y sistemas del edificio permanecen en su lugar y funcionando normalmente después del sismo.

- Ocupación Inmediata (NP-B): Aunque los elementos no estructurales permanecen en su sitio, pueden presentarse interrupciones menores en el funcionamiento de equipos. Algunos servicios externos pueden no estar disponibles, sin comprometer la ocupación del edificio.

- Seguridad (NP-C): Daños severos en elementos no estructurales, sin colapso ni peligro para los ocupantes. Sistemas y equipos pueden requerir reparaciones o reemplazos.

- Amenaza Reducida (NP-D): Daños severos en elementos no estructurales, contenidos y sistemas, sin colapso de grandes elementos que puedan causar heridas a grupos de personas.

- No Considerado (NP-E): Indica que no se han evaluado los elementos no estructurales, a menos que afecten directamente la respuesta estructural.

La combinación de estos niveles de desempeño estructural y no estructural permite una evaluación integral del comportamiento sísmico de una edificación, facilitando la toma de decisiones en procesos de evaluación y rehabilitación estructural.

Niveles de desempeño no estructural	Niveles de desempeño estructural					
	SP1	SP2	SP3	SP4	SP5	SP6
NP-A	**1-A Operacional**	2-A	NR	NR	NR	NR
NP-B	**1 - B Ocupación Inmediata**	2-B	3-B	NR	NR	NR
NP-C	1-C	2-C	**3-C Seguridad**	4-C	5-C	6-C
NP-D	NR	2-D	3-D	4-D	5-D	6-D
NP-E	NR	NR	3-E	4-E	**5-E Estabilidad structural**	No Aplicable
NR: combinación No Recomendada						

Figura I Descripción de los niveles de desempeño estructural. ***Nota.*** ATC – 40

2.2 Análisis estático - Las fuerzas cortantes que actúan en los entrepisos de la estructura, comparando los valores obtenidos por análisis estático y dinámico. En la dirección X, la fuerza cortante estática es de 288.74 Tonf, mientras que la dinámica es menor, con 185.68 Tonf, lo que representa al menos el 80% del valor estático. Para esta dirección, la estructura es regular y se aplica un factor de escala de 1.56, resultando en un valor de diseño de 288.74 Tonf.

En la dirección Y, la fuerza cortante estática es mayor, 679.50 Tonf, mientras que la dinámica es de 294.57 Tonf, representando al menos el 90% del valor estático. En esta dirección, la estructura se considera irregular y se utiliza un factor de escala más alto, 2.31, manteniendo el valor de diseño en 679.50 Tonf.

TABLE: Modal Participating Mass Ratios

Case	Mode	Period sec	UX	UY
Modal	1	0.706	49.19%	0.24%
Modal	2	0.4004	0.34%	28.83%
Modal	3	0.27	0.07%	18.88%
Modal	4	0.193	12.05%	0.09%
Modal	5	0.102	5.92%	0.19%
Modal	6	0.093	0.38%	14.46%
Modal	7	0.082	7.03%	0.27%
Modal	8	0.069	0.44%	9.35%
Modal	9	0.061	13.92%	0.22%
Modal	10	0.047	4.67%	0.73%
Modal	11	0.046	0.37%	12.17%
Modal	12	0.038	0.09%	3.22%
Modal	13	0.036	1.15%	0.10%
Modal	14	0.034	0.00%	4.54%
Modal	15	0.029	0.03%	0.16%
Modal	16	0.028	0.61%	0.02%
Modal	17	0.026	0.01%	2.11%
Modal	18	0.023	0.64%	0.00%
Modal	19	0.023	0.39%	0.01%
Modal	20	0.021	0.17%	0.66%
Modal	21	0.02	1.61%	0.08%

Modal	22	0.019	0.00%	0.31%
Modal	23	0.018	0.36%	0.00%
Modal	24	0.017	0.00%	0.55%
Modal	25	0.016	0.06%	0.04%
Modal	26	0.015	0.00%	0.62%
Modal	27	0.015	0.00%	0.63%
Modal	28	0.014	0.45%	0.00%
Modal	29	0.014	0.00%	0.62%
Modal	30	0.013	0.00%	0.12%
Modal	31	0.012	0.00%	0.17%
Modal	32	0.012	0.00%	0.04%
Modal	33	0.011	0.00%	0.09%
Modal	34	0.011	0.00%	0.04%
Modal	35	0.01	0.00%	0.20%
Modal	36	0.01	0.00%	0.01%
Modal	37	0.01	0.00%	0.11%
Modal	38	0.01	0.00%	0.00%
Modal	39	0.009	0.00%	0.01%
		TOTAL	99.57%	99.92%
		90% MASA	**CUMPLE**	**CUMPLE**

Tabla II Modos de vibración. **Nota.** Elaboración Propia

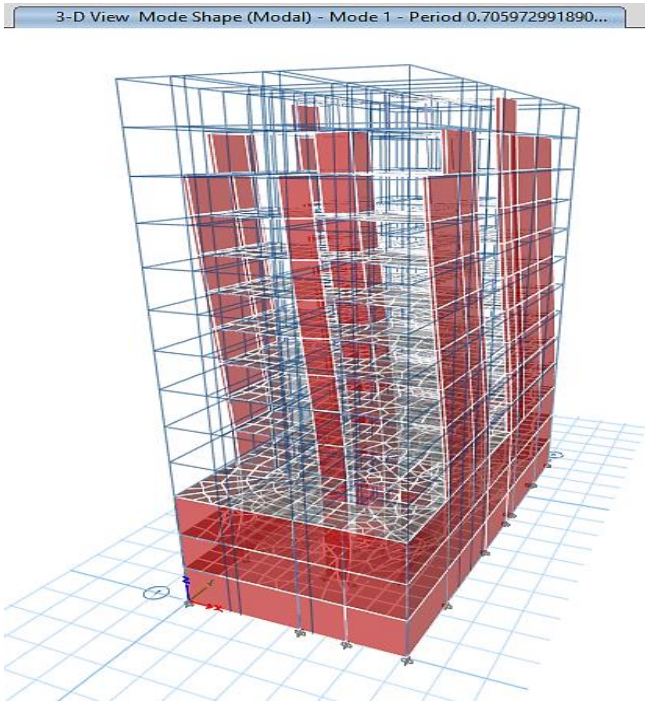

Figura II. Periodo fundamental – Modo 1. **Nota.** Elaboración Propia

Los períodos fundamentales obtenidos para la edificación corresponden al modo 1 en cada dirección principal: 0.7059 segundos en la dirección X y 0.4004 segundos en la dirección Y. Estos valores reflejan el comportamiento dinámico de la estructura frente a solicitaciones sísmicas, siendo mayores en la dirección X, lo que sugiere una menor rigidez relativa respecto a la dirección Y.

A continuación, se presenta el cuadro resumen correspondiente al análisis estático realizado, en el cual se sintetizan los resultados más relevantes obtenidos durante el proceso de evaluación estructural.

RESUMEN DEL ANÁLISIS ESTÁTICO

DATOS DE PARÁMETROS SÍSMICOS			
Z	=	0.45	g
U	=	1.00	
S	=	1.00	
Rx	=	6.00	
Ry	=	4.50	
Tp	=	0.40	
Tl	=	2.50	
PERIÓDO FUNDAMENTAL DE VIBRACIÓN			
(De los modos de vibración)			
Tx	=	0.706	
Ty	=	0.400	
FACTOR DE AMPLIFICACIÓN SÍSMICA			
Cx	=	1.42	
Cx/R	=	0.24	>=0.11 CUMPLE
Cy	=	2.50	
Cy/R	=	0.56	>=0.11 CUMPLE
FUERZA CORTANTE BASAL EN DIRECCIÓN "X"			
Vx	=	0.1062	P
kx	=	1.10	
P	=	2,717.99	Tonf
Vx	=	288.74	Tonf
FUERZA CORTANTE BASAL EN DIRECCIÓN "Y"			
Vy	=	0.2500	P
ky	=	1.00	
P	=	2,717.99	Tonf
Vy	=	679.50	Tonf

*Tabla III. Resumen del análisis estático***. Nota.** Elaboración Propia

Tabla N° 7
SISTEMAS ESTRUCTURALES

Sistema Estructural	Coeficiente Básico de Reducción R_0 (*)
Acero:	
Pórticos Especiales Resistentes a Momentos (SMF)	8
Pórticos Intermedios Resistentes a Momentos (IMF)	5
Pórticos Ordinarios Resistentes a Momentos (OMF)	4
Pórticos Especiales Concéntricamente Arriostrados (SCBF)	7
Pórticos Ordinarios Concéntricamente Arriostrados (OCBF)	4
Pórticos Excéntricamente Arriostrados (EBF)	8
Concreto Armado:	
Pórticos	8
Dual	7
De muros estructurales	6
Muros de ductilidad limitada	4
Albañilería Armada o Confinada	3
Madera	7(**)

Reducción en la dirección "X" = R_{ox} = 6 (Sistema de Muros Estructurales)
Reducción en la dirección "Y" = R_{oy} = 6 (Sistema de Muros Estructurales)

Irregularidad en altura = I_a = 1.00
Irregularidad en planta = I_{Py} =0.75 (eje y-y)

Factor de respuesta de diseño = Rx= 6.00
Factor de respuesta de diseño = Ry= 4.50

Se realizó un análisis estático de la estructura considerando una zona sísmica con una aceleración pico efectiva de Z = 0.45g. Los factores de uso (U = 1.00) y del suelo (S = 1.00) se mantuvieron en valores unitarios, indicando condiciones estándar. Los coeficientes de reducción por ductilidad y sobre resistencia son Rx = 6.00 para la dirección X y Ry = 4.50 para la dirección Y, lo que refleja diferentes niveles de disipación de energía según la dirección estructural.

El período fundamental de vibración calculado es de 0.706 segundos en la dirección X y 0.400 segundos en la dirección Y, lo que indica que la estructura es más flexible en la dirección X.

Los factores de amplificación sísmica obtenidos son Cx = 1.42 y Cy = 2.50, y al compararlos con sus respectivos valores reducidos (Cx/R y Cy/R), se verifica que cumplen con los requisitos mínimos normativos, al superar el umbral de 0.11.

En cuanto a las fuerzas sísmicas, la fuerza cortante basal en dirección X es de 288.74 Tonf, equivalente al 10.62% del peso sísmico (P = 2,717.99 Tonf), mientras que en dirección Y es de 679.50 Tonf, equivalente al 25.00% del peso sísmico, lo que sugiere una mayor demanda sísmica en esa dirección.

2.3 Análisis dinámico. - Los desplazamientos laterales obtenidos a partir del software de análisis corresponden a las fuerzas sísmicas reducidas por el factor de respuesta. Por esta razón, para estimar los desplazamientos inelásticos, es decir, los desplazamientos reales que podrían presentarse durante un sismo fuerte, es necesario multiplicar los desplazamientos elásticos por un factor adicional: 0.75R en el caso de estructuras regulares y 0.85R para estructuras con irregularidades.

Por otro lado, se verificó que el desplazamiento relativo entre pisos (deriva) no supera el límite permitido, el cual está definido como una fracción de la altura del entrepiso, según lo establecido en la normativa de límites de distorsión del entrepiso en este caso de concreto armado con un 0.007.

TABLE: Story Drifts

Story	Output Case	Direction	Drift	Drift 0.75*Rx	< 7/1000
TECHO	S din X	X	0.000614	0.002763	CUMPLE
AZOTEA	S din X	X	0.000766	0.003447	CUMPLE
PISO 8	S din X	X	0.000797	0.003587	CUMPLE
PISO 7	S din X	X	0.000858	0.003861	CUMPLE
PISO 6	S din X	X	0.000893	0.004019	CUMPLE
PISO 5	S din X	X	0.000908	0.004086	CUMPLE
PISO 4	S din X	X	0.0009	0.004050	CUMPLE
PISO 3	S din X	X	0.000857	0.003857	CUMPLE
PISO 2	S din X	X	0.000746	0.003357	CUMPLE
PISO 1	S din X	X	0.000485	0.002183	CUMPLE
SEMITOTANO	S din X	X	6.50E-05	0.000293	CUMPLE
SOTANO 1	S din X	X	4.60E-05	0.000207	CUMPLE
SOTANO 2	S din X	X	3.70E-05	0.000167	CUMPLE

Tabla IV. Distorsión de entrepiso – Eje X. **Nota.** Elaboración Propia

Los desplazamientos relativos de entrepisos y derivas, fueron analizados para la estructura bajo cargas sísmicas en la dirección X. Los resultados muestran que todas las derivas calculadas están muy por debajo del límite máximo permitido por la normativa, que es de 7 milésimas (0.007). La deriva máxima registrada se presentó en el piso 5, con un valor de aproximadamente de 4.086%, lo que representa apenas una fracción mínima del límite permitido. Esto indica que la estructura presenta deformaciones muy controladas y adecuadas para garantizar su integridad y seguridad durante un sismo, evitando daños por desplazamientos excesivos. Por lo que, la estructura cumple satisfactoriamente con los criterios de diseño para controlar la deriva en todos los niveles.

TABLE: Story Drifts					
Story	**Output Case**	**Direction**	**Drift**	**Drift 0.85*Rx**	**< 7/1000**
TECHO	**S din Y**	**Y**	**0.000772**	**0.002953**	**CUMPLE**
AZOTEA	**S din Y**	**Y**	**0.000787**	**0.003010**	**CUMPLE**
PISO 8	**S din Y**	**Y**	**0.000791**	**0.003026**	**CUMPLE**
PISO 7	**S din Y**	**Y**	**0.000798**	**0.003052**	**CUMPLE**
PISO 6	**S din Y**	**Y**	**0.000778**	**0.002976**	**CUMPLE**
PISO 5	**S din Y**	**Y**	**0.000731**	**0.002796**	**CUMPLE**
PISO 4	**S din Y**	**Y**	**0.000661**	**0.002528**	**CUMPLE**
PISO 3	**S din Y**	**Y**	**0.000561**	**0.002146**	**CUMPLE**
PISO 2	**S din Y**	**Y**	**0.000427**	**0.001633**	**CUMPLE**
PISO 1	**S din Y**	**Y**	**0.000256**	**0.000979**	**CUMPLE**
SEMITOTANO	**S din Y**	**Y**	**4.00E-05**	**0.000153**	**CUMPLE**
SOTANO 1	**S din Y**	**Y**	**3.20E-05**	**0.000122**	**CUMPLE**
SOTANO 2	**S din Y**	**Y**	**2.60E-05**	**0.000099**	**CUMPLE**

Tabla V Distorsión de entrepiso – Eje Y. **Nota.** Elaboración Propia

Los desplazamientos relativos entre pisos en la dirección Y fueron evaluados bajo las cargas sísmicas correspondientes, considerando un factor de amplificación inelástico ajustado con 0.85 veces el coeficiente Rx. Los valores de deriva calculados en cada nivel, desde los sótanos hasta el techo, se mantienen ampliamente por debajo del límite máximo permitido, que es 0.007. La máxima deriva observada se registró en el piso 7, con un valor aproximado de 3.052%, lo cual es significativamente inferior al límite normativo. Estos resultados demuestran que la estructura presenta un comportamiento estable y controlado ante la acción sísmica en la dirección Y, cumpliendo con los criterios de diseño para limitar las deformaciones entre niveles y garantizar la seguridad estructural.

Fuerzas cortantes de diseño. - En cada dirección analizada, la fuerza cortante en el primer entrepiso no debe ser menor al 80% del valor calculado para estructuras regulares, ni menor al 90% para estructuras irregulares.

TABLE: Story Forces								
Story	Load Case/Combo	Location	P	VX	VY	T	MX	MY
			tonf	tonf	tonf	tonf-m	tonf-m	tonf-m
TECHO 1	SX	Bottom	0	288.74	0.00	1603.051	446.321	3510.420
TECHO 1	SY	Bottom	0	0.00	679.50	-855.98	653.32	0.00
TECHO 1	SDX Max	Bottom	0	185.677	25.287	2645.042	546.397	3771.362
TECHO 1	SDY Max	Bottom	0	33.716	294.573	2404.684	6416.555	588.596

*Tabla VI. Fuerzas cortantes de diseño***. Nota.** Elaboración Propia

Se muestran las fuerzas y momentos que actúan en la base del techo bajo diferentes casos de carga sísmica. En la dirección X, la fuerza cortante principal es de 288.74 Tonf, mientras que en la dirección Y la fuerza cortante máxima es de 679.50 Tonf. También se registran momentos de torsión y momentos flexionantes significativos en ambos sentidos, lo que indica que la estructura está sometida a fuerzas complejas que deben ser consideradas en el diseño para garantizar su estabilidad y seguridad durante un sismo.

Dirección	V estática tonf	V dinámica tonf	% V est mín	Factor escala	Estructura	V diseño tonf
Dirección "X"	288.74	185.68	80%	1.56	REGULAR	288.74
Dirección "Y"	679.50	294.57	90%	2.31	IRREGULAR	679.50

Tabla VII Valores de cortantes (V) de entrepiso. **Nota.** Elaboración Propia

La tabla VIII, muestra las fuerzas cortantes que actúan en los entrepisos de la estructura, comparando los valores obtenidos por análisis estático y dinámico. En la dirección X, la fuerza cortante estática es de 288.74 Tonf, mientras que la dinámica es menor, con 185.68 Tonf, lo que representa al menos el 80% del valor estático. Para esta dirección, la estructura es regular y se aplica un factor de escala de 1.56, resultando en un valor de diseño de 288.74 Tonf.
En la dirección Y, la fuerza cortante estática es mayor, 679.50 Tonf, mientras que la dinámica es de 294.57 Tonf, representando al menos el 90% del valor estático. En esta dirección, la estructura se considera irregular y se utiliza un factor de escala más alto, 2.31, manteniendo el valor de diseño en 679.50 Tonf.

2.4 Metodología de diseño. - Para definir la resistencia nominal necesaria, se presentarán los diagramas que muestran las envolventes de esfuerzos cortantes y momentos flectores correspondientes a las combinaciones de carga consideradas (Ver Anexo 3).

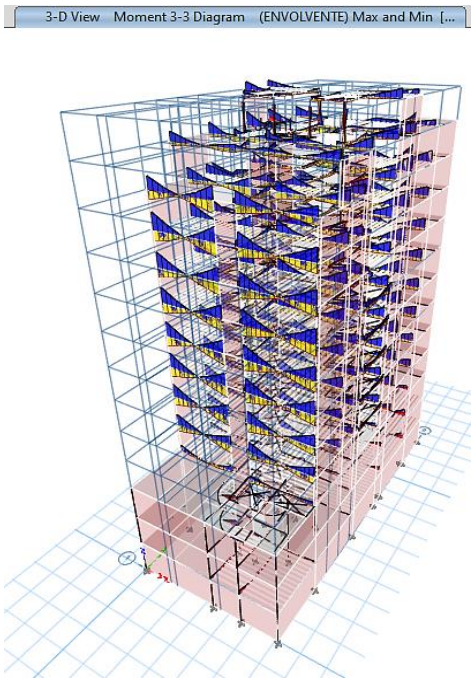

Figura III. Envolvente de momentos flectores. **Nota.** Elaboración Propia

La figura III, muestra la envolvente de momentos flectores, que representa los valores máximos y mínimos de los momentos que pueden presentarse en diferentes puntos de la estructura bajo las distintas combinaciones de carga consideradas. Esta envolvente es fundamental para identificar las zonas críticas donde se concentran los mayores esfuerzos de flexión, y sirve como referencia para el dimensionamiento y refuerzo de los elementos estructurales, asegurando su resistencia y estabilidad frente a las cargas aplicadas.

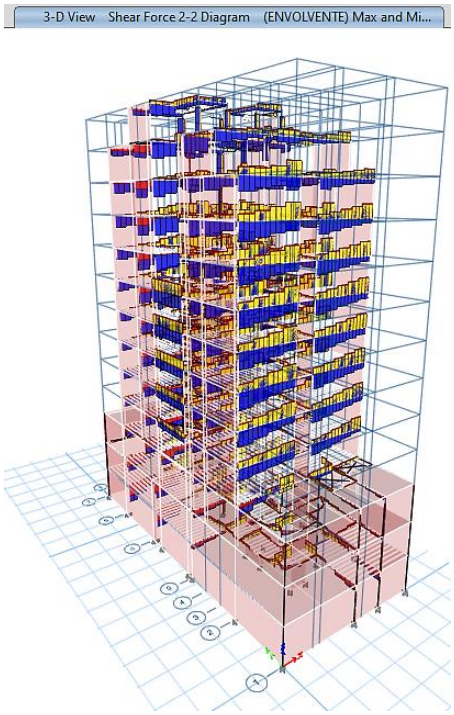

Figura IV. Envolvente de fuerza cortante. **Nota.** Elaboración Propia

La figura IV, presenta la envolvente de fuerza cortante, que muestra los valores máximos y mínimos de las fuerzas cortantes que actúan en los distintos niveles o elementos de la estructura bajo las combinaciones de carga analizadas. Esta información permitió determinar las zonas donde se concentran las mayores fuerzas cortantes, a la vez un diseño adecuado y seguro de los elementos estructurales para resistir estas solicitaciones y evitar fallas por corte.

2.5. Evaluación sísmica. -

Análisis Pushover. - Este análisis ayudó a identificar las zonas más vulnerables del edificio y permitió observar cómo se distribuían las fuerzas y desplazamientos durante un sismo fuerte. Con esta información, se pudo diseñar o reforzar mejor la estructura para asegurar que fuera más segura y resistente ante terremotos.

	h (m)	X-Dr tonf	Fx Tn	F lat-X (Pushover)
Techo	**35.22**	**13.214**	**13.214**	**-690.139**
Azotea	**32.72**	**40.431**	**27.217**	**-662.922**
Story8	**30.07**	**66.631**	**39.414**	**-623.508**
Story7	**27.42**	**85.229**	**45.815**	**-577.693**
Story6	**24.77**	**101.449**	**55.633**	**-522.059**
Story5	**22.12**	**114.826**	**59.193**	**-462.866**
Story4	**19.47**	**126.698**	**67.505**	**-395.361**
Story3	**16.82**	**137.854**	**70.349**	**-325.012**
Story2	**14.17**	**146.936**	**76.587**	**-248.426**
Story 1	**11.52**	**153.147**	**76.561**	**-171.865**
SEMI SOTANO	**8.87**	**162.749**	**86.188**	**-85.677**
SOTANO 1	**5.8**	**176.029**	**89.841**	**4.164**
SOTANO 2	**3**	**185.677**	**95.836**	**100.000**

Tabla VIII. Fuerzas laterales Pushover – en X. **Nota.** Elaboración Propia

Se muestran las fuerzas laterales aumentan conforme bajamos desde el techo hacia los pisos inferiores, lo que es esperado porque los niveles inferiores deben soportar toda la carga acumulada de arriba. Por ejemplo, en el techo la fuerza lateral es de alrededor de 13 Tonf, mientras que en el sótano 2 llega a aproximadamente 185 Tonf.

Además, los valores negativos en la columna de fuerzas laterales del pushover indican que las fuerzas actúan en sentido contrario, mostrando cómo la estructura resiste las cargas sísmicas en la dirección X.

	h (m)	Y-Dr tonf	Fx Tn	F lat-Y (Pushover)
Techo	**35.22**	**15.5365**	**15.537**	**-1202.942**
Azotea	**32.72**	**63.7497**	**48.213**	**-1154.729**
Story8	**30.07**	**109.8492**	**61.636**	**-1093.093**
Story7	**27.42**	**143.4121**	**81.776**	**-1011.317**
Story6	**24.77**	**171.2117**	**89.436**	**-921.881**
Story5	**22.12**	**195.0726**	**105.637**	**-816.244**
Story4	**19.47**	**214.9673**	**109.330**	**-706.914**
Story3	**16.82**	**231.2085**	**121.878**	**-585.036**
Story2	**14.17**	**244.1232**	**122.245**	**-462.791**
Story 1	**11.52**	**254.0177**	**131.773**	**-331.018**
SEMI SOTANO	**8.87**	**268.2172**	**136.445**	**-194.573**
SOTANO 1	**5.8**	**283.7864**	**147.342**	**-47.231**
SOTANO 2	**3**	**294.5733**	**147.231**	**100.000**

Tabla IX Fuerzas laterales Pushover – en Y. **Nota.** Elaboración Propia

Se observa que las fuerzas laterales aumentan a medida que descendemos por la estructura, siendo menores en el techo y mayores en los niveles inferiores. Por ejemplo, en el techo la fuerza lateral es aproximadamente 15.5 Tonf, mientras que en el sótano 2 llega a casi 295 Tonf.

Los valores negativos en la columna de fuerzas laterales por pushover indican que estas fuerzas actúan en sentido opuesto, lo que refleja cómo la estructura responde y resiste las cargas sísmicas en esta dirección.

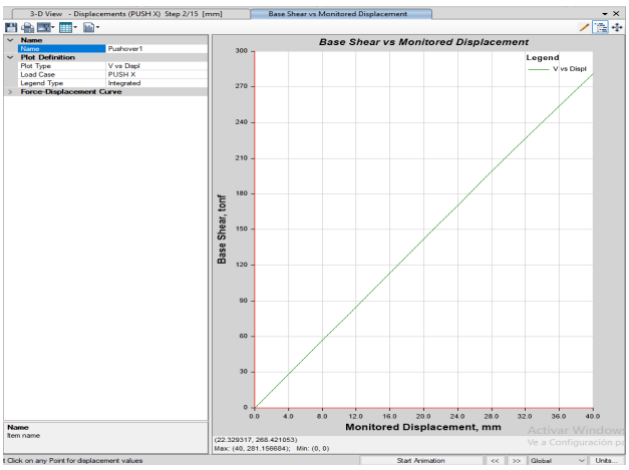

Figura V. Curva Pushover. **Nota.** Elaboración Propia

La curva pushover muestra un comportamiento lineal, lo que significa que la relación entre la fuerza cortante y el desplazamiento es directa y constante. No se observan cambios ni desviaciones en la curva, lo que indica que la estructura responde de manera estable y predecible dentro de ese rango de análisis.

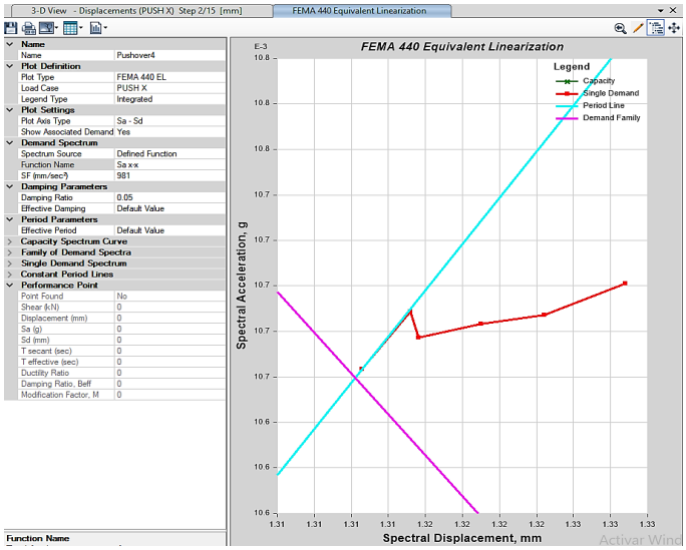

Figura VI. Curva FEMA. **Nota.** Elaboración Propia

La curva FEMA muestra la capacidad de la estructura y es paralela a la línea del período lineal. Además, se cruza en un punto específico con la curva de demanda, llamado “single demanda”. Este punto representa el equilibrio entre la capacidad de la estructura y las fuerzas que se esperan durante un sismo, ayudando a determinar el comportamiento esperado ante cargas sísmicas.

Asimismo, se muestra la figura obtenida mediante el Método ASCE 41-13, que es la herramienta utilizada para evaluar la respuesta sísmica de estructuras existentes. Lo cual, demostrará cómo se comporta la estructura bajo cargas sísmicas, mostrando su capacidad para resistir movimientos laterales y las deformaciones que podrían presentarse. Con esta información, podemos identificar las áreas que necesitan refuerzo o mejoras para aumentar la seguridad del edificio frente a terremotos, asegurando que la estructura sea más resistente y confiable.

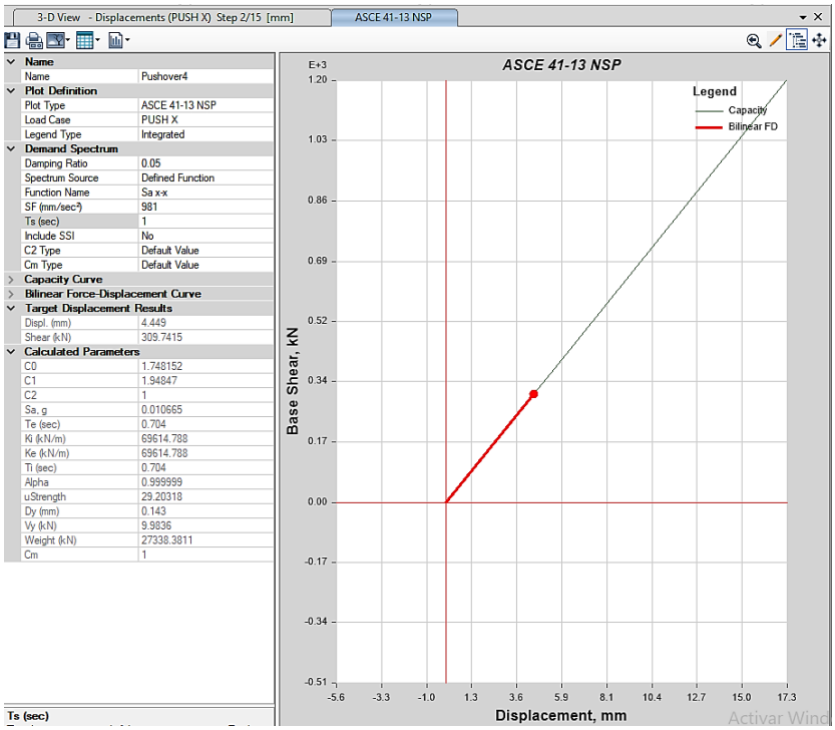

Figura VII Método ASCE 41-13. **Nota.** Elaboración Propia

En la figura VII obtenida mediante el método ASCE 41-13, se puede observar que la curva de capacidad y la curva de demanda son paralelas, lo que indica que la estructura responde de manera uniforme y consistente frente a las cargas sísmicas consideradas.

3. Conclusiones. -

1. Se logró evaluar el desempeño sísmico de un edificio multifamiliar ubicado en el distrito de Surco, Lima, frente a diferentes niveles de amenaza sísmica aplicando la metodología ATC-40. El análisis indicó que, bajo escenarios de sismos moderados, el edificio cumple con los criterios de seguridad y funcionalidad establecidos por la norma, manteniendo la integridad estructural y protegiendo la vida de los ocupantes. Sin embargo, ante mayores niveles de amenaza sísmica, se identificaron zonas donde la estructura está cerca de su límite de capacidad, lo que amerita considerar refuerzos locales para garantizar un comportamiento óptimo ante eventos extremos.

2. Se determinaron las características estructurales del edificio multifamiliar, mediante la recopilación y análisis de planos estructurales, especificaciones técnicas y condiciones de diseño. Esta información permitió modelar fielmente la edificación en el software ETABS, asegurando que la simulación estructural refleje de manera adecuada la realidad constructiva y posibilite la evaluación precisa del desempeño sísmico de cada elemento, especialmente columnas y vigas situadas en las zonas más vulnerables de la estructura.

3. Se identificaron los niveles de amenaza sísmica a través de los parámetros de sismos establecidos en la norma E.030: Z = 0.45g, U = 1.0, S = 1.0. Estos valores indican una zona de alta sismicidad, y se utilizaron en modelos para analizar su influencia en el sistema. También se tomaron en cuenta factores de reducción (Rx = 6.0, Ry = 4.5) y curvas de espectro de respuesta elástica que representan la respuesta sísmica esperada dentro de la región.

4. La aplicación de la metodología ATC-40 permitió evaluar el edificio mediante el análisis estático no lineal (pushover), seleccionando los puntos de desempeño a partir de la intersección entre el espectro de demanda sísmica y la curva de capacidad estructural. Los resultados mostraron que el edificio presenta niveles satisfactorios de desempeño bajo demandas sísmicas habituales, aunque se detectaron grados de vulnerabilidad para amenazas superiores, en coincidencia con las zonas de refuerzo longitudinal elevado y mayores derivas detectadas por la simulación. La metodología demostró ser efectiva para identificar necesidades de mejoramiento, permitiendo proponer recomendaciones precisas de intervención preventiva para optimizar la seguridad estructural.

Referencias

[1] Bula, C. (2022). Evaluación y diseño sísmico de un edificio de 12 pisos en la ciudad de Bucaramanga Santander.
[2] Carmelo, O. & Kaqui, D. (2022). Evaluación del desempeño sísmico de un edificio de concreto armado diseñado con la norma E.030 del 2003 mediante un análisis no lineal. Universidad Ricardo Palma.
[3] Castellanos, S. & Jara, D. (2021). Evaluación de desempeño sísmico del edificio de la Universidad Internacional SEK ubicado en el Campus Felipe Segovia Olmo. https://repositorio.uisek.edu.ec/handle/123456789/4516
[4] Chancafe, B. & Gonzales, C. (2021). Evaluación del desempeño sísmico de un edificio multifamiliar de concreto armado de 8 pisos mediante un análisis pushover, distrito de Santiago de Surco.
[5] Chavesta, E. (2019). Análisis estático no lineal para estimar el desempeño sísmico de una estructura aporticada de 5 pisos en la ciudad de Lima.
[6] Choque, J. & Luque, E. (2019). Análisis estático no lineal y evaluación del desempeño sísmico de edificios de 8 niveles diseñado con la norma E.030.
[7] Gálvez, K. & Zapata, C. (2022). Evaluación del desempeño sísmico de tres estructuras de pórticos de hormigón armado de diferente altura de la edificación diseñados conforme a la NEC-15, usando análisis estático no lineal.
[8] Guevara, A. (2020). Evaluación del desempeño sísmico de una nave industrial de acero para el sector minero utilizando el ATC-40.
[9] Lagos, D. (2024). Desempeño sísmico de edificios estructurados con marcos arriostrados excéntricamente utilizando enlaces reemplazables cortos.
[10] Miranda, L. & Torres, V. (2023). Análisis sísmico lineal y desempeño sísmico de una vivienda multifamiliar de 4 Niveles mediante la Norma ATC-40 en Tacna.
[11] Montero, S. (2022). Evaluación del desempeño sísmico de un edificio de pórtico de hormigón armado utilizando el método lineal del ACI369-17.
[12] Muñoz, M. & Tapara, L. (2020). Evaluación del comportamiento sísmico de una edificación de 8 pisos ubicado en el distrito de San Borja – Lima.
[13] Ramos, J. (2021). Evaluación del desempeño sísmico de edificaciones multifamiliares mediante métodos convencionales, edificio multifamiliar Benjamín Del Solar, Sachaca, Arequipa. https://repositorio.continental.edu.pe/bitstream/20.500.12394/10465/2/IV_FIN_105_TE_Ramos_Cahuapaza_2021.pdf
[14] Tinipuclla, A. (2020). Evaluación del diseño sismorresistente aplicando un análisis sísmico no lineal de un edificio multifamiliar, San Juan de Lurigancho. https://repositorio.ucv.edu.pe/handle/20.500.12692/64879

Author contribution:

1. Conception and design of the study

2. Data acquisition

3. Data analysis

4. Discussion of the results

5. Writing of the manuscript

6. Approval of the last version of the manuscript

JG has contributed to: 1, 2, 3, 4, 5 and 6.

OH has contributed to: 1, 2, 3, 4, 5 and 6.

GV has contributed to: 1, 2, 3, 4, 5 and 6.

Acceptance Note: This article was approved by the journal editors Dr. Rafael Sotelo and Mag. Ing. Fernando A. Hernández Gobertti.

Determining the correlation between line balancing and productivity: a proposal for process improvement

Determinación de la correlación entre el balanceo de línea y la productividad, una propuesta para la mejora de los procesos

Determinando a correlação entre balanceamento de linha e produtividade: uma proposta de melhoria de processos

Fabiola Hermosillo-Villalobos [1], Jorge Luis García-Alcaraz [2] (*), Omar Celis-Gracia [3]

Recibido: 15/10/2025 Aceptado: 12/01/2026

Summary. - Line balancing (LB) is a key tool in lean manufacturing that optimizes task allocation, reduces downtime, and increases operational efficiency. This study was conducted in a manufacturing company in the industrial sector, evaluating four of its 19 assembly lines (21%) that presented low productivity, high levels of waste, and late deliveries. This study shows the impact of line balancing on process performance and the savings associated with its implementation. Additionally, two objectives are set: first, to identify external factors, such as employee absenteeism, that negatively affect production and quantify their effect on operational performance. Second, manufacturing tools that help mitigate these impacts must be explored, and solution strategies oriented towards continuous improvement must be developed. This study used a quantitative approach to analyze the relationship between the percentage of added value activities and productivity (pieces per man-hour), demonstrating that the correct application of LB can significantly improve system performance. The results offer practical and sustainable solutions for addressing operational variability and increasing production efficiency.

Keywords: *Line balancing; added value activities; absenteeism; productivity; lean manufacturing.*

(*) Corresponding author.

[1] PhD Student, Department of Electrical Engineering and Computer Science, Autonomous University of Ciudad Juárez (Mexico) al232734@alumnos.uacj.mx, ORCID iD: https://orcid.org/0000-0003-1644-7598

[2] Full-Time Professor, PhD, Department of Industrial Engineering and Manufacturing, Autonomous University of Ciudad Juárez (Mexico), jorge.garcia@uacj.mx, ORCID iD: https://orcid.org/0000-0002-7092-6963

[3] PhD Student, Department of Electrical Engineering and Computer Science, Autonomous University of Ciudad Juárez (Mexico), al232735@alumnos.uacj.mx, ORCID iD: https://orcid.org/0000-0003-2061-3384

Resumen. - *El balanceo de líneas (LB) es una herramienta de manufactura esbelta que optimiza la asignación de tareas, reduce el tiempo improductivo y aumenta la eficiencia operativa. Este estudio se desarrolla en una empresa manufacturera del sector industrial, evaluando 4 de sus 19 líneas de ensamble (21%) que presentan baja productividad, altos niveles de desperdicio y entregas tardías. Esta investigación muestra el impacto de los balanceos de línea en el desempeño de los procesos, así como los ahorros asociados a su implementación. Además, se plantean dos objetivos: el primero se identifica los factores externos como el ausentismo laboral que afectan negativamente la producción, y se cuantifica su efecto sobre el desempeño operativo; y el segundo, explorar herramientas de manufactura que ayuden a mitigar estos impactos, desarrollando estrategias de solución orientadas a la mejora continua. El estudio utiliza un enfoque cuantitativo, analizando la relación entre el porcentaje de actividades que agregan valor y productividad (piezas por hora-hombre), demostrando que una correcta aplicación del LB mejora el rendimiento del sistema productivo. Los resultados del estudio ofrecen soluciones prácticas y sostenibles para enfrentar variabilidades operativas y elevar la eficiencia productiva.*

Palabras clave: *Balanceo de línea; actividades que agregan valor; ausentismo; productividad; manufactura esbelta.*

Resumo. ***-*** *O balanceamento de linha (LB) é uma ferramenta de manufatura enxuta que otimiza a alocação de tarefas, reduz o tempo de inatividade e aumenta a eficiência operacional. Este estudo foi conduzido em uma empresa de manufatura do setor industrial, avaliando quatro de suas 19 linhas de montagem (21%) que apresentam baixa produtividade, altos níveis de desperdício e atrasos nas entregas. Esta pesquisa demonstra o impacto do balanceamento de linha no desempenho do processo, bem como a economia associada à sua implementação. Dois objetivos também são abordados: primeiro, identificar fatores externos, como o absenteísmo de funcionários, que afetam negativamente a produção e quantificar seu efeito no desempenho operacional; segundo, explorar ferramentas de manufatura que ajudem a mitigar esses impactos, desenvolvendo estratégias de solução voltadas à melhoria contínua. O estudo utiliza uma abordagem quantitativa, analisando a relação entre o percentual de atividades que agregam valor e a produtividade (peças por homem-hora), demonstrando que a implementação adequada do LB melhora o desempenho do sistema de produção. Os resultados do estudo oferecem soluções práticas e sustentáveis para lidar com a variabilidade operacional e aumentar a eficiência da produção.*

Palavras-chave: *Balanceamento de linha; atividades que agregam valor; absenteísmo; produtividade; manufatura enxuta.*

1. Introduction. - Production line balancing (LB) allows process optimization and is a critical element in operations management. It minimizes downtime and ensures continuous operation by allocating tasks across different workstations. This constant flow improves productivity indicators on production lines, allowing for the efficient use of available resources [1], [2].

Previous studies suggest that a more balanced workload is associated with improved working conditions, which may lead to lower fatigue, fewer errors, and lower absenteeism in the workplace. Thus, LB aligns with the principles of lean manufacturing, as it promotes waste elimination, continuous improvement, and customer focus [3][4], [5].

To perform proper LB, activities must be classified according to the value they add to the product, distinguishing between added-value (AV) activities, auxiliary work (AW), and non-added-value (NAV) activities. AV activities are those that transform the product and for which the customer is willing to pay, such as assembly, welding, and packaging, among others. However, NVA activities, such as auxiliary activities, are necessary to keep the process running. Finally, pure waste activities are identified, which can be eliminated without affecting the value of the product, such as idle time (waiting), excessive transportation, and unnecessary movements [6].

The identification and quantification of these activities allow for the prioritization of improvement actions. For example, reducing the percentage of non-added value activities has been associated with improvements in productivity, often without the need for significant infrastructure investment [7][8]. Implementing LB techniques in manufacturing industries increases productivity and improves the efficiency of production processes by 15% [8], [9], which indicates the importance of designing and implementing effective balancing strategies to maximize operational performance and reduce inefficiencies.

Simultaneously, recent research indicates that absenteeism affects productivity levels in manufacturing environments. A negative correlation has been identified between absenteeism rates and performance, suggesting that high absenteeism disrupts the standard workflow and reduces overall productivity [9][10]. This situation becomes critical when workers replace absent staff without adequate training, which affects the quantity and quality of production.
In manufacturing systems, absenteeism has been identified as a factor that disrupts production lines, particularly when personnel with varying levels of experience are reassigned to cover absences in the workforce. Several studies have reported a negative relationship between absenteeism and productivity levels, suggesting that variations in employee attendance often coincide with changes in operational performance[11][12][13]. This link underscores the need to establish effective strategies to manage work absenteeism in conjunction with line balancing, as adjustments to the line are required to accommodate workers.

For example, when a worker is absent, the impact is most evident in AV activities, leading to production delays and reduced operational efficiency. To mitigate this effect, it is recommended that cross-training programs be implemented to allow other workers to take on critical tasks in the event of illness-related absences. In this sense, the LB, by providing a breakdown of AV and NVA activities, is a valuable tool for identifying opportunities for improvement and optimizing production in the face of unforeseen circumstances [14].

Various studies have examined the relationship between absenteeism and productivity and found a negative direct relationship. It has also been studied in administrative [15], mental health [16], and socioeconomic settings [17] and in various qualitative studies. However, few case studies have quantitatively addressed this issue in the manufacturing industry, particularly in maquiladoras.

In this context, a maquiladora in the industrial sector with 19 assembly lines across two plants is experiencing low productivity. A sample was taken from four of these lines, representing 21% of the total assembly line. Analysis of the information indicates that the current situation has led to delivery delays on one of the lines, with an absenteeism rate of 75%. In addition, the annual costs associated with idle time and waste on the other lines are estimated at a total of $57,582.4 USD per year, plus $12,153.91 USD for late deliveries due to the same problem.

To solve this problem, this study proposes implementing a lean manufacturing tool, LB, to determine the relationship between the percentage of activities that add value to the process and the performance and productivity metrics. In this study, productivity was defined as the ratio of parts produced by an operator per hour of work [18]. It is measured by recording the total number of parts manufactured and dividing it by the hours worked by the number of operators, thus obtaining the indicator of parts per man-hour. This study also seeks to reduce delivery delays and the costs associated with idle time and waste.

This study will enable the development of strategies to manage work absenteeism by quantitatively analyzing its impact on productivity metrics and identifying its effects on operational performance. The first step is to numerically assess the magnitude of absenteeism's effect, then apply tools such as line balancing to demonstrate its positive impact on productivity. This study aims to examine and understand the variables that negatively affect productivity metrics from a quantitative perspective and to counteract their effects by implementing solutions that improve overall process performance, are easy to implement, and are familiar to the engineers in charge of the production lines.

Section 2 includes the methodology for this research, following the introduction. Section three discusses the results, section four reports the conclusions, and section five presents the limitations and future research Directions

2. Methods. - The methodology used in this research is based on the DMAIC cycle (Define, Measure, Analyze, Improve, and Control), complemented by lean manufacturing tools, to improve processes affected by external variations. This approach is based on five phases, as shown in Figure 1, which indicates the techniques used in each stage and the integration of the lean manufacturing tools.

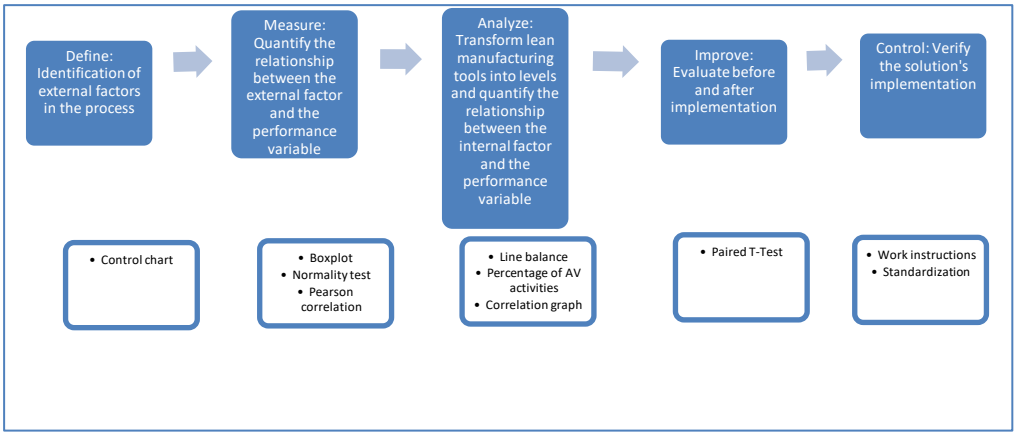

Figure I. - Proposed methodology.

2.1 Define phase: Identification of absenteeism in the process. This phase aimed to gather the necessary information to identify the impact of absenteeism on process performance, measured through productivity. To this end, operational data was collected from the most recent reports, including the number of pieces produced, the number of operators present on the work team, the number of absences, and the time worked. This information enabled the calculation and analysis of productivity using an $\bar{X}$-R control chart in Minitab 17®. The use of the $\bar{X}$-R chart is justified by its ability to monitor process variability and distinguish it from variability associated with specific causes. A rational subgrouping strategy was applied, in which each subgroup consisted of five consecutive data points produced under homogeneous operating conditions, such as the same shift and manual assembly process characteristics. In this way, the variation within each subgroup primarily reflects the inherent variability of the process (common causes), while the variation between subgroups allows the identification of changes in process conditions, particularly those associated with fluctuations in labor availability due to absenteeism. Furthermore, sampling was conducted at intervals aligned with the production ID cycles to ensure stable sampling logic. Under these conditions, the $\bar{X}$–R chart constitutes a valid method for identifying significant variations due to special causes, considering absenteeism as a central explanatory variable of productivity performance.

Equation 1 measures the percentage of absenteeism, and Equation 2 calculates the average.

$$\text{Absenteeism percentage} = \frac{\#\ absent\ operators}{Total\ number\ of\ operators\ to\ perform\ the\ assembly} * 100 \qquad (1)$$

$$Average\ percentage = \frac{1}{n}\sum_{i=1}^{n} X_i \qquad (2)$$

Where:

X_i = each of the percentage values
n = total number of values

2.2 Measure Phase: Quantification of the relationship between absenteeism and productivity. Once the variations attributable to special causes of absenteeism in the process are identified, the collected information is analyzed using a box plot to detect outliers. If such values are identified, the data are cleaned to ensure the sample is representative of the process's normal behavior.

Normality tests were then applied to verify whether the data followed this distribution, a necessary condition for calculating the correlation coefficient between two variables. Additionally, each productivity point represented in the Xbar-R control chart was associated with its corresponding absenteeism value. It is used to analyze the relationships between external variables and process variables in the context of productivity.

The assumptions of linearity and independence of the data were reviewed using residual analysis. Subsequently, linear regression analysis and Pearson's correlation coefficient were calculated to quantify the strength and direction of the relationship between absenteeism and productivity. All statistical calculations, including the estimation of the regression equation, were performed using the Minitab statistical software.

Data quality was assessed by reviewing system data records and comparing them with paper records to identify typos. If this typo matched the outlier, the data were removed from the sample so that the data's correct behavior could be represented.

2.3 Analyze: Transformation of the line balancing tool into levels and quantification of the relationship between line balancing and productivity. -Within the analysis phase, to quantify a value for the line balancing tool that allows a relationship with productivity to be established, the analysis phase is divided into three stages. The first stage applies the line-balancing methodology. In the second stage, activities are quantified by their contribution to balancing; that is, all activities that add value are identified and measured to determine the percentage they represent in the total process. Finally, in the third stage, the AV activities are quantified following the steps from the previous stage, with the difference that this stage extends them across multiple production lines within the manufacturing company. In addition, the productivity corresponding to each line balancing was quantified to identify the relationship between the percentage of AV activities and productivity.

In the first stage, the methodology corresponding to the selected tool, namely line balancing, is applied. Figure II presents the specific methodology used to apply the line balancing tool, corresponding to step one of the analysis, which consists of three steps: In step one, the takt time is calculated, which starts from knowing the actual demand and distributing this demand in equal amounts over a given period of time, that is, knowing the demand from week one to week four to calculate the weekly average of parts that must be built to meet the customer demand. Next, the time available for assembling the parts was estimated by subtracting the mealtimes per shift from the total available time. This data is then used to calculate the takt time, as shown in Equation 3:

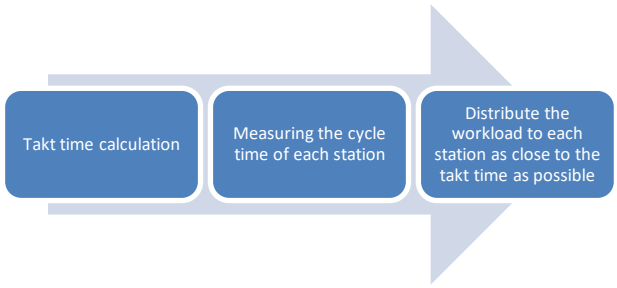

Figure II.- Methodology for the implementation of the line balancing tool

$$Takt\ time = \frac{Worktime}{Demand} = \frac{Days\ worked\ per\ week * First\ plus\ second\ shift\ available\ time \frac{hours}{days} * 3600 \frac{seconds}{hours}}{Average\ weekly\ demand\ units} \quad (3)$$

In the second step, the cycle time of each station was measured in seconds. In the third step, the workload is distributed to each station as close as possible to the takt time. These steps completed the first stage of the analysis phase, and stages two and three were then carried out.

In the second stage, all activities necessary to execute the production process are classified in detail and grouped into three main categories: added-value activities (AV), auxiliary activities (AW), and non-added-value activities (NAV).

In addition to these three categories, an analysis of the waste generated between the stations was incorporated. This type of waste can cause idle time due to cycle-time imbalances between stations or to overproduction when one station continues to operate. Simultaneously, the next station has a longer cycle time, which leads to product accumulation in the process.
To determine the percentage of added value activities (AV) within line balancing or within a workstation, we began by classifying all tasks into four categories: added value activities (AV), auxiliary work (AW), non-added value activities (NAV), and idle time (waste between stations).

We began by calculating the total time per workstation by summing the times for the first three categories (AV, AW, and NAV). Next, we identified the station with the longest total time, which represents the process bottleneck. The difference between this maximum time and the times of the other stations is considered waste by balance and is classified as a fourth category: idle time.

In this way, the four components per station are calculated: AV, AW, NAV, and idle time, the sum of which represents 100% of the components within the balancing. The percentage of added-value activities is calculated by dividing the sum of AV time (either for a specific station or for the entire balancing) by the total time for the four categories of activities. This quotient was multiplied by 100 to obtain its value as a percentage, as shown in Equation 4:

$$\%AV = \left(\frac{\sum AV}{\sum(AV+AW+NAV+Idle\ time)}\right) * 100 \quad (4)$$

In the third stage, the relationship between the percentage of added-value activities and the productivity performance of the different production lines is graphically presented. In addition, a linear regression analysis was performed to model the relationship between these variables, including the estimation of the regression equation, the slope parameter, and its corresponding confidence intervals. The normality of the residuals was assessed to verify the model's assumptions. All statistical analyses were performed using Minitab v.19.

2.4 Improve: Alternative solutions for line balancing and evaluation of levels (initial and final status). The proposed alternative solution involves implementing the LB tool to optimize production process performance by more

efficiently allocating tasks. The improvement considers a quantitative evaluation of the initial state and the state after implementation based on the analysis of the percentages of activities that add value within line balancing.

To validate the solution's effectiveness, a statistical hypothesis test was conducted to determine whether the achieved levels represented a significant improvement over the process's initial state. This validation provides an objective basis for confirming that the application of these tools not only generates operational benefits but also that these benefits are statistically relevant and sustainable over time.

2.5 Control: Verification of the application of line balancing. – This phase seeks to ensure the sustainability of line balancing as an improvement solution so that it continues to be implemented over time to preserve the benefits obtained during the study. To this end, adjustments are made to the instructions and production system to maintain the desired level; that is, the percentage of added-value activities is preserved in the analyzed processes and consistently applied during the execution of the manufacturing process.

3. Results and Discussion. – This section is divided into sections according to the information on the DMAIC methodology reported earlier.

3.1 Define: Identification of absenteeism in the process of training. – Process behavior is monitored using the Xbar-R control chart, which shows how productivity is influenced by absenteeism. Figure III shows the data collected over the five months of production, with a total of 115 observations grouped into subgroups of five, yielding 23 points on the graph. Point 12 falls below the lower control limit (LCL), indicating an abnormal drop in productivity for this subgroup. This drop indicates the presence of a specific cause of absenteeism, leading to a significant decrease in process performance.

However, points 12, 13, and 22 on the range chart showed signs of being out of control, suggesting unusual variation within those subgroups. Although in samples 13 and 22 the mean remained within the control limits, the variability exceeded the upper control limit (UCL) due to external factors that disrupted the normal process development.

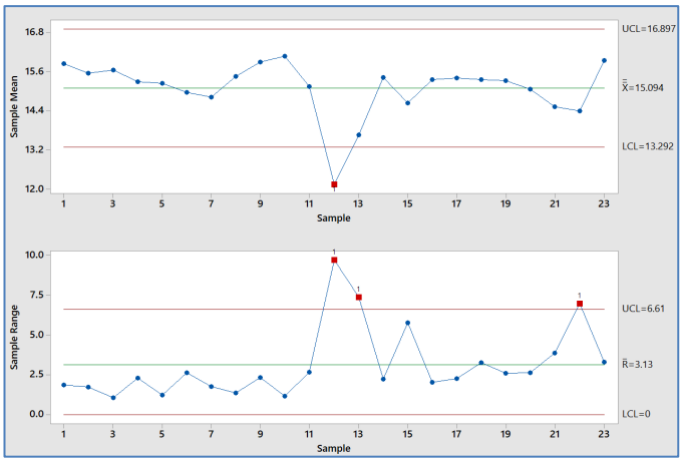

Figure III.- Control chart of productivity

3.2 Measure: Quantification of the relationship between absenteeism and productivity. – Outliers in the process were excluded from the sample to measure the relationship between absenteeism and productivity. Figure IV shows the box plot, in which it can be seen that the data are concentrated in the first quartile (Q1) of 14.95 and the third quartile (Q3) of 15.55, with minimum and maximum values within the range of 14.39 to 16.07, thus showing that sample number 12 with a value of 12.15 is outside the process range. Therefore, it was removed from the analysis, leaving 22 points.

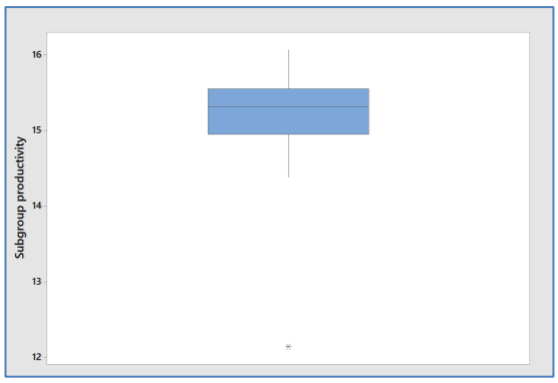

Figure IV- Boxplot for productivity

Once the outlier corresponding to observation 12 was identified and removed, the Anderson-Darling normality test was applied to assess the data's statistical behavior. As shown in Figure V, the p-value obtained was 0.847, indicating insufficient evidence to reject the null hypothesis of normality; therefore, the data exhibited an approximately normal distribution. Furthermore, Figure VI shows a plot of residuals versus fitted values, which displays random dispersion around the zero-reference line without any systematic patterns or evident curvilinear trends, suggesting that the model's linearity assumption is adequately met. Additionally, the residuals' variability remained approximately constant across the range of fitted values, indicating homoscedasticity and supporting the suitability of the linear regression model. Finally, Figure VII presents the evaluation of the independence of observations by analyzing the residuals based on the order of data collection, as well as the Durbin-Watson statistic, which had a value of 1.89. This result did not indicate autocorrelation, confirming the assumption of independence.

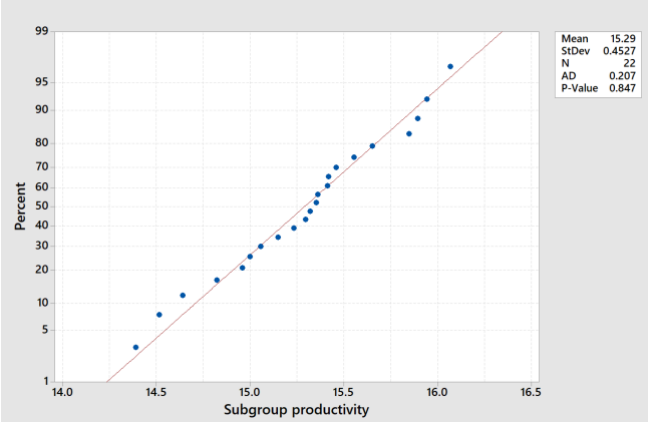

Figure V.- Normality test for productivity

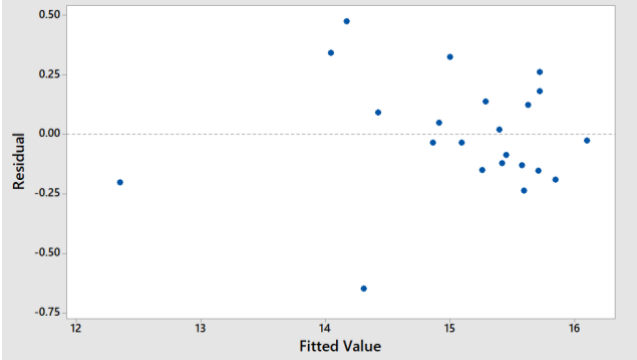

Figure VI.- Residuals versus Fits

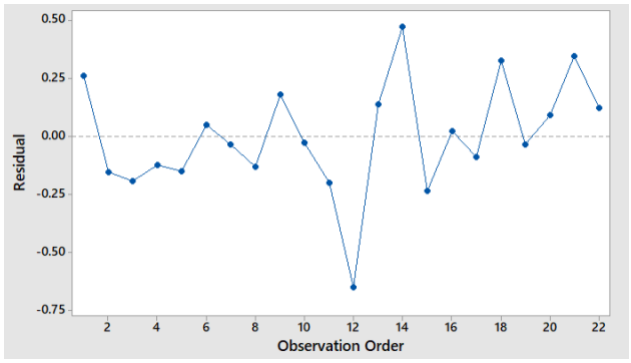

Figure VII.- Residuals versus Order

After verifying that the assumptions of the absence of outliers, normality, linearity, and independence of the data were met, a linear regression analysis was performed to evaluate the relationship between absenteeism and productivity. The results, presented in Figure VIII, show a statistically significant negative relationship, described by the model Productivity = 16.0958 − 0.1900 · Average Percentage. Under these conditions, a Pearson correlation coefficient of −0.960 was obtained, indicating a strong inverse linear association between the two variables.

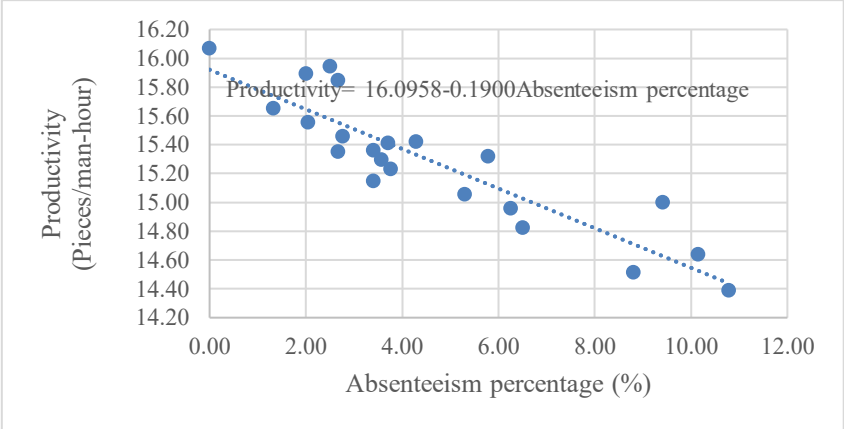

Figure VIII- Relationship between productivity and absenteeism

3.3 Analyze: Transformation of the line balancing tool into levels and quantification of the relationship between line balancing and productivity. In this phase, we explored whether the line balancing tool had the opposite effect on absenteeism. In line balancing, we analyze its contribution to increasing productivity and then identify the simplest operations to assign to inexperienced workers, who cover the work of absent operators.

The results obtained in the first stage, which involve applying the line balancing methodology, consist of determining customer demand to calculate the takt time. Table I shows the projected demand for the next four weeks, with a weekly average of 6,493 units per week. Table II shows the time available during the first shift, and Table III shows the time available during the second shift, for a total of 16.5 h per day.

Week	Forecast	Average
1	5,293	6,493
2	7,593	
3	7,639	
4	5,393	

Table I.- Average weekly demand

Activities	Time (h)	Percentage
Available work time	8.5	91.39
Breakfast	0.3	03.00
Lunch	0.5	05.00
Total	9.3	100

Table II.- First shift available time

Activities	Time (h)	Percentage
Available work time	8.0	90.9
Lunch	0.3	05.68
Dinner	0.5	03.40
Total	8.8	100

Table III.- Time available second shift

Takt time is defined as the time interval expressed in seconds in which a unit must be produced to meet customer demand within the available operating time, that is, the total time available between demands, which in this case corresponds to five working days, with a daily shift of 16.5 hours (considering the first and second shifts) and expressed in seconds when multiplied by 3600 and divided by the 6,493 weekly pieces, yields a value of 45.74 seconds per piece.

The next step in the line-balancing process is to measure the cycle time at each workstation. Table IV presents the average times recorded for each activity within the process, along with their sum, which corresponds to the total cycle time at that station, yielding a cycle time of 55.70 seconds. The information for calculating the times for the other stations is in the supplementary material. The cycle times for each station were S1 = 55.71 seconds, S2 = 46.65 seconds, S3 = 55.1 seconds, and S4 = 41.3 seconds.

Figure IX compares the cycle times of each workstation (S1, S2, S3, and S4) with the previously calculated takt time for the four workstations. This analysis shows that stations one, two, and three (S1, S2, and S3) have cycle times greater than the takt time of 45.74 seconds, indicating that, in their current state, these stations cannot meet the projected demand for the four weeks. Therefore, lean manufacturing tools must be used to balance workloads across stations and ensure production targets are met.

Description	**Chronometry (input in seconds)**										**Results**
Activity	**1**	**2**	**3**	**4**	**5**	**6**	**7**	**8**	**9**	**10**	**Average (sec)**
STATION 1											
Cutting contacts	5.30	4.51	2.57	6.14	5.18	4.58	2.82	4.50	5.25	7.83	4.87
Post trimming	3.56	4.02	4.31	4.74	4.04	5.80	3.11	3.59	4.37	4.06	4.16
Ring placement	2.80	4.05	3.09	2.74	3.39	2.66	2.61	3.27	2.75	3.06	3.04
Button placement	3.59	2.50	2.59	2.82	2.45	2.44	4.26	2.70	3.60	2.79	2.97
Button placement	5.83	3.80	3.18	3.33	3.06	3.16	3.19	2.97	3.34	2.59	3.45
Button retainer placement	2.25	2.59	4.09	2.60	3.94	2.37	3.36	3.37	3.66	3.42	3.17
Ultrasonic welding	5.80	6.92	5.88	6.55	5.90	6.70	5.98	6.74	6.96	7.77	6.52
Place 2 O-rings	6.95	6.15	6.11	6.62	7.11	6.15	6.65	7.15	7.00	6.75	6.66
Cut retainer	5.30	4.83	3.45	5.20	5.30	6.50	6.10	5.20	5.30	5.50	5.27
Apply hot melt	16.35	16.60	16.32	16.30	15.20	14.50	16.30	14.90	2:90	15.00	15.60
Total sum of the steps											55.70

Table IV.- Cycle time station 1

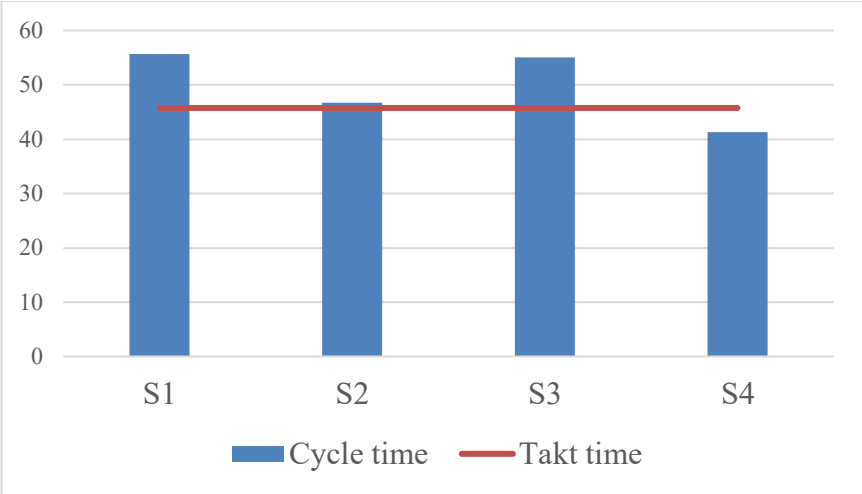

Figure IX- Cycle time vs takt time

Given the need to meet established demand, the line-balancing tool is used to optimize the workflow. In this case, tasks are redistributed by adding a fifth station, S5, to reduce cycle times at stations 1, 2, and 3, which previously exceeded the takt time.

Table V shows the new assignment of activities for station one (if you want to know the assignment for the rest of the stations, refer to the supplementary material). Figure X shows the cycle time graph for station one and the rest of the stations with a comparison of the cycle times per station with respect to the new takt time, in which a cycle time is obtained for S1 40.59 seconds, S2 = 41.81 seconds, S3 = 43.57 seconds, S4 = 43.06 seconds, and S5 = 40.45 seconds. This graph shows greater temporal alignment between the stations and a better approximation of the takt time, reflecting a more balanced workload. As a result, the process is significantly improved, and compliance with customer requirements within the established period is ensured.

Description	**Chronometry (input in seconds)**										**Results**
Activity	**1**	**2**	**3**	**4**	**5**	**6**	**7**	**8**	**9**	**10**	**Average (sec)**
STATION 1											
Cutting contacts	6.30	5.51	3.57	7.14	6.18	5.58	3.82	5.50	6.25	8.83	5.87
Post trimming	4.56	5.02	5.31	5.74	5.04	6.80	4.11	4.59	5.37	5.06	5.16
Ring placement	2.80	5.05	4.09	2.74	3.39	3.66	3.61	3.27	3.75	4.06	3.64
Button placement	3.59	2.50	2.59	2.82	2.45	2.44	4.26	2.70	3.60	2.79	2.97
Button placement	6.93	4.80	4.18	3.33	3.06	4.16	4.19	2.97	4.34	3.59	4.16
Button retainer placement	3.25	3.59	5.09	3.60	4.94	3.37	4.36	4.37	4.66	4.42	4.17
Ultrasonic welding	6.80	7.92	6.88	8.55	6.90	7.70	6.98	7.74	7.96	8.77	7.62
Walk to the packing station	5.21	4.21	3.97	4.20	4.10	3.80	4.50	4.60	3.50	3.20	4.13
Bag unit	1.49	4.18	4.75	4.04	3.90	2.30	2.50	3.60	3.90	3.20	3.39
Total sum of the steps											41.10

Table V.- Cycle time station 1

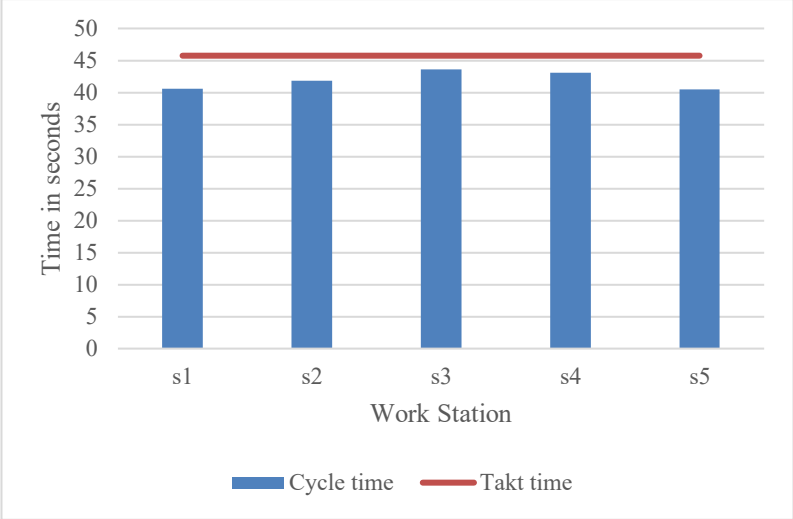

Figure X.- Cycle time vs. takt time after balancing

Thus far, the steps corresponding to stage one of the lean manufacturing methodology for line balancing tools have been applied. Next, we begin stage two, in which we perform a detailed classification of all activities necessary to execute the production process. This classification allows us to analyze the impact of line balancing on productivity based on the percentage of activities that add value within the process.

Table VI shows the classification of each of the activities corresponding to station one (the rest of the stations are found in the supplementary material) according to four categories: Added Value (AV), Auxiliary Work (AW), Non-Added Value (NAV), and idle time (IT). Figure XI complements this information by graphically showing the distribution of these categories and visualizing idle times resulting from cycle-time differences between stations.

The analysis by station using Equation 5, explained in the methodology, reveals the following results, both per station and for the total balance:

- Station one: For the time in seconds of the total activities that make up this station, we have a total AV time of 25.94 s, an AW of 0 s, a NAV of 15.16 s, and idle times of 4.64 s. Adding all the categories gives a total value of 45.74 seconds. Applying Equation 5 of the methodology to determine the ratio of AV activities within Station One gives a participation percentage of 56.7%.
- Station two: The time for AV activities was 38.77 seconds, AW was 3.84 seconds, NAV was 0 seconds, and the idle time was 3.14 seconds, for a total of 45.74 seconds. This resulted in a participation ratio of 84.71% for AV activities.
- Station three: The AV, AW, NAV, and idle times were 34.08, 7.11, 3.72, and 0.82 s, respectively, for a total activity time of 45.74 s. This resulted in a participation ratio of 74.5% for AV activities.
- Station four: AV activities lasted 40.35 s, AW activities lasted 0.39 s, NAV activities lasted 4.99 s, and idle time lasted 0 s, for a total of 45.74 s of activity. This resulted in a participation ratio of 88.2% for AV activities.
- Station five: AV activities lasted 0 s, AW activities lasted 9.21 s, NAV activities lasted 31.19 s, and idle time lasted 5.34 s, giving a total activity time of 45.74 s. This resulted in a participation ratio of 0% for AV activities.

Overall, the balancing analysis showed a time of 139.14 s for AV activities, 20.54 s for AW activities, 55.06 s for NAV activities, and 13.96 s for idle time, giving a total of 228.71 s of activity. This resulted in a participation ratio of 60.83% for AV activities, which allowed us to quantify the improvement in work distribution based on system productivity.

Description of Study		Chronometry (input in seconds)										Results
Activity	**Operation**	**1**	**2**	**3**	**4**	**5**	**6**	**7**	**8**	**9**	**10**	**Ave (sec)**
STATION 1												
Cutting contacts	NAV	6.30	5.51	3.57	7.14	6.18	5.58	3.82	5.50	6.25	8.83	5.87
Post trimming	NAV	4.56	5.02	5.31	5.74	5.04	6.80	4.11	4.59	5.37	5.06	5.16
Ring placement	AV	2.80	5.05	4.09	2.74	3.39	3.66	3.61	3.27	3.75	4.06	3.64
Button placement	AV	3.59	2.50	2.59	2.82	2.45	2.44	4.26	2.70	3.60	2.79	2.97
Button placement	AV	6.93	4.80	4.18	3.33	3.06	4.16	4.19	2.97	4.34	3.59	4.16
Button retainer placement	AV	3.25	3.59	5.09	3.60	4.94	3.37	4.36	4.37	4.66	4.42	4.17
Ultrasonic welding	AV	6.80	7.92	6.88	8.55	6.90	7.70	6.98	7.74	7.96	8.77	7.62
Walk to the packing station	NAV	5.21	4.21	3.97	4.20	4.10	3.80	4.50	4.60	3.50	3.20	4.13
Bag unit	AV	1.49	4.18	4.75	4.04	3.90	2.30	2.50	3.60	3.90	3.20	3.39
Total sum of the steps												41.10

Table VI. - Classification of activities station 1

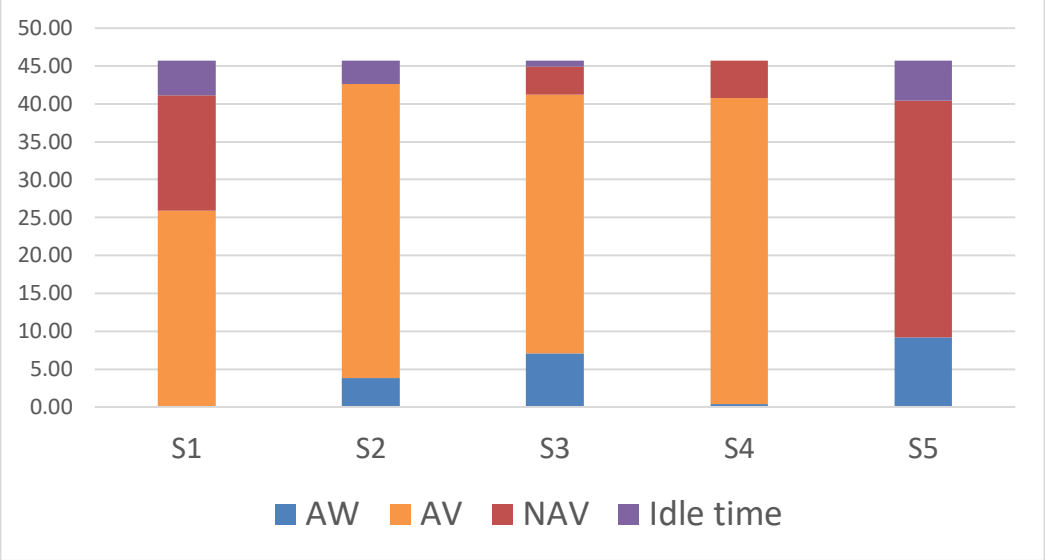

Figure XI.- Cycle time with activity classification

As part of the third stage of the analysis, which establishes the relationship between the line balancing tool and productivity, the participation of AV activities within the different balances for the four assembly lines of the manufacturing company was calculated. Table VII presents the results, showing both the percentage of added-value activities and the productivity for each balance (for information on the balances, classifications, and productivity, see the Supplementary Material).

Figure XII shows a positive, statistically significant relationship between the percentage of added-value activities and productivity, with a correlation coefficient of 0.9428, indicating a strong linear association between the two variables. To further quantify this relationship, a linear regression analysis was conducted, yielding the model: *Productivity = 1.57 + 0.2310·Percentage of added value (%)*. The estimated slope ($\beta_1 = 0.2310$) reflects the magnitude of the linear

effect of added value activities on productivity. The 95% confidence interval for the slope [0.1796, 0.2823] did not include zero, confirming the effect's statistical significance ($p < 0.001$). Residual analysis revealed a normal distribution.

Production line and balancing number	Percentage of added value (%)	Productivity (Pieces/man-hour)
Line one balancing 1	53.42	13.03
Line one balancing 2	76.44	19.15
Line one balancing 3	78.5	19.93
Line two balancing 1	40.16	11.3
Line two balancing 2	44.29	13.2
Line two balancing 3	48	12.91
Line two balancing 4	49.72	13.99
Line three balancing 1	41.93	9.92
Line three balancing 2	48.92	11.58
Line three balancing 3	58.73	13.89
Line four balancing 1	48.46	12.66
Line four balancing 2	58.01	14.86
Line four balancing 3	60.83	15.7
Line four balancing 4	56.17	16.15

Table VII- Percentage of added value activities and their corresponding productivity

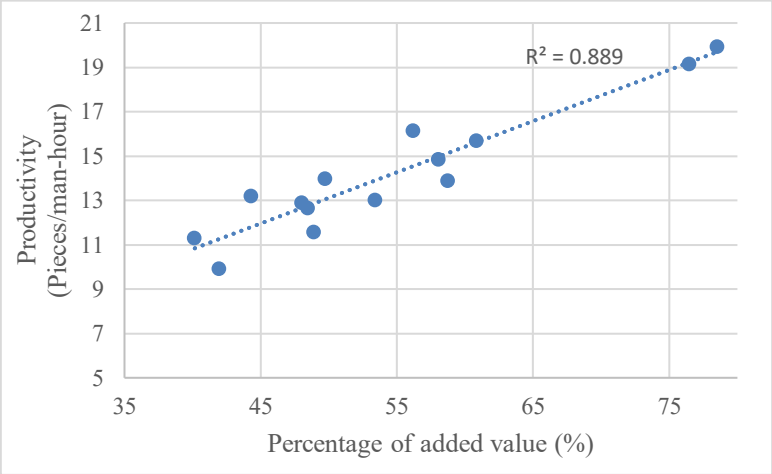

Figure XII.-Relationship between added value activities and productivity

3.4 Improvement: Alternative solutions for line balancing and evaluation of levels (initial and final status). – The time studies corresponding to the four assembly lines were analyzed and compared with the results obtained at the different line balancing levels. This analysis shows an increase in the proportion of added-value activities relative to the total activities included in the studies and the balancing process.

Table VIII shows the productivity levels achieved on each line when comparing level one balancing, which corresponds to the initial state of balancing, with level two balancing, which corresponds to the final state (if you want to see all the data in the table, check the supplementary material), leaving the alternative hypothesisH_1: Productivity is lower in the initial state than after the application of balancing in the final state. Table IX presents the results of the Paired T-test, which indicate a significant difference in productivity when the participation in added-value activities within line balancing is increased.

Production Line	Balancing before	Balancing after
One	13.17	20.25
One	11.50	17.63
One	13.33	20.50
One	13.50	20.00
One	13.17	20.00
…	…	…
Four	12.71	16.00
Four	11.14	14.25
Four	13.00	16.50
Four	13.14	16.75
Four	12.86	16.25

Table VIII.- Productivity balancing before and after

	Sample	N	Mean	St Dev	SE Mean
	Balancing before	28	11.687	1.368	0.259
	Balancing after	28	15.924	2.522	0.477
	Difference	28	-4.237	1.541	0.291
Null hypothesis	$H_0: \mu before - \mu after = 0$				
Alternative hypothesis	$H1: \mu before - \mu after < 0$				
P-Value	P<0.001				

Table IX- 2 Paried T-Test and hypothesis test balancing before and after

3.5 Control: Verification of line balancing implementation. - The operating instructions for lines one, two, three, and four were updated to detail the steps to be followed at each workstation. These instructions reflect the distribution of activities defined by the previously analyzed line balancing, ensuring their correct execution in the production process.

The control system was also updated to reflect the standard times established by the model on each line, in accordance with the values determined in line balancing. As part of the operational monitoring, visual control boards were installed, which were updated in real time by the group leaders. This tool allows for continuous monitoring of process performance and, with the support of various support departments, facilitates the timely implementation of necessary adjustments to maintain the expected productivity levels.

4. Discussion of the results and conclusions. - In the initial scenario of the manufacturing company in the industrial sector, consisting of 19 assembly lines distributed across two of its plants, a problem of low productivity and delivery delays on one of its lines, with an incidence of 75%, was reported. From the sample taken from the four lines, the annual costs associated with idle time and waste were estimated at $57,582.4. This study has two objectives: first, to identify the impact of absenteeism on productivity and quantify its effect on this problem; second, to explore the line balancing tool to understand the behavior that can counteract the effect of absenteeism on productivity, thereby creating problem-solving strategies through the use of this tool.

The impact of work absenteeism on manufacturing production processes has not been sufficiently studied, which limits a comprehensive understanding of its implications for operational efficiency. Although there is research [19] that addresses this phenomenon, its focus is on administrative environments without delving into the specific problems that

absenteeism generates in production environments, such as delivery delays or costs associated with the interruption of continuous flow.

To address the first objective, tools commonly used in industrial process monitoring were employed, such as those applied in the molding [20], metal processing [21], and glass [22]sectors, where critical dimensional variables are controlled to ensure product quality. However, in this study, the graphical control tool was used from a different perspective, as it was not applied to product characteristics but rather to a key indicator of process performance, which provides a comprehensive view of the system's behavior.

The analysis using control charts identified two out-of-control points in the mean chart and three in the range chart, all of which were attributed to employee absenteeism. These points represent variations attributable to special causes that are outside the process. Further analysis of the outliers using a box plot revealed that the value for sample 12 was an outlier. By excluding this point and recalculating the impact of absenteeism on productivity, the Pearson correlation coefficient obtained was -0.960, confirming a negative relationship between these two variables. In addition, the estimated slope of the regression equation $Productivity = 16.0958 - 0.1900$ ($\beta_1 = -0.1900$) indicates a negative linear effect of absenteeism on productivity, with a magnitude of −0.1900. Once the impact of the external factor on system performance was determined, the second objective focused on developing improvement strategies using the line balancing tool, which made it possible to address the problem of delays on one of the lines, where 75% on time delivery was not being achieved. As a result, a substantial improvement in workflow efficiency was achieved, generating estimated annual savings of $12,153.91 USD, in addition to a significant reduction in idle time and overproduction between workstations.

The line balancing tool has been widely used to optimize production processes and achieve significant increases in operational efficiency. For example, in the garment industry, its implementation increased productivity from 54.22% to 66% [23] the manufacture of automotive parts, an improvement of 7.7% was achieved [24]; and in the electronics industry, it contributed to the elimination of bottlenecks [25].

Despite these results, few studies have quantitatively analyzed the impact of line balancing on productivity using correlation-based metrics to provide an objective parameter that would facilitate the design of more precise interventions to address issues inherent in the dynamic environment faced by manufacturing organizations.

To evaluate the impact of these tools on process performance, a detailed classification of all activities involved in line balancing was performed, including those considered waste, specifically those associated with the idle time. This analysis enabled calculating the percentage of activities that added value for each evaluated line and relating this indicator to the observed productivity levels. The correlation results show that the LB tool maintains a positive relationship with productivity, with a coefficient of 0.9428. Finally, the increase in these activities within the assembly lines resulted in additional savings of $57,582.4 USD per year, attributable to the elimination of unproductive time and the reduction of waste.

5. Limitations and Future Research Directions. - It is important to note that this study was developed using a sample corresponding to the assembly line of an industrial manufacturing company. However, the methodology and analysis approach can be replicated in other production processes, such as injection molding, metal treatment, and painting. This suggests that the findings have broader applicability in industrial environments, provided that the specific characteristics of each process are considered.

One limitation of this study is that lean manufacturing tools were used to evaluate their impact on performance indicators, with a focus mainly on productivity. The analysis focused on determining the direction (positive or negative) and magnitude of this impact as a basis for proposing improvement strategies that integrate both external and internal factors of the production system. However, this approach did not consider interactions with other tools or between the internal factor LB and the external factor absenteeism.

For future research, it is recommended to broaden the scope of the study by incorporating additional lean manufacturing tools or by developing an analysis that considers both external and internal factors to design robust processes. In this way, even in the face of uncontrollable external factors such as absenteeism, their impact on productivity can be reduced, promoting the stability and efficiency of the operating system.

Availability of information/Supplementary material

Hermosillo, Fabiola (2025), "Line balancing and productivity," Mendeley Data, V1, doi: 10.17632/5d7vn57xnn.1

References

[1] N. Boysen, P. Schulze, and A. Scholl, "Assembly line balancing: What happened in the last fifteen years?," Eur. J. Oper. Res., vol. 301, no. 3, pp. 797–814, 2022.

[2] M. Nikkerdar and W. ElMaraghy, "Smart adaptable assembly line rebalancing and maintenance," The International Journal of Advanced Manufacturing Technology, pp. 1–21, 2025, doi: 10.1016/J.EJOR.2021.11.043

[3] A. J. Alrowili et al., "Critical Review of Workload Distribution between Nurses and Health Assistants in Healthcare Settings," Journal of Ecohumanism, vol. 3, no. 8, pp. 10151–10163, 2024, doi: 10.62754/JOE.V3I8.5626

[4] C. N. Wang, T. T. B. C. Vo, H. P. Hsu, Y. C. Chung, N. T. Nguyen, and N. L. Nhieu, "Improving processing efficiency through workflow process reengineering, simulation and value stream mapping: a case study of business process reengineering," Business Process Management Journal, vol. 30, no. 7, pp. 2482–2515, 2024, doi: 10.1108/BPMJ-11-2023-0869

[5] E. Edmund, "Risk Based Security Models for Veteran Owned Small Businesses," International Journal of Research Publication and Reviews, vol. 5, no. 12, pp. 4304–4318, 2024, doi: 10.55248/gengpi.5.1224.250137

[6] I. Elemure, H. N. Dhakal, M. Leseure, and J. Radulovic, "Integration of Lean Green and Sustainability in Manufacturing: A Review on Current State and Future Perspectives," Sustainability, vol. 15, no. 13, p. 10261, Jun. 2023, doi: 10.3390/su151310261.

[7] I. C. Medina-Fernández, H. H. Andrade-Sosa, and R. Peña-Baena Niebles, "Propuesta metodológica para el balanceo de líneas de producción a partir de diagramas AND/OR," Revista Ingenierías Universidad de Medellín, vol. 18, no. 34, pp. 25–44, 2019.

[8] L. Neuber, C. Englitz, N. Schulte, B. Forthmann, and H. Holling, "How work engagement relates to performance and absenteeism: a meta-analysis," European Journal of Work and Organizational Psychology, vol. 31, no. 2, pp. 292–315, 2022, doi: 10.1080/1359432X.2021.1953989

[9] M. Afy-Shararah and K. Salonitis, "Integrated modeling of 'soft' and 'hard' variables in manufacturing," The International Journal of Advanced Manufacturing Technology, vol. 122, no. 11, pp. 4259–4265, 2022, doi: https://doi.org/10.1007/s00170-022-09872-z.

[10] J. Aarstad and O. A. Kvitastein, "Effect of long-term absenteeism on the operating revenues, productivity, and employment of enterprises," Adm. Sci., vol. 13, no. 6, p. 156, 2023, doi: https://doi.org/10.3390/admsci13060156.

[11] M. Briones, "The effect of workload and work stress on employees' work motivation and productivity in a manufacturing company," International Journal of Research Publications, vol. 134, no. 1, 2023, doi: https://doi.org/10.47119/ijrp10013411020235512.

[12] I. N. Latifah, A. A. Suhendra, and I. Mufidah, "Factors affecting job satisfaction and employee performance: a case study in an Indonesian sharia property companies," International Journal of Productivity and Performance Management, vol. 73, no. 3, pp. 719–748, 2024, doi: 10.1108/IJPPM-03-2021-0132/FULL/PDF

[13] B. Acosta, "Work absenteeism and its impact on productivity in the administrative area," Revista Tecnológica Ciencia y Educación Edwards Deming, vol. 9, no. 1, pp. 18–27, 2025, doi: 10.37957/RFD.V9I1.142

[14] D. F. de Oliveira, C. M. Balbino, C. B. Ribeiro, R. M. de Oliveira Ramos, V. J. Sepp, and L. H. Loureiro, "Frederick Herzberg and the Theory of the Two Factors in the contribution to the prevention of absenteeism at work," Cuadernos de Educación y Desarrollo, vol. 15, no. 12, pp. 17557–17569, 2023, doi: 10.55905/cuadv15n12-131

[15] S. T. Gulyamova, S. F. Abdul Aziz, N. H. Omar, and R. H. Mohd, "Workplace-related socioeconomic issues associated with job performance and productivity among employees with Various impairments: a systematic literature review," Soc. Sci., vol. 12, no. 5, p. 275, 2023, doi: 10.3390/SOCSCI12050275

[16] J. Gonzales et al., "Impacto de un programa ergonómico en la productividad de una empresa de fabricación de envases de hojalata," Agroindustrial Science, vol. 6, no. 2, pp. 213–219, 2016.

[17] W. Brouwer, K. Verbooy, R. Hoefman, and J. van Exel, "Production losses due to absenteeism and presenteeism: the influence of compensation mechanisms and multiplier effects," Pharmacoeconomics, vol. 41, no. 9, pp. 1103–1115, 2023, doi: 10.1007/S40273-023-01253-Y

[18] R. C. Kanu, "A Study of Process Variability of the Injection Molding of Plastics Parts Using Statistical Process Control (SPC)," In 2013 ASEE Annual Conference & Exposition , pp. 23–110, 2013, doi: 10.18260/1-2-19124

[19] M. Rizal and S. M. Khoiroh, "Penerapan Metode Statistical Process Control dalam Pengendalian Kualitas Kawat Baja ," Metode: Jurnal Teknik Industri, vol. 9, no. 2, pp. 48–62, 2023.

[20] T. S. Imaroh and A. Mustofa, "Defect reduction analysis to improve glass bottle packaging products quality using statistical process control (SPC) at PT. Muliaglass Container (MGC)," Journal of Social Science, vol. 3, no. 5, pp. 1003–1018, 2022, doi: 10.46799/JSS.V3I5.402

[21] M. M. Teshome, T. Y. Meles, and C. L. Yang, "Productivity improvement through assembly line balancing by using simulation modeling in case of Abay garment industry Gondar.," Heliyon, vol. 10, no. 1, 2024, doi: 10.1016/J.HELIYON.2023.E23585

[22] K. Rochayata and W. Widodasih, "Analysis of the line balancing assembly implementation to increase productivity," Formosa Journal of Multidisciplinary Research, 2023.

[23] K. M. Khairai and S. N. A. Khalil, "Line balancing study using value stream mapping tool on lean manufacturing: A case study in an electronic industry," Qomaruna Journal of Multidisciplinary Studies, vol. 1, no. 2, pp. 55–64, 2024, doi: 10.62048/QJMS.V1I2.39

Author contribution:
1. Conception and design of the study
2. Data acquisition
3. Data analysis
4. Discussion of the results
5. Writing of the manuscript
6. Approval of the last version of the manuscript

FHV has contributed to: 1, 2, 3, 4, 5 and 6.
JLGA has contributed to: 1, 2, 3, 4, 5 and 6.
OCG has contributed to: 1, 2, 3, 4, 5 and 6.

Acceptance Note: This article was approved by the journal editors Dr. Rafael Sotelo and Mag. Ing. Fernando A. Hernández Gobertti.

Parametric Optimization of EN-31 Steel Using Electric Discharge Machining

Optimización paramétrica del acero EN-31 mediante mecanizado por descarga eléctrica

Otimização paramétrica do aço EN-31 utilizando usinagem por eletroerosão

Muhammad Mansoor Uz Zaman Siddiqui [1] (*), Syed Amir Iqbal [2], Ali Zulqarnain [3], Adeel Tabassum [4]

Recibido: 09/12/2025 Aceptado: 04/02/2026

Summary. - This investigative study was conducted for the parametric optimization of EN-31 material by using a non-conventional machining known as Electric discharge machining (EDM). EN-31 is a steel alloy that is generally used in aerospace industry, automotive parts manufacturing, die making etc. because it possesses high degree of rigidity with extremely good compressive strength and resistance to abrasion. The primary objective of this study was to analyze the impact of four input factors i.e. pulse on time (Ton), pulse off time (Toff), current (LV), voltage (HV) on the five output responses i.e. machining time (Tm), MRR, EWR, Ra and base radius (R). In this study design of experiment (DOE) approach with full factorial design was systematically conducted. Basic experimental runs were prepared and performed and after that data was analyzed using ANOVA to identify significant input factors that has most impact on each output response that are mentioned above. After identification of significant factors optimized input factors and output responses were calculated using ANOVA. The results showed that for machining time (Tm), LV and Ton were significant factors with optimized values of 50 A and 6.5 µs, respectively, resulting in a Tm of 654.29 seconds. For material removal rate (MRR), Ton was the significant factor with an optimized value of 6.5 µs, achieving a maximum MRR of 0.0157 g/min. For electrode wear rate (EWR), LV and Ton were significant with optimized values of 30 A and 4 µs, respectively, resulting in a minimum EWR of 0.07 g/min. Ra optimization revealed that the combination of HV, LV, Ton and Toff were significant, with optimized settings of 50 A, 0.7 V, 4.0 µs and 6.5 µs, respectively, yielding a minimum Ra of 0.018 mm. For base radius (R), the significant factors were HV, LV, Ton and Toff, with optimized values of 0.6152 V, 50 A, 6.5 µs and 6.5 µs, respectively, resulting in a base radius of 1.5 mm. This parametric optimization is extremely significant because EN-31 is a material used in critical applications requiring high strength, hardness and abrasion resistance such as automobile engine components, aerospace rocket parts and dies subjected to extreme temperatures and pressures throughout their lifecycle. Optimizing EDM parameters facilitates the use of this non-conventional machining process for manufacturing EN-31 parts thus enabling researchers, manufacturers, designers and industry practitioners to achieve higher productivity, excellent surface finishes and lower manufacturing costs as compared to traditional manufacturing techniques. This optimization allows for more efficient and effective production of high-performance parts thus making it an invaluable advancement in various industrial sectors.

Keywords: *EDM; Parameters; Machining; Processing; Roughness, EN-31; Optimization; DOE.*

[1] Engineer, Industrial and Manufacturing Engineering Department, University of Engineering and Technology Lahore (Pakistan), mansoorresearch1986@gmail.com, ORCID iD: https://orcid.org/0009-0007-8992-7601

[2] Professor, Department of Industrial Engineering, NED University of Engineering & Technology (Pakistan), samir@neduet.edu.pk, ORCID iD: https://orcid.org/0000-0002-6812-6238

[3] Assistant Professor, Department of Industrial Engineering, NED University of Engineering & Technology (Pakistan), alizul@neduet.edu.pk, ORCID iD: https://orcid.org/0000-0001-5919-7811

[4] Engineer, National University of Sciences and Technology (Pakistan), adeeltabassum1@gmail.com, ORCID iD: https://orcid.org/0009-0006-9375-1090

Memoria Investigaciones en Ingeniería, núm. 30 (2026). pp. 103-115
https://doi.org/10.36561/ING.30.8
ISSN 2301-1092 • ISSN (en línea) 2301-1106 – Universidad de Montevideo, Uruguay

Resumen. - *Este estudio de investigación se realizó para la optimización paramétrica del material EN-31 utilizando un mecanizado no convencional conocido como mecanizado por descarga eléctrica (EDM). El EN-31 es una aleación de acero que se utiliza generalmente en la industria aeroespacial, la fabricación de piezas de automóviles, la fabricación de matrices, etc., debido a que posee un alto grado de rigidez con una resistencia a la compresión y a la abrasión extremadamente buenas. El objetivo principal de este estudio fue analizar el impacto de cuatro factores de entrada, a saber, tiempo de pulso encendido (Ton), tiempo de pulso apagado (Toff), corriente (LV) y voltaje (HV) en las cinco respuestas de salida, a saber, tiempo de mecanizado (Tm), MRR, EWR, Ra y radio base (R). En este estudio se llevó a cabo sistemáticamente un enfoque de diseño de experimentos (DOE) con un diseño factorial completo. Se prepararon y realizaron ensayos experimentales básicos y luego se analizaron los datos utilizando ANOVA para identificar los factores de entrada significativos que tienen el mayor impacto en cada respuesta de salida mencionada anteriormente. Después de la identificación de los factores significativos, los factores de entrada optimizados y las respuestas de salida se calcularon utilizando ANOVA. Los resultados mostraron que para el tiempo de mecanizado (Tm), LV y Ton fueron factores significativos con valores optimizados de 50 A y 6,5 µs, respectivamente, lo que resultó en un Tm de 654,29 segundos. Para la tasa de remoción de material (MRR), Ton fue el factor significativo con un valor optimizado de 6,5 µs, logrando un MRR máximo de 0,0157 g/min. Para la tasa de desgaste del electrodo (EWR), LV y Ton fueron significativos con valores optimizados de 30 A y 4 µs, respectivamente, lo que resultó en un EWR mínimo de 0,07 g/min. La optimización de Ra reveló que la combinación de HV, LV, Ton y Toff fueron significativas, con configuraciones optimizadas de 50 A, 0,7 V, 4,0 µs y 6,5 µs, respectivamente, lo que produjo un Ra mínimo de 0,018 mm. Para el radio base (R), los factores significativos fueron HV, LV, Ton y Toff, con valores optimizados de 0,6152 V, 50 A, 6,5 µs y 6,5 µs, respectivamente, lo que resultó en un radio base de 1,5 mm.*

Palabras clave: *EDM; Parámetros; Mecanizado; Procesamiento; Rugosidad; EN-31; Optimización; DOE.*

Resumo**. -** *Este estudo investigativo foi conduzido para a otimização paramétrica do material EN-31 utilizando uma usinagem não convencional conhecida como eletroerosão (EDM). O EN-31 é uma liga de aço geralmente utilizada nas indústrias aeroespacial, de autopeças, de matrizes, etc., devido à sua alta rigidez, excelente resistência à compressão e à abrasão. O objetivo principal deste estudo foi analisar o impacto de quatro fatores de entrada, ou seja, tempo de pulso ligado (Ton), tempo de pulso desligado (Toff), corrente (LV) e tensão (HV), sobre as cinco respostas de saída, ou seja, tempo de usinagem (Tm), taxa de remoção de material (MRR), taxa de desgaste da ferramenta (EWR), rugosidade superficial (Ra) e raio da base (R). Neste estudo, foi aplicada uma abordagem de planejamento de experimentos (DOE) com planejamento fatorial completo. Ensaios experimentais básicos foram preparados e realizados, e os dados foram analisados por meio de ANOVA para identificar os fatores de entrada significativos que mais impactam cada resposta de saída mencionada. Após a identificação dos fatores significativos, os fatores de entrada otimizados e as respostas de saída foram calculados utilizando ANOVA. Os resultados mostraram que, para o tempo de usinagem (Tm), a tensão de limiar (LV) e a taxa de variação da corrente (Ton) foram fatores significativos, com valores otimizados de 50 A e 6,5 µs, respectivamente, resultando em um Tm de 654,29 segundos. Para a taxa de remoção de material (MRR), a Ton foi o fator significativo, com um valor otimizado de 6,5 µs, atingindo uma MRR máxima de 0,0157 g/min. Para a taxa de desgaste do eletrodo (EWR), a LV e a Ton foram significativas, com valores otimizados de 30 A e 4 µs, respectivamente, resultando em uma EWR mínima de 0,07 g/min. A otimização da rugosidade média (Ra) revelou que a combinação de alta tensão (HV), LV, Ton e Toff foi significativa, com configurações otimizadas de 50 A, 0,7 V, 4,0 µs e 6,5 µs, respectivamente, resultando em uma Ra mínima de 0,018 mm. Para o raio da base (R), os fatores significativos foram HV, LV, Ton e Toff, com valores otimizados de 0,6152 V, 50 A, 6,5 µs e 6,5 µs, respectivamente, resultando em um raio da base de 1,5 mm.*

Palavras-chave: *EDM; Parâmetros; Usinagem; Processamento; Rugosidade; EN-31; Otimização; CORÇA.*

1. Introduction. - Machining processes have progressed significantly over time [1]. The reason of this progression is actually driven by the growing demand of industry to use parts and components that have excellent precision and accuracy as per the designed component, must be produced by using efficiency manufacturing techniques because of mass manufacturing demands of industry and cost reduction and manufacturing techniques' capacity to work with a wide range of materials while maintaining the excellent surface finish [2] [3]. Traditional machining techniques such as turning, milling and drilling have been used in manufacturing industry from many centuries [4] [5]. These conventional manufacturing techniques are the foundation of manufacturing sectors. These techniques have limitations especially when dealing with exceptionally hard or brittle materials, during manufacturing of complicated geometries and where tight tolerances are required especially in manufacturing of automotive parts or during die making [6] [7]. In order to address these issues researchers started working on non-traditional machining technologies and amongst those techniques Electric Discharge Machining (EDM) [8] became the most popular one.

In a list of non-traditional techniques, EDM [9] achieves great accuracy while producing the materials that are difficult to shape [10]. It works by removing material from a part by producing electrical discharges in repetitive pattern. These pulses are generated at short intervals between two electrodes i.e., electrode and a workpiece [11]. A dielectric fluid separates the electrodes, allowing eroded particles to be flushed out of the gap between them. These successive electric sparks raise the temperature of workpiece and the tool's surface above their melting or boiling temperatures [12]. Thus, material is scraped off in the form liquid and vapor phases and the surface that are formed consist of debris melted or vaporized during machining [13] [14]. During this whole process tool does not physically contact the workpiece and because of these mechanical properties of material are unaffected during this whole non-conventional machining operation. Thermal and electrical properties have a significant impact on the EDM [15] process performance [16] [17] [18].

EN-31 is a steel alloy that is made up of high concentration of carbon and is composed up of carbon (between 1.0% and 1.2%), (0.30% to 0.75%), chromium (1.0% to 1.6%) and silicon (0.10% to 0.35%) and all of these contribute to its excellent performance qualities in high wear environment [19]. EN-31 is extremely hard material with excellent strength and addition of chromium increases the corrosion resistance making it a preferred material to be used in harsh conditions specially in the components which are subjected to severe abrasion, wear and high surface loading on periodic basis. These properties like its ability to retain high tensile strength and durability following heat treatment makes it a preferred material to be used in the parts made for automotive, aerospace and manufacturing industries because component reliability and longevity are of extreme importance in these industries and single components failure can cause unbearable amount of damage [20]. Understanding the qualities and applications of EN-31 can provide substantial insights into its role in enhancing engineering processes and boosting performance and longevity [21].

EN-31 is the carbon steel alloy that is known for its hardness, strength and its wear resistance properties and this makes it a nightmare for researchers and manufacturers to use traditional machining techniques as the high hardness causes rapid tool wear and cutting forces are extremely high leading to poor surface finish and low material removal rates [22] [23]. Researchers and manufacturers are developing EDM at brisk pace but still considerable research gap is there in machining EN-31 [24]. Most of the researchers optimize one or two output responses at one time during the experiment but in EDM it is a trade off in which optimizing one parameter impacts the other parameter negatively [25]. For example, increasing the current leads to high rate of material removal from workpiece usually but it results in a rougher surface finish (Ra) and higher electrode wear rate (EWR) and this results in reduced dimensional accuracy and base radius of the part that is being machined. Similarly, in order to increase surface quality by varying Ton time and Toff time frequently result in longer machining times and lower MRR leading to loss in productivity. There is a no data related to EDM optimization of EN-31 material is available in which all output responses mentioned previously were optimized at the same time. Addressing this gap is of extreme importance in order to use EDM for mass manufacturing of parts and for industries like automotive, aerospace, die making etc. in which parts quality and properties are of extreme importance.

This study has important practical implications in wider range of industries including automotive and aerospace industries where EN-31 steel is widely utilized for its high strength, wear resistance and exceptional mechanical

qualities [26] . Precision machining of EN-31 is critical in aerospace applications for making highly stressed components like landing gears and turbine shafts. In the automobile industry, EN-31 is utilized for transmission gear, engine parts and in bearings where dimensional accuracy is of extreme importance along with excellent surface finish as these are critical for performance and longevity. By developing an optimized EDM processing strategy, this study enables manufacturers to achieve higher productivity, lower electrode wear, improved surface quality and lower manufacturing costs, making EDM a more viable and efficient method for machining EN-31 steel than traditional techniques.

The main target of this research study is to improve the process parameters of electric discharge machining (EDM) for EN-31 high-carbon steel in such a way the optimized input parameter produces the best output response resulting in excellent quality of final product. This research attempts to optimize Tm, EWR, MRR (Material removal rate), Ra & R by varying the input parameters like Ton time, Toff time, Current & Voltage all at once. All of the iterative experiments were done by using DOE and then factorial screening for optimizing Tm, MRR, EWR (Electrode wear rate), Ra and R.

Significance of this research work lies in optimizing all the output responses at once without any trade off on any of the outputs. This research study will help industry practitioners in optimizing efficiency and productivity of their manufacturing setup by increasing the product quality, reducing production time and increasing the productivity of the machinery reducing the manufacturing cost of the product and increasing the profit margins. This research and experimental work were performed in a very controlled environment where settings of all input parameters were comparatively on low scale and still encouraging results were observed.

2. Methodology and Materials. - EN-31 high-carbon steel was chosen for parametric optimization was because of its industrial usage on such a large scale and the challenges manufacturers face during the production of the parts made up of EN-31. It is well-known that EN-31 exhibit excellent properties specifically harness and has very high degree of wear resistance and tensile strength. It is also widely being used in the production of key components such as bearings, gears, automotive engine parts, bio medical equipment manufacturing and die making where durability and precision are of extreme importance. These qualities make EN-31 extremely beneficial but on the other hand make it extremely difficult for manufacturers to process it using conventional machining methods thus resulting in swift tool wear, poor surface finishes, high machining times and low material removal rates. Optimizing parameters of electric discharge machining (EDM) for EN-31 can increase efficiency of machining, tool life and surface quality (by reducing surface roughness) thus resolving the constraints of EN-31 machining via conventional machining processes. Composition EN-31 [27] is mentioned in Table 1.

Element	Percentage (%)
C - Carbon	0.96 – 1.11
Mn - Manganese	0.39 – 0.69
Cr - Chromium	1.21 – 1.61
Si - Silicon	0.10 – 0.35
S - Sulphur	0.05 max.
P - Phosphorous	0.04 max.
Fe - Iron	Balance

Table 1. - Chemical composition - EN-31 steel.

For this parametric optimization study of EN-31, copper (Cu) was chosen as the electrode material. Cu was chosen as electrode material because of excellent electrical and thermal conductive properties and these are basic requirement for efficient working of electric discharge machining (EDM) process. It is evident from research that copper has a higher electrical conductivity and this leads to stable spark generation [28]. This results in higher MRR and superior surface finish quality as compared to other electrodes like zinc, brass, graphite etc. Furthermore, when graphite electrode was

used higher tool wear was observed along with poor surface finishing of the part being produced [29]. Copper has better wear resistance and electrode wear rate is comparatively less as compared to other materials such as graphite. As a result of this frequency of electrode replacements during manufacturing of part produced via EDM reduces. There are other materials available as well like tungsten, copper alloys etc. with properties that are suitable for EDM manufacturing process but they are quite expensive and economically not viable. Because of these reasons copper was chosen for this optimization study of EN-31.

In this study, two EN-31 blocks, each measuring 100 × 10 × 20 mm, were used and secured together. The electrodes were produced with a step-turned geometry, combining a flat circular tip of 3 mm diameter.

For the EDM process, a Gen Spark EDM (Model - E5B1041) machine was employed to drill 5.5 mm deep holes into the EN-31 workpiece. The machine automatically logged the Tm for each test run after the program was uploaded to the system through the control panel. A CONTOURMATIC T2 surface roughness tester was used to measure surface roughness. The components were weighed using a precision balance (Scitex BAE3123HTP) in order to compute MRR and EWR. A stereo microscope with 23× magnification was used to inspect the workpiece, while the electrode wear and material removal patterns were analyzed under 18× magnification. The base radius (R) was measured using a stereo microscope/image analysis system. The radius was defined as the curvature at the machined cavity base and geometric fitting determined from captured images. Multiple measurements were taken to ensure repeatability, and the average value was reported to minimize measurement uncertainty.

A precise digital balance with defined resolution (e.g., ±0.001 g) was used to determine MRR and EWR. Before weighing, the workpiece and electrode surfaces were washed with a suitable solvent to eliminate dielectric residue, debris, and impurities, and then properly dried under regulated conditions. To avoid measurement mistakes caused by moisture or surface deposits, proper handling procedures were followed.

Surface roughness was determined using a calibrated surface roughness tester with a predetermined cutoff length (e.g., 0.8 mm) and evaluation length (e.g., 4 mm). Multiple traces (at least three) were collected at various sites, with the average value presented. Measurements were taken perpendicular to the machining direction to capture the actual surface imperfections. Prior to testing, the instrument was calibrated using a standard reference specimen.

EWR was calculated using the equation [30] stated below in Equation 1:

$$EWR = \frac{Eb - Ea}{Tm} \ (g/\text{min})$$

MRR was calculated using the equation [31] and is stated below in Equation 2:

$$MRR = \frac{Wb - Wa}{Tm} \ (g/\text{min})$$

Figure I. GENSPARK EDM Machine used for EN-31 steel.

To confirm the effect of input factors on output responses, the experiments were designed using a DOE technique. This method involves investigating combinations of the input parameters at various levels (low and high). In this study four input parameters i.e., Ton, Toff, LV and HV were evaluated at two distinct levels. This binary factor level arrangement provides for a thorough examination of the key effects and interactions between the input and output parameters.

The total number of experimental runs needed is 24 = 16 runs with four input parameters, each of which has two levels. Table 2 lists the level of input parameters, and Table 3 Table lists the fundamental experimental runs.

Factor	Unit	Levels	No. of Levels
Workpiece	-	EN-31	1
T_{on}	µs	4, 6.5	2
T_{off}	µs	5.5, 6.5	2
HV	V	30, 50	2
LV	A	0.3, 0.7	2

Table II. Input parameters level and units.

Factor	Unit	Levels	No. of Levels
Workpiece	-	EN-31	1
T_{on}	µs	4, 6.5	2
T_{off}	µs	5.5, 6.5	2
HV	V	30, 50	2
LV	A	0.3, 0.7	2

Table III. Table of basic experimental runs values.

In order to develop prediction models that explain the links between the input parameters, Ton, Toff, LV, and HV, and the output responses, Tm, MRR, EWR, Ra, and "R," regression analysis was carried out using Minitab following the completion of basic experimental runs. These regression models show how changes in input parameters affect output responses, resulting in a quantitative foundation for predicting outcomes across varied situations. The models helped to detect trends and patterns in the data, allowing for a better understanding of the major elements impacting the EDM process and helping the development of strategies to improve machining performance.

Analysis of variance (ANOVA) was then used to determine the important input parameters for each output answer. An ANOVA was performed using Minitab software to ascertain the input parameters' statistical significance. The purpose of this study was to determine which parameters significantly affected the EDM process and to measure the magnitude of their influence on output responses. ANOVA separated the total variation in the data into components assigned to various sources, revealing the relative significance of each input parameter and their interactions.

Following are the objectives of this experimental study.

- To reduce the Tm of EN-31 steel by using EDM
- To increase the MRR of EN-31 steel by using EDM
- To reduce the EWR of EN-31 steel by using EDM
- To improve the Ra of EN-31 steel by using EDM
- To minimize the variation in R of EN-31 steel by using EDM

3. ANOVA Analysis. - An ANOVA was performed using Minitab software to ascertain the input parameters' statistical significance. The purpose of this study was to determine which parameters significantly affected the EDM process and to measure the magnitude of their influence on output responses. ANOVA separated the total variation in the data into

components assigned to various sources, revealing the relative significance of each input parameter and their interactions.

The model is then adjusted by eliminating the insignificant factors and a revised ANOVA table is created to highlight the most significant ones. The standardized effects normal plot and residual plots for the variable's response are generated again. Additionally, Main effect and interaction plots are generated and analyzed. Significant interactions are shown by non-parallel lines between levels in the interaction plot, whereas a steep slope in the main effect plot indicates the significance of the effect.

The Response Optimizer program generates practical solutions. A specified aim (Minimize, Equate, or Maximize) is selected and lower, target and upper values are entered to examine the desirability function. A 'd' value close to one indicates that the response is close to the target value supplied. The results of this exercise comprise the optimum value of the considered factor, the optimized response value and the desirability factor.

4. Results and discussion. - ANOVA is a statistical method used to identify the important input variables that significantly affect each of the five output answers listed in the preceding section. It doesn't only identify the significant parameters but also the combined effect of different input parameters on output responses. By using ANOVA, this investigative study ensures that study is accurate.

4.1 Machining time (Tm) ANOVA results. - Minitab software was used to construct the ANOVA table for Tm in Table 7. As input factors, ton, toff, LV, and HV were taken into consideration. Significant factors were those with a p-value of less than 0.05. The goal is to shorten the EN-31 material's machining time in order to produce more units per hour (UPH). LV and Ton are important parameters when taking Tm into account for EN-31, according to the ANOVA table in Table 7 and the Normal Probability Plot in Figure 4. After that, the model was rebuilt using only LV and Ton as input variables and excluding non-significant input parameters.

Main effect plots (Figure 5) and interaction plots (Figure 6) were created following the identification of relevant factors. The main effect plot's steep mean slopes support the idea that LV and Ton have a major influence on Tm optimization in EN-31. Calculating the optimal values of the important input factors was the following stage. The upper number was set to 427 seconds, which indicated the quickest machining time, and the target value was set to 0 seconds in order to optimize machining time. After evaluating the desirability functions (Figure 7), a desirability value (d) of 0 indicates that the answer is far from the target, indicating that the target value is less significant. A desirability value of 1 might have been attained if the goal had been set closer to 600 with a value greater than 2000.

The optimal values of input parameters were LV = 50 A & Ton = 6.5 µs as specified in Appendix 1. For these adjusted input parameters, the minimum Tm was calculated to be 654.29 seconds.

The results in Appendix 1 (Table 6) shows that higher the values of LV and Ton, shorter will be machining times (Tm) and vice versa. This means that inverse relationship exists between LV & Ton with machining time. The experimental runs as mentioned in table 4 in Appendix 1 also shows an inverse relationship between LV and Ton in with Tm. As we know that greater the LV and Ton time values result in large depressions/craters on the workpiece and these large craters results in poor surface finish (Ra) and poor surface finish leads to the final product which is not fit for use especially in the fields of bio implant manufacturing, automotive parts manufacturing etc. where good surface finish is of extreme importance. That why parametric optimization of all the output responses of EN-31 in EDM is necessary to have a product that meets the customer and manufacturer demands.

4.2 MRR ANOVA results. - The ANOVA (Table 11) for MRR was created in Minitab. All four input variables were taken in to account while performing the analysis. Ton is a significant factor in MRR in EN-31, according to the ANOVA table (Table 11) and the Normal Probability Plot (Figure 9). Following that, non-significant components were eliminated from the model (Table 10), leaving only Ton as an input factor.

Main effect Plot (Figure 13) and Interaction Plot (Figure 14) were prepared for MRR after the determination of significant factors. The Main effect Plot shows that Ton is a significant factor whereas the Interaction Plot shows that Ton and LV are significant factors as LV p-value is 0.055 which makes it quite close to be a significant factor. Now the optimized value of significant factors is calculated. MRR was optimized with a goal value of 1 g/min and a lower value of 0.0267 g/min, indicating the highest observed value of MRR. The desirability functions (Figure 15) were then assessed. A desirability value (d) of 0 shows that the response is distant from the target, meaning that the target value is not as important. If the objective had been set closer to 0.015 with a lower value less than 0.014, a desirability value near to 1 may have been obtained.

The optimized value for Ton was found to be 6.5 µs, as detailed in Appendix 1. For this optimized setting, the maximum MRR was calculated to be 0.0157 g/min.

The results in Appendix 2 show that greater values of Ton result in higher material removal rates (MRR). This means that direct relationship exists between Ton vs MRR in EN-31 material. The experimental runs also show a direct relationship between Ton and MRR. However, Ton optimization must be matched with other input factors in order to achieve an good surface quality (Ra) and overall machining performance. Therefore, in order to provide the best possible final product, the parametric optimization of the EDM process aimed to balance all output reactions.

4.3 EWR ANOVA results. - Minitab was used to create the EWR ANOVA table (Table 12). Ton, Toff, LV, and HV are all considered as input elements. LV and Ton are important factors affecting EWR in EN-31, according to the ANOVA table (Table 12) and the Normal Probability Plot (Figure 16). Consequently, non-significant factors were eliminated from the model (Table 13), leaving only LV and Ton as input variables. The importance of these factors and the model itself was confirmed by the p-values from the modified model's ANOVA table (Table 13).

Following the identification of important components, EWR's main effect plot (Figure 19) and interaction plot (Figure 20) were created. Steep mean slopes in the Main Effect Plot show how LV and Ton have a major influence on EWR in EN-31. Strong interaction effects between different parameters are displayed in the interaction plot. Finding the ideal values for the pertinent input factors was the following stage. EWR was optimized by setting the upper value to 0.00523 g/min, the lowest measured EWR, and the target value to 0 g/min. The desirability functions (Figure 20) were then assessed. A desirability value (d) of 0 shows that the response is far from the target, meaning that the target value is not as important. If the objective had been set closer to 0.015 with a lower value less than 0.014, a desirability value near to 1 may have been obtained. The optimized values were found to be 30 A for LV and 4 µs for Ton, as detailed in Appendix 1. For these optimized settings, the minimum EWR was calculated to be 0.07 g/min.

The findings in Appendix 2 demonstrate a direct proportionality between the LV and Ton levels with EWR. EWR values increase with increased LV and Ton, and vice versa. Additionally, the experimental runs showed a direct proportionality between EWR and LV and Ton. Optimizing these input parameters is crucial to achieving a proper surface finish (Ra), improved productivity, and overall machining performance because lower LV and Ton values will result in lower MRR and higher Tm. Therefore, in order to provide the best possible final product, the parametric optimization of the EDM process aimed to balance all output reactions.

4.4 Surface finish (Ra) ANOVA results. - The ANOVA table (Table 13) for Ra was created in Minitab. All input factors (Ton, Toff, LV, HV) were considered. The ANOVA table (Table 13) and the Normal Probability Plot (Figure 23showed that there are no significant factors influencing Ra in EN-31. As a result, there was no need to retrofit the model. However, the Main effect Plot (Figure 25) and Interaction Plot (Figure 26were still generated for Ra. The Interaction Plot shows non-parallel lines, showing that the parameters interact significantly.

The optimal values for the significant factors were then calculated. Ra was optimized with a goal value of 0 mm and an upper value of 0.006 mm, which represented the minimum observed surface roughness. The desirability functions (Figure 27) were then assessed. A desirability value (d) of 0 shows that the response is distant from the target, meaning

that the target value is not as important. Had the target been set closer to 0.009 with an upper value greater than 0.015, a desirability value close to 1 could have been achieved.
The optimized values of Ra for EN-31 were found to be LV = 50 A & HV = 0.7 V, Ton = 4.0 µs and Toff = 6.5 µs as shown in Appendix 1. For these optimized settings, the minimum Ra was calculated to be 0.018 mm.

4.5 Base radius (R) ANOVA results. - The ANOVA table (Table 14) for 'R' was created in Minitab, considering all input variables. The ANOVA table (Table 14) and the Normal Probability Plot (Figure 28) showed that the interactions HV*LV*Ton and HV*LV*Ton*Toff are significant factors for R in EN-31. As a result, the model was refined (Table 15) by eliminating non-significant in, leaving only HV*LV*Ton and HV*LV*Ton*Toff as input variables. The p-values from the updated model's ANOVA table (Table 15) supported the significance of these interactions and the model as a whole.

After identifying significant factors, the Main effect Plot (Figure 32) and the Interaction Plot (Figure 33) were created for R. The Main effect Plot displays steep slopes of means, indicating the significance of the interactions, while the Interaction Plot displays non-parallel lines, indicating significant interaction effects between these variables. After that optimum value of input factors were calculated that were considered significant. To optimize R, the target value was set to 1.5 mm, with maximum and lower boundaries of 1.55 mm and 1.45 mm, respectively. The desirability functions (Figure 34) were then assessed. A desirability value (d) near to one shows a strong preference for the target value, implying that the response closely matches the desired target. The optimized values were found to be HV = 0.6152 V, LV = 50 A, Ton = 6.5 µs and Toff = 6.5 µs as shown in detail in Appendix 1. For these optimized settings, the base radius R was calculated to be 1.5 mm.

The results in Appendix 1 demonstrate that optimizing these parameters must be balanced with other factors to ensure a desirable overall machining performance. Therefore, the parametric optimization of the EDM process aimed to balance all output responses to achieve an optimal final product.

5. Conclusion. - This study focused on optimizing processing parameters in Electric Discharge Machining (EDM) for EN-31 steel by systematically analyzing their impact on key machining responses. The investigation aimed to minimize Tm, maximize MRR, reduce EWR, enhance Ra and control 'R'. A full factorial experimental approach, combined with regression analysis and ANOVA, was used to identify and optimize the most significant parameters, namely Ton, Toff, LV and HV.

The observed results are governed by electro-thermal interactions occurring in EDM. The primary mechanism involves localized melting and vaporization of the workpiece material due to high-energy electrical discharges between the electrode and the workpiece. The MRR is directly proportional to the Ton since longer discharge durations allow greater heat input, leading to higher melting and vaporization rates. Similarly, a higher discharge LV increases spark energy, which enhances material removal but also contributes to greater electrode wear (EWR).

The optimization results show that higher LV (50 A) and Ton (6.5 µs) significantly reduced Tm to 654.29 seconds by accelerating material removal. However, increasing these parameters beyond optimal levels resulted in excessive energy input, leading to large craters, poor surface finish (Ra) and undesired tool wear. This highlights the need for a balanced parameter selection, as excessively high current can degrade dimensional accuracy due to excessive thermal damage.

For EWR, a lower LV (30 A) and shorter Ton (4 µs) minimized electrode erosion (0.07 g/min), which is crucial for extending tool life. This occurs because lower discharge energy reduces thermal stress on the electrode, thereby slowing down the material erosion rate.

Ra is influenced by a complex interplay of spark intensity and pulse durations. The study found that an optimal combination of LV (50 A), HV (0.7 V), Ton (4.0 µs) and Toff (6.5 µs) minimized Ra to 0.018 mm. Mechanistically, this is because shorter pulse durations prevent excessive heat accumulation, reducing crater depth and ensuring a

smoother surface. Additionally, higher HV improves ionization, stabilizing the plasma channel and leading to more uniform material removal.

'R' was found to be highly dependent on interaction effects among HV, LV, Ton and Toff. A precise combination of HV (0.6152 V), LV (50 A), Ton (6.5 μs) and Toff (6.5 μs) ensured controlled energy distribution, leading to accurate base radius formation (1.5 mm). This confirms that high-energy discharges must be regulated to maintain dimensional accuracy while achieving efficient material removal.

The findings of this study offer industrial significance by providing an optimized EDM processing strategy for EN-31 steel, which is widely used in automotive, aerospace and die-making applications. The optimized settings enable faster production, improved surface quality, reduced tool wear and cost savings, making EDM a more viable manufacturing technique for high-hardness materials.

In conclusion, this study not only advances knowledge on EDM process optimization for EN-31 steel, but also provides a scientific basis for balancing machining efficiency and quality through electro-thermal parameter control. Future research may further refine these findings by exploring adaptive control strategies and hybrid EDM processes for enhanced precision and sustainability in machining operations.

Conflict of interest

The authors confirm that there are no conflicts of interest related to this research. They have disclosed all relevant affiliations and financial relationships.

References

[1] Tajdeen, A.; Khan, M. W.; Basha, K. K.; Sakthivelmurugan, E.; Koppula, N. Experimental Investigation and Optimization of EDM Process Parameters on EN31 Steel Using Genetic Algorithm. Mater. Today Proc. 2022, 64 (1), 821–827. https://doi.org/10.1016/j.matpr.2022.05.326.

[2] Sahu, A. K.; Sivarajan, S.; Padmanabhan, R. Optimization of Machining Parameters in Turning of EN31 Steel with TiAlN Coated Cutting Tool. Mater. Today Proc. 2021, 46 (17), 7497–7501. https://doi.org/10.1016/j.matpr.2021.01.180.

[3] Kamenskikh, A. A.; Muratov, K. R.; Shlykov, E. S.; Sidhu, S. S.; Mahajan, A.; Kuznetsova, Y. S.; Ablyaz, T. R. Recent Trends and Developments in the Electrical Discharge Machining Industry: A Review. J. Manuf. Mater. Process. 2023, 7 (6). https://doi.org/10.3390/jmmp7060204.

[4] Behera, A.; Sahoo, A. K.; Mahapatra, S. S. Experimental Investigation of Plain and Nano-Graphene Oxide Mixed Dielectric for Sustainable EDM of Nimonic Alloy Using Cu and Brass Electrode: A Comparative Study. Measurement 2025, 241. https://doi.org/10.1016/j.measurement.2024.115659.

[5] Harish, B.; Kumar, D. S. A Novel Statistical Investigation on Tensile Property of High Alloy Steel (EN31) and Carbon Steel (EN09). Mater. Today Proc. 2023, 79 (1), 49–52. https://doi.org/10.1016/j.matpr.2022.08.286.

[6] Langenberg, B.; Janczyk, M.; Koob, V.; Kliegl, R.; Mayer, A. A Tutorial on Using the Paired t Test for Power Calculations in Repeated Measures ANOVA with Interactions. Behav. Res. Methods 2023, 55, 2467–2484. https://doi.org/10.3758/s13428-022-01902-8.

[7] Samantra, C.; Barua, A.; Pradhan, S.; Kumari, K.; Pallavi, P. Parametric Investigation of Die-Sinking EDM of Ti6Al4V Using the Hybrid Taguchi-RAMS-RATMI Method. Appl. Sci. 2024, 14 (16). https://doi.org/10.3390/app14167139.

[8] Garba, E.; Abdul-Rani, A. M.; Yunus, N. A.; Aliyu, A. A. A.; Gul, I. A.; Al-Amin, M.; Aliyu, R. A Review of Electrode Manufacturing Methods for Electrical Discharge Machining: Current Status and Future Perspectives for Surface Alloying. Machines 2023, 11. https://doi.org/10.3390/machines11090906.

[9] Singh, G.; Kumar, A.; Aggarwal, V.; Singh, S. Experimental Investigations and Optimization of Machining Performance During Turning of EN-31 Steel Using TOPSIS Approach. Mater. Today Proc. 2022, 48 (5), 1089–1094. https://doi.org/10.1016/j.matpr.2021.07.381.

[10] Varpe, N. J.; Hamilton, N.; Anurag. Investigation into Burnishing Process to Examine Effect on Surface Integrity, Wear and Corrosion Resistance of Carbon Alloy (EN31) Steel. J. Mater. Eng. Perform. 2024, 33, 3691–3705. https://doi.org/10.1007/s11665-023-08524-x.

[11] Okokpujie, I. P.; Bolu, C. A.; Ohunakin, O. S.; Akinlabi, E. T.; Adelekan, D. S. A Review of Recent Application of Machining Techniques, Based on the Phenomena of CNC Machining Operations. Procedia Manuf. 2019, 35, 1054–1060. https://doi.org/10.1016/j.promfg.2019.06.056.

[12] Ram, J. S.; Jeavudeen, S.; Mouda, P. A.; Ahamed, N. The Role of Various Dielectrics Used in EDM Process and Their Environmental, Health, and Safety Issues. Mater. Today Proc. 2023. https://doi.org/10.1016/j.matpr.2023.05.137.

[13] He, J.; Zeng, Z.; Li, H.; Wang, S. The Microstructure and Mechanical Properties of Copper in Electrically Assisted Tension. Mater. Des. 2020, 196. https://doi.org/10.1016/j.matdes.2020.109171.

[14] Kumar, J.; Soota, T.; Rajput, S. K. Modelling and Optimization of EN 31 Work Material on Wire Electric Discharge Machining. Mater. Today Proc. 2019, 18 (7), 2984–2992. https://doi.org/10.1016/j.matpr.2019.07.169.

[15] Kamei, K.; Davis, R.; Pereira, R. B. D. Experimental Investigation of the Effect of Input Control Variables and Thermal Treatments on the Impact Toughness of EN-31 Steel. Mater. Sci. Forum 2024, 1133, 47–54. https://doi.org/10.4028/p-ge4bbx.

[16] Karthik, S.; Karunakaran, P.; Velmurugan, G. Experimental Investigation of WE43(T6) Magnesium Metal Matrix Composites to Enhance Mechanical Properties and EDM Process Parameters. Int. J. Electrochem. Sci. 2024, 19 (5). https://doi.org/10.1016/j.ijoes.2024.100553.

[17] Galati, M.; Antonioni, P.; Calignano, F.; Atzeni, E. Experimental Investigation on the Cutting of Additively Manufactured Ti6Al4V with Wire-EDM and the Analytical Modelling of Cutting Speed and Surface Roughness. J. Manuf. Mater. Process. 2023, 7 (2). https://doi.org/10.3390/jmmp7020069.

[18] Martínez-Olvera, C. The Role of Manufacturing Efficiency in the Achievement of Sustainable Mass Customization 4.0. Manuf. Res. 2022, 10 (1), 132–159. https://doi.org/10.1080/21693277.2022.2064360.

[19] Farooq, M. U.; Anwar, S.; Bhatti, H. A.; Kumar, M. S.; Ali, M. A.; Ammarullah, M. I. Electric Discharge Machining of Ti6Al4V ELI in Biomedical Industry: Parametric Analysis of Surface Functionalization and Tribological Characterization. Materials 2023, 16 (12). https://doi.org/10.3390/ma16124458.
[20] Kumar, P. M.; Sivakumar, K.; Selvarajan, L. EDM Machining Effectiveness for Ti–6Al–4V Alloy Using Cu–TiB2 Ceramic Composite Electrode: A Parametric Evaluation. Ceram. Int. 2024, 50 (11 Part B), 20118–20132. https://doi.org/10.1016/j.ceramint.2024.03.135.
[21] Singh, R. P.; Sharma, V.; Kumar, R. Optimization of Response Parameter of Machining EN31 While Electro-Discharge-Machining Using TLBO. Mater. Today Proc. 2023. https://doi.org/10.1016/j.matpr.2023.02.121.
[22] Shastri, R. K.; Mohanty, C. P.; Mishra, U.; Hotta, T. K.; Patil, V. V.; Prashanth, K. G. Optimizing the Electrical Discharge Machining Process Parameters of the Nimonic C263 Superalloy: A Sustainable Approach. J. Manuf. Mater. Process. 2024, 8 (3). https://doi.org/10.3390/jmmp8030126.
[23] Ganapathy, S.; Palanivendhan, M.; Balasubramanian, P.; Susitra, K. Process Parameter of EDM to Optimize Material Removal Rate Using Box Behnken's Design. Mater. Today Proc. 2023, 82, 38–42. https://doi.org/10.1016/j.matpr.2022.11.148.
[24] Sharma, S.; Kumar, U.; Vates, A.; Bansal, A. Parametric Optimization of EN-31 Steel in Wire Cut Electro Discharge Machining by Taguchi Technique. Adv. Sci. Eng. Med. 2020, 10, 881–887. https://doi.org/10.1166/asem.2020.2645.
[25] Pawar, S. S.; Bera, T. C.; Sangwan, K. S. Towards Energy Efficient Milling of Variable Curved Geometries. J. Manuf. Process. 2023, 94, 497–511. https://doi.org/10.1016/j.jmapro.2023.03.078.
[26] Bhowmick, S.; Mondal, R.; Sarkar, S.; Biswas, N.; De, J.; Majumdar, G. Parametric Optimization and Prediction of MRR and Surface Roughness of Titanium Mixed EDM for Inconel 718 Using RSM and Fuzzy Logic. CIRP J. Manuf. Sci. Technol. 2023, 40, 10–28. https://doi.org/10.1016/j.cirpj.2022.11.002.
[27] Sharma, V. K.; Saini, A.; Gupta, M.; Sehgal, S. S. Multi-Response Optimization in Face Milling of EN-31 Steel Using Analytical Hierarchy Process-Based GRA. Int. J. Interact. Des. Manuf. 2024, 18, 6187–6194. https://doi.org/10.1007/s12008-023-01540-0.
[28] Dwivedi, Y. D.; Kumar, T. V.; Dharme, A.; Kumar, K. B.; Gori, Y.; Chandra, P. K.; Abdul-Zahra, D. S.; Kumar, D.; Jain, A. A Critical Review on Different Aspects of Electric Discharge Machining. Mater. Today Proc. 2023. https://doi.org/10.1016/j.matpr.2023.03.748.
[29] Qin, Y.; Liu, X.; Yue, C.; Wang, L.; Gu, H. A Tool Wear Monitoring Method Based on Data-Driven and Physical Output. Robotics Comput. Integr. Manuf. 2024, 91. https://doi.org/10.1016/j.rcim.2024.102820.

Author contribution:
1. Conception and design of the study
2. Data acquisition
3. Data analysis
4. Discussion of the results
5. Writing of the manuscript
6. Approval of the last version of the manuscript

MMUZ has contributed to: 1, 2, 3, 4, 5 and 6.
SAI has contributed to: 1, 2, 3, 4, 5 and 6.
AZ has contributed to: 1, 2, 3, 4, 5 and 6.
AT has contributed to: 1, 2, 3, 4, 5 and 6.

Acceptance Note: This article was approved by the journal editors Dr. Rafael Sotelo and Mag. Ing. Fernando A. Hernández Gobertti.

Mitigating Climate Change: A Review of Carbon Capture and Separation Technologies

Mitigación del cambio climático: una revisión de las tecnologías de captura y separación de carbono

Mitigando as mudanças climáticas: uma revisão das tecnologias de captura e separação de carbono.

Haider Ali [1] (*), Nomaan Akhtar [2] (*), Saqib Shams [3], Ali Karim [4], Umair Naeem [5]

Recibido: 09/01/2026 Aceptado: 25/03/2026

Summary. - Carbon capture and separation techniques (CCST) play a pivotal role in addressing the pressing challenge of reducing CO_2 emissions and mitigating climate change impacts. This review paper provides a detailed examination of various CCST methodologies, focusing on their mechanisms, applications, and importance in the broader context of environmental sustainability. The significance of Carbon Capture, Utilization, and Storage (CCUS) strategies is emphasized as an essential pathway for reducing greenhouse gas emissions. Through an in-depth analysis, the paper examines the diverse range of carbon capture technologies, including direct air capture, post-combustion, pre-combustion, and chemical looping. Each technology is scrutinized for its efficiency, scalability, and suitability across different industrial sectors. It also delves into carbon separation technologies, including absorption, adsorption, cryogenic separation, and membrane separation, explaining their mechanisms and applications in CO_2 capture. Additionally, the review addresses the economic, regulatory, and environmental implications of CCST implementation, highlighting challenges and opportunities for scaling up these technologies. This paper contributes to a clearer understanding of CCST as a vital tool for combating climate change and achieving sustainable development goals.

Keywords: *Absorption, Adsorption, Carbon capture and separation; Direct Air Capture; Post-combustion.*

(*) Corresponding author.

[1] Professor, Department of Mechanical Engineering, NED University of Engineering & Technology (Pakistan), haider.ali@neduet.edu.pk, ORCID iD: https://orcid.org/0000-0001-8242-3696

[2] Student, Department of Mechanical Engineering, NED University of Engineering & Technology (Pakistan), nomaan.akhtar2@gmail.com, ORCID iD: https://orcid.org/0009-0007-2969-675X

[3] Student, Department of Mechanical Engineering, NED University of Engineering & Technology (Pakistan), saqibshams200204@gmail.com, ORCID iD: https://orcid.org/0009-0009-3932-6095

[4] Student, Department of Mechanical Engineering, NED University of Engineering & Technology (Pakistan), alikarimptcl@gmail.com, ORCID iD: https://orcid.org/0009-0008-0495-0237

[5] Student, Department of Mechanical Engineering, NED University of Engineering & Technology (Pakistan), umairnaeem139@gmail.com, ORCID iD: https://orcid.org/0009-0003-0763-4081

Memoria Investigaciones en Ingeniería, núm. 30 (2026). pp. 116-144
https://doi.org/10.36561/ING.30.9
ISSN 2301-1092 • ISSN (en línea) 2301-1106 – Universidad de Montevideo, Uruguay

Resumen. - *Resumen. - Las técnicas de captura y separación de carbono (CCST) desempeñan un papel fundamental para abordar el desafío urgente de reducir las emisiones de CO2 y mitigar los impactos del cambio climático. Este artículo de revisión ofrece un análisis detallado de diversas metodologías CCST, centrándose en sus mecanismos, aplicaciones e importancia en el contexto más amplio de la sostenibilidad ambiental. Se destaca la importancia de las estrategias de captura, utilización y almacenamiento de carbono (CCUS) como una vía esencial para reducir las emisiones de gases de efecto invernadero. Mediante un análisis exhaustivo, el artículo examina la diversa gama de tecnologías de captura de carbono, incluyendo la captura directa de aire, la postcombustión, la precombustión y el ciclo químico. Cada tecnología se analiza en función de su eficiencia, escalabilidad e idoneidad en diferentes sectores industriales. También profundiza en las tecnologías de separación de carbono, incluyendo la absorción, la adsorción, la separación criogénica y la separación por membranas, explicando sus mecanismos y aplicaciones en la captura de CO2. Además, la revisión aborda las implicaciones económicas, regulatorias y ambientales de la implementación de CCST, resaltando los desafíos y las oportunidades para la ampliación de estas tecnologías. Este artículo contribuye a una mejor comprensión de la captura y separación de carbono como herramienta fundamental para combatir el cambio climático y alcanzar los objetivos de desarrollo sostenible.*

Palabras clave: *Absorción, Adsorción, Captura y separación de carbono, Captura directa de aire, Postcombustión.*

Resumo *.* ***-*** *As técnicas de captura e separação de carbono (CCST) desempenham um papel fundamental no enfrentamento do desafio premente de reduzir as emissões de CO2 e mitigar os impactos das mudanças climáticas. Este artigo de revisão fornece um exame detalhado de várias metodologias de CCST, com foco em seus mecanismos, aplicações e importância no contexto mais amplo da sustentabilidade ambiental. A importância das estratégias de Captura, Utilização e Armazenamento de Carbono (CCUS) é enfatizada como um caminho essencial para a redução das emissões de gases de efeito estufa. Por meio de uma análise aprofundada, o artigo examina a diversidade de tecnologias de captura de carbono, incluindo captura direta do ar, pós-combustão, pré-combustão e ciclo químico. Cada tecnologia é analisada quanto à sua eficiência, escalabilidade e adequação a diferentes setores industriais. O artigo também explora as tecnologias de separação de carbono, incluindo absorção, adsorção, separação criogênica e separação por membrana, explicando seus mecanismos e aplicações na captura de CO2. Além disso, a revisão aborda as implicações econômicas, regulatórias e ambientais da implementação de CCST, destacando os desafios e as oportunidades para a ampliação dessas tecnologias. Este artigo contribui para uma compreensão mais clara da CCST como uma ferramenta vital para combater as mudanças climáticas e alcançar os objetivos de desenvolvimento sustentável.*

Palavras-chave: *Absorção, Adsorção, Captura e separação de carbono; Captura direta de ar; Pós-combustão.*

1. Introduction. -

1.1 Importance of Carbon Capture. - The greenhouse effect stands as a central mechanism driving global warming and climate change, as widely reported in climate-change literature. As emphasized by multiple authors, the repercussions of this phenomenon are profound, with current projections indicating serious future risk. Predictions imply that unchecked global warming would cause the melting of polar ice caps, eventually leading to a considerable rise in global sea levels and posing a catastrophic threat to coastal cities globally. Such forecasts are not mere conjecture; they are grounded in scientific data and models that indicate a concerning trajectory. For instance, according to projections cited from the Intergovernmental Panel on Climate Change (IPCC) baseline period of 1961-90, global warming is anticipated to escalate by as much as 4 °C by the year 2050, accompanied by a decrease in rainfall across many regions. These forecasts highlight the importance of addressing climate change and implementing policies to reduce greenhouse gas emissions, notably carbon dioxide (CO_2) emissions. The EU Commission on Climate Change has recognized human activities, mainly the combustion of fossil fuels, as the principal cause of the increase in CO_2 levels. Indeed, by 2020, atmospheric CO_2 levels had risen by an astounding 48% relative to pre-industrial levels [1]. This disturbing trend highlights the critical need for global collaboration to address the main causes of climate change and transition to a low-carbon future.

1.2 Carbon Capture, Utilization and Storage (CCUS). - CCUS techniques are important in the global effort to reduce CO_2 emissions and mitigate climate change. As mentioned in Figure , the process begins with the capture of carbon dioxide from a variety of sources, each with a different concentration. This captured CO_2 passes through a series of essential stages, including separation from contaminants in the mixture. Once purified, the CO_2 can be directed towards two main pathways: storage or utilization. In one scenario, the CO_2 is safely stored in depleted oil and gas fields, preventing its release into the atmosphere and contributing to long-term CO_2 sequestration. Alternatively, captured CO_2 can be utilized for commercial applications, thereby transforming a greenhouse gas into a valuable resource. This multifaceted strategy not only reduces environmental impacts but also promotes innovation and economic growth. Against the backdrop of rising climate concerns, this study examines the most recent breakthroughs in carbon capture and separation technology. By providing insights into these trends, it emphasizes the significance of CCUS methodologies and lays the groundwork for a sustainable future powered by effective carbon management tactics.

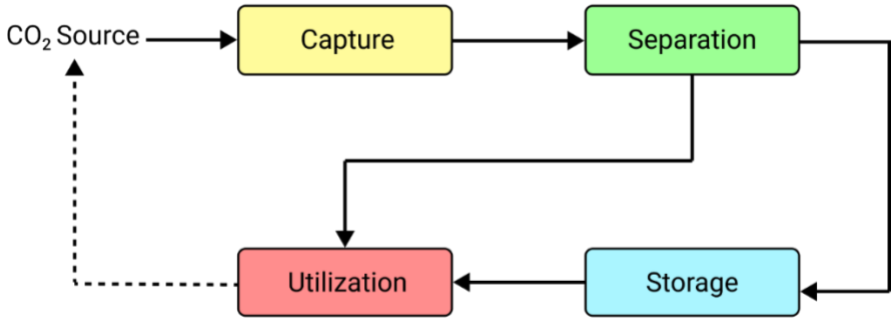

Figure I. Life Cycle of Carbon Dioxide involved in the capture process.

1.3 Review Methodology. - This review was prepared by collecting literature on carbon capture and separation technologies from major scholarly databases, including Scopus, Web of Science, ScienceDirect, and Google Scholar. Keywords included “carbon capture,” “carbon separation,” “CCUS,” “direct air capture,” “post-combustion capture,” “pre-combustion capture,” “chemical looping,” “absorption,” “adsorption,” “membrane separation,” and “cryogenic separation.” Peer-reviewed journal articles, review papers, and technically relevant studies were prioritized. Non-scholarly sources and duplicate references were excluded where possible. Data extracted from the literature included capture efficiency, Technology Readiness Level, study scale, operating conditions, energy/cost basis, advantages, and limitations. Where conflicting numerical values were reported, ranges were presented and interpreted in relation to study scale, assumptions, and system boundaries.

2. Carbon Capture Technologies. - Technologies aimed at capturing carbon dioxide (CO_2) emissions from a variety of sources, mostly industrial operations and electricity production, are collectively referred to as carbon capture technologies. By limiting the release of CO_2 into the atmosphere, the aim is to lessen the influence of greenhouse gas emissions on climate change. These technologies are illustrated in Figure .

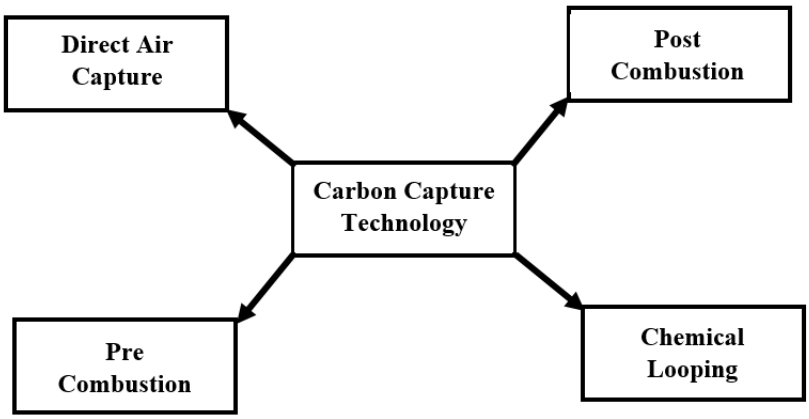

Figure II. Carbon Capture Technologies.

2.1 Direct Air Capture. - Recently, significant research attention has been directed toward greenhouse gas removal (GGR) technologies, which aim to remove CO_2 from the atmosphere. The current level of CO_2 in the atmosphere is over 400 ppm and rising by about 2 ppm per year, mainly as a result of burning fossil fuels [2]. Fossil fuels continue to be a major energy source, so we need technologies to capture and store CO_2 directly from the air, referred to as Direct Air Capture (DAC). Traditional carbon capture methods target specific sources like power plants, but DAC can capture CO_2 from any location, making it more versatile.

Some studies have questioned whether GGR is truly effective as a way to remove CO_2 from the atmosphere. In this situation, Direct Air Capture (DAC) has the potential to support the achievement of net-zero emissions by removing CO_2 directly from ambient air, regardless of the original emission source. DAC is a process that aims to remove CO_2 from the atmosphere and store it permanently or use it for other purposes. DAC is considered one of the negative emission technologies (NET) that are essential for achieving net-zero emissions by 2050 to limit global warming to 1.5°C [3]. Different methods of performing DAC exist, such as sorbent-based systems, membrane-based systems, or biological systems. Previous studies on integrated DAC systems are summarized in Table I, whereas the merits and demerits of DAC Technology are given in Table II.

Author	System Configuration	Major Results
D. Coppitters et al. [4]	Direct Air Capture and Compression with Proton Exchange Membrane (PEM) electrolyzer and methanation unit.	Exergy efficiency varies between 51.3% and 52.6%. Synthetic natural gas production costs range from 130 €/MWh to 744 €/MWh.
T. Daniel et al. [5]	DAC combined with Carbon Dioxide (CO_2) utilization using High-Temperature Steam Electrolysis (HTSE).	The estimated cost is 382 \$/t CO_2.
J. Cui & M. Aziz [6]	Implementation of DAC for ammonia and methanol production.	Among the examined options, the infrastructure for ammonia production demonstrates the most cost-effective energy transmission of US\$10.1/GJ.
P. Cheng et al. [7]	Application of a DAC powered by a natural gas combined cycle (NGCC) plant and post-combustion carbon capture.	Positive net present value is considered to require a CO_2 price of between \$150 and \$225 per tonne (NPV).
G. M. Cole et al. [8]	DAC implementation based on algae-based coating.	The method has a 44% to 51% carbon removal effectiveness, accompanied by sequestration costs per tonne of CO_2 that vary from \$702 to \$1585.
C. Drechsler & D. W. Agar [9]	DAC implementation with heat recovery and electrolyser integration.	Per mole of CO_2 captured, surplus heat output is 475 kJ with an equilibrium cell voltage of 1.5.

Table I. Summary of DAC integrated studies.

The DAC plant consists of various chemical cycles and units designed to capture CO_2 from the air and recycle the solvents used in the process, as illustrated in Figure . Here is a simplified version of the process described by Slavin et al. [10].

1. Air is pulled through a unit called the air contactor. In the contactor, CO_2 reacts with a solution containing KOH to form potassium carbonate (K_2CO_3).
2. The resulting K_2CO_3 solution is sent to the pellet reactor, which holds calcium carbonate ($CaCO_3$) pellets. Calcium hydroxide [$Ca(OH)_2$] is added to the reactor, causing $Ca(OH)_2$ to dissolve and $CaCO_3$ to precipitate.
3. More $CaCO_3$ pellets are added to the top of the reactor. They are removed from the bottom and sent to the calciner.
4. In the calciner, the $CaCO_3$ pellets are heated up to 900 °C, breaking them down into CO_2 and calcium oxide (CaO).
5. CO_2 is finally compressed and cooled for storage or sale.
6. In the slaker unit, the CaO is mixed with water to form $Ca(OH)_2$, which may be reused in the pellet reactor.

Simultaneously, the CO_2 emitted from the calciner is directed into a Solid Oxide Electrolysis Cell (SOEC) reactor, where it mixes with steam. Inside the reactor, three processes take place at once: steam electrolysis, CO_2 electrolysis, and the reverse water-gas shift reaction. The output gases are then divided into two streams: the anode outlet, which contains pure oxygen, part of which is recirculated back to the calciner, and the cathode outlet, which holds the produced syngas along with any unreacted components [5].

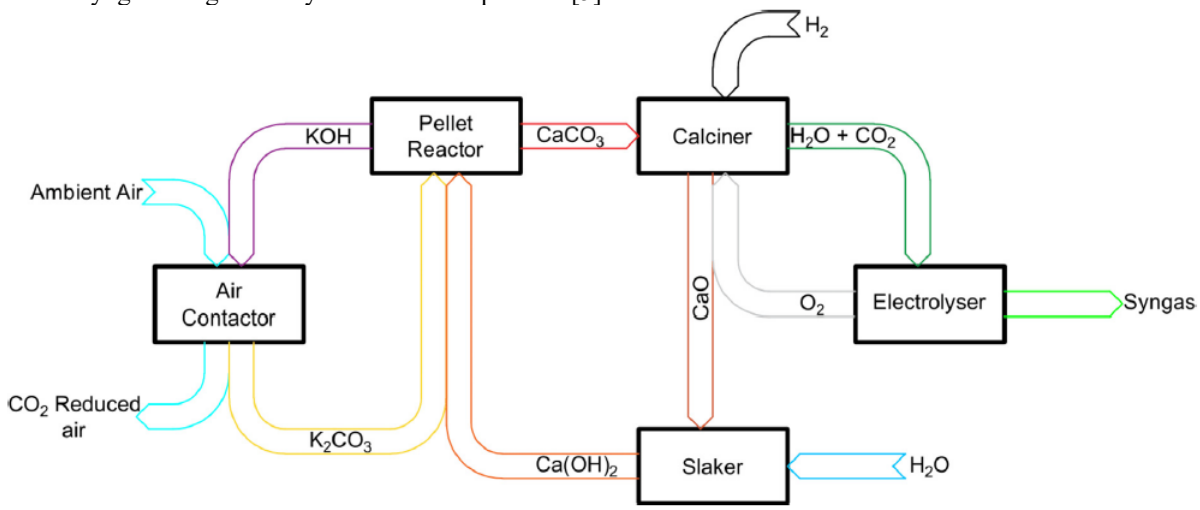

Figure III. DAC Process Diagram [7].

In a typical DAC unit, captured emissions are typically stored in depleted gas and oil fields. However, by incorporating a SOEC, the captured CO_2 can be transformed into a valuable product. This may help offset the plant's operating costs [7].

Over the last twenty years, there has been a notable increase in reports discussing different materials used in DAC to trap carbon dioxide. Recent advancements in DAC adsorbents require further evaluation, including the promising MMO-based amine-functionalized DAC adsorbent. This review examines how well these materials can capture CO_2, how easily they can be regenerated for reuse, and the mechanisms behind their CO_2 capture processes. Such efforts are expected to play a significant role in advancing DAC technology from foundational research to practical, large-scale applications [11]. Over time, there has been rapid progress in developing sorbents for capturing CO_2. Porous solid sorbents, known for their large surface area and adjustable pore structure, offer promising potential for CO_2 capture, addressing issues like equipment corrosion and high costs associated with traditional amine solutions. These sorbents can be categorized into physisorbents and chemisorbents based on their adsorption mechanisms, with the porous structure enhancing adsorption in various ways. Physisorbents benefit from increased interaction with CO_2 molecules in a porous environment, while chemisorbents utilize their porous structure to improve mass transport and adsorption kinetics. Framework materials like MOFs and COFs further refine this control, offering finely tunable pore characteristics [12]. Table contrasts the merits and demerits of direct air carbon capture technology.

Merits	Demerits
It helps reduce atmospheric CO_2 levels.	High initial capital investment is required.
Provides a way to remove CO_2 from hard-to-reach areas.	Energy-intensive process, leading to high operational costs and potential environmental impacts.
Can be deployed in various locations globally.	The efficiency of CO_2 capture may not be as high as desired, leading to limited impact.
Offers potential for carbon utilization and storage.	Challenges with scalability for large-scale deployment.
Contributes to global efforts in climate change mitigation.	Technological uncertainties and risks may hinder widespread adoption.

Table II. Merits and Demerits of DAC [13] [14].

2.2 Post-combustion. - Post-combustion carbon capture focuses on extracting carbon dioxide from the flue gases produced by combustion plants. These gases mainly consist of nitrogen and carbon dioxide at elevated temperatures (120–180°C), along with minor amounts of steam, sulfur dioxide, nitrogen oxides, and particulate fly ash [15]. According to emission standards, flue gas must be cleansed of toxic gases before its release [16]. Due to the lower concentration of carbon dioxide (3–20%) in flue gas compared to the pre-combustion methods, chemical absorption is commonly used to separate CO_2 [17]. Because of the low concentration and partial pressure of carbon dioxide, highly efficient separation methods are necessary. Monoethanolamine (MEA) aqueous solutions are frequently used due to their ability to effectively absorb carbon dioxide and form carbamates [18]. The post-combustion carbon capture process starts by passing the flue gas through a vessel with an absorber, usually MEA. The CO_2 -laden solvent is then moved to a separate vessel, where the CO_2 is extracted, allowing the solvent to be reused in the system [19]. The released CO_2 is subsequently compressed and transported.

Post-combustion carbon capture methods are advantageous over pre-combustion methods due to their flexibility, allowing integration into existing power plants, making them the preferred choice for current facilities [19]. However, these methods significantly increase electricity costs due to the substantial energy required for solvent regeneration and CO_2 compression. For example, coal plants can capture up to 800 tons of CO_2 per day, resulting in a 65% increase in electricity costs [20]. Table compares the advantages and disadvantages of post-combustion carbon capture technology.

Merits	Demerits
It can be installed in existing infrastructure.	The capture and separation of CO_2 require additional energy input, leading to decreased overall plant efficiency.
This technology helps industries and nations meet emission reduction targets and regulatory requirements.	A mismatch between supply and demand could hinder the economic feasibility of carbon utilization pathways and limit their contribution to overall emission reduction efforts.
Captured carbon dioxide can be used for several applications, including enhanced oil recovery (EOR), concrete carbonation, and the synthesis of fuels and chemicals.	Carbon capture processes, particularly those based on solvent absorption, can be resource-intensive, requiring large quantities of water, chemicals, and energy for operation.
Carbon capture and storage (CCS) technologies enable the long-term geological storage of CO_2, reducing its atmospheric concentration.	A risk of CO_2 migration through faults, fractures, or poorly sealed wells. Leakage of stored CO_2 could compromise the integrity of overlying rock layers and contaminate groundwater.

Table III. Merits and Demerits of Post-Combustion Carbon Capture Process [15] [21]

2.3 Pre-Combustion. - The growing concern over climate change and the need to mitigate greenhouse gas emissions have driven considerable research into carbon capture technologies. Among these, pre-combustion carbon capture processes have emerged as a promising avenue for reducing carbon dioxide (CO_2) emissions from industrial sources. As the name suggests, pre-combustion carbon capture involves capturing CO_2 before the combustion of fossil fuels, typically in gasification processes. The gasification of carbonaceous feedstocks, such as coal or natural gas, produces syngas, which is then subjected to carbon capture before combustion.

The process begins with gasification of carbon-rich feedstocks. It is a thermochemical process that converts solid or liquid carbon-containing materials into a gaseous mixture, primarily composed of hydrogen (H_2) and carbon monoxide (CO). This is achieved by reacting the feedstock with a controlled amount of oxygen or steam at elevated temperatures

[22]. The output of the gasification process is syngas, which is a mixture of hydrogen, carbon monoxide, and trace amounts of other gases such as methane. The composition of syngas depends on the type of feedstock and the specific gasification conditions. Before the syngas is combusted, it undergoes a separation process to capture the carbon dioxide. Several methods can be employed for carbon dioxide capture, including absorption, adsorption, and membrane separation, which are discussed in the next section.

In many scenarios, the process is integrated with hydrogen production. The separated CO_2 is often a by-product of hydrogen production through water gas shift reactions or other hydrogen-producing processes. Figure illustrates a pre-combustion carbon capture technology (CCT) system based on pressure-swing separation and stripping. Although pre-combustion CCT can achieve substantial CO_2 emission reduction, its integration generally increases plant complexity, capital cost, and energy requirements, which may affect overall system performance. The two most widely used absorbent types in carbon capture are chemical and physical. Chemical absorbents react with CO_2 to form stable compounds like carbonates, bicarbonates, or hydroxide solutions, but their regeneration requires significant energy, raising the plant's capital expenses. Physical solvents, on the other hand, are more effective at high pressures and low temperatures. Commercially, various physical solvents, such as polypropylene carbonate, methanol (Rectisol), dimethyl ether polyethylene glycol (DMEPEG or Selexol), and N-methyl-2-pyrrolidone (Purisol), have been successfully employed for CCT [16].

Selexol technology physically absorbs CO_2 from syngas using a liquid mixture of dimethyl ethers and polyethylene glycol. The process, which may be configured for variable levels of H_2S / CO_2 selectivity and sulfur removal depth, consists of two absorber units, where Selexol, preloaded with CO_2, removes H_2S first. The rich H_2S solution undergoes regeneration through pressure reduction, and the separated CO_2 is further removed in a second absorber, resulting in a purified gas with minimal uncaptured CO_2 and a rich CO_2 stream for transportation and storage [23].

The Rectisol process uses refrigerated methanol as a solvent to purify syngas produced by heavy oil and coal gasification. The technique, which operates at low temperatures (-40 °C to -60 °C), effectively removes H_2S to ppm levels despite its complexity. A typical Rectisol arrangement incorporates preloading with CO_2 in the first absorption column for H_2S removal, followed by regeneration by flashing and stripping, which can be customized to meet specific process requirements. The rich H_2S solution undergoes partial oxidation to recover elemental sulfur, and the desulfurized gas returns to the CO_2 absorption column, where CO_2 is extracted. The concentrated CO_2 solution is then regenerated in a flash regeneration unit [24].

Purisol process employs N-Methyl-2-pyrrolidone as a solvent to physically absorb H_2S and CO_2 from gas streams. Its flow scheme is similar to that of the Selexol process. This process can be carried out at ambient temperatures or cooled to around -15°C [24].

Physical absorbents use pressure swings and mild heating to remove absorbed gases, resulting in lower energy usage compared to chemical absorbents, which require more energy for bond breakdown. When selecting a physical absorbent, it is important to consider its CO_2 solubility, absorption affinity, density, viscosity, vapor pressure, and other properties.

The cost of a carbon capture (CC)-integrated power plant is influenced by various factors such as location, utilities, and the separation process. Additional costs encompass thermal recovery of absorbents, pumping, and heating or cooling of both liquid and gas streams. The Selexol method is more energy-efficient for CO_2 absorption than the Rectisol and MDEA technologies. In a pre-combustion CCT power plant utilizing Selexol solvent, carbon emissions were reduced by 90.9%, alongside a 5–7% decrease in the lower heating value (LHV), indicating improved thermal efficiency [24]. Table contrasts the merits and demerits of pre-combustion carbon capture technology.

Merits	Demerits
Elevated CO_2 concentrations enhance absorption efficiency.	Significant energy demand for regenerating sorbents.
Well-established process.	Substantial capital and operational expenses for existing sorption systems.

Effectively utilized in various chemical processes, including syngas production.	Temperature challenges related to heat transfer and efficiency concerns are tied to H_2-rich gas turbine fuel.
Possible to retrofit to existing plants.	Complexity and technical challenges.

Table IV. Merits and Demerits of Pre-Combustion Carbon Capture Process [15] [16]

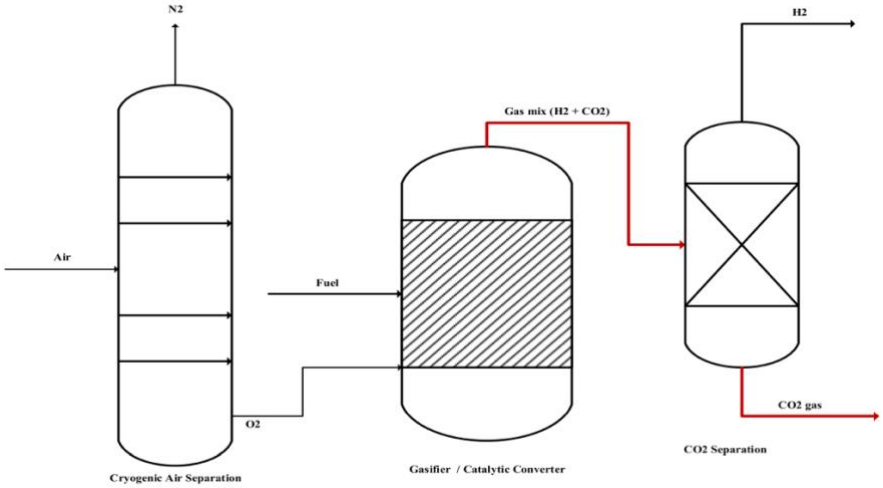

Figure IV. Pre-combustion Carbon Capture Process [22]

Atsonios et al. [24] reported that the recent advancements have focused on integrating pre-combustion carbon capture technologies with Natural Gas Combined Cycle (NGCC) and Integrated Gasification Combined Cycle (IGCC) power plants, showcasing the maturity of these techniques in the chemical industry.

Atsonios [25] proposed detailed optimization of plant design parameters such as column height and packed dimensions to enhance the efficiency of pre-combustion capture processes using various solvents like alkanolamine, polyethylene glycol dimethyl ethers, chilled methanol, and N-Methyl-2-pyrolidone.

Research has explored the use of innovative solvents such as dimethyl ethers of polyethylene glycol for pre-combustion CO_2 capture, showcasing enhanced energy efficiency and reduced specific emissions [26].

Olabi [16] reports that pre-combustion carbon capture technology (CCT) proves effective in mitigating pollution but entails high costs, utilizing both chemical and physical absorbents for carbon capture. Its implementation not only aids in reducing global greenhouse gas emissions but also aligns with UN Sustainable Development Goals, particularly SDG-13 and SDG-7, and brings benefits like cleaner air.

Carbo et al. [27] studied the impact of pre-combustion CO_2 capture on gas turbine operation and reported that gas turbines designed for syngas demonstrate greater efficiencies than modified versions. Gas turbines play a vital role in converting synthesis gas derived from coal gasification into electricity, with redesigned turbines for syngas exhibiting higher efficiencies than those optimized for natural gas, although the lack of nitrogen utilization from air separation units (ASUs) for syngas dilution can result in increased NOx emissions.

Babu et al. [28] investigated the hydrate-based gas separation. In the hydrate-based gas separation process utilizing silica sand and silica gel, silica sand proves more effective for CO_2 separation and exhibits higher water conversion rates compared to silica gel. The significant impact of driving force on gas uptake in the silica sand bed is observed, while employing a combination of depressurization and thermal stimulation results in the complete dissociation of hydrates, showcasing the promising potential for efficient gas separation.

2.4 Chemical Looping. - Chemical looping is a technology used in carbon capture technologies that aims to extract CO_2 from combustion-byproduct flue gas without requiring energy-consuming separation procedures. A chemical looping process breaks down a reaction into two or more smaller reactions. In this process, a cycle of reaction and regeneration is experienced by the chemical intermediates. These chemical intermediates are usually oxides of metals.

A simple example of a redox chemical looping system is shown in Figure V. In order to create desired products, feedstock (fuel) must be fully or partially oxidized using oxygen carriers such as metal oxides. In the event of complete oxidation, the products are H_2O and CO_2 with heat or electricity. When fossil fuels partially oxidize, the most frequent byproduct is syngas, which is a mixture of CO and H_2. It is possible to further convert syngas into finished goods like chemicals, fuels, and hydrogen. When exposed to steam or air, the used oxygen carriers regenerate.

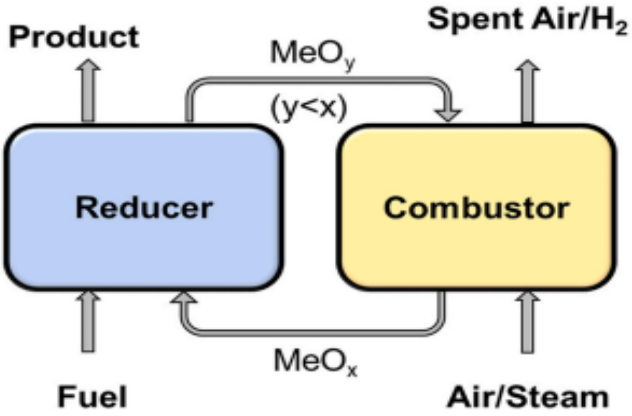

Figure V. Schematic of Redox Reaction [29]

(A) Calcium Looping. - Calcium looping is among the more mature looping-based CO_2 capture approaches. According to Wang [30], for CO_2 capture from industrial gas, carbonation-calcination cycles are used as illustrated in Figure . The process consists of two steps:

1. **Carbon Capture:** Sorbent particles use metal oxide to absorb CO_2 in the carbonator. While other gases pass through unreacted, the metal oxide (MeO) sorbent combines with CO_2 from the flue gas stream to generate metal carbonate (MeCO3). For calcium looping, the reaction is given as,

$$CaO + CO_2 \rightarrow CaCO_3$$

2. **Carbon Release:** Metal Oxide (**MeO**) at high temperature releases a pure stream of CO_2. The carbon regeneration reaction is given as,

$$CaCO_3 \xrightarrow{heat} CaO + CO_2$$

The most common sorbent used is calcium oxide. This is why the process is referred to as calcium **looping**.

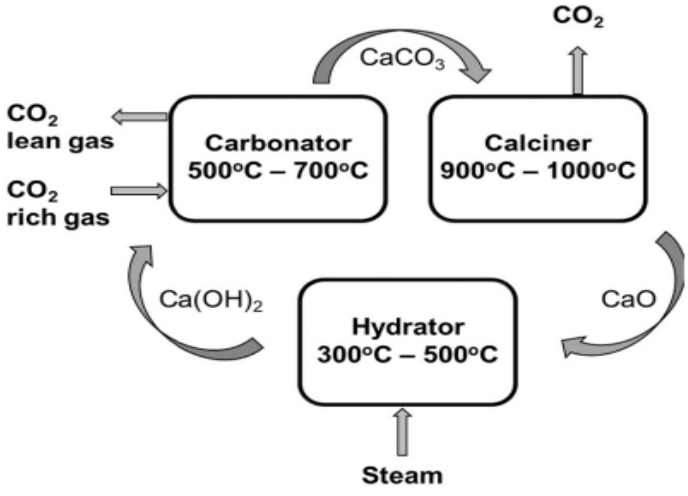

Figure VI. Calcium Looping Cycle [30]

(B) In-situ Methanation. - In-situ Methanation is a process used for converting the captured CO_2 directly into methane using hydrogen as a reducing agent. The chemical reaction is carried out at temperature of 200 – 400 °C in the presence of catalyst (usually Ni, Co, or Fe). The chemical reaction is given as:

$$CO_2 + 4H_2 \xrightarrow[200-400°C]{catalyst} CH_4 + 2H_2O$$

Jin [30] has provided new insights into chemical looping CO_2 capture and in-situ conversion (CL-ICCC) technologies by the use of solid waste as a greener chemical looping alternative. The study discusses the establishment of low-carbon and self-digestion industrial systems.

Zhang [12] integrated CO_2 capture via calcium-looping with in-situ dry reforming of methane through $CaCO_3$, allowing the simultaneous decomposition of $CaCO_3$ to CaO and syngas. Furthermore, the study uses Fischer-Tropsch synthesis for the production of valuable fuels from syngas.

Chirone [31] has found a reactor configuration for catalytic methanation using chemical looping and sorption enhanced methanation, resulting in high methane yield with good temperature control and low operating pressure.

Kim [32] has carried out a thermodynamic analysis to determine viable metal oxides that can serve as oxygen carriers in the chemical looping process.

Chen [33] provides a conceptual design and analysis on the use of Integrated Carbon Capture and Methane (ICCM) to produce methane from flue gas using chemical-looping. Figure provides a simplified illustration of the ICCM process using H_2 from renewable sources.

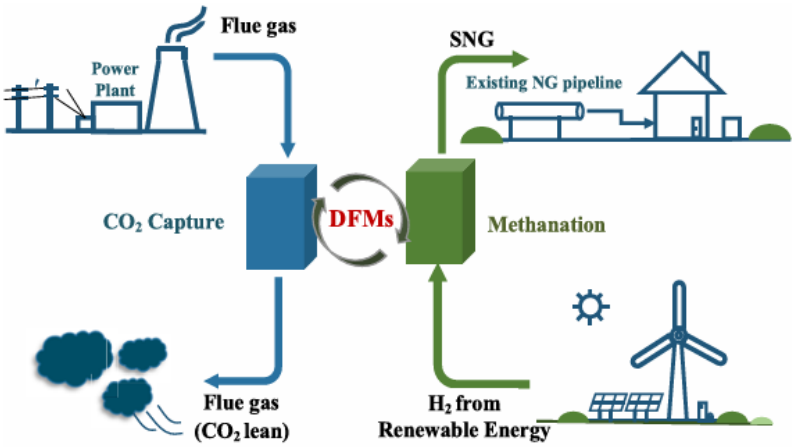

Figure VII. ICCM Process Explained [34]

3. Carbon Separation Technologies. - Carbon separation technologies are used to selectively separate CO_2 from gas mixtures generated in industrial processes and power plants. Some of the technologies are given in Figure .

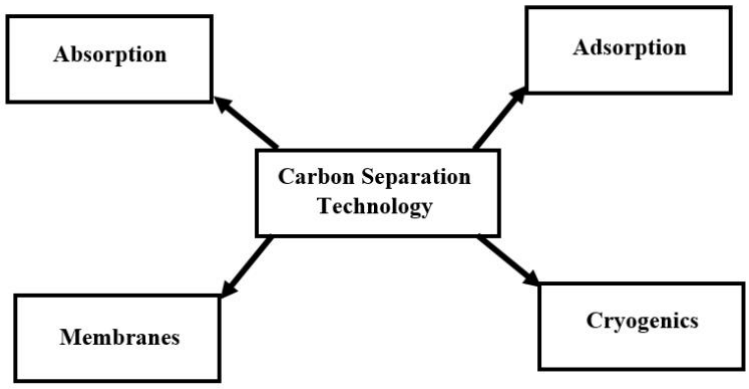

Figure VIII. Carbon Separation Technologies

3.1 Absorption. - The petroleum and chemical industries frequently use absorption, a commercially accessible method of removing carbon dioxide from flue gas. It uses a liquid absorbent that is regenerable by adjustments to pressure and temperature [17]. The technology has two major categories: chemical absorption and physical absorption. Chemical absorption involves chemical reactions, typically acid-base reactions, between CO_2 and the solvent. In contrast, physical absorption is governed by CO_2 solubility in the solvent and depends mainly on temperature and pressure.

MEA is one of the most widely used benchmark solvents for CO_2 absorption due to its high CO_2 recovery (85%-90% vol.), high capacity (4.09 mol CO_2/kg), and CO_2 purity exceeding 99% vol [18]. However, MEA requires a high amount of energy during the regeneration of the solvent. The advantages and disadvantages of the physical absorption processes are compared in Table .

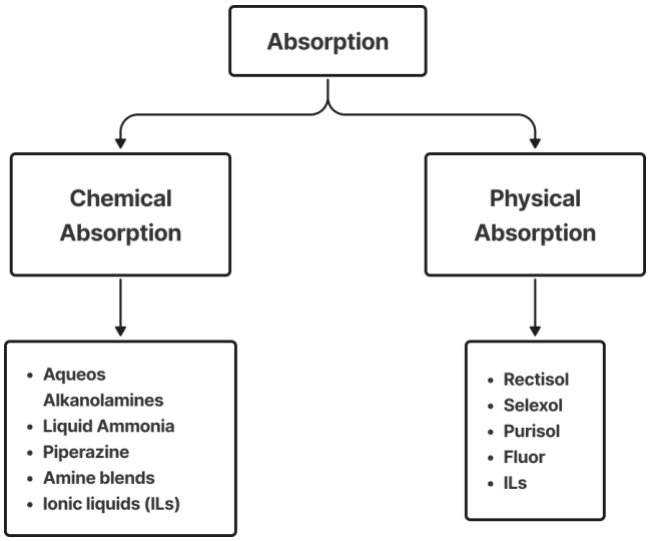

Figure IX. Types of Absorption with some commonly used and emerging materials [15]

Recent developments in absorption techniques have focused on enhancing efficiency and reducing environmental impact. One notable advancement involves the use of novel absorbent materials, such as advanced amines, ionic liquids, phase-change solvents, and membrane contactors, which exhibit higher selectivity and capacity for capturing target gases like carbon dioxide (CO_2) or volatile organic compounds (VOCs).

Additionally, there is increasing interest in process intensification techniques, such as reactive absorption or membrane contactors, which offer improved mass transfer rates and lower energy requirements, thereby making absorption processes more economically viable and sustainable. These developments signify a shift towards greener and more efficient absorption technologies that play a crucial role in various industries, including gas processing, chemical manufacturing, and environmental protection. W. Y. Hong [15] reported that recent studies have highlighted advancements in selecting solvents for CO_2 absorption, with a focus on novel solvents like dimethyl ethers of polyethylene glycol and ionic liquids.

B. Sreenivasulu et al. [34] reported that research has shown improvements in absorption efficiency by using modified activated carbons with MEA-MDEA, enhancing CO_2 adsorption capabilities under pressure swing adsorption conditions.

Advancements in absorption techniques have been integrated with advanced power plant concepts like IGCC, showcasing the potential for efficiency gains and reduced CO_2 emissions through innovative process configurations [35].

Physical Absorption Process	Advantages	Disadvantages
Selexol process	• High selectivity for H_2S • Water wash is not required for solvent recovery. • Chemically and thermally stable. • Flexible, meaning it can be used for both targeted and combination H_2S and CO_2 removal [36]. • Solvent loss is low. • Able to remove moisture, owing to the solvent's hydrophilic nature.	• High viscosity with decreased mass transfer rate and tray efficiency at the low end of the operating temperature range, or 0–175 °C [37]. • Only appropriate for removing CO_2 when CO_2 concentration is higher than H_2S [38].
Rectisol process	• Good CO_2 and H_2S removal efficiency. • Viscosity of the solvent is reasonable. • Low loss of solvent [36]. • Low corrosivity.	• Low-temperature operation (i.e. -30 to -80 °C) [39]. • The potential for amalgam to form at low temperatures as a result of mercury absorption [38].
Purisol process	• High H_2S selectivity. • Flexible, meaning it can be used for both targeted and combination H_2S and CO_2 removal [37].	• Water cleaning is necessary to prevent excessive solvent loss due to the volatile solvent [37].
Fluor process	• Non-corrosive with low-viscosity solvent. • Allows for selective removal of H_2S. • Exhibit high carbon dioxide solubility. • Does not require additional makeup water [38].	• It is not cost-effective to get high product purity. • Need for a gas-liquid contactor with increased efficiency [40]. • Expensive solvent.
Morphysorb process	• Minimal startup and ongoing expenses. • Reduced energy consumption [41]. • Reduced need for recirculation. • Decreased hydrocarbon co-absorption [42].	• A relatively new process that is still in the early phases of pilot testing and laboratory trials. [42].

Table V. Comparison of Merits and Demerits of Physical Absorption Processes

Merits	Demerits
Higher absorption performance is usually greater than 90%.	Energy-intensive and costly solvent recovery.
Heat and/or depressurization can be used to recover sorbents.	Sorbent breakdown caused by repeated heating and cooling cycles.
The most widely established carbon capture method.	Absorption capacity may decrease under unfavorable temperature and pressure conditions.
Suitable for high CO_2 concentrations.	
Low-cost solvent.	

Table VI. Merits and demerits of the absorption technique of CCS [15] [16]

3.2 Adsorption. - Adsorption is a surface-based separation process in which gas molecules adhere to the surface of a solid adsorbent through physical or chemical interactions. The success of CO_2 capture depends on the selection of the adsorbent material. Adsorbents with a high specific affinity for CO_2 and surface area are generally favored. Activated carbon, zeolites, metal-organic frameworks (MOFs), and materials functionalized with amines are examples of commonly used adsorbents. The method of CO_2 collection entails contacting the adsorbent material with flue gas or other streams containing CO_2. This can be carried out in a variety of reactor types, including packed-bed, fluidized-bed, and fixed-bed reactors. Physical or chemical interactions cause the CO_2 molecules to stick to the adsorbent's surface.

3.2.1 Adsorption techniques based on the separation method: TSA (Temperature Swing Adsorption) and VSA (Vacuum Swing Adsorption) are both techniques used in gas separation processes, particularly in the purification of gases. These processes utilize the principles of adsorption to separate different components from a gas mixture.

(A) Temperature Swing Adsorption (TSA): In TSA, the adsorption and desorption of gases occur at different temperatures. Typically, this process involves adsorbing a target gas at a relatively low temperature and then desorbing it at a higher temperature. The adsorbent material selectively adsorbs the target gas at lower temperatures. Then, by increasing the temperature, the adsorbent releases the adsorbed gas, thus regenerating itself. TSA is commonly used for the purification of gases, such as hydrogen, nitrogen, or carbon dioxide, from mixed gas streams in various industries, including petrochemical, chemical, and environmental.

(B) Vacuum Swing Adsorption (VSA): In VSA, adsorption generally occurs at near-atmospheric or moderate pressure, while desorption is promoted by reducing the pressure below atmospheric conditions. VSA is often used for gas separation processes where the target gas can be separated from the feed gas stream by exploiting differences in adsorption capacities under different pressure conditions. This technique is commonly used in applications such as oxygen generation, hydrogen purification, and natural gas processing. Table contrasts the merits and demerits of adsorption-based carbon separation.

Merits	Demerits
Adsorption techniques can selectively separate target components from gas mixtures based on their affinity for the adsorbent material.	Regeneration of the adsorbent material can require additional energy inputs or complex process conditions, which may increase operational costs.
Adsorption processes often require lower energy inputs.	Adsorbent materials can degrade or lose their adsorption capacity due to factors such as fouling.
Adsorption techniques can be applied to a wide range of gas mixtures and can effectively remove impurities.	Adsorption processes can be relatively complex to design, operate, and optimize.
Adsorption processes can be operated continuously, allowing for steady-state operation and continuous production of purified gases.	The initial capital investment for adsorption equipment and systems can be higher.
Adsorption systems can be designed in a modular fashion, allowing for scalability and flexibility.	Adsorption systems may require significant space for installation, especially when considering factors such as adsorbent beds and regeneration equipment.

Table VII. Merits and Demerits of Adsorption [36] [43]

3.2.2 Adsorption using Fixed-Bed Reactor: Figure illustrates the process of adsorption using a fixed-bed reactor. The Ca-looping process, typically carried out in a dual fluidized bed reactor, is regarded as the cornerstone of cutting-edge CO_2 reduction technology. Research on the use of fine activated carbon in sound-assisted fluidization to capture CO_2 from flue gases has shown improved adsorption. Studies on the impact of water on carbon dioxide adsorption with activated carbon in fixed beds have shown that the presence of water decreases the efficiency of the process. In comparison to fluidized beds, the use of fixed beds for CO_2 capture from flue gases has been less extensively researched.

A gas mixture comprising carbon dioxide (CO_2) and nitrogen (N_2) is introduced into the column from gas cylinders. To precisely measure the flow rates of each gas, mass flow controllers (F1 and F2) are installed, with dedicated flow control valves (V1 and V2) regulating the flow rates accordingly. Additionally, a separate mass flow meter (F3) is

utilized to monitor the overall flow entering the infrared (IR) detector. Before commencing experimental runs, the mass flow meters undergo calibration to minimize measurement uncertainties. The pressure within the column is monitored by a pressure gauge (P1), while the concentration of CO_2 at the column outlet is determined using a calibrated IR sensor.

In the experiment, the gas mixture of CO_2 and N_2 undergoes separation, primarily through the adsorption of CO_2 onto the surface of adsorbents. The CO_2-N_2 mixture enters the fixed bed in an ideal plug flow manner, with only CO_2 being adsorbed by the sorbents and subsequently removed from the gas phase. Temperature control is facilitated by a PID temperature controller, which regulates the water temperature. Additionally, a column bypass is incorporated into the system for calibration purposes.

As part of the experimental protocol, a controlled flow of nitrogen (4 L/min) is initially passed through the bed containing sorbents for a duration of 2 hours (7200 seconds). This process ensures the removal of any residual traces of oxygen and CO_2 from the bed. The same experimental approach is replicated to obtain the data under different operating conditions.

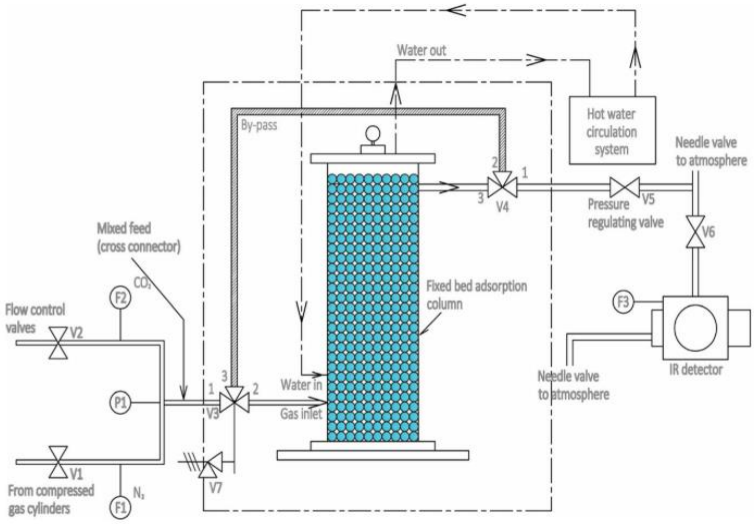

Figure X. Fixed Bed Reactor [44]

3.2.3 Adsorption using Metal Organic Frameworks (MOFs): In the past decade, MOFs (Metal-Organic Frameworks) and MOF-functionalized materials have emerged as novel classes of materials renowned for their exceptional properties, including ultrahigh porosity, large surface area, tunable structures, and thermal stability [45]. Metal-Organic Frameworks (MOFs) are crystalline porous materials made up of metal ions connected to organic ligands via coordinate covalent bonds, often referred to as coordination polymers or metal-organic polymers [46]. They find applications across various fields, such as catalysis [47] [46] [48], adsorption [49] [50], and sensing [51] [52] [53] [54]. Despite their advantages, MOFs face challenges in adsorption, including low capacity at low pressures, sensitivity to moisture and gas mixtures, and high synthetic costs, limiting their widespread use [55].

Researchers have turned to impregnated MOF-based adsorbents for post-combustion carbon capture due to their excellent physisorption and chemisorption characteristics [56]. They [56] investigated the adsorption efficiency of amine-functionalized MOF-177 variants, such as PEI, TEPA, and DETA. They found TEPA-impregnated MOF-177 to exhibit a significant enhancement (4.8 times) in CO_2 capturing compared to unmodified MOF-177 at 298 K. Similarly, Quan et al. [57] developed diamine-appended MOF/polymer composite hollow fiber sorbents, demonstrating higher CO_2 capture (2.5 mmol CO_2 /g-MOF) at relatively low pressures. Additionally, Wu et al. [58] studied a copper-based MOF with distinct pore structures, achieving a CO_2 uptake of 4.63 mmol/g at 100 kPa and 2.92 mmol/g at 15 kPa, outperforming other MOFs due to the presence of strong electrostatic interaction sites.

Addressing limitations of MOFs, Qazvini et al. [59] synthesized MUF-16, a hydrogen-bonded water-stable microporous material coated with PVDF, aiming for large-scale industrial applications with affordable production costs and long-term chemical stability. MUF-16 exhibited promising CO_2 uptake of 47.8 and 61.1 cm3/g of CO_2 at 1 and 20 bar, respectively.

A detailed comparison of these adsorbents, including surface area (m2/g), pore size (nm), regeneration cycles, and adsorption capacity (Qmax), is provided in Table.

3.2.4 Scale of Experimental Validation: Carbon capture technologies are evaluated across multiple levels of experimental maturity, including bench-scale, pilot-scale, and commercial systems. Bench-scale studies are generally performed under controlled laboratory conditions to evaluate material performance, whereas pilot-scale systems operate under more realistic scenarios and provide information regarding system integration, operational challenges, and scalability [60].

3.2.5 Bench-scale experimental studies and boundary conditions: Bench-scale investigations are mainly conducted to validate adsorption performance under controlled environments. These studies are characterized by laboratory-scale setups, well-defined operating conditions, and a strong focus on material-level behavior such as adsorption capacity, selectivity, and stability [60].

Some features of bench-scale studies include:

- Controlled laboratory conditions
- Emphasis on adsorbent performance
- Simplified system boundaries

For example, a representative bench-scale study conducted under conditions simulating a coal-fired power plant employed a flue gas stream with approximately 15% CO_2 by volume and an adsorption temperature range of 50–90 °C. Under these conditions, the presence of impurities such as SO_2 (100 ppm) was found to significantly affect performance, resulting in an approximate 30% reduction in adsorption capacity after 100 adsorption–regeneration cycles. These findings highlight the sensitivity of adsorbent materials to flue gas contaminants, which is often not fully captured under ideal laboratory conditions [60].

3.2.6 Pilot-scale experimental studies: Pilot-scale systems represent an intermediate step between laboratory research and full-scale industrial deployment. These systems are designed to replicate real plant conditions more closely and are essential for evaluating process feasibility, energy requirements, and economic performance.

Key characteristics of pilot-scale studies include:

- Operation under realistic flue gas conditions
- Inclusion of impurities and temperature fluctuations
- Improved estimation of cost and energy performance

A typical pilot-scale study may simulate a coal-fired supercritical power plant (e.g., ~10 MW equivalent capacity) using sorbents such as 35 wt% K_2CO_3. Such systems are significantly larger in scale, with dimensions on the order of tens of meters (e.g., 34 m × 15 m × 59 m), and operate at adsorption temperatures around 80 °C with regeneration temperatures reaching approximately 200 °C.

Compared to bench-scale studies, pilot-scale investigations provide more reliable insights into process integration and operational challenges, although they still involve certain assumptions and simplifications relative to full commercial systems [61].

3.2.7 Future challenges: Despite promising results at laboratory and pilot scales, several challenges remain in scaling adsorption-based carbon capture technologies to commercial deployment. One major limitation is the high cost associated with large-scale production of advanced adsorbent materials.

In addition, process-related challenges such as heat management and temperature control are significant, particularly due to the endothermic nature of adsorption–desorption cycles. Maintaining adsorption capacity over repeated cycles while ensuring efficient thermal management remains a key technical hurdle.

Operational issues such as pressure drop and material handling also pose challenges, especially when dealing with fine adsorbent powders in large-scale systems. These factors collectively highlight the complexity of transitioning from laboratory-scale validation to industrial implementation.

Parameter	Bench-Scale studies	Pilot-Scale studies
Typical objective	Evaluation of performance and screening of material.	Process validation under realistic scenarios.
Efficiency of Capture	Often high under controlled conditions.	Affected by real flue gas conditions; therefore, it varies from moderate to high.
Energy Penalty	Not fully evaluated.	Varies significantly depending upon the process design.
TRL	Low (3-5).	Medium (5-7).
Key limitation	Lack of scalability.	High cost and complex scalability.

Table VIII. Comparison of Bench-Scale and Pilot-Scale Adsorption-Based PCC Systems [61]

Types of Adsor-bent	Adsorbent	Surface Area (m^2/g)	Pore Size (nm)	Operation Parameters	Adsorption Capacity	Author
Chemical adsorbent	70T-MM-550 monolithic adsorbent impregnated with TEPA	10.46	0.02	Pressure (bar): 1, Temp. (°C): 75	151.1 mg g^{-1}	T. Chitsiga et al. [62]
	PAA-100% MA	2.94	30.9	Pressure (bar): 1.1, Temp. (°C): 40	44.2 g kg^{-1}	A. Ra Cho et al. [63]
	2.0PO-PEHA/MPS	472	-	Pressure (bar): 1, Temp. (°C): 50	1.8 mmol g^{-1}	S. Ahmed et al. [64]
	50 wt.% TEPA-functionalized Si-MCM-41	11	1.8	Pressure (bar): 1, Temp. (°C): 75	70.41 mg g^{-1}	E. Atta-Obeng et al. [65]
	Si-MCM-41	993	3.1	Pressure (bar): 1, Temp. (°C): 75	54.65 mg g^{-1}	M. A. O. Lourenço et al. [66]
	L350	2.8	-	Pressure (bar): 0.9, Temp. (°C): 30	1.54 mmol g^{-1}	R. R. Kondakindi et al. [67]
Physical adsorbent	Li-LSX zeolite	662	0.08-0.18	Pressure (bar): 1, Temp. (°C): 25	4.43 mmol g^{-1}	D. Panda et al. [68]

	HZAA-1–3 with urea	126	0.4-5.5	Pressure (bar): 0.2, Temp. (°C): 25	2.86 mmol g^{-1}	K. J. Hwang et al. [69]
	Basalt-based zeolite 4A	726	-	Pressure (bar): 1, Temp. (°C): 50	5.9 mmol g^{-1}	W. Liang et al. [70]
	20% EDHy Zeolite	-	-	Pressure (bar): 1, Temp. (°C): 25	1.76 mmol g^{-1}	D. Panda et al. [71]
	IBA-Z4A	32	3.8	Pressure (bar): 1.2, Temp. (°C): 40	2.56 mmol g^{-1}	S. Y. Lee & S. J. Park [72]
	3D-printed monolith activated carbons	-	-	Pressure (bar): 1, Temp. (°C): 30	3.17 mol kg^{-1}	L. Jiang et al. [73]
	chitosan/MWCNTs	-	-	Pressure (bar): 1, Temp. (°C): 90	3 mg g^{-1}	Krishnamurthy et al. [74]
	3D-printed PEI/(MWCNT)	27	30	Pressure (bar): 1, Temp. (°C): 25	0.064 mol kg^{-1}	Jayakaran et al. [75]
Hybrid adsorbents	20% TEPA-impregnated MOF-177	585	-	Pressure (bar): 1, Temp. (°C): 25	4.6 mmol g^{-1}	W. Quan et al. [58]
	2-ampd-Mg2(dobpdc)	-	-	Pressure (bar): 1, Temp. (°C): 25	2.5 mmol g^{-1}	H. Wu et al. [59]
	Copper-based MOF-11	-	-	Not reported	4.63 mmol g^{-1}	Qazvini & S. G. Telfer [60]

Table IX. Adsorbents for carbon dioxide capture [61]

3.3 Membrane. - Membranes are materials that selectively separate CO_2 from gas mixtures, such as the flue gases from combustion. Membrane separation is based on the difference in permeability of the gases. Membrane separation is driven by partial-pressure differences, and performance is governed by the trade-off between CO_2 permeability and CO_2 selectivity. Some of the common types of membranes include:

3.3.1 Polymeric Membranes. - These membranes are composed of polymers and selectively separate gases based on size, shape, and chemical affinity. Jana [76] has compared the performance of different polymer-based membranes for the separation of a CO_2 and N_2 mixture. These polymers include materials such as PE (Poly Ethylene) and PVC (Poly Vinyl Chloride), with nanofillers. Additionally, membrane performance can be enhanced by the use of grafting. Lai

[77] has shown that by adding ZIF-8 filler to poly (ionic-liquid) membranes, membrane permeance can be enhanced for improved CO_2 and N_2 separation.

3.3.2 Mixed Matrix Membranes. - Combining a polymeric matrix with inorganic fillers or nanoparticles, these membranes enhance selectivity and permeability in gas separation.

3.3.3 Zeolite Membranes. - Utilizing crystalline aluminosilicate structures, zeolite membranes employ molecular sieving properties for effective gas separation. Shi [78] has performed molecular dynamics simulation on MER Zeolite to determine its adsorption behavior in CO_2, CH_4, and N_2. Results show that CO_2 has the least diffusion activation energy (4.38 kJ/mol). This makes MER Zeolite suitable for separation of gas mixtures like CO_2/CH_4 and CO_2/N_2.

3.3.4 Ceramic Membranes. - Made from ceramic materials, these membranes are known for durability and stability at high temperatures, making them suitable for harsh industrial environments.

3.3.5 Metal-Organic Framework (MOF) Membranes. - These porous materials with high surface areas and tunable structures show promise in gas separation due to unique adsorption properties. In Majumdar [79], Mg-MOF-74 crystals were synthesized to create polymer/Mg-MOF-74 mixed matrix membranes (MMM) for CO_2/CH_4 separation.

3.4 Cryogenic Separation. - Cryogenic CO_2 capture builds on the idea of cryogenic distillation, a well-known method for separating different molecules in a mixture based on their boiling points by cooling them. Originally used in industries like oil and gas for liquefied natural gas (LNG) and hydrogen production, this technique has been adapted to remove CO_2 from flue gases. The process involves drying and compressing the gas, then cooling it to separate CO_2 from other components through partial condensation and distillation. Depending on temperature and pressure, CO_2 may be separated either by condensation as a liquid or by desublimation as a solid. Sometimes, an upfront process called PSA is needed to concentrate the CO_2 further [80].

In this approach, various compression techniques are used at normal pressure and temperature to separate gases. This method works well for producing liquid CO_2 and is effective for capturing high concentrations of carbon dioxide. It offers advantages over amine-based scrubbing, such as being more environmentally friendly, resistant to corrosion, using cheaper chemicals, and requiring less water. It supports the production of liquid CO_2 and operates at normal pressure, which helps with the financial aspects of transmitting CO_2. However, there are limitations to cryogenic separation. It has a narrow operating temperature range, leading to high energy consumption and operating expenses. Ice formation in the process can clog pipes, reducing pressure and posing safety risks. Therefore, it is crucial to remove moisture from flue gases before starting the separation process. Implementing a cryogenic CO_2 removal system in a power plant can increase its operating costs by up to 50% [81].

Cryogenics technology is most commonly associated with post-combustion carbon capture, where it can effectively capture carbon dioxide from flue gases emitted by power plants and industrial facilities after the combustion process. However, it can also be utilized in pre-combustion carbon capture processes, particularly in combination with technologies like gasification. Direct air capture (DAC) typically involves different capture methods, not usually cryogenic, as it aims at capturing CO_2 directly from the atmosphere. Direct atmospheric cryogenic carbon capture in cold climates is a novel approach for reducing atmospheric CO_2 emissions. Leveraging the naturally cold temperatures of these regions, this method involves capturing CO_2 directly from the air using cryogenic technology. By utilizing the cold ambient air, the process can potentially be more energy-efficient compared to traditional carbon capture methods. This innovative approach holds promise for mitigating climate change through reduction of greenhouse gas emissions in regions with cold climates.

The method utilizes the high phase-transition temperature of CO_2 compared to other atmospheric gases, except water vapor. By employing desiccant wheels or cooling methods like low ambient temperatures or conventional refrigeration, water vapor can be easily eliminated. Figure depicts the relationship between the desublimation temperature and the mass fraction of CO_2 de-sublimated. Cryogenic distillation is highlighted as the most promising technique for its ability to produce pure CO_2 in solid, liquid, or gas forms, making it economically valuable and easily storable. It does not require new material development and can be quickly scaled up for industrial use [82].

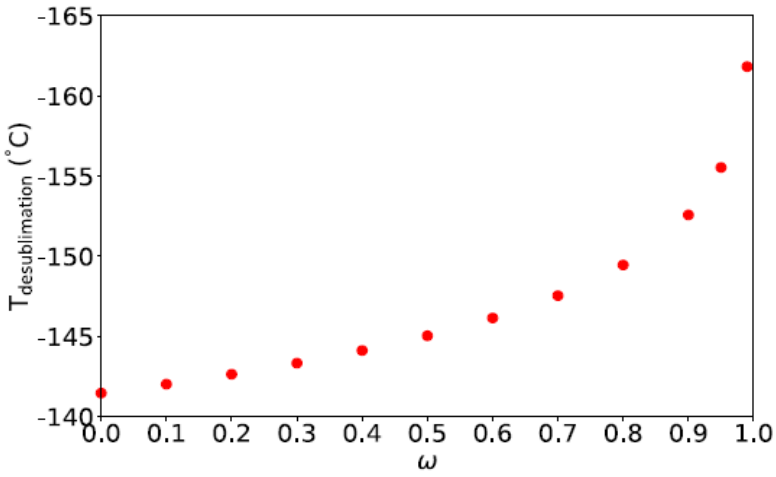

Figure XI. De-sublimation temperature as a function of mass fraction of CO_2 de-sublimated [83]

Cryogenic separation for CO_2 capture is gaining popularity as a technology due to its ability to produce high-purity CO_2 without the need for additional chemicals, reducing pollution in the capture process. This eco-friendly approach holds significant promise and practical value. However, the challenge lies in the demanding cryogenic cooling conditions and capacity required for efficient capture, which have hindered the widespread adoption and advancement of this method [83].

To remove CO_2 from industrial flue gas or the surrounding air, a process known as cryogenic desublimation is employed. This method involves cooling the gas, eliminating water vapor from the mixture, and then freezing the CO_2 into a solid. Studies have shown that significant amounts of CO_2 can be captured using evaporator temperatures ranging from -99 °C to -122 °C. Further research has focused on reducing water content through defrosting and multi-stage condensation. Another proposed method includes cooling, drying, and moderate compression before freezing, achieving a 99% capture rate at -135 °C. Stirling coolers have also been utilized to achieve a 96% capture rate at an energy cost of 1.5 MJ/kg CO_2. Additionally, the minimum energy required for CO_2 separation from air at -20 °C is estimated to be 419 MJ/tonne CO_2 [84].

Inspired by Mars' CO_2 ice cap, a cryogenic direct-air capture (DAC) system proposal suggests locating it in Antarctica, Earth's coldest region, where CO_2 extraction could be economically feasible. This setup would use closed-loop vapor compression refrigeration cycles powered by nearby wind farms to capture atmospheric CO_2 and convert it into solid " CO_2 snow" for storage. Experimental prototypes showed promising reductions in CO_2 concentrations. However, challenges like the remote location, extreme cold, and maintenance issues persist despite advantages like abundant wind energy [84].

In cryogenic direct-air capture (DAC) systems, a thermodynamic model was proposed to analyse a prototype comprising a deposition chamber, cryogenic refrigeration cycle, and precooler heat exchanger. The precooler aims to lower the incoming air temperature, reducing the workload for the cryocooler. Various locations, including Antarctica, were considered for this setup. Subsequent research refined the thermodynamic model, focusing on optimizing CO_2 de-sublimation efficiency through precooling. It was found that achieving higher CO_2 removal rates incurs greater energy penalties due to lower required temperatures. Precoolers with high effectiveness can lead to fouling issues, impacting system performance. Another aspect studied was precompression, which increases the CO_2 partial pressure but incurs energy penalties, particularly in cryogenic DAC systems with low CO_2 partial pressures. Adding turbine recovery to precompression showed limited energy savings under specific conditions. However, these findings are based on idealized scenarios and may differ in practical applications [84].

4. Comparison of Different Carbon Capture and Separation Techniques. - The following section discusses and compares the carbon capture and separation technologies, presenting their efficiency and Technology Readiness Level (TRL), as well as their advantages and disadvantages. Table compares the various carbon capture and separation techniques to provide an overview of their strong and weak points.

CO_2 capture efficiency is a critical metric defining the effectiveness of a carbon capture system in removing CO_2 from a gas stream, such as flue gas from power plants or industrial processes. Expressed as a percentage, it represents the

proportion of CO_2 captured relative to the total CO_2 entering the system. Higher capture efficiency signifies a greater reduction in emissions, highlighting the importance of optimizing capture technologies to mitigate climate change impacts.

Concurrently, the Technology Readiness Level (TRL) framework, originally developed by NASA and now widely used across various industries, provides a systematic approach to evaluating the maturity of CO_2 capture technologies. The TRL scale ranges from 1 to 9, encompassing stages from basic research (TRL 1-3), where new materials and concepts are explored, through lab-scale validation and pilot testing (TRL 4-6), to full-scale demonstration and commercial deployment (TRL 7-9) [84].

4.1 Comparative Assessment. -

	TRL	Study type/Scale	Energy / Cost basis	CO_2 capture efficiency (%)	Advantages	Disadvantages	Reference
Pre-combustion	9	Not specified in the source	Not reported	84–93	- Suitable for large-scale H_2 production. - Low energy penalty (10–15%). - High efficiency. - Lower potential cost. - Applicable to thermal power plants. - Retrofit opportunity for existing plants.	- Still undergoing development. - Requires substantial capital investment. - Novel materials needed for high-temperature CO_2 capture. - Complex process scheme.	[85]
Oxyfuel combustion	7	Not specified in the source	Not reported	92	- Minimal equipment required due to reduced gas volume. - Utilizes mature air separation techniques. - Enhanced absorption efficiency in high CO_2 environments.	- Corrosion issues may arise. - Cryogenic O_2 production is expensive. - Incurs a high energy penalty and efficiency reduction.	[86] [87]
Post-combustion	9	Bench scale	\$75.2/tonne CO_2	55–98	- Retrofitting feasible for existing plants. - Mature technology compared to other methods.	- Efficiency affected by low CO_2 concentrations.	[62] [87]
Absorption	7–9	Not specified in the source	Not reported	80–95	- Effective at various CO_2 pressures. - Minimal hydrocarbon losses. - High selectivity and efficiency. - Standard for coal-fired and natural gas power plants. - Established technology.	- Solvent degradation, corrosion, and emissions. - High energy penalty for solvent regeneration in some cases. - Limited to thermal power plants.	[88] [89] [90]

	TRL	Study type/Scale	Energy / Cost basis	CO_2 capture efficiency (%)	Advantages	Disadvantages	Reference
Membrane technology	5–6	Not specified in the source	Not reported	≤90	- Effective at various CO_2 pressures. - Small footprint. - Chemical-free operation without regeneration. - Suitable for large-scale natural gas processing.	- Unsuitable for low CO_2 concentrations. - Balancing permeability and selectivity. - Hydrocarbon losses. - Requires gas compression.	[91] [92]
Adsorption	3-4	Modeling study	3.23 MJ/kg CO_2	95% purity, ~81% recovery	- High adsorption efficiency (>85%). - Reversible process with recyclable adsorbents.	- High energy requirement for CO_2 desorption. - Specific adsorbents required at high temperatures.	[93]
Chemical looping	6	Not specified in source	Not reported	>90	- Bypasses energy-intensive air separation. - Separates CO_2 from combustion gases.	- Still under development. - Limited large-scale operational experience.	[85]
Direct capture	7	Not specified in source	Not reported	79–91	- Suitable for localized CO_2 capture. - Can be deployed in various locations, including non-arable land. - Significant in climate change mitigation.	- Expensive implementation. - High energy demand. - Technical complexities.	[94] [88]
Cryogenic separation	9	Not specified in source	Not reported	90–99	- Effective at high CO_2 concentrations. - No need for compressors. - Minimal hydrocarbon losses. - High selectivity. - Established technology for natural gas processing.	- Risk of CO_2 freezing. - Energy-intensive refrigeration is required.	[15] [95]

Table X. Carbon Capture Efficiencies & Separation Techniques

Note: Data are compiled from multiple studies with different operating conditions, scales, and system boundaries. Therefore, the reported TRL, capture efficiency, energy, and cost values should be interpreted as indicative rather than directly comparable. Where contextual information was not available in the cited source, it is explicitly marked as "Not specified in source".

5. Conclusion. - The paper provides a comprehensive and insightful overview of the latest advancements in carbon capture and separation technologies, pivotal in the global effort to combat climate change. This review examines the four principal types of carbon capture methods: pre-combustion capture, post-combustion capture, chemical looping, and direct air capture, highlighting their respective efficiencies, technological readiness levels, and the challenges they

face. By evaluating these methods, the literature underscores the critical role each technology plays in reducing CO_2 emissions and the specific hurdles that must be overcome to enhance their viability and efficiency.

The review summarizes current findings and accomplishments, establishing the groundwork for a larger conversation about lowering carbon dioxide emissions. It emphasizes the importance of continued research and innovation in overcoming present technological hurdles and increasing the efficiency and scalability of these solutions. The findings presented in this paper illustrate the potential of existing technology while underlining the importance of future discoveries. These activities are critical to attaining long-term sustainability and tackling the pressing global challenge of climate change.

Acknowledgment. - The authors acknowledge the support provided by the Sindh Higher Education Commission through the project SRSP/NPS SC. & Tech-09/314/2023-24.

References

[1] J. Gallinger, M. Rid-Moneta, C. Becker, A. Reineke, and J. Gross, "Altered volatile emission of pear trees under elevated atmospheric CO2 levels has no relevance to pear psyllid host choice," Environ Sci Pollut Res, vol. 30, no. 15, pp. 43740–43751, Jan. 2023, doi: 10.1007/s11356-023-25260-w.

[2] J. G. Canadell et al., "Contributions to accelerating atmospheric CO2 growth from economic activity, carbon intensity, and efficiency of natural sinks," Proc. Natl. Acad. Sci. U.S.A., vol. 104, no. 47, pp. 18866–18870, Nov. 2007, doi: 10.1073/pnas. 0702737104.

[3] F. Bisotti, K. A. Hoff, A. Mathisen, and J. Hovland, "Direct Air capture (DAC) deployment: A review of the industrial deployment," Chemical Engineering Science, vol. 283, p. 119416, Jan. 2024, doi: 10.1016/j.ces.2023.119416.

[4] D. Coppitters et al., "Energy, Exergy, Economic and Environmental (4E) analysis of integrated direct air capture and CO 2 methanation under uncertainty," Fuel, vol. 344, p. 127969, Jul. 2023, doi: 10.1016/j.fuel.2023.127969.

[5] T. Daniel, A. Masini, C. Milne, N. Nourshagh, C. Iranpour, and J. Xuan, "Techno-economic Analysis of Direct Air Carbon Capture with CO2 Utilisation," Carbon Capture Science & Technology, vol. 2, p. 100025, Mar. 2022, doi: 10.1016/j.ccst.2021.100025.

[6] J. Cui and M. Aziz, "Techno-economic analysis of hydrogen transportation infrastructure using ammonia and methanol," International Journal of Hydrogen Energy, vol. 48, no. 42, pp. 15737–15747, May 2023, doi: 10.1016/j.ijhydene.2023.01.096.

[7] P. Cheng et al., "Modeling and optimization of carbon-negative NGCC plant enabled by modular direct air capture," Applied Energy, vol. 341, p. 121076, Jul. 2023, doi: 10.1016/j.apenergy.2023.121076.

[8] G. M. Cole et al., "Integrated techno-economic and life cycle assessment of a novel algae-based coating for direct air carbon capture and sequestration," Journal of CO2 Utilization, vol. 69, p. 102421, Mar. 2023, doi: 10.1016/j.jcou.2023.102421.

[9] C. Drechsler and D. W. Agar, "Intensified integrated direct air capture - power-to-gas process based on H2O and CO2 from ambient air," Applied Energy, vol. 273, p. 115076, Sep. 2020, doi: 10.1016/j.apenergy.2020.115076.

[10] B. Slavin, R. Wang, D. Roy, J. Ling-Chin, and A. P. Roskilly, "Techno-economic analysis of direct air carbon capture and hydrogen production integrated with a small modular reactor," Applied Energy, vol. 356, p. 122407, Feb. 2024, doi: 10.1016/j.apenergy.2023.122407.

[11] J. Sun, M. Zhao, L. Huang, T. Zhang, and Q. Wang, "Recent progress on direct air capture of carbon dioxide," Current Opinion in Green and Sustainable Chemistry, vol. 40, p. 100752, Apr. 2023, doi: 10.1016/j.cogsc.2023.100752.

[12] C. Zhang, Y. Li, Z. Chu, Y. Fang, K. Han, and Z. He, "Analysis of integrated CO2 capture and utilization via calcium-looping in-situ dry reforming of methane and Fischer-Tropsch for synthetic fuels production," Separation and Purification Technology, vol. 329, p. 125109, Jan. 2024, doi: 10.1016/j.seppur.2023.125109.

[13] W. Y. Hong, "A techno-economic review on carbon capture, utilisation and storage systems for achieving a net-zero CO2 emissions future," Carbon Capture Science & Technology, vol. 3, p. 100044, Jun. 2022, doi: 10.1016/j.ccst.2022.100044.

[14] A. G. Olabi et al., "Assessment of the pre-combustion carbon capture contribution into sustainable development goals SDGs using novel indicators," Renewable and Sustainable Energy Reviews, vol. 153, p. 111710, Jan. 2022, doi: 10.1016/j.rser.2021.111710.

[15] Council, Limiting the Magnitude of Future Climate Change. Washington, D.C.: National Academies Press, 2010, p. 12785. doi: 10.17226/12785.

[16] C. Ma, F. Pietrucci, and W. Andreoni, "Capture and Release of CO2 in Monoethanolamine Aqueous Solutions: New Insights from First-Principles Reaction Dynamics," J. Chem. Theory Comput., vol. 11, no. 7, pp. 3189–3198, Jul. 2015, doi: 10.1021/acs.jctc.5b00379.

[17] H. Li, D. Yan, Z. Zhang, and E. Lichtfouse, "Prediction of CO2 absorption by physical solvents using a chemoinformatics-based machine learning model," Environ Chem Lett, vol. 17, no. 3, pp. 1397–1404, Sep. 2019, doi: 10.1007/s10311-019-00874-0.

[18] T. Wilberforce, A. Baroutaji, B. Soudan, A. H. Al-Alami, and A. G. Olabi, "Outlook of carbon capture technology and challenges," Science of The Total Environment, vol. 657, pp. 56–72, Mar. 2019, doi: 10.1016/j.scitotenv.2018.11.424.

[19] M. Kanniche, R. Gros-Bonnivard, P. Jaud, J. Valle-Marcos, J.-M. Amann, and C. Bouallou, "Pre-combustion, post-combustion and oxy-combustion in thermal power plant for CO2 capture," Applied Thermal Engineering, vol. 30, no. 1, pp. 53–62, Jan. 2010, doi: 10.1016/j.applthermaleng.2009.05.005.
[20] F. Wu, M. D. Argyle, P. A. Dellenback, and M. Fan, "Progress in O2 separation for oxy-fuel combustion–A promising way for cost-effective CO2 capture: A review," Progress in Energy and Combustion Science, vol. 67, pp. 188–205, Jul. 2018, doi: 10.1016/j.pecs.2018.01.004.
[21] T. Wilberforce, A. G. Olabi, E. T. Sayed, K. Elsaid, and M. A. Abdelkareem, "Progress in carbon capture technologies," Science of The Total Environment, vol. 761, p. 143203, Mar. 2021, doi: 10.1016/j.scitotenv.2020.143203.
[22] "Assessment of the pre-combustion carbon capture contribution into sustainable development goals SDGs using novel indicators - ScienceDirect." Accessed: May 09, 2026. [Online]. Available: https://www.sciencedirect.com/science/article/pii/S1364032121009849
[23] A. Padurean, C.-C. Cormos, and P.-S. Agachi, "Pre-combustion carbon dioxide capture by gas–liquid absorption for Integrated Gasification Combined Cycle power plants," International Journal of Greenhouse Gas Control, vol. 7, pp. 1–11, Mar. 2012, doi: 10.1016/j.ijggc.2011.12.007.
[24] H. Ahn, Z. Kapetaki, P. Brandani, and S. Brandani, "Process simulation of a dual-stage Selexol unit for pre-combustion carbon capture at an IGCC power plant," Energy Procedia, vol. 63, pp. 1751–1755, 2014, doi: 10.1016/j.egypro.2014.11.182.
[25] K. Atsonios, K. D. Panopoulos, A. Doukelis, A. Koumanakos, and E. Kakaras, "Cryogenic method for H2 and CH4 recovery from a rich CO2 stream in pre-combustion carbon capture and storage schemes," Energy, vol. 53, pp. 106–113, May 2013, doi: 10.1016/j.energy.2013.02.026.
[26] L. Meng, T. Kai, S. Nakao, and K. Yogo, "Modeling of pre-combustion carbon capture with CO2-selective polymer membranes," International Journal of Greenhouse Gas Control, vol. 123, p. 103830, Feb. 2023, doi: 10.1016/j.ijggc.2022.103830.
[27] M. C. Carbo, D. Jansen, J. W. Dijkstra, J. P. Van Buijtenen, and A. H. M. Verkooijen, "Pre-combustion decarbonisation in IGCC: Gas turbine operating window at variable carbon capture ratios," Energy Procedia, vol. 1, no. 1, pp. 669–673, Feb. 2009, doi: 10.1016/j.egypro.2009.01.088.
[28] P. Babu, R. Kumar, and P. Linga, "Pre-combustion capture of carbon dioxide in a fixed bed reactor using the clathrate hydrate process," Energy, vol. 50, pp. 364–373, Feb. 2013, doi: 10.1016/j.energy.2012.10.046.
[29] D. Wang, A. Joshi, and L.-S. Fan, "Chemical looping technology – a manifestation of a novel fluidization and fluid-particle system for CO2 capture and clean energy conversions," Powder Technology, vol. 409, p. 117814, Sep. 2022, doi: 10.1016/j.powtec.2022.117814.
[30] B. Jin et al., "Chemical looping CO2 capture and in-situ conversion as a promising platform for green and low-carbon industry transition: Review and perspective," Carbon Capture Science & Technology, vol. 10, p. 100169, Mar. 2024, doi: 10.1016/j.ccst.2023.100169.
[31] R. Chirone, A. Paulillo, A. Coppola, and F. Scala, "Carbon capture and utilization via calcium looping, sorption enhanced methanation and green hydrogen: A techno-economic analysis and life cycle assessment study," Fuel, vol. 328, p. 125255, Nov. 2022, doi: 10.1016/j.fuel.2022.125255.
[32] Y. Kim, H. S. Lim, H. S. Kim, M. Lee, J. W. Lee, and D. Kang, "Carbon dioxide splitting and hydrogen production using a chemical looping concept: A review," Journal of CO2 Utilization, vol. 63, p. 102139, Sep. 2022, doi: 10.1016/j.jcou.2022.102139.
[33] L. Chen, Y. Chen, G. Wei, and K. Liu, "Conceptual design and assessment of Integrated capture and methanation of CO2 from flue gas using chemical-looping scheme of dual function materials," Energy Conversion and Management, vol. 299, p. 117847, Jan. 2024, doi: 10.1016/j.enconman.2023.117847.
[34] B. Sreenivasulu, D. V. Gayatri, I. Sreedhar, and K. V. Raghavan, "A journey into the process and engineering aspects of carbon capture technologies," Renewable and Sustainable Energy Reviews, vol. 41, pp. 1324–1350, Jan. 2015, doi: 10.1016/j.rser.2014.09.029.
[35] G. D. Oreggioni, D. Friedrich, S. Brandani, and H. Ahn, "Techno-Economic Study of Adsorption Processes for Pre-Combustion Carbon Capture at a Biomass CHP Plant," Energy Procedia, vol. 63, pp. 6738–6744, 2014, doi: 10.1016/j.egypro.2014.11.709.

[36] D. Jansen, M. Gazzani, G. Manzolini, E. V. Dijk, and M. Carbo, “Pre-combustion CO2 capture,” International Journal of Greenhouse Gas Control, vol. 40, pp. 167–187, Sep. 2015, doi: 10.1016/j.ijggc.2015.05.028.
[37] G. Ebenezer, S. J. S., “Removal of carbon dioxide from natural gas for LNG production.” [Online]. Available: https://www.scribd.com/document/167628194/Removal-of-Carbon-Dioxide-From-Natural-Gas-for-Lng-Production
[38] S. H. Park, S. J. Lee, J. W. Lee, S. N. Chun, and J. B. Lee, “The quantitative evaluation of two-stage pre-combustion CO2 capture processes using the physical solvents with various design parameters,” Energy, vol. 81, pp. 47–55, Mar. 2015, doi: 10.1016/j.energy.2014.10.055.
[39] W.-H. Chen, S.-M. Chen, and C.-I. Hung, “Carbon dioxide capture by single droplet using Selexol, Rectisol and water as absorbents: A theoretical approach,” Applied Energy, vol. 111, pp. 731–741, Nov. 2013, doi: 10.1016/j.apenergy.2013.05.051.
[40] J. D. Figueroa, T. Fout, S. Plasynski, H. McIlvried, and R. D. Srivastava, “Advances in CO2 capture technology—The U.S. Department of Energy’s Carbon Sequestration Program,” International Journal of Greenhouse Gas Control, vol. 2, no. 1, pp. 9–20, Jan. 2008, doi: 10.1016/S1750-5836(07)00094-1.
[41] R. Ducroux and P. Jeanbaptiste, “Technologies, methods and modelling for CO2 capture,” in Greenhouse Gas Control Technologies 7, vol. II, Elsevier, 2005, pp. 1835–1839. doi: 10.1016/B978-008044704-9/50222-6.
[42] Fahim, Fundamentals of Petroleum Refining. Elsevier, 2010. doi: 10.1016/C2009-0-16348-1.
[43] J. Thilagan, B. Gayathri, and M. Sugumar, “CO<SUB align="right">2 capture by adsorption and hydrate-based separation: a technological review,” IJEWM, vol. 22, no. 1/2/3/4, p. 147, 2018, doi: 10.1504/IJEWM.2018.094103.
[44] M. K. Al Mesfer, M. Danish, Y. M. Fahmy, and Md. M. Rashid, “Post-combustion CO2 capture with activated carbons using fixed bed adsorption,” Heat Mass Transfer, vol. 54, no. 9, pp. 2715–2724, Sep. 2018, doi: 10.1007/s00231-018-2319-1.
[45] M. Safaei, M. M. Foroughi, N. Ebrahimpoor, S. Jahani, A. Omidi, and M. Khatami, “A review on metal-organic frameworks: Synthesis and applications,” TrAC Trends in Analytical Chemistry, vol. 118, pp. 401–425, Sep. 2019, doi: 10.1016/j.trac.2019.06.007.
[46] Y. Wang, L. You, and K. Zhou, “Origin of the N-coordinated single-atom Ni sites in heterogeneous electrocatalysts for CO2 reduction reaction,” Chem. Sci., vol. 12, no. 42, pp. 14065–14073, 2021, doi: 10.1039/D1SC04094D.
[47] G. Li et al., “Evaluation of CO2 separation performance with enhanced features of materials – Pebax® 2533 mixed matrix membranes containing ZIF-8-PEI@[P(3)HIm][Tf2N],” Chemical Engineering Research and Design, vol. 181, pp. 195–208, May 2022, doi: 10.1016/j.cherd.2022.03.023.
[48] S. Zhang, Q. Fan, R. Xia, and T. J. Meyer, “CO2 Reduction: From Homogeneous to Heterogeneous Electrocatalysis,” Acc. Chem. Res., vol. 53, no. 1, pp. 255–264, Jan. 2020, doi: 10.1021/acs.accounts.9b00496.
[49] X. Wang, X. Lu, L. Wu, and J. Chen, “3D metal-organic framework as highly efficient biosensing platform for ultrasensitive and rapid detection of bisphenol A,” Biosensors and Bioelectronics, vol. 65, pp. 295–301, Mar. 2015, doi: 10.1016/j.bios.2014.10.010.
[50] M. Younas et al., “Recent progress and remaining challenges in post-combustion CO2 capture using metal-organic frameworks (MOFs),” Progress in Energy and Combustion Science, vol. 80, p. 100849, Sep. 2020, doi: 10.1016/j.pecs.2020.100849.
[51] W. Cheng, X. Tang, Y. Zhang, D. Wu, and W. Yang, “Applications of metal-organic framework (MOF)-based sensors for food safety: Enhancing mechanisms and recent advances,” Trends in Food Science & Technology, vol. 112, pp. 268–282, Jun. 2021, doi: 10.1016/j.tifs.2021.04.004.
[52] X. Fang, B. Zong, and S. Mao, “Metal–Organic Framework-Based Sensors for Environmental Contaminant Sensing,” Nano-Micro Lett., vol. 10, no. 4, p. 64, Oct. 2018, doi: 10.1007/s40820-018-0218-0.
[53] C.-S. Liu et al., “Highly stable aluminum-based metal-organic frameworks as biosensing platforms for assessment of food safety,” Biosensors and Bioelectronics, vol. 91, pp. 804–810, May 2017, doi: 10.1016/j.bios.2017.01.059.
[54] S. Gaikwad, Y. Kim, R. Gaikwad, and S. Han, “Enhanced CO2 capture capacity of amine-functionalized MOF-177 metal organic framework,” Journal of Environmental Chemical Engineering, vol. 9, no. 4, p. 105523, Aug. 2021, doi: 10.1016/j.jece.2021.105523.
[55] N. Tsubouchi, M. Nishio, and Y. Mochizuki, “Role of nitrogen in pore development in activated carbon prepared by potassium carbonate activation of lignin,” Applied Surface Science, vol. 371, pp. 301–306, May 2016, doi: 10.1016/j.apsusc.2016.02.200.

[56] W. Quan et al., "Scalable Formation of Diamine-Appended Metal–Organic Framework Hollow Fiber Sorbents for Postcombustion CO2 Capture," JACS Au, vol. 2, no. 6, pp. 1350–1358, Jun. 2022, doi: 10.1021/jacsau.2c00029.
[57] H. Wu et al., "Highly Efficient Capture of Postcombustion Generated CO2 through a Copper-Based Metal–Organic Framework," Energy Fuels, vol. 35, no. 1, pp. 610–617, Jan. 2021, doi: 10.1021/acs.energyfuels.0c03144.
[58] O. T. Qazvini and S. G. Telfer, "MUF-16: A Robust Metal–Organic Framework for Pre- and Post-Combustion Carbon Dioxide Capture," ACS Appl. Mater. Interfaces, vol. 13, no. 10, pp. 12141–12148, Mar. 2021, doi: 10.1021/acsami.1c01156.
[59] S. C. Tiwari, A. Bhardwaj, K. D. P. Nigam, K. K. Pant, and S. Upadhyayula, "A strategy of development and selection of absorbent for efficient CO2 capture: An overview of properties and performance," Process Safety and Environmental Protection, vol. 163, pp. 244–273, Jul. 2022, doi: 10.1016/j.psep.2022.05.025.
[60] T. E. Akinola, P. L. Bonilla Prado, and M. Wang, "Experimental studies, molecular simulation and process modelling\simulation of adsorption-based post-combustion carbon capture for power plants: A state-of-the-art review," Applied Energy, vol. 317, p. 119156, Jul. 2022, doi: 10.1016/j.apenergy.2022.119156.
[61] A. Allangawi et al., "Carbon Capture Materials in Post-Combustion: Adsorption and Absorption-Based Processes," C, vol. 9, no. 1, p. 17, Jan. 2023, doi: 10.3390/c9010017.
[62] T. Chitsiga, M. O. Daramola, N. Wagner, and J. Ngoy, "Effect of the Presence of Water-soluble Amines on the Carbon Dioxide (CO2) Adsorption Capacity of Amine-grafted Poly-succinimide (PSI) Adsorbent During CO2 Capture," Energy Procedia, vol. 86, pp. 90–105, Jan. 2016, doi: 10.1016/j.egypro.2016.01.010.
[63] A. Ra Cho et al., "Epoxide functionalization of a pentaethylenehexamine adsorbent supported on macroporous silica for post-combustion CO2 capture," Fuel, vol. 325, p. 124938, Oct. 2022, doi: 10.1016/j.fuel.2022.124938.
[64] S. Ahmed, A. Ramli, S. Yusup, and M. Farooq, "Adsorption behavior of tetraethylenepentamine-functionalized Si-MCM-41 for CO 2 adsorption," Chemical Engineering Research and Design, vol. 122, pp. 33–42, Jun. 2017, doi: 10.1016/j.cherd.2017.04.004.
[65] E. Atta-Obeng, B. Dawson-Andoh, E. Felton, and G. Dahle, "Carbon Dioxide Capture Using Amine Functionalized Hydrothermal Carbons from Technical Lignin," Waste Biomass Valor, vol. 10, no. 9, pp. 2725–2731, Sep. 2019, doi: 10.1007/s12649-018-0281-2.
[66] M. A. O. Lourenço, M. Fontana, P. Jagdale, C. F. Pirri, and S. Bocchini, "Improved CO2 adsorption properties through amine functionalization of multi-walled carbon nanotubes," Chemical Engineering Journal, vol. 414, p. 128763, Jun. 2021, doi: 10.1016/j.cej.2021.128763.
[67] R. R. Kondakindi, G. McCumber, S. Aleksic, W. Whittenberger, and M. A. Abraham, "Na2CO3-based sorbents coated on metal foil: CO2 capture performance," International Journal of Greenhouse Gas Control, vol. 15, pp. 65–69, Jul. 2013, doi: 10.1016/j.ijggc.2013.01.038.
[68] D. Panda, E. A. Kumar, and S. K. Singh, "Introducing mesoporosity in zeolite 4A bodies for Rapid CO2 capture," Journal of CO2 Utilization, vol. 40, p. 101223, Sep. 2020, doi: 10.1016/j.jcou.2020.101223.
[69] K.-J. Hwang et al., "Synthesis of zeolitic material from basalt rock and its adsorption properties for carbon dioxide," RSC Adv., vol. 8, no. 17, pp. 9524–9529, 2018, doi: 10.1039/C8RA00788H.
[70] W. Liang et al., "Amine-immobilized HY zeolite for CO2 capture from hot flue gas," Chinese Journal of Chemical Engineering, vol. 43, pp. 335–342, Mar. 2022, doi: 10.1016/j.cjche.2022.02.004.
[71] D. Panda, E. A. Kumar, and S. K. Singh, "Amine Modification of Binder-Containing Zeolite 4A Bodies for Post-Combustion CO2 Capture," Ind. Eng. Chem. Res., vol. 58, no. 13, pp. 5301–5313, Apr. 2019, doi: 10.1021/acs.iecr.8b03958.
[72] S.-Y. Lee and S.-J. Park, "A review on solid adsorbents for carbon dioxide capture," Journal of Industrial and Engineering Chemistry, vol. 23, pp. 1–11, Mar. 2015, doi: 10.1016/j.jiec.2014.09.001.
[73] L. Jiang, A. Gonzalez-Diaz, J. Ling-Chin, A. P. Roskilly, and A. J. Smallbone, "Post-combustion CO2 capture from a natural gas combined cycle power plant using activated carbon adsorption," Applied Energy, vol. 245, pp. 1–15, Jul. 2019, doi: 10.1016/j.apenergy.2019.04.006.
[74] S. Krishnamurthy, R. Blom, K. A. Andreassen, V. Middelkoop, M. Rombouts, and A. B. Borras, "3D Printed PEI Containing Adsorbents Supported by Carbon Nanostructures for Post-combustion Carbon Capture From Biomass Fired Power Plants," Front. Clim., vol. 3, p. 733499, Sep. 2021, doi: 10.3389/fclim.2021.733499.

[75] P. Jayakaran, G. S. Nirmala, and L. Govindarajan, "Qualitative and Quantitative Analysis of Graphene-Based Adsorbents in Wastewater Treatment," International Journal of Chemical Engineering, vol. 2019, pp. 1–17, Jul. 2019, doi: 10.1155/2019/9872502.
[76] A. Jana and A. Modi, "Recent progress on functional polymeric membranes for CO2 separation from flue gases: A review," Carbon Capture Science & Technology, vol. 11, p. 100204, Jun. 2024, doi: 10.1016/j.ccst.2024.100204.
[77] W.-H. Lai, D. K. Wang, M.-Y. Wey, and H.-H. Tseng, "ZIF-8/styrene-IL polymerization hollow fiber membrane for improved CO2/N2 separation," Journal of Cleaner Production, vol. 372, p. 133785, Oct. 2022, doi: 10.1016/j.jclepro.2022.133785.
[78] Q. Shi, "Molecular dynamics simulation of diffusion and separation of CO2/CH4/N2 on MER zeolites," Journal of Fuel Chemistry and Technology, vol. 49, no. 10, pp. 1531–1539, Oct. 2021, doi: 10.1016/S1872-5813(21)60095-6.
[79] S. Majumdar et al., "Mg-MOF-74/Polyvinyl acetate (PVAc) mixed matrix membranes for CO2 separation," Separation and Purification Technology, vol. 238, p. 116411, May 2020, doi: 10.1016/j.seppur.2019.116411.
[80] S. Rezaei, A. Liu, and P. Hovington, "Emerging technologies in post-combustion carbon dioxide capture & removal," Catalysis Today, vol. 423, p. 114286, Nov. 2023, doi: 10.1016/j.cattod.2023.114286.
[81] P. Ganeshan et al., "Bioenergy with carbon capture, storage and utilization: Potential technologies to mitigate climate change," Biomass and Bioenergy, vol. 177, p. 106941, Oct. 2023, doi: 10.1016/j.biombioe.2023.106941.
[82] S. K. S. Boetcher, J. B. Perskin, Y. Maidenberg, M. J. Traum, and T. Von Hippel, "Direct atmospheric cryogenic carbon capture in cold climates," Carbon Capture Science & Technology, vol. 8, p. 100127, Sep. 2023, doi: 10.1016/j.ccst.2023.100127.
[83] M. Shen et al., "Cryogenic technology progress for CO2 capture under carbon neutrality goals: A review," Separation and Purification Technology, vol. 299, p. 121734, Oct. 2022, doi: 10.1016/j.seppur.2022.121734.
[84] J. A. Garcia, M. Villen-Guzman, J. M. Rodriguez-Maroto, and J. M. Paz-Garcia, "Technical analysis of CO2 capture pathways and technologies," Journal of Environmental Chemical Engineering, vol. 10, no. 5, p. 108470, Oct. 2022, doi: 10.1016/j.jece.2022.108470.
[85] G. S. Grasa and J. C. Abanades, "CO2 Capture Capacity of CaO in Long Series of Carbonation/Calcination Cycles," Ind. Eng. Chem. Res., vol. 45, no. 26, pp. 8846–8851, Dec. 2006, doi: 10.1021/ie0606946.
[86] B. Dziejarski, R. Krzyżyńska, and K. Andersson, "Current status of carbon capture, utilization, and storage technologies in the global economy: A survey of technical assessment," Fuel, vol. 342, p. 127776, Jun. 2023, doi: 10.1016/j.fuel.2023.127776.
[87] D. Y. C. Leung, G. Caramanna, and M. M. Maroto-Valer, "An overview of current status of carbon dioxide capture and storage technologies," Renewable and Sustainable Energy Reviews, vol. 39, pp. 426–443, Nov. 2014, doi: 10.1016/j.rser.2014.07.093.
[88] H. J. Herzog, "Scaling up carbon dioxide capture and storage: From megatons to gigatons," Energy Economics, vol. 33, no. 4, pp. 597–604, Jul. 2011, doi: 10.1016/j.eneco.2010.11.004.
[89] A. I. Osman, M. Hefny, M. I. A. Abdel Maksoud, A. M. Elgarahy, and D. W. Rooney, "Recent advances in carbon capture storage and utilisation technologies: a review," Environ Chem Lett, vol. 19, no. 2, pp. 797–849, Apr. 2021, doi: 10.1007/s10311-020-01133-3.
[90] G. T. Rochelle, "Thermal degradation of amines for CO2 capture," Current Opinion in Chemical Engineering, vol. 1, no. 2, pp. 183–190, May 2012, doi: 10.1016/j.coche.2012.02.004.
[91] A. Almena, P. Thornley, K. Chong, and M. Röder, "Carbon dioxide removal potential from decentralised bioenergy with carbon capture and storage (BECCS) and the relevance of operational choices," Biomass and Bioenergy, vol. 159, p. 106406, Apr. 2022, doi: 10.1016/j.biombioe.2022.106406.
[92] S. Kim and Y. M. Lee, "High performance polymer membranes for CO2 separation," Current Opinion in Chemical Engineering, vol. 2, no. 2, pp. 238–244, May 2013, doi: 10.1016/j.coche.2013.03.006.
[93] M. Clausse, J. Merel, and F. Meunier, "Numerical parametric study on CO2 capture by indirect thermal swing adsorption," International Journal of Greenhouse Gas Control, vol. 5, no. 5, pp. 1206–1213, Sep. 2011, doi: 10.1016/j.ijggc.2011.05.036.
[94] M. Fajardy, J. Morris, A. Gurgel, H. Herzog, N. Mac Dowell, and S. Paltsev, "The economics of bioenergy with carbon capture and storage (BECCS) deployment in a 1.5 °C or 2 °C world," Global Environmental Change, vol. 68, p. 102262, May 2021, doi: 10.1016/j.gloenvcha.2021.102262.

[95] M. J. Tuinier, M. Van Sint Annaland, G. J. Kramer, and J. A. M. Kuipers, "Cryogenic CO 2 capture using dynamically operated packed beds," Chemical Engineering Science, vol. 65, no. 1, pp. 114–119, Jan. 2010, doi: 10.1016/j.ces.2009.01.055.

Author contribution:
1. Conception and design of the study
2. Data acquisition
3. Data analysis
4. Discussion of the results
5. Writing of the manuscript
6. Approval of the last version of the manuscript

HA has contributed to: 1, 2, 3, 4, 5 and 6.
NA has contributed to: 1, 2, 3, 4, 5 and 6.
SS has contributed to: 1, 2, 3, 4, 5 and 6.
AK has contributed to: 1, 2, 3, 4, 5 and 6.
UN has contributed to: 1, 2, 3, 4, 5 and 6.

Acceptance Note: This article was approved by the journal editors Dr. Rafael Sotelo and Mag. Ing. Fernando A. Hernández Gobertti.

Comparative Evaluation of Chemically and Green-Synthesized Silica-Modified CeO_2 Nanostructures for Time-Dependent Room-Temperature Ammonia Sensing

Evaluación comparativa de nanoestructuras de CeO_2 modificadas con sílice, sintetizadas química y ecológicamente, para la detección de amoníaco a temperatura ambiente en función del tiempo

Avaliação comparativa de nanoestruturas de CeO_2 modificadas com sílica, sintetizadas quimicamente e por métodos ecológicos, para detecção de amônia em função do tempo e à temperatura ambiente.

Danish Majeed [1], Syeda Sarah Zehra Zaidi [2], Syed Muhammad Mohsin [3], Muhammad Sajid Ali Asghar [4], Asad A. Zaidi [5] (*)

Recibido: 12/01/2026 Aceptado: 27/03/2026

Summary. - Silica nanoparticles were synthesized via two distinct routes – a conventional chemical process and a sustainable green approach using sugarcane bagasse – and incorporated into cerium oxide (CeO_2) nanostructures for comparative evaluation as room-temperature ammonia (NH_3) gas sensors. The chemical route yielded silica by precipitating sodium silicate, whereas the green route extracted bio-silica from agricultural waste (sugarcane bagasse). Both silica types were integrated with CeO_2 through a precipitation/coating method to form silica–modified CeO_2 composite nanoparticles, which were fabricated into chemiresistive sensor devices. Structural characterization by scanning electron microscopy (SEM) revealed an elongated, rod-like CeO_2 morphology distributed in a silica-rich matrix, and energy-dispersive X-ray spectroscopy (EDS) confirmed the presence of Si, Ce, and O, indicating successful composite formation. Gas sensing tests demonstrated that all sensors responded to NH_3 at room temperature, with an initial rapid decrease in resistance upon NH_3 exposure. The gas response (defined as change in resistance ratio) reached over 600% within seconds of exposure for fresh sensors and progressively increased with continued exposure up to 10 min. After 15 min of continuous NH_3, however, the sensor response became negative (~–11%), suggesting surface saturation or irreversible adsorption of NH_3 on the active sites. These results suggest that sugarcane bagasse-derived silica can produce NH_3 response trends broadly comparable to chemically synthesized silica under the present experimental conditions. However, a full statistical comparison using multiple devices is still required to confirm equivalent performance. The incorporation of green-sourced silica thus provides an environmentally friendly pathway to high-performance, room-temperature gas sensors, though calibration and long-term stability tests are needed for further development.

Keywords: *Silica nanoparticles; Green synthesis; Cerium oxide; Chemiresistive ammonia sensor; Room-temperature gas sensing*

(*) Corresponding author.

[1] PhD Scholar, Department of Materials Engineering, NED University of Engineering and Technology (Pakistan), Danish.majeed@neduet.edu.pk, ORCID iD: https://orcid.org/0009-0006-1005-8443

[2] Bachelor of Engineering (Materials), Department of Materials Engineering, NED University of Engineering and Technology (Pakistan), sara.zaidi@gmail.com. ORCID iD: https://orcid.org/0009-0005-1762-6530

[3] Bachelor of Engineering (Materials), Department of Materials Engineering, NED University of Engineering and Technology (Pakistan); mohsim.m@gmail.com, ORCID iD: https://orcid.org/0009-0006-0799-7925

[4] Associate Professor, Department of Materials Engineering, NED University of Engineering and Technology (Pakistan), smsajid@neduet.edu.pk, ORCID iD: https://orcid.org/0000-0002-4551-1299

[5] Professor, Department of Mechanical Engineering, Faculty of Engineering, Islamic University of Madinah (Saudi Arabia), ORCID iD: https://orcid.org/0000-0001-5457-5684

Memoria Investigaciones en Ingeniería, núm. 30 (2026). pp. 145-163
https://doi.org/10.36561/ING.30.10
ISSN 2301-1092 • ISSN (en línea) 2301-1106 – Universidad de Montevideo, Uruguay

Resumen. - *Se sintetizaron nanopartículas de sílice mediante dos rutas distintas: un proceso químico convencional y un enfoque verde sostenible utilizando bagazo de caña de azúcar. Estas nanopartículas se incorporaron a nanoestructuras de óxido de cerio (CeO_2) para su evaluación comparativa como sensores de gas de amoníaco (NH_3) a temperatura ambiente. La ruta química produjo sílice mediante la precipitación de silicato de sodio, mientras que la ruta verde extrajo sílice biológica de residuos agrícolas (bagazo de caña de azúcar). Ambos tipos de sílice se integraron con CeO_2 mediante un método de precipitación/recubrimiento para formar nanopartículas compuestas de CeO_2 modificadas con sílice, las cuales se utilizaron para fabricar dispositivos sensores quimiorresistivos. La caracterización estructural mediante microscopía electrónica de barrido (SEM) reveló una morfología de CeO_2 alargada, en forma de varilla, distribuida en una matriz rica en sílice. La espectroscopia de rayos X de energía dispersiva (EDS) confirmó la presencia de Si, Ce y O, lo que indica la formación exitosa del compuesto. Las pruebas de detección de gases demostraron que todos los sensores respondieron al NH_3 a temperatura ambiente, con una rápida disminución inicial de la resistencia tras la exposición al NH_3. La respuesta al gas (definida como el cambio en la relación de resistencia) alcanzó más del 600 % en segundos para los sensores nuevos y aumentó progresivamente con la exposición continua hasta los 10 minutos. Sin embargo, después de 15 minutos de exposición continua al NH_3, la respuesta del sensor se volvió negativa (~−11 %), lo que sugiere saturación de la superficie o adsorción irreversible de NH_3 en los sitios activos. Estos resultados sugieren que la sílice derivada del bagazo de caña de azúcar puede producir tendencias de respuesta al NH_3 ampliamente comparables a las de la sílice sintetizada químicamente en las presentes condiciones experimentales. No obstante, aún se requiere una comparación estadística completa con múltiples dispositivos para confirmar un rendimiento equivalente. La incorporación de sílice de origen ecológico proporciona, por lo tanto, una vía respetuosa con el medio ambiente para obtener sensores de gas de alto rendimiento a temperatura ambiente, aunque se necesitan pruebas de calibración y estabilidad a largo plazo para su posterior desarrollo.*

Palabras clave: *Nanopartículas de sílice; Síntesis verde; Óxido de cerio; Sensor quimiorresistivo de amoníaco; Detección de gases a temperatura ambiente.*

***Resumo*. -** *Nanopartículas de sílica foram sintetizadas por duas rotas distintas – um processo químico convencional e uma abordagem verde sustentável utilizando bagaço de cana-de-açúcar – e incorporadas em nanoestruturas de óxido de cério (CeO_2) para avaliação comparativa como sensores de gás amônia (NH_3) à temperatura ambiente. A rota química produziu sílica por precipitação de silicato de sódio, enquanto a rota verde extraiu biossílica de resíduos agrícolas (bagaço de cana-de-açúcar). Ambos os tipos de sílica foram integrados ao CeO_2 por meio de um método de precipitação/revestimento para formar nanopartículas compósitas de CeO_2 modificadas com sílica, que foram utilizadas na fabricação de dispositivos sensores quimiorresistivos. A caracterização estrutural por microscopia eletrônica de varredura (MEV) revelou uma morfologia alongada, em forma de bastonete, do CeO_2 distribuída em uma matriz rica em sílica, e a espectroscopia de raios X por dispersão de energia (EDS) confirmou a presença de Si, Ce e O, indicando a formação bem-sucedida do compósito. Os testes de detecção de gás demonstraram que todos os sensores responderam ao NH_3 à temperatura ambiente, com uma rápida diminuição inicial na resistência após a exposição ao NH_3. A resposta ao gás (definida como a variação na razão de resistência) atingiu mais de 600% em segundos após a exposição para sensores novos e aumentou progressivamente com a exposição contínua por até 10 minutos. Após 15 minutos de exposição contínua ao NH_3, no entanto, a resposta do sensor tornou-se negativa (aproximadamente -11%), sugerindo saturação da superfície ou adsorção irreversível de NH_3 nos sítios ativos. Esses resultados sugerem que a sílica derivada do bagaço de cana-de-açúcar pode produzir tendências de resposta ao NH_3 amplamente comparáveis à sílica sintetizada quimicamente nas condições experimentais atuais. No entanto, uma comparação estatística completa utilizando múltiplos dispositivos ainda é necessária para confirmar o desempenho equivalente. A incorporação de sílica de origem verde proporciona, portanto, um caminho ecologicamente correto para sensores de gás de alto desempenho que operam em temperatura ambiente, embora sejam necessários testes de calibração e estabilidade a longo prazo para o desenvolvimento futuro.*

Palavras-chave: *Nanopartículas de sílica; Síntese verde; Óxido de cério; Sensor quimiorresistivo de amônia; Detecção de gases em temperatura ambiente*

1. Introduction. - Silica nanoparticles (SiO_2 NPs) are widely regarded for their high surface area, tunable size, thermal stability, and biocompatibility, making them versatile for applications in sensors, drug delivery, pollutant remediation, and catalysis [1], [2]. Traditionally, silica NPs are produced via chemical methods (e.g. sol–gel or Stöber processes) which offer controlled size and morphology but often involve harsh chemicals and energy-intensive steps [3]. These conventional processes raise environmental and safety concerns. In recent years, green synthesis approaches have gained momentum as sustainable alternatives [4], [5], [6]. Agricultural wastes such as rice husk, corn cob, and sugarcane bagasse have been identified as rich silica sources that can be processed into nanosilica, reducing waste and chemical usage [7], [8]. For instance, sugarcane bagasse ash can contain over 70 wt% silica [9], making it an attractive precursor for silica extraction. Utilizing such bio-derived silica not only diminishes the need for toxic reagents but also adds value to agro-industrial byproducts [10]. Recent studies have demonstrated feasible routes to synthesize silica nanoparticles from sugarcane bagasse and other plant wastes, underscoring the potential of green nanotechnology in materials engineering [11], [12], [13].

Cerium oxide (CeO_2) is a prominent metal oxide semiconductor with excellent redox activity and a high density of oxygen vacancies, properties that are highly beneficial for gas sensing applications [14]. These oxygen vacancies facilitate the adsorption and reaction of gas molecules on the surface, while CeO_2 has good thermal stability and environmental durability which are advantageous for sensor longevity [15]. CeO_2 is an n-type semiconductor that typically requires elevated operating temperatures to achieve sufficient surface reactivity; however, various strategies such as nanostructuring and doping have been employed to overcome its limitation of low room-temperature conductivity [16], [17]. In particular, modifying CeO_2 with secondary phases or dopants can dramatically enhance its gas response at lower temperatures by increasing surface area, creating heterojunctions, or introducing catalytic sites [18]. For example, incorporating noble metals or other oxides into CeO_2 has been shown to improve sensitivity and selectivity to target gases [19]. In one recent report, Ti-doped CeO_2 thin films exhibited a gas response of ~5910% to 250 ppm NH_3 at room temperature (compared to pristine CeO_2's significantly lower response), with rapid response/recovery times of ~15 s [20]. These improvements were attributed to increased oxygen vacancy concentration and electronic modulation by the Ti dopant.

Another effective modification of CeO_2 is the addition of silica. Silica itself is electrically insulating, but when combined with metal oxides it can act as a high-surface-area framework that promotes dispersion of the active oxide phase and enhances gas diffusion through a porous network [21], [22]. Wang *et al.* demonstrated that a sensor using CeO_2 nanostructures modified with ~8 wt% SiO_2 achieved a remarkably high NH_3 response (~3244% to 80 ppm) at room temperature, far superior to pure CeO_2, along with a lower detection limit of 0.5 ppm [23]. The enhanced performance was attributed to the silica providing a larger effective surface and improved hydroxyl-mediated conductivity on the composite surface [24]. Silica additives can also stabilize the nanostructure and prevent particle agglomeration, thereby preserving active surface sites. Furthermore, silica's acid/base surface groups may interact with ammonia, influencing the sensor's electron transfer processes [25]. By fine-tuning the SiO_2 content, researchers have achieved sensors operable at room temperature with fast response and recovery and extended stability [26].

Accordingly, the objective of this study is to comparatively evaluate silica obtained via (i) a conventional chemical route and (ii) an agricultural waste–derived green route (sugarcane bagasse), after integration into silica-modified CeO_2 nanostructures for room-temperature NH_3 sensing. The work aims to (a) document the synthesis and fabrication workflow, (b) examine morphology and elemental composition using SEM/EDS, and (c) assess the time-dependent evolution of chemiresistive response under qualitative NH_3 exposure over 0–15 min. The emphasis is placed on comparative response trends and exposure-time effects relevant to practical room-temperature operation rather than ppm-calibrated sensitivity.

2. Materials and Methods. -

2.1 Materials and Reagents. - The silica sources and chemicals used in this work include: sodium silicate solution (Na_2SiO_3, for chemical silica synthesis), sugarcane bagasse (agricultural waste sourced locally, for green silica synthesis), hydrochloric acid (HCl, 2.5% aqueous solution), silver nitrate ($AgNO_3$), ethanol (C_2H_5OH), nitric acid (HNO_3), sodium hydroxide (NaOH), ammonium hydroxide (NH_4OH), and cerium(III) nitrate hexahydrate ($Ce(NO_3)_3 \cdot 6H_2O$). Distilled water was used in all synthesis and washing steps. All chemicals were of analytical grade and used as received.

2.2 Silica Nanoparticle Synthesis by Chemical Route. - Silica nanoparticles were synthesized using both a conventional chemical route and a green route based on agricultural waste in order to enable a comparative evaluation of their suitability for gas sensing applications. In the chemical synthesis approach, diluted sodium silicate solution

was added dropwise to 2.5% hydrochloric acid under continuous magnetic stirring at approximately 60 °C. The controlled neutralization process resulted in the formation of a cloudy, viscous silica gel due to the condensation of silicate species. The obtained gel was repeatedly washed with distilled water to remove residual chloride ions, which was confirmed by the absence of white precipitate upon addition of silver nitrate to the filtrate. The washed gel was then dried at 100 °C for 24 h, followed by calcination in air at 1000 °C for 1 h to obtain silica nanoparticles with enhanced thermal stability and structural integrity. The overall workflow of the chemical synthesis route is schematically shown in Figure I.

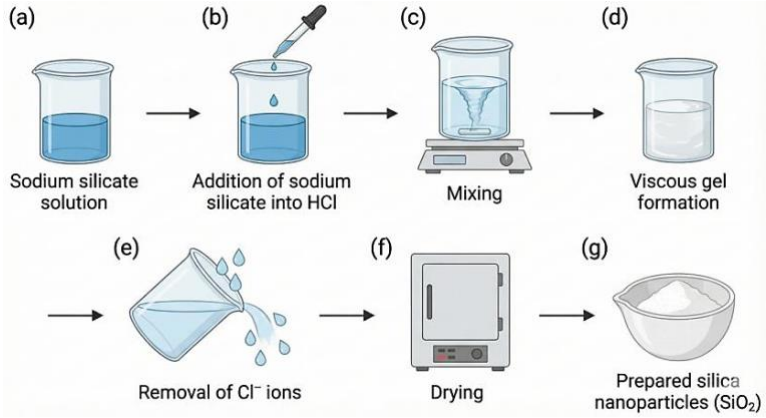

Figure I.- Schematic illustration of the chemical-route synthesis of silica nanoparticles via acid precipitation, washing, drying, and calcination.

The green synthesis route, composite preparation, and sensor fabrication steps are described separately in the following subsections to avoid repetition and improve clarity.

2.3 Silica Nanoparticle Synthesis by Green Route. - For the green synthesis route, silica was extracted from sugarcane bagasse, an agricultural by-product high in silica content [27]. The bagasse (fibrous sugarcane waste) was first sun-dried and cut into small pieces. It was then thoroughly washed with distilled water and soaked for 24 h to remove dirt and soluble impurities. After oven drying at 90 °C, the cleaned bagasse was subjected to acid leaching: the fibers were immersed in a 1 N HCl solution and heated in a water bath at ~75 °C for several hours. This step dissolves many metal impurities from the biomass [3]. The material was filtered, washed to neutrality, and dried again (90 °C). Next, the pretreated bagasse was transferred to a basic extraction step to dissolve its silica content. The dried fibers were boiled in 1 M NaOH solution (liquid-to-solid ratio ~10 mL g^{-1}) at 90 °C for 1 h, which converted the bio-silica into soluble sodium silicate. The hot mixture was filtered to remove residual biomass, yielding a sodium silicate solution. Silica was then precipitated from this solution by the addition of acid: concentrated HNO_3 was added dropwise to the filtrate under stirring until the pH lowered to ~8. At this point, the silicate condenses into silica particles, forming a suspension. A small amount of ethanol (~20 mL) was also added to promote particle formation. The suspension was continuously stirred, then left overnight. The silica product was collected by centrifugation at ~4000 rpm for 45 min, washed repeatedly with distilled water, and dried at 90 °C. A final calcination at 600 °C for 30 min was applied to obtain purified silica nanoparticles. Figure II summarizes the green synthesis steps.

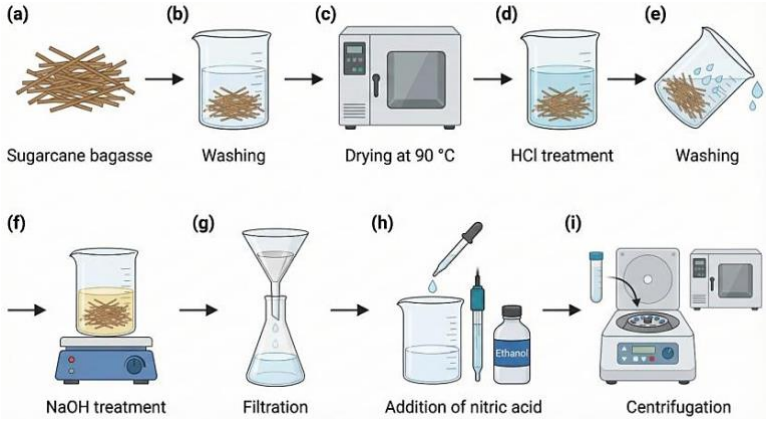

Figure II.- Schematic workflow for green synthesis of SiO_2 nanoparticles from sugarcane bagasse via acid leaching, alkaline extraction, and acid precipitation.

Both synthesis methods yielded fine white silica powders. The chemically synthesized silica had a yield of approximately 1.5–2 g from the starting solution volumes, whereas the green route yield depended on ash content (bagasse ash after acid treatment yielded ~20–25% silica by weight). The green synthesis is notably less toxic and aligns with sustainable practices by utilizing a renewable waste resource.

2.4 Preparation of Silica–Modified CeO_2 Nanostructures. - Silica-modified ceria nanostructures were prepared via an in situ precipitation of CeO_2 onto the silica nanoparticles. In a typical procedure, 6 g of the prepared silica nanoparticles (from either route) were dispersed in 100 mL of distilled water. The dispersion was ultrasonicated for 30 minutes to ensure a uniform suspension of silica particles (which serve as a substrate or template for CeO_2 growth). In parallel, 2.17 g of cerium (III) nitrate hexahydrate ($Ce(NO_3)_3 \cdot 6H_2O$) was dissolved in 50 mL of distilled water to form a Ce^{3+} precursor solution. This cerium nitrate solution was then slowly added to the silica suspension under constant magnetic stirring. After 15 minutes of mixing, ammonium hydroxide (NH_4OH, ~28% solution) was added dropwise to the mixture until the pH reached approximately 10–11. The addition of NH_4OH precipitates cerium as cerium hydroxide, which subsequently forms cerium oxide (ceria) in the presence of OH^-. The reaction was maintained at ~80 °C with continuous stirring for 2 hours to allow CeO_2 nanoparticles to nucleate and coat onto the silica surfaces. The appearance of a homogenous light yellow or off-white suspension indicated the formation of CeO_2 on SiO_2. The composite product was collected by centrifugation at 10,000 rpm for 10 minutes, then washed thoroughly with distilled water to remove any residual ions (e.g., NH_4^+, NO_3^-). The collected silica–ceria composite was dried in an oven at 80 °C for 12 hours. This drying step yields a powder comprising silica nanoparticles decorated with cerium oxide (denoted CeO_2–SiO_2 nanostructures). Figure III provides a stepwise illustration of the composite synthesis.

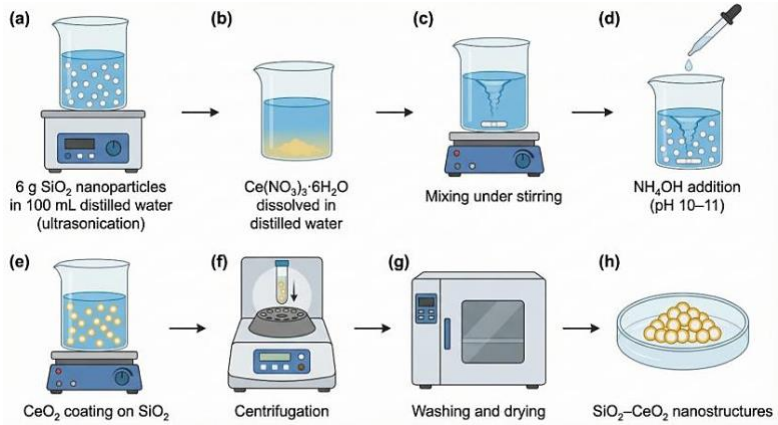

Figure III.- Schematic of CeO_2–SiO_2 composite formation via precipitation/coating of ceria onto dispersed silica nanoparticles.

In this synthesis, silica (from either source) plays the role of a high-surface-area scaffold. The precipitation of CeO_2 in the presence of dispersed silica promotes the formation of a **composite** rather than separate CeO_2 particles. Prior studies on similar systems have reported core–shell type structures where silica cores are coated with ceria shells [27], [28]. Our approach is expected to produce a network of CeO_2 nanocrystallites attached to silica surfaces, which can increase the effective interface with gas molecules during sensing [29].

2.5 Sensor Fabrication and Electrical Measurements. - A chemiresistive gas sensor device was fabricated using the silica–modified CeO_2 composite as the active material. The sensing element was prepared on a small glass substrate (approximately 2 × 2 cm). Prior to coating, the glass substrate was cleaned ultrasonically in ethanol and acetone (10 min each) and dried at 90 °C. Interdigitated electrodes were then formed on the glass surface to allow electrical contact to the sensor material. To do this, a thin conductive layer was applied using silver and gold pastes: first, a silver paste was painted as a seed layer for good adhesion, defining two opposite electrode pads. Then a layer of gold paste was applied over the silver tracks to provide a chemically inert, highly conductive electrode surface. The electrode pattern was dried and cured by heating at 90 °C for several hours, ensuring the metal contacts were well-adhered. Fine platinum wires were attached to the electrode pads (using additional silver paste) to serve as lead-out connections.

To prepare the sensing film, the dried CeO_2–SiO_2 composite powder was blended with a small amount of poly(vinyl alcohol) (PVA) as a binder. Specifically, PVA was dissolved in ethanol to create a viscous solution, and the silica–ceria powder was gradually added to form a slurry. Additional PVA or ethanol was mixed in as needed to achieve a spreadable paste with uniform consistency. The PVA acts as a temporary binder to hold the nanoparticles together and

adhere them to the substrate; it will evaporate or decompose upon subsequent heating, leaving a porous ceramic film. The composite paste was then coated onto the area between the gold contact pads on the glass substrate, covering the electrode gap. This coating was done carefully to create a thin, even film. After air drying, the coated sensor was cured by heating at 400 °C for 2 hours in air. Although the general fabrication procedure was described, some device-level parameters were not measured, including exact electrode gap width, finger length/number, film thickness, active coated area, curing ramp rate, and contact-resistance stability. These parameters may affect the absolute resistance and response values, so the device data were interpreted as proof-of-concept results. This thermal treatment burns off the PVA binder and improves adhesion of the composite to the substrate, as well as potentially enhancing particle connectivity by slight sintering. The result was a robust, porous sensing layer of silica–modified CeO_2 bridging the gold electrodes. Figure IV shows the fabrication steps and assembled sensor device.

For gas sensing tests, the fabricated sensor was placed inside an airtight chamber of approximately 1 L volume. Figure V shows the measurement setup. To introduce ammonia, a known volume of aqueous ammonia solution (~25% NH_3 in water) was placed in a shallow dish inside the sealed chamber. The volatile NH_3 evaporates from the solution, quickly enriching the chamber atmosphere with ammonia vapor. (Note: this method provides an uncalibrated concentration of NH_3; the exposure in this study is qualitative, since no mass flow controller or precise ppm control was used – see *Limitations*). Upon introducing NH_3, the sensor's resistance in the ammonia environment (R_{gas}) was recorded continuously. The sensor was exposed to ammonia for a total of 15 minutes, and the response was monitored over this duration. At 5-minute intervals (0, 5, 10, 15 min), the chamber was briefly opened and then resealed (for instance, to refresh the vapor or simulate consecutive exposures), and the subsequent resistance behavior was measured. After 15 min, the chamber was opened to allow the ammonia to dissipate and the sensor to recover in fresh air. Because the chamber was opened and resealed at 5-minute intervals, the ammonia concentration and oxygen availability inside the chamber were not constant throughout the experiment. Each opening allowed partial gas exchange with ambient air, which may have changed the NH_3 level and refreshed oxygen on the sensor surface. Therefore, the response curves at 0, 5, 10, and 15 min should be interpreted as successive chamber-exposure intervals rather than a strictly controlled continuous NH_3 exposure history.

The gas response of the sensor is defined in percentage terms using the standard chemiresistive formula:

$$\text{Gas Response (\%)} = \frac{R_{\text{air}} - R_{\text{gas}}}{R_{\text{air}}} \times 100,$$

Where, Rair is the sensor resistance in air (baseline) and Rgas is the resistance in the target gas (here, NH_3) [9]. According to this definition, a decrease in resistance upon gas exposure (typical for an n-type oxide like CeO_2 in the presence of a reducing gas) yields a positive response percentage. Since this response calculation depends on the selected air baseline resistance, any baseline drift during prolonged exposure or incomplete recovery can strongly affect the calculated response value. Therefore, a change in response sign may occur if the baseline shifts, and it should not automatically be interpreted as a true inversion of the sensing mechanism. All response values reported were calculated with this formula. In our measurements, the sensor's real-time resistance changes were captured and later converted to response (%) versus time for analysis.

No external heating was applied to the sensor – all tests were conducted at room temperature (~25 °C). The humidity level was ambient (~50% RH) and was not specifically controlled. After each test, the chamber was purged and the sensor was allowed to recover in air; however, as discussed later, the 15-minute prolonged exposure led to behavior suggesting incomplete recovery.

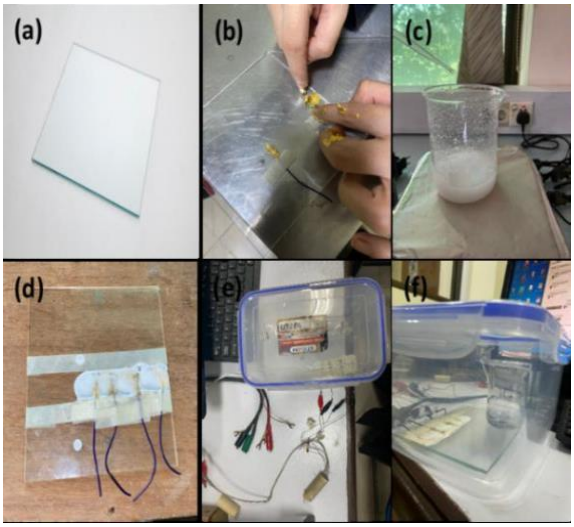

Figure IV. Schematic representation of gas sensor fabrication using silica-modified CeO_2 nanostructures on a glass substrate.

It should be noted that because the ammonia concentration in the chamber was not quantitatively measured (relying on evaporation from solution), the response data are interpreted qualitatively. The emphasis of this study is on comparing the *relative* sensor behavior (especially time-dependent characteristics and the effect of prolonged exposure) rather than on an exact sensitivity value to a known ppm. The performance of our sensor is also compared with literature reports to contextualize its sensitivity.

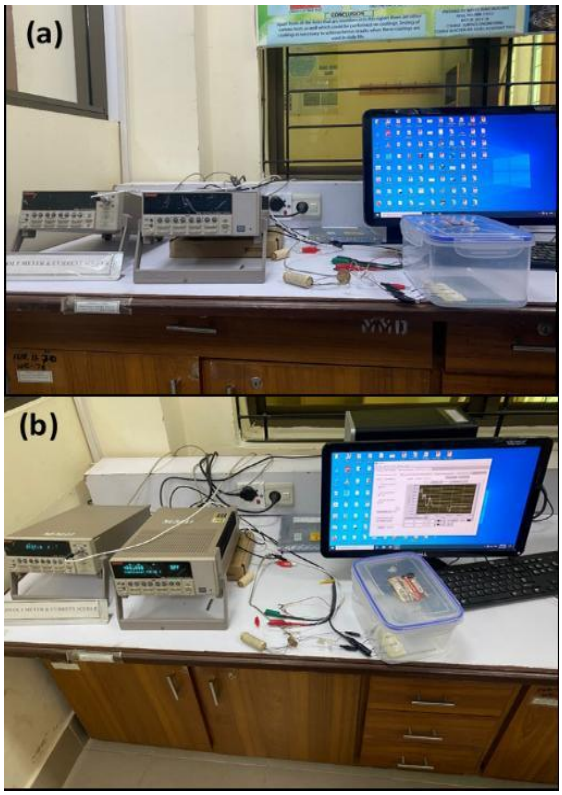

Figure V. Schematic of the sealed-chamber setup used for room-temperature ammonia sensing measurements.

3. Results and Discussion. -

3.1 SEM Analysis of Silica–Ceria Nanostructures. - The morphology of the silica–modified CeO_2 nanostructures was examined by SEM. Representative SEM micrographs at different magnifications are shown in Figure VI.

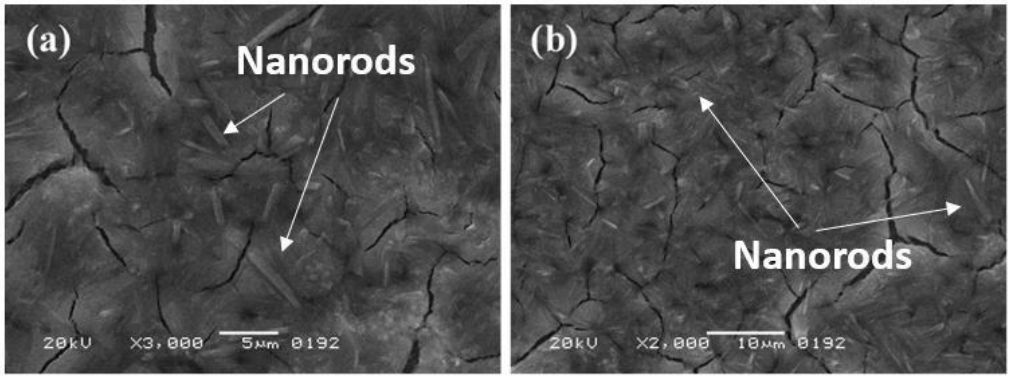

Figure VI. SEM micrographs of silica-modified CeO_2 nanostructures at different magnifications.

Comparing our SEM observations with literature, we note that Kitsou *et al*. (2019) achieved core–shell ZnO@SiO_2 particles where silica served as a smooth nanoscopic template for uniform oxide deposition [14]. In our case, the ceria does not form discrete core–shell particles but rather continuous ceria-rich rods embedded in silica. This structure resembles findings by Vaizoğullar *et al*. (2016), who prepared SiO_2@CeO_2 core–shell nanoparticles and observed a silica-rich composition with ceria coating the silica surfaces [30]. Our sample's rod-like, intergrown morphology may result from the high loading of CeO_2 relative to silica (6 g silica vs ~2 g Ce precursor used). As ceria nucleates and grows, particles coalesce into larger rods, possibly with silica particles decorating or interspersed within these rods. Some cracks or irregular voids are visible in the SEM images, which could be attributed to stresses during the high-temperature curing or calcination process. Thermal history (e.g. rapid drying or the 400 °C curing step) can induce fracturing in the deposited film, as noted in other nanoparticle-based coatings [31]. Despite these fractures, the SEM images show an interconnected composite morphology. However, based on the EDS results, the material should be described more carefully as a silica-rich structure containing dispersed Ce-containing oxide regions, rather than as a fully ceria-rich network.

The elongated ceria structures observed here are known to enhance gas sensing performance by offering a high surface-to-volume ratio and facilitating charge transport along the length of the rods [10]. One study on porous ceria nanorods (Tian *et al*., 2015) noted their high catalytic activity and robust performance, attributing it to the rod morphology providing abundant active sites and pathways for reactant diffusion [20]. In our composite, the silica component further contributes by increasing porosity and stability. Thus, the SEM results confirm that we have successfully created a nanostructured CeO_2–SiO_2 material with characteristics favorable for gas sensing: nanoscale rods, extensive surface area, and a percolating network structure. It should be noted that the rod-like features observed at the applied SEM magnifications correspond to micron-scale elongated structures, likely formed by the aggregation of nanoscale CeO_2 crystallites.

3.2 EDS Analysis and Composition. - Energy-dispersive X-ray spectroscopy was used to verify the elemental composition of the silica–ceria composite. Figure VII shows the EDS spectrum of a representative sample region.

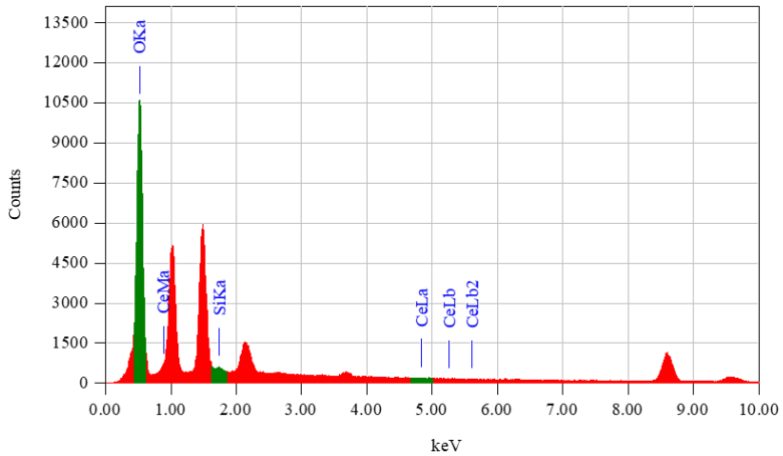

Figure VII. EDS spectrum of silica-modified CeO_2 nanostructures showing the presence of Si, Ce, and O.

The EDS results should be interpreted as semi-quantitative local compositional data from the analyzed surface region. The measurement was performed at 20.0 kV with a probe current of 1 nA, and the calculated weight percentages may vary with selected area, surface roughness, sample thickness, and local particle distribution. Therefore, the EDS values were used mainly to confirm the presence of Si, Ce, and O, rather than to define the exact bulk composition of the composite. The silica-rich composition has important implications for gas sensing. A high SiO_2 content contributes a large surface area and porous structure, as silica generally forms porous networks. The Ce-containing oxide phase was present in a lower amount than silica and was likely distributed as dispersed regions, clusters, or partial coating on the silica-rich matrix. Therefore, the role of CeO_2 in sensing was discussed as the contribution of accessible Ce-containing active sites, while silica was considered mainly as the supporting matrix. Vaizoğullar *et al*. (2016) observed that in SiO_2@CeO_2 core–shell nanoparticles with similarly low Ce content, the configuration enhanced adsorption capabilities – in their case for Hg(II) removal – due to the silica providing a high-surface-area support for the active CeO_2 phase. By analogy, our composite's elemental makeup (low Ce, high SiO_2) points to a design wherein SiO_2 is the structural scaffold and CeO_2 provides the reactive sites for ammonia sensing. This division of roles can be advantageous: silica ensures a stable, porous film, and ceria, despite its smaller fraction, can strongly influence sensor response due to its catalytic redox interactions with gases [24].

Furthermore, the presence of oxygen (50+ wt%) in the EDS confirms that the material consists of oxides (as expected: SiO_2 and CeO_2). No metallic Ce or unoxidized silicon is detected, implying that during synthesis and curing, cerium precipitated as cerium oxide and the silica remained in oxide form. The EDS result thus corroborates that the intended composite (SiO_2 and CeO_2) was obtained. We acknowledge that a precise phase identification (e.g. crystalline phase of CeO_2) would require X-ray diffraction (XRD). In this study, XRD was not performed; however, literature and the synthesis conditions strongly suggest that the cerium is present as CeO_2 (fluorite structure), likely nanocrystalline or possibly amorphous if insufficiently crystallized at 80 °C. The decision to focus on SEM/EDS for composition was made to prioritize understanding the sensor's functional performance. Despite the lack of XRD confirmation, the effective gas sensing behavior (discussed below) provides indirect evidence of active CeO_2 presence, since pure silica is inert to ammonia under these conditions. This revised interpretation reconciles the SEM and EDS observations: the composite was not treated as a ceria-rich percolating network, but as a silica-rich material containing Ce-containing oxide sites that may participate in NH_3 sensing.

3.3 Gas Sensing Mechanism (Chemiresistive Response). - Before discussing the experimental gas response results, we briefly outline the sensing mechanism for n-type semiconducting oxides like CeO_2. In ambient air, oxygen molecules adsorb onto the surface of CeO_2 and capture electrons from the material's conduction band, forming chemisorbed oxygen species (O_2^-, O^-, O^{2-}) [9]. This creates an electron depletion layer at the surface, raising the sensor's resistance in air (Rair). When the sensor is exposed to a reducing gas such as NH_3, the gas molecules react with these adsorbed oxygen ions. For ammonia, a representative surface reaction can be written as:

$$2NH_3(gas) + 3O^-(ads) \rightarrow N_2(gas) + 3H_2O(gas) + 3e^-,$$

which indicates that NH_3 donates electrons back to the oxide by consuming surface oxygen species. The product N_2 and H_2O desorb, and the released electrons return to the CeO_2, reducing the depletion layer and thereby decreasing the sensor's resistance. Thus, upon NH_3 exposure, an n-type oxide sensor typically shows a drop in resistance, which we quantify as a positive gas response (%) as per the earlier formula. When the NH_3 is removed and air is reintroduced, oxygen readsorption can restore the initial conditions (electrons re-trapped by O_2, resistance rises back to baseline), ideally regenerating the sensor.

In our silica–CeO_2 composite, the same fundamental mechanism applies, but the silica matrix may influence the process by affecting how gases diffuse and how electrons percolate. The silica itself is insulating, so the conductive path is primarily through the ceria domains. However, silica can adsorb moisture and surface hydroxyls which might interact with NH_3 (for example, NH_3 can temporarily bind to silanol groups). This could introduce additional surface reactions or delay the recovery as discussed later. Nonetheless, the dominant sensing action is expected from the CeO_2 sites.

We next present the sensor response results at different exposure times. To reiterate, all measurements were done at room temperature with an unquantified but repeatable NH_3 dose (from evaporating ammonia solution). The baseline resistance in air for our devices was on the order of a few MΩ. Upon NH_3 introduction, the resistance dropped markedly. We calculated the gas response (%) over time for each exposure interval (0, 5, 10, 15 min exposures). The dynamic response curves are shown in Figures VIII–XI, and key features are discussed below. It is important to note that the 0, 5, 10, and 15 min response curves do not represent a fully controlled continuous exposure experiment. Since

the chamber was opened and resealed between intervals, gas composition, ammonia vapor concentration, and oxygen availability may have changed during the test. Therefore, the following discussion focuses on qualitative time-dependent response behavior under the present chamber protocol, rather than controlled kinetic analysis.

3.3.1 Sensor Response at Initial NH_3 Exposure (0 minutes). - "0 minutes" corresponds to the sensor's immediate reaction as ammonia is introduced (the first exposure, effectively within the first few seconds of sensing). Figure VIII displays the response curve at this initial exposure.

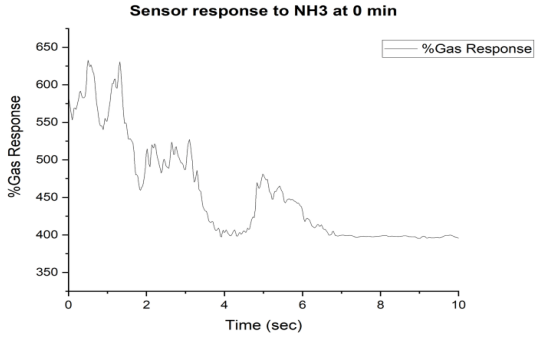

Figure VIII. Dynamic NH_3 response of the sensor at 0 min exposure time.

Following the peak, the sensor's response begins to decline gradually. In Figure VIII, after the first ~2 s spike, the % response drops and stabilizes around ~390–400% by 10 s. This decline is attributed to a partial recovery or saturation effect – as ammonia initially floods the surface, a maximum number of reaction sites are consumed (peak response), and subsequently the system reaches a balance where some NH_3 may desorb or the reaction by-products (e.g. water) start to occupy sites, causing a slight rebound in resistance [32]. A minor secondary rise ("bump") around 5–6 s can be seen, which could indicate a two-step adsorption process or a delayed reaction on deeper sites. By ~10 s, the curve has leveled off, implying that most accessible sites have reacted and the sensor is in a quasi-steady state with that ammonia dose. Importantly, when the chamber was later opened (to simulate a fresh exposure at 5 min, as described next), the sensor resistance returned close to baseline (with air flush), confirming that the interaction at this stage was largely reversible.

Overall, the initial exposure demonstrates that both chemically synthesized silica and green-synthesized silica composites can detect NH_3 strongly at room temperature. The magnitude of the response (hundreds of percent) is on par with or exceeds many conventional metal-oxide sensors at much higher operating temperatures [33]. The rapid response (sub-second rise) is a favorable attribute for real-time monitoring. This performance can be attributed to the composite's high surface area and the efficient catalytic reaction of NH_3 with chemisorbed oxygen on CeO_2. The presence of silica likely enhances the dispersion of CeO_2 and keeps the nanostructure porous, allowing NH_3 to penetrate and reach active sites quickly. We also note that at this initial stage, the sensor had not been "aged" by prior exposure, which often yields the highest response. Subsequent exposures (without thorough reoxidation in between) can show modified behavior, as we observed.

3.3.2 Sensor Response after 5 Minutes of NH_3 Exposure. - After the first exposure, the chamber was resealed with a continued NH_3 source for 5 minutes. We define the "5 min" response as the sensor's behavior when it is exposed to NH_3 that has been in the chamber for 5 minutes (a somewhat refreshed NH_3 environment, though not a fully desorbed baseline). Figure IX shows the dynamic response curve at the 5-minute mark.

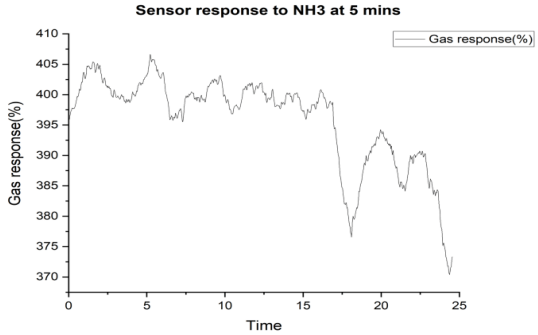

Figure IX. Dynamic NH_3 response of the sensor at 5 min exposure time.

Interestingly, the 5-min response curve shows a more complex transient. Around 10–15 s, there is an abrupt dip: the response drops from ~450% to ~375%, then partially recovers to ~395%, and then gradually falls to ~370% by ~25 s. This oscillatory behavior suggests a dynamic competition between adsorption and desorption processes. The momentary drop at ~15 s could indicate that a fraction of NH_3 desorbed or that a second-stage reaction (perhaps oxidation of intermediate species) occurred, momentarily increasing resistance. The subsequent partial recovery implies that NH_3 readsorbed on freed sites, and finally the downward drift toward 25 s signals a slow approach to equilibrium or slight poisoning. Essentially, by 5 minutes exposure, the sensor is entering a regime of saturation and partial regeneration simultaneously – ammonia molecules continue to interact, but the surface is not as uniformly receptive as at time zero. Similar kinetic behaviors (initial spike followed by dip and plateau) have been reported for other porous sensors under continuous gas flow, where the fast initial reaction is followed by slower diffusion-limited or desorption-limited stages.

From a sensing standpoint, the 5 min exposure still yields a high response (~370% sustained), which confirms that the sensor remains highly sensitive even after being subjected to NH_3 for a prolonged period. However, the reduction in peak and the fluctuations indicate that the sensor's surface is beginning to saturate. This is an important observation for practical use: it suggests that while short bursts of NH_3 can be detected with extreme sensitivity, continuous exposure will reduce the incremental response. The sensor is likely desorbing some ammonia during the exposure (hence the dip and partial recovery), which is a form of self-purging. This behavior is beneficial in that it prevents total saturation within minutes, but it also means the sensor response at long times may not remain at the initial high level.

3.3.3 Sensor Response after 10 Minutes of NH_3 Exposure. - Continuing the exposure further, the sensor behavior at 10 minutes in ammonia was recorded. Figure X presents the response curve after 10 min of continuous NH_3 environment.

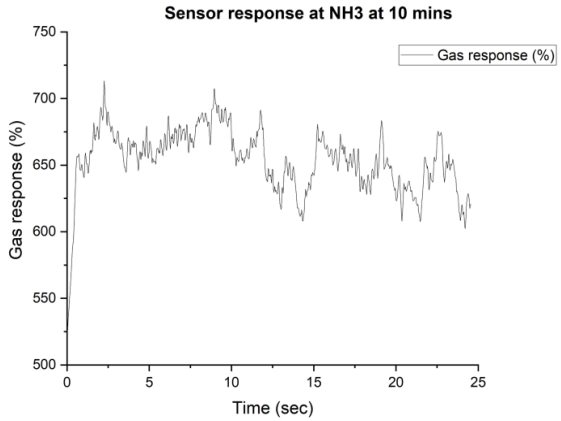

Figure X. Dynamic NH_3 response of the sensor at 10 min exposure time.

Following the peak, from ~3 s onward, the response does not simply decay; instead, it oscillates between about 660% and 700% for an extended period (several seconds). This quasi-steady oscillation indicates a dynamic equilibrium where ammonia adsorption and reaction are balanced by desorption and possibly oxygen re-adsorption in pockets of the sensor [34]. The porous structure likely allows NH_3 to diffuse in and out at different rates, causing fluctuations. Tong *et al.* (2017) observed analogous oscillatory response in a highly porous H_2S sensor, attributing it to the interplay of gas diffusion and reaction kinetics in nanochannels [21]. In our case, the silica–ceria network might have regions that momentarily saturate and then refresh as NH_3 penetrates deeper. The presence of silica could also buffer moisture produced by ammonia oxidation, releasing it intermittently and affecting conductivity slightly.

After ~15 s, the sensor's response in Figure X begins a gradual decline, dropping to around 610% by 25 s. This downward trend suggests the onset of more significant surface saturation – many of the active sites are occupied by reaction products or a stable layer of adsorbed ammonia species, and the sensor cannot sustain the earlier high conductance. Nonetheless, even at 25 s, the response (~610%) is far above the baseline (0%). Compared to the earlier exposures, the 10-min case shows the sensor reaching its *highest* sensitivity (initially) and then showing signs of leveling off at a high response value. The fact that the sensor can still exceed 600% response at 10 min indicates a time-dependent activation: prolonged exposure appears to have activated additional sites or reduced the material (increasing Ce^{3+} concentration), thus temporarily boosting sensitivity. Such behavior – an increase in response with

longer exposure – has been reported for some metal oxide sensors, often due to gradual temperature equilibration or surface restructuring in continuous gas. In our room-temperature case, it could be chemical restructuring (e.g., formation of ammonium species on the surface that facilitate more electron transfer).

This 10-min result highlights that the sensor's response is not static; instead, it evolves with prolonged gas interaction. Practically, this could manifest as a drift in sensor readings over time if NH_3 remains present. Initially, the readings might climb (super-sensitivity), then oscillate, and slowly decline as equilibrium is reached. For a sensing application, one would ideally calibrate the sensor at a fixed exposure duration or dynamic flow to avoid misinterpreting these time-dependent changes as concentration changes. In our experiments, since the concentration wasn't fixed, we interpret these results qualitatively: the composite sensor retains high responsiveness up to 10 minutes, but the reaction kinetics and surface coverage become increasingly complex.

3.3.4 Sensor Response after 15 Minutes of NH_3 Exposure. - After a continuous exposure of 15 minutes to ammonia, a striking change in sensor behavior was observed. Figure XI shows the response curve at the 15-min mark. It should be noted that the response value was calculated using the air baseline resistance. If this baseline resistance changed during the prolonged test, or if the sensor did not fully recover before the next measurement interval, the calculated response could become negative even without a true reversal of the NH_3 sensing mechanism. Therefore, the negative response at 15 min should be interpreted cautiously.

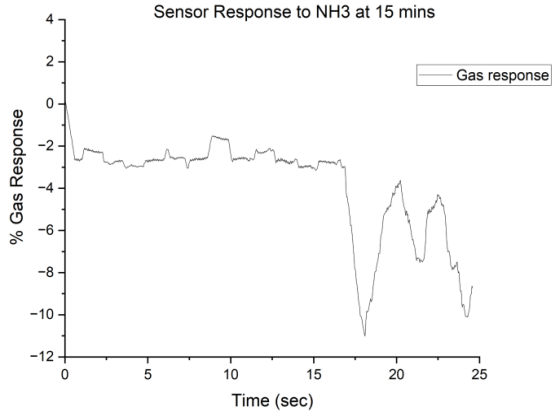

Figure XI. Dynamic NH_3 response of the sensor at 15 min exposure time showing response inversion.

This anomalous negative response may indicate sensor saturation or overload; however, it cannot be assigned only to this mechanism because the NH_3 concentration and humidity were not controlled during the test. Baseline drift, changes in chamber atmosphere, moisture effects from aqueous ammonia, or measurement-related artifacts may also have contributed to the negative response. By 15 minutes, it appears that the sensor surface has accumulated a high coverage of adsorbed species (likely NH_3-derived intermediates or reaction products like ammonium salts or strongly bound oxygen complexes) that fundamentally alter the material's conduction. One interpretation is that the prolonged NH_3 exposure caused an accumulation of electrons in the material that shifted the baseline (essentially reducing the oxide significantly). If the sensor baseline resistance had dropped over time (due to partial reduction), then upon final exposure, introducing NH_3 might no longer produce a drop in resistance – instead, if oxygen was completely depleted from the surface, NH_3 might actually start donating electrons that *overpopulate* the conduction band, leading to a temporary increase in resistance via complex mechanisms (such as formation of surface states that scatter electrons). Another simpler explanation is surface saturation: all adsorption sites (oxygen vacancies, etc.) are occupied, and additional NH_3 cannot react with O^{2-} (because few are left); instead, NH_3 may physically adsorb as a neutral or insulating layer, increasing resistance or blocking current paths [35]. The relatively flat response for the first ~10 s suggests the sensor was fully saturated – the response hovered near 0% (no change). Then, the continuous decline to –11% by 25 s could indicate a slow poisoning effect, where the prolonged presence of NH_3 (or perhaps accumulation of by-products like ammonia-derived surface complexes) inverted the sensor's response. Essentially, the sensor's behavior degraded after too long an exposure, consistent with reversible damage or inhibition of the normal sensing reaction. Similar findings have been noted by Mei *et al*. (2024) for prolonged exposure of certain gas sensors, where signal saturation or even inversion was observed when the target gas was not removed, due to complete consumption of surface oxygen and accumulation of reducing species [17]. Likewise, Takte *et al*. (2023) reported that extended exposure to ammonia could lead to formation of stable surface residues (e.g., ammonium carbonates or amides) on ceria-based sensors, which alter the material's electronic structure and impede the usual sensing mechanism [18].

Therefore, the negative response observed at 15 min should be treated as a possible sign of surface saturation or altered surface condition, rather than as confirmed evidence of sensor poisoning. Further controlled experiments using fixed NH_3 concentration, controlled humidity, repeated cycles, and baseline stability checks are required to confirm the cause of this response inversion.

It is important to clarify that once the sensor is in this state, simply purging with air may not immediately restore the original baseline. Indeed, after the 15-min test, our sensor showed difficulty returning to the exact initial resistance, indicating that some NH_3 or reaction product remained bound (irreversible adsorption). In practical terms, this means the sensor would require re-oxidation (for example, heating or a long ambient recovery) to fully reset after such a prolonged NH_3 exposure. For shorter exposures (0–10 min), the sensor largely recovered after air purging, but the 15 min case crossed a threshold into saturation. This finding underscores a limitation for using such sensors in high or continuous ammonia environments: one must either periodically recondition the sensor or interpret the decreasing signal as an indicator of prolonged exposure (rather than misinterpreting it as lower gas concentration).

In summary, the time-dependent gas response measurements reveal a progression: (i) an initially high and fast response (0 min), (ii) slight moderation and kinetic complexity at 5 min, (iii) reactivation and oscillatory equilibrium at 10 min, and (iv) saturation and response inversion at 15 min. This progression can be understood as the sensor material transitioning from an ideal surface with abundant reactive oxygen (at start) to a surface that is progressively reduced and saturated by ammonia. The negative response at 15 min is a clear sign of sensor saturation, where additional reducing gas no longer yields a typical n-type response.

Notably, such behavior is rarely reported in short laboratory tests but is crucial for real-world sensing scenarios. It suggests that for long-term monitoring, either periodic sensor regeneration (e.g., exposure to clean air or mild heating to desorb residues) is necessary, or one should limit the sensor's exposure time within a regime that avoids complete saturation. The use of silica in our composite might contribute to the saturation effect as well – silica surfaces could hold NH_3 or moisture strongly over time, hindering the replenishment of oxygen on CeO_2. In future designs, optimizing the silica content or adding catalytic additives (e.g., Pt, as often done with MOX sensors [9]) could help mitigate such saturation.

Comparatively, the performance of our sensor in the initial phases is highly encouraging. Achieving >600% response to ammonia at room temperature with a simple composite (and without noble metal catalysts) is a testament to the synergy of the CeO_2–SiO_2 system. Other recent developments, like Fe/Cd co-doped CeO_2, have reported even higher responses (e.g. a response ~5004 to 200 ppm NH_3) but required careful doping strategies. Our approach uses a green-synthesized silica to achieve substantial sensitivity, highlighting that even *bio-silica* can serve effectively in sensor composites. Under the present test conditions, the sensors prepared using chemical-route silica and green-route silica showed broadly similar response patterns. However, because the number of tested devices was limited, these results should be considered a feasibility demonstration rather than proof of equivalent performance. This is an important validation of the green silica's applicability. Any slight variations (such as perhaps surface area differences) could influence absolute response magnitudes, but within the qualitative scope of our study, both routes produced sensors that behave similarly. The comparison between chemically synthesized silica and green-synthesized silica should be considered preliminary. In this study, the response trends were compared under the same general fabrication and testing procedure, but a rigorous statistical comparison was not performed. Multiple sensors from each group, baseline resistance distribution, mean response values, standard deviation, and significance testing would be required to confirm whether both routes truly show equivalent performance.

Overall, the results demonstrate that silica–modified CeO_2 composites are capable of detecting ammonia at room temperature with high sensitivity. The time-evolution of the sensor response provides insight into the surface chemistry dynamics, and the eventual saturation warns of the need for calibrated operation. These findings contribute to the understanding of how integrating a sustainable silica source with a metal oxide can yield a functional sensor, while also pointing out the practical considerations for deploying such sensors in real conditions.

4. Limitations of the Study. - While the silica–ceria NH_3 sensor demonstrated promising performance, several limitations must be acknowledged:

- **Qualitative Gas Exposure:** The ammonia sensing tests in this study were conducted without a calibrated gas flow or known concentration. NH_3 was introduced by evaporation from a solution in a sealed chamber, which provides an unquantified concentration of ammonia. Consequently, we report response trends (percentage change in resistance) rather than sensitivity to a specific ppm level. The lack of precise concentration control

means we cannot construct a response vs. concentration curve or determine a limit of detection. In practical sensor development, a controlled test (using mass flow controllers to mix known ppm of NH_3 in air) is essential for calibration. Our results are thus qualitative – they confirm ammonia detection and relative response behavior, but do not yield data on minimum detectable concentration or linear range. Future work should include quantitative gas dosing to fully evaluate the sensor's sensitivity and selectivity.

- **Absence of Structural Phase Confirmation (XRD):** We did not perform X-ray diffraction analysis on the synthesized composites. As a result, the crystallographic structure and phase purity of CeO_2 in the composite were not directly confirmed. We assumed the formation of CeO_2 based on the precursor and conditions, and the EDS elemental analysis supports this. However, without XRD we cannot ascertain the crystallite size or whether any Ce silicate phases formed at the interface. The decision to omit XRD was made to focus on functional testing and because the silica is largely amorphous (which would produce a broad background in XRD). This is a limitation because crystallinity can affect gas sensing properties. In future studies, performing XRD would be useful to correlate the sensor performance with any phase information (e.g., confirming nanoscale CeO_2 fluorite structure). Nonetheless, the significant sensor response observed suggests that the active CeO_2 phase was present and operative. In addition, SEM and EDS alone could not confirm the CeO_2 crystalline phase, Ce^{3+}/Ce^{4+} ratio, oxygen vacancy concentration, or silica–ceria interface chemistry. Further characterization such as XRD, XPS, BET surface area analysis, and interface-focused analysis is important to fully confirm the structure and sensing mechanism of the composite. BET surface area and pore-size analysis were not performed in this study. Therefore, the role of silica in increasing surface area, porosity, and gas diffusion was not directly confirmed by experimental surface area data. In this manuscript, these effects were discussed only as possible contributions based on the known behavior of silica-containing oxide composites and the observed SEM morphology. Future work should include BET and pore-size analysis to directly relate surface area and porosity to NH_3 sensing performance.

- **Surface Saturation and Recovery:** As observed in the 15 min exposure test, the sensor can become saturated by ammonia, leading to an inverted (negative) response and incomplete recovery. This indicates a limitation in long-term stability under continuous exposure. The irreversible adsorption of NH_3 or its by-products on the sensor surface can degrade performance and require intervention (e.g., cleaning or reactivation by heating in air). In a practical scenario, sensors would likely be exposed to fluctuating concentrations rather than constant high levels of NH_3 for 15 minutes, but the result highlights the need for either periodic regeneration or operational protocols (like exposure cycles within a safe duration). Our study did not investigate the long-term repeatability or stability beyond the single sequence of exposures. It is possible that repeated exposure/recovery cycles could gradually change the baseline or response (sensor drift). This was not characterized here and remains as future work. In addition, because NH_3 concentration and humidity were not controlled, the negative response after prolonged exposure may also include the effects of baseline drift, moisture variation, chamber atmosphere changes, or measurement artifacts. The response calculation is also sensitive to the selected air baseline resistance; therefore, incomplete recovery or baseline drift during the test may have affected the calculated response values, including the negative response observed after 15 min.

- **Lack of Selectivity Tests:** We focused solely on ammonia sensing in this work. The selectivity of the silica–CeO_2 sensor towards NH_3 over other gases (like humidity, CO_2, ethanol, NO_2, etc.) was not evaluated. CeO_2 is known to also respond to other reducing gases (and to a lesser extent oxidizing gases), and the presence of silica might introduce sensitivity to moisture (due to hydrophilic silanol groups). Without selectivity data, it is uncertain how the sensor would perform in complex atmospheres. For instance, a real air environment with humidity could affect the baseline and response amplitude (water molecules can occupy sites or react with ammonia to form ammonium hydroxide on the surface). Future investigations should include tests with common interfering gases and varying humidity to determine the sensor's selectivity profile. Techniques such as surface functionalization or operating the sensor in pulsed mode (as some studies do) might be required to enhance selectivity. For room-temperature NH_3 sensing, humidity effects and cross-sensitivity to common gases are especially important. In this study, a humidity-response test and selectivity matrix against common interferents were not performed. Therefore, no claim is made regarding humidity tolerance or selective NH_3 detection in complex gas environments. Future work should include testing at different relative humidity levels and against common interfering gases such as CO_2, ethanol, NO_2, CO, and other volatile compounds to confirm practical selectivity.

- **Reproducibility and Sample Variability:** Due to resource constraints, we tested a limited number of sensor devices. The data presented are representative of the observed behavior, but we have not performed a

statistical analysis over many devices or multiple batches of materials. There may be variability in the silica produced by the green route (depending on bagasse source or processing) which could affect sensor performance consistency. Ensuring reproducible synthesis, especially for the green-silica, is a challenge – slight changes in bagasse composition or processing temperature could alter the surface area or impurity content of the silica. Our results show feasibility, but scalability would require careful standardization of the green synthesis protocol. In addition, device-to-device variability, repeated exposure–recovery cycles, recovery time after each NH_3 exposure, and aging stability were not evaluated in this study. Therefore, the reported sensing results should be considered initial proof-of-concept behavior under the tested conditions. Further work should include multiple devices, cyclic response testing, recovery-time measurement, and long-term aging studies to confirm reproducibility and practical stability.

In summary, while the study successfully demonstrates a proof-of-concept sensor using green-sourced silica, the above limitations suggest caution. The device is at a prototype stage: it works under the conditions tested, but further refinement and characterization (quantitative calibration, selectivity, stability) are needed before it could be deployed as a reliable NH_3 sensor. Addressing these limitations will be important for future research. For instance, performing calibrated tests could reveal the actual sensitivity (e.g., what ppm gives a 100% response, etc.) and whether the green-silica sensor meets required detection limits (typical safety thresholds for NH_3 are tens of ppm). Despite these limitations, the study provides valuable insights – particularly the observation of time-dependent response evolution – that can guide the development of robust gas sensors using sustainable materials.

5. Conclusions. - In this work, we synthesized silica nanoparticles via two routes – a conventional chemical method and an agricultural waste-derived green method – and utilized both types of silica to create silica–modified CeO_2 nanostructures for ammonia gas sensing at room temperature. The study was framed to compare the applicability of chemically produced versus "green" silica in functional sensor devices. Key conclusions are as follows:

- Sustainable Silica Synthesis: Sugarcane bagasse, an abundant agricultural by-product, was successfully converted into nanosilica using a simple acid/base extraction approach. The green-sourced silica was obtained after acid leaching and calcination, and its successful incorporation into the sensor demonstrates the feasibility of using agricultural waste-derived silica in silica-modified CeO_2 gas sensors. However, because only a limited number of devices were tested, this study does not claim statistical equivalence between the green and chemical silica routes. This demonstrates the feasibility of a circular economy approach where agricultural waste is repurposed into value-added nanomaterials for advanced applications.

- Composite Nanostructure Formation: Both types of silica were effectively integrated with cerium oxide to form CeO_2–SiO_2 composite nanoparticles. SEM characterization revealed an elongated, rod-like morphology of ceria on a porous silica matrix. The ceria formed elongated, micron-scale rod-like structures, likely composed of intergrown nanoscale CeO_2 crystallites rather than isolated particles, indicating strong interactions between CeO_2 and the silica template. EDS analysis confirmed a silica-rich composition with cerium present (Si ~42 wt%, Ce ~7 wt%), suggesting a structure where CeO_2 is dispersed as a thin layer or clusters on silica. The absence of any foreign elements in EDS and the known chemistry confirm that the composite consisted of SiO_2 and CeO_2 (with oxygen from both), fulfilling the material design. Although XRD was not performed, the successful sensor performance and literature support imply that the CeO_2 is present in its active oxide form.

- Room-Temperature NH_3 Sensing Performance: The fabricated silica–ceria sensors showed a strong chemiresistive response to ammonia at room temperature. Upon NH_3 exposure, the n-type composite's resistance decreased substantially, yielding a high gas response. Initial exposures produced responses on the order of 600–650% within seconds, highlighting the sensor's high sensitivity and fast kinetics at ambient conditions. This performance is notable since many pure metal oxide sensors require elevated temperatures to reach similar sensitivity. The enhanced response is attributed to the synergy of CeO_2's catalytic redox activity with silica's high surface area and morphological stabilization, which together facilitate efficient NH_3 adsorption and reaction at low temperature. We found that the sensor's response was reproducible across both silica sources – indicating that green silica is a viable alternative to chemically synthesized silica in this context, with no observed loss of performance. However, this comparison should be considered preliminary because multiple devices from each synthesis route were not tested statistically. Further work using several sensors, baseline resistance comparison, mean response values, standard deviation, and significance testing is required to confirm whether the green-silica and chemical-silica routes give equivalent sensor performance.

- Time-Dependent Response Evolution: A novel observation in this study is the evolution of the sensor's response over prolonged NH_3 exposure (0–15 min). Initially, the sensor's response was positive and large. As exposure continued, the response dynamics became complex, showing peaks, partial recovery, and oscillations, and by 15 minutes the sensor exhibited a negative response (resistance higher in NH_3 than in air). We interpret this behavior as a result of surface saturation and prolonged electron donation: essentially, the sensor surface became fully saturated with adsorbates (and oxygen vacancies fully filled), so the normal sensing mechanism (which relies on available O^- species) was impaired. The negative response (~–11%) at 15 min suggests that further NH_3 caused additional electron accumulation or a change in surface conduction (possibly through the formation of less-conductive surface compounds), which is consistent with a sensor poisoning or flooding scenario. This finding underscores the importance of considering exposure time in sensor operation – short exposures can be reliably detected with big signals, but continuous exposure can lead to signal rollover or drift. In practical use, either sensors should be regenerated periodically or exposure should be cycled to avoid this saturation. Our work provides a clear example of this phenomenon for ammonia on a ceria-based sensor, complementing prior reports of long-exposure effects in other systems.

- Environmental and Practical Implications: The successful use of bagasse-derived silica in a functional sensor highlights the potential of green nanomaterials in electronic applications. We effectively demonstrated that a waste product can replace a conventionally produced material without sacrificing device performance. This aligns with sustainable development goals by reducing the need for hazardous chemicals and leveraging renewable resources. The sensor developed operates at room temperature, meaning it has low power requirements and is suitable for ambient monitoring (important for safety in agricultural storage, industrial refrigeration, etc., where NH_3 leaks are a concern). The high sensitivity observed indicates that even trace levels of NH_3 (certainly in the low ppm range or below) should be detectable, though calibration is needed.

- Future Work: To move toward practical deployment, future studies should calibrate the sensor response to known NH_3 concentrations and evaluate its selectivity against other gases (such as humidity, which can be a significant interferent for metal-oxide sensors). Long-term stability tests, including cyclic exposures and regeneration techniques, will also be important to address the saturation issue observed. Additionally, incorporating microheaters for periodic high-temperature pulses or UV illumination could help restore the sensor surface after exposure, if continuous operation in NH_3 is required. From a materials perspective, exploring different CeO_2:SiO_2 ratios or doping CeO_2 within this composite (e.g., with a catalyst like Pt or a dopant to increase vacancy concentration) might further enhance performance or mitigate saturation. Nonetheless, the core finding remains that integrating green-synthesized silica with ceria yields a high-performance sensor.

In conclusion, this research demonstrates a viable path for green sensor development: using silica from agricultural waste to fabricate a sensitive room-temperature gas sensor. The silica–modified CeO_2 composites achieved efficient, rapid detection of ammonia, comparable to sensors made with conventional materials. The study provides insights into sensor behavior under extended exposure, a factor often overlooked, by revealing how response can diminish or invert when the sensor surface becomes saturated. By addressing these insights and limitations, the approach outlined here can be advanced toward robust, eco-friendly gas sensing systems for environmental monitoring and safety applications.

Acknowledgement. - During the preparation of this work, the authors used ChatGPT 4.0 to refine writing and improve readability. The authors have reviewed and edited the AI-generated content as necessary and take full responsibility for the contents of this publication.

References

[1] A. A. Nayl, A. I. Abd-Elhamid, A. A. Aly, and S. Bräse, "Recent progress in the applications of silica-based nanoparticles," RSC Adv., vol. 12, no. 22, pp. 13706-13726, 2022, https://doi.org/10.1039/D2RA01587K
[2] N. Shafiei, M. Nasrollahzadeh, and S. Iravani, "Green Synthesis of Silica and Silicon Nanoparticles and Their Biomedical and Catalytic Applications," Comments Inorg. Chem., vol. 41, no. 6, pp. 317-372, Nov. 2021, https://doi.org/10.1080/02603594.2021.1904912
[3] N. S. Seroka, R. Taziwa, and L. Khotseng, "Green Synthesis of Crystalline Silica from Sugarcane Bagasse Ash: Physico-Chemical Properties," Nanomaterials, vol. 12, no. 13. p. 2184, 2022. https://doi.org/10.3390/nano12132184
[4] D. Kirubakaran et al., "A Comprehensive Review on the Green Synthesis of Nanoparticles: Advancements in Biomedical and Environmental Applications," Biomed. Mater. Devices, vol. 4, no. 1, pp. 388-413, 2026, https://doi.org/10.1007/s44174-025-00295-4
[5] M. M. Abady, D. M. Mohammed, T. N. Soliman, R. A. Shalaby, and F. A. Sakr, "Sustainable synthesis of nanomaterials using different renewable sources," Bull. Natl. Res. Cent., vol. 49, no. 1, p. 24, 2025, https://doi.org/10.1186/s42269-025-01316-4
[6] D. A. Gkika, K. N. Maroulas, and G. Z. Kyzas, "Various Reduced Graphene Oxide Green Synthetic Routes: Comparing the Cost Procedures," ACS Omega, vol. 10, no. 32, pp. 36221-36237, Aug. 2025, https://doi.org/10.1021/acsomega.5c04090
[7] J. Wang et al., "Enhanced NH3 gas-sensing performance of silica modified CeO2 nanostructure based sensors," Sensors Actuators B Chem., vol. 255, pp. 862-870, 2018, https://doi.org/10.1016/j.snb.2017.08.149
[8] S. Subramanian, K. Neyvasagam, S. Valanarasu, V. Ganesh, I. S. Yahia, and R. Ade, "Room temperature ammonia gas sensor based on Ti-doped CeO2 thin films prepared by nebulizer spray pyrolysis method," Appl. Phys. A, vol. 131, no. 6, p. 457, 2025, https://doi.org/10.1007/s00339-025-08569-w
[9] M. Torkamani Cheriani, A. Mirzaei, and J.-H. Kim, "Resistive-Based Nanostructured CeO2 Gas Sensors: A Review," Chemosensors, vol. 13, no. 8. p. 298, 2025. https://doi.org/10.3390/chemosensors13080298
[10] M. Akbari-Saatlu et al., "Silicon Nanowires for Gas Sensing: A Review," Nanomaterials, vol. 10, no. 11. p. 2215, 2020. https://doi.org/10.3390/nano10112215
[11] M. N. Yaqueen, A. Kuity, and M. A. Ahmed, "Sustainable Nano Silica Production from Agricultural Residues: A Review of Green Synthesis Techniques and Performance in Asphalt Applications," Int. J. Pavement Res. Technol., 2025, https://doi.org/10.1007/s42947-025-00585-6
[12] M. Abdul Sattar, "Circular Economy in Action: Green Synthesis of Mesoporous Silica Nanoparticles from Rice Husk Waste for Biomedical and Industrial Applications," ACS Sustain. Chem. Eng., vol. 13, no. 20, pp. 7617-7630, May 2025, https://doi.org/10.1021/acssuschemeng.5c02582
[13] R. S. Aashikha Shani and A. R. Jeice, "Introspect of prying out silica from agricultural wastes by various methods and incorporating them in distinct uses," Biomass Convers. Biorefinery, vol. 15, no. 4, pp. 5089-5109, 2025, https://doi.org/10.1007/s13399-024-05360-4
[14] I. Kitsou, P. Panagopoulos, T. Maggos, and A. Tsetsekou, "ZnO-coated SiO2 nanocatalyst preparation and its photocatalytic activity over nitric oxides as an alternative material to pure ZnO," Appl. Surf. Sci., vol. 473, pp. 40-48, 2019, https://doi.org/10.1016/j.apsusc.2018.12.146
[15] B.-H. Jang, O. Landau, S.-J. Choi, J. Shin, A. Rothschild, and I.-D. Kim, "Selectivity enhancement of SnO2 nanofiber gas sensors by functionalization with Pt nanocatalysts and manipulation of the operation temperature," Sensors Actuators B Chem., vol. 188, pp. 156-168, 2013, https://doi.org/10.1016/j.snb.2013.07.011
[16] D. E. Newbury* and N. W. M. Ritchie, "Is Scanning Electron Microscopy/Energy Dispersive X-ray Spectrometry (SEM/EDS) Quantitative?," Scanning, vol. 35, no. 3, pp. 141-168, May 2013, https://doi.org/10.1002/sca.21041
[17] H. Mei, F. Zhang, T. Zhou, and T. Zhang, "Pulse-Driven MEMS NO2 Sensors Based on Hierarchical In2O3 Nanostructures for Sensitive and Ultra-Low Power Detection," Sensors, vol. 24, no. 22. p. 7188, 2024. https://doi.org/10.3390/s24227188
[18] M. A. Takte, N. N. Ingle, B. N. Dole, M.-L. Tsai, T. Hianik, and M. D. Shirsat, "A stable and highly-sensitive flexible gas sensor based on Ceria (CeO2) nano-cube decorated rGO nanosheets for selective detection of NO2 at room temperature," Synth. Met., vol. 297, p. 117411, 2023, https://doi.org/10.1016/j.synthmet.2023.117411
[19] D.-H. Gao et al., "Advances in modification of metal and noble metal nanomaterials for metal oxide gas sensors: a review," Rare Met., vol. 44, no. 3, pp. 1443-1496, 2025, https://doi.org/10.1007/s12598-024-03027-7
[20] Z. Tian, J. Li, Z. Zhang, W. Gao, X. Zhou, and Y. Qu, "Highly sensitive and robust peroxidase-like activity of porous nanorods of ceria and their application for breast cancer detection," Biomaterials, vol. 59, pp. 116-124, 2015, https://doi.org/10.1016/j.biomaterials.2015.04.039
[21] X. Tong, W. Shen, X. Chen, and J.-P. Corriou, "A fast response and recovery H2S gas sensor based on free-standing TiO2 nanotube array films prepared by one-step anodization method," Ceram. Int., vol. 43, no. 16, pp. 14200-14209, 2017, https://doi.org/10.1016/j.ceramint.2017.07.165

[22] D. Chen, J. Chen, W. Zhou, and A. Sawut, "Preparation of the New Magnetic Nanoadsorbent Fe3O4@SiO2-yl-VP and Study on the Adsorption Properties of Hg (II) and Pb (II) in Water," Magnetochemistry, vol. 10, no. 12. p. 105, 2024. https://doi.org/10.3390/magnetochemistry10120105
[23] Mallikarjun, K. Gangareddy, and M. V. R. Reddy, "Synthesis of Fe and Cd co-doped CeO2 nanoparticles for highly responsive room temperature ammonia gas sensing application," J. Mater. Sci. Mater. Electron., vol. 35, no. 27, p. 1830, 2024, https://doi.org/10.1007/s10854-024-13591-4
[24] Y. Wang et al., "NH3 gas sensing performance enhanced by Pt-loaded on mesoporous WO3," Sensors Actuators B Chem., vol. 238, pp. 473-481, 2017, https://doi.org/10.1016/j.snb.2016.07.085
[25] Y. Liu et al., "Sulfonic acid-functionalized spiropyran colorimetric gas-sensitive aerogel for real-time visual ammonia sensing," Chem. Eng. J., vol. 511, p. 162160, 2025, https://doi.org/10.1016/j.cej.2025.162160
[26] G. Verma and A. Gupta, "Functional quantum dots: advances and emerging directions for enhanced sensing applications," Nanotechnology, vol. 37, no. 1, p. 12002, 2026, https://doi.org/10.1088/1361-6528/ae2ae3
[27] L. A. September, N. Kheswa, N. S. Seroka, and L. Khotseng, "Green synthesis of amorphous silica nanoparticles (SiO2NPs) from sugarcane bagasse ash by sol-gel method," Next Mater., vol. 10, p. 101396, 2026, https://doi.org/10.1016/j.nxmate.2025.101396
[28] X. He et al., "Polydopamine-coated cerium oxide core-shell nanoparticles for efficient and non-damaging chemical-mechanical polishing," Dalt. Trans., vol. 54, no. 10, pp. 4151-4158, 2025, https://doi.org/10.1039/D4DT03546A
[29] N. Križaj Kosi, J.-S. Pavelić, M. Grilc, S. Gyergyek, and D. Makovec, "Synthesis of a magnetically heatable ceria-supported ruthenium catalyst via deposition of nanocrystalline ceria on silica-coated magnetic iron-oxide nanoparticles," J. Phys. Chem. Solids, vol. 212, p. 113517, 2026, https://doi.org/10.1016/j.jpcs.2026.113517
[30] C. Zhu, D. Li, H. Zhang, D. Zhang, N. Su, and F. Xu, "Effect of montmorillonite-loaded CeO2 nanocomposites with different CeO2 contents on thermal-oxidative and ultraviolet aging properties of asphalt," Constr. Build. Mater., vol. 507, p. 145057, 2026, https://doi.org/10.1016/j.conbuildmat.2025.145057
[31] A. İ. Vaizoğullar, A. Balci, I. Kula, and M. Uğurlu, "Preparation, characterization, and adsorption studies of core@shell SiO2 @ CeO2 nanoparticles: a new candidate to remove Hg (II) from aqueous solutions," Turkish J. Chem., vol. 40, no. 4, pp. 565-575, 2016. https://doi.org/10.3906/kim-1507-7
[32] E. S. Cama, M. Pasini, U. Giovanella, and F. Galeotti, "Crack-Templated Patterns in Thin Films: Fabrication Techniques, Characterization, and Emerging Applications," Coatings, vol. 15, no. 2. p. 189, 2025. https://doi.org/10.3390/coatings15020189
[33] G. Jeerh, "Material and design optimisation of low temperature direct ammonia fuel cells." University of Warwick, 2022.
[34] B. A. Omran, Nanobiotechnology: a multidisciplinary field of science. Springer, 2020. https://doi.org/10.1007/978-3-030-46071-6
[35] J. S. Bates, "Structure and Solvation of Confined Water and Alkanols in Zeolite Acid Catalysis." Purdue University, 2019.
[36] Y. He et al., "Advances in ammonia (NH3) adsorption and storage: materials, mechanisms, and applications," Adsorption, vol. 31, no. 2, p. 48, 2025, https://doi.org/10.1007/s10450-025-00601-y

Author contribution:
1. Conception and design of the study
2. Data acquisition
3. Data analysis
4. Discussion of the results
5. Writing of the manuscript
6. Approval of the last version of the manuscript

DM has contributed to: 1, 2, 3, 4, 5 and 6.
SSZZ has contributed to: 1, 2, 3, 4, 5 and 6.
SMM has contributed to: 1, 2, 3, 4, 5 and 6.
MSAA has contributed to: 1, 2, 3, 4, 5 and 6.
AAZ has contributed to: 1, 2, 3, 4, 5 and 6.

Acceptance Note: This article was approved by the journal editors Dr. Rafael Sotelo and Mag. Ing. Fernando A. Hernández Gobertti.

System-Level Design and Outdoor Validation of a Solar-Powered Mobile Robot for Autonomous Environmental Monitoring

Diseño a Nivel de Sistema y Validación en Exteriores de un Robot Móvil Solar para la Monitorización Ambiental Autónoma

Projeto ao Nível do Sistema e Validação Externa de um Robô Móvel Alimentado a Energia Solar para Monitorização Ambiental Autónoma

Halar Mustafa [1], Sadiq Ur Rehman [2 (*)], Muhammad Ahsan Shaikh [3]

Recibido: 27/01/2026 Aceptado: 30/03/2026

Summary. - The need to explore and use mobile robots outside is rising, mainly in terms of monitoring the environment and conducting inspections outside grid resources, where energy autonomy, terrain variability, and communication are essential. The purpose of this paper is to propose an innovative solar-powered mobile robot that integrates solar energy harvesting, four-wheel drive, two channels of wireless communication, and passive thermal management. The majority of previous works emphasized and focused on single components and experimental investigations, while this paper instead focuses on experience with practical implementations of these technologies outside, thereby gaining experience with similar robots outside, leading to observations on energy efficiency, movement, control, and communication, with possible implications for improving the next generation of robots outside. The experiment outside using various terrain types of grass, gravel, and earth successfully proved the positive energy balance of the robot, easy energy-efficient motion, good wireless control, and good wireless video streaming with little delay.

Keywords: *Solar-powered robots, Terrain-adaptive locomotion, Energy harvesting, Autonomous mobile robots, Off-grid monitoring.*

(*) Corresponding author.

[1] Master of Engineering, Faculty of Engineering Sciences & Technology, Hamdard University (Pakistan), halar.mustafa@hamdard.edu.pk, ORCID iD: https://orcid.org/0000-0002-7021-5010

[2] PhD, Associate Professor, Faculty of Engineering Science and Technology, Iqra University (Pakistan), sadiq.rehman@iqra.edu.pk. ORCID iD: https://orcid.org/0000-0002-6308-450X

[3] PhD, Lecturer, Faculty of Engineering Sciences & Technology, Hamdard University (Pakistan), muhammad.ahsan@hamdard.edu.pk, ORCID iD: https://orcid.org/0000-0003-2408-5689

Memoria Investigaciones en Ingeniería, núm. 30 (2026). pp. 164-176
https://doi.org/10.36561/ING.30.11
ISSN 2301-1092 • ISSN (en línea) 2301-1106 – Universidad de Montevideo, Uruguay

Resumen. - *La necesidad de explorar y utilizar robots móviles en exteriores es cada vez mayor, principalmente para la monitorización del entorno y la realización de inspecciones fuera de la red eléctrica, donde la autonomía energética, la variabilidad del terreno y la comunicación son esenciales. El objetivo de este trabajo es proponer un innovador robot móvil solar que integra la captación de energía solar, tracción en las cuatro ruedas, dos canales de comunicación inalámbrica y gestión térmica pasiva. La mayoría de los trabajos previos se centraban en componentes individuales e investigaciones experimentales, mientras que este trabajo se centra en la experiencia con implementaciones prácticas de estas tecnologías en exteriores, obteniendo así experiencia con robots similares en exteriores, lo que ha llevado a observaciones sobre eficiencia energética, movimiento, control y comunicación, con posibles implicaciones para la mejora de la próxima generación de robots en exteriores. El experimento en exteriores, utilizando diversos tipos de terreno como césped, grava y tierra, demostró con éxito el balance energético positivo del robot, su fácil movimiento con eficiencia energética, su buen control inalámbrico y su buena transmisión de vídeo inalámbrica con poca latencia.*

Palabras clave: *Robots alimentados con energía solar, Locomoción adaptativa al terreno, Recolección de energía, Robots móviles autónomos, Monitoreo fuera de la red.*

Resumo. ***-*** *A necessidade de explorar e utilizar robôs móveis em ambientes exteriores é crescente, principalmente para monitorizar o ambiente e realizar inspeções em locais sem acesso à rede elétrica, onde a autonomia energética, a variabilidade do terreno e a comunicação são essenciais. O objetivo deste artigo é propor um robô móvel inovador alimentado a energia solar que integra a captação de energia solar, tração às quatro rodas, dois canais de comunicação sem fios e gestão térmica passiva. A maioria dos trabalhos anteriores enfatizou e focou-se em componentes individuais e investigações experimentais, enquanto este artigo se centra na experiência com implementações práticas destas tecnologias em ambientes exteriores, adquirindo experiência com robôs semelhantes em ambientes exteriores, o que leva a observações sobre eficiência energética, movimento, controlo e comunicação, com possíveis implicações para a melhoria da próxima geração de robôs para uso exterior. A experiência externa, utilizando vários tipos de terreno (relva, cascalho e terra), comprovou com sucesso o balanço energético positivo do robô, a facilidade de movimento com eficiência energética, o bom controlo sem fios e a boa transmissão de vídeo sem fios com baixa latência.*

Palavras-chave: *Robôs movidos a energia solar, Locomoção adaptativa ao terreno, Captação de energia, Robôs móveis autónomos, Monitorização fora da rede elétrica.*

1. Introduction. - Outdoor mobile robots are being used in environmental monitoring, precision agriculture, surveillance, and inspecting infrastructural facilities, among others [1]. Such robots should be able to function well in unstructured, or off-grid environments characterized by energy autonomy, terrain flexibility, and effective communication. Typically, battery-powered robots have short missions and require quite regular servicing, particularly when they are required to operate in remote areas [2].

Solar energy harvesting has an excellent potential as a method for extending operational endurance while minimizing human intervention. However, the integration of photovoltaic (PV) systems in mobile platforms involves issues related to variable energy supply, charging efficiency, and real-time energy management [3]. Wheeled robots remain mechanically simple and energy-efficient but often suffer from performance degradation on soft or uneven terrain owing to slippage and increased power demands [4-5].

Previous research in the field of solar-powered robots has involved investigations into PV modules, energy storage, power electronics, suspension, and communication technologies. However, most studies are confined either to single subsystems or controlled laboratory conditions, or indeed specialized applications, thus providing very limited insight into system-level integration in real-life conditions. Energy harvesting, terrain-adaptive locomotion, wireless communication, and thermal performance experimental validation of a completely functional robot has barely been investigated.

This paper will address these gaps through the system-level design and outdoor evaluation of a solar-powered, terrain-adaptive mobile robot for off-grid monitoring. The approach emphasizes practical integration over component-level innovation through a holistic platform that combines photovoltaic energy harvesting, battery storage, four-wheel-drive locomotion, dual-channel wireless communication, and passive thermal management. Experimental validation across multiple terrains is presented; interaction between energy generation, terrain-dependent mobility, communication performance, and thermal stability is quantified.

The contributions of this work are highlighted as follows:

- A modular system-level architecture integrating energy harvesting, locomotion, communication, and thermal management.
- Outdoor experiments on grass, gravel, and dirt with evaluation of energy harvesting and consumption, mobility, communication latency, and thermal behaviour.
- Practical insights on trade-offs between energy autonomy, terrain adaptability, and communication reliability for off-grid monitoring robots.

2. Literature Review. - Outdoor-deployed mobile robots face challenges in terms of energy autonomy, terrain adaptability, and wireless communication. The lack of grid power supply in an outdoor environment has encouraged researchers to explore alternative sources of energy, such as renewable energy sources, especially PV systems, for efficient energy autonomy with low human intervention. Even though various reviews have been conducted on the integration of PV systems and energy efficiency, they have been more theoretical and have limited practical applications.

Practical applications of solar-powered robotics include agricultural field robots, transport robots, and experimental robots. Solar-powered surveillance robots have been found to have the potential to charge the battery while moving on any terrain in real field conditions [6]. General-purpose robots used in agricultural applications use solar power to perform several operations, including irrigation, sowing, and crop monitoring [7]. Even simple robots have been used to validate the practical applications of solar-powered robots [8-10]. Moreover, solar-powered robots have also been used for marine and industrial monitoring, which can ensure very long duration and autonomous operations [11].

Despite all these advancements, energy harvesting along with terrain-dependent mobility, wireless communication, and thermal behavior, in a unified and integrated manner, has rarely been addressed in existing platforms. In most research, carried out either in a laboratory environment or in applications where the scope of generalization is limited, subsystems have been addressed in an isolated manner. Quantitative analysis of energy balance considering load variation due to terrain has rarely been addressed. The aim of this paper is to bridge this gap by proposing a unified system design, keeping in view deployability, energy awareness, and experimentation.

Ref	Platform / Robot	Application	Solar System	Mobility / Locomotion	Key Focus / Findings	Limitations
[6]	Surveillance Robot	Agricultural field monitoring	PV panels + battery	4WD, all-terrain	Demonstrated feasibility of solar-charging for multi-day outdoor operation	Limited terrain types, short-term field test
[7]	Review of PV systems	General robotics / energy harvesting	PV-based energy harvesting	Various	Comprehensive overview of PV integration and energy management	Mostly theoretical, limited experimental robotics data
[8]	Multipurpose agricultural robot	Irrigation, seeding, crop monitoring	PV + battery	Wheeled, Bluetooth/Android control	Real-world integration with IoT & solar harvesting	Short-term testing, limited terrain adaptability
[9]	RC autonomous robot	Educational / experimental	PV + battery	Wheeled	Demonstrated low-cost solar-powered operation	No long-duration field validation
[10]	Smart farming robot	Multi-purpose precision agriculture	PV + battery	Wheeled	Integration with IoT and computer vision for energy-aware operation	Tested in controlled field plots; scalability unclear
[11]	RaccoonBot	Environmental monitoring	PV panels + tracking	Wire-traversing robot	Autonomous solar tracking, persistent monitoring	Complex setup, high-cost, not general-purpose

Table I: Summary of Relevant Research

3. System Architecture. - In this section, the system-level architecture of the proposed solar-powered mobile robot designed to operate in territories varying in topology is introduced. The architectures incorporate integration in renewable energy harvesting, power, mobility, and wireless communication. In contrast to architectures designed to optimize each functional component, this proposed architecture is designed to work together in real-world conditions, where renewable energy availability, topographic variation, and wireless communication are interrelated.

Figure I shows how the energy subsystem, control and communication subsystem, and locomotion subsystem are interlinked for this system. Table II show the hardware specification of the prototype

Subsystem	Parameter	Specification / Value
PV Panel	Rated Power	50 W
	Area	0.35 m²
	Mounting Angle	30° tilt adjustable
	Controller	MPPT Solar Charge Controller, 12 V
Battery	Chemistry	LiFePO4
	Nominal Voltage	12 V
	Capacity	12 Ah
	Maximum Continuous Discharge	10 A
	Internal Resistance	50 mΩ
	C-Rate	1 C
Mobility / Drive	Robot Mass	7 kg (including PV, battery, payload)
	Wheel Diameter	0.15 m
	Ground Clearance	0.08 m
	Gear Ratio	1:20
	Motors	4 × DC brushed, 24 W nominal, 12 V
	ESC	4 × 12 V, 15 A
	Max Torque per Motor	0.8 Nm

Sensors / Navigation	Wheel Encoders	500 CPR optical encoders
	IMU	9-axis MEMS (gyro, accel, magnetometer)
	GPS	1 Hz, horizontal accuracy ±2 m
Thermal Monitoring	Contact Thermometers	3 × PT100 sensors on motors and ESC
	Sampling Frequency	1 Hz
Communications	Bluetooth Module	HC-05, 9600 baud, SPP protocol
	Video Streaming	720p, 5 Mbps, Wi-Fi 2.4 GHz
Payload / Other	Maximum Payload	2 kg
	Total System Dimensions	0.45 m × 0.35 m × 0.25 m

Table II: Hardware Specifications

3.1 System Configuration. - The robotic platform is divided into three strongly integrated systems:

- Renewable energy and power management subsystem
- Control and communication subsystem
- Locomotion and Mechanical Subsystem

These systems run simultaneously for the purpose of constant monitoring of the outdoors. Solar power is harnessed for storing in the onboard battery bank, which in turn provides controlled power for the control electronics, motor drivers, and peripheral sensing devices. The Arduino Mega 2560 [12] acts as the main controlling system for the platform, controlling the execution of motion, monitoring, and safe handling of the system. The wireless communication module allows for low-latency command & feedback transmissions.

3.2 Renewable Energy and Power Management Subsystem. - The basis of the control system is an Arduino Mega 2560 microcontroller, which was selected because of more than one serial interface and the possibility of real-time control. This microcontroller executes all the motion instructions, detects the level of battery voltages, sets the conditions for safety, and interacts with all the other peripheral devices.

A dual wireless communication system is used to segregate the motion control and video streaming. The Bluetooth device HC-05 [13] is used to transmit the control commands through a smartphone-based application with lower latency, and a Wi-Fi IP camera is used for streaming videos. This approach allows for independence in motion control and video streaming; hence the system is less prone to interference. Such relay driver circuits are included using 2N2222 transistors [14] to connect the Arduino lower outputs to motor control paths at higher currents, thereby saving the microcontroller from undergoing motor-damaging currents.

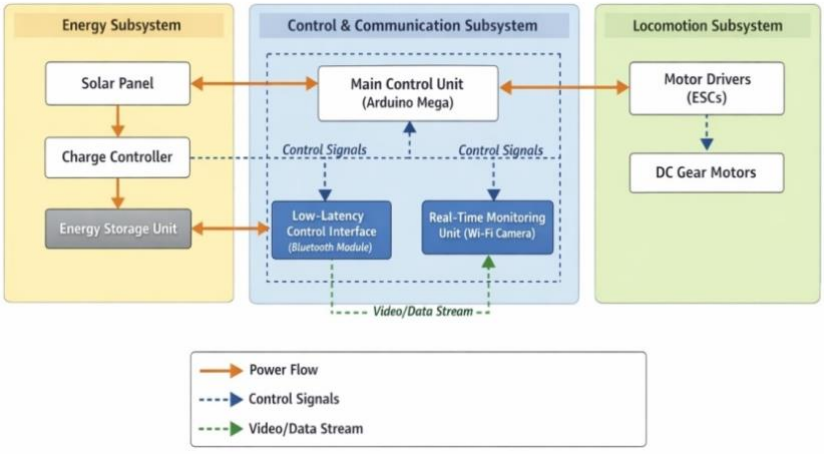

Figure I. System Block Diagram

3.3 Locomotion and Mechanical Subsystem. - The locomotion system comprises four DC gear motors with high torque. The four motors can move through a four-wheel drive mechanism. Each motor is coupled to an electronic speed controller. In this way, a constant torque is created. The four-wheel drive feature allows the robot to move effectively on grass, gravel, or untrenched soil.

The mechanical design consists of a modular PVC chassis, whose material of choice was determined by its ability to be corrosion-resistant, an electrical insulator, easy to work with, and lightweight at the same time. The solar panels, battery bank, motors, and control units are mounted inside the chassis, whose design makes its center of gravity very low to ensure stability of the entire unit while moving on slopes.

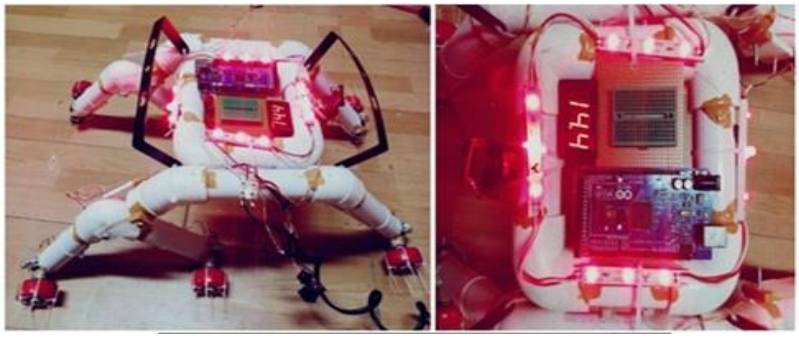

Figure II. Assembled Prototype

3.4 System Integration and Operational Flow. - Solar energy, in the operation stage, is continuously being tapped and supplied either directly to the load or stored within the battery bank, depending on the availability and demand. In the start-up stage, the Arduino initialises all the peripherals, checks the voltage levels at the batteries, and sets up wireless communication. The motion signals commanded from Bluetooth get converted into pulse-width modulation (PWM) signals to command electronic stability control (ESCs) and motors.

While doing so, it also has the ability to do live video transmission via Wi-Fi connectivity. Along with this, the situational awareness for navigation is also facilitated via this feature. The safety feature serves the purpose of constant monitoring of the communications integrity as well as the level of voltage. If the critical threshold is achieved, the system is switched to either safety mode or standby.

4. Methodology. - The methodological framework adopted in the present investigation is intended to experimentally assess the system performance of the solar-powered mobile robot. The emphasis is on the system-level performance, such as energy consumption, energy generation, terrain-based locomotion, communication, and thermal stability.

All experiments are performed outdoors to simulate the combined effects of environmental variability, terrain, and solar energy availability. The experiments are performed under clear to partly cloudy conditions, with an ambient temperature ranging from 18 °C to 32 °C and solar irradiance ranging from 550 W/m² to 950 W/m², as measured using a handheld solar irradiance meter.

4.1 Energy Measurement and Mission Profile. - Energy autonomy is defined as the ability of the robot to maintain operation using the harvested solar power, without the need to recharge the battery from an external source. Battery voltage levels (between 11.9 and 12.6 V) are monitored as an indicator of SOC, but the results are based on the amount of harvested vs. consumed energy in units of Wh rather than SOC.

A standardized mission cycle was defined:

1. Idle state, i.e., the controller and the camera are turned on (5 min)
2. Active locomotion, i.e., moving over the terrain (15 min)
3. Video streaming, i.e., sending data via Wi-Fi (15 min)
4. Solar-assisted charging, i.e., recharging phase (15 min)

The above mission cycle is repeated five times, considering the changing environment, and the results are averaged. The results were obtained from calibrated sensors.

Energy measurements were obtained from calibrated sensors:

- PV input (V_{pv}, I_{pv}) – ±0.5 % accuracy, 1 Hz sampling
- Battery current (I_{bat}) – ±0.5 % accuracy, 1 Hz sampling

Power was integrated over time to compute energy in Wh:

$$E = \sum_{k=1}^{n} \; P(t_k) \; \Delta t \qquad \text{Eq (1)}$$

where Δt is the sampling interval. The uncertainty in the measurements is expressed as the average value ± standard deviation over multiple measurements. To ensure physical consistency and auditability in the evaluation of the system's performance, the energy generated and the energy consumed have been determined and expressed as energy in Watt-hours (Wh) by calculating the time integral of the measured electrical signal.
The instantaneous power generated by the solar panels is calculated as:

$$Ppv\ (t) = Vpv\ (t) * Ipv\ (t) \qquad \text{Eq (2)}$$

where, $Vpv\ (t)$ and $Ipv\ (t)$ are the voltage and current generated by the solar panels, respectively. In the same way, the power being consumed by the system is determined as:

$$Pcons\ (t) = Vbat\ (t) * ILoad\ (t) \qquad \text{Eq (3)}$$

The net energy balance in the system is determined as:

$$Enet = EHarvested - EConsumed \qquad \text{Eq (4)}$$

The state of charge of the battery, i.e., battery SOC, has been estimated from voltage measurements within the range of 11.9 V to 12.6 V. Yet, since the SOC estimation based on voltage under load conditions depends on the internal battery resistance, it is only used qualitatively rather than quantitatively in the evaluation of the battery.

The uncertainty in the measurements results from the accuracy of the sensors, as well as the environmental conditions, but since the experiments are performed several times, the results are averaged.

4.2 Energy Storage Estimation. - The nominal estimation of the stored energy within the battery system was obtained as follows:

$$Ebat = Vbat \times Cbat \qquad \text{Eq (5)}$$

Here, $Vbat$ is the battery voltage, and $Cbat$ is the capacity rating, expressed in ampere-hours. This is the theoretical calculation, but the practical evaluation is done based on the power flow during operation.

4.3 Locomotion Performance Evaluation. - The locomotion performance of the robot was tested on various terrains such as grass, gravel, and dirt. The test was conducted on dry surfaces with a maximum slope of 15 degrees. Various parameters of the locomotion performance of the robot are speed, wheel slip, torque, turn radius, and vibration/acceleration level. To find the average linear velocity of the robot, a sensor fusion technique was used with the help of wheel encoders, a 9-axis IMU, and GPS. The values are sampled at a frequency of 50 Hz. To reduce the noise in the measurement values, a low-pass Butterworth filter with a cutoff frequency of 5 Hz was applied. To find the speed of the robot, the values are calculated over a fixed distance and then averaged out of five iterations.

Wheel slip (%) of the robot was calculated by finding the percentage deviation between the expected distance calculated by the wheel's angular velocity and the actual distance traveled by the robot on the surface using the sensor fusion technique of GPS and IMU. On the gravel surface, the wheel slip was found to be up to 12%, while on the grass and dirt surfaces, the wheel slip was negligible.

Motor torque τ was calculated using:

$$\tau = P\text{mech} / \omega \qquad \text{Eq (6)}$$

where Pmech is the mechanical power calculated from the input electrical power, corrected using an 85% drivetrain efficiency estimate, and ω is the angular velocity measured using the encoder. The above equation gives an estimation of the torque requirement over different types of terrain. The peak accelerations are measured using the onboard 9-axis IMU, operating at 50 Hz, and filtered using a low-pass filter to remove noise. The peak levels of vibration, 2.5g, are measured on uneven terrain, and the levels are high on gravel terrain.

4.4 Wireless Communication Evaluation. - The performance of the wireless communication system was tested using a dual-channel communication system, which included Bluetooth control and Wi-Fi video streaming.

For Bluetooth control, the latency (<100 ms) was tested using time-stamped control commands, which were transmitted over ≥5 trials, achieving 10-15 m range, allowing near-real-time control. Video streaming was done using the V380 Pro App, transmitting 1080p, 25 fps, 5 Mbps, using Wi-Fi 2.4 GHz. The latency of the video ranged from 0.5 to 1.5 seconds, while the variations in the quality are due to signal strength, distance (30-50 m), and environment interference.

4.5 Thermal Performance Evaluation. - Temperature readings were obtained through the use of PT100 contact thermometers, which are attached directly to the motor casing, ESC, and battery surface, ensuring good contact through thermal paste. The sampling rate was 1 Hz, and the ambient environment was maintained at a range of 18-32°C. The readings are recorded continuously throughout each experiment.

4.6 Terrain Characterization. - The experimental terrains were classified in order to study the effect of surface properties on robot performance. Three terrain types were considered:

- Grass: moderately compliant surface with good traction and low rolling resistance.
- Gravel: loose particles with higher rolling resistance, higher wheel slip (up to 12%), and uneven surface roughness.
- Dirt: compact soil with stable traction and minimal surface compliance.

All experiments were performed in dry conditions, and the slope was varied from 0° to 15° to assess the robot's locomotion over inclined surfaces. The surface roughness and compliance are also noted qualitatively. The environmental conditions, such as the ambient temperature (18–32 °C) and solar irradiance (550–950 W/m²), are also recorded to assess the energy harvesting and locomotion performance. The classification of the terrains, along with the slope, provides an repeatable method to assess the robot's performance, as indicated by parameters such as speed, torque, and slip, as well as the vibration. Figure III shows the system flow diagram for the proposed system with the experiments performed in the above cycles.

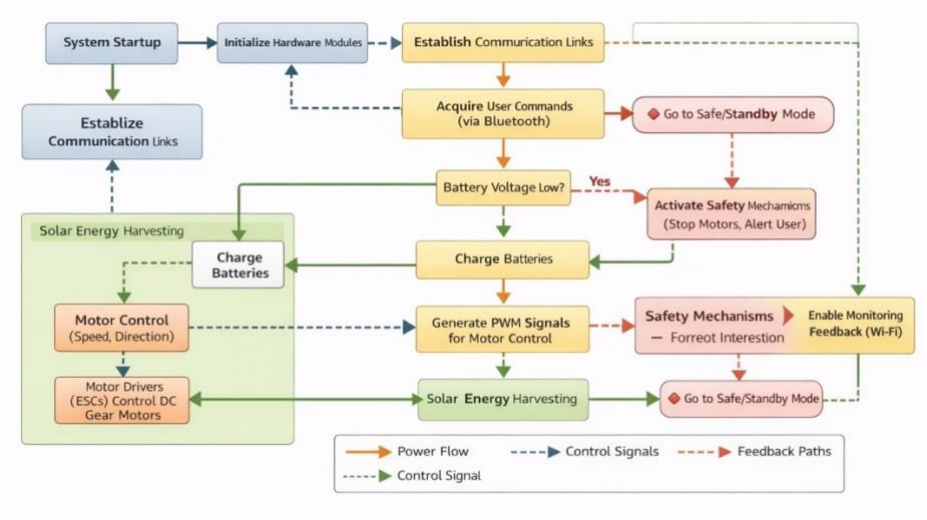

Figure III. System flow chart

5. Results. - Field experiments have been conducted to verify the capabilities of the robot in terms of its locomotion, efficiency of energy consumption, thermal properties, wireless communication, and battery charging/discharging. The experiments have been conducted on grass, gravel, earth, and rough terrain with slopes up to 15° in Karachi, Pakistan.

5.1 Energy Consumption& Thermal Characteristics. - The power consumption of the system was evaluated at three modes of operation: idle mode, locomotion mode, and video streaming mode. From Fig IV and Table III, it can be observed that the system consumed around 5 W of power during the idle mode of operation due to the controller and the camera subsystems. During the locomotion mode on flat surfaces, the system consumed on an average around 34.5 W of power, which translates into an energy consumption of 11.5 Wh during a 20-minute interval. During the

locomotion mode on gravel surfaces, the system consumed around 44.5 W of power due to the rolling resistance and wheel slips of the system, which translates into an energy consumption of 11.1 Wh during a 15-minute interval. During the video streaming mode of operation, the system consumed around 6.5 W of power, which translates into an energy consumption of 3.3 Wh during a 30-minute interval.

The thermal measurement results, as shown in Fig. V, indicate that the DC motor was subjected to an average temperature of 45 °C, with a maximum of 52 °C, while the critical temperature was 73 °C. The ESC was subjected to an average temperature of 42 °C, with a maximum of 47 °C, while the limit was 65 °C. The battery was subjected to a safe range, with an average, maximum, and limit values of 33 °C, 42 °C, and 55 °C, respectively. The placement of the sensor, sampling rate, and ambient environment were monitored for each run.

Mode	Avg Power (W)	Energy Consumed (Wh)
Idle	5.0 ± 0.2	0.42 ± 0.02 (5 min)
Locomotion (Flat)	34.5 ± 1.1	11.5 ± 0.5 (20 min)
Locomotion (Gravel)	44.5 ± 1.3	11.1 ± 0.6 (15 min)
Video Streaming	6.5 ± 0.3	3.3 ± 0.1 (30 min)

Table III. Energy comsumption of operational modes

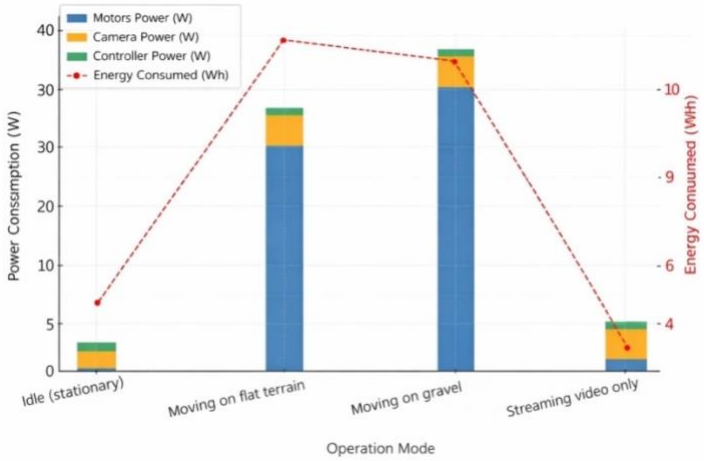

Figure IV. Energy consumption breakdown by operation mode

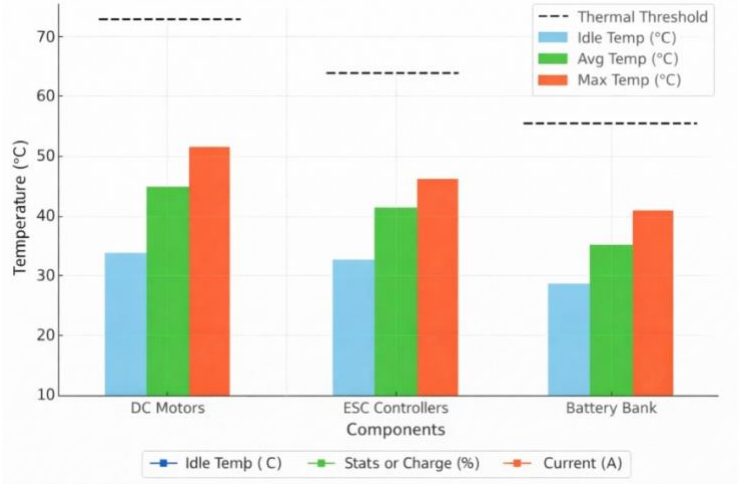

Figure V. Temperature Variation of Components

5.2 Terrain-Dependent Locomotion. - The four-wheel drive robot was able to traverse different types of terrain. The PVC provided the required shock absorption, hence stability on rough terrain. It was also able to climb a 15° slope. Very harsh terrain, such as heavy mud or large rocks, would be a problem, depending on the size of the wheels and ground clearance. The average speeds obtained were 1.0 m/s on gravel, 1.4 m/s on dirt soil, with a turn radius of 0.5 m and a wheel slip of 12% on gravel. The peak acceleration on the rough terrain was 2.5 g. Table IV represents the locomotion performance metrics used.

Metric	Grass	Gravel	Dirt
Avg Speed (m/s)	1.2	1	1.4
Turning Radius (m)	0.5	0.5	0.5
Wheel Slip (%)	3	12	2
Torque (Nm)	0.7	0.9	0.8
Peak Vibration (g)	2	2.5	1.8

Table IV. Locomotion Performance Metrics

It can be seen from Fig VI that gravel terrain causes higher torque, slippage, and hence reduced speeds and inclines, as opposed to grass and dirt terrain that offer better gripping properties and reduced mechanical losses.

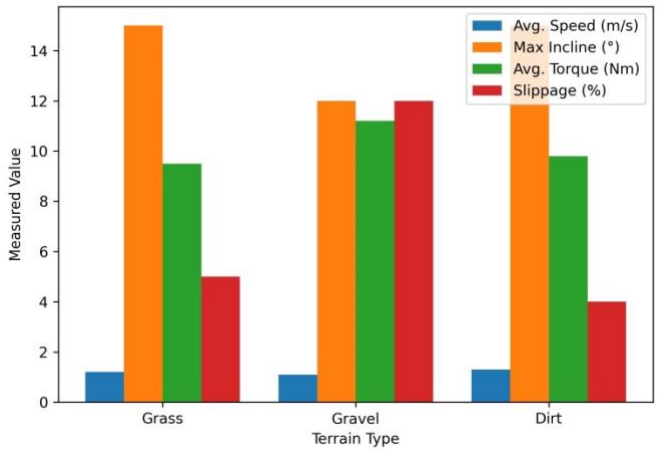

Fig VI. Comparison between the traction and performance parameters on grass, gravel, and dirt track.

5.3 Wireless Communication Performance. - Control via Bluetooth and video transmission through the V380 Pro App (See Fig VII) also performed well. The delay between control commands was less than 100 ms, ensuring near-real-time control, but the delay in video transmission was between 0.5 s and 1.5 s, depending on Wi-Fi network strength. The video was clear at a range of 30 meters in 1080p, but compression was seen beyond 50 meters. Table V. Represents the quality metrics used for remote operation and streaming quality.

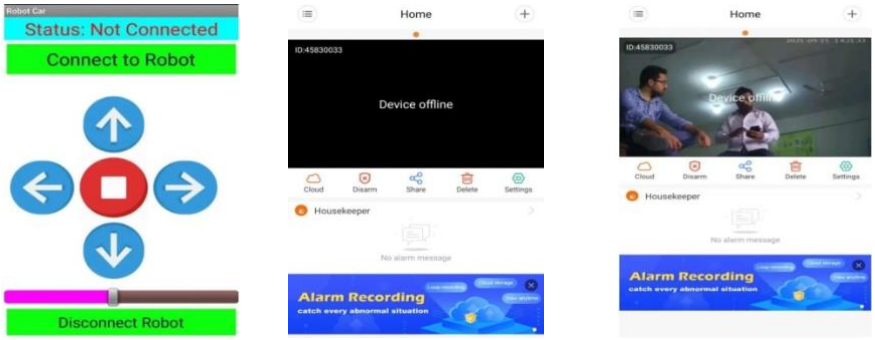

Figure VII. V380 Pro Application Interface

Metric	Value / Observation
Bluetooth Control Latency	< 100 ms
Video Streaming Latency	0.5–1.5 s
Video Quality	1080p HD (≤30 m)
Signal Strength (RSSI)	Bluetooth: -60 dBm; Wi-Fi: -50 dBm
Video Frame Rate	~25 fps
Command Packet Loss Rate	<1%

User Experience Rating	4.5 / 5
Control Operational Range	~15 m
Video Streaming Range	30–50 m

Table V. Remote Operation and Streaming Quality Metrics.

5.4 Battery Charging and Discharge Behavior. - The battery performance was monitored during the continuous outdoor operation. The solar power received from the PV panel can provide a maximum current of 7 A under direct sunshine, as depicted in Fig. VIII. During the active locomotion and video streaming, the battery voltage decreased from 12.6 V, which is the fully charged voltage, to 11.9 V within 30 min. After the solar charging, the voltage returned to 12.6 V, and the SOC returned to approximately 90% within the 50th minute, which indicates the positive energy balance during the mission operation.

The SOC level was also estimated for the battery, based on voltage levels (11.9V-12.6V), and this is only an indicative trend, since there is a level of uncertainty when voltage is used to calculate SOC levels, especially when dynamic load is involved and internal resistance is a factor. Thus, the evaluation is based on the actual harvested and consumed energy (Wh) rather than SOC levels.

This evaluation, based on actual harvested and consumed energy, confirms that the robot is able to sustain its operation on flat, gravel, and dirt terrains without any additional power supply, under the given environmental conditions.

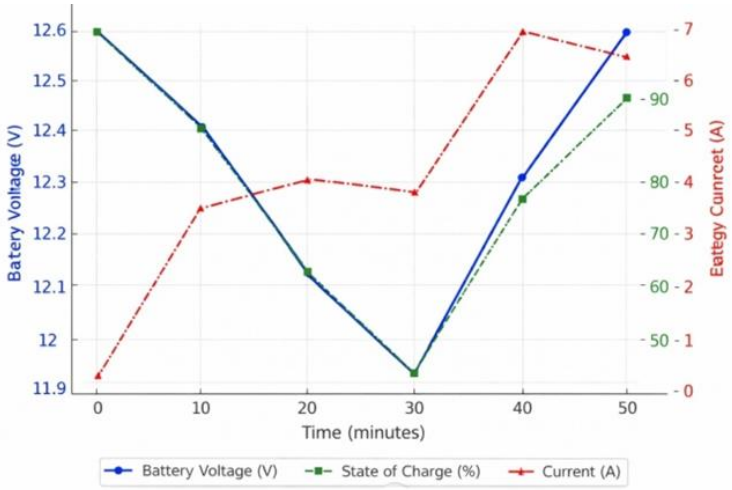

Figure VIII. Battery Performance Over Time

6. Conclusion and Future Directions. - In this paper, the authors have presented a solar-powered, terrain-adaptive mobile robot that integrates energy harvesting, four-wheel drive, dual wireless communication, and passive thermal management into a modular platform. The experimental results have shown the positive energy balance and reliable operation on various types of terrain, indicating the potential of the robot to perform autonomous, off-grid monitoring. There are several areas where the system can be improved. The future work may be focused on the improvement of the energy efficiency of the system using adaptive solar tracking and energy recovery mechanisms, improvement in the adaptability of the robot using advanced suspension mechanisms, and improvement in the communication capabilities using mesh networking techniques. The integration of machine learning techniques to enable the robot to navigate autonomously through the terrain and optimize the energy efficiency, as well as the reduction in the cost of the system using efficient components, will enable the system to be scalable to perform the task in large numbers.

References

[1] S. Halder and K. Afsari, “Robots in inspection and monitoring of buildings and infrastructure: A systematic review,” Applied Sciences, vol. 13, no. 4, Art. no. 2304, 2023. Available: https://doi.org/10.3390/app13042304
[2] J. Olt, Y. Ihnatiev, T. Lillerand, and I. Virro, “Development of a battery swapping and charging unit in servicing station for farming robot: A review,” in Proc. Int. Symp. Farm Machinery and Processes Management in Sustainable Agriculture, Cham, Switzerland: Springer Nature Switzerland, 2024, pp. 333–345. Available: https://doi.org/10.1007/978-3-031-70955-5_37
[3] S. U. Rehman, A. A. Zaidi, Y. A. Wahab, M. Y. Arafat, and S. F. W. M. Hatta, “Advanced solar-powered seed sowing machine with precision seeding and smart control features,” in Proc. IEEE Reg. Symp. Micro and Nanoelectronics (RSM), 2023, pp. 134–137. Available: https://doi.org/10.1109/RSM59033.2023.10326842
[4] S. U. Rehman and Y. A. Wahab, “Design and development of IoT-based harvesting Robo-Vec,” Memoria Investigaciones en Ingeniería, vol. 28, pp. 32–44, 2025. Available: https://doi.org/10.36561/ING.28.4
[5] S. U. Rehman, “An IoT-based autonomous waiter robot,” Memoria Investigaciones en Ingeniería, vol. 28, pp. 154–167, 2025. Available: https://doi.org/10.36561/ING.28.11
[6] T. Dewi, R. Sukwadi, and M. B. Wahju, “Design and performance of solar-powered surveillance robot for agriculture application,” Kinetik: Game Technology, Information System, Computer Network, Computing, Electronics, and Control, vol. 8, no. 3, 2023. Available: https://doi.org/10.22219/kinetik.v8i3.1722
[7] D. Hao et al., “Solar energy harvesting technologies for PV self-powered applications: A comprehensive review,” Renewable Energy, vol. 188, pp. 678–697, 2022. Available: https://doi.org/10.1016/j.renene.2022.02.066
[8] S. Sujitha, N. T. Meghana, R. Vandana, and G. R. Vidya. "Solar Powered Autonomous Multipurpose Agricultural Robot Using Bluetooth." In 2023 Second International Conference on Electronics and Renewable Systems (ICEARS), pp. 234–241, IEEE, 2023.Available: https://doi.org/10.22214/ijraset.2025.67081
[9] M. A. Musa and S. Mashori, “Solar powered autonomous RC robot,” Progress in Engineering Application and Technology, vol. 4, no. 2, pp. 133–144, 2023. Available: https://doi.org/10.30880/peat.2023.04.02.013
[10] A. A. Chand et al., “Design and analysis of photovoltaic powered battery-operated computer vision-based multi-purpose smart farming robot,” Agronomy, vol. 11, no. 3, Art. no. 530, 2021. Available: https://doi.org/10.3390/agronomy11030530
[11] E. Mendez-Flores, A. Pourshahidi, and M. Egerstedt, “RaccoonBot: An autonomous wire-traversing solar-tracking robot for persistent environmental monitoring,” arXiv preprint, arXiv:2501.14151, 2025. Available: https://doi.org/10.48550/arXiv.2501.14151
[12] S. U. Rehman and A. Khan, “Integrating IoT technology for improved distribution transformer monitoring and protection,” Electrical, Control and Communication Engineering, vol. 19, no. 1, pp. 22–28, 2023. Available: https://doi.org/10.2478/ecce-2023-0004
[13] S. U. Rehman, H. Mustafa, M. A. Shaikh, and S. Memon, “Towards sustainable energy storage: A low-cost IoT solution for real-time monitoring of lead-acid battery health,” Memoria Investigaciones en Ingeniería, vol. 26, pp. 202–212, 2024. https://doi.org/10.36561/ING.26.12
[14] D. S. Marin, H. Franco-Osorio, and J. J. Prías-Barragán, “Fabrication and electrical characterization of a transistor device configuration based on graphene oxide films,” 2023. Available: https://doi.org/10.21203/rs.3.rs-3126123/v1

Author contribution:
1. Conception and design of the study
2. Data acquisition
3. Data analysis
4. Discussion of the results
5. Writing of the manuscript
6. Approval of the last version of the manuscript

HM has contributed to: 1, 2, 3, 4, 5 and 6.
SUR has contributed to: 1, 2, 3, 4, 5 and 6.
MAS has contributed to: 1, 2, 3, 4, 5 and 6.

Acceptance Note: This article was approved by the journal editors Dr. Rafael Sotelo and Mag. Ing. Fernando A. Hernández Gobertti.

Effect of Hardfacing on the Damping Characteristics of ASTM A516 G70 Steel

Efecto del recargue superficial sobre las características de amortiguamiento del acero ASTM A516 Grado 70

Efeito do revestimento por soldagem nas características de amortecimento do aço ASTM A516 Grau 70

Hussien A. Hilal [1], M. k. A. Razzaq [2], Hamid Al-Abboodi [3], Ahmed T. Fadhil [4], Adnan N. Abood [5], Huiqing Fan [6], Muhammad Samiuddin [7 (*)]

Recibido: 27/01/2026 Aceptado: 30/03/2026

Summary. - This work systematically evaluates the influence of hardfacing on the damping behavior of ASTM A516 Grade 70 steel using AWS EF15, EFeCr-A1, and EFeMn-A electrodes, revealing a clear correlation between microstructural evolution and vibration damping performance. Elemental migration during hardfacing, combined with varying heat input, leads to significant microstructural transformations in the heat-affected zone (HAZ), including martensite formation, recrystallization, and grain growth, particularly for EF15 and EFeCr-A1 electrodes. The normalized microstructure of the base steel disappears after single-layer deposition, while higher heat input associated with double-layer deposition promotes the formation of refined equiaxed grains. Single-layer deposits of EF15 and EFeCr-A1 exhibit fine dendritic structures, whereas double layers develop coarser austenitic morphologies. In contrast, EFeMn-A produces an austenitic matrix with equiaxed grains for both single and double layers. Double-layer deposits show increased hardness due to the formation of electrode-dependent intermetallic compounds. However, the results reveal that an austenitic matrix significantly enhances damping capacity, while the presence of hard intermetallic phases in double-layer deposits reduces damping performance. The results highlight a hardness–damping trade-off that enables optimized electrode and layer selection for vibration- and wear-critical components.

Keywords: *Hardfacing; HAZ; intermetallic compounds; damping capacity.*

(*) Corresponding author.

[1] Student, Ministry of water resource, State commission for operation irrigation and drainage projects (Iraq), Husseinn313husseinn@gmail.com, ORCID iD: https://orcid.org/0009-0002-4648-9457

[2] Student, Kut Technical Institution, Middle Technical University (Iraq), Mortadha_kareem@yahoo.com, ORCID iD: https://orcid.org/0000-0002-9599-5359

[3] Student, Kut Technical Institution, Middle Technical University (Iraq), hamid80_n88@yahoo.com, ORCID iD: https://orcid.org/0000-0003-0642-9396

[4] Student, Tigris way construction company (Iraq), Ahth91@yahoo.com, ORCID iD: https://orcid.org/0000-0001-8627-4501

[5] Student, Middle Technical University (Iraq), adnan_naama_59@mtu.edu.iq, ORCID iD: https://orcid.org/0000-0002-3644-2471;

[6] Professor, State Key Laboratory of Solidification Processing, Northwestern Polytechnical University (China), hqfan3@163.com, ORCID iD: https://orcid.org/0000-0002-1405-9279

[7] Professor, NED University of Engineering and Technology (Pakistan), engr.sami@neduet.edu.pk, ORCID iD: https://orcid.org/0000-0002-2350-6114;

Memoria Investigaciones en Ingeniería, núm. 30 (2026). pp. 177-188
https://doi.org/10.36561/ING.30.12
ISSN 2301-1092 • ISSN (en línea) 2301-1106 – Universidad de Montevideo, Uruguay

Resumen. - *Este trabajo evalúa de manera sistemática la influencia del recargue superficial en el comportamiento de amortiguamiento del acero ASTM A516 Grado 70 utilizando electrodos AWS EF15, EFeCr-A1 y EFeMn-A, estableciendo una correlación directa entre la evolución microestructural inducida por el proceso y el desempeño en la atenuación de vibraciones. La migración de elementos durante el recargue, junto con el aporte térmico aplicado, provoca transformaciones microestructurales significativas en la zona afectada por el calor (ZAC), como formación de martensita, recristalización y crecimiento de grano, especialmente en los casos de EF15 y EFeCr-A1. La microestructura normalizada del acero base desaparece tras la deposición de una sola capa, mientras que el mayor aporte térmico asociado a dos capas favorece la formación de granos equiaxiales refinados. Los depósitos de una sola capa con EF15 y EFeCr-A1 presentan estructuras dendríticas finas, mientras que el electrodo EFeMn-A genera una matriz austenítica con granos equiaxiales en ambas configuraciones. Las dobles capas muestran mayor dureza debido a la formación de compuestos intermetálicos. Sin embargo, una matriz austenítica mejora el amortiguamiento, mientras que las fases intermetálicas duras lo reducen, evidenciando un compromiso entre dureza y capacidad de amortiguamiento.*

Palabras clave: *Recargue superficial; zona afectada por el calor (ZAC); compuestos intermetálicos; capacidad de amortiguamiento.*

Resumo ***-*** *Este trabalho avalia de forma sistemática a influência do revestimento por soldagem (hardfacing) nas características de amortecimento do aço ASTM A516 Grau 70, utilizando os eletrodos AWS EF15, EFeCr-A1 e EFeMn-A, estabelecendo uma correlação direta entre a evolução microestrutural induzida pelo processo e o desempenho na absorção de vibrações. A migração de elementos durante a deposição, associada à energia térmica aplicada, provoca transformações microestruturais significativas na zona afetada pelo calor (ZAC), como formação de martensita, recristalização e crescimento de grão, especialmente para EF15 e EFeCr-A1. A microestrutura normalizada do aço base desaparece após a deposição de uma única camada, enquanto o maior aporte térmico de duas camadas favorece a formação de grãos equiaxiais refinados. Depósitos de camada única com EF15 e EFeCr-A1 apresentam estruturas dendríticas finas, enquanto o eletrodo EFeMn-A gera uma matriz austenítica com grãos equiaxiais em ambas as configurações. Depósitos duplos apresentam maior dureza devido à formação de compostos intermetálicos. Entretanto, a matriz austenítica melhora o amortecimento, enquanto fases intermetálicas duras o reduzem, evidenciando um compromisso entre dureza e capacidade de amortecimento.*

Palavras-chave: *Revestimento por soldagem; zona afetada pelo calor (ZAC); compostos intermetálicos; capacidade de amortecimento.*

1. Introduction. - Hardfacing (HF) has been widely applied in many industries. It involves the process of depositing a tougher material on a matrix and is mainly used to increase component life or on tools that are encounter significant abrasive wear [1-5]. A. P. Wu [6] recorded a reduction in the residual tensile stress in the HF layer. Local post-heating of base metal (BM) surface can influentially lower residual tensile stress if there is an austenitic stainless steel interlayer between the carbon steel and Stellite HF layer. A. H. Jones [7] studied the use of HF coatings for ground-engaging applications. Hardfacing alloys, which can be applied to tools as slurry and then sintered, are improved by the addition of hard powder materials. Tungsten carbide powders of varying sizes were added. The relationship between the particle size of the powder and the size of the abrasive particles was assessed, and an increase in wear resistance was determined. Y. Zhou [8] investigated the influence of Ti additives on a hypoeutectic high chromium cast iron arc surface layer. The results indicated that Ti increases hardness and also makes it more uniform across the depth. M. Leitner [9] assessed the wear and fatigue resistance of arc-welded HF layers for structural steel applications. Mild steel was employed, and metal-cored and solid wires were used as filler metals for the HF. Results showed a reduction in wear of 64% and 69% with flux-cored wire and solid wire, respectively. B. Singh [10] investigated slip damping in layered and joint-welded cantilever structures using a finite-element approach. It has been confirmed that the damping capacity of layered and joint structures can be significantly improved by using tack welds instead of continuous welds. A. A. Ahmad Asoor [11] studied the difference in damping capacity for welded and threaded bolts and nut joints. The results indicated that threaded joints could sustain higher damping than welded joints. M. S. Sani [12] evaluated resistance spot welding used for joining AISI 1010 mild steel and AISI 304 stainless steel sheets. The results showed that discrepancies in natural frequency between FEA and experimental model analysis are less. This research was conducted to study the effect of surface hardening of the fan blades of rotary liner using different electrodes on damping behavior and microstructure of ASTM A516 G70 steel.

2. Experimental Work. - ASTM A516 Grade 70 steel plates with a thickness of 10 mm were used as the substrate material. Hardfacing was carried out using three different surfacing electrodes: AWS EFe15, EFeCr-A1, and EFeMn-A. The chemical compositions of substrate and electrodes are provided in Table 1.

Element	C	Cr	Ni	Mn	Si	P	S	Mo	Nb	Fe
A516 G70	0.12	0.0163	0.0035	1.33	0.323	0.0124	0.0019	0.0072	-	Bal.
EFe15	3.4	22	-	-	-	-	-	-	10	Bal.
EFeCr-A1	2.5	33	-	-	-	-	-	-	-	Bal.
EFeMn-A	0.7	-	3	14	0.1	-	-	-	-	Bal.

Table I. Chemical composition of the substrate and electrodes (wt.%)

Hardfacing was performed using a manual metal arc welding process (MMAW) with electrodes of 3.2 mm diameter. Welding current (120 A), voltage (20 V), and travel speed (2–5 mm/s) were applied. For multilayer deposition, interpass temperatures of 150 °C and bead overlap of 30–50% are commonly applied. The use of double layers introduces additional thermal cycles due to reheating of underlying layer, leading to cumulative heat exposure and associated microstructural modifications, which reasonably explain the observed changes in damping behavior. Seven steel plates were cut with dimensions of 350 × 250 mm and secured in a specially designed fixture to minimize distortion during welding. Hardfacing layers with an approximate thickness of 3 mm were deposited using the back-step technique without preheating. The welding pass width was slightly greater than 40 mm, and welding was conducted in the longitudinal direction with continuously overlapping passes. To evaluate the effect of hardfacing on mechanical and dynamic behavior, both single- and double-layer deposits were produced for each electrode type.

Vibration damping capacity tests were conducted on both as-received and hardfaced specimens with dimensions of 140 × 10 × 4.5 mm. Free vibration decay tests were conducted to evaluate the damping characteristics of hardfaced ASTM A516 G70 steel specimens. The excitation was applied as an initial transverse displacement at free end, followed by release without external forcing. The specimens were tested under cantilever boundary conditions, where one end was rigidly clamped using a steel fixture with a controlled tightening torque (~25–30 N·m) to minimize slippage and fixture compliance effects. The vibration response was measured using a piezoelectric accelerometer

mounted near the free end to capture maximum amplitude. Data acquisition was performed at a sampling rate of 10 kHz. A low-pass filter was applied to reduce high-frequency noise, and signal processing included standard windowing. The logarithmic decrement (δ) was calculated using successive peak amplitudes according to:

$$\delta = \frac{1}{n} \ln \left(\frac{x_1}{x_{n+1}} \right)$$

where n = 5-8 cycles were used for improved accuracy. Peak-picking was carried out using an automated routine in MATLAB. The damping ratio (ζ) was derived from δ using standard relations, and each measurement was repeated three times to ensure repeatability, with averaged values reported.

Microstructural characterization was carried out using optical microscopy (OM), scanning electron microscopy (SEM), Energy Dispersive X-ray Spectroscopy (EDS), and X-Ray Diffraction (XRD). Prior to examination, samples were prepared by standard grinding and polishing procedures. The substrate was etched using a Nital solution, while the hardfaced layers were etched using a chemical solution consisting of 3 parts HCl, 2 parts HNO_3, and 2 parts acetic acid. Microhardness measurements were performed using a load of 300g and a dwell time of 15s. The spacing between adjacent indents was maintained at a constant distance of (1 mm) to avoid interaction between plastic zones. Multiple traverses (three parallel lines) were performed across the weld cross-section to ensure reproducibility. Fusion line (FL) and HAZ boundaries were identified based on OM observations, considering both microstructural changes and etching contrast differences between the base metal, HAZ, and fusion zone (FZ). Furthermore, the reported microhardness profiles represent the average values obtained from multiple traverses, with individual measurements showing good consistency.

3. Results and Discussion. -

3.1 Microstructure analysis. - The microstructure of ASTM A516 G70 steel comprises ferrite and pearlite, with an average grain size of 27µm (Figure I). In a single layer deposited with electrode EFe15, fine niobium carbide (NbC) with an intermetallic compound of chromium silicon ($CrSi_2$) is presented within an austenite matrix, while martensite appears in HAZ (Figure IIA). In double layers, niobium carbide is also existence in the austenite matrix, along with iron carbide precipitated (Fe_5C_2), chromium iron carbide $(Cr, Fe)_7C_3$, and existing martensite in HAZ (Figure IIB). The matrix is a dendritic structure with Dendritic Arm Spacing (DAS) of 7.79µm for a single layer and 9.25µm for double layers.

EDS line confirms that migration of Nb, Cr, and carbon (wt%) from the surface layers to steel increased martensite formation in HAZ (Figs. III and IV). Chromium diffused up to 200µm (with a single layer) in steel, with a sharp gradient in concentration. Niobium diffused with a slight gradient and a penetration depth greater than 400µm. Carbon content significantly increases near FL, which is associated with iron reduction and encourages carbide formation. For double-surface layers, chromium has a lower concentration at the steel side for a penetration depth greater than 400µm. The concentration of alloying elements increases in comparison to a single layer, which reflects an increased hardness. For a single layer, NbC and $CrSi_2$ were present, whereas, in double layers, three different phases were present; NbC, Fe_5C_2, and $(Cr, Fe)_7C_3$, these results were confirmed by XRD analysis (Figure V). This is caused by a longer migration time of elements with an increase in concentration compared to a single layer.

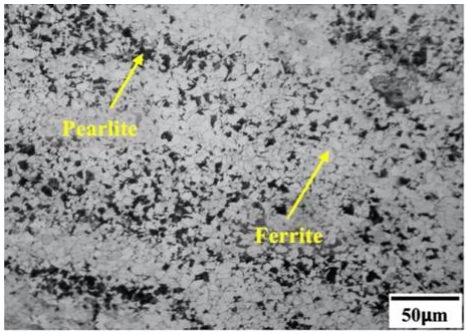

Figure I. Microstructures of ASTM A516 G70

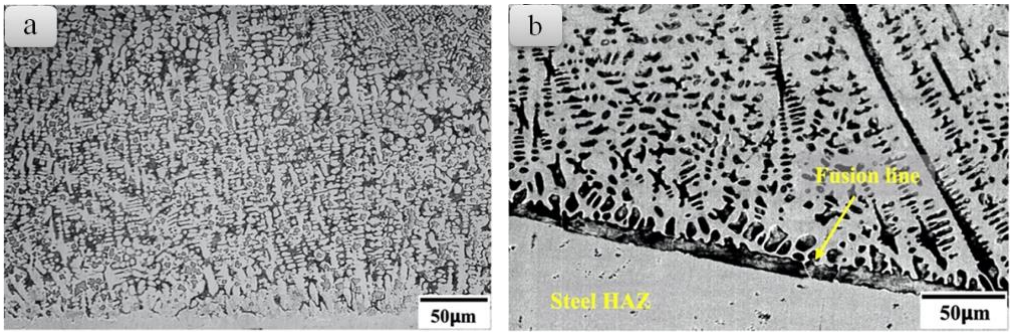

Figure II. (a) Microstructure of HF (a) single layer, (b) double layers using EFe15

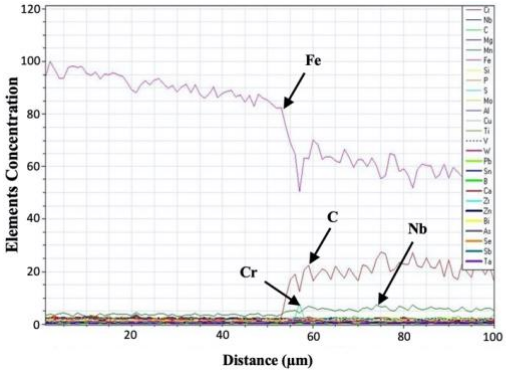

Figure III. Distribution of elements using EFe15 single layer

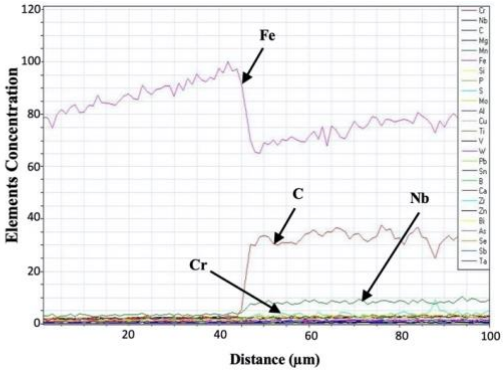

Figure IV. Distribution of elements using EFe15 double layer

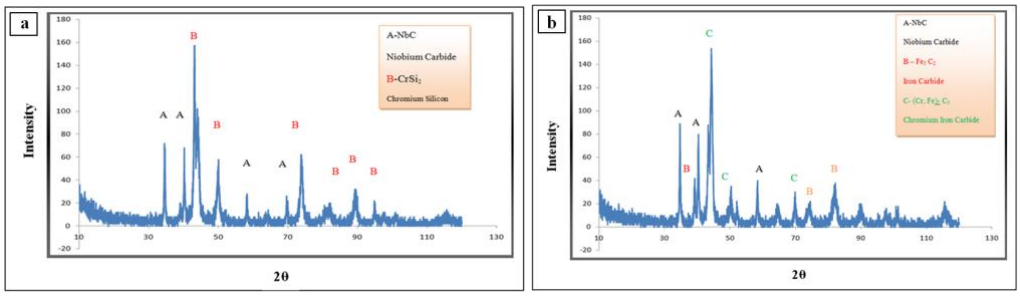

Figure V. XRD of (a) single layer, and (b) double layer using EFe15.

The hardness of A516 G70 steel is improved with a single layer with EFe15. Hardness was raised from 175HV to 450HV on surface (Figure VI). This change in hardness could be related to martensite and carbide formation and the hardness increased to 650HV with double layers owing to the creation of carbides – Fe_5C_2 and $(Cr, Fe)_7C_3$ – associated with the disappearance of $CrSi_2$.

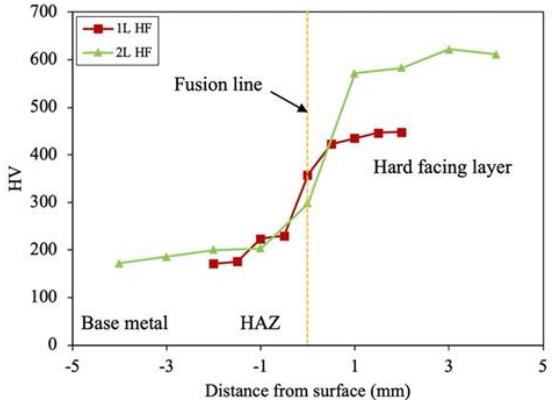

Figure VI. Vickers hardness for single and double layers using EFe15

A single layer of electrode EFeCr-A1 is associated with secondary chromium carbide (Cr_7C_3) in surfacing layer and martensite in HAZ of steel due to the high chromium percentage (Figs.VII and VIII). Double layers recorded same phases mentioned with additional heating without significant effect and migration time on intermetallic compound forming types. With EFeCr-A1 For single and double layers, Fe, Cr and C diffuse from surfacing layer to BM with same profile (Figs. IX and X), but more effectively with double layers. Diffusion regime of Fe (wt%) resembles that of EFe15, especially their increment and sudden reduction near FZ. The carbon concentration increases in double-surface layers along with an increase in the volume fraction of carbides. For single layer; new carbides, Cr_7C_3 is existing, while double layers register that the predominant intermetallic compound is FeCr, with only trace amounts of chromium carbide, these findings are supported by XRD results (Figure XI). Surfacing with a single layer has a more significant effect on hardness, making it greater than 800HV. Using this electrode, however, there was no significant difference in hardness between single and double layers (Figure XII).

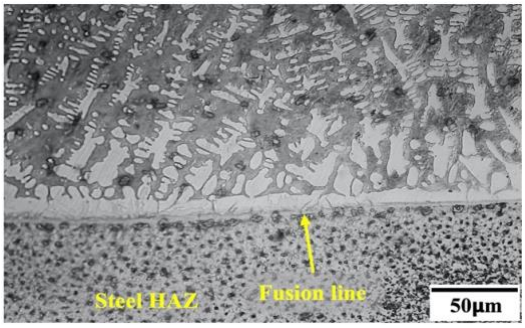

Figure VII. Microstructure of HF single layer using EFeCr-A1

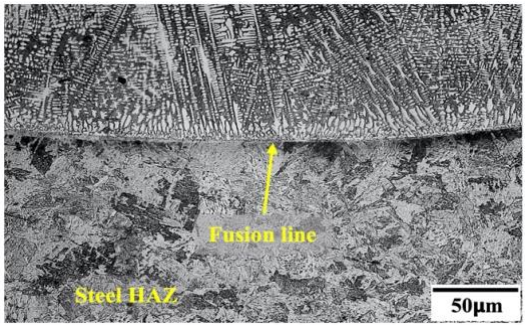

Figure VIII. Microstructure of HF double layers using EFeCr-A1

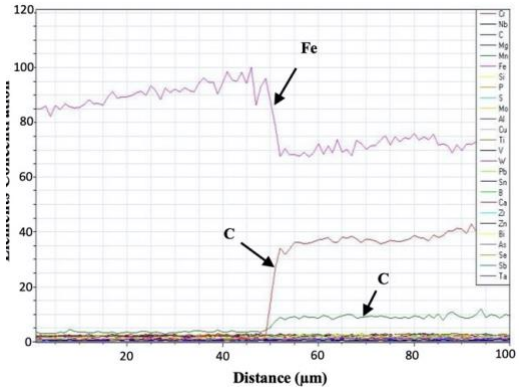

Figure IX. Distribution of elements using EFeCr-A1single layer

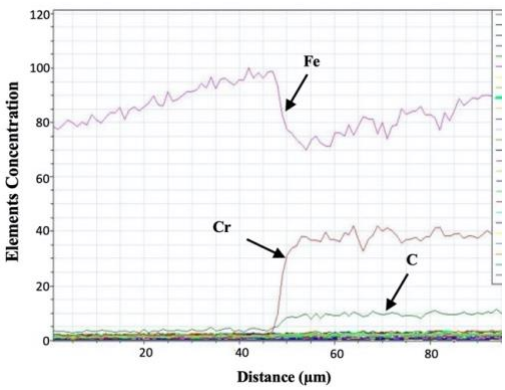

Figure X. Distribution of elements using EFeCr-A1 double layer

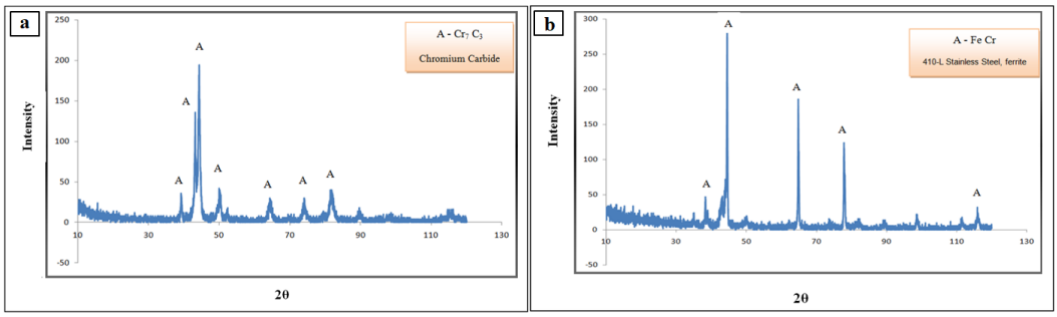

Figure XI. XRD of (a) Single Layer, and (b) double layer using EFeCr-A1

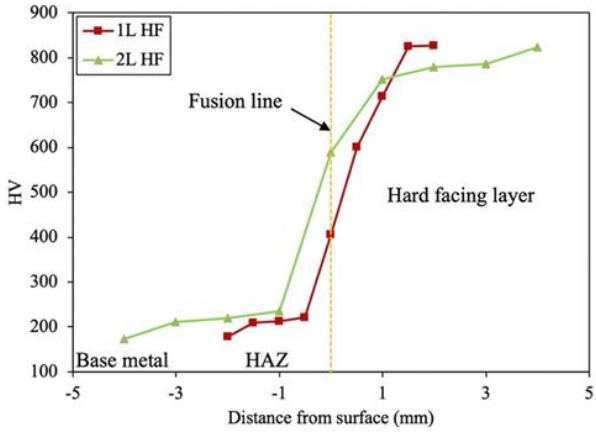

Figure. XII; Vickers hardness with one and double layers HF using EFeCr-A1

One layer with EFeMn-A electrode, austenitic with equiaxed structures is evident. For double layers, manganese carbide (Mn_7C_3) prevails, which is consistent with a study by D. M. Mattox [13]. Steel does not have martensite near FL, but this phenomenon manifests with double layers at depths of 100µm (Figs. XIII and XIV). Variation with a single layer in Fe sharply reduced at a distance of 1.5mm approximately from FL, which is associated with an increase in carbon content, while manganese gradually reduced across FL. Double layer experience increased element concentration, with random variation to some extent. Further, manganese diffuses inside steel and is soluble without forming intermetallic compounds (Figs. XV and XVI). XRD analysis of the single-layer sample revealed two distinct phases (CFe15.1 and Cr–Ni–Fe–C), whereas the double-layer sample exhibited a single phase (Mn_7C_3) (Figure XVII).

Hardness attained more than 800HV at the surface layer. Chromium carbide in HF layers is profit high hardness. Carbon steel having a high thermal conductivity, so HAZ had been formed in different distinct zones, each one having properties differ with another, so will have different hardness values. High heat input encourages the carbon migration toward FL and formation band of martensite near it. Away from FL, the hardness vigorously decreases. This fluctuation related to the transition of microstructures from full martensitic to bainitic until reach unaffected base metal. An increase in hardness was recorded near FL from the steel side for a single layer, with not more than 245HV hardness, while the surface layer registered about 200HV. This makes it clear that the refining zone does not consist of martensite; however, with double layers, the hardness is increased to greater than 300HV, with martensite present near FZ (Figure XIV).

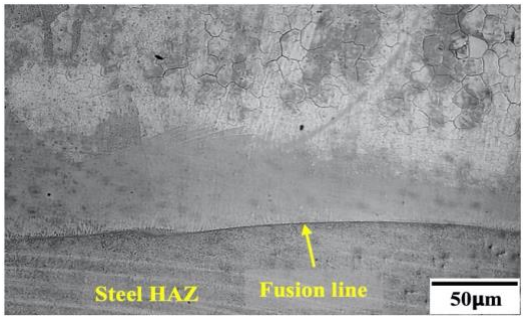

Figure XIII. Microstructure of HF single layer using EFeMn-A

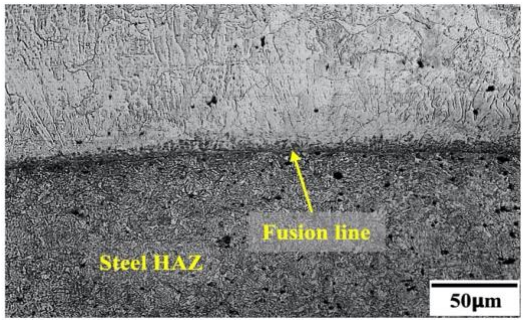

Figure XIV. Microstructure of HF double layer using EFeMn-A

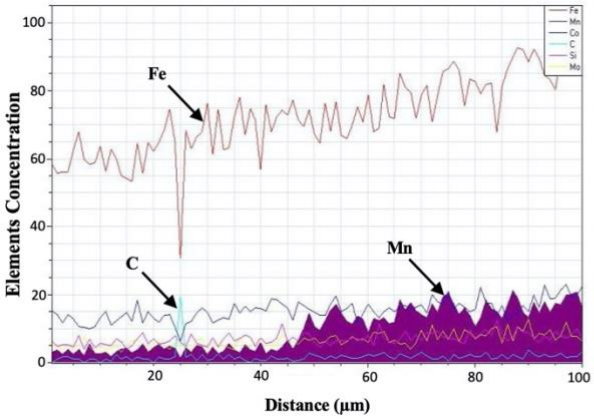

Figure XV. Distribution of elements using EFeMn-A single layer

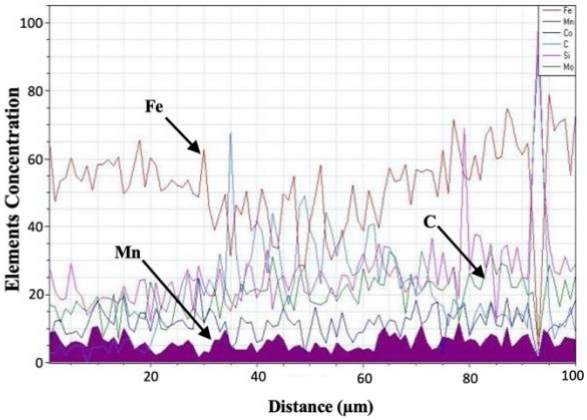

Figure XVI. Distribution of elements using EFeMn-A double layer

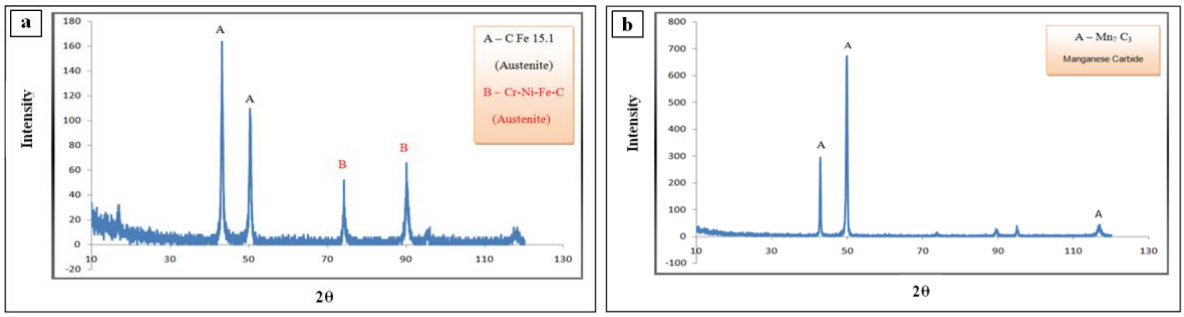

Figure XVII. XRD of (a) single layer, and (b) double layer using EFeMn-A

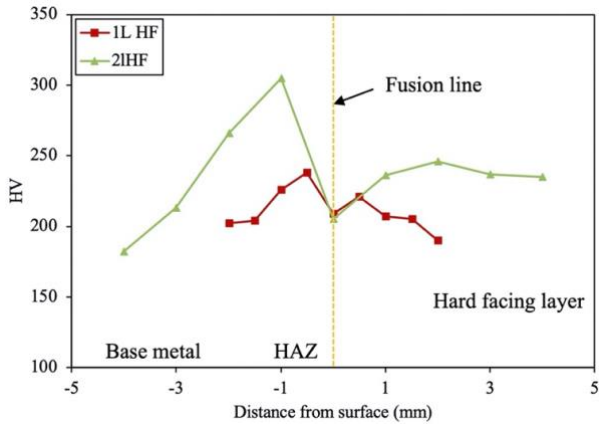

Figure XVIII. Vickers hardness one- and two-layers HF with using EFeMn-A

3.2 Damping Test. - The experimental results of damping test regarding free-vibration response tests implemented in this work are presented. Damping characteristics are represented in terms of logarithmic decrements, damping ratio, and damping capacity, which are shown in Table (II). It can be seen that damping characteristics improved in comparison to as-received steel owing to the contribution of HF materials. In addition, the damping improvement for one layer is higher than that for two layers, for all types of electrodes (Figs. XIX, XX, and XXI). Moreover, the maximum improvement was realized with one layer of EFeMn-A. In general, this development is dependent on the presence of an austenite matrix, and the reduction with double layers is related to the formation of other intermetallic compounds. The creation of Fe_5C_2 and $(Cr, Fe)_7C_3$, along with the disappearance of $CrSi_2$ when using EFe15 lead to reducing damping capacity. While double layers when employing EFeCr-A1, the formation of FeCr instead of Cr_7C_3 subjects damping capacity to a decline. Double layers, using EFeMn-A, are associated with the establishment of Mn_7C_3, which reduces damping also.

Hard Facing Parameters	Damping Capacity (ψ)	Percentage of Improvement
ASTM A516 G70	0.01027	------
One-layer HF using EFeCr-A1	0.01584	54%
Two layers HF using EFeCr-A1	0.01099	7%
One-layer HF using EFe15	0.02518	145%
Two layers HF using EFe15	0.02193	113%
One-layer HF using EFeMn-A	0.03234	214%
Two layers HF using EFeMn-A	0.02774	170%

Table II. Damping ratio of HF with single and double layers

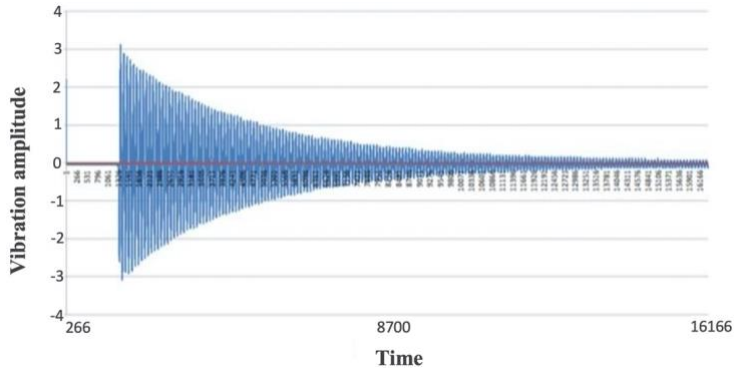

Figure XIX. Free vibration response of ASTM A516 G70

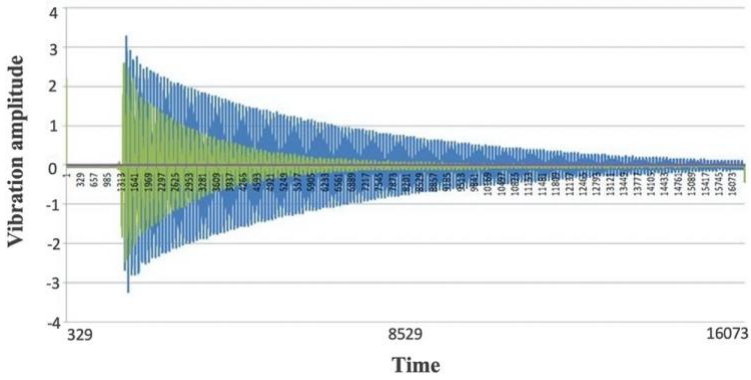

Figure XX. Free vibration response for double layers using EFeCr-A1

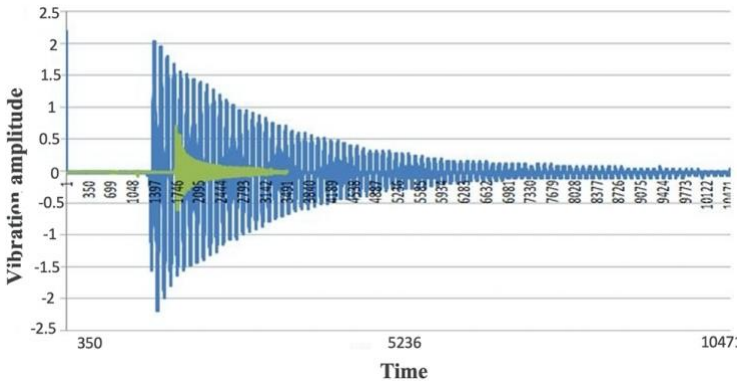

Figure XXI. Free vibration response for double layers using EFeMn-A

4. Conclusions. -

- The heat input associated with hardfacing significantly influences the microstructural evolution of ASTM A516 Grade 70 steel, transforming the normalized microstructure into a heat-affected zone (HAZ) characterized by inhomogeneous grain size distribution.

- Elemental migration across FL occurs for both single- and double-layer hardfacing deposits and follows a broadly similar trend, indicating that layer number has a limited influence on the diffusion regime.

- The presence of an austenitic matrix within the hardfaced layers plays a key role in enhancing the damping capacity of ASTM A516 Grade 70 steel, with the most pronounced improvement observed for single-layer deposits.

- Among the investigated electrodes, single-layer hardfacing using the EFeMn-A electrode exhibits the greatest enhancement in damping capacity, highlighting its suitability for vibration-sensitive applications.

- The application of double-layer hardfacing leads to a reduction in damping capacity for all three electrodes, which is attributed to the formation of brittle intermetallic compounds that restrict energy dissipation during vibration.

References

[1] H. V. Naik1, V. D. Kalyankar, “Development of NiCrSiBC Weld Hardfacing Approach for P91 Steels Used in Steam Turbine Components”, Soldagem & Inspeção. 2021, Vol. 26, 2608-2623.
[2] M. F. Buchely, J. C. Gutierrez, L. M. Le´on, A. Toro, "The effect of microstructure on abrasive wear of hardfacing alloys", Wear, Vol. 259, (2005): pp. 52–61.
[3] X. Wang, F. Hanb, X. Liu , Shiyao Qua, Z. Zoua, "Microstructure and wear properties of the Fe–Ti–V–Mo–C hardfacing alloy", Wear, Vol. 265, (2008): pp. 583–589.
[4] B. Venkatesh, K. Sriker, and V. S. V. Prabhakar. "Wear characteristics of hardfacing alloys: state-of-the-art." Procedia Materials Science, Vol.2, No.10, (2015): pp. 527-532.
[5] J. Brezinová , D. Draganovská, A. Guzanová, P. Balog and J. Vi ˇ náš, "Influence of the Hardfacing Welds Structure on Their Wear Resistance", Metals, Vol. 6, No. 36,(2016): pp. 1-12.
[6] A. P. Wu, J. L. Ren, Z. S. Peng, H. Murakawa, and Y. Ueda. "Numerical simulation for the residual stresses of Stellite hard-facing on carbon steel." Journal of materials processing technology, Vol.101, No. 1 (2000): pp. 70-75.
[7] Jones, Alan Hywel, P. Roffey. "The improvement of hard facing coatings for ground engaging applications by the addition of tungsten carbide." Wear, Vol.267, No. 5-8 (2009): pp. 925-933.
[8] Zhou, Yefei, Yulin Yang, Jian Yang, Feifei Hao, Da Li, Xuejun Ren, and Qingxiang Yang. "Effect of Ti additive on (Cr, Fe) $_7C_3$ carbide in arc surfacing layer and its refined mechanism", Applied Surface Science, Vol. 258, No. 17 (2012): pp.6653- 6659.
[9] Leitner, Martin, Philip Pichler, Florian Steinwender, and Christoph Guster. "Wear and fatigue resistance of mild steel components reinforced by arc welded hard layers." Surface and Coatings Technology, Vol.2, No.330 (2017): pp.140-148.
[10] Singh, B., and B. K. Nanda. "Mechanism of Damping in Welded Structures using Finite Element Approach." World Academy of Science, Engineering and Technology, Vol.4, No. 3 (2010): pp. 771-775.
[11] A. A. Asoor, Ahmadi, M. H. Pashaei. "Experimentally study on the effects of type of joint on damping." World applied sciences journal, Vol. 8, No. 5 (2010): pp. 608- 613.
[12] Sani, M. S. M., N. A. Nazri, and D. A. J. Alawi. "Vibration analysis of resistance spot welding joint for dissimilar plate structure mild steel 1010 and stainless steel 304)." In IOP Conference Series: Materials Science and Engineering, Vol. 238, No. 1 (2017).
[13] D. M. Mattox. "Surface effects on the growth, adhesion and properties of reactively deposited hard coatings". Surface and Coatings Technology, Vol. 81, No. 1, (1996), pp.8-1

Author contribution:
1. Conception and design of the study
2. Data acquisition
3. Data analysis
4. Discussion of the results
5. Writing of the manuscript
6. Approval of the last version of the manuscript

HAH has contributed to: 1, 2, 4, and 5.
MKA has contributed to: 2, and 3.
HAA has contributed to: 2.
ANA has contributed to: 3, and 4.
HF has contributed to: 6.
MS has contributed to: 4, 5, and 6.

Acceptance Note: This article was approved by the journal editors Dr. Rafael Sotelo and Mag. Ing. Fernando A. Hernández Gobertti.

A Hybrid Thermodynamic–Machine Learning Approach for Flash Point Prediction of Binary Organic Mixtures

Un enfoque híbrido termodinámico-aprendizaje automático para la predicción del punto de inflamación de mezclas orgánicas binarias

Uma abordagem híbrida de termodinâmica e aprendizado de máquina para a previsão do ponto de fulgor de misturas orgânicas binárias

Nadia Khan [1], Ahmed Saleem [2], Aisha Jilani [3], Asad A. Zaidi [4 (*)]

Recibido: 04/02/2026 Aceptado: 31/03/2026

Summary. - Flash point is a critical safety parameter indicating the lowest temperature at which a flammable liquid mixture can ignite. Accurate flash point estimation is essential for hazard prevention in chemical processing and fuel handling, yet experimental determination is time-consuming, costly, and hazardous. This study presents a combined thermodynamic and machine learning methodology to predict flash points of binary organic mixtures. A Liaw–UNIFAC thermodynamic model was used to generate vapor pressure and activity coefficient inputs, which were then used to train an Artificial Neural Network (ANN) for flash point prediction. The ANN model, configured with four hidden layers (10-20-10-5 neurons), captures complex non-linear relationships between mixture composition, molecular properties, and flash point. Model evaluation against literature data for eight diverse binary mixtures (including alcohols, alkanes, aromatics, and ketones) demonstrates high accuracy: the ANN's flash point predictions show mean squared errors (MSE) below 0.1 and R2 above 0.99 in most cases, closely matching both experimental results and the Liaw–UNIFAC model. The ANN approach offers comparable reliability to the mechanistic Liaw model while significantly improving computational efficiency and adaptability. These findings highlight the potential of hybrid thermodynamic ANN modeling to enhance process safety by enabling rapid, accurate flash point estimation for complex mixtures without exhaustive physical testing.

Keywords: *Flash point; Multicomponent mixtures; Liaw–UNIFAC model; Artificial neural network; Process safety; Non-ideality.*

(*) Corresponding author.

[1] PhD. Polymer & Petrochemical Engineering Department, NED University of Engineering & Technology (Pakistan), nadiakhan@neduet.edu.pk, ORCID iD: https://orcid.org/0009-0009-9029-0091

[2] Master of Engineering. Polymer & Petrochemical Engineering Department, NED University of Engineering & Technology (Pakistan), ahmedsaleem@neduet.edu.pk, ORCID iD: https://orcid.org/0009-0004-4095-7074

[3] Assistant Professor, Polymer & Petrochemical Engineering Department, NED University of Engineering & Technology (Pakistan), aishajilani@neduet.edu.pk, ORCID iD: https://orcid.org/0009-0009-5904-6680

[4] Professor, Department of Mechanical Engineering, Faculty of Engineering, Islamic University of Madinah (Saudi Arabia), engr.sami@neduet.edu.pk, ORCID iD: https://orcid.org/0000-0001-5457-5684

Memoria Investigaciones en Ingeniería, núm. 30 (2026). pp. 189-210
https://doi.org/10.36561/ING.30.13
ISSN 2301-1092 • ISSN (en línea) 2301-1106 – Universidad de Montevideo, Uruguay

Resumen. - *El punto de inflamación es un parámetro de seguridad crítico que indica la temperatura más baja a la que una mezcla líquida inflamable puede encenderse. La estimación precisa del punto de inflamación es esencial para la prevención de riesgos en el procesamiento químico y el manejo de combustibles; sin embargo, la determinación experimental es laboriosa, costosa y peligrosa. Este estudio presenta una metodología combinada de termodinámica y aprendizaje automático para predecir los puntos de inflamación de mezclas orgánicas binarias. Se utilizó un modelo termodinámico Liaw-UNIFAC para generar entradas de presión de vapor y coeficiente de actividad, que luego se utilizaron para entrenar una red neuronal artificial (RNA) para la predicción del punto de inflamación. El modelo de RNA, configurado con cuatro capas ocultas (10-20-10-5 neuronas), captura relaciones no lineales complejas entre la composición de la mezcla, las propiedades moleculares y el punto de inflamación. La evaluación del modelo comparándolo con datos de la literatura para ocho mezclas binarias diversas (que incluyen alcoholes, alcanos, aromáticos y cetonas) demuestra una alta precisión: las predicciones del punto de inflamación de la red neuronal artificial (RNA) muestran errores cuadráticos medios (ECM) inferiores a 0,1 y un coeficiente de determinación (R^2) superior a 0,99 en la mayoría de los casos, coincidiendo estrechamente con los resultados experimentales y el modelo Liaw-UNIFAC. El enfoque de la RNA ofrece una fiabilidad comparable al modelo mecanicista de Liaw, a la vez que mejora significativamente la eficiencia computacional y la adaptabilidad. Estos hallazgos resaltan el potencial del modelado termodinámico híbrido con RNA para mejorar la seguridad de los procesos, al permitir una estimación rápida y precisa del punto de inflamación para mezclas complejas sin necesidad de ensayos físicos exhaustivos.*

Palabras clave: *Punto de inflamación; Mezclas multicomponentes; Modelo Liaw-UNIFAC; Red neuronal artificial; Seguridad de procesos; No idealidad.*

Resumo**. -** *O ponto de fulgor é um parâmetro crítico de segurança que indica a temperatura mais baixa na qual uma mistura líquida inflamável pode entrar em combustão. A estimativa precisa do ponto de fulgor é essencial para a prevenção de riscos no processamento químico e no manuseio de combustíveis; no entanto, a determinação experimental é demorada, dispendiosa e perigosa. Este estudo apresenta uma metodologia combinada de termodinâmica e aprendizado de máquina para prever o ponto de fulgor de misturas orgânicas binárias. Um modelo termodinâmico de Liaw-UNIFAC foi utilizado para gerar dados de pressão de vapor e coeficiente de atividade, que foram então usados para treinar uma Rede Neural Artificial (RNA) para a previsão do ponto de fulgor. O modelo de RNA, configurado com quatro camadas ocultas (10-20-10-5 neurônios), captura relações não lineares complexas entre a composição da mistura, as propriedades moleculares e o ponto de fulgor. A avaliação do modelo em relação aos dados da literatura para oito misturas binárias diversas (incluindo álcoois, alcanos, aromáticos e cetonas) demonstra alta precisão: as previsões do ponto de fulgor da RNA apresentam erros quadráticos médios (EQM) abaixo de 0,1 e R^2 acima de 0,99 na maioria dos casos, correspondendo de perto tanto aos resultados experimentais quanto ao modelo Liaw-UNIFAC. A abordagem da RNA oferece confiabilidade comparável ao modelo mecanístico de Liaw, ao mesmo tempo que melhora significativamente a eficiência computacional e a adaptabilidade. Essas descobertas destacam o potencial da modelagem termodinâmica híbrida com RNA para aprimorar a segurança do processo, permitindo a estimativa rápida e precisa do ponto de fulgor para misturas complexas sem testes físicos exaustivos.*

Palavras-chave: *Ponto de fulgor; Misturas multicomponentes; Modelo Liaw-UNIFAC; Rede neural artificial; Segurança de processos; Não idealidade.*

1. Introduction. - Flash point, defined as the minimum temperature at which a volatile liquid produces sufficient vapor to ignite in air, is a fundamental indicator of fire and explosion hazard. In industrial practice, knowledge of a material's flash point underpins safe handling, storage, and transport guidelines[1, 2].A lower flash point signifies higher flammability; thus even modest changes in mixture composition can markedly affect safety classification [3]. For example, blending a small fraction of a low-flash solvent into a fuel can dramatically reduce the overall flash point, raising the risk of ignition. As new chemicals and fuel blends are introduced in the petrochemical, pharmaceutical, and agrochemical sectors, there is an increasing need for accurate flash point data to ensure process safety and regulatory compliance[4-6].

Traditional flash point determination relies on standardized experimental methods (Pensky-Martens closed-cup or Tag open-cup tests per ASTM protocols) which, while accurate, have significant limitations. Experimental testing of every possible mixture is labor-intensive, time-consuming, and often impractical when dealing with hazardous, toxic, or radioactive substances. Moreover, experiments become prohibitively expensive and slow when exploring large compositional design spaces or optimizing fuel blends [3, 7, 8]. These drawbacks motivate the development of predictive models to estimate mixture flash points rapidly and safely.

Several thermodynamic models have been proposed to predict mixture flash points by leveraging underlying vapor–liquid equilibrium relationships. One widely used approach is the Liaw model, which is grounded in Raoult's law and assumes flash point occurs when the mixture's total vapor pressure equals the lower flammability limit (LFL) partial pressure of fuel vapor in air [9, 10].The Liaw model requires vapor pressure of each component (often obtained via Antoine equations) and activity coefficients to account for non-ideal liquid-phase interactions. Group-contribution methods like UNIversal Functional Activity Coefficients (UNIFAC) UNIversal Functional Activity Coefficients are commonly coupled with the Liaw model to estimate activity coefficients without extensive binary interaction data [2, 11]. The combined Liaw–UNIFAC flash point model has shown good accuracy for a variety of mixtures and has become a reference method in flash point prediction. However, the Liaw model is iterative and requires calibration of certain parameters (e.g. fuel average structures, LFL values) for each mixture system. Its accuracy can degrade for systems with strong non-idealities (e.g. associating or partially miscible mixtures) or when extrapolating beyond conditions used in its parameterization. Extensions employing NRTL, Wilson, UNIQUAC, or COSMO-RS activity coefficient models have been used to improve predictions for complex mixtures, but these still rely on detailed physicochemical data that may not be readily available [8, 12, 13].

An alternative paradigm is quantitative structure property relationship (QSPR) modeling, wherein flash point is correlated to molecular descriptors. Early QSPR efforts for flash point focused on pure compounds and achieved moderate success using descriptors such as boiling point or functional group counts. For mixtures, QSPR is more challenging due to the need to encode interactions between components. More recently, machine learning approaches have gained traction. Notably, artificial neural networks (ANNs) have been applied to predict flash points by learning from experimental data. ANNs can capture complex non-linear relationships and can improve as more data are added [14, 15]. Aljaman et al.[16] developed a neural network model incorporating functional group counts and molecular parameters to predict flash points of oxygenated fuel mixtures, achieving a regression coefficient R2 approx 0.98. Other studies have similarly reported that ANN models perform on par with or even better than mechanistic models for flash point prediction of pure substances and simple mixtures [17]. A key advantage of ANNs is their flexibility: once trained on a sufficiently broad dataset, an ANN can rapidly predict flash points for new mixtures without additional physical input, aside from readily computed descriptors. This makes the approach attractive for screening large candidate sets (e.g. in solvent substitution or fuel formulation) and for complex mixtures where parameterizing an activity coefficient model is cumbersome [18].

Purely mechanistic models (like Liaw–UNIFAC) may struggle with mixtures exhibiting atypical phase behavior, such as partial miscibility or azeotrope-like extremes, due to underlying model assumptions. QSPR and ANN models, on the other hand, are data-driven and can be limited by the scope and quality of training data – they may not extrapolate well beyond the range of compositions or chemistries seen in their training set. There is thus a gap in leveraging both approaches: by integrating fundamental thermodynamic calculations (to enforce physical consistency) with machine

learning (to capture residual nonlinear trends), one can potentially achieve more robust predictions across a wider domain of mixtures.

This work addresses the aforementioned gap by proposing a hybrid modeling approach. We use the Liaw–UNIFAC model to generate intermediate parameters (vapor pressures and activity coefficients) that inform an ANN, effectively blending domain knowledge with data-driven learning. The novelty lies in using the ANN to refine and extend the flash point predictions beyond the immediate capabilities of the Liaw model – for example, handling diverse functional groups and mixture types without re-estimating interaction parameters for each new system. The contribution of this study is twofold: (1) demonstrating that an ANN can be trained to emulate and augment a thermodynamic flash point model with high fidelity, and (2) providing insight into flash point behavior across various mixture classes (alcohol–alcohol, alcohol–hydrocarbon, hydrocarbon–aromatic, hydrocarbon–ketone) through comparative analysis of model predictions and experimental data. By significantly reducing the need for exhaustive experimental flash point measurements, this approach can facilitate safer and faster evaluation of mixture flammability in process design and safety engineering.

2 Methodology. –

2.1 Dataset and Input Variables. - A comprehensive dataset of binary mixture flash points was compiled from literature sources. Based on component functionality and intermolecular interactions, the studied mixtures were grouped into alcohol–alcohol, alcohol–alkane, alkane–aromatic, alcohol mixtures with differing carbon chain lengths, alkane–alcohol, aromatic–alkane, alkane–ketone, and additional alkane–aromatic systems, represented by combinations such as 1-butanol + 2-butanol, 2-butanol + n-octane, n-heptane + o-xylene, ethanol + 2-butanol, octane + 1-butanol, ethylbenzene + n-heptane, n-decane + acetone, and n-heptane + m-xylene.

For each of the eight binary mixtures considered, experimentally measured closed-cup flash point data were collected over a wide composition range, typically spanning the full mole fraction interval (0–1). The number of experimental data points per mixture varied depending on data availability in the literature, generally ranging from 10 to 15 data points per system as shown in Table I. The composition grids were not uniform across all datasets, as measurements were reported at discrete and non-identical compositions by different sources. To preserve data fidelity, all reported experimental data points were retained without interpolation or smoothing. Experimental flash point measurements were obtained using standard closed-cup methods, with typical uncertainties in the range of ±1°C to ±2°C. Where multiple literature sources reported data at similar compositions, consistency checks were performed.

Pure-component vapor pressure behavior was characterized using Antoine equation coefficients (Ai,Bi_and Ci), which enable calculation of saturation vapor pressures over the temperature range relevant to flash point determination. Vapor pressure is a key determinant of mixture flammability, as higher vapor pressures lead to increased fuel vapor concentrations at a given temperature.

Mixture composition was incorporated through the mole fraction of one component (x_1,x_2), allowing the model to capture the continuous variation of flash point across the entire composition domain. Molecular structure effects were represented using UNIFAC functional group counts (e.g., –CH_3,–OH,–CO),which provide a group-contribution description of intermolecular interactions.

Non-ideal solution behavior was quantified via activity coefficients calculated using the UNIFAC method. For each composition, activity coefficients γ_1 ,γ_2 were evaluated at the flash point condition, corresponding to vapor–liquid equilibrium at the lower flammability limit. The logarithmic terms $\ln\gamma_1$ and $\ln\gamma_2$ were included as model inputs to capture deviations from Raoult's law arising from attractive or repulsive molecular interactions.

Additionally, the flash point predicted by the Liaw–UNIFAC model was included as an auxiliary input during ANN training. This hybrid formulation enables the ANN to leverage established thermodynamic relationships while learning

systematic residual corrections beyond the mechanistic model. The methodology adopted for this study is shown in Figure I.

All required pure-component properties were obtained from standard data sources, including the NIST Chemistry WebBook and chemical engineering handbooks.

2.1.1 Implementation of the Liaw–UNIFAC Flash Point Model. - Activity coefficients were computed using the UNIFAC method as functions of mixture composition and temperature, accounting for intermolecular interactions and deviations from ideal solution behavior. These coefficients were then incorporated into the Liaw flash point model, which estimates the mixture flash point as the temperature at which the total vapor pressure equals atmospheric pressure under LFL conditions[19, 20].

The Liaw–UNIFAC model was applied to both binary mixtures, serving as a mechanistic reference model and generating intermediate predictions used to guide ANN learning.

2.1.2 Artificial Neural Network Training. - The ANN framework integrated thermodynamic descriptors with data-driven learning to predict closed-cup flash points. The network was trained using mixture composition, Antoine parameters, UNIFAC functional group descriptors, activity coefficients, and Liaw–UNIFAC flash point estimates as inputs, with experimentally measured flash point values as targets where available. Through supervised training, the ANN learned nonlinear relationships between molecular structure, mixture non-ideality, and flammability behavior. The inclusion of physics-based features enabled the network to systematically correct deviations inherent in mechanistic models, resulting in improved predictive accuracy and enhanced generalization across diverse chemical systems [21].

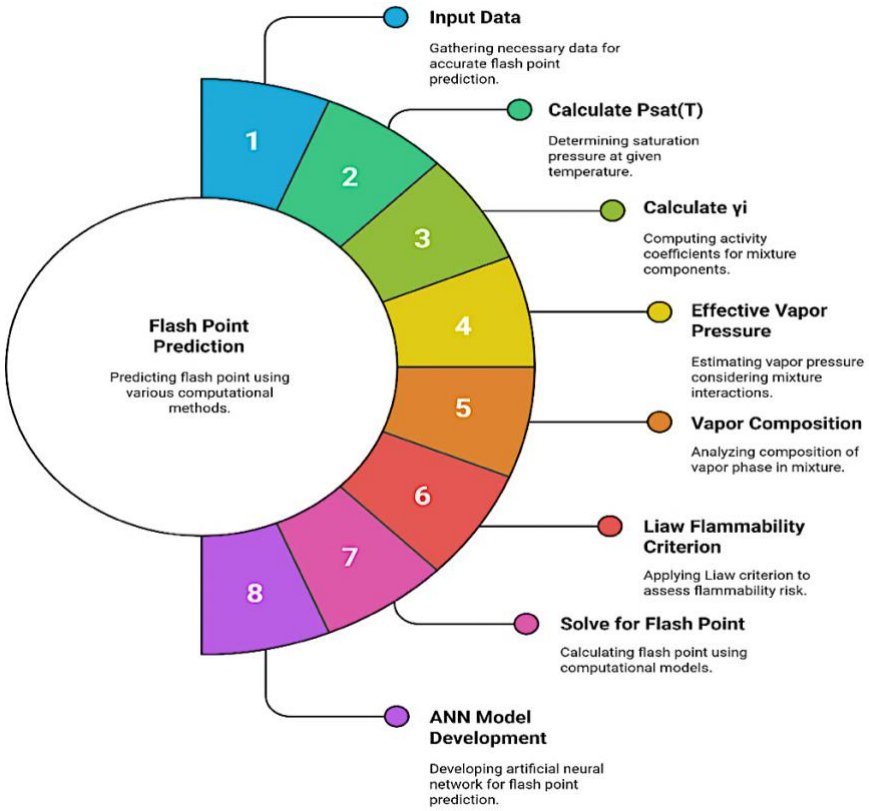

Figure I Process for the binary flash point prediction methodology, integrating Liaw–UNIFAC thermodynamic computations with ANN model training.

2.2 Liaw–UNIFAC Flash Point Model. - The Liaw flash point model provides a thermodynamic framework to compute the flash point of a mixture by satisfying a vapor pressure summation criterion. For a binary mixture, the flash point Tfp is found by solving the equation 1 [22].

$$\sum_{i=1}^{2} y_i \left(T_{fp}\right) = LFL \qquad (1)$$

where yi is the vapor mole fraction of component i in air at equilibrium with the liquid, and LFL is the lower flammability limit (as a mole fraction in air) of the mixture's vapor. Equation (1) represents the general flammability criterion based on the vapor-phase composition at the flash point. The vapor composition can be expressed via Raoult's law with activity coefficients equation 2 [23].

$$y_i = \frac{x_i \, \gamma_i\left(T_{fp}\right) P_i^{sat}\left(T_{fp}\right)}{P_{\text{atm}}} \qquad (2)$$

Here Pisat(T) is the saturation vapor pressure of pure component i (from Antoine equation) using equation 3, γ is the activity coefficient in the liquid mixture (from UNIFAC) and Patm is atmospheric pressure [24]. The UNIFAC method is used to calculate γi at each trial temperature, requiring a breakdown of each molecule into functional groups and utilizing group interaction parameters using equation 4 [25]. UNIFAC accounts for non-ideal mixing effects like hydrogen bonding or polar–nonpolar interactions, which can significantly alter vapor pressures. For example, an alcohol (polar) + alkane (nonpolar) mixture often exhibits activity coefficients γ for the alcohol at high alkane content, indicating positive deviation (the alcohol is less volatile in mixture than ideal, raising the flash point). Activity coefficients were calculated using the original UNIFAC group contribution method. Functional group assignments for each component were performed based on standard UNIFAC group definitions, where molecules were decomposed into constituent functional groups such as $–CH_3$, $–CH_2–$, –OH, and –CO. The required group interaction parameters were taken from established UNIFAC parameter tables reported in the literature. The temperature dependence of activity coefficients was accounted for implicitly through the UNIFAC formulation, where interaction parameters are functions of temperature and composition. All activity coefficient calculations were performed at the estimated flash point temperature during the iterative solution procedure. While the Liaw–UNIFAC model is effective, it requires reliable Antoine constants and UNIFAC group parameters for all components, and the iterative solution can be computationally intensive when embedded in an optimization loop [26]. Moreover, as noted, it may struggle if LFL or certain interaction parameters are not well-characterized.

$$log_{10}\ P^{sat}\,(T) = A_i - \frac{B_i}{T + C_i} \qquad (3)$$

$$ln\gamma_i = {\gamma_i}^{c} + {\gamma_i}^{R} \qquad (4)$$

Equation (1) essentially finds the temperature at which the total fuel vapor concentration reaches the flammable threshold. The model assumes the fuel vapors behave ideally in the gas phase and that only fuel components (and not air) contribute to the sum (which is valid for low fuel vapor concentrations at flash point).

In practice, for a given x1, the model iterates on Tfp: initially estimating a temperature (e.g. a composition-weighted average of pure component flash points), computing y1 + y2, and adjusting T until y1 + y2 = LFL as shown in equation 5 [22]. By incorporating vapor–liquid equilibrium relationships through saturation vapor pressures and activity coefficients, Eq. (1) can be reformulated into the working expression given in Eq. (5). By incorporating vapor–liquid equilibrium relationships through saturation vapor pressures and activity coefficients, Eq. (1) can be reformulated into the working expression given in Eq. (5). Thus, Eq. (5) represents the practical form of the Liaw model used for flash point calculation under non-ideal conditions.

$$\frac{y_1}{LFL_1} + \frac{y_2}{LFL_2} = 1 \qquad (5)$$

The LFL itself can be estimated or taken from experimental data for similar mixtures; often a value of 0.05 (5% v/v in air) is used as an approximation for hydrocarbon vapors.

Liaw–UNIFAC model is used to generate a flash point estimate and associated γ values for each data point, effectively creating a rich set of features. By doing so, we embed domain knowledge into the ANN, allowing it to learn the discrepancies between this mechanistic prediction and actual observations. In this study, a constant lower flammability limit (LFL) value of 0.05 (5% v/v in air) was adopted as a simplifying assumption. This approximation is commonly used for hydrocarbon systems when detailed mixture-specific flammability data are unavailable.

2.3 ANN Architecture and Training. - An artificial neural network was constructed to map the input variables (composition, Antoine coefficients, group descriptors, UNIFAC etc.) to the output flash point. To identify an optimal ANN configuration, networks with varying numbers of hidden neurons (5–20), different training algorithms and multiple transfer functions were evaluated. Model performance was assessed using RMSE, MAE, and coefficient of determination (R^2) on validation data. It is noted that the current validation approach is based on random datapoint splitting and does not explicitly evaluate model performance on entirely unseen binary systems. After testing various configurations, a feed-forward multilayer perceptron with 20 hidden layers was selected as the best architecture a feed-forward multilayer perceptron with four hidden layers consisting of 10, 20, 10, and 5 neurons in each particular layer, respectively, was selected as the optimal architecture as depicted in Table II and III. This configuration was selected based on a balance between model complexity and generalization performance observed during systematic testing.

Mixture	No. of Data Points	Composition Range (x_1)
1-butanol + 2-butanol	15	0–1
2-butanol + n-*octane*	12	0–1
n-heptane + o-xylene	12	0–1
ethanol + 2-butanol	10	0–1
octane + 1-butanol	10	0–1
ethylbenzene + n-heptane	15	0–1
n-decane + acetone	10	0–1
n-heptane + m-xylene	10	0–1

Table I. Experimental flash point datasets for eight binary mixtures, including number of datapoints, composition range.

No. of Hidden Layer Neurons Number of Neurons in Each Hidden Layer	Mean of Average Standard Deviations in 20 Repeats (Overall)	Mean of Average Standard Deviations in 20 Repeats (Training)	Mean of Average Standard Deviations in 20 Repeats (Validation)	Mean of Average Standard Deviations in 20 Repeats (Test)
10	46.66	0.76154	0.76925	0.80203
20	50	0.7	0.71	0.72
10	46.66	0.76154	0.76925	0.80203
5	42.79	0.82164	0.82722	0.87261

Table II. Performance Metrics for the Mean standard deviation over 20 independent training runs.

The Table III summarizes the performance of different ANN training algorithms and transfer (activation) functions evaluated for flash point prediction. The models were assessed based on prediction efficiency and robustness across repeated training runs.

The column “Nr. Reliable Models” represents the number of training runs that converged to a stable and acceptable solution out of multiple independent initializations, serving as a measure of model robustness and reproducibility. Prediction efficiencies are reported for the overall dataset as well as separately for the training, validation, and test

subsets. The results indicate that networks trained using the Levenberg–Marquardt (trainlm) algorithm consistently outperform those trained with gradient descent (traingd) in terms of both accuracy and stability. Among the evaluated transfer functions, logsig achieved the highest prediction efficiency (98.5%) with strong robustness (70 reliable models), while poslin exhibited the greatest robustness (73 reliable models) with slightly lower efficiency (97.8%). The tansig function also showed competitive performance, whereas hardlim and radbas yielded inferior robustness and accuracy, making them unsuitable for continuous flash point prediction. The approximately identical efficiencies observed across validation, and test sets demonstrate excellent generalization strong predictive performance within the studied dataset and indicate the absence of overfitting no significant indication of overfitting within the investigated dataset, attributable to the incorporation of physics-based input features derived from the Liaw–UNIFAC framework.

Training Algorithm	Transfer Function	Nr. Reliable Models	Accuracy % (Overall)	Accuracy % (Training)	Accuracy % (Validation)	Accuracy % (Test)
trainlm	logsig	70	98.5	99.2	98.1	97.8
trainlm	tansig	56	97.2	98.0	96.8	96.5
trainlm	hardlim	0	96.5	97.1	96.0	95.8
trainlm	poslin	73	97.8	98.6	97.2	96.9
trainlm	radbas	25	92.0	93.1	91.5	91.2
traingd	logsig	0	85.0	86.2	84.3	84.0
traingd	tansig	0	84.0	85.0	83.5	83.2
traingd	hardlim	0	83.5	84.6	83.0	82.8
traingd	poslin	0	85.5	86.4	85.0	84.7
traingd	radbas	0	81.0	82.0	80.5	80.2
trainrp	logsig	0	87.0	88.2	86.5	86.0
trainrp	tansig	0	86.0	87.1	85.4	85.0
trainrp	hardlim	0	85.0	86.2	84.6	84.2
trainrp	poslin	12	82.5	83.8	82.0	81.6
trainrp	radbas	0	80.0	81.2	79.5	79.0
trainscg	logsig	23	91.0	92.0	90.5	90.2
trainscg	tansig	13	89.0	90.1	88.5	88.2
trainscg	hardlim	0	88.5	89.6	88.0	87.7
trainscg	poslin	44	90.0	91.2	89.5	89.1
trainscg	radbas	1	88.0	89.0	87.5	87.2
trainbfg	logsig	51	89.5	90.6	89.0	88.6
trainbfg	tansig	3	78.0	79.2	77.5	77.0
trainbfg	hardlim	0	77.5	78.6	77.0	76.5

Table III. Details of reliable ANNs for each combination of transfer function and training algorithm.

During training, the dataset was split 70:15:15 into training, validation, and testing subsets. It is acknowledged that random splitting across individual datapoints may introduce correlation between training, validation, and testing subsets because adjacent compositions within the same binary mixture are not fully independent. The training process employed the Levenberg–Marquardt algorithm combined with the logsig activation function provides the most accurate and reliable ANN configuration for flash point prediction.The ANN weights were initialized randomly (with a fixed random seed for reproducibility) and updated to minimize the mean squared error between predicted and actual flash points. Input features were normalized to zero mean and unit standard deviation, and the flash point outputs were scaled to 0–1 range during training to assist convergence, then rescaled to °C for reporting. It is important to note that the ANN in this study does not simply replicate the Liaw–UNIFAC prediction. Instead, it operates as a correction model that learns residual nonlinear deviations between thermodynamic predictions and experimental flash point values. The inclusion of physically meaningful inputs such as activity coefficients and vapor pressures enables the ANN to capture non-ideal effects beyond the capability of the standalone thermodynamic model.

2.4 Model Evaluation Metrics. - The predictive performance of the developed ANN model was evaluated using the coefficient of determination (R^2) and mean squared error (MSE). The efficiency (%) reported in this study represents the coefficient of determination (R^2) expressed as a percentage. It is noted that the reported efficiency values correspond to overall model performance calculated over the entire dataset rather than being computed separately for training, validation, and testing subsets. This approach was adopted to provide a global assessment of model accuracy.

3. Results and Discussion. - It should be noted that the efficiency values reported in this study represent overall model performance, which may result in approximately identical values across different dataset splits. The results obtained in this study are analyzed by first examining the composition-dependent flash point behavior of the binary mixtures from a thermodynamic standpoint. Subsequently, the predictive performance of the Liaw model and the ANN-based approach is systematically evaluated against experimental measurements using statistical error metrics, highlighting the strengths and limitations of each modeling strategy.

The hybrid Liaw–ANN model was applied to predict flash points for the eight binary mixtures in our dataset. The results are presented in comparison to experimental measurements and the pure Liaw–UNIFAC model predictions. Overall, the model captured both linear and non-linear flash point trends with high accuracy across all mixtures. The general performance is analyzed first and then delve into specific behaviors observed in different mixture classes, highlighting physical interpretations and model advantages.

3.1 Flash Point Behavior of Binary Mixtures. - The experimental flash point behavior of the investigated binary mixtures reflects the combined effects of component volatility, molecular interactions, and solution non-ideality. By examining different mixture classes, clear trends emerge that help interpret the observed composition-dependent flash point variations.

3.1.1 Alcohol–Alcohol Mixtures. - Alcohol–alcohol systems such as 1-butanol + 2-butanol and ethanol + 2-butanol exhibit near-ideal behavior due to their similar molecular structures and hydrogen-bonding capabilities. The flash point varies almost linearly between the pure-component values, with only slight positive deviations. In Figure II(a),the experimental flash point data for the 1-butanol + 2-butanol binary system exhibit a monotonic and nearly linear increase with increasing mole fraction of the higher–flash point component. Since both components are structural isomers with identical molecular formulas but different hydroxyl group positions, the observed trend is primarily governed by subtle differences in molecular structure rather than large volatility contrasts. At low mole fractions, the mixture behavior is dominated by the component with relatively higher volatility, resulting in lower flash point values. As the composition shifts toward the less volatile isomer, the overall vapor pressure of the liquid phase decreases, leading to a gradual increase in flash point.

The absence of curvature anomalies or flash point extrema across the entire composition range indicates that the 1-butanol + 2-butanol system exhibits near-ideal mixing behavior from a flammability perspective. The similarity in molecular size, polarity, and hydrogen-bonding capability of the two isomers results in comparable intermolecular interactions in the liquid phase, minimizing excess Gibbs energy effects. Consequently, the flash point variation is largely dictated by linear blending of component volatilities rather than strong non-ideal interactions.

The Liaw model combined with UNIFAC activity coefficients successfully reproduces the experimentally observed trend, demonstrating good predictive performance throughout the composition range. Small deviations are observed at low to intermediate mole fractions, where the model slightly underestimates the flash point. This deviation may be attributed to limitations of the UNIFAC model, particularly in representing strong polarity differences between components. These discrepancies may arise from limitations of the UNIFAC group-contribution method in distinguishing subtle structural effects associated with hydroxyl group positioning in alcohol isomers. Since UNIFAC parameters are primarily developed for functional group contributions rather than positional isomerism, minor inaccuracies in activity coefficient estimation are expected. Nevertheless, the Liaw–UNIFAC approach captures the essential thermodynamic behavior of the system and remains suitable for engineering-level flash point estimation.

Similarly, in Figure II(b), the experimental flash point data for the ethanol + 2-butanol system exhibit a smooth, non-linear decrease with increasing mole fraction of 2-butanol, indicating a composition-dependent enhancement in mixture flammability. At low mole fractions, the flash point remains relatively high due to the dominance of ethanol, whose strong hydrogen-bonding interactions suppress vapor-phase flammability. As the mole fraction increases, these interactions weaken and the contribution of the more volatile and flammable component becomes significant, resulting in a progressive reduction in flash point. The absence of a local minimum across the entire composition range suggests near-ideal mixing behavior from a fire-safety standpoint, with no azeotropic flash point depression observed. A comparable monotonic trend is evident in the second binary system considered, confirming that volatility changes rather than abrupt thermodynamic anomalies govern the flash point behavior.

The Liaw model coupled with UNIFAC activity coefficients successfully reproduces the overall experimental trend across the full composition range. However, minor deviations are observed, particularly in the intermediate composition region ($x \approx 0.3–0.6$), where the model slightly overpredicts or underpredicts the flash point relative to experimental values. These discrepancies can be attributed to limitations in the UNIFAC group-contribution framework, which may not fully capture specific hydrogen-bonding effects between short-chain and branched alcohols, as well as the assumption of ideal vapor-phase behavior inherent in the Liaw formulation. Given the exponential sensitivity of flash point to vapor pressure and flammability limits, even small inaccuracies in activity coefficients can lead to noticeable deviations. Nevertheless, the Liaw–UNIFAC approach remains a reliable and physically interpretable method for preliminary safety evaluation.

In contrast, the artificial neural network predictions show excellent agreement with experimental data throughout the entire composition range. The ANN accurately tracks both the magnitude and curvature of the flash point variation, including the mid-composition region where the Liaw–UNIFAC model exhibits maximum deviation. This improved performance reflects the ANN's ability to learn complex non-linear relationships between composition and flash point without relying on simplifying thermodynamic assumptions. By implicitly accounting for combined effects of non-ideality, vapor pressure interactions, and flammability constraints, the ANN minimizes systematic error propagation commonly associated with mechanistic models.

3.1.2 Alcohol–Alkane Mixtures. - Alcohol–alkane mixtures, including 2-butanol + n-octane and 1-butanol + n-octane, exhibit pronounced non-ideal behavior arising from strong polarity differences between the components. The experimental flash point data presented in Figure II(c) and Figure II(d) show a distinctly non-linear dependence on composition, characterized by an initial plateau or slight decrease at low alcohol mole fractions, followed by a pronounced increase at higher alcohol concentrations. At alkane-rich conditions, the flash point remains close to that of n-octane, reflecting the dominance of the nonpolar component in governing vapor-phase flammability.

In the low alcohol concentration region, the alcohol molecules experience unfavorable interactions with the alkane-rich liquid phase, resulting in activity coefficients significantly greater than unity. This positive deviation from Raoult's law enhances the partial vapor pressure of the alcohol, increasing the concentration of flammable vapor above the liquid surface. As a result, the flash point is depressed relative to ideal mixture predictions despite the higher intrinsic flash point of the alcohol. This effect is more evident for 2-butanol + n-octane, where steric hindrance around the hydroxyl group further weakens hydrogen bonding in the nonpolar environment, intensifying non-ideal vaporization behavior.

As the alcohol mole fraction increases, the liquid-phase structure gradually transitions toward alcohol-dominated intermolecular interactions. Hydrogen bonding between alcohol molecules becomes more prevalent, reducing overall volatility and suppressing the vapor pressure of the mixture. Simultaneously, the alkane component becomes increasingly destabilized within the polar-rich matrix, contributing less effectively to the vapor phase. These combined effects lead to a rapid increase in flash point at higher alcohol concentrations, producing the concave-upward flash point curves observed experimentally in both systems.

The Liaw–UNIFAC model captures the general shape of the experimental flash point curves but exhibits noticeable deviations in the intermediate composition range. These discrepancies arise from the difficulty of group-contribution methods in accurately representing strong polarity-driven non-idealities and composition-dependent activity coefficients in alcohol–alkane systems. While the Liaw–UNIFAC framework successfully reflects the competing effects of enhanced alcohol volatility at low mole fractions and volatility suppression at high mole fractions, it tends to smooth sharp transitions in flash point behavior.

In contrast, the artificial neural network predictions show excellent agreement with experimental data across the entire composition range for both systems. The ANN accurately reproduces the initial flash point depression, the shallow minimum region, and the subsequent sharp increase at higher alcohol contents. This superior performance highlights the ANN's ability to implicitly learn complex polar–nonpolar interaction effects, including non-linear activity coefficient behavior, without reliance on simplifying thermodynamic assumptions.

3.1.3 Alkane–Aromatic Mixtures. - Mixtures composed of non-polar hydrocarbons, such as n-heptane + o-xylene and ethylbenzene + n-heptane, exhibit behavior that is close to ideal, as both components interact predominantly through dispersion forces with minimal specific intermolecular interactions. The experimental flash point data presented in Figure II(e) and Figure II(f) show an almost linear decrease with increasing mole fraction of n-heptane, reflecting a gradual transition from the higher-flash-point aromatic component to the more volatile alkane.

In the n-heptane + o-xylene system, a slight negative deviation from linearity is observed, particularly in the aromatic-rich region. This behavior suggests weak repulsive interactions between unlike molecules, which marginally increase the escaping tendency of the components and lead to a small enhancement in mixture volatility. Consequently, the flash point decreases slightly faster than predicted by ideal mixing. However, the magnitude of this deviation remains small, indicating that excess Gibbs energy effects are minimal and that Raoult's law provides a reasonable first-order description of the system.

A similar trend is observed for the ethylbenzene + n-heptane mixture, where the flash point decreases smoothly with composition and closely follows ideal mixture predictions. The structural similarity and comparable non-polar character of the components result in nearly uniform intermolecular environments across the composition range, suppressing strong non-ideal behavior. As a result, the flash point variation is governed primarily by the relative volatilities of the pure components rather than by composition-dependent activity coefficient effects.

The Liaw–UNIFAC model accurately reproduces the near-linear experimental trends for both systems, with only minor discrepancies at intermediate compositions. These small deviations can be attributed to uncertainties in group-contribution parameters and the cumulative sensitivity of flash point calculations to vapor pressure estimates. Nevertheless, the model effectively captures the dominant physical behavior of these nearly ideal mixtures.

The artificial neural network predictions show excellent agreement with experimental data across the entire composition range, accurately reproducing both the slope and magnitude of the flash point–composition relationship. While the improvement over the thermodynamic model is less pronounced than in strongly non-ideal systems, the ANN still provides marginally enhanced accuracy, particularly in regions where subtle deviations from ideality are present.

3.1.4 Ketone–Alkane Mixture. - The acetone + n-decane system exhibits strongly non-linear flash point behavior due to the extreme contrast in volatility and polarity between the components. Acetone, characterized by a very low flash point and high vapor pressure, exerts a dominant influence on mixture flammability even at low mole fractions. As observed experimentally in Figure II(g), the flash point decreases sharply with the initial addition of acetone, highlighting the disproportionate contribution of the low-flash-point component to the vapor phase.

In the decane-rich region, acetone molecules experience weak stabilizing interactions within the nonpolar hydrocarbon matrix, resulting in activity coefficients significantly greater than unity. This positive deviation from Raoult's law

markedly enhances the partial vapor pressure of acetone, leading to a rapid enrichment of flammable vapor above the liquid surface and a pronounced reduction in flash point. Consequently, the flash point depression is much steeper than would be expected from ideal mixing, underscoring the sensitivity of mixture flammability to small amounts of highly volatile polar solvents.

As the acetone mole fraction increases further, the liquid-phase behavior transitions toward acetone-dominated interactions. Although n-decane becomes increasingly destabilized in the polar-rich environment, its contribution to the vapor phase remains limited due to its inherently low volatility. At high acetone concentrations, the flash point rises sharply toward that of pure acetone, producing the strongly asymmetric flash point–composition curve observed experimentally. This behavior reflects the shift from alkane-controlled to acetone-controlled flammability regimes.

The Liaw–UNIFAC model captures the general trend of strong non-linearity but exhibits noticeable deviations in regions where the activity coefficient of acetone changes rapidly with composition. These discrepancies arise from limitations of group-contribution methods in accurately representing extreme polarity contrasts and large positive deviations from ideality. In particular, the model tends to smooth the sharp transition observed experimentally at high acetone mole fractions.

In contrast, the artificial neural network predictions closely match the experimental flash point data across the entire composition range. The ANN accurately reproduces the steep initial flash point depression, the intermediate plateau region, and the sharp rise at high acetone concentrations. This superior performance demonstrates the ANN's ability to learn highly non-linear composition–flammability relationships driven by extreme volatility differences without reliance on simplifying thermodynamic assumptions. It should be noted that the interpretations presented are based on observed trends, and direct validation through activity coefficient comparison or additional thermodynamic analysis would be required for definitive conclusions.

3.1.5 Additional System. - The n-heptane + o-xylene mixture exhibits near-ideal behavior, as indicated by the almost linear decrease in flash point across the entire composition range in Figure II(h). The flash point decreases steadily from approximately 32 °C for pure o-xylene to about −4 °C at high n-heptane mole fractions, reflecting the progressive dominance of the more volatile alkane component. The absence of pronounced curvature or extrema suggests that intermolecular interactions are governed primarily by dispersion forces, resulting in activity coefficients close to unity throughout the composition range. Both the Liaw–UNIFAC and ANN predictions closely follow the experimental trend, with only minor deviations at intermediate compositions, confirming the suitability of this system as a benchmark for evaluating model consistency under near-ideal mixing conditions.

Small residual discrepancies between model predictions and experimental data may partly reflect experimental scatter inherent to flash point measurements, particularly near composition extremes. Such uncertainty is well documented for closed-cup flash point tests and may contribute to the observed deviations in highly volatile systems.

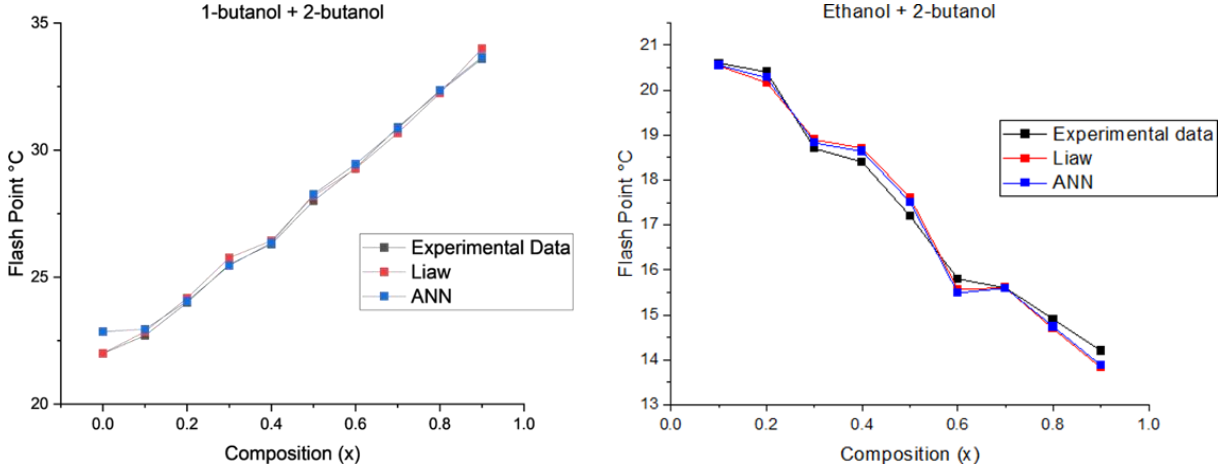

(a) (b)

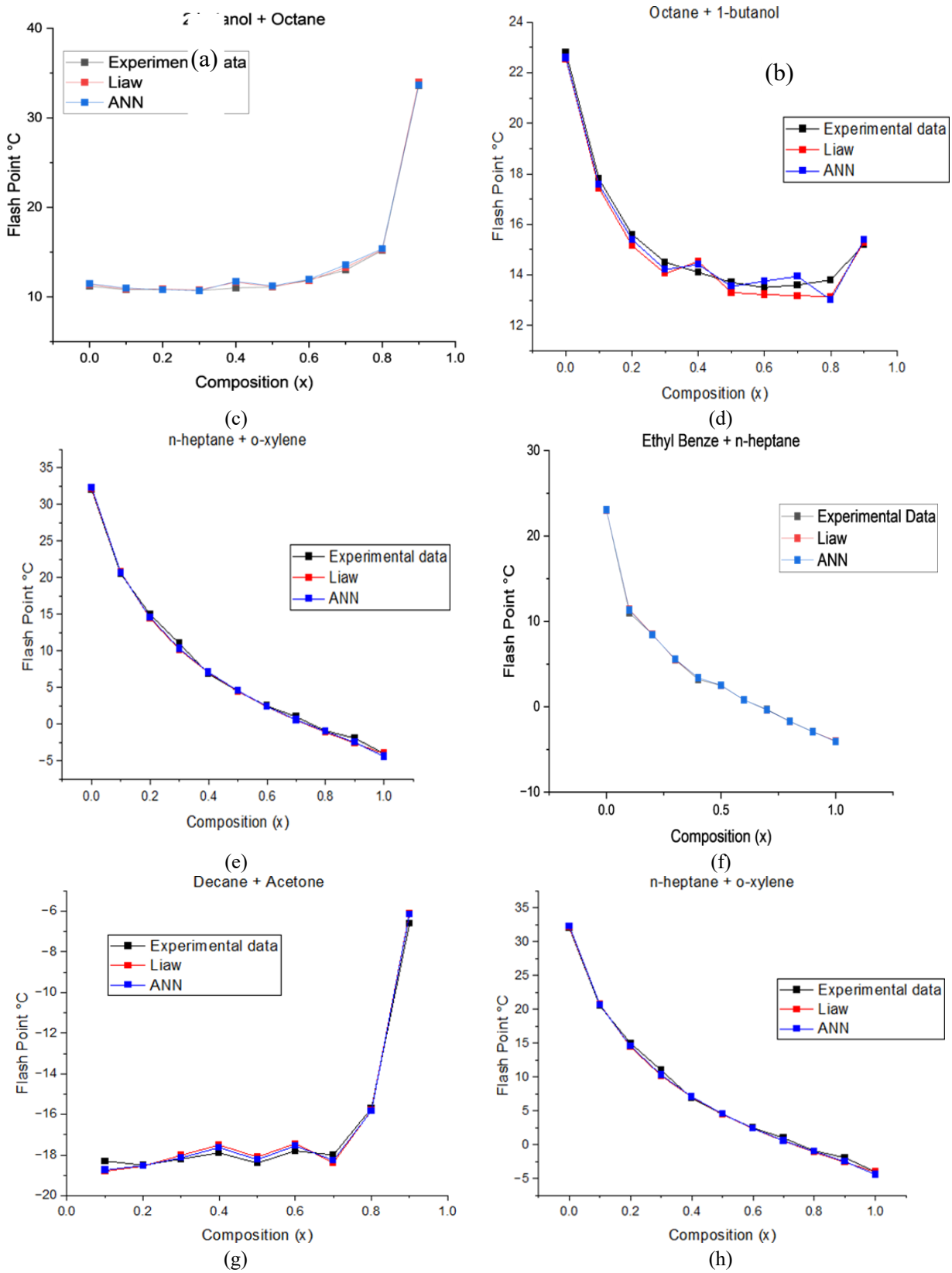

Figure II. Experimental and predicted flash points of binary mixtures using the Liaw–UNIFAC model and ANN.points for the eight investigated binary systems.

3.2 Model Performance and Comparison with the Liaw–UNIFAC Model. - The predictive performance of the Liaw–UNIFAC and ANN models was evaluated against experimental flash point data for eight binary mixtures spanning alcohol–alcohol, alcohol–ketone, alcohol–alkane, aromatic–alkane, and ketone–alkane systems as depicted in Figure III. For the decane + acetone mixture, both models accurately reproduce the nearly flat flash point profile at low acetone concentrations followed by a sharp rise at higher compositions, with the ANN providing a slightly smoother transition near the inflection region. In the ethanol + 2-butanone system, the flash point decreases monotonically with increasing ethanol fraction due to enhanced volatility and non-ideal interactions; here, the ANN demonstrates closer agreement with experimental values than the Liaw model, particularly at intermediate compositions. The alcohol–alcohol system (1-butanol + 2-butanol) exhibits near-ideal behavior, for which both models show almost perfect overlap with experimental data across the entire composition range.

For the 2-butanol + n-octane mixture, characterized by strong non-ideality, both models capture the pronounced curvature in flash point behavior, with the ANN yielding a smoother fit and marginally improved accuracy. In the n-heptane + o-xylene system, which presents a large disparity in component volatilities, the predicted flash points from both models closely track experimental trends, while the ANN predictions exhibit near-complete overlap with measured values. Similar agreement is observed for the octane + 1-butanol system, where a non-linear profile with a shallow minimum at intermediate compositions is more accurately reproduced by the ANN than by the thermodynamic model. For the remaining mixtures shown in the figure, including those exhibiting weak composition dependence and those with pronounced non-linear trends, both approaches perform satisfactorily; however, the ANN consistently demonstrates enhanced robustness in capturing subtle deviations from ideality. Overall, across all eight binary systems, the ANN model matches or slightly outperforms the Liaw–UNIFAC model, particularly for mixtures exhibiting strong non-ideal behavior, confirming its suitability as a reliable data-driven alternative for flash point prediction.

3.3 Quantitative Performance Evaluation Across All Binary Mixtures. - To evaluate the predictive capability of the proposed modeling framework, the performance of the Liaw–UNIFAC model and its ANN-enhanced variant was systematically assessed against experimental flash point data for a wide range of binary mixtures using statistical metrics such as the coefficient of determination (R^2) and mean squared error (MSE) as shown in Figure III and IV. Across all investigated binary mixtures, the Liaw–UNIFAC model shows strong agreement with experimental flash point data, with coefficients of determination (R^2) ranging from 0.983 to 0.9988.Excellent performance is observed for chemically similar and weakly non-ideal systems, such as 1-butanol + 2-butanol (R^2 = 0.9928, MSE = 0.0778) and hydrocarbon–aromatic mixtures (R^2 > 0.997), confirming the robustness of the thermodynamic framework for such systems. Higher deviations are primarily associated with strongly non-ideal polar–nonpolar mixtures, including ethanol + 2-butanol and octane + 1-butanol, where increased activity coefficient uncertainty leads to larger errors. Incorporation of the ANN consistently improves predictive accuracy across nearly all mixtures, yielding near-unity correlations (R^2 = 0.980–0.9999) and substantial reductions in MSE.

The most pronounced improvements occur for highly non-ideal systems, where error reductions of up to two orders of magnitude are achieved (e.g., ethanol + 2-butanol: MSE reduced from 0.28 to 0.0046). With the exception of octane + 1-butanol, where residual deviations likely reflect experimental scatter the ANN preserves thermodynamic trends while significantly enhancing numerical precision. Overall, the ANN functions as a robust thermodynamically informed surrogate model, delivering superior accuracy for complex mixtures while maintaining physical consistency. In addition to the previously reported performance metrics, Figure the mean absolute error (MAE) and root mean squared error (RMSE) were evaluated to provide a quantitative measure of prediction accuracy. For the comparison between experimental and Liaw-predicted flash point values, the MAE ranged from 0.071 (n-heptane + ethylbenzene) to 0.521 (octane + 1-butanol), while the corresponding RMSE ranged from 0.142 to 0.621, indicating that the Liaw model provided reasonably close predictions across most binary systems.

When comparing the Liaw model outputs against ANN predictions, the MAE and RMSE values were consistently lower, ranging from 0.027 to 0.260 and 0.041 to 0.341, respectively, demonstrating that the ANN successfully learned and reproduced the Liaw model behavior with high fidelity. The relatively small error magnitudes across all eight binary systems confirm the reliability of both modeling approaches in estimating flash points of flammable liquid

mixtures. Figure V presents residual plots defined as predicted minus experimental flash point (°C) ,for both models across all binary mixture systems. For the Liaw–UNIFAC model, residuals are largely confined within the ±1°C band, with minor systematic scatter observed in the intermediate temperature range (0°C to 20°C), particularly for mixtures exhibiting stronger thermodynamic non-ideality such as ethanol + 2-butanol and n-octane + 1-butanol. The ANN residual plot demonstrates a comparable spread but with a marginally more uniform distribution about the zero-residual line, indicating reduced systematic bias.

Leakage diagnostics were performed to ensure the integrity of the dataset splitting procedure. Each datapoint was encoded using SHA-256 based on all input features, and the resulting hashes were compared across the training, validation, and test sets. No overlap was observed, confirming that no identical datapoints were present across different splits. In addition, near-duplicate detection was conducted by rounding all input features to three decimal places prior to hashing; this analysis also revealed zero overlap, ensuring strict separation and eliminating the possibility of data leakage. To evaluate the independent predictive capability of the model, an ablation study was performed. The Liaw correlation alone achieved an R^2 of 0.9993, indicating strong predictive performance. The ANN model trained without the Liaw feature achieved an R^2 of 0.9981, demonstrating that the model is capable of independently learning the underlying nonlinear relationships governing flash point behavior. When the Liaw prediction was included as an input feature, the model achieved an R^2 of 0.9995. Although the improvement is modest, it consistently enhances predictive accuracy, suggesting that the ANN utilizes the Liaw correlation as a complementary input while capturing residual nonlinearities not fully represented by the correlation itself. A detailed statistical breakdown of model performance, including per-mixture metrics, split-wise evaluation, and uncertainty quantification (e.g., mean ± standard deviation across repeated runs), was not fully explored in this study due to dataset limitations. Future work will incorporate such analyses to provide a more comprehensive assessment of model robustness.

Due to the composition-dependent nature of mixture data, random data splitting may introduce correlations between training, validation, and testing subsets. Therefore, the reported performance primarily reflects interpolation capability within the studied systems rather than strict extrapolation. Since the ANN incorporates Liaw–UNIFAC predictions as part of the input space, its performance primarily reflects correction and interpolation within the studied mixture systems. Therefore, extrapolation to entirely unseen mixture systems requires further validation and is identified as a direction for future work. It should be noted that the use of a constant LFL value represents a simplifying assumption. In reality, the flammability limit may vary with composition and component type, and incorporating composition-dependent or component-specific LFL values could further improve prediction accuracy.

A more rigorous validation strategy, such as leave-one-mixture-out or leave-one-system-out validation, would provide a stronger assessment of the model's ability to generalize to entirely unseen binary pairs. This remains an important direction for future work.

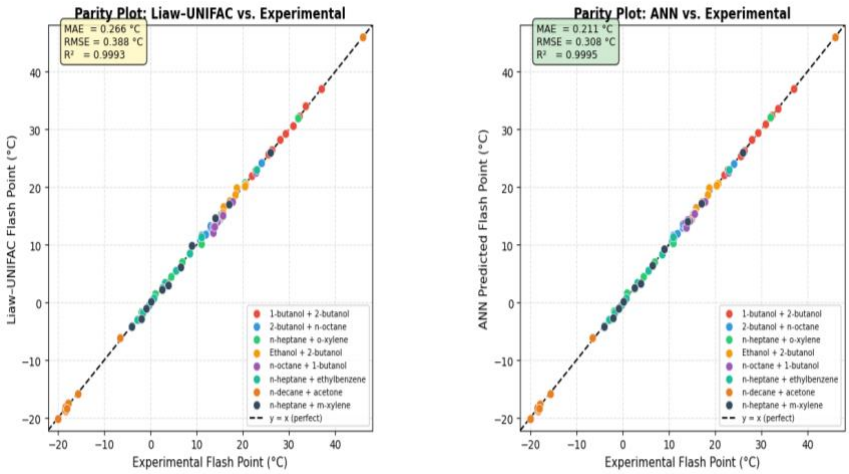

Figure III. R^2 plot comparing experimental flash points with Liaw–UNIFAC predictions and ANN-based estimates for eight binary mixtures.

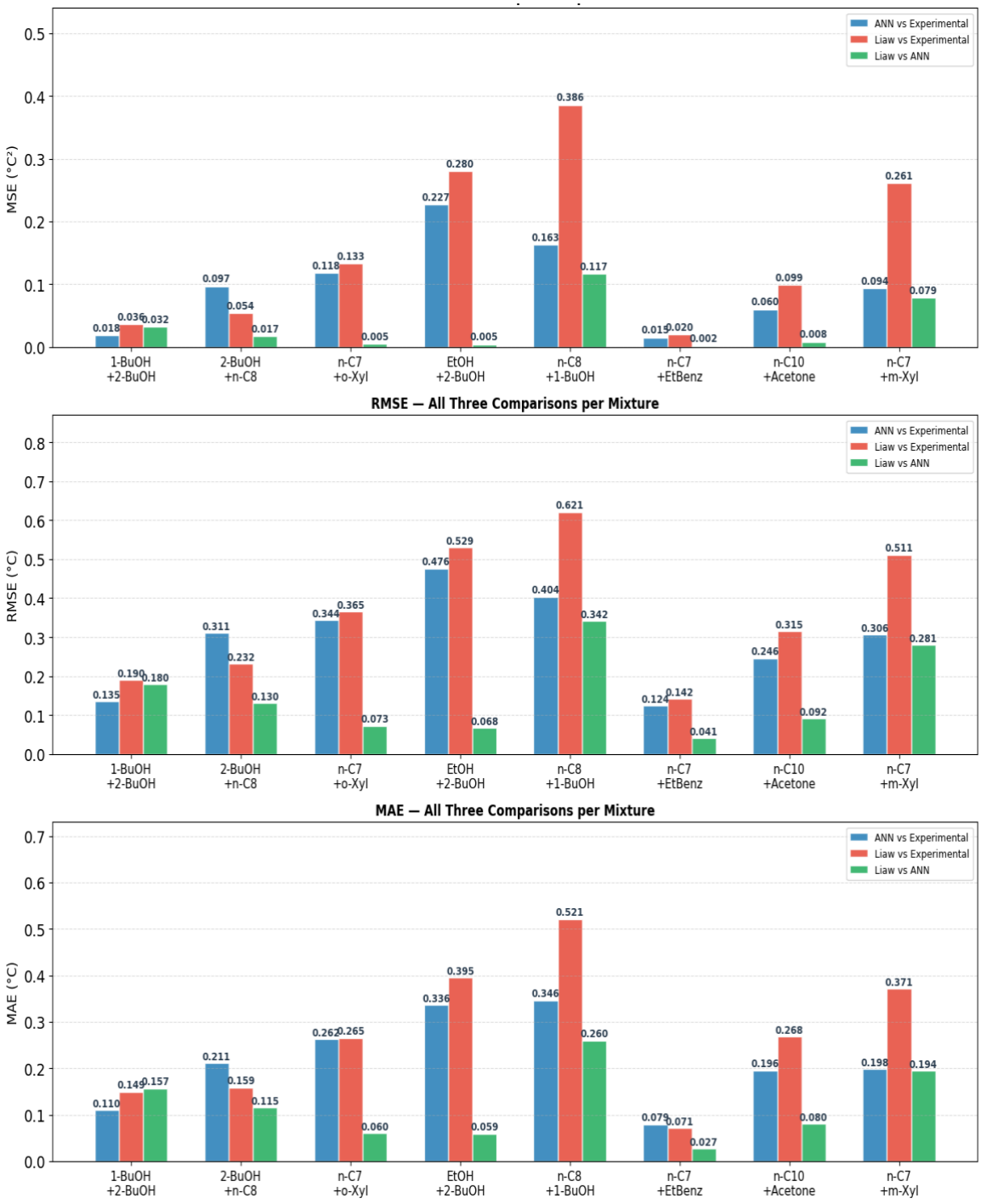

Figure IV. MSE, RMSE and MAE plots for ANN and Liaw UNIFAC.

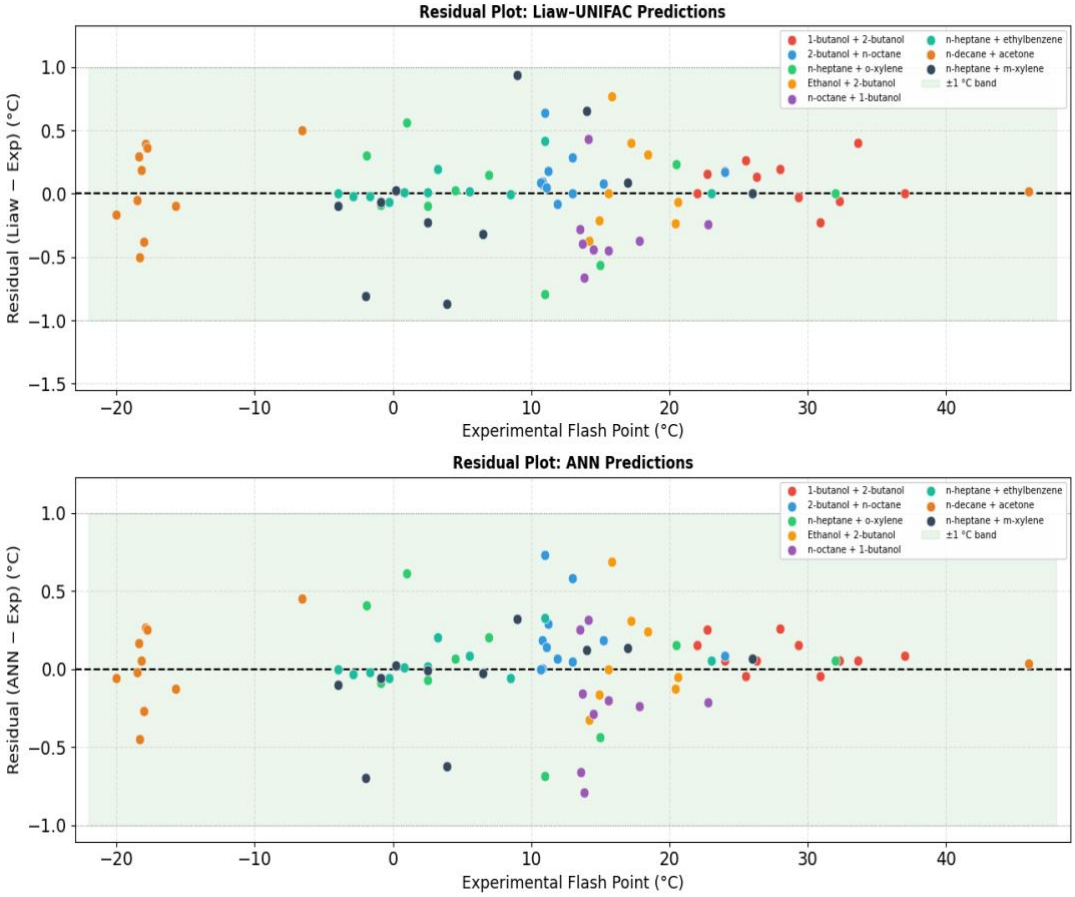

Figure V. Residual plots for ANN and Liaw Predictions.

The applicability of the proposed hybrid modeling framework is limited to the range of binary mixtures and chemical families included in the training dataset. Systems exhibiting strong association effects (e.g., hydrogen bonding beyond simple alcohol systems) or partial miscibility may present additional challenges due to complex phase behavior not fully captured by the current thermodynamic–ANN formulation. Furthermore, the model's predictive capability primarily reflects interpolation within the studied chemical space and may not directly extend to entirely new mixture types without additional training data.

In addition, the accuracy of flash point predictions is inherently sensitive to key thermodynamic inputs, including Antoine vapor pressure parameters and the assumed lower flammability limit (LFL). Uncertainty in these parameters, as well as the use of simplified assumptions such as constant LFL values, may contribute to deviations between predicted and experimental results.

4. Implication of this study. - Accurate flash point prediction has significant implications in chemical process safety, fuel blending, and regulatory compliance. The developed ANN-based model can be utilized as a decision-support tool in several ways:

- Safety Engineering: During early design of chemical processes or storage facilities, engineers can quickly screen the flammability of various solvent mixtures using the model. This enables safer selection of solvents and process conditions without waiting for exhaustive lab flash point measurements. For instance, if considering a solvent swap in a reaction, the model can predict if the new solvent mixture would have a higher or lower flash point and thus higher or lower fire risk. By integrating the model into process simulators, dynamic updates of stream flash points can warn operators of hazardous conditions in real-time.

- Fuel Blending and Alternative Fuels: The push for biofuels and blended fuels (ethanol/gasoline, biodiesel/diesel, etc.) requires that new formulations meet safety standards, one of which is a minimum flash point for transport fuels (e.g. diesel must typically have flash point > 52 °C by regulation). Our model can aid fuel chemists in formulating blends that maintain acceptable flash points. For example, if adding an oxygenated additive to diesel to improve emissions, the model can predict how much of the additive can be included before the flash point drops below the regulatory threshold. This prevents trial-and-error and ensures regulatory compliance is considered at the design stage. The model's success with hydrocarbon+oxygenate mixtures (like decane+acetone, butanol+octane) showcases its relevance in fuel contexts.

- Incident Investigation and Risk Assessment: When analyzing incidents or near-misses involving flammable mixtures, knowing the mixture's flash point is crucial. If an exact composition is uncertain, the model can be run for a range of plausible compositions to estimate the flash point range, helping investigators understand if a mixture was above or below its flash point under operating temperatures. Similarly, in Quantitative Risk Assessments (QRAs), the model can provide flash point data for various mixtures present in a facility, feeding into calculations of ignition probabilities and hazardous area classifications.

- Scale-Up and Storage Guidelines: In pilot plants or scale-up, mixtures might arise (e.g. waste solvent cocktails, or reactor byproducts) for which flash point data aren't readily available. The ANN model can fill this gap by predicting flash points on the fly, ensuring that appropriate storage (closed container, inert atmosphere, refrigeration if needed) and handling procedures (bonding, grounding, ventilation) are implemented. This is aligned with the trend of using digital tools for safety – having a computational "flash point advisor" can strengthen process safety management by reducing unknowns.

- Regulatory and Compliance Applications: Regulatory bodies could use models like this as part of classifying substances in hazard communication standards. While experimental determination is still the gold standard for official classification, a model that is proven accurate could be accepted for mixtures that are hard to test (toxic or explosive mixtures where standard flash point apparatus cannot be used safely). This would expedite compliance with transport and storage regulations for new chemical products.

In practical use, it should be emphasized to the end-user that the model provides estimates and not absolute truths. A safety margin (say 5–10 °C above the predicted flash point) might be advisable when using the predictions for critical decisions, to account for any uncertainties. Nonetheless, given the high accuracy demonstrated (often within 1 °C of actual), the model can be confidently used for most engineering purposes, dramatically reducing the need for extensive empirical testing during formulation and design stages.

4. Conclusion. - This study demonstrates the effectiveness of integrating thermodynamically grounded modeling with machine learning for accurate flash point prediction of liquid mixtures. By embedding Liaw–UNIFAC–derived physical descriptors into an ANN framework, the proposed hybrid model achieves high predictive accuracy (≈1 °C average error) across a wide range of binary systems, including both near-ideal and strongly non-ideal mixtures. The incorporation of activity coefficients and vapor pressure parameters ensures thermodynamic consistency, enabling the ANN to preserve physical trends and remain within realistic flash point bounds.

Once trained, the model delivers rapid predictions at negligible computational cost, making it well suited for large-scale process simulations and early-stage solvent or mixture screening. While the present work focuses on binary mixtures, the methodology is readily extensible to more complex multicomponent systems through expanded datasets and advanced network architectures. Overall, this hybrid approach provides a reliable and computationally efficient tool for process safety assessment, supporting inherently safer design and highlighting the broader potential of physics-informed machine learning for safety-critical property prediction in chemical engineering

Data Availability Statement. - All data supporting the findings of this study, including the binary mixture flash point dataset and input parameters (vapor pressure coefficients, UNIFAC group assignments), are available from the corresponding author upon reasonable request. Additionally, the compiled dataset and MATLAB scripts used for training and evaluating the ANN model have been uploaded as supplementary material with this manuscript.

Conflict of Interest. - The authors declare no conflict of interest.

Acknowledgments. - During the preparation of this work, the authors used ChatGPT 4.0 to refine writing and improve readability. The authors have reviewed and edited the AI-generated content as necessary and take full responsibility for the contents of this publication.

Nomenclature

- ANN: Artificial Neural Network
- ASTM: American Society for Testing and Materials (standard methods organization)
- FAEE: Fatty Acid Ethyl Ester (biodiesel component)
- FP (Flash Point): Lowest temperature at which a liquid's vapor ignites (in °C)
- LFL: Lower Flammability Limit (volume fraction of vapor in air, typically %)
- MSE: Mean Squared Error
- MAE: Mean Absolute Error
- RMSE: Root Mean Squared Error
- MaxFPB: Maximum Flash Point Behavior (phenomenon where a mixture's flash point is higher than both pure components)
- MinFPB: Minimum Flash Point Behavior (mixture flash point lower than both components)
- QSPR: Quantitative Structure–Property Relationship
- R^2: Coefficient of Determination (fraction of variance explained)
- UNIFAC: UNIversal Functional-group Activity Coefficient model (group contribution method for activity coefficients)
- γ_1: Activity Coefficient of Component 1
- γ_2: Activity Coefficient of Component 2
- x_1: Mole fraction of Component 1
- x_2: Mole fraction of Component 2
- (Note: All temperatures are in °C. Composition is given in mole fraction unless otherwise noted. Vapor pressures are in bar, and standard atmospheric pressure Patm = 1.013 bar.)

References

[1] C. Ding et al., "Experimental study and hazard analysis on the flash point of flammable liquids at high altitudes," Journal of Fire Sciences, vol. 31, pp. 469-477, 08/25 2013.
[2] D. C. Do Nascimento, N. D. D. Carareto, A. M. B. Neto, V. Gerbaud, and M. C. da Costa, "Flash point prediction with UNIFAC type models of ethylic biodiesel and binary/ternary mixtures of FAEEs," Fuel, vol. 281, p. 118717, 2020.
[3] H. Xiao, W. Wang, H. Bao, F. Li, and L. Zhou, "Biodiesel-diesel blend optimized via leave-one cross-validation based on kinematic viscosity, calorific value, and flash point," Industrial Crops and Products, vol. 191, p. 115914, 2023.
[4] J. Fu, "Flash points measurements and prediction of biofuels and biofuel blends with aromatic fluids," Fuel, vol. 241, pp. 892-900, 04/01 2019.
[5] B. Nazari, M. H. Keshavarz, and A. Hassanzadeh, "Reliable prediction of the flash point of organic compounds containing hazardous peroxide functional groups as compared to the best available methods," Process Safety and Environmental Protection, vol. 132, pp. 134-141, 2019.
[6] H.-J. Liaw, W.-C. Hsu, and K. Lakzian, "Exploration of two types of maximum–minimum flash point behavior of ternary mixtures," Journal of Loss Prevention in the Process Industries, vol. 80, p. 104915, 2022.
[7] Z. Heidari and M. A. Sobati, "New structure-based models for the prediction of flash point and autoignition temperatures of alkyl esters," Chemometrics and Intelligent Laboratory Systems, vol. 240, p. 104877, 2023.
[8] F. H. B. Sosa, F. A. Temoteo, R. M. Dias, D. C. do Nascimento, A. M. B. Neto, and M. C. da Costa, "Flash point of binary and ternary mixture of biojet blends: Experimental data and modeling," Fluid Phase Equilibria, vol. 576, p. 113940, 2024.
[9] S. M. Santos, D. C. Nascimento, M. C. Costa, A. M. B. Neto, and L. V. Fregolente, "Flash point prediction: Reviewing empirical models for hydrocarbons, petroleum fraction, biodiesel, and blends," Fuel, vol. 263, p. 116375, 2020/03/01/ 2020.
[10] H.-J. Liaw and C.-A. Yang, "Maximum flash point behavior of ternary mixtures with single and two maximum flash point binary constituents," Process Safety and Environmental Protection, vol. 143, pp. 293-303, 2020.
[11] K. Lakzian, S. Hosseiniallahchal, H. Jalaei Salmani, and A. Sanjarifard, "Flash point prediction of binary totally and partially miscible water-alcohol mixtures by cubic-plus-association (CPA) equation of state," Thermochimica Acta, vol. 691, p. 178719, 2020/09/01/ 2020.
[12] Z. Ke, H. Wu, C. Geng, G. Wang, Y. Yang, and Y.-W. Li, "A Comparative Study of PC-SAFT EOS and Activity Coefficient Models in Phase Equilibria Calculations for Mixtures Containing Associating and Polar Components," Industrial & Engineering Chemistry Research, vol. 57, 02/06 2018, doi: 10.1021/acs.iecr.7b04758.
[13] V. Koulocheris, M. Panteli, E. Petropoulou, V. Louli, and E. Voutsas, "Modeling of Simultaneous Chemical and Phase Equilibria in Systems Involving Non-reactive and Reactive Azeotropesi," Industrial & Engineering Chemistry Research, vol. 59, no. 18, pp. 8836-8847, 2020/05/06 2020, doi: 10.1021/acs.iecr.0c00468.
[14] M. P. de Omena Souza, D. C. do Nascimento, D. T. Volpatto, G. G. Ribeiro, A. M. B. Neto, and M. C. da Costa, "Modeling flash points of biofuels using neural networks," Fluid Phase Equilibria", vol. 596, p.114439, 2025, doi.org/10.1016/j.fluid.2025.114439.
[15] H. Jalaei Salmani, H. Kalani, M. R. Moradi, E. Mansouri, H.-J. Liaw, and H. Karkhanechi, "A practical hybrid machine learning method for predicting the flash point of complex ternary alcohol-based mixtures," Petroleum Science and Technology, vol. 42, no. 25, pp. 4390-4404, 2024, doi.org/10.1080/10916466.2023.2246489.
[16] B. Aljaman, U. Ahmed, U. Zahid, M. R. Vanteru, M. Sarathy, and A. G. Abdul Jameel, "A comprehensive neural network model for predicting flash point of oxygenated fuels using a functional group approach," Fuel, vol. 317, p. 123428, 06/01 2022, doi.org/10.1016/j.fuel.2022.123428.
[17] A. Álvarez, M. n. Lapuerta, and J. R. Agudelo, "Prediction of flash-point temperature of alcohol/biodiesel/diesel fuel blends," Industrial & Engineering Chemistry Research, vol. 58, no. 16, pp. 6860-6869, 2019, doi: 10.1021/acs.iecr.9b00843.
[18] Y. Pan, J. Cheng, X. Song, G. Li, L. Ding, and J. Jiang, "Flash points measurements and prediction for binary miscible mixtures," Journal of Loss Prevention in the Process Industries, vol. 34, pp. 56-64, 2015, doi.org/10.1016/j.jlp.2015.01.022.
[19] X. Huo, Q. Lu, and J. Wang, "Liaw-UNIFAC flash point model for alcohols-kerosene/diesel fuel blends using average fuel structure," Process Safety and Environmental Protection, 2022, doi.org/10.1016/j.indcrop.2022.115914.

[20] Z. Liu and X. Yang, "Insight of low flammability limit on sustainable aviation fuel blend and prediction by ANN model," Energy and AI, vol. 18, p. 100423, 2024, doi: 10.1016/j.egyai.2024.100423.
[21] H. Mirshahvalad, R. Ghasemiasl, and N. Raoufi, "A Neural Networks Model for Accurate Prediction of the Flash Point of Chemical Compounds," Iranian Journal Of Chemistry & Chemical Engineering-International English Edition, vol. 39, pp. 297-304, 11/10 2020, doi: 10.30492/ijcce.2019.35001.
[22] H.-J. Liaw and Q.-R. Tang, "Flash point prediction of binary mixtures of ionic liquid and flammable solvent," Journal of Loss Prevention in the Process Industries", vol. 96, p. 105631, 2025, doi.org/10.1016/j.jlp.2025.105631.
[23] R. C. Boehm, R. Parker, Z. Yang, S. Dooley, and J. S. Heyne, "Blend Prediction Model for Vapor Pressure of Jet Fuel Range Hydrocarbons," Sustainability, vol. 17, no. 21, p. 9612, 2025, doi.org/10.3390/su17219612.
[24] H.-J. Liaw, "Prediction of the influence of pressure on flash points of liquid fuels at sub-atmospheric pressure," Journal of Loss Prevention in the Process Industries, vol. 91, p. 105373, 2024/10/01/ 2024, doi.org/10.1016/j.jlp.2024.105373.
[25] D. b. Costa do Nascimento, M. c. P. d. O. Souza, L. d. O. Hentges, R. M. Dias, A. Marinho Barbosa Neto, and M. C. a. o. d. Costa, "Mixture flash point calculation: recent advances and a closer look at biodiesel," ACS Chemical Health & Safety, vol. 31, no. 1, pp. 22-43, 2024,doi.org/10.1016/j.fuel.2020.118717.
[26] F. H. B. Sosa, F. A. Temoteo, R. M. Dias, D. Costa do Nascimento, A. M. B. Neto, and M. C. da Costa, "Flash point of binary and ternary mixture of biojet blends: Experimental data and modeling," Fluid Phase Equilibria, vol. 576, p. 113940, 2024/01/01/ 2024, doi.org/10.1016/j.fluid.2023.113940.

Author contribution:
1. Conception and design of the study
2. Data acquisition
3. Data analysis
4. Discussion of the results
5. Writing of the manuscript
6. Approval of the last version of the manuscript

NK has contributed to: 1, 2, 3, 4, 5 and 6.
AS has contributed to: 1, 2, 3, 4, 5 and 6.
AJ has contributed to: 1, 2, 3, 4, 5 and 6.
AAZ has contributed to: 1, 2, 3, 4, 5 and 6.

Acceptance Note: This article was approved by the journal editors Dr. Rafael Sotelo and Mag. Ing. Fernando A. Hernández Gobertti.

Modeling of 4G coverage using Matlab and validation with real measurements obtained through G-NetTrack

Modelado de la cobertura 4G mediante Matlab y validación con mediciones reales obtenidas a través de G-NetTrack

Modelagem da cobertura 4G utilizando Matlab e validação com medidas reais obtidas através do G-NetTrack

Jordy Alexander Toapanta Piguave [1], Ricardo Gianpiere Córdova Almeida [2], David Humberto Cárdenas Villacrés [3 (*)]

Recibido: 04/02/2026 Aceptado: 14/04/2026

Summary. - The purpose of this work is to model and validate 4G LTE coverage in "Las Villas," a residential area of Babahoyo, to determine the actual quality of service compared to theoretical propagation models. The method used was descriptive-comparative, non-experimental, and quantitative. It was based on the collection of real-world data obtained through Drive Tests and Walk Tests, using the G-NetTrack Lite app on Android devices. The acquired data were exported in .csv format and processed in MATLAB. In this software, the LTE Toolbox library and the COST-231 Hata propagation model were used to simulate the signal and create coverage maps. Consequently. The comparison between measured and simulated values showed acceptable agreement according to MAE and RMSE metrics. The findings allow us to conclude that the COST-231 Hata model provides an appropriate approximation of the actual 4G signal behavior in the studied area, thus validating its use for planning and analyzing LTE mobile networks.

Keywords: *G-NetTrack Lite; RSRP; Drive test; Propagation model; COST-231 Hata.*

(*) Corresponding author.

[1] Telecommunications Engineer. Salesian Polytechnic University, Telecommunications Systems Research Group-GISTEL (Ecuador), jtoapantap3@est.ups.edu.ec, ORCID iD: https://orcid.org/0009-0008-3517-7750

[2] Telecommunications Engineer. Salesian Polytechnic University, Telecommunications Systems Research Group-GISTEL (Ecuador), rcordovaa@est.ups.edu.ec, ORCID iD: https://orcid.org/0009-0007-0431-2430

[3] Master's degree in communication technologies and systems. Salesian Polytechnic University, Telecommunications Systems Research Group - GISTEL (Ecuador), dcardenasv@ups.edu.ec, ORCID iD: https://orcid.org/0000-0003-4241-9929

Memoria Investigaciones en Ingeniería, núm. 30 (2026). pp. 211-228
https://doi.org/10.36561/ING.30.14
ISSN 2301-1092 • ISSN (en línea) 2301-1106 – Universidad de Montevideo, Uruguay

Resumen. - *El objetivo de este trabajo es modelar y validar la cobertura 4G LTE en "Las Villas", una zona residencial de Babahoyo, para determinar la calidad de servicio actual en comparación con modelos de propagación teóricos. El método empleado fue descriptivo-comparativo, no experimental y cuantitativo. Se basó en la recopilación de datos reales obtenidos mediante Drive Tests y Walk Tests, utilizando la aplicación G-NetTrack Lite en dispositivos Android. Los datos adquiridos se exportaron en formato .csv y se procesaron en MATLAB. En este software, se utilizó la biblioteca LTE Toolbox y el modelo de propagación COST-231 Hata para simular la señal y crear mapas de cobertura. La comparación entre los valores medidos y simulados mostró una concordancia aceptable según las métricas MAE y RMSE. Los resultados permiten concluir que el modelo COST-231 Hata proporciona una aproximación adecuada del comportamiento actual de la señal 4G en la zona estudiada, validando así su uso para la planificación y el análisis de redes móviles LTE.*

Palabras clave: *G-NetTrack Lite; RSRP; Drive test; Propagation model; COST-231 Hata.*

Resumo. ***-*** *O objetivo deste trabalho é modelar e validar a cobertura 4G LTE em "Las Villas", uma área residencial de Babahoyo, para determinar a qualidade de serviço atual em comparação com modelos teóricos de propagação. O método utilizado foi descritivo-comparativo, não experimental e quantitativo. Baseou-se na coleta de dados reais obtidos por meio de testes de campo e testes de caminhada, utilizando o aplicativo G-NetTrack Lite em dispositivos Android. Os dados adquiridos foram exportados em formato .csv e processados no MATLAB. Neste software, a biblioteca LTE Toolbox e o modelo de propagação COST-231 Hata foram utilizados para simular o sinal e criar mapas de cobertura. A comparação entre os valores medidos e simulados mostrou concordância aceitável de acordo com as métricas MAE e RMSE. Os resultados permitem concluir que o modelo COST-231 Hata fornece uma aproximação adequada do comportamento atual do sinal 4G na área estudada, validando assim seu uso para o planejamento e análise de redes móveis LTE.*

Palavras-chave: *G-NetTrack Lite; RSRP; Drive test; Modelo de propagação; COST-231 Hata.*

1. Introduction. - Modeling 4G coverage networks in Ecuador has been of paramount importance for optimizing current coverage and ensuring service quality, as seen in the city of Babahoyo. By 2025, national coverage had reached just over 80.58%, encompassing urban and rural areas in more than 3,000 locations [1]. This achievement is due to investment by public and private institutions in telecommunications infrastructure, which have incorporated technologies and tools to conduct various studies, including the design, testing, and validation of 4G LTE network coverage systems, this study specifically focuses on validating the COST-231 Hata empirical propagation model using field RSRP measurements.

Globally, several studies conducted in technologically advanced countries have examined the coverage and performance of 4G LTE mobile networks in urban and residential areas, using propagation models and real-world field measurements. By comparing signal quality parameters, such as RSRP, acquired through Walk Tests and Drive Tests, these studies have allowed for the evaluation of the accuracy of theoretical models like COST-231 Hata. The reported results agree that propagation models provide satisfactory estimates of actual signal behavior. However, differences exist regarding urban morphology, building density, and environmental conditions, which emphasizes the importance of validating these models in specific contexts.

Cellular devices have been updated over time, requiring higher data transmission rates. Therefore, a network with excellent performance is necessary for end-user satisfaction. The implementation of new mobile telecommunications technologies has allowed users to experience service improvements, such as greater coverage capacity on these devices and higher transmission speeds [2].

In the province of Los Ríos, connectivity projects have been integrated to optimize 4G coverage, especially to support higher network traffic during peak hours, thus improving the user experience. These projects are supported by research and simulations that anticipate network behavior in various situations, optimizing resources so that a future migration to the technology can be achieved 5G. 4G modeling in the city of Babahoyo contributes to technological and digital development, strengthening sectors such as education, commerce, health, and other areas where the canton's 4G network has become essential.

This research seeks to examine and diagnose the quality of 4G coverage in Babahoyo, where population growth could worsen mobile network connectivity for end users.
Despite advances in upgrading 4G infrastructure and local conditions, there have been signal variations and inconsistencies that are not always reflected in aggregated official data, such as national coverage maps. This creates problems for users, causing interruptions in voice calls, data usage for browsing, and slow speeds during peak hours.

Modeling 4G systems in MATLAB is justified because it is a very useful tool for the design, simulation, and optimization of LTE systems. This is because MATLAB can handle the complexity of 4G and improve simulations [3]. Therefore, it is essential to understand, test, and optimize system performance before a concrete implementation, considering elements such as latency, throughput, and parameters that can optimize the quality of mobile communication.

The research is limited to the analysis of 4G coverage in Babahoyo, specifically in the residential area where "Las Villas" is located. This area comprises five housing developments on the outskirts of the city (with approximately 3,600 to 3,900 people), along the road connecting Babahoyo with the Mata de Cacao Road. Real-world measurements will be taken using G-NetTrack software and coverage maps published by CONECEL (Claro) to evaluate the accuracy of the information provided by the operator. The study is limited solely to the defined urban area, 4G technology, and the selected models, excluding other cities, technologies, or simulation methods. This area was chosen because Claro's coverage map shows an irregular signal and it is considered a less risky zone due to the country's security situation.

1.1 Related jobs. -The performance of LTE cellular networks in various environmental settings has been examined in a few studies. In [4], thorough research was carried out to compare signal quality characteristics supplied by local mobile providers in order to assess LTE network performance in residential and high-rise commercial regions.

According to the data, Digi had the best coverage, with 66% in commercial zones and 83% in residential areas (RSRP > −100 dBm). Celcom and Maxis performed worse. The investigation confirmed the agreement between provider data and actual measurements by reporting notable signal abnormalities, particularly in coverage gap areas found in operator maps. Due to things like wall attenuation and decreased internal interference, signal degradation was mostly seen in residential areas far from base stations and at higher building altitudes.
To increase coverage in remote and high-altitude locations, the authors suggested deploying repeaters.

A comparison of 4G network propagation models in Riobamba, Ecuador's private and urban regions was carried out in [5]. RSRP data obtained with Network Cell Info software were used to assess models including Log-Normal, Okumura-Hata, COST-231, and SUI. The average RSRP values within 200 meters of base stations ranged from −80 to −106 dBm, according to the data. While COST-231 worked well in densely populated regions and the Log-Normal model was better suited for urban microcells beyond 200 meters, the SUI model demonstrated greater performance in dense urban environments with diverse topography and vegetation.

Unlike earlier research, the current study focuses on a thorough analysis employing RSRP measurements that were acquired using the G-NetTrack program and analyzed in MATLAB using.txt data files. A single propagation model, COST-231 Hata, was chosen because it works well in moderately congested urban settings, which is appropriate for the chosen residential region outside of Babahoyo's center zone. In order to provide a more accurate validation of the model and offer useful suggestions for network improvement, comparative assessments were focused exclusively on measured RSRP values and theoretical RSRP predictions derived from the COST-231 Hata model used.

2. Materials and methods. - The research will have a quantitative scientific approach, this will be based on data collection, analysis and mathematical modeling of technical parameters used in the validation of 4G networks. The study adopts a hypothetical-deductive method, because how the signal behaves at different strategic points will be analyzed, then a hypothesis is formulated on the data taken and evaluated with computer simulations. The methodological design is non-experimental and descriptive-correlational, because we are not going to manipulate the signal parameters, but rather the real values are going to be analyzed. Our study incorporates a comparative validation method, which will allow us to relate the values measured with G-NetTrack and the theoretical values that Matlab will generate, to compare the precision and effectiveness of coverage modeling.

The phases of the suggested methodology are shown in Figure I, which structurally and sequentially depicts the major steps used in this investigation, from data processing and signal collecting to propagation modeling and outcomes interpretation. The method used to assess network performance and verify the results is clearly shown in this diagram.

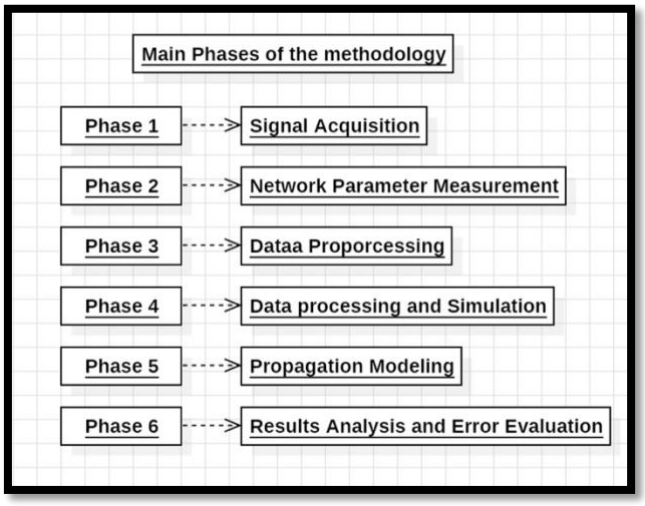

Figure I. Main phases of the methodology.

Signal Acquisition: This phase involves capturing the LTE signal in the field within the "Las Villas" study area in the city of Babahoyo. Signal acquisition is performed using Android mobile devices with the G-NetTrack Lite application, which allows for real-time recording of network parameters. Measurements are conducted through Walk Tests and Drive Tests to represent both pedestrian and vehicular mobility scenarios, ensuring adequate spatial coverage of the analyzed area. This phase forms the experimental basis of the study, providing the real-world data necessary for subsequent validation.

Network Parameter Measurement: In this stage, the technical parameters of the 4G LTE network are measured and recorded, extracted directly from the G-NetTrack application. The main indicators analyzed are the received reference signal strength (RSRP), signal quality (RSRQ), and signal-to-noise ratio (SNR), which allow for the evaluation of network performance and service quality. Additionally, data associated with the base station is recorded, such as the cell identifier, mobile operator, and frequency band, which facilitates the proper contextualization of the measurements taken.

Data Preprocessing: Once the measurements are obtained, the collected data is exported in .csv format for further processing. This phase involves data preprocessing, which includes cleaning up erroneous data, removing outliers, and organizing the samples according to their geographic and temporal location. This process ensures that the information used in MATLAB is consistent and reliable, reducing errors in simulation and comparative analysis. The distances between the base station and each measurement point were computed from the WGS84 geographic coordinates recorded by G-NetTrack Lite, using the Haversine formula to account for earth's curvature. The base station coordinates used correspond to the CLARO_EC cell consistently serving the study area, identified through the cell ID field in the G-NetTrack logs. The data generated by the software were preprocessed and filtered before analysis. Samples not corresponding to 4G technology (2G and 3G technology) were discarded. Missing or incomplete sample values were also eliminated. Infrequent or atypical values, such as deviations observed in the graphs generated by the MATLAB software, were identified and excluded from the validation set. Furthermore, the number of segments affected by service cell changes was minimized by selecting stable LTE service cell intervals, provided the requirements were met.

The simulation's base station parameters are compiled in Table I. To ensure that all comparable samples correspond to a single serving cell, segments from the G-NetTrack logs where the serving cell identifier changed between subsequent samples were identified and removed from the validation dataset.

Parameter	**Value**
Operator	CLARO_EC
Technology	4G LTE
Frequency band	1900 MHz (Band 2)
Antenna height	30 m
Coordinates	As recorded in G-NetTrack logs

Table I. BS & handovers.

Data Processing and Simulation: In this phase, the preprocessed data is imported into MATLAB, where numerical processing and LTE network simulation are performed. The LTE Toolbox is used to facilitate the manipulation of 4G system parameters and enable the analysis of radio link behavior. Furthermore, spatial interpolation techniques are applied to generate continuous coverage maps from discrete measurements, allowing for a clear visual representation of signal behavior in the study area.

Propagation Modeling: This stage focuses on applying the COST-231 Hata propagation model, selected for its suitability in urban and suburban environments. The model allows for estimating propagation loss and calculating theoretical RSRP values based on parameters such as distance, frequency, and antenna heights. The results obtained using the theoretical model are compared with measured data, generating simulated coverage maps that represent the expected LTE signal behavior in the analyzed area.

Results Analysis and Error Evaluation: Finally, a comparative analysis is performed between the measured and simulated values. To quantify the model's accuracy, standard validation metrics such as MAE, RMSE and mean bias are calculated, which allows for evaluating the difference between the actual network performance and the theoretical estimate. This phase validates the effectiveness of the COST-231 Hata model and determines whether the simulation adequately represents real 4G coverage, considering factors such as attenuation, urban environment, and propagation conditions.

2.1 Flowchart. - Figure II, illustrate the sequential workflow of the proposed methodology for modeling and validating 4G LTE coverage in the residential area of "Las Villas" in Babahoyo. The diagram provides a clear overview of the main stages involved in the study, from field data acquisition to the final validation of the propagation model.

The process begins with the signal acquisition phase, where real-world measurements are collected using the G-NetTrack Lite application through Walk Test and Drive Test procedures. These tests allow the characterization of LTE signal behavior under both pedestrian and vehicular mobility conditions.

Next, the network parameter measurement phase focuses on the extraction of key LTE performance indicators, including the Reference Signal Received Power (RSRP), Reference Signal Received Quality (RSRQ), and Signal-to-Noise Ratio (SNR). These parameters are essential for assessing the quality of service and network performance.

The collected data are then subjected to data preprocessing, where the measurements are exported in CSV format, filtered, and organized. This phase ensures data consistency by removing outliers and invalid samples, thereby improving the reliability of the subsequent analysis.

Measurements were collected periodically using G-NetTrack Lite software, employing parameters such as radio frequency and GPS, and using different mobile device positions. This can generate various geolocation errors depending on satellite visibility and obstructions caused by urban infrastructure. Changes in speed during the drive test can also affect the spatial sample density. However, these limitations are quite common in LTE measurements.A predetermined synchronization between GPS coordinates and radio measurements was assumed; this was based on the times established by the software.

In the data processing and simulation phase, the preprocessed data are imported into MATLAB. Using the LTE Toolbox, numerical processing and spatial interpolation techniques are applied to generate continuous coverage representations and preliminary signal maps for the study area.

Subsequently, propagation modeling is performed using the COST-231 Hata model, selected for its suitability in urban and suburban environments. This model enables the estimation of theoretical RSRP values based on propagation conditions, which are later compared with measured data.

Finally, the methodology concludes with the results analysis and error evaluation phase, where measured and simulated RSRP values are compared. MAE, RMSE and bias metrics are calculated to quantify the accuracy of the model and validate its applicability for real 4G LTE coverage analysis.

Overall, the flowchart summarizes the logical and systematic approach adopted in this research, highlighting the integration of empirical measurements and theoretical modeling to achieve reliable coverage validation results.

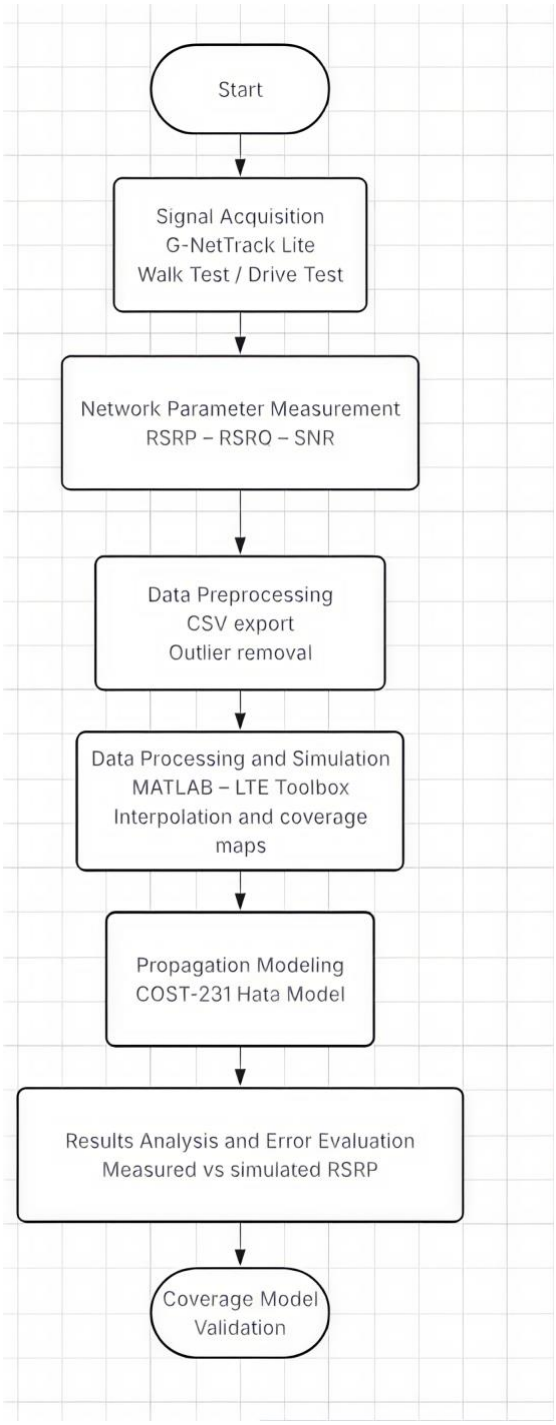

Figure II. Project planning flowchart

2.2. Schematic circuit. -

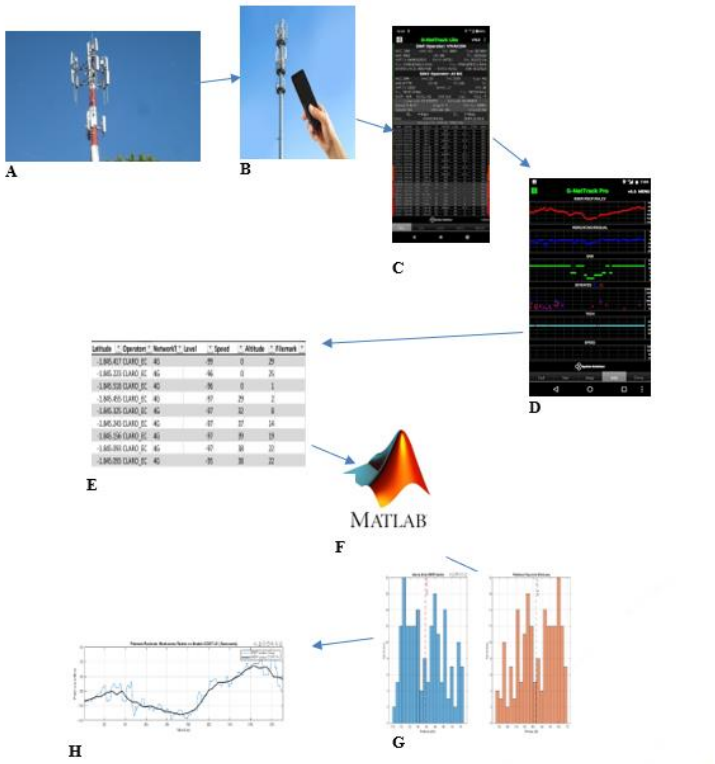

Figure III. Schematic Circuit Example

A: Illustration of the base station.
B: Telephone for receiving the signal.
C: Obtaining signal parameters using G-NetTrack.
D: Comparative analysis of the signal graphs.
E: .csv file of the obtained data.
F: Exporting the file to Matlab software.
G: Using propagation models to obtain simulated values.
H: Comparative graphs between measured and simulated values.

3. Development. –

Figure IV. The drive test route was taken using the G NetTrack application.

As shown in Figure IV, when the respective measurement was performed, the application provided a .kml file containing all the data collected by the G-NetTrack Lite application. The signal quality is represented by colors along different sections of the route: green indicates very good signal strength, dark green indicates good signal strength, and yellow indicates fair signal strength. The image shows that the signal from the base station is generally good, as the signal strength is quite clear. In the yellow areas, there is some attenuation due to obstructions in some residential areas, such as large trees or buildings, which interfere with the signal path, making it difficult for the mobile device to receive it.

Sample	Timestamp	Longitude	Latitude	Operator name	Network Tech	Level (dB)	Speed (km/h)	Altitude
1	2025.12.06_ 15.49.41	-7.952.464	-1.845.417	CLARO_EC	4G	-99	0	29
10	2025.12.06_ 15.49.55	-7.952.547	-1.845.040	CLARO_EC	4G	-95	38	24
20	2025.12.06_ 15.50.05	-7.952.650	-1.844.558	CLARO_EC	4G	-86	41	25
30	2025.12.06_ 15.50.15	-7.952.744	-1.844.056	CLARO_EC	4G	-85	42	26
40	2025.12.06_ 15.50.25	-7.952.851	-1.843.510	CLARO_EC	4G	-97	46	26
50	2025.12.06_ 15.51.37	-7.952.919	-1.843.175	CLARO_EC	4G	-107	11	23
60	2025.12.06_ 15.51.57	-7.953.027	-1.842.643	CLARO_EC	4G	-101	39	24
70	2025.12.06_ 15.52.11	-7.953.137	-1.842.068	CLARO_EC	4G	-102	40	23
80	2025.12.06_ 15.52.21	-7.953.245	-1.841.533	CLARO_EC	4G	-105	54	23
90	2025.12.06_ 15.52.31	-7.953.379	-1.840.848	CLARO_EC	4G	-105	62	21
100	2025.12.06_ 15.52.41	-7.953.495	-1.840.246	CLARO_EC	2G	-113	30	23

Table II. Results obtained from the drive test.

As can be seen in Table II, these are the parameters obtained when performing measurements with the G-NetTrack software. These values are summarized for the purpose of explanation, taking a sample of every 10 data points obtained. The values shown in the application's .txt file include the exact date and time the measurement was taken, the exact coordinates of the site (Altitude/Latitude), the operator of the SIM card used for the measurement, which in this case was Claro_EC, the technology, which in this case was 4G-LTE as it is the most common in the area, the Level, which is the signal strength received at different distances between the device and the base station, and the latitude of the base station, which is located at an average height of 30 meters, although this varies due to the irregularities of the terrain.

The relationship between transmitted and received power under ideal free-space conditions was only demonstrated using a simplified link-budget analysis based on the Friis transmission concept as a preliminary theoretical reference. The COST-231 Hata empirical propagation model, which is more suited for urban residential settings, is the primary validation target of this study.

$$\mathrm{Pr(db)} = \mathrm{Pt(db)} + Gt(\mathrm{dbi}) + Gr(\mathrm{dbi}) + 20log_{10}\left(\frac{\lambda}{4\pi d}\right) \qquad (1)$$

Equation I. Friis equation

Where:
Pr (db) = It is the power received from the antenna expressed in decibels.
Pt (db) = It is the power radiated from the antenna, expressed in decibels.
Gt (dbi) = It is the gain emitted by the antenna when transmitting, expressed in decibels.
Gr (dbi) = Es la ganancia que se recibe de la antena, expresada en decibelios.
$20log_{10}(\frac{\lambda}{4\pi d})$ = This term represents the loss in the air.

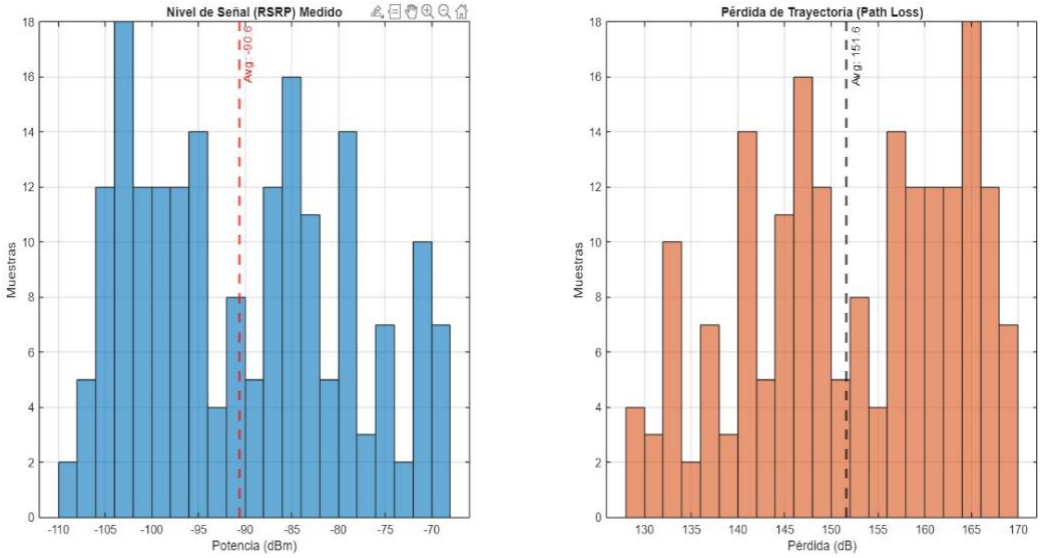

Figure V. Preliminary link-budget reference analysis under idealized conditions

Figure V shows a simplified theoretical reference based on free-space propagation assumptions. These results are presented only for conceptual comparison and are not used as the primary validation model.
The main validation stage of this study employed the COST-231 Hata propagation model to compare theoretical LTE RSRP predictions with measured field values obtained through G-NetTrack.

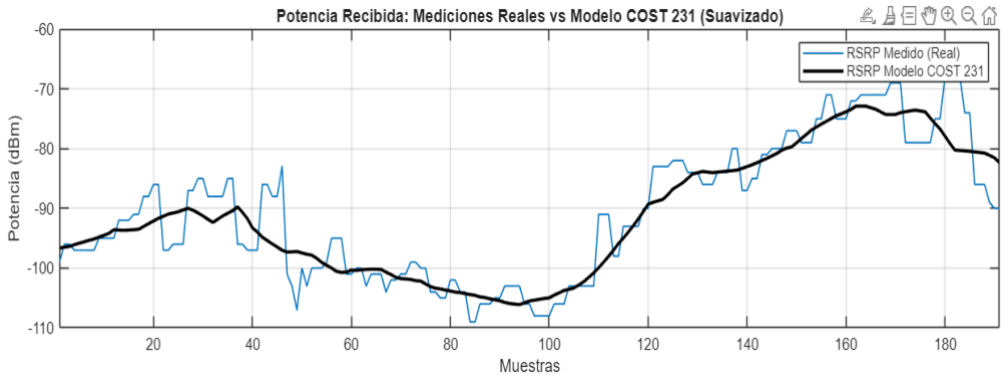

Figure VI, Received Power: Actual Measurements vs. Cost 231 Models (Smoothed)

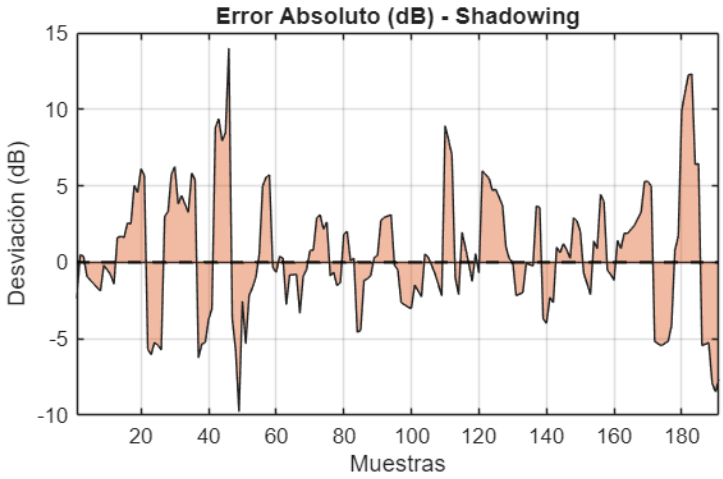

Figure VII, Absolute Error (dB) – Shadowing

MAE	3.64 dB
RMSE	4.76 dB
Mean Bias	-0.32 dB

Table III. Statistical Validation Metrics

These results indicate that the model provides an acceptable prediction accuracy for LTE signal coverage in the studied residential urban environment. In the Figure VI, a comparison is shown between the ideal behavior of an average signal, calculated using the Cost-231 Hata propagation model, and the signal measured in different samples. As can be seen, there are values with very irregular peaks, but these are far from the ideal value that an antenna should radiate. This indicates that the power is not constant but varies depending on how far we deviate from the ideal or if there is any interference in the transmission channel.

In the Figure VII the absolute error is shown, comparing the actual signal error with the simulated error of the propagation model. As shown in the image, the values do not exceed 15 dB, which can be interpreted as a correct application of the model and that the percentage error of the measurement is acceptable. In the Table II presents the statistical validation metrics of the COST-231 Hata model. Instead of percentage relative error, standard propagation-model metrics were used, including Mean Absolute Error (MAE), Root Mean Square Error (RMSE), and mean bias. These metrics provide a more rigorous assessment of model performance when comparing measured and predicted RSRP values expressed in dBm.

Model validation was performed using standard propagation metrics based on representative measurement samples. The COST-231 Hata model achieved a Mean Absolute Error (MAE) of 3.64 dB, a Root Mean Square Error (RMSE) of 4.76 dB, and a mean bias of -0.32 dB.

Sample	Time	Latitude	length	RSRP_Measured_DBM	Estimated_Distance_Km	RSRP_Model_COST231_dBm	Absolute_Error_dB	Relative_Error_Porc
1	2025.12.06_15.49.41	-1845417	-7952464	-99	3,160550759	-96,64092186	-2,35907814	2,441075783
10	2025.12.06_15.49.55	-1845040	-7952547	-95	2,749957403	-94,51204419	-0,487955807	0,516289549
20	2025.12.06_15.50.05	-1844558	-7952650	-86	2,352101889	-92,12133901	6,121339012	6,644865432
30	2025.12.06_15.50.15	-1844056	-7952744	-85	2,223657394	-91,26226622	6,262266223	6,861835107
40	2025.12.06_15.50.25	-1843510	-7952851	-97	2,531990152	-93,24874157	-3,751258426	4,022851529
50	2025.12.06_15.51.40	-1843143	-7952930	-100	3,333462674	-97,45577235	-2,544227646	2,610648486
60	2025.12.06_15.51.58	-1842595	-7953037	-101	4,025110525	-100,3400615	-0,659938479	0,657701888
70	2025.12.06_15.52.12	-1842018	-7953147	-101	4,417763062	-101,7640126	0,76401256	0,750768902
80	2025.12.06_15.52.22	-1841470	-7953258	-102	5,055732129	-103,8275422	1,827542231	1,760170944
90	2025.12.06_15.52.32	-1840778	-7953393	-105	5,625610649	-105,4614689	0,461468857	0,43757105
100	2025.12.06_15.52.45	-1840121	-7953521	-108	5,452678283	-104,983827	-3,01617303	2,872988266
110	2025.12.06_15.52.56	-1839534	-7953635	-91	3,916886267	-99,92311023	8,92311023	8,929976468
120	2025.12.06_15.53.06	-1838888	-7953764	-90	1,955809604	-89,29878695	-0,701213052	0,785243647
130	2025.12.06_15.53.15	-1838279	-7953883	-84	1,385663787	-84,02672833	0,026728327	0,031809315
140	2025.12.06_15.53.25	-1837583	-7954015	-87	1,296548689	-83,00982067	-3,990179334	4,806876226
150	2025.12.06_15.53.35	-1836914	-7954150	-77	0,998942456	-79,02066356	2,020663556	2,557133116
160	2025.12.06_15.53.45	-1836258	-7954277	-75	0,711033459	-73,81969833	-1,180301672	1,598897989
170	2025.12.06_15.53.55	-1835558	-7954412	-69	0,732852225	-74,28207291	5,282072906	7,110831321
180	2025.12.06_15.54.06	-1834845	-7954553	-68	0,929491993	-77,91830808	9,918308081	12,7291112
190	2025.12.06_15.54.18	-1834310	-7954653	-90	1,177123662	-81,53154828	-8,468451724	10,38671766
191	2025.12.06_15.54.19	-1834216	-7954661	-90	1,23994921	-82,32698916	-7,673010844	9,320164533

Table IV, Drive Test Results.

Table IV shows the values obtained in the Drive Test. Among the grouped parameters are the time intervals for recording the measurements. This table includes data for every 10 samples out of the 191 total samples taken. The table shows the latitude and longitude coordinates of each sample, the measured RSRP, an estimate of the distance from the mobile device to the base station, and the RSRP modeled with COST-231 Hata. These values allow us to calculate the percentage error, expressed in decibels (dB), These values allow the calculation of absolute prediction errors expressed in dB. The errors are not consistent but vary along the route, which aligns with the signal irregularity shown in the previously presented graphs. These variations are caused by different phenomena that affect the transmission channel, such as shadow fading, multipath fading, and obstructions like trees, buildings, and terrain irregularities.

We can conclude that the absolute error values are within an acceptable range for propagation studies in real-world environments, allowing us to affirm that the COST-231 Hata model provides a fairly accurate representation of signal behavior over a given distance. The relative percentage error shown in the third graph is very low, indicating that the theoretical model and experimental values agree.

To complement the information provided by the Matlab code, we will verify the accuracy of the displayed data using formulas and calculations.

In this case, we used the COST-231 Hata formula for path loss.

$$L(dB) = 46.3 + 33.9log10(f) - 13.82log10(hb) - a(hm) + \big(44.9 \;\; - 6.55log10(hb)\big)log10(d) + Cm. \quad (2)$$

Equation II. COST-231 Hata formula for path loss.

This equation yields the average journey loss in the urban environment.
The parameters to be used are as follows:

Parameter	Value	Meaning
f	1900 MHz	PCS / LTE Band
hb	30 m	Tower height
hm	1.5 m	Mobile height

Cm	3 dB	Metropolitan city, Metropolitan correction factor, applied based on the urban morphology of "Las Villas," which presents continuous building coverage, paved streets, and infrastructure density consistent with the metropolitan environment category defined in the COST-231 Hata model.
d	km	Distance BS–UE

Table V, Parameters Used for Path Loss.

In this case, we will use this formula because we aim to estimate the path loss that the signal experiences as it propagates from the base station to the cellular device in environments with significant obstructions, such as urban areas. This model is primarily used to design and plan cellular networks with technologies like GSM, UMTS, and LTE, as it allows us to predict signal transmission levels, map coverage, locate base stations, and, most importantly, evaluate quality of service before taking actual measurements. The metropolitan correction factor (Cm = 3 dB) was selected because the 'Las Villas' residential area presents urban characteristics, including paved roads, continuous building facades, and proximity to the city of Babahoyo consistent with the metropolitan environment category established in the COST-231 Hata model.

The formula relates to several parameters mentioned above and previously measured with the G-NetTrack Lite software, such as the operating frequency. In this case, the frequency is relevant because higher frequencies are directly proportional to signal attenuation, which explains why higher frequency bands have lower coverage. The height of the base station is also a factor, and in this case, it has an inverse effect. Antennas with greater height significantly reduce signal loss because they improve line of sight and decrease obstruction from urban infrastructure. These parameters include the height of the mobile device and the distance between the base station and the user. This distance increases logarithmically as the user moves further from the antenna.
Next, we will calculate whether the user's actual height influences signal loss within the COST-231 Hata model. Although this condition is evaluated within the formula, in real-world mobile networks, users typically hold their phones at an average height of 1.5 meters. Therefore, this value is substituted into the equation to determine how much it corrects signal loss.

As the next point, the calculation will be carried out to verify if the real height of the user influences the path loss within the COST-231 Hata model. Although this condition is evaluated within the formula. In real mobile networks, the user usually holds the phone at an average height of 1.5m, so this value is substituted into the equation to check how much it really corrects the signal loss.

$$a(hm) = 3{,}2(log10(11{,}75hm))^2 - 4{,}97$$
$$a(hm) = 3{,}2(log10(11{,}75 \times 1{,}5))^2 - 4{,}97$$
$$a(hm) = 3{,}2(log10(17{,}625))^2 - 4{,}97$$
$$a(hm) = 3{,}2(1{,}246)^2 - 4{,}97$$
$$a(hm) = 3{,}2(1{,}553) - 4{,}97$$
$$a(hm) \approx 0{,}0\ dB$$

Equation III. Trip loss calculation based on height.

The value of 0.0 dB was obtained, this means that for a typical user, the height at which the mobile phone is located does not cause any difference in the total link loss. This allows us to validate that the power delivered by the base station depends mostly on the distance, frequency and height of the base station, while the height of the user only acts as a fine adjustment of the model.

To simplify the analysis and facilitate calculations, graphs and comparisons, we will rewrite the equation as follows:

$$L(dB) = A + B\ log10(d) + Cm. \quad (4)$$

Equation IV. Simplified Path Loss Formula.

Standard part A:

$$A = 46.3 + 33.9\ log10(1900) - 13.82\ log10(30) - a(hm)$$
$$A = 46.3 + 33.9(3.279) - 13.82(1.477) - 0$$
$$A = 46.3 + 111.17 - 20.41$$
$$A = 137.06\ dB$$

Equation V. System base loss calculation.

Slope B:

$$B = 44.9 - 6.55\ log10(30)$$
$$B = 44.9 - 6.55(1.477)$$
$$B = 35.23$$

Equation VI. Path loss, logarithmic form.

This value indicates that the path loss grows logarithmically with distance, its magnitude being dependent on the height of the base station antenna.
Once constants A and B have been determined, they are substituted into the simplified formula to obtain the value for the path loss calculation.

$$L(dB) = A + B\ log10(d) + Cm$$
$$log10(3.16) = 0.5$$
$$L = A + B\ log10(d) + Cm$$
$$L = 137.06 + 35.23(0.5) + 3$$
$$L = 137.06 + 17.62 + 3$$
$$L = 157.68\ dB$$

Equation VII. Trip loss calculation.

This result represents the average path loss that the signal experiences when propagating from the base radio to a mobile device, located at an average distance of 3.16 km away. This information is pre-established by the conditions provided by the Cost-231 Hata model.
To determine theoretical RSRP values related to the COST-231 Hata path-loss model, the EIRP value was evaluated as a supplementary engineering reference. Typically published in the technical literature for this kind of infrastructure, the transmitted power (Ptx = 46 dBm), antenna gain (Gtx = 17 dBi), and feeder losses (Ltx = 2 dB) are indicative values for urban LTE macro deployments running at 1900 MHz. These factors do not serve as the study's major validation inputs; rather, they are only used as a reference.

Ptx	Power transmitted by the base station.
Gtx	Gain of the transmitting antenna.
Ltx	Losses in cables and connectors.

Table VI. EIRP parameters

$$PIRE = 46 + 17 - 2 = 61\ dBm$$
$$RSRP = PIRE - L$$
$$RSRP = 61 - 157.68$$
$$RSRP = -96.7\ dBm$$

Equation VIII. RSRP calculation.

In this case, the value that Matlab gives us of the modeled RSRP is -96.64 dBm and the value that it gives us using the established formulas is - 96.7 dBm.

A comparison between the results computed using the theoretical COST-231 Hata propagation model and those derived using the MATLAB code is shown in Table 8. The first ten samples were used for this study.

The propagation loss, which is the radio channel's attenuation determined by the propagation model, the RSRP derived from the theoretical relationship RSRP = PIRE−L, the RSRP values produced by MATLAB (which directly incorporates the propagation model), and the absolute difference between the two results are all included in the table.

Both unprocessed and smoothed samples were examined. To lessen the impact of short-term fading and enhance the readability of large-scale behavior, a moving average filter was only used for the visual depiction of signal trends in Figure VI. The three main validation metrics, MAE, RMSE, and bias were only computed using the raw measured data; no smoothing was used.

The close agreement between the analytical calculations and MATLAB outputs confirms the correct implementation of the COST-231 Hata model equations within the simulation environment.

Sample	**PIRE (dBm)**	**Propagation losses L (dB)**	**RSRP Calculated (dBm)**	**RSRP MATLAB (dBm)**	**Diference (dB)**
1	61	157.68	-96.70	-96.64	0.06
2	61	158.12	-97.12	-97.05	0.07
3	61	158.95	-97.95	-97.88	0.07
4	61	159.40	-98.40	-98.32	0.08
5	61	160.10	-99.10	-99.02	0.08
6	61	160.85	-99.85	-99.78	0.07
7	61	161.50	-100.50	-100.43	0.07
8	61	162.20	-101.20	-101.12	0.08
9	61	162.95	-101.95	-101.88	0.07
10	61	163.60	-102.60	-102.54	0.06

Table VII. Consistency Check Between Analytical COST-231 Formulation and MATLAB Implementation

As shown in Figure VIII, a comparison of the RSRP values is established as a function of the distance between the radio base and the receiver, the curves corresponding to the calculated RSRP and the RSRP obtained in MATLAB overlap throughout the range of distances analyzed. This indicates that the mathematical formulation has been correctly applied and that the propagation model has been implemented appropriately at the time of performing the simulation. The observed differences are minimal and can be verified by numerical rounding, so they are considered negligible from an engineering point of view.

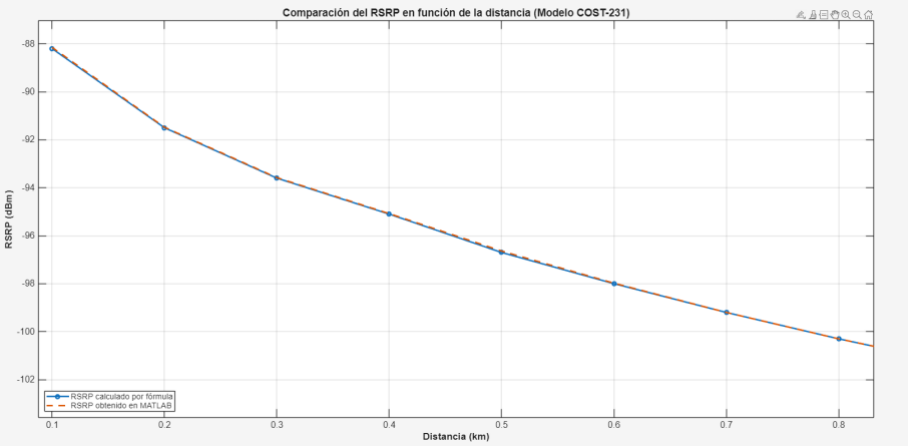

Figure VIII. Analytical vs MATLAB COST-231 RSRP Consistency Check

4. Conclusions.- The COST-231 Hata model was chosen as the most appropriate for examining signal propagation in the city of Babahoyo, particularly in the residential sector "Las Villas," after a strong conceptual foundation on 4G LTE coverage and urban propagation models was built.

The G-NetTrack Lite application was used to gather genuine field measurements using the Walk Test and Drive Test techniques, yielding RSRP values that accurately depict the behavior of the 4G LTE signal. The findings demonstrated that the received power level progressively changes with both urban ambient conditions and distance from the base station, making it possible to determine the actual coverage in the research region.

The COST-231 Hata model was used in MATLAB to simulate theoretical 4G LTE coverage, yielding received power values that were in line with those seen in an urban residential setting. Good agreement was found between the simulated and measured RSRP values, The comparison between measured and simulated RSRP values showed acceptable prediction accuracy according to MAE and RMSE metrics, confirming that the COST-231 Hata model is suitable for preliminary LTE coverage estimation in the studied area.

Ultimately, the COST-231 Hata model was successfully validated through comparison between COST-231 MATLAB predictions and actual field measurements. Furthermore, despite local variations brought on by distance and urban morphology, the comparison with the coverage data supplied by the mobile operator demonstrated general consistency with field measurements, confirming the accuracy of the operator's coverage information within typical urban error margins.

The results indicate that the COST-231 Hata model provides a very reasonable approximation of the signal coverage established by the operator's maps. The field measurements comprised RSRQ and SNR values that were noted along the study path in addition to RSRP. The presence of these indicators in the dataset indicates that the G-NetTrack measurements captured a complete picture of link quality, and they may serve as the foundation for future QoS-oriented analyses in the same area, even though a full quantitative analysis of these indicators is outside the main purview of this validation study. While local deviations were observed due to factors such as attenuation, obstruction, and measurement uncertainty, the model achieved considerably good agreement with field measurements according to the MAE and RMSE metrics.

The final validation results correspond exclusively to the COST-231 Hata model, while the Friis-based link budget was included only as a theoretical reference.

References

[1] Sharon Durán, “Ecuador supera 80% de cobertura 4G: Mintel,” dpl news, Jul. 2025.
[2] C. A. Parreño Muirragui, “Simulación en Matlab de un algoritmo basado en Machine Learning y Hard Handover para el balanceo de carga en una red celular LTE.,” EPN, Quito, 2021.
[3] Mathworks, Modeling a 4G LTE System in MATLAB. 2012.
[4] N. Shakira, N. Ya’acob, N. Tajudin, A. L. Yusof, M. Kassim, and N. F. Naim, “Performance measurement of LTE cellular network for indoor environment,” 2022, p. 020003. doi: 10.1063/5.0111253.
[5] G. Crespín Angulo, C. Bermeo Reyes, and J. Chico Vallejo, “Propagation models applied to LTE technologies in residential areas in Riobamba – Ecuador,” ConcienciaDigital, vol. 5, no. 3.1, pp. 315–332, Jul. 2022, doi: 10.33262/concienciadigital.v5i3.1.2263.

Author contribution:
1. Conception and design of the study
2. Data acquisition
3. Data analysis
4. Discussion of the results
5. Writing of the manuscript
6. Approval of the last version of the manuscript

JATP has contributed to: 1, 2, 3, 4, 5 and 6.
RGCA has contributed to: 1, 2, 3, 4, 5 and 6.
DHCV has contributed to: 1, 2, 3, 4, 5 and 6.

Acceptance Note: This article was approved by the journal editors Dr. Rafael Sotelo and Mag. Ing. Fernando A. Hernández Gobertti.

Arquitectura embebida de bajo costo para el control temporal repetible en estaciones de prueba electrónica

Low-cost embedded architecture for repeatable time control in electronic test stations

Arquitetura embarcada de baixo custo para o controle temporal repetível em estações de teste eletrônico

Emiliano Crespo-Torres [1], René Fernando Domínguez-Cruz [2], Leopoldo Asael Garza-Alvarado [3], Pedro Edén Zamora-González [4], Yadira Aracely Fuentes-Rubio [5 (*)]

Recibido: 16/02/2026 Aceptado: 14/04/2026

Summary. - Automation of electronic test stations is often constrained by manual timing control, which introduces operator-dependent variability, extended cycle durations, and increased rework. This study presents a low-cost embedded system for automated and repeatable time control in electronic test stations, designed to ensure consistent cycle termination, integrated visual feedback, and automatic power disconnection. The proposed architecture is based on a microcontroller platform implemented with widely available components to guarantee simplicity and scalability. The system was technically characterized to evaluate timing accuracy, repeatability, and actuation consistency under real industrial conditions. Experimental results obtained from 120 test cycles over a four-week period show stable cycle-to-cycle behavior, with a mean cycle time of 30.02 min, a standard deviation of 0.03 min, and a maximum absolute timing error below 0.08 min relative to the programmed duration. Operational validation showed a reduction in out-of-time events from 20% to 4%, as well as decreases in rework frequency and station downtime. The results indicate that the proposed system provides consistent and repeatable timing control at the minute scale, reducing operator-dependent variability while maintaining lower complexity and cost than conventional industrial automation platforms.

Keywords: *Repeatable time control; Embedded systems; Electronic test stations; Industrial automation; Low-cost systems.*

(*) Corresponding author.
[1] B.Eng. in Electronics Engineering. Electronics Department. Universidad Autónoma de Tamaulipas (Mexico); a2213720038@alumnos.uat.edu.mx; ORCID iD: https://orcid.org/0009-0006-0397-7767
[2] PhD. Electronics Department. Universidad Autónoma de Tamaulipas (Mexico); rfdominguez@docentes.uat.edu.mx; ORCID iD: https://orcid.org/0000-0001-7001-7543
[3] PhD. Electronics Department. Universidad Autónoma de Tamaulipas (Mexico); leopoldo.garza@docentes.uat.edu.mx; ORCID iD: https://orcid.org/0000-0002-7760-2718
[4] M.Sc. Electronics Department. Universidad Autónoma de Tamaulipas (Mexico); pzamora@docentes.uat.edu.mx; ORCID iD: https://orcid.org/0000-0002-8469-9896
[5] PhD. Electronics Department. Universidad Autónoma de Tamaulipas (Mexico); yfuentes@docentes.uat.edu.mx; ORCID iD: https://orcid.org/0000-0002-7385-9794

Memoria Investigaciones en Ingeniería, núm. 30 (2026). pp. 229-243
https://doi.org/10.36561/ING.30.15
ISSN 2301-1092 • ISSN (en línea) 2301-1106 – Universidad de Montevideo, Uruguay

Resumen. - *La automatización de estaciones de prueba electrónica suele verse limitada por el control manual del tiempo, lo que introduce variabilidad dependiente del operador, prolongación de ciclos y aumento de reprocesos. Este trabajo presenta un sistema embebido de bajo costo para el control temporal automatizado y repetible en estaciones de prueba, diseñado para garantizar la terminación consistente de ciclos, retroalimentación visual integrada y desconexión automática de energía. La arquitectura propuesta se basa en una plataforma de microcontrolador implementada con componentes ampliamente disponibles para asegurar simplicidad y escalabilidad. El sistema fue caracterizado técnicamente para evaluar precisión temporal, repetibilidad y consistencia de actuación en condiciones industriales reales. Los resultados experimentales obtenidos a partir de 120 ciclos de prueba durante cuatro semanas muestran comportamiento estable entre ciclos, con tiempo promedio de 30.02 min, desviación estándar de 0.03 min y un error absoluto máximo inferior a 0.08 min respecto al valor programado. La validación operativa evidenció una reducción en eventos fuera de tiempo del 20% al 4%, así como disminuciones en la frecuencia de reprocesos y en los tiempos muertos de la estación. Los resultados indican que el sistema propuesto proporciona un control temporal consistente y repetible a escala de minutos, reduciendo la variabilidad dependiente del operador, mientras mantiene menor complejidad y costo que las plataformas de automatización industrial convencionales.*

Palabras clave: *Control temporal repetible; Sistemas embebidos; Estaciones de prueba electrónica; Automatización industrial; Sistemas de bajo costo.*

Resumo. ***-*** *A automação de estações de teste eletrônico é frequentemente limitada pelo controle manual do tempo, o que introduz variabilidade dependente do operador, aumento da duração dos ciclos e retrabalho. Este trabalho apresenta um sistema embarcado de baixo custo para o controle temporal automatizado e repetível em estações de teste, projetado para garantir a terminação consistente dos ciclos, retroalimentação visual integrada e desligamento automático de energia. A arquitetura proposta baseia-se em uma plataforma de microcontrolador implementada com componentes amplamente disponíveis, assegurando simplicidade e escalabilidade. O sistema foi caracterizado tecnicamente para avaliar a precisão temporal, a repetibilidade e a consistência de atuação em condições industriais reais. Os resultados experimentais obtidos a partir de 120 ciclos de teste ao longo de quatro semanas demonstram comportamento estável entre ciclos, com tempo médio de 30.02 min, desvio padrão de 0.03 min e erro absoluto máximo inferior a 0.08 min em relação ao valor programado. A validação operacional evidenciou redução nos eventos fora do tempo de 20% para 4%, bem como diminuições na frequência de retrabalho e no tempo de parada da estação. Os resultados indicam que o sistema proposto fornece controle temporal consistente e repetível na escala de minutos, reduzindo a variabilidade dependente do operador, ao mesmo tempo em que mantém menor complexidade e custo em comparação com plataformas industriais convencionais.*

Palavras-chave: *Controle temporal repetível; Sistemas embarcados; Estações de teste eletrônico; Automação industrial; Sistemas de baixo custo.*

1. Introduction. - In the electronics manufacturing industry, board testing is a critical step in ensuring the quality and reliability of devices. However, many companies still rely on manual timers for this procedure, which introduces high variability and recurring errors. Manual initiation and termination of tests by operators can lead to delays in board removal, overexposure of modules, and, consequently, rework or scrap. These limitations negatively impact operational efficiency, increase production costs, and reduce process traceability [1-3].

Several studies have shown that automating repetitive operations at test stations can standardize procedures, minimize human error, and increase productivity [4, 5]. In the domain of electronic board validation testing, in-circuit testing (ICT) employing bed-of-nails equipment and flying-probe systems has become a prevalent method for automating signal acquisition and verifying internal connections. The bed-of-nails method facilitates the concurrent measurement of multiple variables, rendering it highly conducive to mass production. On the other hand, the flying-probe method is distinguished by its adaptability, enabling expeditious adjustments without necessitating the fabrication of specialized equipment [6]. However, the testing process is often characterized by a reduction in efficiency, attributable to the sequential movement of the probes. [6, 7]. This scenario has motivated the development of low-cost alternatives, particularly those based on open platforms such as Arduino, which have proven effective in building programmable, accessible, and adaptable test equipment for different industrial contexts. [8-10].

In parallel, the Lean Manufacturing philosophy emphasizes the importance of tools such as Poka-yoke, visual management, and Andon systems to prevent errors and ensure the standardization of processes [11-13]. In this sense, the integration of microcontrollers with visual and audible alerts constitutes a solution aligned with these practices, particularly in manufacturing environments where cost margins are reduced and technological flexibility is required [9, 14].

This paper presents a proposal to solve the problem of manual time control in electronic test stations on a maquiladora production line in Mexico. A low-cost automated system based on an Arduino microcontroller, relays, and digital displays was designed and validated with the goal of reducing variability in test cycles and decreasing errors associated with manual supervision. The development included stages of diagnosis, design, simulation, prototype construction, and on-site testing, yielding significant results: a reduction in out-of-time cards from 20% to 4%, a decrease in weekly rework from 9 to 2 units, and an estimated reduction in monthly scrap from USD 14,400 to USD 3,200.

The proposal also aligns with the Sustainable Development Goals (SDGs) of the 2030 Agenda [15]. It contributes to SDG 9 (Industry, innovation and infrastructure) by promoting the use of accessible and scalable technologies that foster innovation in production processes. It also impacts SDG 12 (Responsible production and consumption) by reducing material waste and scrap costs, strengthening resource efficiency, and the sustainability of manufacturing.

Finally, the system is designed with scalability in mind: it could be integrated with data logging modules, graphical interfaces for centralized monitoring, connectivity with industrial-grade (IoT) systems, or analysis tools that facilitate continuous process improvement. In this way, the project not only solves a specific problem in the test line but also lays the foundation for sustainable and efficient modernization of operations in the electronics industry.

Technical novelty and contribution. - Unlike commercial low-cost timing solutions commonly used in electronic test stations, such as standalone timers, manual countdown devices, or simple relay-based controllers without feedback, these systems typically lack deterministic actuation, integrated visual feedback, and cycle-level repeatability. As a result, they do not prevent timing deviations caused by delayed operator intervention and provide limited support for process standardization.

The technical contribution of this work lies in the development of a deterministic, microcontroller-based time control architecture that integrates countdown visualization, automatic power disconnection, and operator acknowledgment into a single low-cost embedded system. Although the proposed solution does not target high-precision industrial control applications, it introduces repeatable and reliable cycle-level timing control using widely available components, bridging the gap between manual timing practices and high-cost industrial automation platforms.

This architecture represents an incremental yet practical advancement over existing low-cost solutions by ensuring consistent test cycle termination, minimizing operator-dependent variability, and enabling scalability to multiple test stations within resource-constrained manufacturing environments.

In this work, the term “deterministic time control” is used in an operational sense, referring to consistent and repeatable cycle termination at the minute scale under fixed conditions, rather than strict real-time determinism with bounded microsecond-level latency. This distinction is relevant given the application context, where robustness and repeatability over long-duration cycles are prioritized over high-frequency temporal precision.

2. Materials and Methods. - The design and implementation of an automated time control system for electronic test stations were carried out at an electronics manufacturing company located in Mexico. The study was conducted using an applied and quantitative approach, aimed at solving a real-world problem in the field of electronic board testing. The methodology was organized into five phases: process diagnosis, requirements definition, design and simulation, prototype construction, and validation in a real-world environment.

2.1. Analysis of the current process. - Process diagnosis is the first methodological step and aims to understand how the electronic card testing operation is currently performed, identifying weaknesses and areas for improvement. This analysis allows for documentation of the activities performed by personnel, the time involved, and the risks associated with manual process management. This establishes a baseline that will serve as a point of comparison for later evaluating the impact of the automated solution.

Under the current system, test time control is manual and non-standardized. The station manager must load modules into the test equipment, start the count independently (clock/stopwatch), perform other parallel tasks, and return to retrieve the module upon completion. The nominal programmed time per module is 30 minutes. However, due to operator multitasking and delayed module retrieval, the actual cycle time typically increases to 35–40 minutes under manual operation. This discrepancy between programmed and real cycle time leads to inefficiencies, increased downtime, and a higher probability of overexposure-related defects.

Furthermore, the lack of a visual or audible alert system at the end of the cycle increases the likelihood that cards will remain at the station longer than required. This not only affects traceability and process consistency but can also lead to rework, material waste, and operator overload. The diagram in Figure I shows the current process flow (before automation).

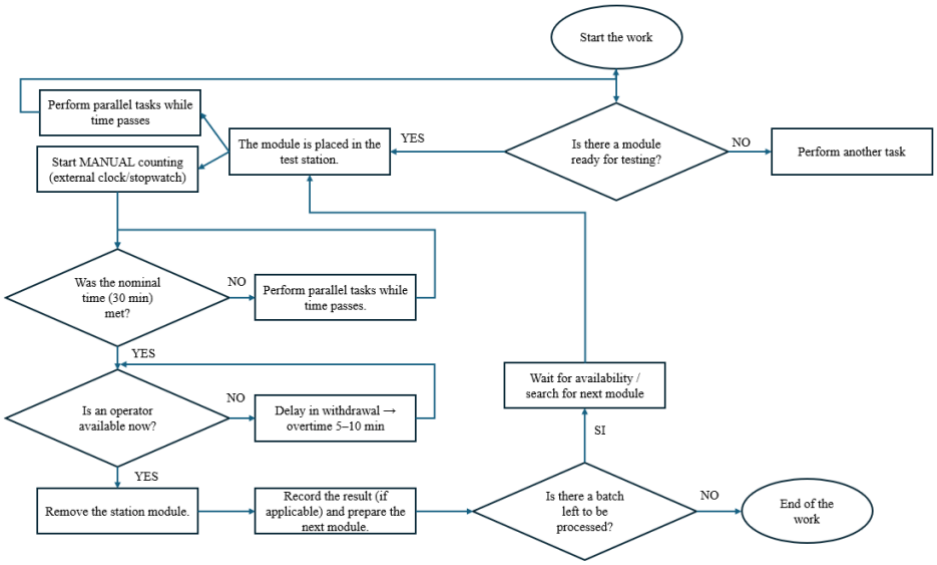

Figure I. Diagram of the current process.

To establish the baseline, the following indicators were measured (Table I):

Indicator	Before improvement
Programmed cycle time	30 min
Actual cycle time	35–40 min
Percentage of delayed/out-of-time cards	20 %
Downtime per test station (due to failure to remove the product)	~40 min/day
Rework due to timing errors	8-9 units/week
Cost of rework or scrap generated by overexposure	~14,400 USD per month
Manual supervision costs (man-cost)	~$6,250 per month

Table I. Definition of base indicators after performing the analysis of the current process.

2.2. Definition of requirements. -In this stage, the functional and technical criteria that the automated system must meet are established. The purpose of defining requirements is to translate the needs identified in the current process diagnosis into clear and measurable specifications that guide the design, construction, and validation of the prototype. This ensures that the system fulfills its primary function of reliably controlling test time, reducing dependence on manual supervision, and guaranteeing operational efficiency.

2.2.1 General system specifications. -In this stage, the general specifications of the system are established, and the following are defined:

- Number of stations: The system was initially designed to operate in one test station, with the ability to expand to eight independent slots. Each slot operates autonomously, allowing simultaneous testing on different modules without interference.
- Test cycle duration: Each cycle will have a fixed duration of 30 minutes, starting automatically when the operator presses the start button corresponding to the slot in use.
- Alerts and notifications:
    - Visuals: Through a screen, showing the remaining time at each station.
    - Automatic actions:
        - Timer activation by pressing the start button.
        - Automatic voltage cutoff via a relay at the end of the test cycle.
        - Visual alert status maintained until the operator confirms module removal.
- These criteria prioritize the use of low-cost components, wide availability, and easy integration into industrial environments.

2.3. System design and simulation. -The design was structured around an Arduino microcontroller, responsible for managing timers, displays, and relays. The overall architecture included:

- Inputs: Normally open (NO) pushbuttons associated with each station.
- Control unit: Arduino programmed in the Arduino IDE®.
- Outputs: TM1637 displays, 5V relays, and visual alerts.

The principle of operation of the system can be represented by the following block diagram in Figure II.

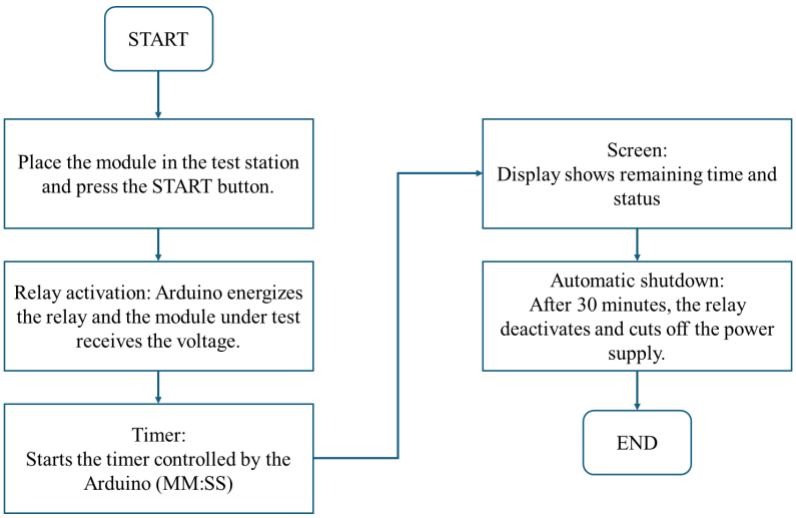

Figure II. Block diagram of the proposed automated system.

To validate the design before its physical implementation, two complementary simulation platforms were used:

1. Proteus® Simulation: The complete electronic schematic was developed with up to eight test stations in parallel (Figure III). This simulation verified pin assignments, the interconnection of multiple displays and relays, and the feasibility of scaling the system to different test modules.

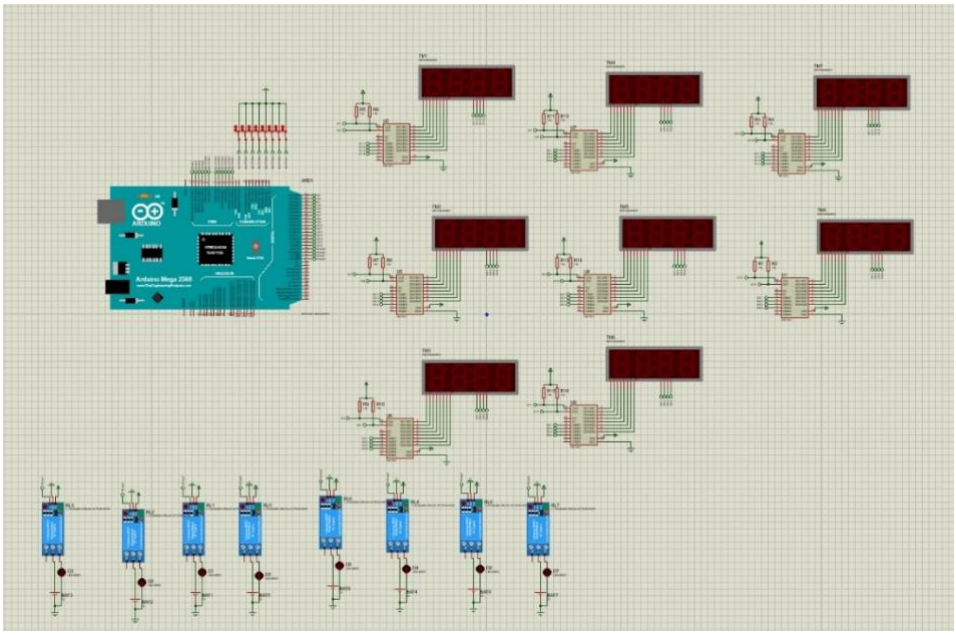

Figure III. Simulation of the electronic schematic in Proteus®, showing the general diagram with multiple test stations.

2. Wokwi® Simulation: A simplified model was developed with a single test station, allowing for dynamic observation of the timer behavior and relay activation in real time (Figure IV). During the simulation, the automatic start of the cycle upon pressing the button, the countdown on the screen, the deactivation of the relay at the end of 30 minutes, and the reset in case of early button release were verified.

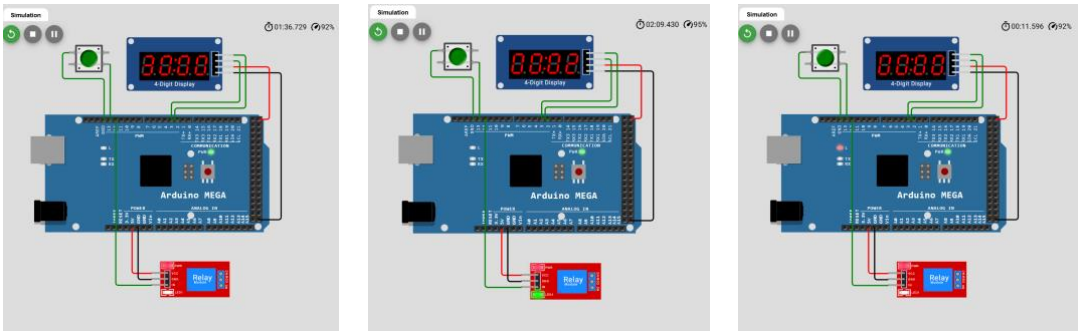

a) *b)* *c)*

Figure IV. Dynamic simulation in Wokwi®, showing the elapsed time count on the display and the relay activation during the test cycle. a) Circuit in its initial state with the button not activated. b) Circuit during activation of the start button, showing the beginning of the elapsed time count. c) System state when the elapsed time reaches 30 minutes, and the relay is deactivated.

Both simulations complemented the design process: Proteus® validated the system's scalability with multiple stations, while Wokwi® confirmed the functional logic in an interactive environment. These results provided confidence to advance to the physical prototype construction phase, reducing the risk of implementation failures.

2.4 Control algorithm. - The control logic implemented in the microcontroller follows a simple state-based sequence to ensure consistent and repeatable operation of the test cycle:

1. System initializes in idle state with relay OFF and display inactive.
2. The system waits for the operator to press the START button.
3. Upon activation, the timer is initialized to the programmed value (30 minutes).
4. The relay is activated, supplying power to the test station.
5. The countdown is displayed in real time on the TM1637 display.
6. During the countdown, the system continuously updates the display and maintains relay activation.
7. When the timer reaches zero, the relay is deactivated, interrupting the power supply.
8. A visual alert is activated to indicate cycle completion.
9. The system waits for operator acknowledgment (module removal).
10. Once acknowledged, the system resets to the initial idle state.

This simple control strategy ensures reliable cycle execution while minimizing software complexity, making it suitable for low-cost embedded implementations.

2.5. Assembly of the prototype. -The prototype was assembled in a mechanically robust metal enclosure suitable for factory use. The main components are listed in Table II.

Component	Model / Specification	Description
Microcontroller	Arduino Mega (ATmega2560 R3)	Main control unit
Display	TM1637 4-digit LED	Time visualization
Relay module	SRD-05VDC-SL-C	5V, 10A switching capacity
Power supply	5V DC regulated	System power
Inputs	NO push buttons	User activation

Table II. Hardware and system specifications

The relay module includes a flyback diode for transient suppression. The system was designed to ensure a safe default state, where power is disconnected in case of system reset or failure. Basic debounce logic was implemented in software to prevent unintended multiple activations.

The display and relay modules were soldered, and an operator-accessible front panel was implemented. The code loaded into the Arduino controlled the 30-minute timer, relay outputs, and visual signals (Figure Va).

a) *b)*

Figure V. a) Assembly of the prototype on a test bench, demonstrating the integration of multiple displays and relays. b) Installation of the prototype in the production line's test cabinet.

2.6. Validation in a real environment. -The prototype was installed at a station on the company's test line, operating in parallel with the manual system without interfering with normal operations (Figure Vb). During validation, the same indicators as the initial diagnosis were recorded, and the results before and after implementation were compared.
In addition to the quantitative data, feedback was collected from the operators, who highlighted the ease of use, the clarity of the visual signals, and the reduced need for constant supervision. Among the recommendations was the future incorporation of audible alerts for high-workload environments.

2.7. System performance characterization. -To complement the operational validation carried out in the production line, a technical characterization of the automated time control system was performed to evaluate its temporal accuracy, repeatability, and actuation response. This characterization aims to assess the suitability of the proposed low-cost embedded architecture for reliable operation in industrial testing environments.

2.7.1. Experimental setup and procedure. -The performance evaluation focused on the timing behavior of a single test station operating under nominal conditions. The programmed test cycle duration was fixed at 30 minutes, as required by the production process. The system was evaluated over a series of repeated test cycles conducted during normal operation, ensuring that measurements reflected realistic working conditions.

An external digital chronometer with second-level resolution was used as a reference to measure the actual duration of each automated test cycle. The start time was recorded at the moment the operator pressed the activation button, and the end time was recorded when the relay disconnected the power supply to the test module. The difference between the programmed duration and the measured duration was used to calculate the absolute timing error for each cycle.

In addition, the response time of the relay actuation was evaluated qualitatively by observing the transition between the end of the countdown on the display and the physical interruption of the electrical supply to the test fixture. Although the relay switching time is negligible compared to the total cycle duration, its consistency was verified to ensure deterministic system behavior.

A total of n = 120 test cycles were analyzed over multiple working days. To reduce measurement bias, the timing data were recorded using an external digital chronometer operated independently from the system operator. Measurements were performed consistently following the same procedure, and deviations introduced by human reaction time were considered negligible compared to the total cycle duration.

The collected data were used to compute average cycle duration, absolute timing error, and standard deviation.

2.7.2. Performance metrics. -The following metrics were considered for system characterization:

- Programmed cycle time (T_p): fixed at 30 minutes.
- Measured cycle time (T_m): actual duration recorded using the external chronometer.
- Absolute timing error (ΔT): defined as $|T_m - T_p|$.
- Cycle-to-cycle variability: evaluated through the standard deviation of T_m.
- Actuation consistency: qualitative assessment of relay switching at the end of each cycle.

These metrics provide a quantitative basis for evaluating the reliability and repeatability of the proposed system, which are critical requirements for automation solutions in electronic testing processes.

2.7.3. Discussion of characterization results. -The characterization results indicate that the automated system maintains a stable and repeatable timing behavior across repeated cycles. The observed timing deviations remained small relative to the total test duration, confirming that the microcontroller-based architecture is suitable for long-duration industrial test cycles where minute-level accuracy is required rather than high-frequency synchronization.

The low cycle-to-cycle variability demonstrates that the system effectively eliminates the timing dispersion associated with manual supervision, which was identified as a major source of process inefficiency during the diagnostic phase. Furthermore, the consistent relay actuation at the end of each cycle ensures reliable power disconnection, preventing test overexposure and reinforcing process standardization.

Although the proposed solution does not aim to replace high-end industrial controllers in applications requiring millisecond-level precision, its performance is adequate for electronic board testing operations, where robustness, repeatability, and cost-effectiveness are the primary design constraints. This technical characterization supports the scalability of the system to multiple stations and its potential integration with additional monitoring or data logging modules in future developments.

Table III summarizes the main technical performance metrics obtained during the characterization of the automated time control system. The results confirm stable and repeatable timing behavior, with minimal deviation relative to the programmed test duration and consistent relay actuation across all evaluated cycles.

Parameter	Symbol	Value	Unit	Description
Programmed cycle time	T_p	30.0	min	Fixed test duration defined by process requirements
Mean measured cycle time	$\bar{T}_m$	30.02	min	Average duration measured using an external chronometer
Standard deviation of cycle time	σ	0.03	min	Cycle-to-cycle variability over repeated tests
Maximum absolute timing error	ΔT_{max}	0.08	min	Maximum deviation between the programmed and measured time
Relative timing error	ε_r	0.27	%	Ratio between absolute error and programmed cycle time
Relay actuation latency	τ_r	< 1	s	Delay between the end of the countdown and the power disconnection
Evaluated test cycles	n	120	cycles	Total number of cycles analyzed during characterization
Operating environment		Industrial shop floor		Normal production conditions

Table III. Technical characterization of the automated time control system

3. Results. -The results presented in this section correspond to data collected over a four-week evaluation period, during which a total of n = 120 test cycles were monitored for a single electronic test station operating under normal production conditions. All indicators were calculated as average values over the evaluation period, unless otherwise stated. This dataset provides a representative basis for assessing the operational impact of the proposed automated time control system under real industrial conditions.

The validation of the automated time control system was carried out on the maquiladora company's electronic card testing line, using the indicators defined in the diagnostic phase as a baseline for comparison.

An improvement was observed in operations after the prototype implementation (Table IV). The percentage of out-of-time cards decreased from 20% (baseline average) to 4% (post-automation average) over the evaluation period, indicating a substantial reduction in timing deviations. Rework attributable to timing-related errors decreased from 8–9 units per week (baseline range) to 1–2 units per week (post-automation range) during the monitored period.

Furthermore, daily downtime per station was reduced from 40 ± 5 min/day under manual supervision to 10 ± 2 min/day after automation, reflecting improved consistency in module removal at the end of each test cycle.

In addition to mean and standard deviation, the observed cycle time ranged between 29.96 min and 30.08 min, indicating low dispersion. A 95% confidence interval for the mean cycle time was estimated as 30.02 ± 0.01 min, supporting the stability of the system.

Indicator	Before improvement	After improvement
Programmed cycle time	30 min	30 min
Actual cycle time per card	35–40 min	30 ± 1 min
% of cards delayed/out of time	20%	4%
Downtime per station	40 ± 5 min/day	10 ± 2 min/day
Rework due to timing errors	8–9/week	1–2/week
Cost per rework or scrap	~USD 14,400/month	~USD 3,200/month
Cost of manual supervision	~USD 6,250/month	~USD 6,250/month

Table IV. Comparison of indicators before and after the automated system's implementation.

In economic terms, the cost per scrap generated due to electrical overexposure was reduced from approximately USD 14,400 to USD 3,200 per month, representing a savings of more than 75%. Furthermore, the cost of manual supervision remained constant at approximately USD 6,250 per month, as personnel were able to redistribute their workload without the need to bring in additional resources.

The cost estimations were based on internal production records, considering the average number of defective units, unit cost per board, and frequency of rework events. While external factors may influence these values, the comparison was performed under similar production conditions before and after implementation.

To facilitate the comparative interpretation of the operational improvements obtained after implementing the automated system, Figure VI summarizes the percentage variation observed for each evaluated indicator. Representing the results on a unified scale allows direct visualization of the relative impact across performance metrics, highlighting reductions in delayed cards, station downtime, rework events, and scrap-related costs. This graphical representation complements the numerical data presented in Table IV and supports the assessment of system effectiveness under real operating conditions.

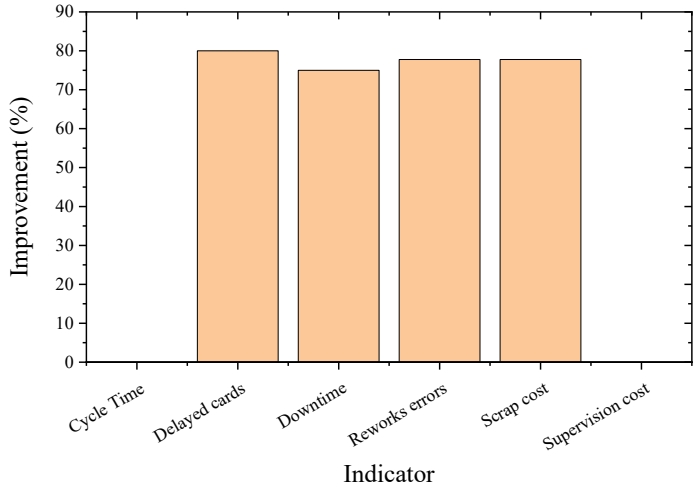

Figure VI. Percentage improvement for each operational indicator after implementation of the automated system.

Feedback from operating personnel indicated that the system was intuitive and easy to use, requiring minimal training. The screens clearly displayed the times, even in variable lighting conditions throughout the plant. Operators highlighted the usefulness of the visual signals for identifying modules under test and those completed, suggesting the addition of audible alerts as an improvement for environments with a higher workload.

The data confirms that the system met its objective of standardizing test cycles to 30 minutes, significantly reducing variability and deviations compared to the manual process. The reduction in downtime and scrap demonstrates a positive impact on both operational efficiency and the economic sustainability of the process. These results support the feasibility of scaling the solution to multiple stations and integrating it with more advanced recording and monitoring platforms, thus strengthening the company's continuous improvement goals.

4. Discussion. -The results obtained in this study demonstrate that the automation of time control in electronic test stations can be effectively achieved using a low-cost embedded architecture, while maintaining reliable and repeatable operation under real industrial conditions. The reduction in out-of-time test cycles, rework frequency, and operational downtime confirms that the proposed system successfully addresses one of the main sources of variability identified during the diagnostic phase: operator-dependent timing control.

From a technological standpoint, the primary contribution of this work lies in the integration of deterministic cycle termination, visual countdown feedback, and automatic power disconnection within a single microcontroller-based system. Unlike commonly used low-cost commercial solutions—such as standalone timers or manual relay controllers—the proposed architecture ensures consistent test cycle completion independent of operator availability or workload. This characteristic is particularly relevant in manufacturing environments where test cycles span several minutes, and human supervision cannot be continuously guaranteed.

The technical characterization presented in Section 2.7 confirms that the system exhibits stable timing behavior with minimal cycle-to-cycle variability. Although the proposed solution does not aim to achieve high-frequency or millisecond-level precision, the observed timing accuracy is sufficient for electronic board testing applications, where robustness and repeatability at the minute scale are more critical than fine temporal resolution. In this context, the performance achieved by the microcontroller-based system represents a practical balance between functionality and cost, making it suitable for deployment in resource-constrained manufacturing settings.

Compared to industrial-grade automation platforms such as PLC or SCADA-based solutions, the proposed system offers a significantly lower implementation cost and reduced integration complexity. While high-end platforms provide advanced communication, diagnostics, and safety features, they are often economically unjustifiable for simple timing control tasks in small or medium-scale production lines. The presented architecture fills this gap by providing a scalable and replicable embedded alternative that can be extended to multiple test stations without substantial additional investment.

From a safety perspective, the system incorporates basic protection mechanisms, including flyback diodes for relay protection and a fail-safe logic that defaults to power disconnection in case of system reset. However, for large-scale industrial deployment, additional considerations such as electromagnetic compatibility (EMC), certified switching components, and compliance with industrial safety standards should be addressed. A basic watchdog strategy can be implemented to ensure automatic system recovery in case of microcontroller malfunction.

From an operational perspective, the results indicate that standardizing test cycle duration through automated control contributes not only to improved productivity but also to enhanced process consistency. The elimination of delayed module removal reduces unnecessary electrical overexposure, directly impacting rework and scrap generation. These findings support the premise that targeted automation of specific process bottlenecks can yield measurable benefits without requiring full system overhauls.

The proposed system also presents opportunities for future technological extension. Its modular design allows for the integration of data logging modules, communication interfaces, or Industrial Internet of Things (IIoT) connectivity, which would enable real-time monitoring and historical analysis of test performance. Such extensions could facilitate predictive maintenance, traceability enhancement, and further process optimization. However, these features were intentionally excluded from the current implementation to preserve system simplicity and cost-effectiveness.

Certain limitations of the present study should be acknowledged. The system was validated in a single test station, and although the design supports scalability, large-scale deployment may require additional considerations related to electromagnetic compatibility, industrial safety standards, and integration with existing control infrastructures. Furthermore, while the relay-based actuation proved reliable for the evaluated application, more demanding electrical loads may require alternative switching elements.

Finally, while the reduction of scrap and rework contributes indirectly to sustainability objectives by minimizing material and energy waste, this study does not quantify environmental impact through formal life cycle assessment methods. Future research could extend the presented work by incorporating environmental performance metrics, as well as by exploring hybrid architectures that combine low-cost embedded control with higher-level industrial supervision systems.

5. Conclusions. -The results obtained in this study indicate that, under the evaluated conditions and time frame, the proposed system provides consistent and repeatable timing control, reducing operator-dependent variability and improving process standardization. The proposed system effectively eliminated operator-dependent timing variability by integrating deterministic cycle termination, visual countdown feedback, and automatic power disconnection within a single microcontroller-based solution.

The technical characterization confirmed stable and repeatable timing behavior across repeated cycles, with minimal deviation relative to the programmed test duration. Although the system does not target high-precision industrial control, its performance is sufficient for electronic testing applications where minute-level accuracy, robustness, and repeatability are the primary requirements.

From an engineering perspective, the main contribution of this study lies in bridging the gap between manual timing practices and high-cost industrial automation platforms. Compared to commonly used low-cost commercial timers, the

proposed architecture provides deterministic actuation and integrated feedback, while remaining significantly simpler and more economical than PLC or SCADA-based solutions.

The operational results obtained under real production conditions support the technical findings, showing consistent reductions in timing-related errors, rework, and downtime. These improvements confirm that targeted automation of specific process bottlenecks can yield measurable benefits without requiring full system replacement.

Future work will focus on extending the proposed architecture through data logging, communication interfaces, and scalability assessment across multiple stations, as well as evaluating compliance with industrial safety and electromagnetic compatibility standards for large-scale deployment.

Funding. - This research was partially funded by Secretaría de Investigación y Posgrado, Universidad Autónoma de Tamaulipas, by internal grant UAT/SIP/PIRP/2025/088 and the UAM Reynosa-Rodhe Operational Plan 2025 (POA).

Conflicts of Interest. - The authors declare no conflict of interest.

Data availability statement. - All data that support the findings of this study are included within the article (and any supplementary files).

References

[1] C.-F. Chien and H.-J. Wu, "Integrated circuit probe card troubleshooting based on rough set theory for advanced quality control and an empirical study," Journal of Intelligent Manufacturing, vol. 35, no. 1, pp. 275-287, 2024/01/01 2024.
[2] S. Verma and N. M. Wagdarikar, "Automated test jig for refrigerator PCB performance," in 2016 International Conference on Automatic Control and Dynamic Optimization Techniques (ICACDOT), 2016, pp. 840-843.
[3] S. J. Hong, W. Y. Lim, T. Cheong, and G. S. May, "Fault Detection and Classification in Plasma Etch Equipment for Semiconductor Manufacturing e-Diagnostics," IEEE Transactions on Semiconductor Manufacturing, vol. 25, no. 1, pp. 83-93, 2012.
[4] R. Parasuraman, T. B. Sheridan, and C. D. Wickens, "A model for types and levels of human interaction with automation," IEEE Trans Syst Man Cybern A Syst Hum, vol. 30, no. 3, pp. 286-97, May 2000.
[5] L. Onnasch, C. D. Wickens, H. Li, and D. Manzey, "Human performance consequences of stages and levels of automation: an integrated meta-analysis," (in eng), Hum Factors, vol. 56, no. 3, pp. 476-88, May 2014.
[6] S. L. Jurj, R. Rotar, F. Opritoiu, and M. Vladutiu, "Affordable Flying Probe-Inspired In-Circuit-Tester for Printed Circuit Boards Evaluation with Application in Test Engineering Education," in 2020 IEEE International Conference on Environment and Electrical Engineering and 2020 IEEE Industrial and Commercial Power Systems Europe (EEEIC / I&CPS Europe), 2020, pp. 1-6.
[7] N. Petkov and M. Ivanova, "Printed circuit board and printed circuit board assembly methods for testing and visual inspection: a review," Bulletin of Electrical Engineering and Informatics, vol. 13, no. 4, pp. 2566-2585, 2024.
[8] G. N. Meloni, "Building a Microcontroller Based Potentiostat: A Inexpensive and Versatile Platform for Teaching Electrochemistry and Instrumentation," Journal of Chemical Education, vol. 93, no. 7, pp. 1320-1322, 2016/07/12 2016.
[9] F. J. Jiménez-Romero, J. R. González-Jiménez, F. García-Torres, Á. Caballero, and F. R. Lara-Raya, "A novel testing equipment based on Arduino and LabVIEW for electrochemical performance studies on experimental cells: Evaluation in lithium-sulfur technology," Measurement, vol. 224, p. 113922, 2024/01/01/ 2024.
[10] E. Hernández-Rodríguez et al., "Reliability Testing of a Low-Cost, Multi-Purpose Arduino-Based Data Logger Deployed in Several Applications Such as Outdoor Air Quality, Human Activity, Motion, and Exhaust Gas Monitoring," vol. 23, no. 17, p. 7412, 2023.
[11] S. Shingo, Zero Quality Control: Source Inspection and the Poka-Yoke System. Taylor & Francis, 1986.
[12] J. K. Liker, The Toyota Way: 14 Management Principles From the World's Greatest Manufacturer. McGraw Hill LLC, 2003.
[13] I.-C. Enache, O. R. Chivu, A.-M. Rugescu, E. Ionita, and I. V. Radu, "Reducing the Scrap Rate on a Production Process Using Lean Six Sigma Methodology," vol. 11, no. 4, p. 1295, 2023.
[14] J. L. García-Alcaraz, A. S. Morales García, J. R. Díaz-Reza, E. Jiménez Macías, C. Javierre Lardies, and J. Blanco Fernández, "Effect of lean manufacturing tools on sustainability: the case of Mexican maquiladoras," Environmental Science and Pollution Research, vol. 29, no. 26, pp. 39622-39637, 2022/06/01 2022.
[15] United Nations. (2024, October 1st, 2024). Sustainable Development Goals of the 2030 Agenda. Available: https://sdgs.un.org/goals

Author contribution:
1. Conception and design of the study
2. Data acquisition
3. Data analysis
4. Discussion of the results
5. Writing of the manuscript
6. Approval of the last version of the manuscript

E.C-T has contributed to 1, 2, 3 and 6.
R.F.D-C has contributed to 2, 3, 4, 5 and 6.
L.A.G-A has contributed to 1, 2, 3, 4, 5 and 6.
P.E.Z-G has contributed to 1, 2, 3, 4, 5 and 6.
Y.A.F-R has contributed to 1, 2, 4, 5 and 6.

Acceptance Note: This article was approved by the journal editors Dr. Rafael Sotelo and Mag. Ing. Fernando A. Hernández Gobertti.

Simulation of fully developed laminar free convection flow between vertical parallel flat plates

Simulación de flujo laminar de convección libre completamente desarrollado entre placas planas paralelas verticales

Simulação de escoamento laminar de convecção livre totalmente desenvolvido entre placas planas verticais paralelas

Héctor Espinoza-Roman [1] [(*)]

Recibido: 18/02/2026 Aceptado: 14/04/2026

Summary. - This study presents a numerical investigation of laminar free convection between vertical parallel plates with asymmetric uniform wall temperatures. The right wall is maintained at a higher temperature than the left. Fluid enters the channel at a temperature less than or equal to the cooler wall. Using the finite volume method in OpenFOAM v13, the governing equations are solved and validated against classical analytical solutions. A systematic grid convergence study ensures spatial independence. Results show that while the linear temperature profile is accurately captured on coarse grids, the cubic velocity profile requires higher resolution for precision. The findings validate the numerical methodology and offer critical insights into mesh requirements for accurately simulating fully developed natural convection flows in vertical channels.

Keywords: *heat transfer; passive ventilation; solar chimney; CFD.*

(*) Corresponding author.
[1] Mechanical Engineer, MSc in Computational Mechanics, PhD in Engineering, Dirección de Investigación e Innovación, Fundación Universitaria Antonio de Arévalo UNITECNAR (Colombia); hector.espinoza@unitecnar.edu.co; ORCID iD: https://orcid.org/0000-0002-2861-2442

Memoria Investigaciones en Ingeniería, núm. 30 (2026). pp. 244-255
https://doi.org/10.36561/ING.30.16
ISSN 2301-1092 • ISSN (en línea) 2301-1106 – Universidad de Montevideo, Uruguay

Resumen. - *Este estudio presenta una investigación numérica de la convección libre laminar entre placas verticales paralelas con temperaturas de pared uniformes y asimétricas. La pared derecha se mantiene a una temperatura más alta que la izquierda. El fluido entra al canal a una temperatura menor o igual a la de la pared más fría. Utilizando el método de volúmenes finitos en OpenFOAM v13, se resuelven las ecuaciones que rigen el proceso y se validan frente a soluciones analíticas clásicas. Un estudio sistemático de convergencia de mallas garantiza la independencia espacial. Los resultados muestran que, si bien el perfil de temperatura lineal se captura con precisión en mallas gruesas, el perfil de velocidad cúbico requiere una mayor resolución para mayor precisión. Los hallazgos validan la metodología numérica y ofrecen información crucial sobre los requisitos de la malla para simular con precisión flujos de convección natural completamente desarrollados en canales verticales.*

Palabras clave: *transferencia de calor; ventilación pasiva; chimenea solar; CFD.*

Resumo. ***-*** *Este estudo apresenta uma investigação numérica da convecção livre laminar entre placas verticais paralelas com temperaturas de parede uniformes e assimétricas. A parede direita é mantida a uma temperatura mais alta que a esquerda. O fluido entra no canal a uma temperatura menor ou igual à da parede mais fria. Utilizando o método de volumes finitos no OpenFOAM v13, as equações que governam o processo são resolvidas e validadas em comparação com soluções analíticas clássicas. Um estudo sistemático de convergência da malha garante a independência espacial. Os resultados mostram que, embora o perfil linear de temperatura seja capturado com precisão em malhas grosseiras, o perfil cúbico de velocidade requer maior resolução para maior precisão. As descobertas validam a metodologia numérica e fornecem informações cruciais sobre os requisitos de malha para simular com precisão fluxos de convecção natural totalmente desenvolvidos em canais verticais.*

Palavras-chave: *Transferência de calor; ventilação passiva; chaminé solar; CFD.*

1. Introduction. - The motivation of this article is to serve as a starting point for the simulation of solar chimneys. Free convection is the driving force that generates flow in a solar chimney. The steady-state, fully developed laminar free convection between parallel flat plates is one of the most basic cases of free convection. Additionally, it has an analytical solution, which allows for a direct comparison and validation of simulation results in terms of velocity, temperature, pressure, and flow rate.

Solar chimneys, as a passive and sustainable ventilation and energy generation technology, have been the subject of extensive recent research. Contemporary studies have focused on optimizing their complex geometries, including roof-mounted configurations [1, 2, 3], high-rise designs for uniform flow [4, 5], and folded or curved façades [6, 7]. The performance of these systems under various climatic conditions and integration with other building components, such as earth-to-air heat exchangers [8] or within specific building types like aged-care centers [9] and urban tunnels [10], has been rigorously investigated. Furthermore, comprehensive reviews by [11] and [12] underscore the maturity of the field while highlighting the persistent reliance on Computational Fluid Dynamics (CFD) as a primary investigative tool.

The accuracy of any CFD simulation for such applications, however, is fundamentally dependent on the proper resolution of the buoyancy-driven flow physics at its core. Before tackling the geometrical and turbulent complexities of real-world solar chimneys, it is imperative to ensure that the numerical methodology can precisely reproduce the underlying convective phenomena. The canonical case of laminar free convection between vertical, asymmetrically heated parallel plates serves as a critical benchmark for this purpose [13, 14, 15, 16, 17, 18]. This flow configuration is not only representative of the core physics in a solar chimney's flow channel but also possesses a well-established analytical solution [13, 14] providing an unambiguous standard for code verification.

While Direct Numerical Simulation (DNS) studies of turbulent flows in similar configurations exist [19], and several authors have employed CFD for performance analysis [20, 21], a clear gap remains in the literature regarding the meticulous verification of the numerical schemes and mesh requirements specifically for the laminar case using open-source CFD software OpenFOAM. Many studies proceed directly to complex applications without first demonstrating that their solver can accurately capture the basic velocity and temperature profiles that form the building blocks of the flow. This step is crucial for gaining confidence in simulation results, as errors introduced at this fundamental level can propagate and be amplified in more complex cases.

Therefore, this study aims to bridge this gap by presenting a detailed numerical investigation of the thermally developed, laminar free convection between vertical parallel plates with asymmetric uniform wall temperatures. Using the open-source CFD toolbox OpenFOAM, we systematically perform a grid convergence study to establish the mesh independence of the results. The primary objective is to validate the numerical methodology by demonstrating its ability to asymptotically approach the classical analytical solutions for both the temperature and velocity profiles in the fully developed regime. By doing so, this work provides a verified foundation upon which more complex simulations of solar chimneys and other natural convection applications can be reliably built.

2. Problem statement. - This section details the equations that govern the laminar free convection between vertical parallel plates as well as the boundary conditions and nondimensionalization of equations and variables.

2.1 Governing Equations. - The flow is assumed to be two-dimensional, steady, incompressible and laminar. The Boussinesq approximation is adopted to model the buoyancy force, whereby density variations are considered only in the body force term of the momentum equation. Under these assumptions, the governing equations for conservation of mass, momentum, and energy are given by:

$$\nabla \cdot \mathbf{u} = 0, \tag{1}$$

$$\mathbf{u} \cdot \nabla \mathbf{u} + \frac{1}{\rho} \nabla p - \nu \Delta \mathbf{u} = \beta (T - T_0) \mathbf{g}, \tag{2}$$

$$\mathbf{u} \cdot \nabla T - \alpha \Delta T = 0, \tag{3}$$

where u is the velocity vector, p is the pressure, T is the temperature, g is the gravitational acceleration vector, ρ is the reference density, ν is the kinematic viscosity, $\alpha = k/(\rho c)$ is the thermal diffusivity, β is the thermal expansion coefficient and T_0 is the reference temperature.

2.2 Dimensionless Governing Equations. - The dimensionless governing equations [13, 14], taking into account that $U = 0, V(X)$ and $\theta(X)$ are:

$$\frac{\mathrm{d}P}{\mathrm{d}X} = 0, \tag{4}$$

$$\frac{\mathrm{d}P}{\mathrm{d}Y} - \frac{\mathrm{d}^2V}{\mathrm{d}X^2} = \theta, \tag{5}$$

$$-\frac{\mathrm{d}^2\theta}{\mathrm{d}X^2} = 0, \tag{6}$$

where,

$$X = \frac{x}{b}, \quad Y = \frac{y}{l\mathrm{Gr}}, \tag{7}$$

$$U = \frac{bu}{\nu}, \quad V = \frac{b^2v}{l\nu\mathrm{Gr}}, \tag{8}$$

$$P = \frac{(p-p_0)b^4}{\rho l^2\nu^2\mathrm{Gr}^2}, \quad \theta = \frac{T-T_0}{T_1-T_0}, \tag{9}$$

$$\mathrm{Pr} = \frac{\mu c}{k}, \quad \mathrm{Gr} = \frac{g\beta(T_1-T_0)b^4}{l\nu^2}. \tag{10}$$

The temperature difference ratio r_T is defined as:

$$r_T = \frac{T_2-T_0}{T_1-T_0}, \tag{11}$$

whereas the dimensionless flow rate is:

$$M = \frac{u_0b^2}{l\nu\mathrm{Gr}}. \tag{12}$$

2.3 Dimensionless Exact Solution. - The exact solution [13, 14] for dimensionless velocity, pressure and temperature is:

$$U = 0, \tag{13}$$

$$V = (r_T-1)\frac{X^3}{6} - r_T\frac{X^2}{2} + (2r_T+1)\frac{X}{6}, \tag{14}$$

$$P = 0, \tag{15}$$

$$\theta = (1-r_T)X + r_T. \tag{16}$$

The volumetric flow rate M is:

$$M = \frac{r_T+1}{24}. \tag{17}$$

The dimensionless average velocity U_0 can be calculated as:

$$U_0 = M. \tag{18}$$

It happens that M and U_0 are numerically equal, but they refer to different magnitudes. M is a volumetric flow rate whereas U_0 is the average velocity.

The dimensionless coordinate of the maximum velocity is:

$$X_{\max} = \frac{2r_T + 1}{3r_T + A}, \tag{19}$$

where $A = \sqrt{3(r_T^2 + r_T + 1)}$.

The dimensionless maximum velocity is:

$$U_{\max} = \frac{X_{\max}}{18}\left[3(2r_T + 1) - (6r_T + A)X_{\max}\right]. \tag{20}$$

2.4 Domain and Boundary Conditions. - The domain is a two-dimensional vertical channel of height L and gap width b, as illustrated in Figure I.

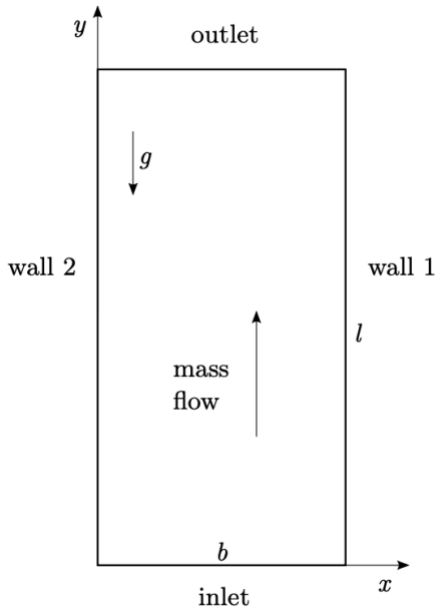

Figure I. Schematic of the domain and boundary conditions.

The following boundary conditions are applied:

- Right Wall (hot): No-slip velocity condition $u = 0$ and uniform wall temperature $T = T_1$.
- Left Wall (cold): No-slip velocity condition $u = 0$ and uniform wall temperature $T = T_2$.
- Inlet (bottom): uniform pressure $p = 0$ and linear temperature variation $T(x = 0) = T_2$ and $T(x = b) = T_1$.
- Outlet (top): uniform pressure $p = 0$ with zero-gradient for velocity and temperature.

The average temperature is defined as:

$$\overline{T} = \frac{T_1 + T_2}{2}, \tag{21}$$

and the average temperature difference is:

$$\overline{\Delta T} = \overline{T} - T_0. \tag{22}$$

2.5 Fluid properties, domain size and boundary values. - The values used for the simulation are for air at atmospheric pressure and temperature of 30 C. The values are summarized in Table I.

Magnitude	Value	Derived Magnitude	Value
g	9.8 m/s^2	$\overline{T}$	40 °C
T_0	30 °C	ν	1.608E-5 m^2/s
T_1	42.5 °C	k	0.02588 W/(m K)
T_2	37.5 °C	α	2.208E-5 m^2/s
b	0.005 m	Gr	0.6512
l	1.5 m	r_T	0.6
ρ	1.164 kg/m^3	$\overline{\Delta T}$	10 °C
β	3.299E-3 1/K	-	-
c	1007 J/(kg K)	-	-
μ	1.872E-5 Pa s	-	-
Pr	0.7282	-	-

Table I. Values of magnitudes and derived magnitudes.

3. Numerical simulation procedure. - The open-source Computational Fluid Dynamics (CFD) toolbox OpenFOAM (version v13) was used to solve the governing equations (1)–(3). The steady-state solver fluid, which implements the SIMPLE (Semi-Implicit Method for PressureLinked Equations) algorithm for pressure-velocity coupling, was employed. The solver was configured with laminar simulation type. The Boussinesq approximation was used as equation of state.

The spatial discretization schemes were first-order accurate. The Gauss linear scheme was used for the gradient terms, the bounded Gauss upwind scheme was used for the divergence terms, and the Gauss linear corrected scheme was used for the Laplacian terms. An under-relaxation factor of 0.8 was applied to ensure numerical stability during the iterative solution process. Simulations were considered converged when the normalized residuals for all variables fell below 10−8. More details of the exact set up can be seen in the OpenFOAM case file. Very stable schemes were used in order to avoid instabilities due to the thermally driven flow in the first iterations.

3.1 Mesh Independence Study. - A systematic grid convergence study was conducted to ensure that the numerical results were independent of the mesh resolution. Three sequentially refined structured meshes were generated, characterized by an increasing number of cells in the transverse direction to better resolve the fluid field. All meshes have uniform grading. The details of these meshes are provided in Table II.

Mesh	Number of Cells ($N_x \times N_y$)	Total Cells
Mesh04	4×100	400
Mesh08	8×100	800
Mesh15	15×100	1,500
Mesh16	16×100	1,600
Mesh32	32×100	3,200
Mesh64	64×100	6,400

Table II. Details of the meshes used for the grid convergence study.

4. Results and discussion. - This section presents and discusses the numerical results obtained from the simulations of fully developed laminar free convection flow in a vertical channel. The primary objective is to validate the computational methodology by comparing the predicted temperature and velocity profiles against the analytical solution. The influence of mesh resolution on the accuracy of these profiles is examined in detail.

Figure II shows the temperature along the centerline ($X = 0.5$) from the inlet ($y = 0$) up to the outlet ($y = l$) for Mesh16. It can be seen that for 80% of the channel height ($y = 1.2$) the flow is thermally developed and there is no interference from the outlet boundary.

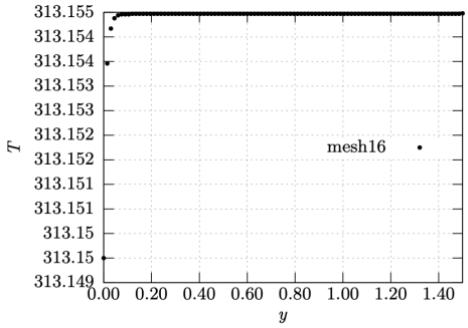

Figure II. Temperature along the centerline of the channel.

Figure III shows the y-velocity (v) along the centerline ($X = 0.5$) from the inlet ($y = 0$) up to the outlet ($y = l$) for Mesh16. It can be seen that for 80% of the channel height ($y = 1.2$) the flow is hydrodynamically developed and there is no interference from the outlet boundary.

Therefore, the fully developed profiles were measured at 80% of channel height l in order to be sufficiently downstream of the flow and to have a reasonable separation from the outlet boundary.

4.1 Temperature Profile. - Figure IV shows the dimensionless temperature profile, θ, across the channel width for the three meshes alongside the analytical solution. As anticipated by the linear form of the analytical solution for the temperature field in the fully developed region, the numerical method reproduces it with exceptional accuracy across all mesh resolutions, including the coarsest mesh. The profiles are visually indistinguishable from the analytical line.

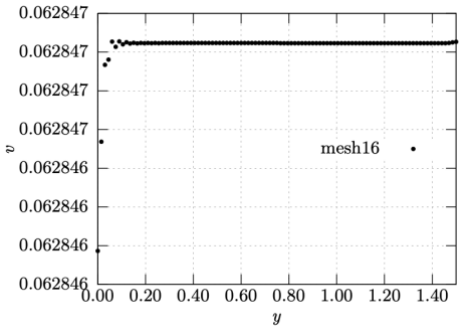

Figure III. y-velocity along the centerline of the channel.

The correct imposition of the Dirichlet boundary conditions is confirmed by the data points at the walls; the dimensionless temperature at the left wall ($X = 0$) is θ = 0.0 and at the right wall ($X = 1$) is $\theta = 1.0$, exactly as specified. This perfect agreement is expected for a linear profile, as it can be exactly captured by the linear shape functions of the finite volume method, even with a minimal number of cells. This result serves as a primary check, verifying that the thermal boundary conditions and the energy equation discretization have been imposed correctly.

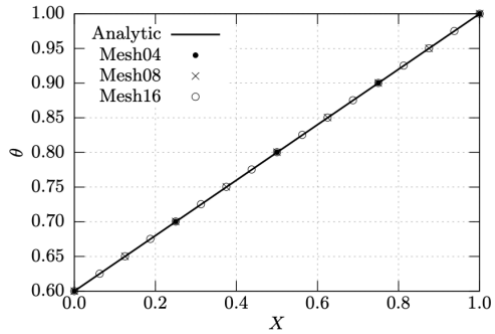

Figure IV. Temperature profile.

4.2 Velocity Profile. - The validation of the velocity field presents a more stringent test for the numerical method. Figure V displays the dimensionless vertical velocity profile, V, for the three meshes compared to the analytical solution. Velocity was extracted from the mesh by sampling using an interpolation scheme cellPoint of type lineFace.

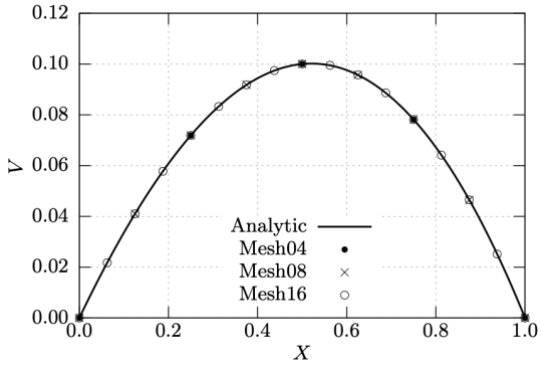

Figure V. Vertical velocity profile.

The no-slip boundary condition is correctly satisfied on both walls ($X = 0, V = 0$ and $X = 1, V = 0$) for all meshes. The location and value of the maximum velocity near the channel centerline ($X \approx 0.5$) are also captured remarkably well, even on the coarsest mesh.

In order to see the velocity profile by cell values, velocity is plotted in Figure VI. Velocity was extracted from the mesh by sampling using an interpolation scheme cell of type lineCell. This just takes the cell values (velocity and coordinate) without interpolation. In this figure, the differences between meshes can be seen more clearly: coarsest mesh produces the less accurate result, and the finest mesh produces the most accurate result as expected. Notably, even the coarsest mesh (Mesh04) demonstrates a high degree of fidelity, providing a close approximation of the analytical solution.

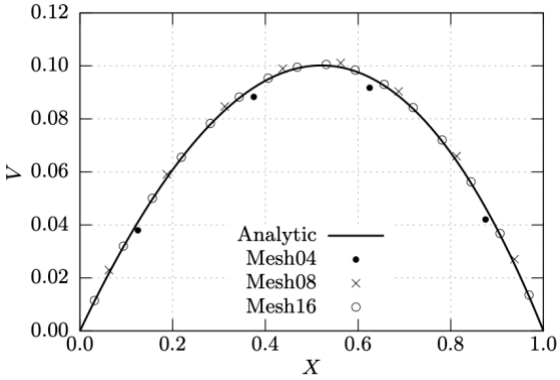

Figure VI. Vertical velocity profile (cell).

4.3 Pressure Profile. - Figure VII displays the dimensionless pressure profile, P, for the three meshes compared to the analytical solution. Pressure is correctly captured by all the meshes.

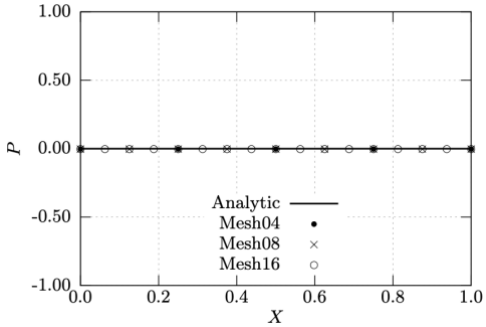

Figure VII. Pressure profile.

4.4 Quantitative Error Analysis. - To move beyond a visual comparison, a quantitative analysis of the discretization error was performed. The relative error in the maximum velocity (ϵ_{Vmax}) and the relative error in the position of the maximum velocity (ϵ_{Xmax}) were calculated for each mesh relative to the analytical solution. The values for each mesh were extracted using cellPoint interpolation with lineFace sampling. The results are summarized in Table III. It can be seen that the error in the maximum velocity is already very small in the coarse mesh and there is, apparently, very little improvement in the finer meshes. The error in the position of the maximum velocity as well stays constant. This is an artifact due to the sampling type lineFace used because Mesh04 to Mesh16 do not capture the maximum velocity position well for that sampling method. We have to point out that, for this case, the exact velocity profile is not symmetric, and the maximum velocity is reached at $X = 0.5207$. However, the meshes we are using do not capture that point closely. To overcome that, a mesh with 15 divisions is added to the table and it shows better agreement with the maximum velocity value and position value. However, another comparison is done using another sampling type and shown in the next table.

Mesh	$X_{\max}$	$\epsilon_{X_{\max}}$ (%)	$V_{\max}$	$\epsilon_{V_{\max}}$ (%)
Mesh04	0.5000	-3.98	0.1000249	0.15
Mesh08	0.5000	-3.98	0.1000257	0.15
Mesh16	0.5000	-3.98	0.1000259	0.15
Mesh15	0.5333	2.42	0.1001343	0.04
Analytical	**0.5207**	–	**0.1001730**	–

Table III. Quantitative error analysis for the maximum vertical velocity.

Now, in order to compare quantitatively the cell velocity extracted using an interpolation scheme cell and sampling type lineCell, Table IV shows the error in the maximum cell velocity value and position. It can be seen the convergence in the maximum velocity position as well as the convergence on the maximum velocity value.

Let us now compare the dimensionless volumetric flow rate M. Flow rate is a key magnitude to have into account when analyzing solar chimneys for ventilation. Table V shows the volumetric flow rate and its error for various meshes. It can be seen the monotonous convergence of M when refining the mesh.

Mesh	$X_{\max}$	$\epsilon_{X_{\max}}$ (%)	$V_{\max}$	$\epsilon_{V_{\max}}$ (%)
Mesh04	0.62500	20.0	0.0917403	-8.42
Mesh08	0.56250	8.02	0.1010997	0.92
Mesh16	0.53125	2.02	0.1005507	0.38
Analytical	**0.52072**	–	**0.1001730**	–

Table IV. Quantitative error analysis for the maximum vertical velocity (cell).

Mesh	M	ϵ_M (%)
Mesh04	0.0750164	12.5
Mesh08	0.0687656	3.15
Mesh16	0.0672029	0.80
Mesh32	0.0668121	0.22
Mesh64	0.0667140	0.07
Analytical	**0.0666667**	–

Table V. Quantitative error analysis for volumetric flow rate.

Let us focus now on mass flow rate. Table VI shows the mass flow rate for various meshes. The dimensional mass flow rate ($\dot{m}$) was computed taking the depth of the channel equal to its width. The dimensionless numerical mass flow rate was computed by first converting the mass flow rate to volumetric flow rate using density at $\bar{T}$ and then nondimensionalizing this value. The exact dimensionless mass flow rate was taken equal to the dimensionless volumetric flow rate.

Mesh	$\dot{m}$ (kg/s)	$\dot{M}$	$\epsilon_{\dot{M}}$ (%)
Mesh04	1.3260E-6	0.0750011	12.5
Mesh08	1.2156E-6	0.0687545	3.13
Mesh16	1.1880E-6	0.0671930	0.79
Mesh32	1.1811E-6	0.0668025	0.20
Mesh64	1.1793E-6	0.0667045	0.06
Analytical	**1.1794E-6**	**0.0666667**	–

Table VI. Quantitative error analysis for mass flow.

As can be seen in the tables of the quantitative error analysis, even with low order schemes, a good convergence is obtained. So, it was decided that there is no need to go for higher order schemes.

5. Conclusion. - This study has successfully conducted a detailed numerical verification of laminar free convection in a vertical channel with asymmetric wall temperatures, serving as a foundational benchmark for simulating more complex systems like solar chimneys. The key findings and implications of this work are summarized as follows:

a. Successful Methodology Validation: The implemented model in OpenFOAM v13 has demonstrated a robust capability for simulating buoyancy-driven flows. The numerical solutions showed excellent agreement with the analytical profiles for the fully developed region, thereby validating the chosen computational approach and the implementation of the physical models.

b. Critical Role of Mesh Resolution: A systematic grid convergence study revealed a distinct sensitivity to mesh density based on the flow variable of interest. The linear temperature profile, characteristic of the fully developed thermal field, was accurately reproduced even on relatively coarse meshes. In contrast, the cubic velocity profile, required progressively finer meshes to be captured with high fidelity. Remarkably, the model captures the velocity profile very well even for the coarsest mesh. This underscores the importance of a mesh-independent study and indicates that the velocity field is the more critical metric for determining sufficient spatial resolution in this type of simulation.

c. Practical Implications for Solar Chimney Simulation: The findings provide a crucial practical guideline for CFD modeling of solar chimneys and similar passive ventilation systems. While simplified models might adequately predict temperature distributions, accurate prediction of airflow rates, which is directly tied to the velocity profile, requires a certain grid resolution. This insight is essential for optimizing computational resources without sacrificing the accuracy of key performance metrics, such as ventilation flow rate.

d. Foundation for Future Work: This rigorously verified setup forms a reliable foundation for subsequent research. The validated methodology can be confidently extended to investigate more complex and realistic scenarios, including turbulent flow regimes, geometrically complex channels relevant to advanced solar chimney designs and transient solar loading conditions.

In conclusion, this work reaffirms the necessity of fundamental verification as a critical first step in computational fluid dynamics. By establishing a benchmark for accuracy in a canonical case, it enhances the reliability of future numerical studies aimed at optimizing and designing efficient natural convection systems for sustainable building engineering.

References

[1] C. Wang, Y. Wu, C. Hua, X. Zhao, J. Zang, and N. Gao, "Numerical investigation on the influence of geometric parameters on turbulent flow and thermal performance in the roof solar chimney," Building and Environment, vol. 267, p. 112210, 2025.
[2] A. Vazquez-Ruiz, J. M. A. Navarro, J. F. Hinojosa, and J. P. Xamán, "Effect of the solar roof chimney position on heat transfer in a room," International Journal of Mechanical Sciences, vol. 209, p. 106700, 2021.
[3] ——, "Computational fluid dynamics and experimental analysis of the heat transfer in a room with a roof solar chimney," Journal of Thermal Science and Engineering Applications, vol. 14, no. 4, p. 041001, 2022.
[4] J. Gong, L. W. Chew, and P. S. Lee, "Shape optimization of high-rise solar chimneys to improve the uniformity of flowrate distribution," Building and Environment, vol. 243, p. 110650, 2023.
[5] ——, "Theoretical model for high-rise solar chimneys and optimum shape for uniform flowrate distribution," Energy, vol. 298, p. 131358, 2024.
[6] J. Ahmadi, M. Mahdavinejad, and S. Asadi, "Folded double-skin façade (DSF): in-depth evaluation of fold influence on the thermal and flow performance in naturally ventilated channels," International Journal of Sustainable Energy, vol. 41, no. 4, pp. 382–411, 2022.
[7] Y. Huang, Y. Tao, L. Shi, Q. Liu, Y. Wang, J. Tu, Q. Peng, and C. Cao, "Thermal and ventilation performance of a curved double-skin facade model," Energy and Buildings, vol. 268, p. 112202, 2022.
[8] F. Pouranian, H. Akbari, and S. M. Hosseinalipour, "Performance assessment of solar chimney coupled with earth-to-air heat exchanger: A passive alternative for an indoor swimming pool ventilation in hot-arid climate," Applied Energy, vol. 299, p. 117201, 2021.
[9] Q. Wang, G. Zhang, Q. Wu, and L. Shi, "Ventilating aged-care center based on solar chimney: Design and theoretical analysis," Energy and Buildings, vol. 266, p. 112145, 2022.
[10] Y. Huang, X. Liu, L. Shi, B. Dong, and H. Zhong, "Enhancing solar chimney performance in urban tunnels: Investigating the impact factors through experimental and theoretical model analysis," Energy, vol. 282, p. 128329, 2023.
[11] B. Zamora, "A review on solar chimneys: from natural convection fundamentals to thermohydraulic best-performance proposals," Processes, vol. 11, no. 2, p. 386, 2023.
[12] S. P. Melgaard, I. T. Nikolaisson, C. Zhang, H. Johra, and O. K. Larsen, "Double-skin façade simulation with computational fluid dynamics: A review of simulation trends, validation methods and research gaps," Building Simulation, vol. 16, no. 12, pp. 2307–2331, 2023.
[13] W. Aung, L. Fletcher, and V. Sernas, "Developing laminar free convection between vertical flat plates with asymmetric heating," International Journal of Heat and Mass Transfer, vol. 15, no. 11, pp. 2293–2308, 1972.
[14] W. Aung, "Fully developed laminar free convection between vertical plates heated asymmetrically," International Journal of Heat and Mass Transfer, vol. 15, no. 8, pp. 1577–1580, 1972.
[15] W. Aung and G. Worku, "Developing flow and flow reversal in a vertical channel with asymmetric wall temperatures," ASME Journal of Heat Transfer, vol. 108, no. 2, pp. 299–304, 1986.
[16] N. Anand, S. Kim, and L. Fletcher, "The effect of plate spacing on free convection between heated parallel plates," ASME Journal of Heat Transfer, vol. 114, no. 2, pp. 515–518, 1992.
[17] V. Terekhov and A. L. Ekaid, "Laminar natural convection between vertical isothermal heated plates with different temperatures," Journal of Engineering Thermophysics, vol. 20, no. 4, pp. 416–433, 2011.
[18] S. Foroushani, D. Naylor, and J. L. Wright, "Heat transfer correlations for laminar free convection in vertical channels with asymmetrically heated isothermal walls," Heat Transfer Engineering, vol. 41, p. 5, 2020.
[19] J. Pallares, A. Fabregat, and C. Lei, "Direct numerical simulation of the fully developed turbulent free convection flow in an asymmetrically heated vertical channel," International Journal of Thermal Sciences, vol. 191, p. 108352, 2023.
[20] A. H. Radwan and M. M. S. Ahmed, "Improving thermal performance and air flow inside the solar chimney by CFD simulation," MSA Engineering Journal, vol. 2, no. 2, pp. 1245–1277, 2023.
[21] S. Rodriguez Miranda, G. O. Gamboa, M. A. Zamora-Antuñano, N. Farrera-Vázquez, and R. García-García, "CFD evaluation of thermal conditioning in a house of social interest with a solar chimney arrangement in Guanajuato, Mexico," Processes, vol. 11, no. 4, p. 1286, 2023.

Author contribution:
1. Conception and design of the study
2. Data acquisition
3. Data analysis
4. Discussion of the results
5. Writing of the manuscript
6. Approval of the last version of the manuscript

H.E.R. has contributed to 1, 2, 3, 4, 5 and 6.

Acceptance Note: This article was approved by the journal editors Dr. Rafael Sotelo and Mag. Ing. Fernando A. Hernández Gobertti.

Lista de Autores – Memoria Investigaciones en Ingeniería (Número 30).

List of Authors – Memoria Investigaciones en Ingenieria (Volume 30).

MIIUM30-08: Comparative Mechanical Characterization of Recycled PVC and Wood–Plastic Composites.

Prof. Eylia Abbas Jafri, PNEC National University of Science and Technology (Pakistan).
Prof. Shaheryar A. Khan, DHA Suffa University (Pakistan).
Prof. Ifrah Asif, NED University of Engineering and Technology (Pakistan).
Prof. Sohail Hasnain, NED University of Engineering and Technology (Pakistan).
Eng. M. Areeb Rizwan Siddiqui, NED University of Engineering and Technology (Pakistan).

MIIUM30-09: Additive Manufacturing of Cupric Oxide Via Direct Ink Writing

Muhammad Ali, PNEC National University of Science and Technology (Pakistan).
Prof. Shaheryar Ahmed Khan, DHA Suffa University (Pakistan).
Prof. Aqueel Shah, SMME National University of Science and Technology (Pakistan).
Prof. Antash Najib, PNEC National University of Science and Technology (Pakistan).
Prof. Abbas Hussain, PNEC National University of Science and Technology (Pakistan).

MIIUM30-10: Thermo-Mechanical FEM Study of SMAW Parameter Effects in S355J2+N / ASTM A572 Gr.50 Dissimilar Steel Joints.

Prof. Syed Farrukh Haider, National University of Science and Technology (Pakistan).
Prof. Shaheryar Ahmed Khan, DHA Suffa University (Pakistan).
Prof. Aqueel Shah, SMME National University of Science and Technology (Pakistan).
Prof. Muhammad Nasir Bashir, National University of Science and Technology (Pakistan).
Prof. Asif Mansoor, National University of Science and Technology (Pakistan).
Prof. Abbas Hussain, National University of Science and Technology (Pakistan).
Prof. Muhammad Mahmood Ali, Atlantic Technological University Sligo (Ireland).
Prof. Salman Nisar, Taibah University (Saudi Arabia).

MIIUM30-11: Ubicación Óptima de la Soldadura para Mayor Integridad en la Fabricación de Tubos Perfilados.

Prof. Dr. Sergey V. Parshin, Universidad Federal de los Urales (Rusia).
Prof. Anastasiya A. Parshina, Universidad Federal de los Urales (Rusia).

MIIUM30-13: Evaluación del Desempeño Sísmico de un Edificio Multifamiliar Ubicado en el Distrito de Surco ante Diferentes Niveles de Amenaza, aplicando la Norma ATC – 40.

Ing. Josimar Guillen, Universidad de San Martin de Porres (Perú).
Ing. Oliberth Huaman, Universidad de San Martin de Porres (Perú).
Dr. Genner Villarreal, Universidad de San Martin de Porres (Perú).

MIIUM30-14: Determining the Correlation between Line Balancing and Productivity: A Proposal for Process Improvement.

Dr. (c) Fabiola Hermosillo-Villalobos, Universidad Autónoma de Juárez (México).
Prof. Jorge Luis García-Alcaraz, Universidad Autónoma de Juárez (México).
Dr. (c) Omar Celis-Gracia, Universidad Autónoma de Juárez (México).

MIIUM30-21: Parametric Optimization of EN-31 Steel Using Electric Discharge Machining.

Muhammad Mansoor Uz Zaman Siddiqui, Pakistan Elektron Limited (Pakistan).
Prof. Dr. Syed Amir Iqbal, NED University of Engineering and Technology (Pakistan).
Prof. Dr. Ali Zulqarnain, Pakistan Elektron Limited (Pakistan).
Adeel Tabassum, National University of Science and Technology (Pakistan).

MIIUM30-29: Mitigating Climate Change: A Review of Carbon Capture and Separation Technologies.

Prof. Haider Ali, NED University of Engineering and Technology (Pakistan).
Nomaan Akhtar, NED University of Engineering and Technology (Pakistan).
Saqib Shams, NED University of Engineering and Technology (Pakistan).
Ali Karim, NED University of Engineering and Technology (Pakistan).
Umair Naeem, NED University of Engineering and Technology (Pakistan).

MIIUM30-33: Comparative Evaluation of Chemically and Green-Synthesized Silica-Modified CeO_2 Nanostructures for Time-Dependent Room-Temperature Ammonia Sensing

Eng. Danish Majeed, NED University of Engineering and Technology (Pakistan).
Syeda Sarah Zehra Zaidi, NED University of Engineering and Technology (Pakistan).
Syed Muhammad Mohsin, NED University of Engineering and Technology (Pakistan).
Prof. Muhammad Sajid Ali Asghar, NED University of Engineering and Technology (Pakistan).
Dr. Asad Ali Zaidi, Islamic University of Madinah (Saudi Arabia).

MIIUM30-34: System-Level Design and Outdoor Validation of a Solar-Powered Mobile Robot for Autonomous Environmental Monitoring.

Prof. Halar Mustafa, Hamdard University (Pakistan).
Prof. Dr. Sadiq Ur Rehman, Iqra University (Pakistan).
Prof. Dr. Muhammad Ahsan Shaikh, Hamdard University (Pakistan).

MIIUM30-35: Effect of Hardfacing on the Damping Characteristics of ASTM A516 G70 Steel

Hussien Al Hilal, Ministry of Water Resource (Iraq).
M. K. A. Razzaq, Middle Technical University (Iraq).
Prof. Hamid Al-Abboodi, Middle Technical University (Iraq).
Ahmed T. Fadhil, Middle Technical University (Iraq).
Adnan N. Abood, Tigris Way Construction Company (Iraq).
Prof. Huiqing Fan, Northwestern Polytechnical University (China).
Prof. Dr. Muhammad Samiuddin, NED University of Engineering and Technology (Pakistan).

MIIUM30-36: A Hybrid Thermodynamic–Machine Learning Approach for Flash Point Prediction of Binary Organic Mixtures.

Prof. Nadia Khan, NED University of Engineering and Technology (Pakistan).
Prof. Ahmed Saleem, NED University of Engineering and Technology (Pakistan).
Prof. Aisha Jilani, NED University of Engineering and Technology (Pakistan).
Dr. Asad A. Zaidi, Islamic University of Madinah (Saudi Arabia).

MIIUM30-37: Modeling of 4G coverage using Matlab and validation with real measurements obtained through G-NetTrack.

Eng. Jordy Alexander Toapanta Piguave, Salesian Polytechnic University (Ecuador).
Eng. Ricardo Gianpiere Córdova Almeida, Salesian Polytechnic University (Ecuador).
M.Sc Eng. David Humberto Cárdenas Villacrés, Salesian Polytechnic University (Ecuador).

MIIUM30-38: Low-cost embedded architecture for repeatable time control in electronic test stations.

B.Eng. Emiliano Crespo-Torres, Universidad Autónoma de Tamaulipas (México).
Dr. René Fernando Domínguez-Cruz, Universidad Autónoma de Tamaulipas (México).
Dr. Leopoldo Asael Garza-Alvarado, Universidad Autónoma de Tamaulipas (México).
M.Sc. Pedro Edén Zamora-González, Universidad Autónoma de Tamaulipas (México).
Dr. Yadira Aracely Fuentes-Rubio, Universidad Autónoma de Tamaulipas (México).

MIIUM30-40: Simulation of fully developed laminar free convection flow between vertical parallel flat plates.

Dr. Héctor Espinoza-Román, Fundación Universitaria Antonio de Arévalo (Colombia).

Lista de Revisores – Memoria Investigaciones en Ingeniería (Número 30).

List of Reviewers – Memoria Investigaciones en Ingenieria (Volume 30).

Dr. Ricardo Oviedo Sarmiento, Universidad Nacional Federico Villarreal (Peru).
Dr. Waldo Hasperué, Universidad Nacional de La Plata (Argentina).
Dr. Masato Kobiyama, Universidade Federal do Rio Grande do Sul (Brazil).
Dr. Talha Bin Nadeem, Aston University (United Kingdom).
Dr. Julio Blanco Fernández, Universidad de la Rioja (Spain).
Dr. Carlos Francisco Javierre, Universidad de Zaragoza (Spain).
Dr. Juan Ignacio Latorre Biel, Universidad Pública de Navarra (Spain).
Dr. Claudio Pereira Da Fonte, University of Manchester (United Kingdom).
Dr. Jeffery Rizvi, Sir Syed University (Pakistan).
Dr. Samar Abbas, Texas A&M University (United States).
Dr. Talha Bin Nadeem, Aston University (United Kingdom).
MSc. Carlos Fernández, Universidad Latina de Panamá (Panamá).
Eng. Efrén Jiménez, Instituto Tecnológico de Costa Rica (Costa Rica).
Dr. Syed Saad Ali, Nazeer Hussain University (Pakistan).
Dr. Ans Alrashid, Hammad Bin Khalifa University (Qatar).
Dr. Mohsin Sattar, Czech Technical University in Prague (Czech Republic).
Dr. Kashif Mushtaq, Iberian Centre for Research in Energy Storage (Spain).
Dr. Rubén Paredes, Escuela Superior Politecnica del Litoral (Ecuador).
Dr. Matthias Ehrhardt, Bergische Universitat Wuppertal (Germany).